

# IMPROVE

INTERAGENCY MONITORING OF PROTECTED VISUAL ENVIRONMENTS

## SPATIAL AND SEASONAL PATTERNS AND TEMPORAL VARIABILITY OF HAZE AND ITS CONSTITUENTS IN THE UNITED STATES



COLORADO STATE  
UNIVERSITY

REPORT VI  
2023





We dedicate this report to all of the hard working operators, technicians, and scientists who have contributed to the success of the IMPROVE network over the years.

Description of the cover:

Deep Lake in the Bridger Wilderness, Wyoming (photo credit: Scott Copeland)

**Spatial and Seasonal Patterns and Temporal Variability of Haze  
and its Constituents in the United States**  
**Report VI**

**Principal Author:**  
**Jenny L. Hand<sup>1</sup>**

**<sup>1</sup>Cooperative Institute for Research in the Atmosphere  
Colorado State University  
Fort Collins, CO 80523-1375**

**Contributors:**

**Scott A. Copeland<sup>1</sup>  
Judy Chow<sup>2</sup>  
Ann M. Dillner<sup>3</sup>  
Nicole P. Hyslop<sup>3</sup>  
William C. Malm<sup>1</sup>  
Anthony J. Prenni<sup>4</sup>**

**Sean M. Raffuse<sup>3</sup>  
Bret A. Schichtel<sup>4</sup>  
John G. Watson<sup>2</sup>  
Dominique E. Young<sup>3</sup>  
Xiaolu Zhang<sup>3</sup>**

**<sup>2</sup>Desert Research Institute  
Reno, NV 89512**

**<sup>3</sup>Air Quality Research Center  
University of California  
Davis, CA 95618**

**<sup>4</sup>National Park Service  
Air Resources Division  
Lakewood, CO 80225**

**Disclaimer**

The assumptions, findings, conclusions, judgments, and views presented herein are those of the authors and should not be interpreted as necessarily representing the National Park Service or National Oceanic and Atmospheric Administration policies.

## TABLE OF CONTENTS

Executive Summary .....	S-1
S.1 Introduction .....	S-1
S.2 Aerosol Data.....	S-2
S.3 Spatial Patterns in Rural and Urban Speciated Annual Mean Aerosol Concentrations .....	S-6
S.3.1 Ammonium Sulfate .....	S-7
S.3.2 Ammonium Nitrate .....	S-7
S.3.3 Particulate Organic Matter .....	S-8
S.3.4 Elemental Carbon .....	S-9
S.3.5 Fine Dust .....	S-9
S.3.6 Sea Salt .....	S-10
S.3.7 PM <sub>2.5</sub> Gravimetric Mass .....	S-10
S.3.8 Coarse Mass.....	S-11
S.3.9 Discussion .....	S-11
S.4 Seasonal Distributions in Aerosol Mass Concentrations .....	S-12
S.4.1 Ammonium Sulfate .....	S-13
S.4.2 Ammonium Nitrate .....	S-19
S.4.3 Particulate Organic Matter .....	S-20
S.4.4 Elemental Carbon .....	S-20
S.4.5 Fine Dust Mass .....	S-21
S.4.6 PM <sub>2.5</sub> Sea Salt .....	S-22
S.4.7 PM <sub>2.5</sub> Gravimetric Fine Mass.....	S-22
S.4.8 Discussion .....	S-23
S.5 Spatial and Seasonal Patterns in Relative Reconstructed Aerosol Light Extinction Coefficients.....	S-25
S.5.1 Annual Mean Reconstructed Light Extinction Coefficient .....	S-25
S.5.2 Ammonium Sulfate Light Extinction Coefficients .....	S-27
S.5.3 Ammonium Nitrate Light Extinction Coefficients .....	S-32
S.5.4 Particulate Organic Matter Light Extinction Coefficients .....	S-33
S.5.5 Elemental Carbon Light Extinction Coefficients .....	S-34
S.5.6 Fine Dust Light Extinction Coefficients .....	S-34
S.5.7 PM <sub>2.5</sub> Sea Salt Light Extinction Coefficients .....	S-35
S.5.8 Coarse Mass Light Extinction Coefficients.....	S-35

S.5.9 Discussion .....	S-36
S.6 Trends in IMPROVE Speciated Aerosol Mass Concentrations .....	S-38
S.6.1 Sulfate Ion Trends.....	S-39
S.6.2 Nitrate Ion Trends .....	S-40
S.6.3 Organic Carbon Trends .....	S-42
S.6.4 Elemental Carbon Trends .....	S-43
S.6.5 Fine Dust Trends.....	S-44
S.6.6 Gravimetric PM <sub>2.5</sub> Fine Mass Trends.....	S-46
S.6.7 Coarse Mass Trends .....	S-47
S.6.8 Discussion .....	S-49
REFERENCES .....	S-52
Chapter 1. Interagency Monitoring of Protected Visual Environments (IMPROVE) Network: Configuration and Measurements .....	1-1
1.1 Introduction .....	1-1
1.2 Overview of the Improve Monitoring Network .....	1-4
1.2.1 Site Locations .....	1-4
1.2.2 Aerosol Sampling and Analysis.....	1-15
1.2.3 Optical Monitoring and Analysis.....	1-24
1.3 Protocol and Equipment Changes .....	1-29
1.3.1 Analytical Changes .....	1-29
1.3.1.1 Carbon Analyzer Replacements .....	1-29
1.3.1.2 Environmentally Controlled Chamber Measurements of PM <sub>2.5</sub> and PM <sub>10</sub> Gravimetric Mass.....	1-30
1.3.1.3 Transition from Custom-built XRF Instruments to PANalytical Epsilon 5 Instruments .....	1-31
1.3.1.4 Changes to Filter Light Absorption Measurement (f <sub>abs</sub> ).....	1-33
1.3.1.5 Fourier Transform-Infrared Spectroscopy (FT-IR).....	1-35
1.3.1.6 Summary of Data Advisories .....	1-36
1.3.1.7 Quality Assurance Reports .....	1-40
1.3.2 Sampling Equipment Changes .....	1-40
1.3.2.1 New Sampler Controller .....	1-40
1.3.2.2 Teflon Manufacture Change .....	1-40
1.3.3 Data Processing Changes .....	1-41
1.3.4 Summary of Changes .....	1-43
1.3.5 IMPROVE Technical System Audits.....	1-44

1.4 Chemical Speciation Network .....	1-45
REFERENCES .....	1-55
Chapter 2. Spatial Patterns of Speciated PM <sub>2.5</sub> Aerosol Mass Concentrations .....	2-1
2.1 Aerosol Species Composition.....	2-2
2.2 Spatial Patterns in Annual Mean Mass Concentrations .....	2-4
2.2.1 PM <sub>2.5</sub> Ammonium Sulfate Mass .....	2-4
2.2.2 PM <sub>2.5</sub> Ammonium Nitrate Mass.....	2-7
2.2.3 PM <sub>2.5</sub> Particulate Organic Matter Mass .....	2-10
2.2.4 PM <sub>2.5</sub> Elemental Carbon Mass .....	2-13
2.2.5 Filter Light Absorption (f <sub>abs</sub> ) .....	2-16
2.2.6 PM <sub>2.5</sub> Fine Dust Mass.....	2-17
2.2.7 PM <sub>2.5</sub> Sea Salt Mass .....	2-21
2.2.8 PM <sub>2.5</sub> Gravimetric Fine Mass .....	2-24
2.2.9 PM <sub>2.5</sub> Reconstructed Fine Mass .....	2-26
2.2.10 PM <sub>2.5</sub> Residual .....	2-27
2.2.11 PM <sub>10</sub> Mass .....	2-29
2.2.12 Coarse Mass.....	2-30
2.2.13 Summary.....	2-33
REFERENCES .....	2-36
Chapter 3. Seasonal Distributions of PM <sub>2.5</sub> Aerosol Mass .....	3-1
3.1 PM <sub>2.5</sub> Ammonium Sulfate .....	3-2
3.1.1 IMPROVE .....	3-2
3.1.2 CSN .....	3-8
3.2 PM <sub>2.5</sub> Ammonium Nitrate .....	3-14
3.2.1 IMPROVE .....	3-14
3.2.2 CSN .....	3-15
3.3 PM <sub>2.5</sub> Particulate Organic Matter.....	3-16
3.3.1 IMPROVE .....	3-16
3.3.2 CSN .....	3-17
3.4 PM <sub>2.5</sub> Elemental Carbon.....	3-18
3.4.1 IMPROVE .....	3-18
3.4.2 CSN .....	3-19
3.5 PM <sub>2.5</sub> Dust Mass .....	3-19
3.5.1 IMPROVE .....	3-19

3.5.2 CSN .....	3-20
3.6 PM <sub>2.5</sub> Sea Salt Mass .....	3-21
3.6.1 IMPROVE .....	3-21
3.6.2 CSN .....	3-22
3.7 PM <sub>2.5</sub> Gravimetric Fine Mass .....	3-23
3.7.1 IMPROVE .....	3-23
3.7.2 CSN .....	3-23
3.8 Coarse Mass.....	3-23
3.9 Discussion .....	3-27
REFERENCES .....	3-30
 Chapter 4. Reconstructed Aerosol Light Extinction Coefficients .....	4-1
4.1 IMPROVE Aerosol Light Extinction Coefficient Algorithm .....	4-1
4.2 Spatial Patterns in Annual Mean Aerosol Light Extinction Coefficients .....	4-5
4.2.1 PM <sub>2.5</sub> Ammonium Sulfate Light Extinction Coefficients .....	4-5
4.2.2 PM <sub>2.5</sub> Ammonium Nitrate Light Extinction Coefficients.....	4-8
4.2.3 PM <sub>2.5</sub> Particulate Organic Matter Light Extinction Coefficients .....	4-11
4.2.4 PM <sub>2.5</sub> Elemental Carbon Light Extinction Coefficients .....	4-14
4.2.5 PM <sub>2.5</sub> Fine Dust Light Extinction Coefficients.....	4-17
4.2.6 PM <sub>2.5</sub> Sea Salt Extinction Coefficients.....	4-20
4.2.7 Coarse Mass Light Extinction Coefficients.....	4-22
4.2.8 Reconstructed Aerosol Light Extinction Coefficients.....	4-25
4.2.9 Reconstructed Total Light Extinction Coefficients.....	4-27
4.2.10 Deciview .....	4-28
4.2.11 Summary.....	4-29
REFERENCES .....	4-32
 Chapter 5. Seasonal Distribution of Reconstructed Aerosol Light Extinction Coefficients .	5-1
5.1 PM <sub>2.5</sub> Ammonium Sulfate Light Extinction Coefficients .....	5-1
5.1.1 IMPROVE .....	5-1
5.1.2 CSN .....	5-8
5.2 PM <sub>2.5</sub> Ammonium Nitrate Light Extinction Coefficients .....	5-14
5.2.1 IMPROVE .....	5-14
5.2.2 CSN .....	5-16
5.3 PM <sub>2.5</sub> Particulate Organic Matter Light Extinction Coefficients.....	5-17
5.3.1 IMPROVE .....	5-17

5.3.2 CSN .....	5-19
5.4 PM <sub>2.5</sub> Elemental Carbon Light Extinction Coefficient .....	5-20
5.4.1 IMPROVE .....	5-20
5.4.2 CSN .....	5-21
5.5 PM <sub>2.5</sub> Fine Dust Light Extinction Coefficients .....	5-22
5.5.1 IMPROVE .....	5-22
5.5.2 CSN .....	5-23
5.6 PM <sub>2.5</sub> Sea Salt Light Extinction Coefficients .....	5-24
5.6.1 IMPROVE .....	5-25
5.6.2 CSN .....	5-26
5.7 Coarse Mass Light Extinction Coefficients.....	5-26
5.7.1 IMPROVE .....	5-26
5.7.2 CSN .....	5-28
5.8 Reconstructed Aerosol Light Extinction Coefficients .....	5-29
5.8.1 IMPROVE .....	5-29
5.8.2 CSN .....	5-30
5.9 Deciview.....	5-31
5.9.1 IMPROVE .....	5-31
5.9.2 CSN .....	5-31
5.10 Summary .....	5-32
Chapter 6. Trends in IMPROVE Speciated Aerosol Concentrations .....	6-1
6.1 Sulfate Ion Trends.....	6-2
6.2 Nitrate Ion Trends .....	6-6
6.3 Organic Carbon Trends .....	6-10
6.4 Elemental Carbon Trends .....	6-14
6.5 Fine Dust Mass Trends.....	6-18
6.6 Gravimetric PM <sub>2.5</sub> Fine Mass Trends .....	6-22
6.7 PM <sub>10</sub> Trends.....	6-26
6.8 Coarse Mass Trends .....	6-29
6.9 f <sub>abs</sub> Trends .....	6-33
6.10 Discussion.....	6-36
REFERENCES .....	6-40
Chapter 7. Trends in IMPROVE Reconstructed Light Extinction Coefficients .....	7-1
7.1 Ammonium Sulfate Light Extinction Coefficient Trends.....	7-2

7.2 Ammonium Nitrate Light Extinction Coefficient Trends .....	7-5
7.3 Particulate Organic Matter Light Extinction Coefficient Trends .....	7-8
7.4 Elemental Carbon Light Extinction Coefficient Trends .....	7-12
7.5 Fine Dust Light Extinction Coefficient Trends .....	7-15
7.6 Coarse Mass Light Extinction Coefficient Trends .....	7-19
7.7 Aerosol Extinction Coefficient Trends .....	7-23
7.8 Total Extinction Coefficient Trends .....	7-26
7.9 Deciview Trends .....	7-29
7.10 Discussion.....	7-32
REFERENCES .....	7-37
Chapter 8. IMPROVE Bibliography 2010 to Present.....	8-1

## LIST OF FIGURES

- Figure S.2.1. Locations of IMPROVE sites for all discontinued and current sites. IMPROVE regions are indicated by shading and bold text. Urban IMPROVE sites are identified by stars. Blue circles indicate sites with data used in the analyses in this report. .... S-4
- Figure S.2.2. Current and discontinued Chemical Speciation Network (CSN) sites (grey and orange) operated by the Environmental Protection Agency. Regions are shown as shaded areas and bold text. Sites included in the analyses in this report are shown as orange circles. .... S-5
- Figure S.3.1. 2016–2019 PM<sub>2.5</sub> ammonium sulfate (AS) annual mean mass concentrations ( $\mu\text{g m}^{-3}$ ) for (a) IMPROVE and (b) IMPROVE and CSN..... S-7
- Figure S.3.2. 2016–2019 PM<sub>2.5</sub> ammonium nitrate (AN) annual mean mass concentrations ( $\mu\text{g m}^{-3}$ ) for (a) IMPROVE and (b) IMPROVE and CSN..... S-8
- Figure S.3.3. 2016–2019 PM<sub>2.5</sub> particulate organic matter (POM) annual mean mass concentrations ( $\mu\text{g m}^{-3}$ ) for (a) IMPROVE and (b) IMPROVE and CSN. .... S-8
- Figure S.3.4. 2016–2019 PM<sub>2.5</sub> elemental carbon (EC) annual mean mass concentrations ( $\mu\text{g m}^{-3}$ ) for (a) IMPROVE and (b) IMPROVE and CSN. .... S-9
- Figure S.3.5. 2016–2019 PM<sub>2.5</sub> fine dust (FD) annual mean mass concentrations ( $\mu\text{g m}^{-3}$ ) for (a) IMPROVE and (b) IMPROVE and CSN..... S-10
- Figure S.3.6. 2016–2019 PM<sub>2.5</sub> sea salt (SS) annual mean mass concentrations ( $\mu\text{g m}^{-3}$ ) for (a) IMPROVE and (b) IMPROVE and CSN..... S-10
- Figure S.3.7. 2016–2019 PM<sub>2.5</sub> gravimetric annual mean fine mass (FM) concentrations ( $\mu\text{g m}^{-3}$ ) for (a) IMPROVE and (b) IMPROVE and CSN. .... S-11
- Figure S.3.8. 2016–2019 annual mean gravimetric coarse mass (CM = PM<sub>10</sub> - PM<sub>2.5</sub>) ( $\mu\text{g m}^{-3}$ ) for (a) IMPROVE and (b) IMPROVE and EPA..... S-11
- Figure S.4.1. IMPROVE 2016–2019 regional monthly mean PM<sub>2.5</sub> mass concentrations ( $\mu\text{g m}^{-3}$ ) for the eastern United States. Letters on the x-axis correspond to month and “A” corresponds to annual mean. Shaded areas in the map correspond to regions that include the sites used in the analysis, shown as blue dots. .... S-14
- Figure S.4.2. IMPROVE 2016–2019 regional monthly mean PM<sub>2.5</sub> mass concentrations ( $\mu\text{g m}^{-3}$ ) for the northwestern United States. Letters on the x-axis correspond to month and “A” corresponds to annual mean. Shaded areas in the map correspond to regions that include the sites used in the analysis, shown as blue dots. .... S-15
- Figure S.4.3. IMPROVE 2016–2019 regional monthly mean PM<sub>2.5</sub> mass concentrations ( $\mu\text{g m}^{-3}$ ) for the southwestern United States. Letters on the x-axis correspond to month and “A” corresponds to annual mean. Shaded areas in the map correspond to regions that include the sites used in the analysis, shown as blue dots. .... S-16
- Figure S.4.4. CSN 2016–2019 regional monthly mean PM<sub>2.5</sub> mass concentrations ( $\mu\text{g m}^{-3}$ ) for the eastern United States. Letters on the x-axis correspond to month and “A” corresponds to annual mean. Shaded areas in the map correspond to regions that include the sites used in the analysis, shown as orange dots. .... S-17
- Figure S.4.5. CSN 2016–2019 regional monthly mean PM<sub>2.5</sub> mass concentrations ( $\mu\text{g m}^{-3}$ ) for the northwestern United States. Letters on the x-axis correspond to month and “A” corresponds

to annual mean. Shaded areas in the map correspond to regions that include the sites used in the analysis, shown as orange dots. .... S-18

Figure S.4.6. CSN 2016–2019 regional monthly mean PM<sub>2.5</sub> mass concentrations ( $\mu\text{g m}^{-3}$ ) for the northwestern United States. Letters on the x-axis correspond to month and “A” corresponds to annual mean. Shaded areas in the map correspond to regions that include the sites used in the analysis, shown as orange dots. .... S-19

Figure S.5.1. 2016–2019 annual mean ambient total reconstructed light extinction coefficient ( $b_{\text{ext\_tot}}$ ) ( $\text{Mm}^{-1}$ ) for (a) IMPROVE and (b) IMPROVE and CSN. Annual mean deciview (dv) for (c) IMPROVE and (d) IMPROVE and CSN. Wavelength corresponds to 550 nm. .... S-26

Figure S.5.2. IMPROVE 2016–2019 regional monthly mean speciated fractional contributions to ambient aerosol light extinction coefficients ( $b_{\text{ext}}$ ) for the eastern United States. Letters on the x-axis correspond to the month and “A” corresponds to annual mean. Shaded areas in the map correspond to regions that include sites used in the analysis, shown as blue dots. Wavelength corresponds to 550 nm. .... S-27

Figure S.5.3. IMPROVE 2016–2019 regional monthly mean speciated fractional contributions to ambient aerosol light extinction coefficients ( $b_{\text{ext}}$ ) for the northwestern United States. Letters on the x-axis correspond to the month and “A” corresponds to annual mean. Shaded areas in the map correspond to regions that include sites used in the analysis, shown as blue dots. Wavelength corresponds to 550 nm. .... S-28

Figure S.5.4. IMPROVE 2016–2019 regional monthly mean speciated fractional contributions to ambient aerosol light extinction coefficients ( $b_{\text{ext}}$ ) for the southwestern United States. Letters on the x-axis correspond to the month and “A” corresponds to annual mean. Shaded areas in the map correspond to regions that include sites used in the analysis, shown as blue dots. Wavelength corresponds to 550 nm. .... S-29

Figure S.5.5. CSN 2016–2019 regional monthly mean speciated fractional contributions to ambient aerosol light extinction coefficients ( $b_{\text{ext}}$ ) for the eastern United States. Letters on the x-axis correspond to the month and “A” corresponds to annual mean. Shaded areas in the map correspond to regions that include sites used in the analysis, shown as orange dots. Wavelength corresponds to 550 nm. .... S-30

Figure S.5.6. 2016–2019 regional monthly mean speciated fractional contributions to ambient aerosol light extinction coefficients ( $b_{\text{ext}}$ ) for the northwestern United States. Letters on the x-axis correspond to the month and “A” corresponds to annual mean. Shaded areas in the map correspond to regions that include sites used in the analysis, shown as orange dots. Wavelength corresponds to 550 nm. .... S-31

Figure S.5.7. CSN 2016–2019 regional monthly mean speciated fractional contributions to ambient aerosol light extinction coefficients ( $b_{\text{ext}}$ ) for the southwestern United States. Letters on the x-axis correspond to the month and “A” corresponds to annual mean. Shaded areas in the map correspond to regions that include sites used in the analysis, shown as orange dots. Wavelength corresponds to 550 nm. .... S-32

Figure S.6.1.1. Annual mean sulfate ion mass trends ( $\% \text{ yr}^{-1}$ ) for short-term (2000–2019) periods. Filled triangles correspond to statistically significant trends ( $p \leq 0.05$ ). .... S-39

Figure S.6.1.2. Short-term (2000–2019) regional seasonal mean sulfate ion trends ( $\% \text{ yr}^{-1}$ ) for major U.S. regions for winter, spring, summer, fall, and annual means. Regions are arranged

from western to eastern United States (AK = Alaska, HI = Hawaii, NW = Northwest, CA = California, SW = Southwest, Cen = Central, MiS = Midsouth, NE = Northeast, SE = Southeast, VIIS = Virgin Islands, and US = all sites). Statistically significant trends ( $p \leq 0.05$ ) are denoted with “\*”. ..... S-40

Figure S.6.2.1. Annual mean nitrate ion mass trends ( $\% \text{ yr}^{-1}$ ) for short-term (2000–2019) periods. Filled triangles correspond to statistically significant trends ( $p \leq 0.05$ ). ..... S-41

Figure S.6.2.2. Short-term (2000–2019) regional seasonal mean nitrate ion trends ( $\% \text{ yr}^{-1}$ ) for major U.S. regions for winter, spring, summer, fall, and annual means. Regions are arranged from western to eastern United States (AK = Alaska, HI = Hawaii, NW = Northwest, CA = California, SW = Southwest, Cen = Central, MiS = Midsouth, NE = Northeast, SE = Southeast, VIIS = Virgin Islands, and US = all sites). Statistically significant trends ( $p \leq 0.05$ ) are denoted with “\*”. ..... S-41

Figure S.6.3.1. Annual mean organic carbon mass trends ( $\% \text{ yr}^{-1}$ ) for short-term (2000–2019) periods. Filled triangles correspond to statistically significant trends ( $p \leq 0.05$ ). ..... S-42

Figure S.6.3.2. Short-term (2000–2019) regional seasonal mean organic carbon (OC) trends ( $\% \text{ yr}^{-1}$ ) for major U.S. regions for winter, spring, summer, fall, and annual means. Regions are arranged from western to eastern United States (AK = Alaska, HI = Hawaii, NW = Northwest, CA = California, SW = Southwest, Cen = Central, MiS = Midsouth, NE = Northeast, SE = Southeast, VIIS = Virgin Islands, and US = all sites). Statistically significant trends ( $p \leq 0.05$ ) are denoted with “\*”. ..... S-43

Figure S.6.4.1. Annual mean elemental carbon mass trends ( $\% \text{ yr}^{-1}$ ) for short-term (2000–2019) periods. Filled triangles correspond to statistically significant trends ( $p \leq 0.05$ ). ..... S-44

Figure S.6.4.2. Short-term (2000–2019) regional seasonal mean elemental carbon (EC) trends ( $\% \text{ yr}^{-1}$ ) for major U.S. regions for winter, spring, summer, fall, and annual means. Regions are arranged from western to eastern United States (AK = Alaska, HI = Hawaii, NW = Northwest, CA = California, SW = Southwest, Cen = Central, MiS = Midsouth, NE = Northeast, SE = Southeast, VIIS = Virgin Islands, and US = all sites). Statistically significant trends ( $p \leq 0.05$ ) are denoted with “\*”. ..... S-44

Figure S.6.5.1. Annual mean fine dust (FD) mass trends ( $\% \text{ yr}^{-1}$ ) for short-term (2000–2019) periods. Filled triangles correspond to statistically significant trends ( $p \leq 0.05$ ). ..... S-45

Figure S.6.5.2. Short-term (2000–2019) regional seasonal mean fine dust mass trends ( $\% \text{ yr}^{-1}$ ) for major U.S. regions for winter, spring, summer, fall, and annual means. Regions are arranged from western to eastern United States (AK = Alaska, HI = Hawaii, NW = Northwest, CA = California, SW = Southwest, Cen = Central, MiS = Midsouth, NE = Northeast, SE = Southeast, VIIS = Virgin Islands, and US = all sites). Statistically significant trends ( $p \leq 0.05$ ) are denoted with “\*”. ..... S-46

Figure S.6.6.1. Annual mean PM<sub>2.5</sub> gravimetric fine mass (FM) trends ( $\% \text{ yr}^{-1}$ ) for short-term (2000–2019) periods. Filled triangles correspond to statistically significant trends ( $p \leq 0.05$ ). ..... S-47

Figure S.6.6.2. Short-term (2000–2019) regional seasonal mean gravimetric PM<sub>2.5</sub> fine mass (FM) trends ( $\% \text{ yr}^{-1}$ ) for major U.S. regions for winter, spring, summer, fall, and annual means. Regions are arranged from western to eastern United States (AK = Alaska, HI = Hawaii, NW = Northwest, CA = California, SW = Southwest, Cen = Central, MiS = Midsouth, NE = Northeast,

SE = Southeast, VIIS = Virgin Islands, and US = all sites). Statistically significant trends ( $p \leq 0.05$ ) are denoted with “*”.....	S-47
Figure S.6.7.1 Annual mean coarse mass (CM) trends ( $\% \text{ yr}^{-1}$ ) for short-term (2000–2019) periods. Filled triangles correspond to statistically significant trends ( $p \leq 0.05$ ).....	S-48
Figure S.6.7.2. Short-term (2000–2019) regional seasonal mean coarse mass (CM) trends ( $\% \text{ yr}^{-1}$ ) for major U.S. regions for winter, spring, summer, fall, and annual means. Regions are arranged from western to eastern United States (AK = Alaska, HI = Hawaii, NW = Northwest, CA = California, SW = Southwest, Cen = Central, MiS = Midsouth, NE = Northeast, SE = Southeast, VIIS = Virgin Islands, and US = all sites). Statistically significant trends ( $p \leq 0.05$ ) are denoted with “*”.....	S-48
Figure S.6.8. Short-term (2001–2019) timelines of IMPROVE regional, annual mean mass concentrations ( $\mu\text{g m}^{-3}$ ) for sulfate ion, nitrate ion, organic carbon (OC), elemental carbon (EC), and fine dust (FD). .....	S-48
Figure 1.1. Class I areas of the United States. Shading identifies the managing agency of each CIA.....	1-3
Figure 1.2. Locations of IMPROVE sites for all discontinued and current sites. IMPROVE regions are indicated by shading and bold text. Urban IMPROVE sites are identified by stars. Blue circles indicate sites with data used in the analyses in this report.....	1-5
Figure 1.3. IMPROVE sampler showing the four modules with separate inlets and pumps. Substrates with analyses performed for each module are also shown. ....	1-15
Figure 1.4. Version II IMPROVE sampler PM <sub>2.5</sub> module.....	1-16
Figure 1.5. IMPROVE XRF field blank concentrations ( $\text{ng m}^{-3}$ ) for elemental species from January 2019 to January 2021. ....	1-20
Figure 1.6. IMPROVE monthly median field blank concentrations ( $\mu\text{g m}^{-3}$ ) for ions for 2016 through 2020.....	1-21
Figure 1.7. IMPROVE carbon fraction monthly median field blank concentrations ( $\mu\text{g m}^{-3}$ ) from 2016 through 2020.....	1-23
Figure 1.8. Locations of nephelometers and web cameras. ....	1-25
Figure 1.9. Fraction of IMPROVE network samples from January 2019 through June 2020 weighed on the MTL automated weighing system (Luna), the manual balance, or a mix of the two (e.g., pre-sampling mass from MTL automated weighing system and post-sampling mass from manual balance).....	1-31
Figure 1.10. Timeline of elemental characterization methods used to analyze IMPROVE samples at UC Davis. PANalytical XRF is abbreviated “E5”.....	1-32
Figure 1.11. Scatterplots showing the agreement between XRF analytical instruments for elements routinely measured above 3 times the reported MDLs. Black dotted lines show the reported MDLs for each element and instrument while gray dashed lines show a 1:1 agreement, not a regression line. Data are for three sites (GRSM1, MORA1, and PORE1).....	1-33
Figure 1.12. Time series of PM <sub>2.5</sub> ( $\mu\text{g/filter}$ ) on Teflon filter field blanks (1 January 2011 through 30 June 2020). Blue vertical lines indicate manufacturer lot transition, where Pall	

Corporation is the manufacturer. Red vertical line indicates manufacturer transition to Measurement Technology Laboratories (MTL) as manufacturer..... 1-41

Figure 1.13. Time series of PM<sub>10</sub> ( $\mu\text{g}/\text{filter}$ ) on Teflon filter field blanks (1 January 2011 through 30 June 2020). Blue vertical lines indicate manufacturer lot transition, where Pall Corporation is the manufacturer. Red vertical line indicates manufacturer transition to Measurement Technology Laboratories (MTL) as manufacturer..... 1-41

Figure 1.14. IMPROVE field site audits from 2016–2022. Blue symbols correspond to audited sites; red symbols are sites yet to have a technical audit. ..... 1-45

Figure 1.15. Current and discontinued Chemical Speciation Network (CSN) sites operated by the Environmental Protection Agency. Regions are shown as shaded areas and bold text. Sites included in the analyses in this report are shown as orange circles. ..... 1-48

Figure 1.16. Comparisons of monthly mean 2016–2019 PM<sub>2.5</sub> aerosol mass concentration data ( $\mu\text{g m}^{-3}$ ) for four collocated IMPROVE and CSN sites (see text) for (a) organic carbon (OC), (b) elemental carbon (EC), (c) ammonium sulfate (AS), (d) ammonium nitrate (AN), (e) fine dust, (f) sea salt (SS), (g) PM<sub>2.5</sub> gravimetric fine mass (FM), and (h) reconstructed fine mass (RCFM). ..... 1-53

Figure 2.2.1a. IMPROVE 2016–2019 PM<sub>2.5</sub> ammonium sulfate (AS) annual mean mass concentrations ( $\mu\text{g m}^{-3}$ ). ..... 2-5

Figure 2.2.1b. IMPROVE and CSN 2016–2019 PM<sub>2.5</sub> ammonium sulfate (AS) annual mean mass concentrations ( $\mu\text{g m}^{-3}$ ). ..... 2-6

Figure 2.2.1c. IMPROVE 2016–2019 annual mean fraction contributions of ammonium sulfate (AS) to PM<sub>2.5</sub> reconstructed fine mass (RCFM). ..... 2-6

Figure 2.2.1d. IMPROVE and CSN 2016–2019 annual mean fraction contributions of ammonium sulfate (AS) to PM<sub>2.5</sub> reconstructed fine mass (RCFM). ..... 2-7

Figure 2.2.2a. IMPROVE 2016–2019 PM<sub>2.5</sub> ammonium nitrate (AN) annual mean mass concentrations ( $\mu\text{g m}^{-3}$ ). ..... 2-9

Figure 2.2.2b. IMPROVE and CSN 2016–2019 PM<sub>2.5</sub> ammonium nitrate (AN) annual mean mass concentrations ( $\mu\text{g m}^{-3}$ ). ..... 2-9

Figure 2.2.2c. IMPROVE 2016–2019 annual mean fraction contributions of ammonium nitrate (AN) to PM<sub>2.5</sub> reconstructed fine mass (RCFM). ..... 2-10

Figure 2.2.2d. IMPROVE and CSN 2016–2019 annual mean fractions of ammonium nitrate (AN) to PM<sub>2.5</sub> reconstructed fine mass (RCFM). ..... 2-10

Figure 2.2.3a. IMPROVE 2016–2019 PM<sub>2.5</sub> particulate organic matter (POM) annual mean mass concentrations ( $\mu\text{g m}^{-3}$ ). ..... 2-12

Figure 2.2.3b. IMPROVE and CSN 2016–2019 PM<sub>2.5</sub> particulate organic matter (POM) annual mean mass concentrations ( $\mu\text{g m}^{-3}$ ). ..... 2-12

Figure 2.2.3c. IMPROVE 2016–2019 annual mean fraction contributions of particulate organic matter (POM) to PM<sub>2.5</sub> reconstructed fine mass (RCFM). ..... 2-13

Figure 2.2.3d. IMPROVE and CSN 2016–2019 annual mean fraction contributions of particulate organic matter (POM) to PM<sub>2.5</sub> reconstructed fine mass (RCFM). ..... 2-13

Figure 2.2.4a. IMPROVE 2016–2019 PM <sub>2.5</sub> elemental carbon (EC) annual mean mass concentrations ( $\mu\text{g m}^{-3}$ ) .....	2-15
Figure 2.2.4b. IMPROVE and CSN 2016–2019 PM <sub>2.5</sub> elemental carbon (EC) annual mean mass concentrations ( $\mu\text{g m}^{-3}$ ).....	2-15
Figure 2.2.4c. IMPROVE 2016–2019 annual mean fraction contributions of elemental carbon (EC) to PM <sub>2.5</sub> reconstructed fine mass (RCFM).....	2-16
Figure 2.2.4d. IMPROVE and CSN 2016–2019 annual mean fraction contributions of elemental carbon (EC) to PM <sub>2.5</sub> reconstructed fine mass (RCFM).....	2-16
Figure 2.2.5. IMPROVE 2016–2019 PM <sub>2.5</sub> annual mean filter absorption ( $f_{\text{abs}}$ ) ( $\text{Mm}^{-1}$ ) ..	2-17
Figure 2.2.6a. IMPROVE 2016–2019 PM <sub>2.5</sub> fine dust annual mean mass concentrations ( $\mu\text{g m}^{-3}$ ) .....	2-19
Figure 2.2.6b. IMPROVE and CSN 2016–2019 PM <sub>2.5</sub> fine dust annual mean mass concentrations ( $\mu\text{g m}^{-3}$ ) .....	2-20
Figure 2.2.6c. IMPROVE 2016–2019 annual mean fraction contributions of fine dust to PM <sub>2.5</sub> reconstructed fine mass (RCFM) .....	2-20
Figure 2.2.6d. IMPROVE and CSN 2016–2019 annual mean fraction contributions of fine dust to PM <sub>2.5</sub> reconstructed fine mass (RCFM) .....	2-21
Figure 2.2.7a. IMPROVE 2016–2019 PM <sub>2.5</sub> sea salt (SS) annual mean mass concentrations ( $\mu\text{g m}^{-3}$ ).....	2-22
Figure 2.2.7b. IMPROVE and CSN 2016–2019 PM <sub>2.5</sub> sea salt (SS) annual mean mass concentrations ( $\mu\text{g m}^{-3}$ ) .....	2-23
Figure 2.2.7c. IMPROVE 2016–2019 annual mean fraction contributions of sea salt to PM <sub>2.5</sub> reconstructed fine mass (RCFM) .....	2-23
Figure 2.2.7d. IMPROVE and CSN 2016–2019 annual mean fraction contributions of sea salt (SS) to PM <sub>2.5</sub> reconstructed fine mass (RCFM).....	2-24
Figure 2.2.8a. IMPROVE 2016–2019 PM <sub>2.5</sub> annual mean gravimetric fine mass (FM) concentrations ( $\mu\text{g m}^{-3}$ ) .....	2-25
Figure 2.2.8b. IMPROVE and CSN 2016–2019 PM <sub>2.5</sub> annual mean gravimetric fine mass (FM) concentrations ( $\mu\text{g m}^{-3}$ ) .....	2-25
Figure 2.2.9a. IMPROVE 2016–2019 PM <sub>2.5</sub> annual mean reconstructed fine mass (RCFM) concentrations ( $\mu\text{g m}^{-3}$ ) .....	2-26
Figure 2.2.9b. IMPROVE and CSN 2016–2019 PM <sub>2.5</sub> annual mean reconstructed fine mass (RCFM) concentrations ( $\mu\text{g m}^{-3}$ ) .....	2-27
Figure 2.2.10a. IMPROVE 2016–2019 annual mean PM <sub>2.5</sub> residuals (FM - RCFM) between PM <sub>2.5</sub> gravimetric fine mass (FM) and reconstructed fine mass (RCFM) ( $\mu\text{g m}^{-3}$ ).....	2-28
Figure 2.2.10b. IMPROVE and CSN 2016–2019 annual mean PM <sub>2.5</sub> residuals (FM - RCFM) between PM <sub>2.5</sub> gravimetric fine mass (FM) and reconstructed fine mass (RCFM) ( $\mu\text{g m}^{-3}$ )....	2-28
Figure 2.2.11a. IMPROVE 2016–2019 annual mean PM <sub>10</sub> mass ( $\mu\text{g m}^{-3}$ ).....	2-30
Figure 2.2.11b. IMPROVE and EPA 2016–2019 annual mean PM <sub>10</sub> mass ( $\mu\text{g m}^{-3}$ ) .....	2-30

Figure 2.2.12a. IMPROVE 2016–2019 annual mean coarse mass (CM = PM <sub>10</sub> - PM <sub>2.5</sub> ) ( $\mu\text{g m}^{-3}$ ) .....	2-31
Figure 2.2.12b. IMPROVE and EPA 2016–2019 annual mean coarse mass (CM = PM <sub>10</sub> - PM <sub>2.5</sub> ) ( $\mu\text{g m}^{-3}$ ) .....	2-32
Figure 2.2.12c. IMPROVE 2016–2019 annual mean fraction contributions of CM to PM <sub>10</sub> gravimetric mass .....	2-33
Figure 2.2.12d. IMPROVE and EPA 2016–2019 annual mean fraction contributions of CM to PM <sub>10</sub> gravimetric mass .....	2-33
Figure 3.1.1. IMPROVE 2016–2019 regional monthly mean PM <sub>2.5</sub> mass concentrations ( $\mu\text{g m}^{-3}$ ) for the eastern United States. Letters on the x-axis correspond to month and “A” corresponds to annual mean. Shaded areas in the map correspond to regions that include the sites used in the analysis, shown as blue dots .....	3-3
Figure 3.1.2. IMPROVE 2016–2019 regional monthly mean PM <sub>2.5</sub> mass concentrations ( $\mu\text{g m}^{-3}$ ) for the northwestern United States. Letters on the x-axis correspond to month and “A” corresponds to annual mean. Shaded areas in the map correspond to regions that include the sites used in the analysis, shown as blue dots .....	3-4
Figure 3.1.3. IMPROVE 2016–2019 regional monthly mean PM <sub>2.5</sub> mass concentrations ( $\mu\text{g m}^{-3}$ ) for the southwestern United States. Letters on the x-axis correspond to month and “A” corresponds to annual mean. Shaded areas in the map correspond to regions that include the sites used in the analysis, shown as blue dots .....	3-5
Figure 3.1.4. IMPROVE 2016–2019 regional monthly mean PM <sub>2.5</sub> reconstructed fine mass fractions for the eastern United States. Letters on the x-axis correspond to month and “A” corresponds to annual mean. Shaded areas in the map correspond to regions that include the sites used in the analysis, shown as blue dots .....	3-6
Figure 3.1.5. IMPROVE 2016–2019 regional monthly mean PM <sub>2.5</sub> reconstructed fine mass fractions for the northwestern United States. Letters on the x-axis correspond to month and “A” corresponds to annual mean. Shaded areas in the map correspond to regions that include the sites used in the analysis, shown as blue dots .....	3-7
Figure 3.1.6. IMPROVE 2016–2019 regional monthly mean PM <sub>2.5</sub> reconstructed fine mass fractions for the southwestern United States. Letters on the x-axis correspond to month and “A” corresponds to annual mean. Shaded areas in the map correspond to regions that include the sites used in the analysis, shown as blue dots .....	3-8
Figure 3.1.7. CSN 2016–2019 regional monthly mean PM <sub>2.5</sub> mass concentrations ( $\mu\text{g m}^{-3}$ ) for the eastern United States. Letters on the x-axis correspond to month and “A” corresponds to annual mean. Shaded areas in the map correspond to regions that include the sites used in the analysis, shown as orange dots .....	3-9
Figure 3.1.8. CSN 2016–2019 regional monthly mean PM <sub>2.5</sub> mass concentrations ( $\mu\text{g m}^{-3}$ ) for the northwestern United States. Letters on the x-axis correspond to month and “A” corresponds to annual mean. Shaded areas in the map correspond to regions that include the sites used in the analysis, shown as orange dots .....	3-10
Figure 3.1.9. CSN 2016–2019 regional monthly mean PM <sub>2.5</sub> mass concentrations ( $\mu\text{g m}^{-3}$ ) for the northwestern United States. Letters on the x-axis correspond to month and “A” corresponds	

to annual mean. Shaded areas in the map correspond to regions that include the sites used in the analysis, shown as orange dots..... 3-11

Figure 3.1.10. CSN 2016–2019 regional monthly mean PM<sub>2.5</sub> reconstructed fine mass fractions for the eastern United States. Letters on the x-axis correspond to month and “A” corresponds to annual mean. Shaded areas in the map correspond to regions that include the sites used in the analysis, shown as orange dots..... 3-12

Figure 3.1.11. CSN 2016–2019 regional monthly mean PM<sub>2.5</sub> reconstructed fine mass fractions for the northwestern United States. Letters on the x-axis correspond to month and “A” corresponds to annual mean. Shaded areas in the map correspond to regions that include the sites used in the analysis, shown as orange dots..... 3-13

Figure 3.1.12. CSN 2016–2019 regional monthly mean PM<sub>2.5</sub> reconstructed fine mass fractions for the southwestern United States. Letters on the x-axis correspond to the month and “A” corresponds to annual mean. Shaded areas in the map correspond to regions that include the sites used in the analysis, shown as orange dots..... 3-14

Figure 3.8.1. IMPROVE 2016–2019 regional monthly mean coarse mass (CM) concentrations ( $\mu\text{g m}^{-3}$ ) for the eastern United States. Letters on the x-axis correspond to the month and “A” corresponds to annual mean. Shaded areas in the map correspond to regions that include the sites used in the analysis, shown as blue dots..... 3-25

Figure 3.8.2. IMPROVE 2016–2019 regional monthly mean coarse mass (CM) concentrations ( $\mu\text{g m}^{-3}$ ) for the northwestern United States. Letters on the x-axis correspond to the month and “A” corresponds to annual mean. Shaded areas in the map correspond to regions that include the sites used in the analysis, shown as orange dots..... 3-26

Figure 3.8.3. IMPROVE 2016–2019 regional monthly mean coarse mass (CM) concentrations ( $\mu\text{g m}^{-3}$ ) for the southwestern United States. Letters on the x-axis correspond to the month and “A” corresponds to annual mean. Shaded areas in the map correspond to regions that include the sites used in the analysis, shown as orange dots..... 3-27

Figure 4.1. (a) Humidification factors ( $f(\text{RH})$ ) as a function of relative humidity (RH, %) for AS. A lognormal mass size distribution with a geometric mass mean diameter of 0.3  $\mu\text{m}$  and a geometric standard deviation of 2.0 was assumed. (b)  $f(\text{RH})_{\text{SS}}$  for SS with an assumed lognormal mass size distribution with a geometric mass mean diameter of 2.5  $\mu\text{m}$  and a geometric standard deviation of 2.0. A wavelength of 550 nm was used. .... 4-3

Figure 4.2. Comparisons of 2016–2019 monthly mean coarse mass concentrations (CM,  $\mu\text{g m}^{-3}$ ) for four collocated IMPROVE (measured) and CSN (interpolated) sites. CSN CM concentrations were spatially interpolated from EPA Federal Reference Method (FRM) sites. 4-5

Figure 4.2.1a. IMPROVE 2016–2019 PM<sub>2.5</sub> reconstructed ambient annual mean light extinction coefficients for ammonium sulfate ( $b_{\text{ext\_AS}}, \text{Mm}^{-1}$ ). Wavelength corresponds to 550 nm..... 4-6

Figure 4.2.1b. IMPROVE and CSN 2016–2019 PM<sub>2.5</sub> reconstructed ambient annual mean light extinction coefficients for ammonium sulfate ( $b_{\text{ext\_AS}}, \text{Mm}^{-1}$ ). Wavelength corresponds to 550 nm..... 4-6

Figure 4.2.1c. IMPROVE 2016–2019 annual mean fraction contributions of ambient ammonium sulfate light extinction coefficient ( $b_{ext\_AS}$ ) to reconstructed aerosol $b_{ext}$ . Wavelength corresponds to 550 nm. ....	4-7
Figure 4.2.1d. IMPROVE and CSN 2016–2019 annual mean fraction contributions of ambient ammonium sulfate light extinction coefficient ( $b_{ext\_AS}$ ) to reconstructed aerosol $b_{ext}$ . Wavelength corresponds to 550 nm. ....	4-8
Figure 4.2.2a. IMPROVE 2016–2019 PM <sub>2.5</sub> reconstructed ambient annual mean light extinction coefficients for ammonium nitrate ( $b_{ext\_AN}$ , Mm <sup>-1</sup> ). Wavelength corresponds to 550 nm. ....	4-9
Figure 4.2.2b. IMPROVE and CSN 2016–2019 PM <sub>2.5</sub> reconstructed ambient annual mean light extinction coefficients for ammonium nitrate ( $b_{ext\_AN}$ , Mm <sup>-1</sup> ). Wavelength corresponds to 550 nm. ....	4-9
Figure 4.2.2c. IMPROVE 2016–2019 annual mean fraction contributions of ambient ammonium nitrate light extinction coefficient ( $b_{ext\_AN}$ ) to reconstructed aerosol $b_{ext}$ . Wavelength corresponds to 550 nm. ....	4-10
Figure 4.2.2d. IMPROVE and CSN 2016–2019 annual mean fraction contributions of ambient ammonium nitrate light extinction coefficient ( $b_{ext\_AN}$ ) to reconstructed aerosol $b_{ext}$ . Wavelength corresponds to 550 nm. ....	4-11
Figure 4.2.3a. IMPROVE 2016–2019 PM <sub>2.5</sub> reconstructed ambient annual mean light extinction coefficients for particulate organic matter ( $b_{ext\_POM}$ , Mm <sup>-1</sup> ). Wavelength corresponds to 550 nm. ....	4-12
Figure 4.2.3b. IMPROVE and CSN 2016–2019 PM <sub>2.5</sub> reconstructed ambient annual mean light extinction coefficients for particulate organic matter ( $b_{ext\_POM}$ , Mm <sup>-1</sup> ). Wavelength corresponds to 550 nm. ....	4-12
Figure 4.2.3c. IMPROVE 2016–2019 annual mean fraction contributions of particulate organic matter light extinction coefficient ( $b_{ext\_POM}$ ) to reconstructed aerosol $b_{ext}$ . Wavelength corresponds to 550 nm. ....	4-13
Figure 4.2.3d. IMPROVE and CSN 2016–2019 annual mean fraction contributions of particulate organic matter light extinction coefficient ( $b_{ext\_POM}$ ) to reconstructed aerosol $b_{ext}$ . Wavelength corresponds to 550 nm. ....	4-14
Figure 4.2.4a. IMPROVE 2016–2019 PM <sub>2.5</sub> reconstructed ambient annual mean light extinction coefficients for elemental carbon ( $b_{ext\_EC}$ , Mm <sup>-1</sup> ). Wavelength corresponds to 550 nm. ....	4-15
Figure 4.2.4b. IMPROVE and CSN 2016–2019 PM <sub>2.5</sub> reconstructed ambient annual mean light extinction coefficients for elemental carbon ( $b_{ext\_EC}$ , Mm <sup>-1</sup> ). Wavelength corresponds to 550 nm. ....	4-15
Figure 4.2.4c. IMPROVE 2016–2019 annual mean fraction contributions of elemental carbon light extinction coefficient ( $b_{ext\_EC}$ ) to reconstructed aerosol $b_{ext}$ . Wavelength corresponds to 550 nm. ....	4-16
Figure 4.2.4d. IMPROVE and CSN 2016–2019 annual mean fraction contributions of elemental carbon light extinction coefficient ( $b_{ext\_EC}$ ) to reconstructed aerosol $b_{ext}$ . Wavelength corresponds to 550 nm. ....	4-17

Figure 4.2.5a. IMPROVE 2016–2019 PM <sub>2.5</sub> reconstructed ambient annual mean light extinction coefficients for fine dust ( $b_{ext\_FD}$ , Mm <sup>-1</sup> ). Wavelength corresponds to 550 nm. ....	4-18
Figure 4.2.5b. IMPROVE and CSN 2016–2019 PM <sub>2.5</sub> reconstructed ambient annual mean light extinction coefficients for fine dust ( $b_{ext\_FD}$ , Mm <sup>-1</sup> ). Wavelength corresponds to 550 nm. ....	4-18
Figure 4.2.5c. IMPROVE 2016–2019 annual mean fraction contributions of fine dust light extinction coefficient ( $b_{ext\_FD}$ ) to reconstructed aerosol $b_{ext}$ . Wavelength corresponds to 550 nm. ....	4-19
Figure 4.2.5d. IMPROVE and CSN 2016–2019 annual mean fraction contributions of fine dust light extinction coefficient ( $b_{ext\_FD}$ ) to reconstructed aerosol $b_{ext}$ . Wavelength corresponds to 550 nm. ....	4-19
Figure 4.2.6a. IMPROVE 2016–2019 PM <sub>2.5</sub> reconstructed ambient annual mean light extinction coefficients for sea salt ( $b_{ext\_SS}$ , Mm <sup>-1</sup> ). Wavelength corresponds to 550 nm. ....	4-20
Figure 4.2.6b. IMPROVE and CSN 2016–2019 PM <sub>2.5</sub> reconstructed ambient annual mean light extinction coefficients for sea salt ( $b_{ext\_SS}$ , Mm <sup>-1</sup> ). Wavelength corresponds to 550 nm. ....	4-21
Figure 4.2.6c. IMPROVE 2016–2019 annual mean fraction contributions of sea salt light extinction coefficient ( $b_{ext\_SS}$ ) to reconstructed aerosol $b_{ext}$ . Wavelength corresponds to 550 nm. ....	4-22
Figure 4.2.6d. IMPROVE and CSN 2016–2019 annual mean fraction contributions of sea salt light extinction coefficient ( $b_{ext\_SS}$ ) to reconstructed aerosol $b_{ext}$ . Wavelength corresponds to 550 nm. ....	4-22
Figure 4.2.7a. IMPROVE 2016–2019 PM <sub>2.5</sub> reconstructed ambient annual mean light extinction coefficients for coarse mass ( $b_{ext\_CM}$ , Mm <sup>-1</sup> ). Wavelength corresponds to 550 nm. ....	4-23
Figure 4.2.7b. IMPROVE and CSN 2016–2019 PM <sub>2.5</sub> reconstructed ambient annual mean light extinction coefficients for coarse mass ( $b_{ext\_CM}$ , Mm <sup>-1</sup> ). Wavelength corresponds to 550 nm. ....	4-24
Figure 4.2.7c. IMPROVE 2016–2019 annual mean fraction contributions of coarse mass light extinction coefficient ( $b_{ext\_CM}$ ) to reconstructed aerosol $b_{ext}$ . Wavelength corresponds to 550 nm. ....	4-25
Figure 4.2.7d. IMPROVE and CSN 2016–2019 annual mean fraction contributions of coarse mass light extinction coefficient ( $b_{ext\_CM}$ ) to reconstructed aerosol $b_{ext}$ . Wavelength corresponds to 550 nm. ....	4-25
Figure 4.2.8a. IMPROVE 2016–2019 reconstructed ambient annual mean aerosol light extinction coefficients ( $b_{ext\_aer}$ , Mm <sup>-1</sup> ) (no Rayleigh scattering). Wavelength corresponds to 550 nm. ....	4-26
Figure 4.2.8b. IMPROVE and CSN 2016–2019 PM <sub>2.5</sub> reconstructed ambient annual mean aerosol light extinction coefficients ( $b_{ext\_aer}$ , Mm <sup>-1</sup> ) (no Rayleigh scattering). Wavelength corresponds to 550 nm. ....	4-27

Figure 4.2.9a. IMPROVE 2016–2019 annual mean reconstructed ambient total light extinction coefficients ( $b_{ext\_tot}$ , $Mm^{-1}$ ) (aerosol + Rayleigh). Wavelength corresponds to 550 nm. .	4-27
Figure 4.2.9b. IMPROVE 2016–2019 annual mean reconstructed ambient total light extinction coefficients ( $b_{ext\_tot}$ , $Mm^{-1}$ ) (aerosol + Rayleigh). Wavelength corresponds to 550 nm. .	4-28
Figure 4.2.10a. IMPROVE 2016–2019 annual mean deciview (dv). Wavelength corresponds to 550 nm. ....	4-29
Figure 4.2.10b. IMPROVE and CSN 2016–2019 annual mean deciview (dv). Wavelength corresponds to 550 nm. ....	4-29
Figure 5.1.1. IMPROVE 2016–2019 regional monthly mean ambient reconstructed speciated aerosol light extinction coefficients ( $Mm^{-1}$ ) for the eastern United States. Letters on the x-axis correspond to the month and “A” corresponds to annual mean. Shaded areas in the map correspond to regions that include sites used in the analysis, shown as blue dots. Wavelength corresponds to 550 nm. ....	5-2
Figure 5.1.2. IMPROVE 2016–2019 regional monthly mean ambient reconstructed speciated aerosol light extinction coefficients ( $Mm^{-1}$ ) for the northwestern United States. Letters on the x-axis correspond to the month and “A” corresponds to annual mean. Shaded areas in the map correspond to regions that include sites used in the analysis, shown as blue dots. Wavelength corresponds to 550 nm. ....	5-3
Figure 5.1.3. IMPROVE 2016–2019 regional monthly mean ambient reconstructed speciated aerosol light extinction coefficients ( $Mm^{-1}$ ) for the southwestern United States. Letters on the x-axis correspond to the month and “A” corresponds to annual mean. Shaded areas in the map correspond to regions that include sites used in the analysis, shown as blue dots. Wavelength corresponds to 550 nm. ....	5-4
Figure 5.1.4. IMPROVE 2016–2019 regional monthly mean speciated fractional contributions to ambient aerosol light extinction coefficients for the eastern United States. Letters on the x-axis correspond to the month and “A” corresponds to annual mean. Shaded areas in the map correspond to regions that include sites used in the analysis, shown as blue dots. Wavelength corresponds to 550 nm. ....	5-6
Figure 5.1.5. IMPROVE 2016–2019 regional monthly mean speciated fractional contributions to ambient aerosol light extinction coefficients for the northwestern United States. Letters on the x-axis correspond to the month and “A” corresponds to annual mean. Shaded areas in the map correspond to regions that include sites used in the analysis, shown as blue dots. Wavelength corresponds to 550 nm. ....	5-7
Figure 5.1.6. IMPROVE 2016–2019 regional monthly mean speciated fractional contributions to ambient aerosol light extinction coefficients for the southwestern United States. Letters on the x-axis correspond to the month and “A” corresponds to annual mean. Shaded areas in the map correspond to regions that include sites used in the analysis, shown as blue dots. Wavelength corresponds to 550 nm. ....	5-8
Figure 5.1.7. CSN 2016–2019 regional monthly mean ambient reconstructed speciated aerosol light extinction coefficients ( $Mm^{-1}$ ) for the eastern United States. Letters on the x-axis correspond to the month and “A” corresponds to annual mean. Shaded areas in the map	

correspond to regions that include sites used in the analysis, shown as orange dots. Wavelength corresponds to 550 nm ..... 5-9

Figure 5.1.8. CSN 2016–2019 regional monthly mean ambient reconstructed speciated aerosol light extinction coefficients ( $Mm^{-1}$ ) for the northwestern United States. Letters on the x-axis correspond to the month and “A” corresponds to annual mean. Shaded areas in the map correspond to regions that include sites used in the analysis, shown as orange dots. Wavelength corresponds to 550 nm ..... 5-10

Figure 5.1.9. CSN 2016–2019 regional monthly mean ambient reconstructed speciated aerosol light extinction coefficients ( $Mm^{-1}$ ) for the southwestern United States. Letters on the x-axis correspond to the month and “A” corresponds to annual mean. Shaded areas in the map correspond to regions that include sites used in the analysis, shown as orange dots. Wavelength corresponds to 550 nm ..... 5-11

Figure 5.1.10. CSN 2016–2019 regional monthly mean speciated fractional contributions to ambient aerosol light extinction coefficients for the eastern United States. Letters on the x-axis correspond to the month and “A” corresponds to annual mean. Shaded areas in the map correspond to regions that include sites used in the analysis, shown as orange dots. Wavelength corresponds to 550 nm ..... 5-12

Figure 5.1.11. 2016–2019 regional monthly mean speciated fractional contributions to ambient aerosol light extinction coefficients for the northwestern United States. Letters on the x-axis correspond to the month and “A” corresponds to annual mean. Shaded areas in the map correspond to regions that include sites used in the analysis, shown as orange dots. Wavelength corresponds to 550 nm ..... 5-13

Figure 5.1.12. CSN 2016–2019 regional monthly mean speciated fractional contributions to ambient aerosol light extinction coefficients for the southwestern United States. Letters on the x-axis correspond to the month and “A” corresponds to annual mean. Shaded areas in the map correspond to regions that include sites used in the analysis, shown as orange dots. Wavelength corresponds to 550 nm ..... 5-14

Figure 6.0. IMPROVE regions defined to summarize regional mean trends ..... 6-2

Figure 6.1.1. Annual mean sulfate ion mass trends ( $\% \text{ yr}^{-1}$ ) for (a) long-term (1990–2019) and (b) short-term (2000–2019) periods. Filled triangles correspond to statistically significant trends ( $p \leq 0.05$ ) ..... 6-3

Figure 6.1.2. Short-term (2000–2019) regional seasonal mean sulfate ion trends ( $\% \text{ yr}^{-1}$ ) for major U.S. regions for winter, spring, summer, fall, and annual means. Regions are arranged from western to eastern United States (AK = Alaska, HI = Hawaii, NW = Northwest, CA = California, SW = Southwest, Cen = Central, MiS = Midsouth, NE = Northeast, SE = Southeast, VIIS = Virgin Islands, and US = all sites). Statistically significant trends ( $p \leq 0.05$ ) are denoted with “\*”. ..... 6-3

Figure 6.1.3. IMPROVE long-term (1990–2019) trends ( $\% \text{ yr}^{-1}$ ) in (a) 10<sup>th</sup> percentile sulfate ion concentrations and (b) 90<sup>th</sup> percentile concentrations. Filled triangles correspond to statistically significant trends ( $p \leq 0.05$ ) ..... 6-4

Figure 6.1.4. IMPROVE short-term (2000–2019) trends ( $\% \text{ yr}^{-1}$ ) in (a) 10<sup>th</sup> percentile sulfate ion concentrations and (b) 90<sup>th</sup> percentile concentrations. Filled triangles correspond to statistically significant trends ( $p \leq 0.05$ ) ..... 6-5

Figure 6.1.5. Short-term (2000–2019) regional mean trends (% yr<sup>-1</sup>) in 10<sup>th</sup>, 50<sup>th</sup>, and 90<sup>th</sup> percentile sulfate ion concentrations. Regions are arranged from western to eastern United States (AK = Alaska, HI = Hawaii, NW = Northwest, CA= California, SW = Southwest, Cen = Central, MiS = Midsouth, NE = Northeast, SE = Southeast, VIIS = Virgin Islands, and US = all sites). Statistically significant trends ( $p \leq 0.05$ ) are denoted with “\*”..... 6-6

Figure 6.2.1. Annual mean nitrate ion mass trends (% yr<sup>-1</sup>) for (a) long-term (1990–2019) and (b) short-term (2000–2019) periods. Filled triangles correspond to statistically significant trends ( $p \leq 0.05$ ). ..... 6-7

Figure 6.2.2. Short-term (2000–2019) regional seasonal mean nitrate ion trends (% yr<sup>-1</sup>) for major U.S. regions for winter, spring, summer, fall, and annual means. Regions are arranged from western to eastern United States (AK = Alaska, HI = Hawaii, NW = Northwest, CA= California, SW = Southwest, Cen = Central, MiS = Midsouth, NE = Northeast, SE = Southeast, VIIS = Virgin Islands, and US = all sites). Statistically significant trends ( $p \leq 0.05$ ) are denoted with “\*”. ..... 6-8

Figure 6.2.3. IMPROVE long-term (1990–2019) trends (% yr<sup>-1</sup>) in (a) 10<sup>th</sup> percentile nitrate ion concentrations and (b) 90<sup>th</sup> percentile concentrations. Filled triangles correspond to statistically significant trends ( $p \leq 0.05$ ). ..... 6-9

Figure 6.2.4. IMPROVE short-term (2000–2019) trends (% yr<sup>-1</sup>) in (a) 10<sup>th</sup> percentile nitrate ion concentrations and (b) 90<sup>th</sup> percentile concentrations. Filled triangles correspond to statistically significant trends ( $p \leq 0.05$ ). ..... 6-9

Figure 6.2.5. Short-term (2000–2019) regional mean trends (% yr<sup>-1</sup>) in 10<sup>th</sup>, 50<sup>th</sup>, and 90<sup>th</sup> percentile nitrate ion concentrations. Regions are arranged from western to eastern United States (AK = Alaska, HI = Hawaii, NW = Northwest, CA= California, SW = Southwest, Cen = Central, MiS = Midsouth, NE = Northeast, SE = Southeast, VIIS = Virgin Islands, and US = all sites). Statistically significant trends ( $p \leq 0.05$ ) are denoted with “\*”. ..... 6-10

Figure 6.3.1. Annual mean organic carbon (OC) mass trends (% yr<sup>-1</sup>) for (a) long-term (1990–2019) and (b) short-term (2000–2019) periods. Filled triangles correspond to statistically significant trends ( $p \leq 0.05$ ). ..... 6-11

Figure 6.3.2. Short-term (2000–2019) regional seasonal mean organic carbon (OC) trends (% yr<sup>-1</sup>) for major U.S. regions for winter, spring, summer, fall, and annual means. Regions are arranged from western to eastern United States (AK = Alaska, HI = Hawaii, NW = Northwest, CA= California, SW = Southwest, Cen = Central, MiS = Midsouth, NE = Northeast, SE = Southeast, VIIS = Virgin Islands, and US = all sites). Statistically significant trends ( $p \leq 0.05$ ) are denoted with “\*”. ..... 6-12

Figure 6.3.3. IMPROVE long-term (1990–2020) trends (% yr<sup>-1</sup>) in (a) 10<sup>th</sup> percentile organic carbon (OC) concentrations and (b) 90<sup>th</sup> percentile concentrations. Filled triangles correspond to statistically significant trends ( $p \leq 0.05$ ). ..... 6-13

Figure 6.3.4. IMPROVE short-term (2000–2019) trends (% yr<sup>-1</sup>) in (a) 10<sup>th</sup> percentile organic carbon (OC) concentrations and (b) 90<sup>th</sup> percentile concentrations. Filled triangles correspond to statistically significant trends ( $p \leq 0.05$ ). ..... 6-13

Figure 6.3.5. Short-term (2000–2019) regional mean trends (% yr<sup>-1</sup>) in 10<sup>th</sup>, 50<sup>th</sup>, and 90<sup>th</sup> percentile organic carbon (OC) concentrations. Regions are arranged from western to eastern United States (AK = Alaska, HI = Hawaii, NW = Northwest, CA= California, SW = Southwest,

Cen = Central, MiS = Midsouth, NE = Northeast, SE = Southeast, VIIS = Virgin Islands, and US = all sites). Statistically significant trends ( $p \leq 0.05$ ) are denoted with “\*”..... 6-14

Figure 6.4.1. Annual mean elemental carbon (EC) mass trends ( $\% \text{ yr}^{-1}$ ) for (a) long-term (1990–2019) and (b) short-term (2000–2019) periods. Filled triangles correspond to statistically significant trends ( $p \leq 0.05$ )..... 6-15

Figure 6.4.2. Short-term (2000–2019) regional seasonal mean elemental carbon (EC) trends ( $\% \text{ yr}^{-1}$ ) for major U.S. regions for winter, spring, summer, fall, and annual means. Regions are arranged from western to eastern United States (AK = Alaska, HI = Hawaii, NW = Northwest, CA= California, SW = Southwest, Cen = Central, MiS = Midsouth, NE = Northeast, SE = Southeast, VIIS = Virgin Islands, and US = all sites). Statistically significant trends ( $p \leq 0.05$ ) are denoted with “\*”..... 6-16

Figure 6.4.3. IMPROVE long-term (1990–2019) trends ( $\% \text{ yr}^{-1}$ ) in (a) 10<sup>th</sup> percentile elemental carbon (EC) concentrations and (b) 90<sup>th</sup> percentile concentrations. Filled triangles correspond to statistically significant trends ( $p \leq 0.05$ )..... 6-17

Figure 6.4.4. IMPROVE short-term (2000–2019) trends ( $\% \text{ yr}^{-1}$ ) in (a) 10<sup>th</sup> percentile elemental carbon (EC) concentrations and (b) 90<sup>th</sup> percentile concentrations. Filled triangles correspond to statistically significant trends ( $p \leq 0.05$ )..... 6-17

Figure 6.4.5. Short-term (2000–2019) regional mean trends ( $\% \text{ yr}^{-1}$ ) in 10<sup>th</sup>, 50<sup>th</sup>, and 90<sup>th</sup> percentile elemental carbon (EC) percentile concentrations. Regions are arranged from western to eastern United States (AK = Alaska, HI = Hawaii, NW = Northwest, CA= California, SW = Southwest, Cen = Central, MiS = Midsouth, NE = Northeast, SE = Southeast, VIIS = Virgin Islands, and US = all sites). Statistically significant trends ( $p \leq 0.05$ ) are denoted with “\*”.... 6-18

Figure 6.5.1 Annual mean fine dust mass trends ( $\% \text{ yr}^{-1}$ ) for (a) long-term (1990–2019) and (b) short-term (2000–2019) periods. Filled triangles correspond to statistically significant trends ( $p \leq 0.05$ )..... 6-19

Figure 6.5.2. Short-term (2000–2019) regional seasonal mean fine dust mass trends ( $\% \text{ yr}^{-1}$ ) for major U.S. regions for winter, spring, summer, fall, and annual means. Regions are arranged from western to eastern United States (AK = Alaska, HI = Hawaii, NW = Northwest, CA= California, SW = Southwest, Cen = Central, MiS = Midsouth, NE = Northeast, SE = Southeast, VIIS = Virgin Islands, and US = all sites). Statistically significant trends ( $p \leq 0.05$ ) are denoted with “\*”. .... 6-20

Figure 6.5.3. IMPROVE long-term (1990–2019) trends ( $\% \text{ yr}^{-1}$ ) in (a) 10<sup>th</sup> percentile fine dust concentrations and (b) 90<sup>th</sup> percentile concentrations. Filled triangles correspond to statistically significant trends ( $p \leq 0.05$ )..... 6-20

Figure 6.5.4. IMPROVE short-term (2000–2019) trends ( $\% \text{ yr}^{-1}$ ) in (a) 10<sup>th</sup> percentile fine dust concentrations and (b) 90<sup>th</sup> percentile concentrations. Filled triangles correspond to statistically significant trends ( $p \leq 0.05$ )..... 6-21

Figure 6.5.5. Short-term (2000–2019) regional mean trends ( $\% \text{ yr}^{-1}$ ) trends in 10<sup>th</sup>, 50<sup>th</sup>, and 90<sup>th</sup> percentile fine dust concentrations. Regions are arranged from western to eastern United States (AK = Alaska, HI = Hawaii, NW = Northwest, CA= California, SW = Southwest, Cen = Central, MiS = Midsouth, NE = Northeast, SE = Southeast, VIIS = Virgin Islands, and US = all sites). Statistically significant trends ( $p \leq 0.05$ ) are denoted with “\*”..... 6-21

Figure 6.6.1. Annual mean gravimetric PM<sub>2.5</sub> fine mass (FM) trends (% yr<sup>-1</sup>) for (a) long-term (1990–2019) and (b) short-term (2000–2019) periods. Filled triangles correspond to statistically significant trends ( $p \leq 0.05$ ). ..... 6-23

Figure 6.6.2. Short-term (2000–2019) regional seasonal mean gravimetric PM<sub>2.5</sub> fine mass (FM) trends (% yr<sup>-1</sup>) for major U.S. regions for winter, spring, summer, fall, and annual means. Regions are arranged from western to eastern United States (AK = Alaska, HI = Hawaii, NW = Northwest, CA= California, SW = Southwest, Cen = Central, MiS = Midsouth, NE = Northeast, SE = Southeast, VIIS = Virgin Islands, and US = all sites). Statistically significant trends ( $p \leq 0.05$ ) are denoted with “\*”..... 6-23

Figure 6.6.3. IMPROVE long-term (1990–2019) trends (% yr<sup>-1</sup>) in (a) 10<sup>th</sup> percentile gravimetric PM<sub>2.5</sub> fine mass (FM) concentrations and (b) 90<sup>th</sup> percentile concentrations. Filled triangles correspond to statistically significant trends ( $p \leq 0.05$ ). ..... 6-24

Figure 6.6.4. IMPROVE short-term (2000–2019) trends (% yr<sup>-1</sup>) in (a) 10<sup>th</sup> percentile gravimetric PM<sub>2.5</sub> fine mass (FM) concentrations and (b) 90<sup>th</sup> percentile concentrations. Filled triangles correspond to statistically significant trends ( $p \leq 0.05$ ). ..... 6-25

Figure 6.6.5. Short-term (2000–2019) regional mean trends (% yr<sup>-1</sup>) in 10<sup>th</sup>, 50<sup>th</sup>, and 90<sup>th</sup> percentile gravimetric PM<sub>2.5</sub> fine mass (FM) concentrations. Regions are arranged from western to eastern United States (AK = Alaska, HI = Hawaii, NW = Northwest, CA= California, SW = Southwest, Cen = Central, MiS = Midsouth, NE = Northeast, SE = Southeast, VIIS = Virgin Islands, and US = all sites). Statistically significant trends ( $p \leq 0.05$ ) are denoted with “\*”.... 6-25

Figure 6.7.1. Annual mean gravimetric PM<sub>10</sub> mass trends (% yr<sup>-1</sup>) for (a) long-term (1990–2019) and (b) short-term (2000–2019) periods. Filled triangles correspond to statistically significant trends ( $p \leq 0.05$ )..... 6-26

Figure 6.7.2. Short-term (2000–2019) regional seasonal mean gravimetric PM<sub>10</sub> mass trends (% yr<sup>-1</sup>) for major U.S. regions for winter, spring, summer, fall, and annual means. Regions are arranged from western to eastern United States (AK = Alaska, HI = Hawaii, NW = Northwest, CA= California, SW = Southwest, Cen = Central, MiS = Midsouth, NE = Northeast, SE = Southeast, VIIS = Virgin Islands, and US = all sites). Statistically significant trends ( $p \leq 0.05$ ) are denoted with “\*”..... 6-27

Figure 6.7.3. IMPROVE long-term (1990–2019) trends (% yr<sup>-1</sup>) in (a) 10<sup>th</sup> percentile gravimetric PM<sub>10</sub> mass concentrations and (b) 90<sup>th</sup> percentile concentrations. Filled triangles correspond to statistically significant trends ( $p \leq 0.05$ ). ..... 6-28

Figure 6.7.4. IMPROVE short-term (2000–2019) trends (% yr<sup>-1</sup>) in (a) 10<sup>th</sup> percentile gravimetric PM<sub>10</sub> mass concentrations and (b) 90<sup>th</sup> percentile concentrations. Filled triangles correspond to statistically significant trends ( $p \leq 0.05$ ). ..... 6-28

Figure 6.7.5. Short-term (2000–2019) regional mean trends (% yr<sup>-1</sup>) in 10<sup>th</sup>, 50<sup>th</sup>, and 90<sup>th</sup> percentile gravimetric PM<sub>10</sub> mass concentrations. Regions are arranged from western to eastern United States (AK = Alaska, HI = Hawaii, NW = Northwest, CA= California, SW = Southwest, Cen = Central, MiS = Midsouth, NE = Northeast, SE = Southeast, VIIS = Virgin Islands, and US = all sites). Statistically significant trends ( $p \leq 0.05$ ) are denoted with “\*”..... 6-29

Figure 6.8.1. Annual mean coarse mass (CM) trends (% yr<sup>-1</sup>) for (a) long-term (1990–2019) and (b) short-term (2000–2019) periods. Filled triangles correspond to statistically significant trends ( $p \leq 0.05$ ). ..... 6-30

Figure 6.8.2. Short-term (2000–2019) regional seasonal mean coarse mass (CM) trends (% yr<sup>-1</sup>) for major U.S. regions for winter, spring, summer, fall, and annual means. Regions are arranged from western to eastern United States (AK = Alaska, HI = Hawaii, NW = Northwest, CA= California, SW = Southwest, Cen = Central, MiS = Midsouth, NE = Northeast, SE = Southeast, VIIS = Virgin Islands, and US = all sites). Statistically significant trends ( $p \leq 0.05$ ) are denoted with “\*\*” ..... 6-31

Figure 6.8.3. IMPROVE long-term (1990–2019) trends (% yr<sup>-1</sup>) in (a) 10<sup>th</sup> percentile coarse mass (CM) concentrations and (b) 90<sup>th</sup> percentile concentrations. Filled triangles correspond to statistically significant trends ( $p \leq 0.05$ ) ..... 6-32

Figure 6.8.4. IMPROVE short-term (2000–2019) trends (% yr<sup>-1</sup>) in (a) 10<sup>th</sup> percentile coarse mass (CM) concentrations and (b) 90<sup>th</sup> percentile concentrations. Filled triangles correspond to statistically significant trends ( $p \leq 0.05$ ) ..... 6-33

Figure 6.8.5. Short-term (2000–2019) regional mean trends (% yr<sup>-1</sup>) in 10<sup>th</sup>, 50<sup>th</sup>, and 90<sup>th</sup> percentile coarse mass (CM) concentrations. Regions are arranged from western to eastern United States (AK = Alaska, HI = Hawaii, NW = Northwest, CA= California, SW = Southwest, Cen = Central, MiS = Midsouth, NE = Northeast, SE = Southeast, VIIS = Virgin Islands, and US = all sites). Statistically significant trends ( $p \leq 0.05$ ) are denoted with “\*\*” ..... 6-33

Figure 6.9.1. Annual mean filter absorption ( $f_{abs}$ ) short-term (2000–2019) trends (% yr<sup>-1</sup>). Filled triangles correspond to statistically significant trends ( $p \leq 0.05$ ) ..... 6-34

Figure 6.9.2. Short-term (2000–2019) regional seasonal mean filter absorption ( $f_{abs}$ ) trends (% yr<sup>-1</sup>) for major U.S. regions for winter, spring, summer, fall, and annual means. Regions are arranged from western to eastern United States (AK = Alaska, HI = Hawaii, NW = Northwest, CA= California, SW = Southwest, Cen = Central, MiS = Midsouth, NE = Northeast, SE = Southeast, VIIS = Virgin Islands, and US = all sites). Statistically significant trends ( $p \leq 0.05$ ) are denoted with “\*\*” ..... 6-35

Figure 6.9.3. IMPROVE short-term (2000–2019) trends (% yr<sup>-1</sup>) in (a) 10<sup>th</sup> percentile filter absorption ( $f_{abs}$ ) and (b) 90<sup>th</sup> percentile  $f_{abs}$ . Filled triangles correspond to statistically significant trends ( $p \leq 0.05$ ) ..... 6-36

Figure 6.9.4. Short-term (2000–2019) regional mean trends (% yr<sup>-1</sup>) in 10<sup>th</sup>, 50<sup>th</sup>, and 90<sup>th</sup> percentile filter absorption ( $f_{abs}$ ). Regions are arranged from western to eastern United States (AK = Alaska, HI = Hawaii, NW = Northwest, CA= California, SW = Southwest, Cen = Central, MiS = Midsouth, NE = Northeast, SE = Southeast, VIIS = Virgin Islands, and US = all sites). Statistically significant trends ( $p \leq 0.05$ ) are denoted with “\*\*” ..... 6-36

Figure 6.10.1. Short-term (2001–2019) timelines in IMPROVE regional, annual mean mass concentrations ( $\mu\text{g m}^{-3}$ ) for sulfate ion, nitrate ion, organic carbon (OC), elemental carbon (EC), and fine dust (FD) ..... 6-37

Figure 6.10.2. Short-term (2001–2019) timelines in IMPROVE regional, annual mean coarse mass (CM) concentrations ( $\mu\text{g m}^{-3}$ ) ..... 6-39

Figure 7.1.1. Annual mean ammonium sulfate  $b_{ext}$  ( $b_{ext\_AS}$ ) trends (% yr<sup>-1</sup>) for (a) long-term (1990–2019) and (b) short-term (2000–2019) periods. Filled triangles correspond to statistically significant trends ( $p \leq 0.05$ ) ..... 7-2

Figure 7.1.2. Short-term (2000–2019) regional seasonal mean ammonium sulfate  $b_{ext}$  ( $b_{ext\_AS}$ ) trends ( $\% \text{ yr}^{-1}$ ) for major U.S. regions for winter, spring, summer, fall, and annual means. Regions are arranged from western to eastern United States (AK = Alaska, HI = Hawaii, NW = Northwest, CA= California, SW = Southwest, Cen = Central, MiS = Midsouth, NE = Northeast, SE = Southeast, VIIS = Virgin Islands, and US = all sites). Statistically significant trends ( $p \leq 0.05$ ) are denoted with “\*”..... 7-3

Figure 7.1.3. IMPROVE long-term (1990–2019) trends ( $\% \text{ yr}^{-1}$ ) in (a) 10<sup>th</sup> percentile ammonium sulfate  $b_{ext}$  ( $b_{ext\_AS}$ ) and (b) 90<sup>th</sup> percentile  $b_{ext\_AS}$ . Filled triangles correspond to statistically significant trends ( $p \leq 0.05$ ). ..... 7-4

Figure 7.1.4. IMPROVE short-term (2000–2019) trends ( $\% \text{ yr}^{-1}$ ) in (a) 10<sup>th</sup> percentile ammonium sulfate  $b_{ext}$  ( $b_{ext\_AS}$ ) and (b) 90<sup>th</sup> percentile  $b_{ext\_AS}$ . Filled triangles correspond to statistically significant trends ( $p \leq 0.05$ ). ..... 7-4

Figure 7.1.5. Short-term (2000–2019) regional mean trends ( $\% \text{ yr}^{-1}$ ) in 10<sup>th</sup>, 50<sup>th</sup>, and 90<sup>th</sup> percentile ammonium sulfate  $b_{ext}$  ( $b_{ext\_AS}$ ). Regions are arranged from western to eastern United States (AK = Alaska, HI = Hawaii, NW = Northwest, CA= California, SW = Southwest, Cen = Central, MiS = Midsouth, NE = Northeast, SE = Southeast, VIIS = Virgin Islands, and US = all sites). Statistically significant trends ( $p \leq 0.05$ ) are denoted with “\*”..... 7-5

Figure 7.2.1. Annual mean ammonium nitrate  $b_{ext}$  ( $b_{ext\_AN}$ ) trends ( $\% \text{ yr}^{-1}$ ) for (a) long-term (1990–2019) and (b) short-term (2000–2019) periods. Filled triangles correspond to statistically significant trends ( $p \leq 0.05$ )..... 7-6

Figure 7.2.2. Short-term (2000–2019) regional seasonal mean ammonium nitrate  $b_{ext}$  ( $b_{ext\_AN}$ ) trends ( $\% \text{ yr}^{-1}$ ) for major U.S. regions for winter, spring, summer, fall, and annual means. Regions are arranged from western to eastern United States (AK = Alaska, HI = Hawaii, NW = Northwest, CA= California, SW = Southwest, Cen = Central, MiS = Midsouth, NE = Northeast, SE = Southeast, VIIS = Virgin Islands, and US = all sites). Statistically significant trends ( $p \leq 0.05$ ) are denoted with “\*”..... 7-6

Figure 7.2.3. IMPROVE long-term (1990–2019) trends ( $\% \text{ yr}^{-1}$ ) in (a) 10<sup>th</sup> percentile ammonium nitrate  $b_{ext}$  ( $b_{ext\_AN}$ ) and (b) 90<sup>th</sup> percentile  $b_{ext\_AN}$ . Filled triangles correspond to statistically significant trends ( $p \leq 0.05$ ). ..... 7-7

Figure 7.2.4. IMPROVE short-term (2000–2019) trends ( $\% \text{ yr}^{-1}$ ) in (a) 10<sup>th</sup> percentile ammonium nitrate  $b_{ext}$  ( $b_{ext\_AN}$ ) and (b) 90<sup>th</sup> percentile  $b_{ext\_AN}$ . Filled triangles correspond to statistically significant trends ( $p \leq 0.05$ ). ..... 7-8

Figure 7.2.5. Short-term (2000–2019) regional mean trends ( $\% \text{ yr}^{-1}$ ) in 10<sup>th</sup>, 50<sup>th</sup>, and 90<sup>th</sup> percentile ammonium nitrate  $b_{ext}$  ( $b_{ext\_AN}$ ). Regions are arranged from western to eastern United States (AK = Alaska, HI = Hawaii, NW = Northwest, CA= California, SW = Southwest, Cen = Central, MiS = Midsouth, NE = Northeast, SE = Southeast, VIIS = Virgin Islands, and US = all sites). Statistically significant trends ( $p \leq 0.05$ ) are denoted with “\*”..... 7-8

Figure 7.3.1. Annual mean particulate organic matter  $b_{ext}$  ( $b_{ext\_POM}$ ) trends ( $\% \text{ yr}^{-1}$ ) for (a) long-term (1990–2019) and (b) short-term (2000–2019) periods. Filled triangles correspond to statistically significant trends ( $p \leq 0.05$ ). ..... 7-9

Figure 7.3.2. Short-term (2000–2019) regional, seasonal mean particulate organic matter  $b_{ext}$  ( $b_{ext\_POM}$ ) trends ( $\% \text{ yr}^{-1}$ ) for major U.S. regions for winter, spring, summer, fall, and annual means. Regions are arranged from western to eastern United States (AK= Alaska, HI = Hawaii,

NW = Northwest, CA= California, SW = Southwest, Cen = Central, MiS = Midsouth, NE = Northeast, SE = Southeast, VIIS = Virgin Islands, and US = all sites). Statistically significant trends ( $p \leq 0.05$ ) are denoted with “\*\*”. ..... 7-10

Figure 7.3.3. IMPROVE long-term (1990–2019) trends (%  $\text{yr}^{-1}$ ) in (a) 10<sup>th</sup> percentile particulate organic matter  $b_{\text{ext}}(b_{\text{ext\_POM}})$  and (b) 90<sup>th</sup> percentile  $b_{\text{ext\_POM}}$ . Filled triangles correspond to statistically significant trends ( $p \leq 0.05$ ). ..... 7-11

Figure 7.3.4. IMPROVE long-term (1990–2019) trends (%  $\text{yr}^{-1}$ ) in (a) 10<sup>th</sup> percentile particulate organic matter  $b_{\text{ext}}(b_{\text{ext\_POM}})$  and (b) 90<sup>th</sup> percentile  $b_{\text{ext\_POM}}$ . Filled triangles correspond to statistically significant trends ( $p \leq 0.05$ ). ..... 7-11

Figure 7.3.5. Short-term (2000–2019) regional mean trends (%  $\text{yr}^{-1}$ ) in 10<sup>th</sup>, 50<sup>th</sup>, and 90<sup>th</sup> percentile particulate organic matter  $b_{\text{ext}}(b_{\text{ext\_POM}})$ . Regions are arranged from western to eastern United States (AK = Alaska, HI = Hawaii, NW = Northwest, CA= California, SW = Southwest, Cen = Central, MiS = Midsouth, NE = Northeast, SE = Southeast, VIIS = Virgin Islands, and US = all sites). Statistically significant trends ( $p \leq 0.05$ ) are denoted with “\*\*”. ..... 7-12

Figure 7.4.1. Annual mean elemental carbon  $b_{\text{ext}}(b_{\text{ext\_EC}})$  trends for (a) long-term (1990–2019) and (b) short-term (2000–2019) periods. Filled triangles correspond to statistically significant trends ( $p \leq 0.05$ ). ..... 7-13

Figure 7.4.2. Short-term (2000–2019) regional seasonal mean elemental carbon  $b_{\text{ext}}(b_{\text{ext\_EC}})$  trends (%  $\text{yr}^{-1}$ ) for major U.S. regions for winter, spring, summer, fall, and annual means. Regions are arranged from western to eastern United States (AK = Alaska, HI = Hawaii, NW = Northwest, CA= California, SW = Southwest, Cen = Central, MiS = Midsouth, NE = Northeast, SE = Southeast, VIIS = Virgin Islands, and US = all sites). Statistically significant trends ( $p \leq 0.05$ ) are denoted with “\*\*”. ..... 7-13

Figure 7.4.3. IMPROVE long-term (1990–2019) trends (%  $\text{yr}^{-1}$ ) in (a) 10<sup>th</sup> percentile elemental carbon  $b_{\text{ext}}(b_{\text{ext\_EC}})$  and (b) 90<sup>th</sup> percentile  $b_{\text{ext\_EC}}$ . Filled triangles correspond to statistically significant trends ( $p \leq 0.05$ ). ..... 7-14

Figure 7.4.4. IMPROVE short-term (2000–2019) trends (%  $\text{yr}^{-1}$ ) in (a) 10<sup>th</sup> percentile elemental carbon  $b_{\text{ext}}(b_{\text{ext\_EC}})$  and (b) 90<sup>th</sup> percentile  $b_{\text{ext\_EC}}$ . Filled triangles correspond to statistically significant trends ( $p \leq 0.05$ ). ..... 7-15

Figure 7.4.5. Short-term (2000–2019) regional mean trends (%  $\text{yr}^{-1}$ ) in 10<sup>th</sup>, 50<sup>th</sup>, and 90<sup>th</sup> percentile elemental carbon  $b_{\text{ext}}(b_{\text{ext\_EC}})$ . Regions are arranged from western to eastern United States (AK = Alaska, HI = Hawaii, NW = Northwest, CA= California, SW = Southwest, Cen = Central, MiS = Midsouth, NE = Northeast, SE = Southeast, VIIS = Virgin Islands, and US = all sites). Statistically significant trends ( $p \leq 0.05$ ) are denoted with “\*\*”. ..... 7-15

Figure 7.5.1 Annual mean fine dust  $b_{\text{ext}}(b_{\text{ext\_FD}})$  trends (%  $\text{yr}^{-1}$ ) for (a) long-term (1990–2019) and (b) short-term (2000–2019) periods. Filled triangles correspond to statistically significant trends ( $p \leq 0.05$ ). ..... 7-16

Figure 7.5.2. Short-term (2000–2019) regional seasonal mean fine dust  $b_{\text{ext}}(b_{\text{ext\_FD}})$  trends (%  $\text{yr}^{-1}$ ) for major U.S. regions for winter, spring, summer, fall, and annual means. Regions are arranged from western to eastern United States (AK = Alaska, HI = Hawaii, NW = Northwest, CA= California, SW = Southwest, Cen = Central, MiS = Midsouth, NE = Northeast, SE = Southeast, VIIS = Virgin Islands, and US = all sites). Statistically significant trends ( $p \leq 0.05$ ) are denoted with “\*\*”. ..... 7-17

Figure 7.5.3. IMPROVE long-term (1990–2019) trends (% yr<sup>-1</sup>) in (a) 10<sup>th</sup> percentile fine dust b<sub>ext</sub> (b<sub>ext\_FD</sub>) and (b) 90<sup>th</sup> percentile b<sub>ext\_FD</sub>. Filled triangles correspond to statistically significant trends ( $p \leq 0.05$ )..... 7-17

Figure 7.5.4. IMPROVE short-term (2000–2019) trends (% yr<sup>-1</sup>) in (a) 10<sup>th</sup> percentile fine dust b<sub>ext</sub> (b<sub>ext\_FD</sub>) and (b) 90<sup>th</sup> percentile b<sub>ext\_FD</sub>. Filled triangles correspond to statistically significant trends ( $p \leq 0.05$ )..... 7-18

Figure 7.5.5. Short-term (2000–2019) regional mean trends (% yr<sup>-1</sup>) in 10<sup>th</sup>, 50<sup>th</sup>, and 90<sup>th</sup> percentile fine dust b<sub>ext</sub> (b<sub>ext\_FD</sub>). Regions are arranged from western to eastern United States (AK = Alaska, HI = Hawaii, NW = Northwest, CA= California, SW = Southwest, Cen = Central, MiS = Midsouth, NE = Northeast, SE = Southeast, VIIS = Virgin Islands, and US = all sites). Statistically significant trends ( $p \leq 0.05$ ) are denoted with “\*”..... 7-19

Figure 7.6.1. Annual mean coarse mass b<sub>ext</sub> (b<sub>ext\_CM</sub>) trends (% yr<sup>-1</sup>) for (a) long-term (1990–2019) and (b) short-term (2000–2019) periods. Filled triangles correspond to statistically significant trends ( $p \leq 0.05$ )..... 7-19

Figure 7.6.2. Short-term (2000–2019) regional seasonal mean coarse mass b<sub>ext</sub> (b<sub>ext\_CM</sub>) trends (% yr<sup>-1</sup>) for major U.S. regions for winter, spring, summer, fall, and annual means. Regions are arranged from western to eastern United States (AK = Alaska, HI = Hawaii, NW = Northwest, CA= California, SW = Southwest, Cen = Central, MiS = Midsouth, NE = Northeast, SE = Southeast, VIIS = Virgin Islands, and US = all sites). Statistically significant trends ( $p \leq 0.05$ ) are denoted with “\*”..... 7-20

Figure 7.6.3. IMPROVE long-term (1990–2019) trends (% yr<sup>-1</sup>) in (a) 10<sup>th</sup> percentile coarse mass b<sub>ext</sub> (b<sub>ext\_CM</sub>) and (b) 90<sup>th</sup> percentile b<sub>ext\_CM</sub>. Filled triangles correspond to statistically significant trends ( $p \leq 0.05$ )..... 7-21

Figure 7.6.4. IMPROVE short-term (2000–2019) trends (% yr<sup>-1</sup>) in (a) 10<sup>th</sup> percentile coarse mass b<sub>ext</sub> (b<sub>ext\_CM</sub>) and (b) 90<sup>th</sup> percentile b<sub>ext\_CM</sub>. Filled triangles correspond to statistically significant trends ( $p \leq 0.05$ )..... 7-22

Figure 7.6.5. Short-term (2000–2019) regional mean trends (% yr<sup>-1</sup>) in 10<sup>th</sup>, 50<sup>th</sup>, and 90<sup>th</sup> percentile coarse mass b<sub>ext</sub> (b<sub>ext\_CM</sub>). Regions are arranged from western to eastern United States (AK = Alaska, HI = Hawaii, NW = Northwest, CA= California, SW = Southwest, Cen = Central, MiS = Midsouth, NE = Northeast, SE = Southeast, VIIS = Virgin Islands, and US = all sites). Statistically significant trends ( $p \leq 0.05$ ) are denoted with “\*”..... 7-22

Figure 7.7.1 Annual mean aerosol b<sub>ext</sub> (b<sub>ext\_aer</sub>) trends (% yr<sup>-1</sup>) for (a) long-term (1990–2019) and (b) short-term (2000–2019) periods. Filled triangles correspond to statistically significant trends ( $p \leq 0.05$ )..... 7-23

Figure 7.7.2. Short-term (2000–2019) regional seasonal mean aerosol b<sub>ext</sub> (b<sub>ext\_aer</sub>) trends (% yr<sup>-1</sup>) for major U.S. regions for winter, spring, summer, fall, and annual means. Regions are arranged from western to eastern United States (AK = Alaska, HI = Hawaii, NW = Northwest, CA= California, SW = Southwest, Cen = Central, MiS = Midsouth, NE = Northeast, SE = Southeast, VIIS = Virgin Islands, and US = all sites). Statistically significant trends ( $p \leq 0.05$ ) are denoted with “\*”..... 7-24

Figure 7.7.3. IMPROVE long-term (1990–2019) trends (% yr<sup>-1</sup>) in (a) 10<sup>th</sup> percentile aerosol b<sub>ext</sub> (b<sub>ext\_aer</sub>) and (b) 90<sup>th</sup> percentile b<sub>ext\_aer</sub>. Filled triangles correspond to statistically significant trends ( $p \leq 0.05$ )..... 7-24

Figure 7.7.4. IMPROVE short-term (2000–2019) trends (% yr<sup>-1</sup>) in (a) 10<sup>th</sup> percentile aerosol b<sub>ext</sub> (b<sub>ext\_aer</sub>) and (b) 90<sup>th</sup> percentile b<sub>ext\_aer</sub>. Filled triangles correspond to statistically significant trends ( $p \leq 0.05$ ) ..... 7-25

Figure 7.7.5. Short-term (2000–2019) regional mean trends (% yr<sup>-1</sup>) in 10<sup>th</sup>, 50<sup>th</sup>, and 90<sup>th</sup> percentile aerosol b<sub>ext</sub> (b<sub>ext\_aer</sub>). Regions are arranged from western to eastern United States (AK = Alaska, HI = Hawaii, NW = Northwest, CA= California, SW = Southwest, Cen = Central, MiS = Midsouth, NE = Northeast, SE = Southeast, VIIS = Virgin Islands, and US = all sites). Statistically significant trends ( $p \leq 0.05$ ) are denoted with “\*” ..... 7-26

Figure 7.8.1. Annual mean total b<sub>ext</sub> (b<sub>ext\_tot</sub>) trends (% yr<sup>-1</sup>) for (a) long-term (1990–2019) and (b) short-term (2000–2019) periods. Filled triangles correspond to statistically significant trends ( $p \leq 0.05$ ) ..... 7-27

Figure 7.8.2. Short-term (2000–2019) regional seasonal mean total b<sub>ext</sub> (b<sub>ext\_tot</sub>) trends (% yr<sup>-1</sup>) for major U.S. regions for winter, spring, summer, fall, and annual means. Regions are arranged from western to eastern United States (AK = Alaska, HI = Hawaii, NW = Northwest, CA= California, SW = Southwest, Cen = Central, MiS = Midsouth, NE = Northeast, SE = Southeast, VIIS = Virgin Islands, and US = all sites). Statistically significant trends ( $p \leq 0.05$ ) are denoted with “\*” ..... 7-27

Figure 7.8.3. IMPROVE long-term (1990–2019) trends (% yr<sup>-1</sup>) in (a) 10<sup>th</sup> percentile total b<sub>ext</sub> (b<sub>ext\_tot</sub>) and (b) 90<sup>th</sup> percentile b<sub>ext\_tot</sub>. Filled triangles correspond to statistically significant trends ( $p \leq 0.05$ ) ..... 7-28

Figure 7.8.4. IMPROVE short-term (2000–2019) trends (% yr<sup>-1</sup>) in (a) 10<sup>th</sup> percentile total b<sub>ext</sub> (b<sub>ext\_tot</sub>) and (b) 90<sup>th</sup> percentile b<sub>ext\_tot</sub>. Filled triangles correspond to statistically significant trends ( $p \leq 0.05$ ) ..... 7-28

Figure 7.8.5. Short-term (2000–2019) regional mean trends (% yr<sup>-1</sup>) in 10<sup>th</sup>, 50<sup>th</sup>, and 90<sup>th</sup> percentile total b<sub>ext</sub> (b<sub>ext\_tot</sub>). Regions are arranged from western to eastern United States (AK = Alaska, HI = Hawaii, NW = Northwest, CA= California, SW = Southwest, Cen = Central, MiS = Midsouth, NE = Northeast, SE = Southeast, VIIS = Virgin Islands, and US = all sites). Statistically significant trends ( $p \leq 0.05$ ) are denoted with “\*” ..... 7-29

Figure 7.9.1 Annual mean deciview (dv) trends (% yr<sup>-1</sup>) for (a) long-term (1990–2019) and (b) short-term (2000–2019) periods. Filled triangles correspond to statistically significant trends ( $p \leq 0.05$ ) ..... 7-30

Figure 7.9.2. Short-term (2000–2019) regional seasonal mean deciview (dv) trends (% yr<sup>-1</sup>) for major U.S. regions for winter, spring, summer, fall, and annual means. Regions are arranged from western to eastern United States (AK = Alaska, HI = Hawaii, NW = Northwest, CA= California, SW = Southwest, Cen = Central, MiS = Midsouth, NE = Northeast, SE = Southeast, VIIS = Virgin Islands, and US = all sites). Statistically significant trends ( $p \leq 0.05$ ) are denoted with “\*” ..... 7-30

Figure 7.9.3. IMPROVE long-term (1990–2019) trends (% yr<sup>-1</sup>) in (a) 10<sup>th</sup> percentile deciview (dv) and (b) 90<sup>th</sup> percentile dv. Filled triangles correspond to statistically significant trends ( $p \leq 0.05$ ) ..... 7-31

Figure 7.9.4. IMPROVE short-term (2000–2019) trends (% yr<sup>-1</sup>) in (a) 10<sup>th</sup> percentile deciview (dv) and (b) 90<sup>th</sup> percentile dv. Filled triangles correspond to statistically significant trends ( $p \leq 0.05$ ) ..... 7-31

Figure 7.9.5. Short-term (2000–2019) trends (% yr<sup>-1</sup>) trends in 10<sup>th</sup>, 50<sup>th</sup>, and 90<sup>th</sup> percentile deciview (dv). Regions are arranged from western to eastern United States (AK = Alaska, HI = Hawaii, NW = Northwest, CA= California, SW = Southwest, Cen = Central, MiS = Midsouth, NE = Northeast, SE = Southeast, VIIS = Virgin Islands, and US = all sites). Statistically significant trends ( $p \leq 0.05$ ) are denoted with “\*”..... 7-32

Figure 7.10.1. Short-term (2001-2019) timelines in IMPROVE regional, annual mean ambient speciated bext (Mm<sup>-1</sup>) for ammonium sulfate (b<sub>ext\_AS</sub>), ammonium nitrate (b<sub>ext\_AN</sub>), particulate organic matter (b<sub>ext\_POM</sub>), elemental carbon (b<sub>ext\_EC</sub>), fine dust (b<sub>ext\_FD</sub>), and coarse mass (b<sub>ext\_CM</sub>). Wavelength corresponds to 500 nm. .... 7-33

Figure 7.10.2. Split-image of visibility conditions in Great Smoky Mountains NP, Tennessee (GRSM1), for 90<sup>th</sup> percentile total extinction levels in 1990 (left side) and 2019 (right side). 7-35

Figure 7.10.3. Split-image of visibility conditions in San Gorgonio WA, California (SAGO1), for 90<sup>th</sup> percentile total extinction levels in 1990 (left side) and 2019 (right side).. 7-35

Figure 7.10.4. Split-image of visibility conditions in Yosemite NP, California (YOSE1), for 90<sup>th</sup> percentile total extinction levels in 1990 (left side) and 2019 (right side). .... 7-36

## LIST OF TABLES

Table S.2. Comparisons between monthly mean data at collocated IMPROVE and CSN sites from 2016 through 2019. Species include organic carbon (OC), elemental carbon (LAC), ammonium sulfate (AS), ammonium nitrate (AN), fine dust (FD), sea salt (SS), PM <sub>2.5</sub> gravimetric fine mass (FM), and PM <sub>2.5</sub> reconstructed fine mass (RCFM). Positive biases correspond to higher CSN concentrations.....	S-6
Table 1.1. Currently operating and discontinued IMPROVE particulate monitoring sites. Sites are grouped by region, as displayed in Figure 1.2.....	1-6
Table 1.2. Class I areas and representative monitoring sites.....	1-11
Table 1.3. Sites with a fifth collocated module.....	1-18
Table 1.4. IMPROVE nephelometer network site locations.....	1-26
Table 1.5 Web camera network site locations.....	1-28
Table 1.6. Changes and updates made to the UC Davis HIPS system.....	1-34
Table 1.7. Major networkwide changes in sampling, analysis, and data reporting affecting samples collected January 2011 and later.....	1-43
Table 1.8. Chemical Speciation Network (CSN) site location, elevation, setting and region....	1-49
Table 1.9. Comparisons between monthly mean data at collocated IMPROVE and CSN sites from 2016 through 2019. Species include organic carbon (OC), elemental carbon (EC), ammonium sulfate (AS), ammonium nitrate (AN), fine dust (FD), sea salt (SS), PM <sub>2.5</sub> gravimetric fine mass (FM), and PM <sub>2.5</sub> reconstructed fine mass (RCFM). Positive biases correspond to higher CSN concentrations.....	1-53
Table 2.1. Form of molecular species assumed in this report. Units in $\mu\text{g m}^{-3}$ unless otherwise noted.....	2-2
Table 2.2. OM/OC ratios used to calculate POM and applied in the reconstructed mass algorithm for the CSN and IMPROVE networks.....	2-3
Table 6.0. Regions and states (abbreviations) used for regional mean trends. Sites within listed states were included in the corresponding region.....	6-1

## **LIST OF APPENDICES**

Appendix 1.1. A New Cost-Effective Analytical Method for IMPROVE: Nondestructive Infrared Analysis of PTFE Filters to Measure Organic, Elemental, and Total Carbon, Inorganic Ions, Soil Elements, Organic Matter (OM), and Organic Functional Groups

Appendix 1.2. Documentation of Changes in Analytical Methods and Data Processing Due to the Chemical Speciation Network (CSN) Contractor Changes in 2015

Appendix 2.1. Monthly Varying Organic Carbon to Mass Ratio

Appendix 2.2. 2016–2019 IMPROVE and CSN Annual Mean Mass Concentrations

Appendix 2.3. 2016–2019 IMPROVE and CSN Annual Mean Mass Fraction

Appendix 3.1. 2016–2019 IMPROVE and CSN Regional, Monthly Mean Mass Concentration

Appendix 3.2. 2016–2019 IMPROVE and CSN Regional, Monthly Mean Mass Fraction

Appendix 4.1. 2016–2019 IMPROVE Monthly Humidification Factors (f(RH))

Appendix 4.2. 2016–2019 CSN Monthly Humidification Factors (f(RH))

Appendix 4.3. 2016–2019 IMPROVE and CSN Annual Mean Light Extinction Coefficients

Appendix 4.4. 2016–2019 IMPROVE and CSN Annual Mean Light Extinction Coefficients Fraction

Appendix 5.1. 2016–2019 IMPROVE and CSN Regional, Monthly Mean Reconstructed Light Extinction Coefficients

Appendix 5.2. 2016–2019 IMPROVE and CSN Regional, Monthly Mean Reconstructed Light Extinction Coefficient Fraction

Appendix 6.1. IMPROVE Annual Mean Mass Trends

Appendix 6.2. IMPROVE Short-Term (2000–2019) Mass Percentile Trends

Appendix 6.3. IMPROVE Long-Term (1990–2019) Mass Percentile Trends

Appendix 7.1. IMPROVE Annual Mean Light Extinction Coefficient Trends

Appendix 7.2. IMPROVE Short-Term (2000–2019) Light Extinction Coefficient Percentile Trends

Appendix 7.3. IMPROVE Long-Term (1990–2019) Light Extinction Coefficient Percentile Trends

Appendix 8. Regional Haze Rule Metrics

## **Executive Summary**

### **S.1 INTRODUCTION**

The Interagency Monitoring of Protected Visual Environments (IMPROVE) program is a cooperative measurement effort between the U. S. Environmental Protection Agency (EPA), federal land management agencies, and state agencies. The network is designed to

1. establish current visibility and aerosol conditions in 156 mandatory Class I areas (CIAs);
2. identify chemical species and emission sources responsible for existing anthropogenic visibility impairment;
3. document long-term trends for assessing progress towards the national visibility goal;
4. provide regional haze monitoring representing all visibility-protected federal CIAs where practical.

Although the program is focused on visibility objectives, the data acquired and the methodologies developed by the IMPROVE network have been broadly used to address air quality management related to human health, climate change, ecosystem degradation, and material damage.

This IMPROVE report is the sixth in a series that describes the monitoring methods and changes to instrumentation over time, as well as reports on measured aerosol concentrations and aerosol-derived visibility estimates. This report does not include data summaries of the network's direct atmospheric optical monitoring using nephelometers. The IMPROVE<sup>1</sup> and FED<sup>2</sup> web sites include descriptions of the aerosol, optical, and scene monitoring activities and provide access to the aerosol and optical data.

Air quality measurements in the IMPROVE network began in 1988. Due to resource and funding limitations in the early network, measurements in all 156 mandatory CIAs were not possible. Instead, 36 sites were selected to represent aerosol concentrations and visibility over the United States. The first IMPROVE report was published in 1993 and described data that were collected at the initial 36 sites from March 1988 through February 1991 (Sisler et al., 1993). Beginning with the initial report, and in the reports that followed, spatial patterns and seasonal trends in speciated aerosol concentrations and reconstructed light extinction coefficients ( $b_{ext}$ ) were presented. In addition, the first report focused on aerosol measurement quality, aerosol acidity, and transmissometer measurements. In 1996 the second IMPROVE report was published and described data from March 1992 through February 1995 from 43 sites in the network (Sisler et al., 1996). In addition to spatial and seasonal trends, the second report included an exploration of aerosol light extinction efficiencies and long-term trends in fine mass and sulfur, using stacked filter unit measurements. In 2000, the third IMPROVE report was produced that included descriptions of data from 49 sites during the period from March 1996 through February 1999 (Malm et al., 2000). This report also included a discussion of the contributions of aerosol species to periods of high and low mass concentrations. Temporal (long-

---

<sup>1</sup> The IMPROVE website (<http://vista.cira.colostate.edu/Improve/>).

<sup>2</sup> The Federal Environmental Database (FED) website (<http://views.cira.colostate.edu/fed/>).

term and diurnal) trends in visibility and aerosol concentration were also reported. The fourth report was published in 2006 and covered data from 2000 through 2004 (Debell et al., 2006). The number of sites increased to 159 due to the expansion of the network to meet the goals of the Regional Haze Rule (RHR). In addition to data from the IMPROVE sites, data from 84 sites from the EPA's Speciated Trends Network (STN) were included to expand the spatial and seasonal aerosol and  $b_{ext}$  trends to include urban areas and to investigate the differences in urban and rural aerosol concentrations. The 2006 report also included an initial investigation into the comparability of IMPROVE and STN (now Chemical Speciation Network, CSN) data. Focus was also placed on IMPROVE quality assurance procedures. In 2011 the fifth IMPROVE report was published that covered data from 2005–2008 (Hand et al., 2011), and the network consisted of 212 sites (170 current and 42 discontinued sites). Analyses of data from EPA's CSN were also included. Spatial and seasonal trends in aerosol mass and  $b_{ext}$  were reported for major aerosol species, including sea salt. The additional analyses in the fifth report included an examination of urban and rural aerosol differences (“urban excess”) and their spatial patterns using IMPROVE and CSN data. A deeper exploration of the seasonality in speciated aerosol mass concentrations and  $b_{ext}$  was also presented. With the long temporal record of IMPROVE data, “long-term” (1989–2008) and “short-term” (2000–2008) trends in speciated aerosol concentrations for seasonal and statistical parameters were explored. Descriptions of regional haze metrics, including comparisons of visibility between the RHR baseline period (2000–2004) and period 1 (2005–2009) were presented.

The sixth IMPROVE report covers analyses of data from 2016–2019. At the timing of this report, the IMPROVE network consisted of 229 sites (159 current and 70 discontinued sites). Data from the CSN were also included. Analyses of the spatial variability in aerosol mass and  $b_{ext}$  as well as regional and seasonal variability are included for major aerosol species. Long-term (1990–2019) and short-term (2000–2019) trends in speciated aerosol concentrations for annual, seasonal, and percentiles are reported. Several supporting Appendices are also included. The following summary provides highlights of the material contained in the sixth (2023) IMPROVE report; the reader is encouraged to refer to the full report for additional details.

## S.2 AEROSOL DATA

The version II IMPROVE sampler, deployed in 2000, consists of four independent modules (A, B, C, and D) that collect 24-hour samples every third day from midnight to midnight at local time and the data are reported at local conditions. Each module incorporates a separate inlet, filter pack, and pump assembly. Modules A, B, and C are equipped with a 2.5  $\mu\text{m}$  cyclone that allows for sampling of particles with aerodynamic diameters less than 2.5  $\mu\text{m}$ , while module D is fitted with a PM<sub>10</sub> inlet to collect particles with aerodynamic diameters less than 10  $\mu\text{m}$ . Each module contains a filter substrate specific to a particular chemical analysis. Module A is equipped with a PTFE (polytetrafluoroethylene) Teflon® filter (referred to as “Teflon”) that is analyzed for PM<sub>2.5</sub> gravimetric fine mass, elemental concentration, and filter light absorption. Module B is fitted with a Nylasorb (nylon) filter and analyzed for the anions sulfate, nitrate, nitrite, and chloride using ion chromatography. Module C utilizes a quartz fiber filter that are analyzed by thermal optical analysis (TOA) for organic and elemental carbon (Chow et al., 1993). Finally, module D utilizes a Teflon filter that is analyzed for PM<sub>10</sub> gravimetric mass.

Details regarding aerosol sampling and analyses are in Chapter 1. IMPROVE data are available for download from the Federal Environmental Database (FED, <http://views.cira.colostate.edu/fed/>). Current and discontinued IMPROVE sites are listed by region in Table 1.1 in Chapter 1. A map of IMPROVE sites (grouped by region) is shown in Figure S.2.1.

CSN data were also used extensively in this report. CSN sites are operated by state, local, and tribal agencies, primarily in urban/suburban settings (Solomon et al., 2014). All CSN samplers utilize a PM<sub>2.5</sub> inlet and three channels containing Teflon, nylon, and quartz filters. Like the IMPROVE network, CSN samplers operate on a 24-hour schedule from midnight to midnight every third or sixth day. Elemental compositions are analyzed from the Teflon filter, ions from the nylon filter, and carbon from the quartz filter. CSN stopped analyzing PM<sub>2.5</sub> gravimetric mass beginning in 2014, and collocated data from EPA Federal Reference Method (FRM) sites were used. IMPROVE and CSN sampling and analysis methods for each species are provided in Chapter 1 and discussions of aerosol species mass calculations are in Chapter 2. A map of CSN sites is provided in Figure S.2.2. A subset of these sites was used in this report, based on completeness criteria outlined in Chapter 2.

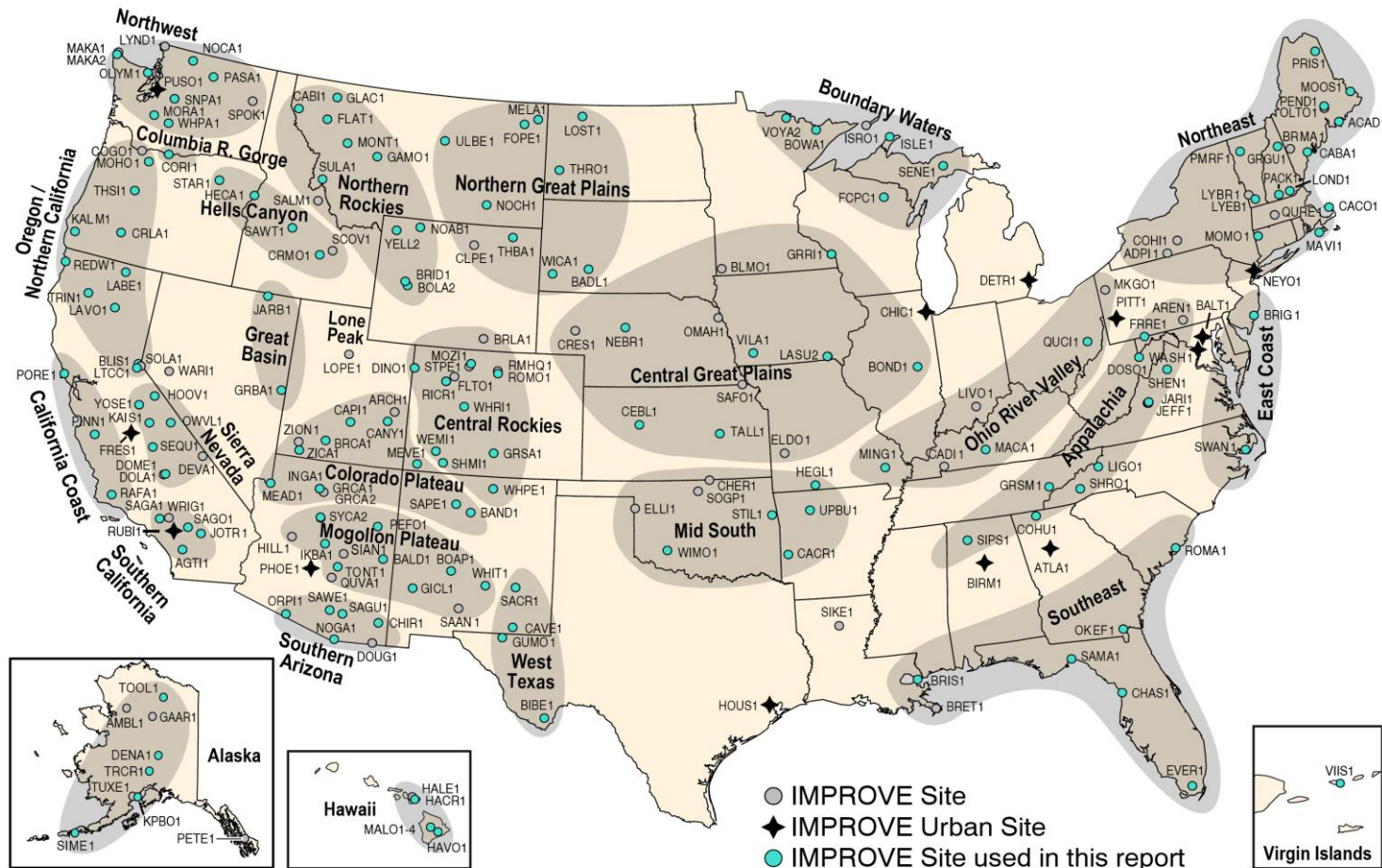
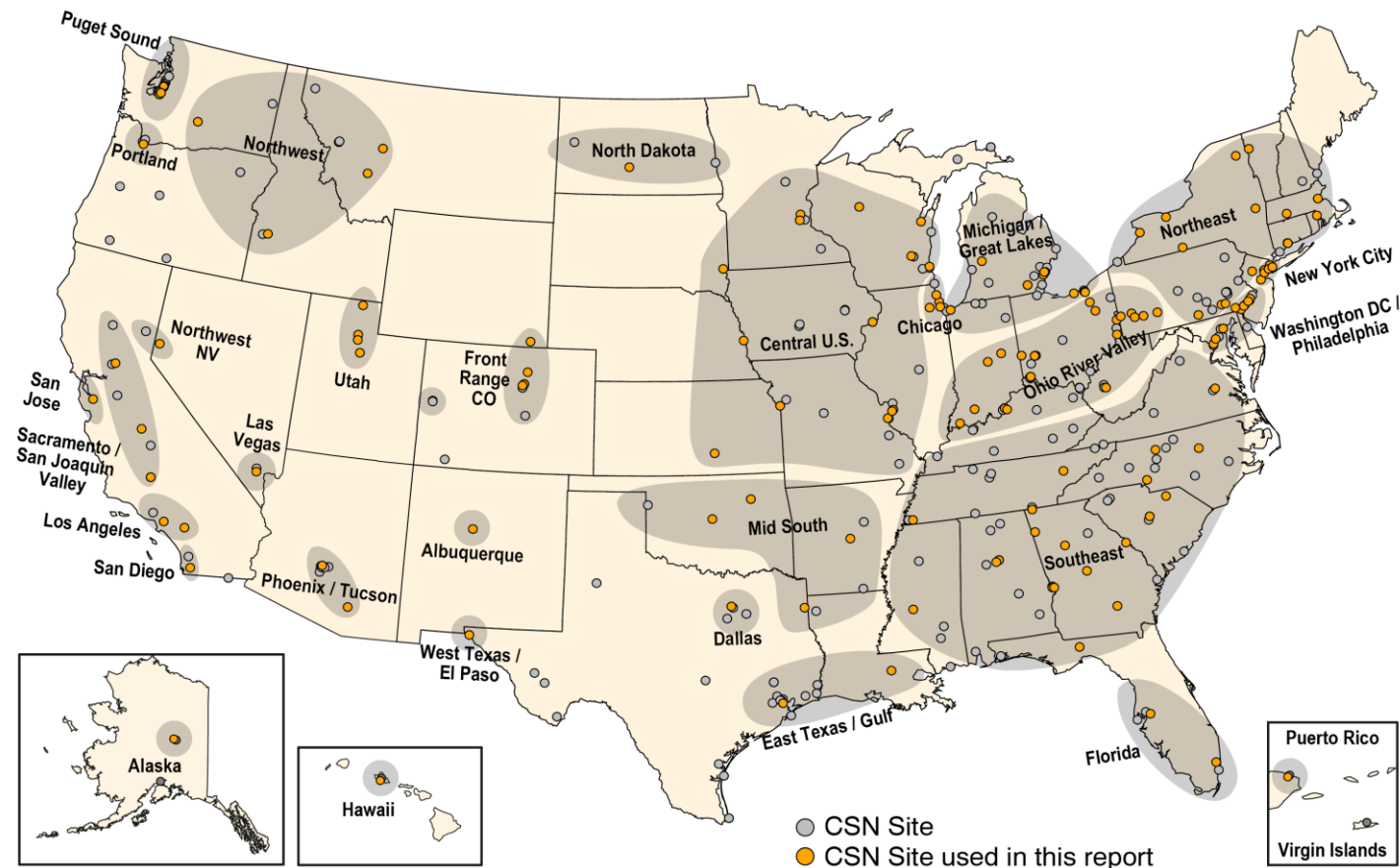


Figure S.2.1. Locations of IMPROVE sites for all discontinued and current sites. IMPROVE regions are indicated by shading and bold text. Urban IMPROVE sites are identified by stars. Blue circles indicate sites with data used in the analyses in this report.



**Figure S.2.2. Current and discontinued Chemical Speciation Network (CSN) sites (grey and orange) operated by the Environmental Protection Agency. Regions are shown as shaded areas and bold text. Sites included in the analyses in this report are shown as orange circles.**

The IMPROVE and CSN networks operate collocated samplers in several urban/suburban sites. Collocated sites with data that met the completeness criteria outlined in Chapter 2 were compared to identify relative biases between IMPROVE and CSN speciated aerosol concentrations. Monthly mean data from Birmingham, Alabama; Fresno, California; Phoenix, Arizona; and Puget Sound, Washington, for 2016–2019 were compared for ammonium sulfate (AS), ammonium nitrate (AN), organic carbon (OC), elemental carbon (EC), fine dust (FD), sea salt (SS), PM<sub>2.5</sub> gravimetric fine mass (FM), and reconstructed fine mass (RCFM, the sum of PM<sub>2.5</sub> species). Descriptions of species mass concentrations calculations are listed in Table 2.1 in Chapter 2. Table S.2 provides comparison statistics. Errors were less than 20% for most species, with the exception of FD (21%) and SS (85%). IMPROVE SS concentrations were computed using chloride ion concentrations ( $1.8 \times \text{Cl}^-$ ), whereas CSN SS concentrations were computed using chlorine concentrations ( $1.8 \times \text{Cl}$ ) from (X-ray fluorescence) XRF analysis. CSN began reporting chloride concentrations in February 2017. Errors for EC were 19%, in part due to changes in TOA for CSN. Biases were typically within  $\pm 15\%$ , except for a -20% bias in FD (IMPROVE higher), -81% bias in SS (IMPROVE higher), and 21% bias in EC (CSN higher). Higher biases and errors associated with coarse-mode species may be due in part to differences in the sharpness of the cut points between IMPROVE and CSN samplers, with sharper CSN cut points resulting in lower concentrations, because less of the tail of the coarse-mode species is collected on the PM<sub>2.5</sub> filter. Additional comparisons between IMPROVE and CSN data are described in Gorham et al. (2021).

**Table S.2. Comparisons between monthly mean data at collocated IMPROVE and CSN sites from 2016 through 2019. Species include organic carbon (OC), elemental carbon (LAC), ammonium sulfate (AS), ammonium nitrate (AN), fine dust (FD), sea salt (SS), PM<sub>2.5</sub> gravimetric fine mass (FM), and PM<sub>2.5</sub> reconstructed fine mass (RCFM, sum PM<sub>2.5</sub> species). Positive biases correspond to higher CSN concentrations.**

Statistic	OC	EC	AS <sup>3</sup>	AN <sup>4</sup>	FD	SS <sup>5</sup>	FM	RCFM
Average IMPROVE ( $\mu\text{g m}^{-3}$ )	2.36	0.69	1.21	1.44	1.21	0.24	8.58	9.04
Average CSN ( $\mu\text{g m}^{-3}$ )	2.59	0.84	1.15	1.40	0.90	0.05	9.42	9.01
Bias <sup>1</sup> (%)	11	21	-6	-6	-20	-81	9	-1
Error <sup>2</sup> (%)	11	19	6	8	21	85	10	4
r	0.99	0.97	0.99	1.00	0.96	0.71	0.97	0.99
IMP/CSN	0.91	0.82	1.06	1.03	1.34	4.75	0.91	1.00

$$^1 \text{Error} = \text{median}\left(\left|\frac{\bar{X}_i - \bar{Y}_i}{\bar{Y}_i}\right|\right)$$

$^2 \text{Bias} = \frac{1}{N} \sum_i \frac{\bar{X}_i - \bar{Y}_i}{\bar{Y}_i}$ ;  $\bar{X}_i$  and  $\bar{Y}_i$  are the daily data for CSN and IMPROVE concentrations, respectively. The number of data points is given by N.

<sup>3</sup>AS =  $1.375 \times [\text{sulfate ion}]$

<sup>4</sup>AN =  $1.29 \times [\text{nitrato ion}]$

<sup>5</sup>Sea salt =  $1.8 \times [\text{chloride ion}]$  for IMPROVE and  $1.8 \times [\text{chlorine}]$  for CSN.

### S.3 SPATIAL PATTERNS IN RURAL AND URBAN SPECIATED ANNUAL MEAN AEROSOL CONCENTRATIONS

Data from 153 IMPROVE and 136 CSN sites that met completeness criteria were combined to explore the spatial variability in the 2016–2019 annual mean concentrations in

major aerosol species. Shown here is a summary of the results in Chapter 2, including spatial variability for AS, AN, particulate organic matter (POM), calculated from OC and a monthly (IMPROVE) or seasonal (CSN) varying organic carbon to organic mass ratio (OM/OC) (POM = (OM/OC) × OC), EC, SS, FD, FM, and coarse mass (CM = PM<sub>10</sub> - PM<sub>2.5</sub>). Urban PM<sub>2.5</sub>, PM<sub>10</sub>, and CM were obtained from the EPA FRM network sites. Maps of interpolated annual mean mass concentrations were created for each species for IMPROVE data alone, and for combined IMPROVE and CSN data. Isopleth maps created using a Kriging algorithm (Isaaks and Mohan Srivastava, 1989) should be viewed and interpreted with caution, as these maps are intended only to help visualize the data and identify large spatial patterns. Maps and discussions of fractional contributions from each PM<sub>2.5</sub> species to RCFM can be found in Chapter 2.

### S.3.1 Ammonium Sulfate

The spatial distribution of AS with the rural IMPROVE sites alone (Figure S.3.1a) was very similar to the pattern of the rural and urban (CSN) sites combined (Figure S.3.1b), suggesting that regional impacts of AS concentrations similarly influenced both urban and rural sites. Notice the difference in site density between the IMPROVE and CSN networks in Figure S.3.1.b, with many more CSN sites in the eastern United States; these sites provide additional detail to the spatial patterns of AS in that section of the country. The combination of high sulfur dioxide (SO<sub>2</sub>) emissions and high relative humidity produced the highest concentrations (2-3  $\mu\text{g m}^{-3}$ ) of AS in the eastern United States that centered on the Ohio River valley and Mid-south areas. AS concentrations decreased sharply towards the western United States. In fact, concentrations in the western United States were typically less than 1  $\mu\text{g m}^{-3}$ , with the lowest concentrations at sites in the Northwest, Montana, and Idaho. Lower concentrations in the West reflected lower SO<sub>2</sub> emissions that lead to secondary particulate AS.

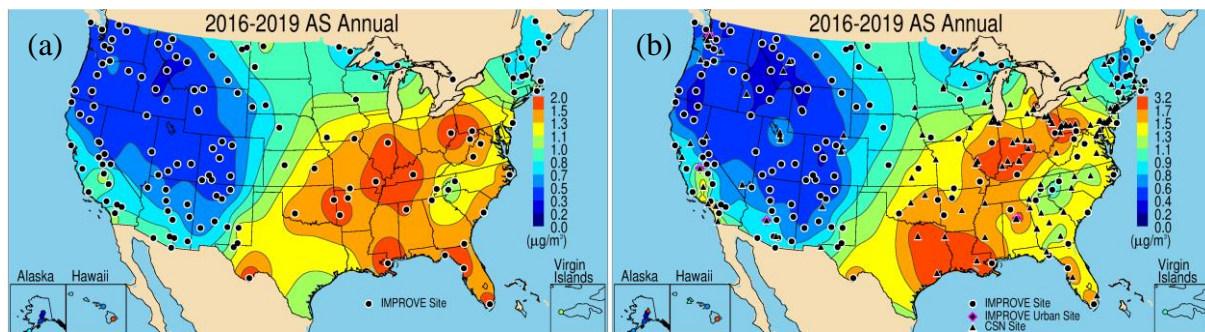


**Figure S.3.1. 2016–2019 PM<sub>2.5</sub> ammonium sulfate (AS) annual mean mass concentrations ( $\mu\text{g m}^{-3}$ ) for (a) IMPROVE and (b) IMPROVE and CSN.**

### S.3.2 Ammonium Nitrate

Higher sources of precursors to AN in agricultural regions in the Midwest resulted in the highest AN concentrations (~2  $\mu\text{g m}^{-3}$ ) for rural sites in the United States (Figure S.3.2a). Generally, urban concentrations of AN were considerably higher than rural concentrations (Figure S.3.2b). Central and southern California were also associated with higher AN concentrations, as were sites in northern North Dakota, with concentrations near 1.0  $\mu\text{g m}^{-3}$ . High concentrations in North Dakota may be associated with oil and gas energy development (Prenni

et al., 2016; Evanoski-Cole et al., 2017; Gebhart et al., 2018). Concentrations were much lower outside of the central United States, especially in the Intermountain West and Northwest, with concentrations less than  $0.5 \mu\text{g m}^{-3}$ . Similarly low annual mean concentrations were observed at sites in the Southeast and Northeast. The inclusion of CSN sites provided more spatial resolution to the rural AN spatial pattern and showed the impact of urban AN concentrations on surrounding areas. High annual mean AN concentrations were associated with urban sites near Lake Michigan, and other hot spots near Denver, Colorado and Salt Lake City, Utah.

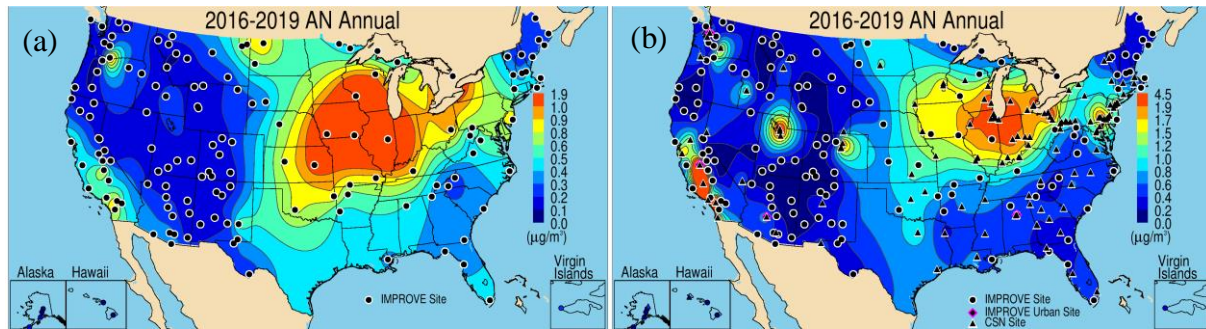


**Figure S.3.2.** 2016–2019 PM<sub>2.5</sub> ammonium nitrate (AN) annual mean mass concentrations ( $\mu\text{g m}^{-3}$ ) for (a) IMPROVE and (b) IMPROVE and CSN.

### S.3.3 Particulate Organic Matter

The highest 2016–2019 annual mean rural IMPROVE POM concentrations occurred at sites in southern Florida, the northwestern United States, and central and northern California due to the influence of biomass burning (Figure S.3.3a). Elevated levels of POM ( $\sim 3.0 \mu\text{g m}^{-3}$ ) also occurred at sites in the Southeast, as well as portions of the Northwest and California. The 2016–2019 period was associated with high fire activity, especially 2017 and 2018 in the Northwest and 2016 in the Southeast. The combined urban and rural POM concentrations demonstrated the influence of urban POM sources, with higher concentrations at sites in the Southeast and along the Central Valley of California (Figure S.3.3b). Sites in Alabama, Georgia, South Carolina, and North Carolina had POM concentrations greater than  $4.0 \mu\text{g m}^{-3}$ . Similar maximum annual mean rural and urban POM concentrations demonstrated the influence of biomass burning on rural POM concentrations.

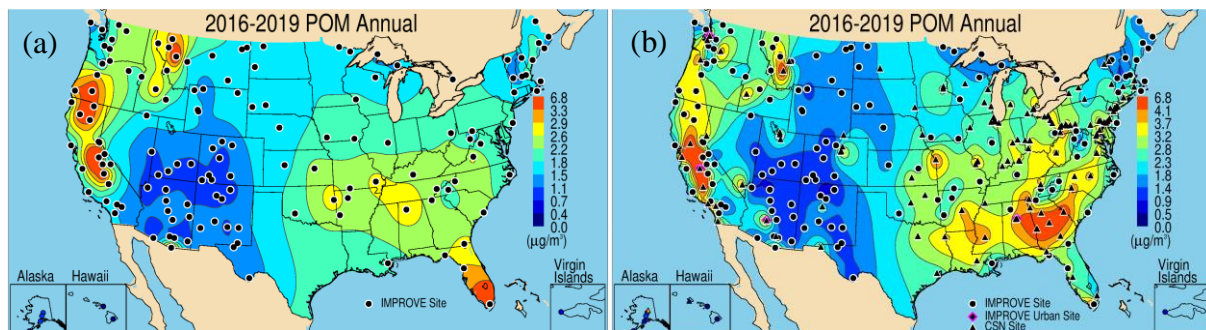


**Figure S.3.3.** 2016–2019 PM<sub>2.5</sub> particulate organic matter (POM) annual mean mass concentrations ( $\mu\text{g m}^{-3}$ ) for (a) IMPROVE and (b) IMPROVE and CSN.

### S.3.4 Elemental Carbon

The IMPROVE rural 2016–2019 annual mean EC concentrations were higher at sites in California and the Northwest ( $\sim 0.25 \mu\text{g m}^{-3}$ ), and at sites in the central and eastern United States ( $> 0.25 \mu\text{g m}^{-3}$ ; see Figure S.3.4a). Urban CSN EC concentrations were generally higher than at IMPROVE sites (Figure S.3.4b). Regionally, urban EC concentrations were highest at sites in the East; however, most impacts of EC were local in extent. Several hot spots occurred in major urban areas, for example, at sites in Colorado, Montana, and Nevada, and several sites in the Central Valley of California. The urban hot spots were indicative of local urban EC emissions (e.g., mobile sources or local residential wood burning) rather than regional sources like biomass combustion from controlled or wild fires. The steep spatial gradient surrounding the hot spots of EC in Figure S.3.4b indicated that the spatial extent of the impact was small and concentrations diluted quickly before they had regional impacts.

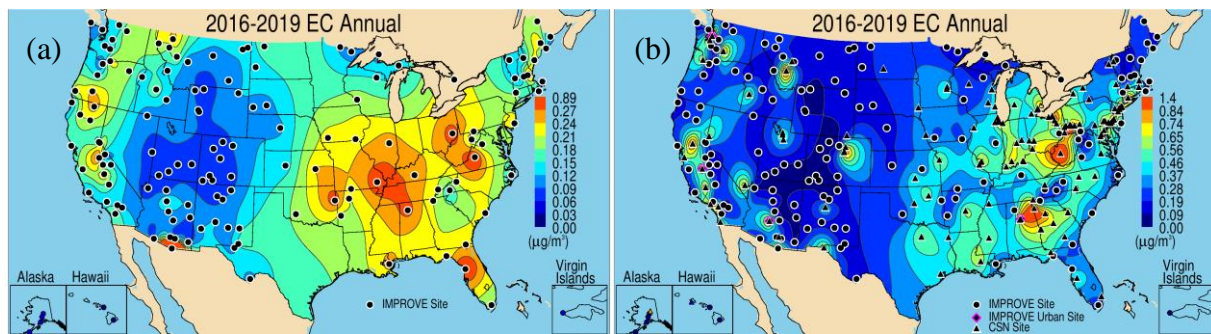
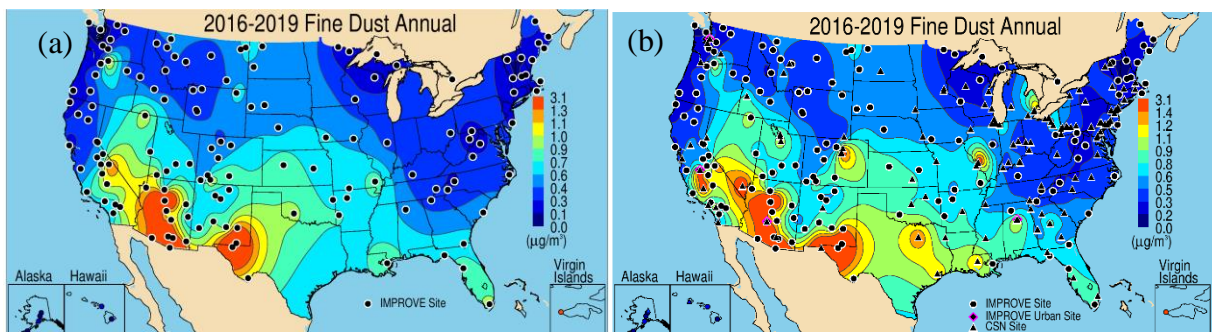


Figure S.3.4. 2016–2019 PM<sub>2.5</sub> elemental carbon (EC) annual mean mass concentrations ( $\mu\text{g m}^{-3}$ ) for (a) IMPROVE and (b) IMPROVE and CSN.

### S.3.5 Fine Dust

The patterns observed in the 2016–2019 annual mean rural IMPROVE FD concentrations were reflective of dominant seasons of elevated FD concentrations, namely the Southwest during spring and the Southeast during summer (Hand et al., 2017). Concentrations at sites around Arizona ranged from  $1.3$  to  $3.1 \mu\text{g m}^{-3}$ . Sites around the Colorado Plateau as well as sites in southern New Mexico and western Texas had annual mean concentrations near  $1 \mu\text{g m}^{-3}$  (see Figure S.3.5a). Unlike other species with spatial gradients along the east/west orientation, gradients in FD concentrations extended north/south. The concentrations at northern sites tended to be lower ( $\sim 0.5 \mu\text{g m}^{-3}$ ). Although the CSN FD concentrations were biased low relative to IMPROVE concentrations, the spatial patterns in combined urban and rural FD generally agreed, with higher concentrations at sites in the Southwest (Figure S.3.5b). There were several urban hot spots with elevated FD concentrations, such as sites in Colorado, Nevada, Missouri, and Texas. Sites in the Central Valley of California had higher FD concentrations relative to surrounding areas.



**Figure S.3.5.** 2016–2019 PM<sub>2.5</sub> fine dust (FD) annual mean mass concentrations ( $\mu\text{g m}^{-3}$ ) for (a) IMPROVE and (b) IMPROVE and CSN.

### S.3.6 Sea Salt

The IMPROVE sites with the highest 2016–2019 annual mean SS concentrations were along coastal regions ( $\sim 2 \mu\text{g m}^{-3}$ , Figure S.3.6a). Outside of coastal regions, SS concentrations were low ( $<0.10 \mu\text{g m}^{-3}$ ). The spatial patterns were generally similar when aggregating IMPROVE and CSN data (Figure S.3.6b), even with the bias between IMPROVE and CSN SS concentrations.

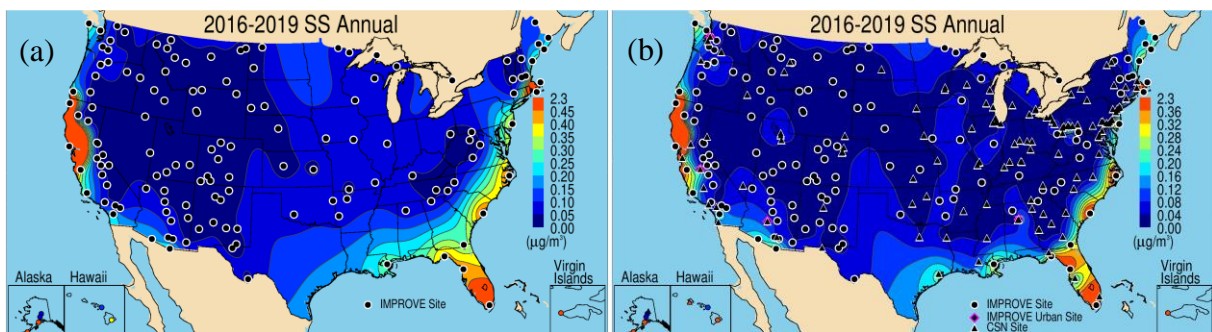


**Figure S.3.6.** 2016–2019 PM<sub>2.5</sub> sea salt (SS) annual mean mass concentrations ( $\mu\text{g m}^{-3}$ ) for (a) IMPROVE and (b) IMPROVE and CSN.

### S.3.7 PM<sub>2.5</sub> Gravimetric Mass

The spatial pattern of 2016–2019 annual mean IMPROVE FM concentrations reflected the combined patterns of annual mean concentrations of AS, AN, and POM (see Figure S.3.7a). Sites in the central and eastern United States had relatively high annual mean FM concentrations ( $\sim 5–6 \mu\text{g m}^{-3}$ ). In addition, sites in California’s Central Valley had higher concentrations. The lowest FM concentrations occurred in the Intermountain West. The urban FM concentrations were somewhat higher than the IMPROVE concentrations, especially at sites in the central and eastern United States (Figure S.3.7b). High annual mean urban FM was also observed at sites in the Central Valley of California, where the highest urban annual mean FM ( $\sim 13 \mu\text{g m}^{-3}$ ) occurred. Several hot spots of annual mean FM occurred at urban sites across the West, such as sites in Colorado, Texas, Utah, Montana, and Washington.

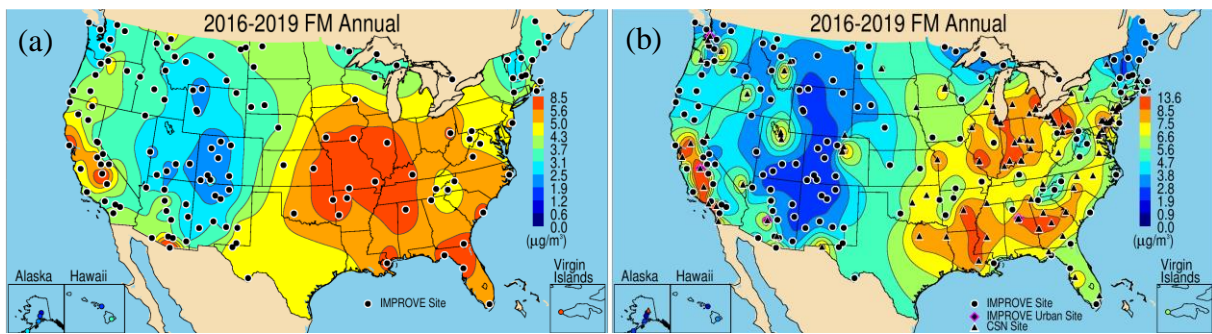


**Figure S.3.7.** 2016–2019 PM<sub>2.5</sub> gravimetric annual mean fine mass (FM) concentrations ( $\mu\text{g m}^{-3}$ ) for (a) IMPROVE and (b) IMPROVE and CSN.

### S.3.8 Coarse Mass

The spatial patterns of CM in the Southwest were similar to those of FD and suggest similar sources (Hand et al., 2017). Higher concentrations also occurred at sites in the California’s Central Valley (Figure S.3.8a). At sites in the central United States, higher concentrations most likely corresponded to agricultural activity and fugitive dust sources (Hand et al., 2019a; Lambert et al., 2020). Lower annual mean CM concentrations occurred at sites across the Intermountain West, the Northwest, and along the eastern United States into the Northeast. The overall spatial patterns in urban annual mean CM concentrations (Figure S.3.8b) were similar to those at rural sites, with higher values at sites in the central United States and along the U.S.–Mexico border and California’s Central Valley.

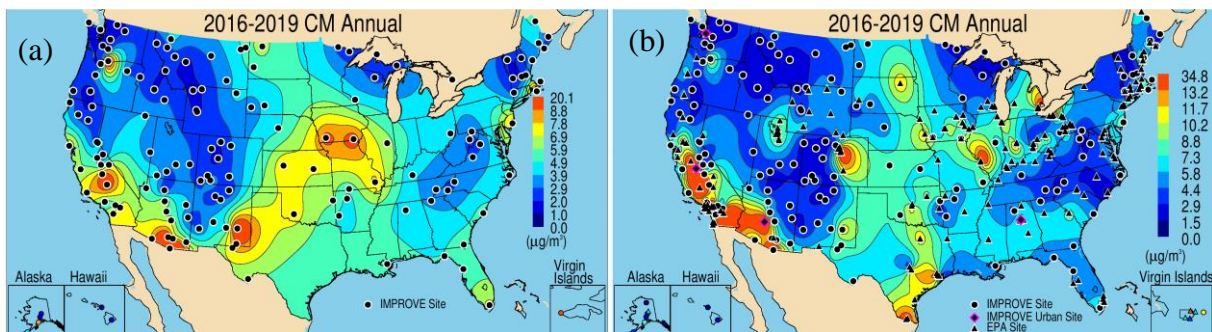


**Figure S.3.8.** 2016–2019 annual mean gravimetric coarse mass (CM = PM<sub>10</sub> - PM<sub>2.5</sub>) ( $\mu\text{g m}^{-3}$ ) for (a) IMPROVE and (b) IMPROVE and EPA.

### S.3.9 Discussion

The spatial variability of FM depends on sources, sinks, and transport of speciated aerosols. A strong spatial gradient in FM was observed, with higher concentrations at sites in the eastern United States. FM decreased rapidly moving westward, with concentrations that were half of those at sites in the East, especially for sites in the Intermountain West. Higher concentrations occurred at sites in California and sites in Oregon and Washington. The spatial patterns did not change significantly with the addition of urban sites, although urban concentrations were higher, including several hot spots at sites in the West, and at sites in the Central Valley of California. The lowest concentrations of annual mean FM occurred at sites in the Intermountain West and Southwest and at sites in the Northeast.

The spatial patterns of FM reflected the combined patterns of AS, AN, and POM. AS concentrations were highest in the eastern United States, where SO<sub>2</sub> emissions were highest, and AS contributed approximately 30% to FM in those regions. Rural annual man AN concentrations were highest at sites in the central United States and contributed 20%-30% to FM at sites in that region. Additional urban sources influenced urban FM sites in the Central Valley of California, as well as other urban hot spots in the West.

Rural POM concentrations were highest at sites in the northwestern United States, where biomass smoke impacts influenced concentrations, and at sites in the eastern United States, due to biogenic emissions and biomass smoke. The lowest annual mean POM concentrations occurred at sites in the Intermountain West and Southwest. The general spatial patterns of urban and rural POM concentration were similar to rural-only patterns, although higher urban concentrations occurred at sites in Southeast and Central Valley. Contributions of POM to RCFM were significant at sites in the western United States, around 70% or greater, and this contribution was similar for CSN sites. At sites in the eastern United States, contributions at CSN sites was around 60% or greater, while for rural sites it was around 50%. Annual mean EC concentrations followed similar patterns to those of POM concentrations at rural sites, with higher concentrations at sites both in the eastern and northwestern United States. Urban EC concentrations were considerably higher than at rural sites, indicating the importance of localized urban sources. Contributions of EC to RCFM at urban sites were roughly double relative to at rural sites (~10% compared to ~5%, respectively).

The spatial pattern of FD reflected its source areas, with high concentrations at both rural and urban sites in the Southwest, where local and regional sources affect FD concentrations. Sites in the Central Valley also had high FD concentrations, especially for urban sites. Higher annual mean FD at sites in the Southeast reflected the influence of North African dust transport to that area, both for rural and urban sites. FD contributions to RCFM at sites in the Southwest were over 50% for many sites in the region. The spatial variability in annual mean CM was similar to FD, especially for sites in the Southwest, suggesting similar sources. However, higher annual mean CM at sites in the central United States, relative to FD patterns, suggested additional sources of coarse-mode aerosol or larger size distributions of FD relative to the Southwest. Urban sites with high CM concentrations occurred in the Central Valley and southern Arizona. CM contributed significantly to PM<sub>10</sub>, especially at sites in the western United States, where annual mean contributions were over 60%. For sites in the eastern United States, the contribution of CM to PM<sub>10</sub> was ~30-40%. Similar contributions occurred for sites in the Northwest.

SS concentrations, while likely underestimated, also followed suspected marine sources, with higher values along coastal areas for both IMPROVE and CSN sites. SS contributions could be significant (>10%) at some sites, especially in Alaska and Hawaii, and along the coasts.

#### S.4 SEASONAL DISTRIBUTIONS IN AEROSOL MASS CONCENTRATIONS

The seasonality of speciated aerosol mass concentrations can be significant depending on species and region and is a function of the source emissions, meteorological parameters, formation processes, and local and long-range transport. Examining aerosol concentrations on a

regional basis, rather than a site-specific basis, can lead to insights regarding air quality issues on regional scales.

IMPROVE and CSN data from 2016 through 2019 were regionally and monthly averaged (see Chapter 3) and plotted as stacked bar charts on maps of three areas of the United States (i.e., East, Northwest, and Southwest). The monthly mean concentrations of PM<sub>2.5</sub> species included AS, AN, POM, EC, FD, and SS. Stacked bar charts provide a detailed view of the changes in monthly mean aerosol concentrations during the year at different regions in the United States. Highlights in seasonality of mass concentrations for IMPROVE and CSN concentrations are included here; additional detail, including regional mass fractions, are provided in Chapter 3.

#### S.4.1 Ammonium Sulfate

In most of the regions in the eastern United States, regional mean AS concentrations rarely exceeded 2  $\mu\text{g m}^{-3}$  year round (Figure S.4.1). In addition, the monthly variability of AS was flat, with a small increase in summer months in some regions (e.g., MidSouth and East Coast). Monthly mean concentrations in regions in the northwestern United States were lower than in the eastern United States (typically  $<1 \mu\text{g m}^{-3}$ ) and had little seasonal variability (see Figure S.4.2). The highest mean AS concentrations in regions in the northwestern United States occurred in the Northern Great Plains and Columbia River Gorge regions, where concentrations approached 1  $\mu\text{g m}^{-3}$ . AS concentrations in the regions of the southwestern United States (Figure S.4.3) were generally  $<2 \mu\text{g m}^{-3}$  and demonstrated more of a summer peak (e.g., Southern California, Southern Arizona, and West Texas regions). Low monthly mean concentrations ( $<1 \mu\text{g m}^{-3}$ ) were observed in the Great Basin, Colorado Plateau, and Central Rockies regions. In the Hawaii region, monthly mean AS concentrations were  $>1 \mu\text{g m}^{-3}$  for most months of the year.

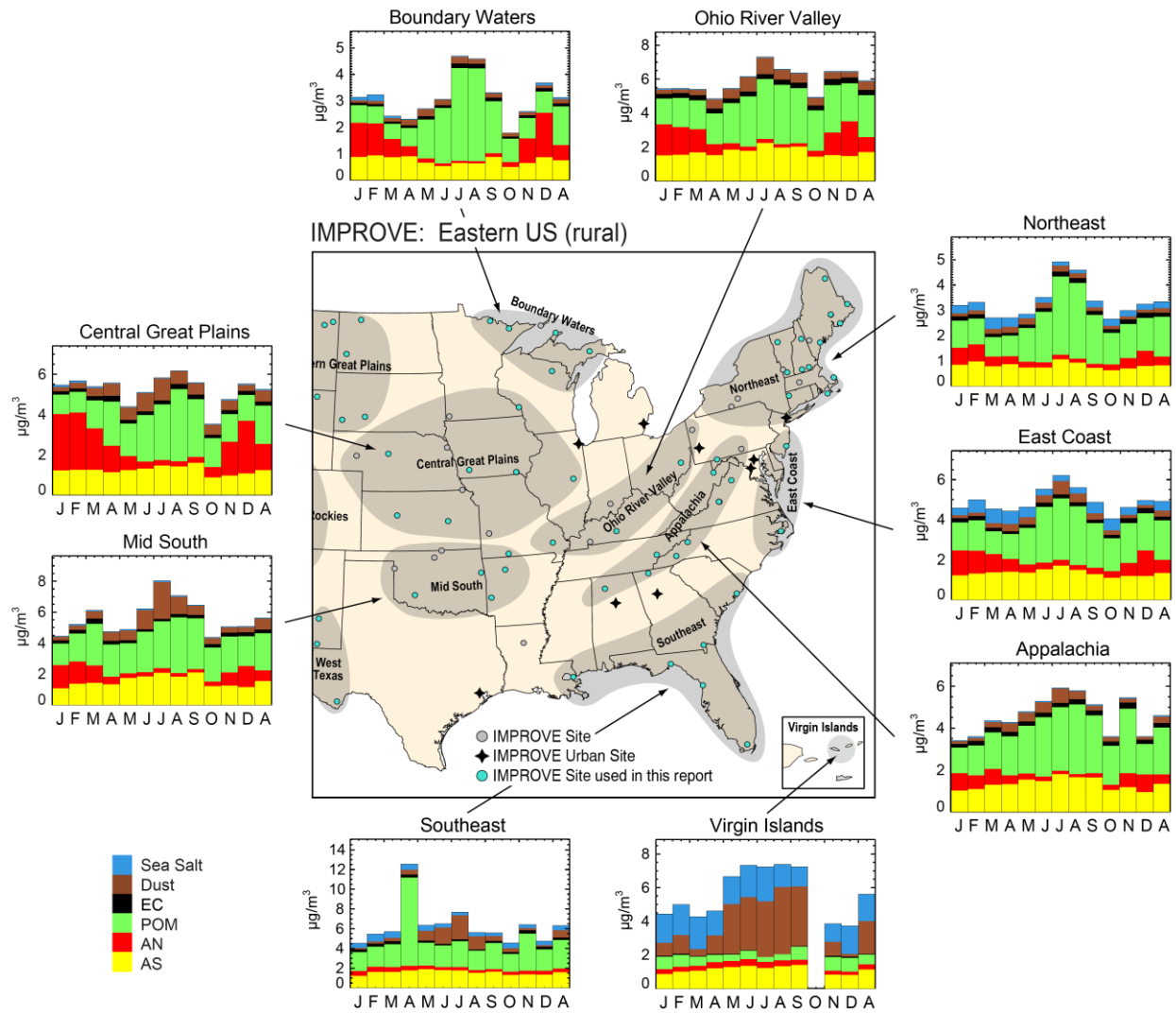


**Figure S.4.1. IMPROVE 2016–2019 regional monthly mean PM<sub>2.5</sub> mass concentrations (µg m<sup>-3</sup>) for the eastern United States. Letters on the x-axis correspond to month and “A” corresponds to annual mean. Shaded areas in the map correspond to regions that include the sites used in the analysis, shown as blue dots.**

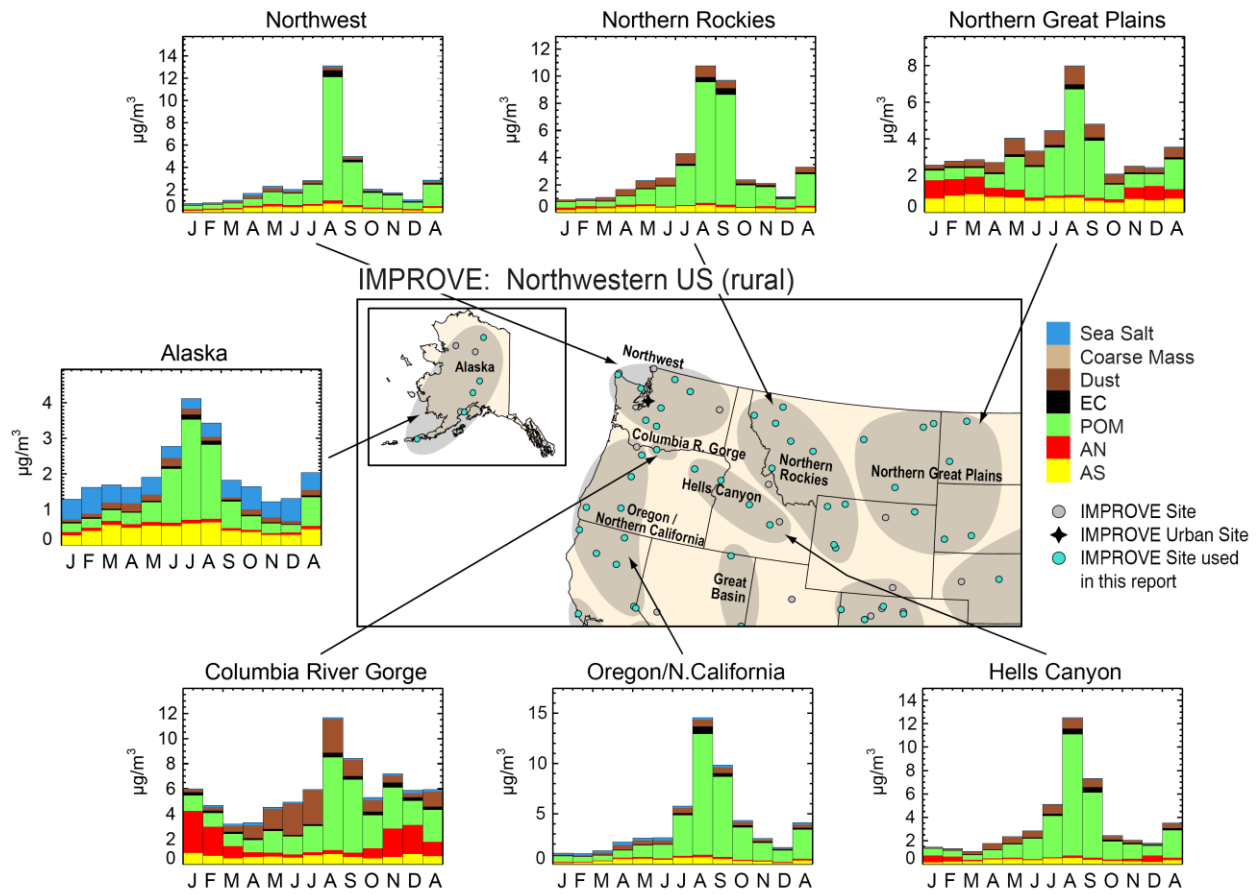


**Figure S.4.2. IMPROVE 2016–2019 regional monthly mean PM<sub>2.5</sub> mass concentrations (µg m<sup>-3</sup>) for the northwestern United States. Letters on the x-axis correspond to month and “A” corresponds to annual mean. Shaded areas in the map correspond to regions that include the sites used in the analysis, shown as blue dots.**

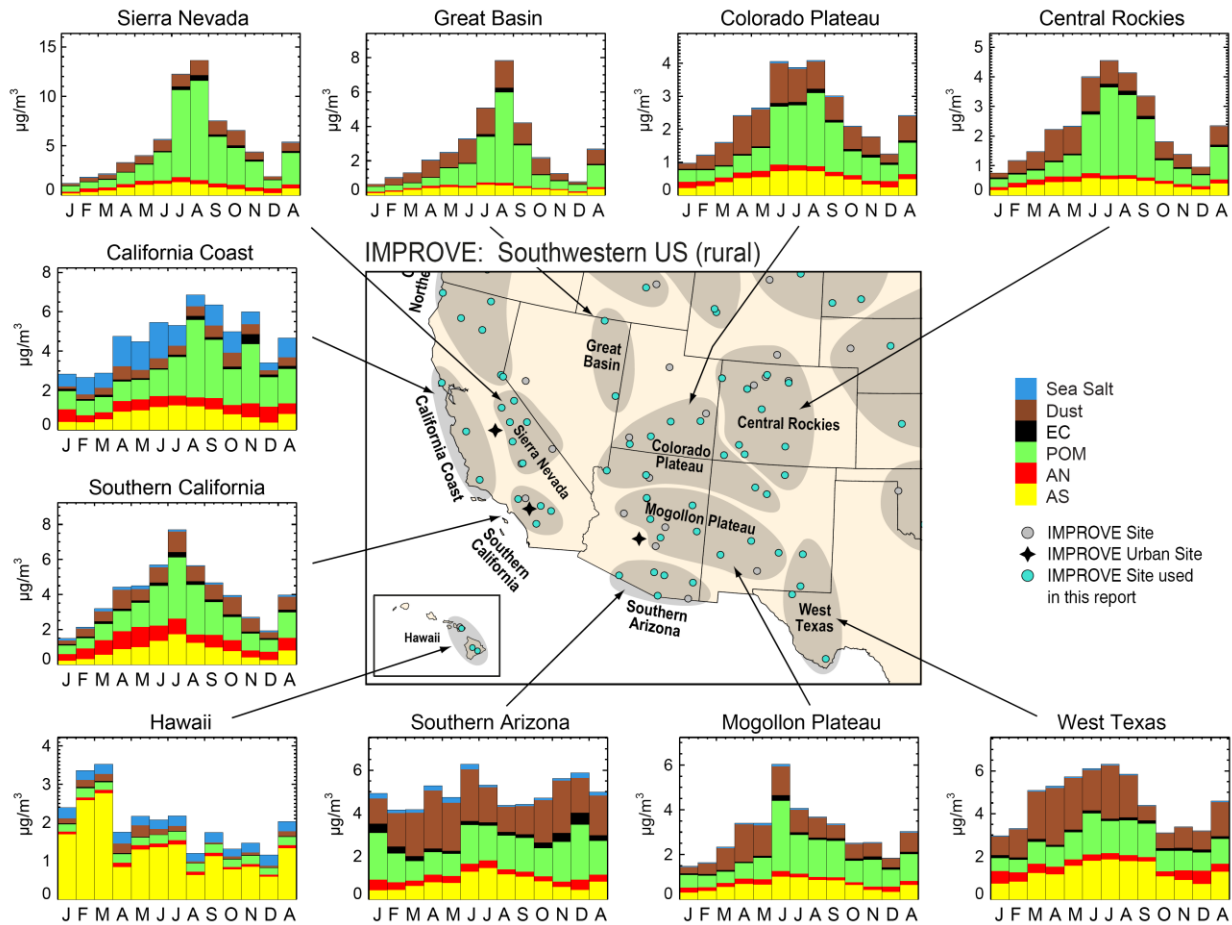


**Figure S.4.3. IMPROVE 2016–2019 regional monthly mean  $\text{PM}_{2.5}$  mass concentrations ( $\mu\text{g m}^{-3}$ ) for the southwestern United States. Letters on the x-axis correspond to month and “A” corresponds to annual mean. Shaded areas in the map correspond to regions that include the sites used in the analysis, shown as blue dots.**

Similar to the IMPROVE regions, in CSN regions AS monthly mean concentrations in the eastern United States rarely reached above  $2 \mu\text{g m}^{-3}$  (see Figure S.4.4). The similarity in seasonal patterns of AS concentrations in the eastern United States pointed to regional sources of AS that influence both urban and rural regions. In addition, the seasonal variability was low, with mostly flat monthly mean concentrations year round. Monthly mean AS concentrations were generally low ( $<1.5 \mu\text{g m}^{-3}$ ) for CSN regions in the northwestern United States (Figure S.4.5) and were seasonally flat, similar to IMPROVE monthly mean concentrations. The exception was the Alaska region, with maximum monthly mean concentrations during cold months. The regional monthly mean AS concentrations in the southwestern United States were generally low ( $<2.0 \mu\text{g m}^{-3}$ ) in most regions but with more seasonal variability than in the eastern United States (Figure S.4.6). Summer maxima were observed for many regions, such as in the Phoenix/Tucson, Albuquerque, Las Vegas, and West Texas regions. The strongest seasonal variability occurred in the Los Angeles and San Diego regions with summer maxima. These patterns also occurred for IMPROVE regions. The Hawaii region experienced some seasonal variability with winter maxima.

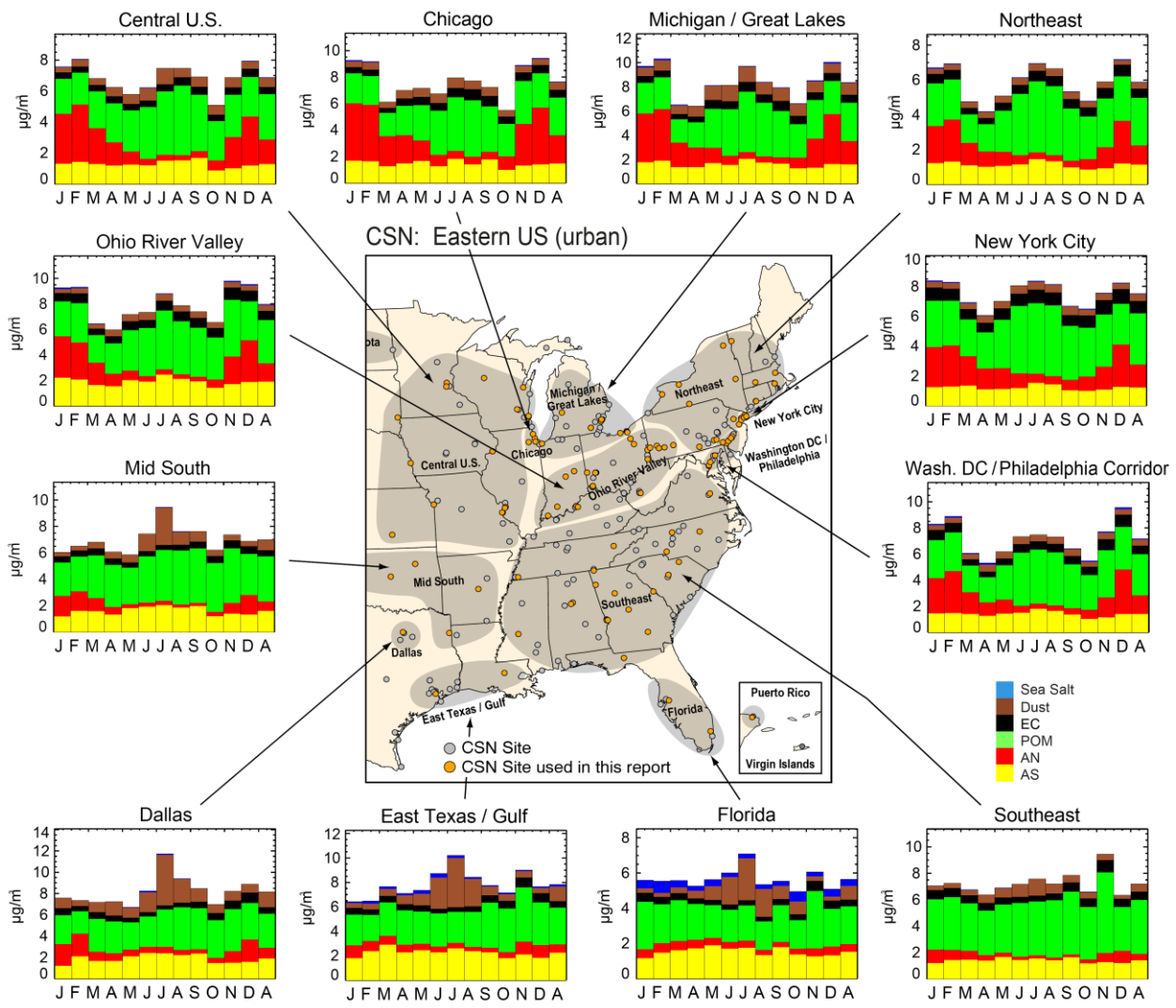


**Figure S.4.4. CSN 2016–2019 regional monthly mean PM<sub>2.5</sub> mass concentrations (µg m<sup>-3</sup>) for the eastern United States. Letters on the x-axis correspond to month and “A” corresponds to annual mean. Shaded areas in the map correspond to regions that include the sites used in the analysis, shown as orange dots.**

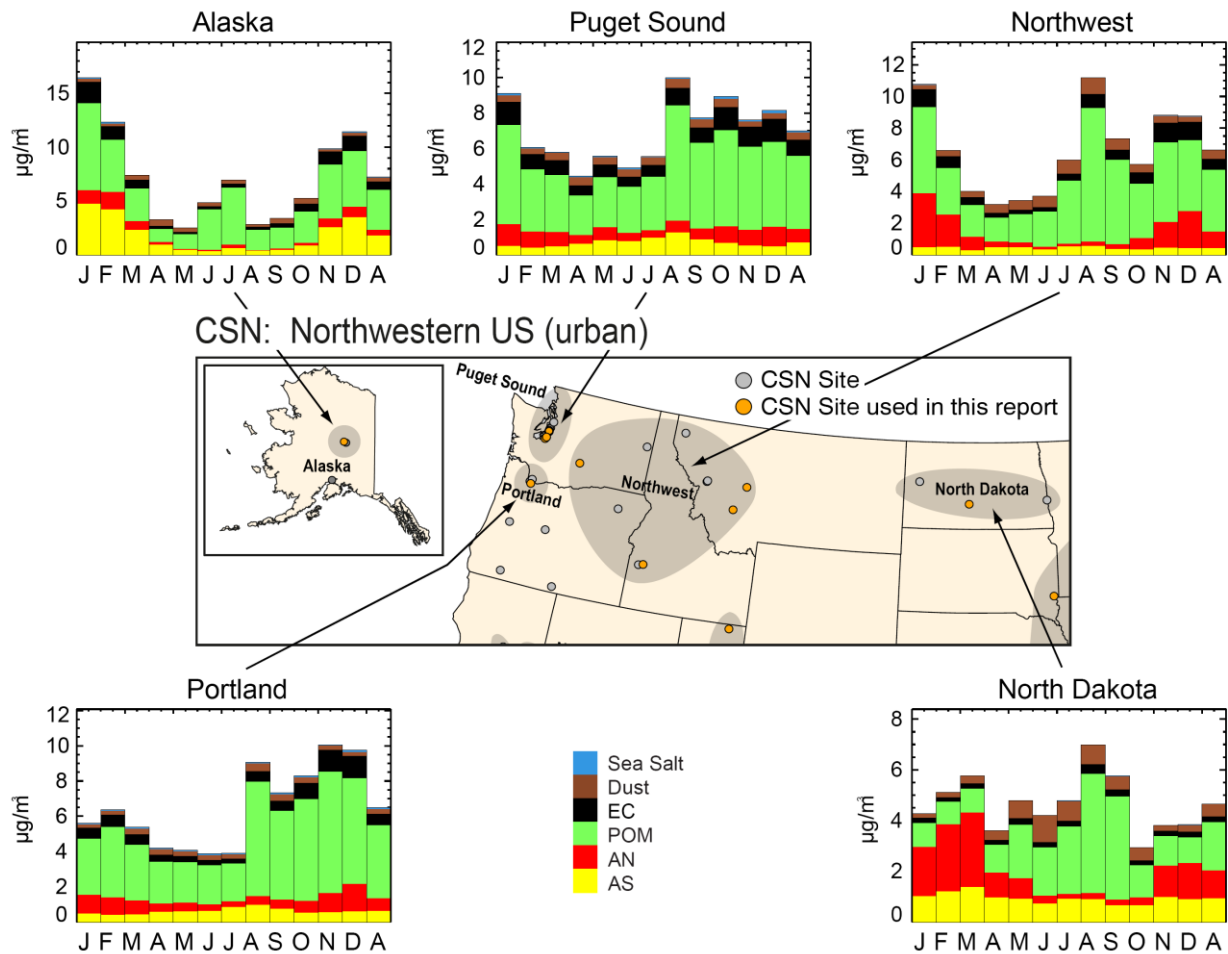


**Figure S.4.5. CSN 2016–2019 regional monthly mean PM<sub>2.5</sub> mass concentrations ( $\mu\text{g m}^{-3}$ ) for the northwestern United States. Letters on the x-axis correspond to month and “A” corresponds to annual mean. Shaded areas in the map correspond to regions that include the sites used in the analysis, shown as orange dots.**

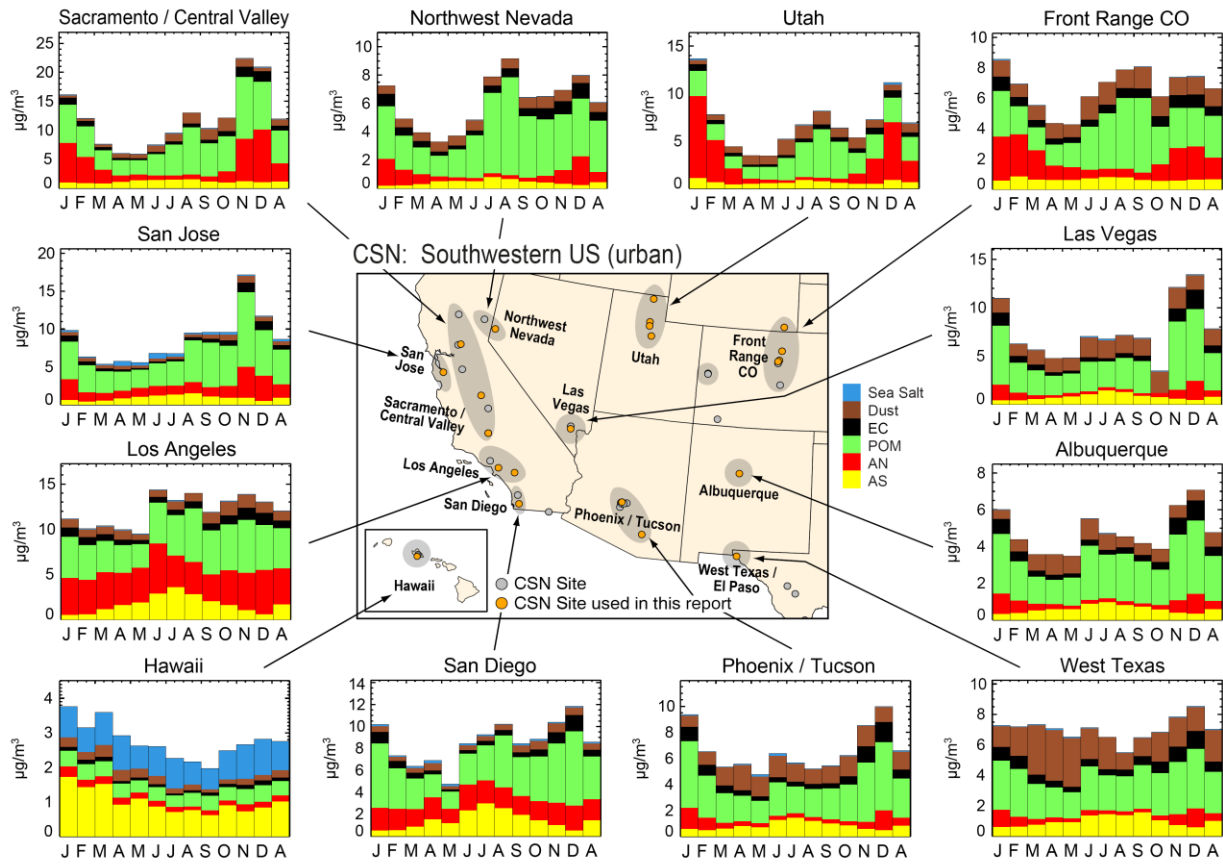


**Figure S.4.6. CSN 2016–2019 regional monthly mean PM<sub>2.5</sub> mass concentrations (µg m<sup>-3</sup>) for the northwestern United States. Letters on the x-axis correspond to month and “A” corresponds to annual mean. Shaded areas in the map correspond to regions that include the sites used in the analysis, shown as orange dots.**

#### S.4.2 Ammonium Nitrate

In the eastern United States, the highest IMPROVE AN monthly mean concentrations occurred during winter months in the Central Great Plains region, near 3 µg m<sup>-3</sup> (Figure S.4.1). Along with the Central Great Plains region, winter monthly mean concentrations were generally higher for regions farther north with mean concentrations nearing 2 µg m<sup>-3</sup>. Farther south, regional mean concentrations were much lower (<1 µg m<sup>-3</sup> year round). In the northwestern United States, the highest monthly mean concentrations occurred during winter months in the Columbia River Gorge and Northern Great Plains regions (Figure S.4.2). Other regions in the northwestern United States experienced relatively low concentrations year round (<0.3 µg m<sup>-3</sup>). Regions in the southwestern United States also had low concentrations (Figure S.4.3). The exceptions were the California Coast and Southern California regions, where concentrations were higher (<1 µg m<sup>-3</sup>). Unlike regions in the eastern United States, regions in the northwestern and southwestern United States had low monthly variability, and, interestingly, the AN monthly mean concentrations in the Southern California region peaked in spring.

In the eastern United States, a strong seasonal pattern in monthly mean AN was observed for CSN regions, with peaks in winter months, especially for regions farther north (Figure S.4.4). High concentrations (~4 µg m<sup>-3</sup>) occurred in winter months in the Central U.S. and

Michigan/Great Lake regions. Concentrations decreased for regions farther south, with lower monthly variability. A similar spatial pattern was observed for IMPROVE regions.

Concentrations were generally lower for regions in the northwestern United States (Figure S.4.5). The Northwest and North Dakota regions had the highest monthly mean concentrations near  $3 \mu\text{g m}^{-3}$  during winter months. Regions in the southwestern United States experienced the highest monthly mean concentrations (see Figure S.4.6). Mean concentrations decreased in regions farther south, such as in the Las Vegas, Albuquerque, West Texas, and Phoenix/Tucson regions, although maxima still occurred in winter months. In contrast, regions in southern California, such as Los Angeles and San Diego, experienced higher concentrations year round.

### S.4.3 Particulate Organic Matter

In the eastern United States, IMPROVE POM monthly, regional mean concentrations were highly seasonal, with peaks in summer months (Figure S.4.1). During July and August, concentrations reached over  $3 \mu\text{g m}^{-3}$  in most regions. The strong peak in POM in April in the Southeast region was due to the influence of biomass smoke. The largest regional mean POM concentrations occurred in the northwestern United States (Figure S.4.2) where peak concentrations ranged from 5 to  $12 \mu\text{g m}^{-3}$ , mainly in August and September due to biomass smoke influence. A strong seasonal pattern in POM was observed at these regions, with relatively low concentrations during winter months ( $<1 \mu\text{g m}^{-3}$ ). This pattern was also observed for more-northerly regions in the southwestern United States (Figure S.4.3), but the magnitude of the concentrations and degree of seasonality decreased farther south.

CSN POM monthly mean concentrations in regions in the eastern United States ranged from 2 to  $5 \mu\text{g m}^{-3}$  and peaked during summer months in many regions farther north (Figure S.4.4). Toward the south, regions had less seasonal variability; however, magnitudes of POM were similar. Higher concentrations were observed in regions in the northwestern United States, likely associated with biomass smoke impacts (Figure S.4.5). The Northwest, Portland, and North Dakota regions experienced monthly mean concentrations of  $6\text{--}8 \mu\text{g m}^{-3}$ , especially during summer and fall months. In the southwestern United States, regions toward the north also experienced high POM concentrations during summer and fall, such as the Northwest Nevada, Sacramento/Central Valley, San Jose, and Front Range CO regions (Figure S.4.6). Farther south, POM concentrations peaked during winter months, such as in the Albuquerque, Phoenix/Tucson, and West Texas regions.

### S.4.4 Elemental Carbon

IMPROVE EC regional mean concentrations are difficult to discern on the bar charts because they are low relative to other aerosol species. In the eastern United States, concentrations rarely exceeded  $0.3 \mu\text{g m}^{-3}$  (Figure S.4.1). Unlike other species, the monthly variability of EC was highly spatially variable. The Boundary Waters region peaked during summer months, Central Great Plains during spring months, Ohio River Valley during fall and winter months, Appalachia during fall months, and in the Southeast during spring and fall months. The monthly mean seasonal and spatial variability suggests localized impacts of sources in regions in the eastern United States. In contrast, monthly mean concentrations in regions in the northwestern United States peaked in late summer and/or early fall for all of the regions (Figure

S.4.2). Concentrations were  $>0.5 \text{ } \mu\text{g m}^{-3}$  in the Hells Canyon, Northern Rockies, Northwest, and Oregon/Northern California regions in August or September, indicating the important role of biomass burning in the area. Lower monthly mean EC concentrations were also observed in regions in the southwestern United States (Figure S.4.3) in summer, except in the Sierra Nevada region in August ( $\sim 0.5 \text{ } \mu\text{g m}^{-3}$ ) and in the California Coast region in November ( $\sim 0.5 \text{ } \mu\text{g m}^{-3}$ ). Farther south, concentrations peaked during winter months in the Southern Arizona region ( $\sim 0.5 \text{ } \mu\text{g m}^{-3}$  in December). Otherwise, monthly mean concentrations in most regions rarely exceeded  $0.2 \text{ } \mu\text{g m}^{-3}$ .

CSN EC monthly mean concentrations in the eastern United States peaked between 0.5 and  $1.0 \text{ } \mu\text{g m}^{-3}$  and were higher in regions such as the Ohio River Valley, Chicago, and New York City regions (Figure S.4.4). Concentrations were generally low in regions farther south, with the exception of the Dallas and Southeast regions, where concentrations almost reached  $1 \text{ } \mu\text{g m}^{-3}$  during cold months. Monthly mean concentrations were generally higher in regions in the northwestern United States than in the eastern United States. Concentrations reached over  $1.0 \text{ } \mu\text{g m}^{-3}$  during fall and winter months, such as in the Puget Sound, Northwest, and Portland regions (Figure S.4.5). In some southwestern regions, monthly mean concentrations also reached values over  $1.0 \text{ } \mu\text{g m}^{-3}$ , such as the Sacramento/Central Valley, San Diego, Los Angeles, Northwest Nevada, Phoenix/Tucson, and Albuquerque regions, often during late fall (Figure S.4.6).

#### S.4.5 Fine Dust Mass

The seasonal and spatial variability of FD in the United States is influenced by local, regional, and long-range transport. A maximum 2016–2019 regional monthly mean IMPROVE FD mass concentration of  $4.01 \text{ } \mu\text{g m}^{-3}$  was observed in August in the Virgin Islands region, a site known to have impacts from North African dust transport, especially during summer (Figure S.4.1). In the eastern United States, the highest FD concentration occurred during summer months, especially at regions farther south, such as the Southeast and Midsouth regions ( $>2.0 \text{ } \mu\text{g m}^{-3}$ ). Concentrations during winter months were relatively low ( $0.1\text{--}0.3 \text{ } \mu\text{g m}^{-3}$ ). Monthly mean FD concentrations in the northwestern United States were highest in the Columbia River Gorge region in summer (Figure S.4.2). Monthly mean concentrations in other regions were relatively low ( $<1 \text{ } \mu\text{g m}^{-3}$ ) but also peaked during summer months. Regional mean concentrations in the southwestern United States were highest ( $2\text{--}3 \text{ } \mu\text{g m}^{-3}$ ) for regions farther south (Figure S.4.3) and peaked in spring and early summer months. Regions farther north, such as the Sierra Nevada and Great Basin regions, had higher concentrations during summer and fall months.

CSN regions farther south in the eastern United States had higher FD concentrations in summer months, such as in the Dallas and East Texas/Gulf regions ( $4\text{--}5 \text{ } \mu\text{g m}^{-3}$  in July) and the Midsouth and Florida regions ( $2\text{--}3 \text{ } \mu\text{g m}^{-3}$  in July), likely associated with long-range transport of North African dust. Monthly mean concentrations in other eastern CSN regions ranged between  $0.5$  and  $1.0 \text{ } \mu\text{g m}^{-3}$  (Figure S.4.4). In the northwestern United States, monthly mean concentrations were typically  $<0.5 \text{ } \mu\text{g m}^{-3}$  in most regions year round. The exception was in the Northwest region, where concentrations reached over  $1.0 \text{ } \mu\text{g m}^{-3}$  in August, and the North Dakota region in June (Figure S.4.5). Relatively high concentrations ( $1\text{--}3 \text{ } \mu\text{g m}^{-3}$ ) were observed in many regions in the southwestern United States (Figure S.4.6) during spring months. Monthly

mean concentrations in the Sacramento/Central Valley region reached over  $2 \mu\text{g m}^{-3}$  during fall months, and in the Los Angeles region monthly mean concentrations were over  $1 \mu\text{g m}^{-3}$  during April and fall months.

#### S.4.6 PM<sub>2.5</sub> Sea Salt

Estimates of SS discussed here are likely an underestimate, as chloride concentrations in the particle phase can be depleted by a gas–particle exchange of chloride to the atmosphere. IMPROVE regional mean SS concentrations were visible on the monthly bar charts relative to other species for only a few regions. In the eastern United States, coastal regions such as the Northeast, East Coast, and Southeast regions had noticeable SS concentrations relative to other species (Figure S.4.1). In the East Coast and Southeast regions, concentrations reached  $0.7 \mu\text{g m}^{-3}$  in the late winter and spring months. In the northwestern United States, monthly mean SS concentrations neared  $0.2 \mu\text{g m}^{-3}$  in the Columbia River Gorge and Northwest regions in April (Figure S.4.2), but in other regions, concentrations were typically  $<0.02 \mu\text{g m}^{-3}$ . In the Alaska region, monthly mean SS concentrations reached  $0.7 \mu\text{g m}^{-3}$  in February. In the southwestern United States, regional mean SS concentrations were higher in the California Coast and Hawaii regions (Figure S.4.3).

CSN regional mean SS concentrations were relatively low and difficult to discern on the bar charts corresponding to regions in the eastern United States (Figure S.4.4), with the exception of the Florida and East Texas/Gulf regions. Monthly mean SS concentrations in the regions in the northwestern United States were quite low, generally around  $0.1 \mu\text{g m}^{-3}$  or less (Figure S.4.5). Regions in the southwestern United States were also associated with low SS regional mean concentrations (Figure S.4.6). The San Jose and Hawaii regions had some of the highest monthly mean concentrations.

#### S.4.7 PM<sub>2.5</sub> Gravimetric Fine Mass

Regional monthly mean FM concentrations mirrored the combined species concentrations on the bar charts shown in previous figures in this section. IMPROVE regional monthly mean concentrations in the eastern United States peaked during summer, around  $6\text{--}8 \mu\text{g m}^{-3}$ . The highest monthly mean concentrations occurred during summer in the Midsouth and Ohio River Valley regions. The Southeast region was influenced by biomass smoke during April, when POM concentrations increased over other months. In the northwestern United States, strong seasonal variability due to the impacts of biomass smoke and increased POM concentrations led to peaks in FM in the Northwest, Northern Rockies, Hells Canyon, and Oregon/Northern California regions, over  $12 \mu\text{g m}^{-3}$ . Biomass smoke impacts also influenced FM concentrations in regions in the southwestern United States, such as the Sierra Nevada region in July and August, when FM was over  $10 \mu\text{g m}^{-3}$ . Summer peaks in FM also occurred in many other southwestern regions but at lower concentrations ( $\sim 6\text{--}8 \mu\text{g m}^{-3}$ ).

Regional, monthly mean CSN FM concentrations peaked in both winter and summer in several northern regions in the eastern United States. Farther south, FM concentrations peaked in summer and were flatter during winter months. Monthly mean FM peaked in both summer and winter at regions in the northwestern United States and reached values near  $10 \mu\text{g m}^{-3}$ . Similar

seasonal patterns in monthly mean FM occurred in regions in the southwestern United States. FM monthly mean concentrations in the West Texas region were relatively flat, while concentrations in the Phoenix/Tucson region peaked during winter. In the Los Angeles region, monthly mean concentrations for the first half of the year were relatively low and increased in June for the rest of the year.

#### S.4.8 Discussion

The differences observed in the seasonal and spatial patterns in species concentrations for the rural regions of the IMPROVE network and the urban/suburban regions in the CSN network were indicative of the spatial extent of aerosol sources, atmospheric processes, regional transport, and sinks. For example, regional mean AS seasonal patterns and concentrations were similar for both the IMPROVE and CSN regions. In the eastern United States, monthly mean AS concentrations were similar in magnitude and had low monthly variability in both urban and rural regions. For nearly all urban and rural regions, monthly mean concentrations were near  $2 \mu\text{g m}^{-3}$  or less and fractional contributions were  $<0.3$ . Concentrations in urban and rural regions in the northwestern United States were lower ( $<2 \mu\text{g m}^{-3}$ ) than in regions in the eastern United States, likely due to lower emissions of SO<sub>2</sub>. The variability of monthly mean AS concentrations was more pronounced in rural regions compared to urban regions in the northwestern United States, in part because of the large contributions from POM during summer. Some urban regions also exhibited this pattern. Contributions of AS to RCFM in northwestern U.S. regions were typically  $<0.2$ , lower than for eastern U.S. regions. In urban CSN regions in the southwestern United States, AS concentrations peaked in summer at many regions. Less monthly variability was seen in rural IMPROVE regions; however, similar magnitudes in concentration were observed.

Seasonal and spatial patterns in monthly mean AN concentrations were similar between urban and rural regions. For example, in the eastern United States, monthly mean concentrations were higher in regions farther north that were closer to areas with extensive agricultural activity, such as the Midwest United States. However, AN concentrations were higher in urban regions. Concentrations peaked during winter months in both urban and rural regions, and often exceeded AS concentrations. Monthly variability and concentration magnitude decreased for regions farther south for both urban and rural regions. Contributions were a significant fraction of RCFM in urban and rural regions, especially during winter months in regions farther north. AN monthly mean concentrations were lower in regions in the northwestern United States, although concentrations in urban regions were still higher than in rural regions. Higher monthly mean concentrations were observed during winter months near areas of agricultural activity for both urban and rural regions. AN concentrations were higher than AS concentrations during winter months in many urban and rural regions in the northwestern United States. In the southwestern United States, higher urban mean AN concentrations were observed relative to rural regions, especially in California, Utah, and Colorado.

The strong summer maxima in regional mean POM concentrations in western IMPROVE regions suggested that wildfire activity was a major contributor to POM concentrations in rural areas, especially in the western and northwestern United States in summer. Biogenic secondary organic aerosol also could have contributed significantly to high summer POM concentrations.

Urban regions experienced maxima in monthly mean POM concentrations during summer but also during winter months, likely due to additional local sources and meteorological conditions. In regions in the southwestern United States, both summer and winter maxima were common in urban regions, whereas most rural regions experienced maxima during summer. Seasonal and spatial variability in rural and urban regions were similar in the eastern United States, with higher concentrations during summer months. Less monthly variability was observed in urban regions farther south, which was not reflected at rural regions. POM monthly mean concentrations in eastern U.S. urban regions were typically higher than at rural regions. POM was the dominant contributor to RCFM at all areas of the United States. In the eastern United States, half of RCFM was composed of POM in both urban and rural regions, especially during summer months. These contributions were greater in both urban and rural regions in the northwestern United States; contributions over 0.7 were common. The contributions decreased for southwestern U.S. regions, but during summer, POM could dominate RCFM at both urban and rural regions, and in some urban regions, POM could be equally important during winter months.

Monthly mean EC concentrations were higher in urban regions across the United States. The urban regional monthly mean maxima were nearly three times higher than those in rural regions. In rural regions, EC seasonal and spatial patterns tended to follow those of POM, especially in northwestern U.S. regions where biomass smoke impacts were significant sources. Summer maxima in monthly mean EC reflected smoke contributions, but higher winter contributions were also observed, especially in urban regions, likely due to residential heating. Contributions to RCFM were also higher in urban regions across the United States.

FD concentrations were influenced by both local and long-range transport. The long-range transport of North African dust influenced both urban and rural regions in the eastern United States during summer in regions farther south. This influence was especially evident in the relative contribution of FD to RCFM. Monthly mean FD concentrations were higher near agricultural areas for both urban and rural regions, such as the Central Great Plains/Central U.S. and Northern Great Plains. The spring dust phenomenon in the southwestern United States also influenced both rural and urban regions. Contributions of FD to RCFM were significant during spring months (~0.5), suggesting both local and regional sources influenced RCFM across the southwestern United States.

SS concentrations and fractional contributions were negligible in most urban and rural regions. Coastal regions (including regions on both the east and west coasts, including the Hawaii and Alaska regions) were the only regions to experience non-negligible impacts from SS on RCFM. SS corresponded to a high degree of seasonality.

FM concentrations were noticeably higher in urban regions than rural regions. The regional mean urban maximum was nearly twice that of rural maximum. The rural monthly mean maximum was likely due to the impact of biomass smoke, given its occurrence in the Oregon/Northern California region in August and the dominant role of POM. The maximum urban monthly mean FM concentration occurred in the Sacramento/Central Valley region in December due to POM and AN concentrations. For most urban and rural regions across the United States, depending on season, the highest FM concentrations occurred due to high

contributions of POM and AN, highlighting their importance to the FM budget, as well the roles of biomass smoke and agricultural influence.

## S.5 SPATIAL AND SEASONAL PATTERNS IN RELATIVE RECONSTRUCTED AEROSOL LIGHT EXTINCTION COEFFICIENTS

Reconstructed total aerosol light extinction coefficients ( $b_{ext\_tot}$ ) were computed from speciated aerosol mass concentrations, multiplied by a species-specific extinction efficiency and a humidification factor ( $f(RH)$ ), and summed over all species. The extinction algorithm used to compute  $b_{ext\_tot}$  is shown in equation (S.5.1):

$$b_{ext\_tot} = 3 \times f(RH) \times [AS] + 3 \times f(RH) \times [AN] + 4 \times [POM] + 10 \times [EC] + 1 \times [FD] + 1.7 \times f(RH)_{ss} \times [SS] + 0.6 \times [CM] + \text{site-specific Rayleigh scattering} \quad (\text{S.5.1})$$

The units of  $b_{ext\_tot}$  and Rayleigh scattering are in inverse megameters ( $Mm^{-1}$ ). The same  $f(RH)$  curve was applied to AS and AN, while a separate  $f(RH)$  was applied to SS ( $f(RH)_{ss}$ , see Chapter 4.1). Mass concentrations of aerosol species (in brackets) are in  $\mu\text{g m}^{-3}$ , and mass scattering and absorption efficiencies have units of  $\text{m}^2 \text{ g}^{-1}$ . Values of  $3 \text{ m}^2 \text{ g}^{-1}$  were used for both AS and AN,  $4 \text{ m}^2 \text{ g}^{-1}$  for POM,  $10 \text{ m}^2 \text{ g}^{-1}$  for EC,  $1 \text{ m}^2 \text{ g}^{-1}$  for soil,  $1.7 \text{ m}^2 \text{ g}^{-1}$  for SS, and  $0.6 \text{ m}^2 \text{ g}^{-1}$  for CM. For CSN sites, CM was interpolated to CSN sites from nearby EPA FRM sites (see Chapter 4). Extinction values correspond to a wavelength of 550 nm.

Visual range and extinction measurements are nonlinear with respect to human perception of visual scene changes caused by haze. The deciview (dv) haze index was derived with a number of assumptions such that uniform changes in haze correspond to approximately uniform incremental changes in visual perception (Pitchford and Malm, 1994). Deciview is calculated from reconstructed  $b_{ext\_tot}$ , using equation (S.5.2):

$$dv = 10 \times \ln(b_{ext\_tot}/10) \quad (\text{S.5.2})$$

For different values of site-specific Rayleigh scattering, as specified in equation (S.5.1), it is possible to have a negative dv for pristine conditions ( $b_{ext\_tot} < 10 \text{ Mm}^{-1}$ ). The spatial variability in dv and  $b_{ext\_tot}$  are similar to the spatial variability in aerosol mass concentrations; however, because of relative humidity (RH) effects and different mass extinction efficiencies, the relative contributions from individual species to  $b_{ext\_tot}$  may be different than their contributions to reconstructed fine mass. Because of the similarity between aerosol speciated mass and  $b_{ext\_tot}$ , only annual mean  $b_{ext\_tot}$  and dv are discussed in Section S.5.1 (see Chapter 4 for individual species).

Regional, monthly mean reconstructed  $b_{ext\_tot}$  and speciated extinction values were computed for the major aerosol species listed earlier and for similar regions discussed in Section S.4 and Chapters 3 and 5. Seasonal patterns of speciated extinction are similar to those for mass, so only the relative contribution of major aerosol species to  $b_{ext\_aer}$  ( $b_{ext\_tot}$  – Rayleigh scattering) are shown in Section S.5.2–S.5.8. See Chapter 5 for additional details.

### S.5.1 Annual Mean Reconstructed Light Extinction Coefficient

The 2016–2019 IMPROVE annual mean  $b_{ext\_tot}$  is presented in Figure S.5.1a. The east–west gradient observed for several species (especially AS) was preserved in the calculation of  $b_{ext\_tot}$ , but sites with the highest  $b_{ext\_tot}$  were in the central United States due to agricultural activity and in Florida due to biomass smoke impacts. Sites with the lowest  $b_{ext\_tot}$  occurred in the southwestern United States and the Intermountain West. Higher  $b_{ext\_tot}$  occurred at sites in California and the northwestern United States.

The addition of CSN sites preserved the large-scale gradients observed with IMPROVE sites, with higher  $b_{ext\_tot}$  in the central and eastern United States compared to lower estimates at sites in the Intermountain West and southwestern United States (Figure S.5.1b). The addition of sites in the eastern United States provided further resolution that focused the area of high  $b_{ext\_tot}$  ( $>50 \text{ Mm}^{-1}$ ) in the central United States, especially at sites in Indiana and Pennsylvania. High  $b_{ext\_tot}$  also occurred at sites in Texas and at Gulf sites ( $>50 \text{ Mm}^{-1}$ ) and along the Central Valley of California.

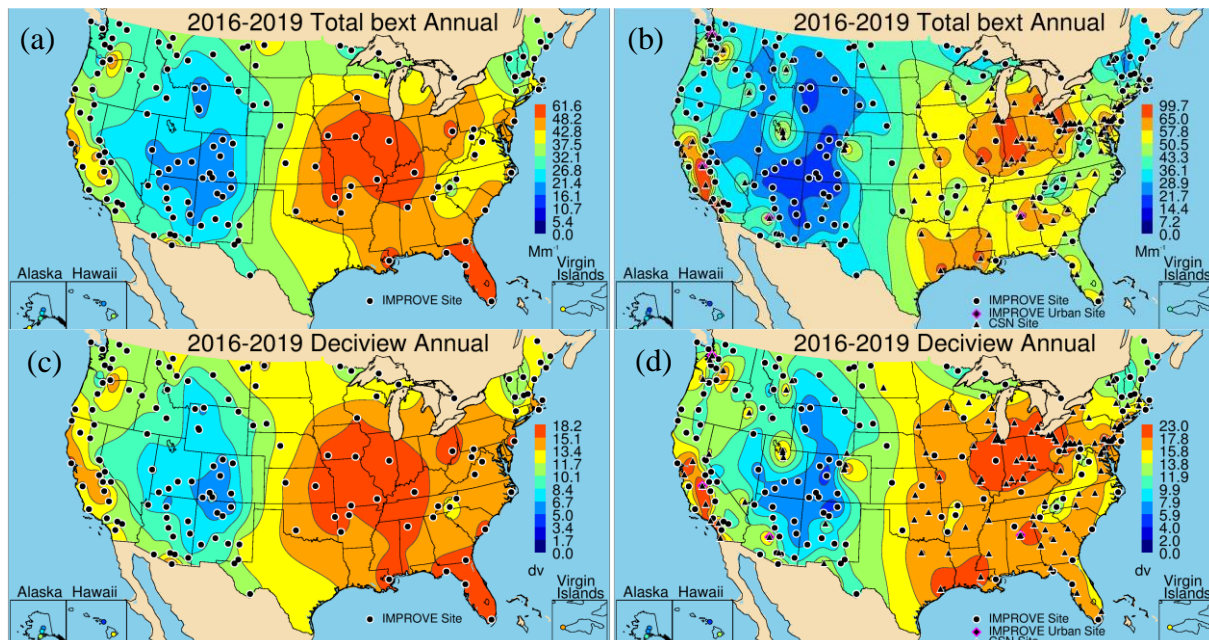


**Figure S.5.1. 2016–2019 annual mean ambient total reconstructed light extinction coefficient ( $b_{ext\_tot}$ ) ( $\text{Mm}^{-1}$ ) for (a) IMPROVE and (b) IMPROVE and CSN. Annual mean deciview (dv) for (c) IMPROVE and (d) IMPROVE and CSN. Wavelength corresponds to 550 nm.**

The 2016–2019 IMPROVE annual mean dv spatial pattern was very similar to the  $b_{ext\_tot}$  pattern, as expected (see Figure S.5.1c). Higher dv values ( $>15 \text{ dv}$ ) were observed at sites in the eastern United States, with the exception of northeastern sites ( $10–11 \text{ dv}$ ). Lower values were observed at sites in the Intermountain West, especially at sites in the central Rocky Mountains of Colorado and northern New Mexico. Higher estimates were observed at sites in California (~15).

Similar to the map of  $b_{ext\_tot}$ , the addition of urban sites to the dv map in Figure S.5.1d provided additional spatial resolution but did not change the overall patterns. The highest annual mean dv occurred at sites in the central United States and the Gulf area, as well as at sites in the Central Valley of California. Additional hot spots included sites in Colorado, Utah, Arizona, and Nevada.

## S.5.2 Ammonium Sulfate Light Extinction Coefficients

The largest IMPROVE fractional contribution from  $b_{ext\_AS}$  to  $b_{ext\_aer}$  ( $\sim 0.5$ ) occurred in the Ohio River Valley and Appalachia regions. Other regions in the eastern United States corresponded to maximum monthly mean fractions around 0.4–0.45 that occurred mostly during summer and early fall months (Figure S.5.2). The seasonality of the fractional contribution of  $b_{ext\_AS}$  to  $b_{ext\_aer}$  in regions in the northwestern United States differed from that observed for eastern regions, with minima in  $b_{ext\_AS}$  contributions in summer months, largely due to the strong contributions from  $b_{ext\_POM}$  during summer (Figure S.5.3). The seasonality of the fractional contribution of  $b_{ext\_AS}$  to  $b_{ext\_aer}$  in regions farther north in the southwestern United States followed those of the northwestern region, with lower contributions that occurred in the summer months due to the role of  $b_{ext\_POM}$  contributions (Figure S.5.4). Contributions of  $b_{ext\_AS}$  in regions farther south tended to have flat seasonality, or summer/early fall maxima.

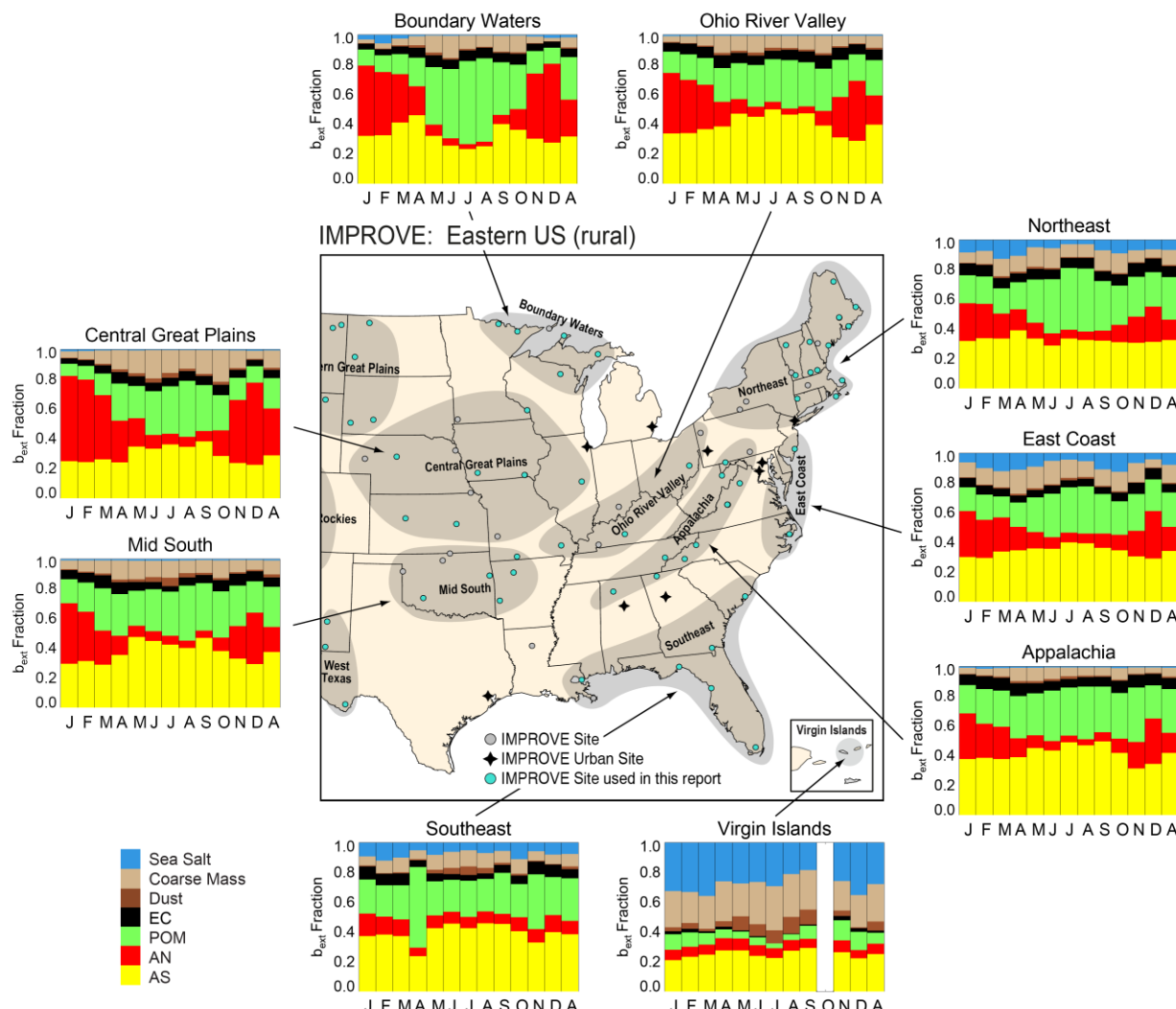


**Figure S.5.2. IMPROVE 2016–2019 regional monthly mean speciated fractional contributions to ambient aerosol light extinction coefficients ( $b_{ext}$ ) for the eastern United States. Letters on the x-axis correspond to the month and “A” corresponds to annual mean. Shaded areas in the map correspond to regions that include sites used in the analysis, shown as blue dots. Wavelength corresponds to 550 nm.**

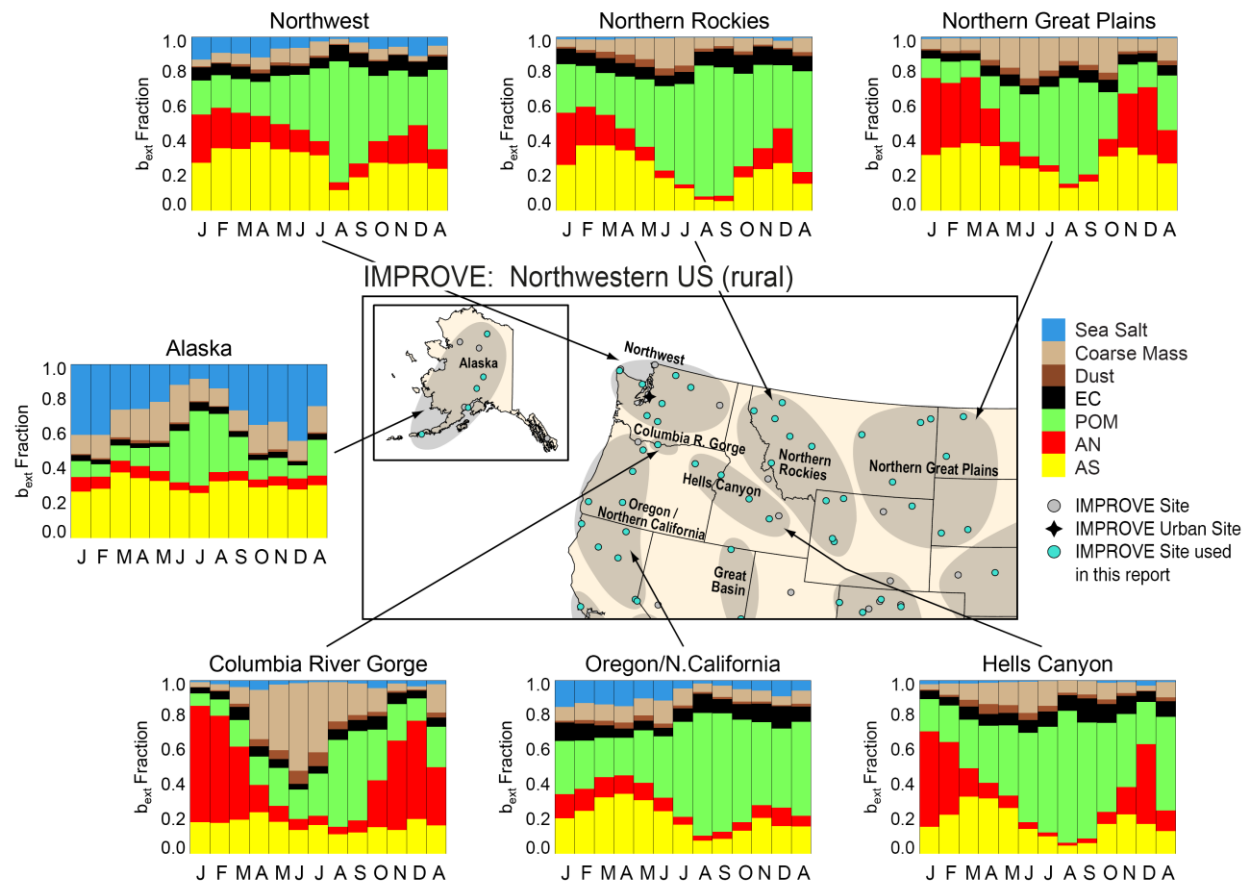


**Figure S.5.3. IMPROVE 2016–2019 regional monthly mean speciated fractional contributions to ambient aerosol light extinction coefficients ( $b_{ext}$ ) for the northwestern United States. Letters on the x-axis correspond to the month and “A” corresponds to annual mean. Shaded areas in the map correspond to regions that include sites used in the analysis, shown as blue dots. Wavelength corresponds to 550 nm.**

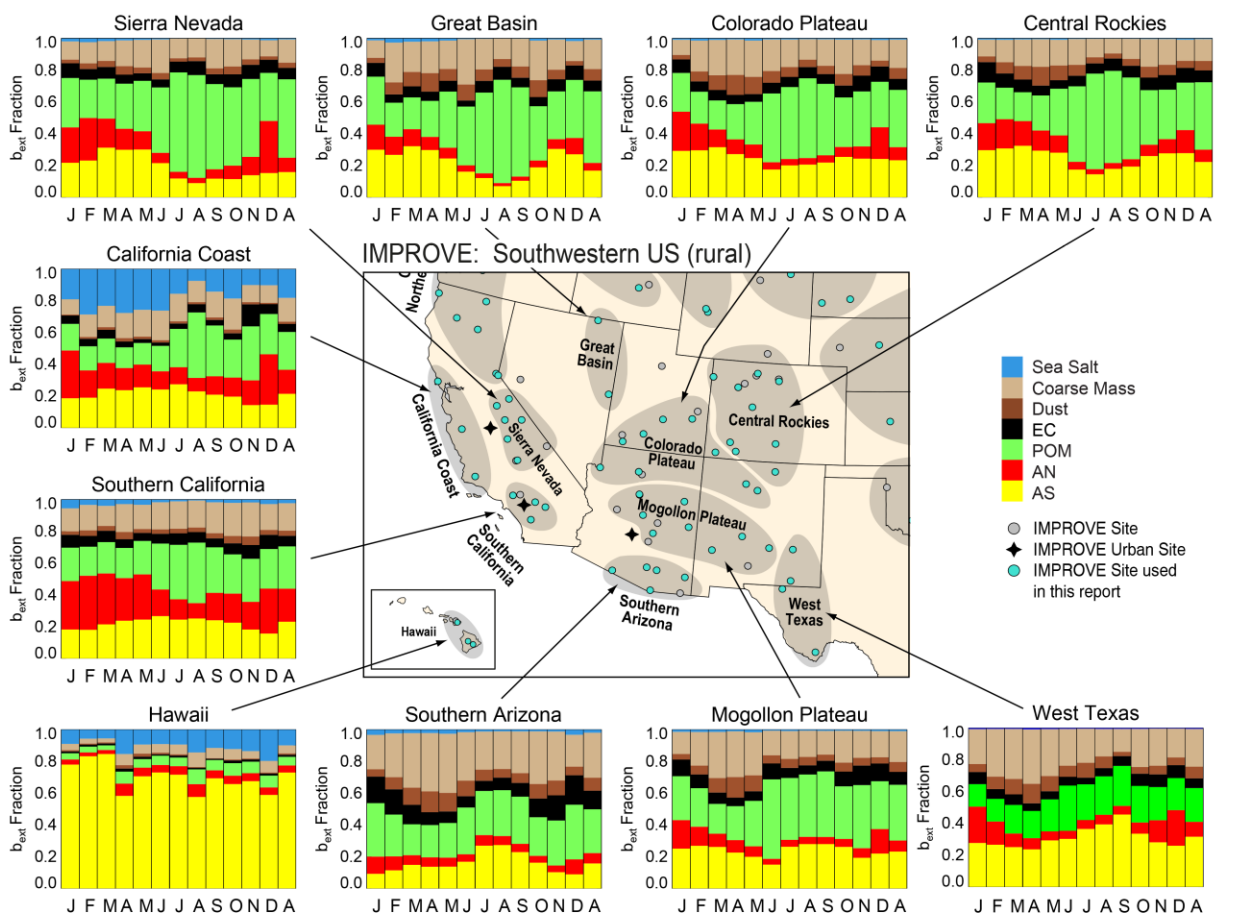


**Figure S.5.4. IMPROVE 2016–2019 regional monthly mean speciated fractional contributions to ambient aerosol light extinction coefficients ( $b_{ext}$ ) for the southwestern United States. Letters on the x-axis correspond to the month and “A” corresponds to annual mean. Shaded areas in the map correspond to regions that include sites used in the analysis, shown as blue dots. Wavelength corresponds to 550 nm.**

The maximum contributions of  $b_{ext\_AS}$  to  $b_{ext\_aer}$  at CSN regions in the eastern United States were typically around 0.3–0.4 in summer and early fall months (Figure S.5.5). The lowest contributions were around 0.2–0.3 in winter months, lending to low seasonal variability in  $b_{ext\_AS}$  contributions in regions in the eastern United States. While the seasonal patterns were quite similar across regions, the maximum contributions occurred in regions farther south. The relative contribution of  $b_{ext\_AS}$  to  $b_{ext\_aer}$  decreased considerably in regions in the western United States. Minimum  $b_{ext\_AS}$  contributions in regions in the northwestern United States were around 0.1 (Figure S.5.6). The maximum contributions for these regions reached 0.2–0.3. Contributions were also relatively flat. Monthly mean contributions of  $b_{ext\_AS}$  to  $b_{ext\_aer}$  were lowest in regions in the southwestern United States relative to other areas of the country (Figure S.5.7). Minimum contributions were below 0.1, and maximum contributions were around 0.2–0.3, with the highest contribution in the San Diego region in July. A stronger seasonal variability occurred at regions in the southwestern United States relative to other regions, with summer maximum contributions common, especially in regions farther south.

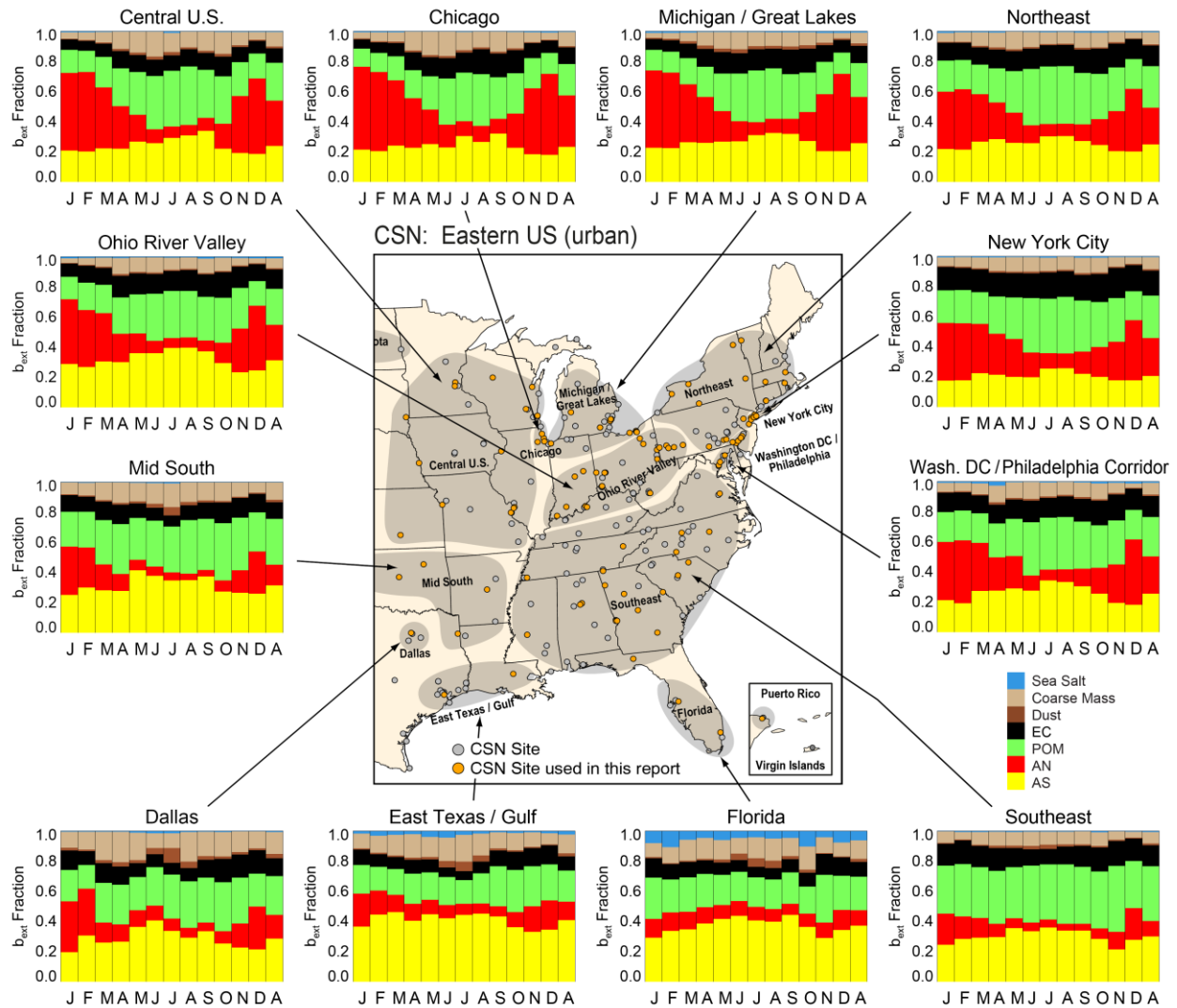


**Figure S.5.5. CSN 2016–2019 regional monthly mean speciated fractional contributions to ambient aerosol light extinction coefficients ( $b_{ext}$ ) for the eastern United States. Letters on the x-axis correspond to the month and “A” corresponds to annual mean. Shaded areas in the map correspond to regions that include sites used in the analysis, shown as orange dots. Wavelength corresponds to 550 nm.**

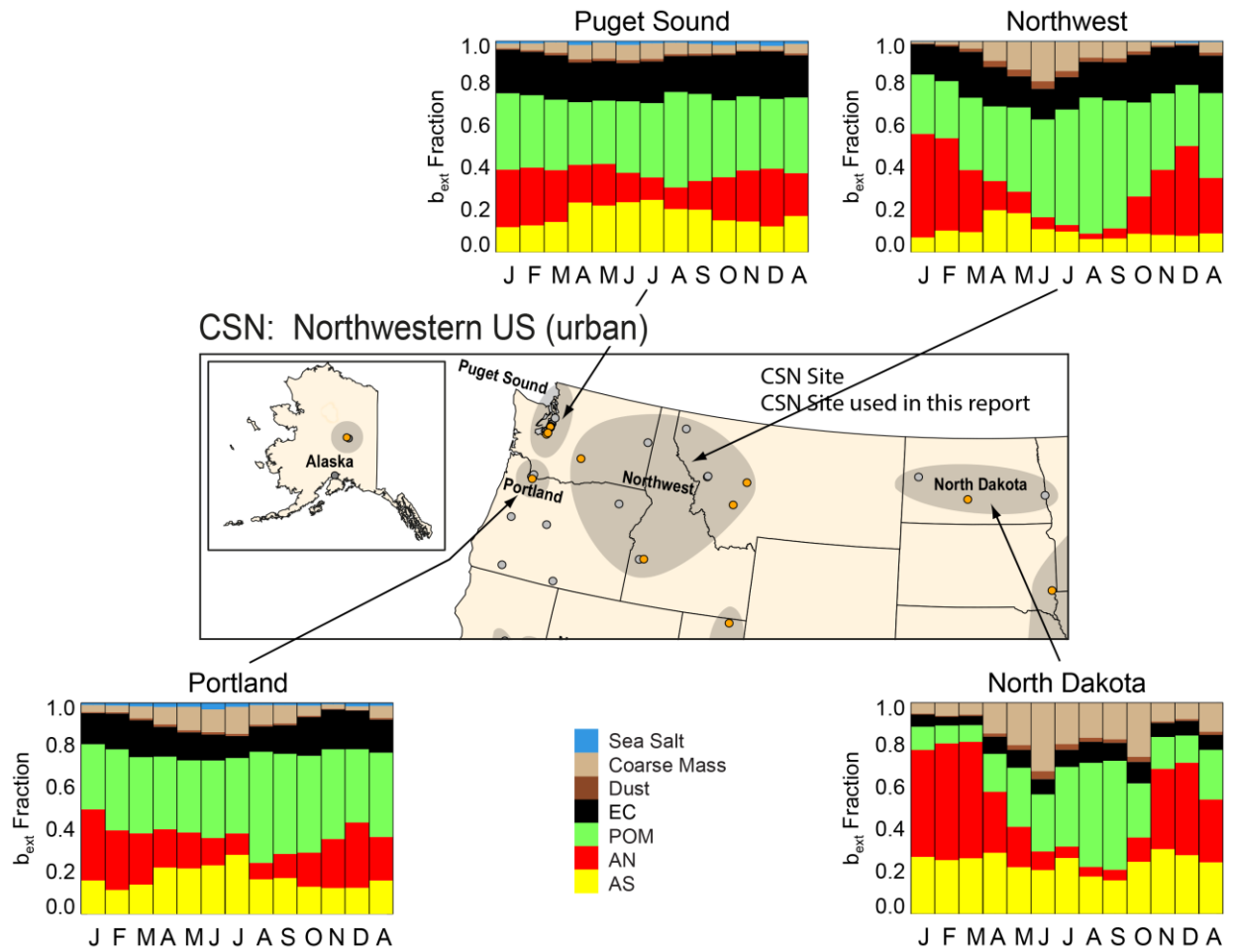


**Figure S.5.6. 2016–2019 regional monthly mean speciated fractional contributions to ambient aerosol light extinction coefficients ( $b_{ext}$ ) for the northwestern United States. Letters on the x-axis correspond to the month and “A” corresponds to annual mean. Shaded areas in the map correspond to regions that include sites used in the analysis, shown as orange dots. Wavelength corresponds to 550 nm.**

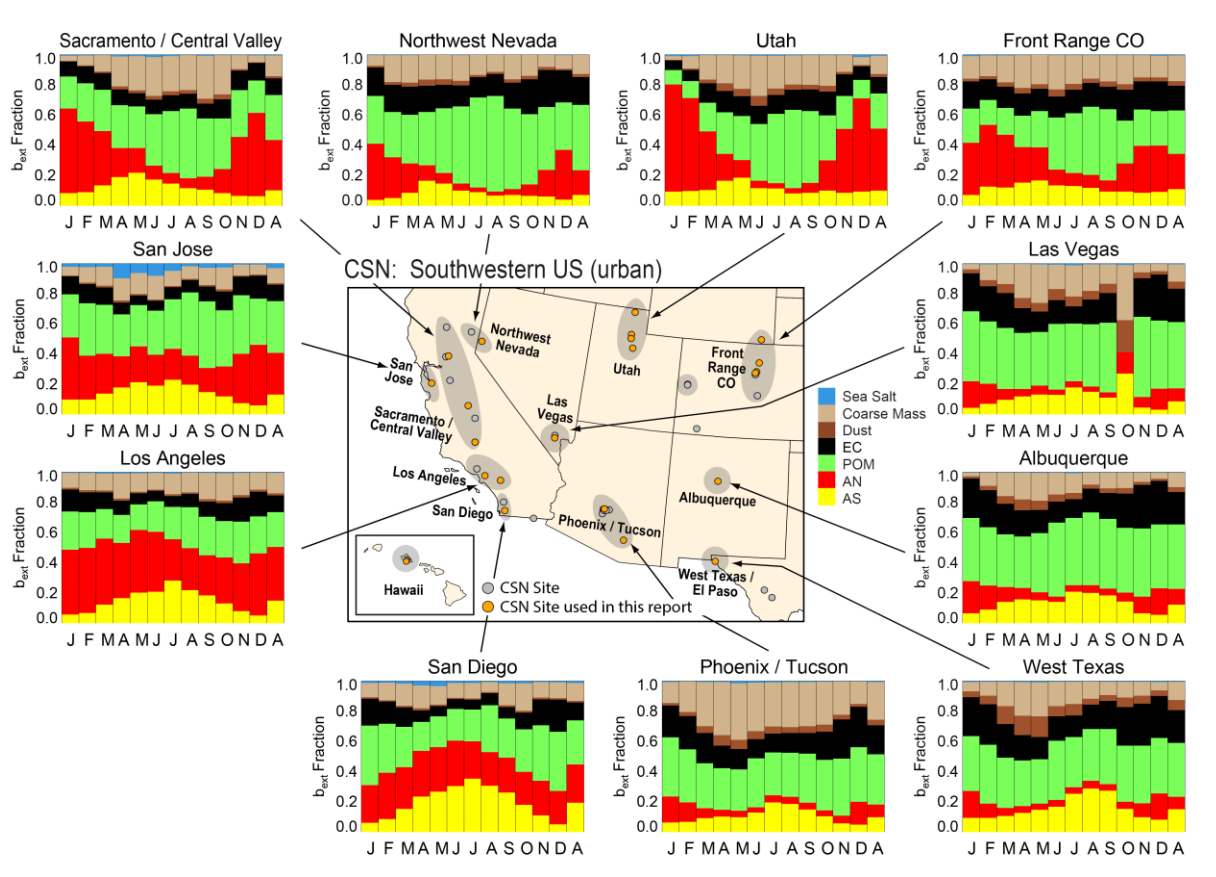


**Figure S.5.7. CSN 2016–2019 regional monthly mean speciated fractional contributions to ambient aerosol light extinction coefficients ( $b_{ext}$ ) for the southwestern United States. Letters on the x-axis correspond to the month and “A” corresponds to annual mean. Shaded areas in the map correspond to regions that include sites used in the analysis, shown as orange dots. Wavelength corresponds to 550 nm.**

### S.5.3 Ammonium Nitrate Light Extinction Coefficients

The contribution of  $b_{ext\_AN}$  to  $b_{ext\_aer}$  at IMPROVE regions farther north in the eastern United States experienced a high degree of seasonality (Figure S.5.2), for example contributions during summer months were around 0.03–0.06, compared to over 0.5 during winter months. Regions farther from agricultural sources, such as the East Coast, Northeast, and Appalachia regions, had lower maximum monthly mean contributions (~0.3 or less) in winter months. Regions farther south, such as the Southeast region, had the lowest year-round monthly mean contributions, ranging from 0.06 to 0.15. In the northwestern United States, the monthly mean contributions of  $b_{ext\_AN}$  to  $b_{ext\_aer}$  ranged from a minimum of 0.030 during summer months to 0.5–0.7 in winter months (Figure S.5.3). The regions with higher contributions were closer to agricultural activity and oil and gas development. Contributions in other regions, such as the Northern Rockies and Northwest regions, reached nearly 0.3 in winter. The relative contribution of  $b_{ext\_AN}$  to  $b_{ext\_aer}$  was lower in the southwestern United States relative to other areas (Figure S.5.4). Monthly mean contributions ranged from ~0.02 to 0.30 in summer and winter months, respectively.

CSN regional monthly mean  $b_{ext\_AN}$  fractional contributions of  $b_{ext\_AN}$  to  $b_{ext\_aer}$  in the eastern United States were highest in regions farther north (Figure S.5.5), similar to IMPROVE regions. During winter months in the Central U.S., Chicago, and Michigan Great Lakes regions,  $b_{ext\_AN}$  contributed over half of  $b_{ext\_aer}$  and decreased to less than 0.1 during summer months. The range in seasonal contributions was much lower in regions farther south, where monthly mean contributions ranged from ~0.05 in summer months to ~0.2 or less during winter months.

Regions in the southwestern United States experienced a strong seasonal contribution from  $b_{ext\_AN}$  to  $b_{ext\_aer}$ . For example, contributions in the North Dakota region ranged from 0.05 to 0.55 from summer to winter months (Figure S.5.6). High levels of contributions occurred in some southwestern U.S. regions. The Utah region had the highest monthly mean contribution in winter months of ~0.7 (Figure S.5.7) but much lower contributions (~0.05) during summer months. Regions in California experienced less seasonality in  $b_{ext\_AN}$  contributions suggesting additional urban sources during summer months. The lowest contributions occurred in regions farther south; these regions experienced higher monthly mean contributions in winter relative to summer but ranged from ~0.03 to ~0.2 or less.

#### S.5.4 Particulate Organic Matter Light Extinction Coefficients

While the patterns of  $b_{ext\_POM}$  were the same as those of POM mass concentrations, its relative contribution to reconstructed  $b_{ext}$  was not because of the hygroscopic and optical properties of other species contributing to  $b_{ext}$ . In the eastern United States, the IMPROVE regional maximum monthly mean  $b_{ext\_POM}$  contribution was ~0.3–0.5 (Figure S.5.2). The April maximum in the Southeast region corresponded to biomass smoke influence. Minimum contributions of  $b_{ext\_POM}$  to  $b_{ext\_aer}$  at southeast U.S. regions occurred mostly during winter months or early spring. Contributions of  $b_{ext\_POM}$  to  $b_{ext\_aer}$  were much higher for many northwestern U.S. regions relative to the eastern United States, and the maximum monthly mean contributions occurred in August for nearly all regions (Figure S.5.3). The  $b_{ext\_POM}$  contributions ranged from 0.071 in the Columbia River Gorge (January) and Alaska (February) regions to 0.76 in the Hells Canyon region (August). For most regions, the maximum monthly mean contributions were over 0.7, highlighting the importance of biomass burning influence on  $b_{ext\_aer}$  in these regions. In the southwestern United States, regions farther north were likely influenced by biomass smoke, similar to regions in the northwestern United States area (Figure S.5.4). Minimum monthly mean contributions were typically around 0.15–0.2 for other regions and occurred in early spring or late winter months. Maximum monthly mean contributions were lower farther south and ranged from 0.3 to 0.4. The maximum contribution in the Southern Arizona region occurred in December; other regions experienced maxima during summer months.

For CSN regions in the eastern United States, monthly mean contributions in the Southeast region were greater than 0.3 during all months (Figure S.5.5). In regions farther north, contributions were greater in the summer months, in part due to contributions of  $b_{ext\_AN}$  to  $b_{ext\_aer}$  during winter months. Nearly all regions experienced their lowest monthly mean  $b_{ext\_POM}$  contributions (~0.12–0.3) during winter months. Months corresponding to maximum contributions varied depending on region but many occurred during summer months. In the northwestern United States, most of the maximum contributions occurred during summer months (~0.45–0.65), and with the exception of the North Dakota region, minimum contributions in

other regions were around 0.3 (Figure S.5.6). Both the Puget Sound and Portland regions experienced relatively flat contributions of  $b_{ext\_POM}$  to  $b_{ext\_aer}$  compared to the Northwest and North Dakota regions, highlighting the importance of  $b_{ext\_POM}$  contributions during winter farther west. Contributions of  $b_{ext\_POM}$  were significant in many southwestern urban regions (Figure S.5.7), ranging from 0.278 in Los Angeles (November) to 0.635 in the Northwest Nevada region in August. Regions farther north experienced maximum contributions during summer, in part due to the contributions of  $b_{ext\_AN}$  during winter months, when  $b_{ext\_POM}$  contributions were lowest. Farther south, maximum contributions around 0.4–0.5 occurred during summer months.

### S.5.5 Elemental Carbon Light Extinction Coefficients

Contributions of  $b_{ext\_EC}$  to  $b_{ext\_aer}$  were less than 0.1 in all IMPROVE eastern regions (Figure S.5.2) and generally higher during fall and winter months. Contributions of  $b_{ext\_EC}$  to  $b_{ext\_aer}$  were higher in regions in the northwestern United States (Figure S.5.3). In the Oregon/Northern California and Hells Canyon region, monthly mean maximum contributions were ~0.13 in December and September, respectively. Minimum monthly mean contributions were around 0.05, meaning that contributions year round were greater than 0.05 in most northwestern U.S. regions. In the southwestern United States, the maximum monthly contribution occurred in the Southern Arizona region (0.185) in December (Figure S.5.4). Maximum contributions in remaining regions were around 0.1, mostly during winter months. Minimum contributions were around 0.05.

Monthly mean contributions of  $b_{ext\_EC}$  to  $b_{ext\_aer}$  were higher in CSN regions compared to IMPROVE regions. In the eastern United States, maximum contributions were around ~0.1 and higher, with a maximum contribution of 0.200 in the New York City region in November (Figure S.5.5). Maximum contributions occurred mostly in fall months. Minimum monthly mean contributions were greater than 0.06 for all regions. In the northwestern United States, CSN  $b_{ext\_EC}$  contributions ranged from 0.042 in the North Dakota region in February to nearly 0.23 in the Puget Sound and Northwest regions in January and October, respectively (Figure S.5.6). The North Dakota region was an outlier in the northwestern United States, where contributions were generally greater than 0.1. Maximum monthly mean  $b_{ext\_EC}$  contributions in the southwestern United States were less than 0.3, with the maximum in Las Vegas. Regions in California had lower maximum contributions compared to those regions farther east (Figure S.5.7).

### S.5.6 Fine Dust Light Extinction Coefficients

IMPROVE maximum monthly mean contributions  $b_{ext\_FD}$  to  $b_{ext\_aer}$  in the eastern United States were negligible, less than 0.03 in most regions, except the Midsouth (0.060) and the Southeast (0.060) regions, both in July (Figure S.5.2), likely due to long-range transport of North African dust. In the northwestern United States, contributions of monthly mean  $b_{ext\_FD}$  to  $b_{ext\_aer}$  were highest (0.080) in the Columbia River Gorge region in July (Figure S.5.3). Maxima in other regions in the northwestern United States were around 0.02–0.05, nearly all in April. Monthly mean contributions of  $b_{ext\_FD}$  to  $b_{ext\_aer}$  in the southwestern United States were highest (0.130) in the Southern Arizona and West Texas regions in April (Figure S.5.4). Other regions had maximum contributions in April of ~0.1.

In the eastern United States, the maximum CSN  $b_{ext\_FD}$  contribution occurred in the Dallas region (0.100) in July (Figure S.5.5). Similar to  $b_{ext\_FD}$ , regions with the highest maximum  $b_{ext\_FD}$  contributions (~0.05) occurred in regions influenced by North African dust transport (e.g., East Texas/Gulf, Midsouth, and Florida regions) in July. Contributions of  $b_{ext\_FD}$  to  $b_{ext\_aer}$  were insignificant in regions in the northwestern United States (Figure S.5.6). Monthly mean maximum contributions were less than 0.04 in all regions. The maximum monthly mean  $b_{ext\_FD}$  contributions in the southwestern United States (~0.2) occurred in the Las Vegas region in October and the West Texas region in May. Other regions in California had low maximum contributions (<0.03), while regions farther south were closer to 0.05–0.07 during spring months (Figure S.5.7). Of all the urban regions, those in the southwestern United States corresponded to the highest contributions of  $b_{ext\_FD}$  to  $b_{ext\_aer}$ .

### S.5.7 PM<sub>2.5</sub> Sea Salt Light Extinction Coefficients

IMPROVE coastal regions in the eastern United States corresponded to higher maximum monthly mean contributions (~0.1–0.2) of  $b_{ext\_SS}$  to  $b_{ext\_aer}$  (Figure S.5.2). Contributions in noncoastal regions in the eastern United States were less than 0.05. Contributions of  $b_{ext\_SS}$  to  $b_{ext\_aer}$  in the northwestern United States were also highest at coastal regions (0.1–0.2). In the other northwestern U.S. regions, the contributions were 0.03 or less year round (Figure S.5.3). Similar to other areas, the southwestern United States had the only significant contributions of  $b_{ext\_ss}$  in coastal regions, such as the California Coast and Hawaii regions (Figure S.5.4).

In the eastern United States the only CSN regions with non-negligible contributions were the Florida region in February (0.104) and the East Texas/Gulf region in June (0.04). All other regions had maximum contributions of 0.01 or less (Figure S.5.5). The maximum  $b_{ext\_SS}$  contribution in the northwestern United States was around 0.02 in the Puget Sound region in December and the Portland region in June (Figure S.5.6). In the southwestern United States, maximum monthly mean  $b_{ext\_SS}$  values were ~0.1 or less (Figure S.5.7). The highest contribution occurred in the San Jose region in April (~0.1). Other regions had maxima of 0.01 or less and were not visible on the regional bar charts.

### S.5.8 Coarse Mass Light Extinction Coefficients

CM concentrations are estimated routinely by the IMPROVE network, and EPA FRM networks were used to interpolate CM to CSN sites in order to calculate  $b_{ext\_CM}$ ,  $b_{ext\_aer}$ ,  $b_{ext\_tot}$ , and dv at CSN sites (see Chapter 4). Therefore, estimates of  $b_{ext\_CM}$  for the CSN have additional uncertainty. In the eastern United States, IMPROVE  $b_{ext\_CM}$  contributions were lowest during winter months for all regions (Figure S.5.2), except the Southeast region (April) and the Virgin Islands region (November). The largest maximum monthly mean  $b_{ext\_CM}$  contribution occurred in the Virgin Islands region (0.30), but in other regions contributions were around 0.1–0.2, with the Central Great Plains region having contributions of ~0.2 in October, perhaps associated with agricultural harvesting. Other contributions were highest during spring and fall months. In the northwestern United States, contributions from  $b_{ext\_CM}$  were the highest in the Columbia River Gorge region (~0.5 in June). Other regions had maximum contributions around 0.13–0.18, all in June (Figure S.5.3). Minimum monthly mean contributions ranged from ~0.03–0.10. Minimum contributions occurred during summer months perhaps due to the strong contributions from  $b_{ext\_POM}$  during summer months. Maximum monthly mean contributions in the southwestern U.S.

regions ranged from ~0.18 in the Central Rockies region in to ~0.4 in the Southern Arizona region in May (Figure S.5.4). Most of the regions had contributions around 0.2 or higher, such as the West Texas region (0.342 in April). For many regions in the southwestern United States,  $b_{ext\_CM}$  was one of the top third contributors to  $b_{ext\_aer}$ , along with  $b_{ext\_AS}$  and  $b_{ext\_POM}$ .

In CSN regions in the eastern United States,  $b_{ext\_CM}$  contributions ranged from ~0.03 (Washington D.C./Philadelphia Corridor region in December) to ~0.2 (Dallas region) in April (Figure S.5.5). Most of the monthly mean maxima were around 0.1–0.2 across eastern regions, and most occurred in late spring to summer months. The maximum monthly mean  $b_{ext\_CM}$  contributions in the northwestern United States were similar in magnitude (0.1–0.2), with the largest in the North Dakota region (Figure S.5.6). Other maxima also occurred in June and July. Lower contributions occurred during winter months, around 0.01–0.05. With the exception of the North Dakota region, contributions of  $b_{ext\_CM}$  were generally similar to or less than contributions from  $b_{ext\_EC}$ . Higher contributions of  $b_{ext\_CM}$  to  $b_{ext\_aer}$  were observed in the southwestern United States (Figure S.5.7). Maximum contributions ranged from ~0.2 in the San Jose region in June to ~0.4 in the Phoenix/Tucson region in May. Otherwise, contributions were 0.2–0.3 in most regions.

## S.5.9 Discussion

The seasonal patterns in  $b_{ext\_tot}$  corresponding to major aerosol species were similar to the seasonal distributions in mass concentrations presented in Chapter 3. This similarity was expected for most species because mass concentrations were converted to  $b_{ext}$ , with mass extinction efficiencies that essentially scaled the values to  $b_{ext}$ . However, for AS, AN, and SS, the conversion to  $b_{ext\_tot}$  accounted for RH effects and hygroscopic growth that can be considerable in environments with high RH. No significant differences were observed between the seasonal distributions in mass compared to  $b_{ext\_tot}$  (see Chapter 5). Occasionally, the season that corresponded to the majority of the maximum and minimum regional absolute  $b_{ext\_tot}$  or relative  $b_{ext\_tot}$  changed for many of the species examined here. In addition, some species that were important for their contributions to RCFM were less important in reconstructed  $b_{ext\_aer}$  (e.g., FD), while others became more important (e.g., EC, POM, and hygroscopic species). Differences in urban and rural  $b_{ext\_aer}$  were evident, especially in seasonal patterns. Many of the urban regions had maximum  $b_{ext\_aer}$  during winter, due to the role of  $b_{ext\_AN}$  and  $b_{ext\_POM}$ , whereas many rural areas across the United States experienced maximum  $b_{ext\_aer}$  during summer months, due to the role of  $b_{ext\_POM}$  and  $b_{ext\_AS}$ . The contributions of  $b_{ext\_CM}$  were important in both urban and rural regions in the southwestern United States.

The highest annual mean  $b_{ext\_AS}$  occurred at urban and rural sites in the eastern United States, where SO<sub>2</sub> emissions are greatest, and high RH in summer can facilitate hygroscopic growth. A strong spatial gradient occurred along the central United States, resulting in relatively low  $b_{ext\_AS}$  at sites across the West, due to lower emissions. Contributions of  $b_{ext\_AS}$  to  $b_{ext\_aer}$  were also highest in the East, typically greater than 0.3, and highest at rural sites. With the exception of sites in Hawaii, the annual mean fractional contribution of  $b_{ext\_AS}$  to  $b_{ext\_aer}$  did not exceed 0.5 at any rural or urban site. Fractional contributions also decreased at sites toward the West. In the eastern United States, contributions reached an average maximum of 0.45 for IMPROVE regions and 0.37 for CSN regions, compared to the northwestern United States (0.35

and 0.26 for IMPROVE and CSN, respectively), and the southwestern United States (0.31 and 0.23 for IMPROVE and CSN, respectively).

Regional average monthly mean maximum  $b_{ext\_AN}$  was higher in urban regions. For all CSN regions, the highest values occurred in regions in the southwestern United States. Rural estimates varied considerably depending on region, with average maximum values in the eastern United States, compared to the lowest maximum values in the southwestern United States. For nearly all regions, monthly mean maximum  $b_{ext\_AN}$  was highest during winter months, reflecting favorable formation conditions. The fraction of  $b_{ext\_aer}$  due to  $b_{ext\_AN}$  was high at sites in the central United States, exceeding 0.3 across the region. Maximum contributions of  $b_{ext\_AN}$  were similar for urban and rural regions in the eastern and northwestern United States (~0.4), but in the southwestern regions, higher contributions occurred in urban (0.36) relative to rural regions (0.23). These contributions were usually higher during winter months, except in some urban and rural regions in the southern part of California that had higher contributions year round.

Biomass smoke impacts at sites in the northwestern United States and Florida strongly influenced the  $b_{ext\_POM}$  spatial pattern at rural sites, where the highest estimates of annual mean rural  $b_{ext\_POM}$  occurred. Estimates were somewhat higher at sites in the southeastern United States, but still lower than at sites highly influenced by smoke. The annual mean  $b_{ext\_POM}$  was higher in many urban areas, such as sites in the southeastern United States and the Central Valley of California, suggesting additional urban sources of POM. Average maximum contributions were higher in the northwestern United States and higher in IMPROVE regions (0.7 versus 0.5 in CSN regions). Although  $b_{ext\_POM}$  contributions in urban and rural regions in the southwestern United States were higher than in the East, like in eastern regions they were similar in magnitude (~0.46–0.48).

The largest urban and rural differences were observed for monthly mean maximum  $b_{ext\_EC}$ . Urban  $b_{ext\_EC}$  was higher, with values four times higher in the eastern and southwestern United States and over two times higher in the northwestern United States. In most urban regions,  $b_{ext\_EC}$  was higher during winter months, suggesting urban sources that led to higher  $b_{ext\_EC}$  relative to summer biomass smoke influence. Contributions from  $b_{ext\_EC}$  to  $b_{ext\_aer}$  were also higher in urban regions for all areas. In the eastern United States, regional average urban maximum contributions of  $b_{ext\_EC}$  were 0.16, compared to 0.09 in rural regions. This range was also observed in the northwestern United States (0.19 versus 0.10) and the southwestern United States (0.22 versus 0.11).

The average maximum  $b_{ext\_FD}$  was similar at urban and rural regions across the United States. The highest monthly mean urban  $b_{ext\_FD}$  occurred in regions in the eastern and southwestern United States, while rural regions experienced maximum  $b_{ext\_FD}$  in the southwestern United States, a region known to experience frequent dust impacts. Similar spatial patterns in  $b_{ext\_FD}$  and  $b_{ext\_CM}$  also were observed at sites in the Central Valley of California, suggesting similar sources. However, unlike  $b_{ext\_FD}$ , annual mean  $b_{ext\_CM}$  was elevated at sites in the central United States, corresponding to areas of agricultural activity. Both  $b_{ext\_FD}$  and  $b_{ext\_CM}$  were elevated at sites in the southeastern United States and the Virgin Islands site, consistent with the influence of transport of dust from North Africa. The contributions of  $b_{ext\_FD}$  and  $b_{ext\_CM}$  to  $b_{ext\_aer}$  were highest at sites in the southwestern United States, around ~0.05–0.15 and 0.2–0.3, respectively, for both urban and rural regions.

Visibility impacts of  $b_{ext\_SS}$  were low, except in coastal regions. Average contributions of  $b_{ext\_SS}$  to  $b_{ext\_aer}$  in CSN regions were 0.01–0.02 and were somewhat higher in rural regions (0.05–0.07).

The spatial patterns in  $b_{ext\_tot}$  and dv were similar and reflected the combined impacts from the species discussed above. Notably, the highest urban and rural  $b_{ext\_tot}$  and dv occurred at sites in the central United States and the Central Valley of California. Both regions corresponded to sites with the highest  $b_{ext\_AN}$ , suggesting the importance of agricultural activity on visibility in these regions. Lower  $b_{ext\_tot}$  and dv occurred at sites along the Appalachian Mountains, the Northeast, and especially the Intermountain West. While the role of biomass smoke is important to  $b_{ext\_tot}$ , with elevated levels at sites in the Northwest and Florida, the role of agriculture appeared to dominate. In both urban and rural regions, the role of  $b_{ext\_AN}$  and  $b_{ext\_POM}$  were very important, often driving the seasonality of the maximum  $b_{ext\_aer}$  due to the seasonality of specific sources (e.g., biomass smoke during summer/fall) or during periods with favorable formation conditions (e.g., winter for  $b_{ext\_AN}$ ). However,  $b_{ext\_AS}$  was within the top third contributing species in most regions, in part due to its hygroscopic nature, and was still an important contributor to  $b_{ext\_aer}$ .

## S.6 TRENDS IN IMPROVE SPECIATED AEROSOL MASS CONCENTRATIONS

One of the main purposes of the IMPROVE network is to document long-term trends for assessing progress towards the national visibility goals. Trend analyses were performed for long-term (1990–2019) and short-term (2000–2019) periods for eight parameters: annual, winter (DJF), spring (MAM), summer (JJA), and fall (SON) means, and 10<sup>th</sup>, 50<sup>th</sup>, and 90<sup>th</sup> percentiles. Temporal trends were calculated for speciated mass concentrations, including sulfate ion, nitrate ion, OC, EC, FD, FM, PM<sub>10</sub>, CM, as well as filter absorption ( $f_{abs}$ ). Trends in SS or chloride ion are not presented because of negative biases in chloride concentrations from 2007 to 2011 (Zhang, 2019). Trends in CSN data were not evaluated because of the many changes that occurred starting in 2016 that resulted in some shifts to the data that require further evaluation before trends could be accurately interpreted (see Appendix 1.2). Full details for trend analyses for mass concentrations can be found in Chapter 6 and for  $b_{ext}$  in Chapter 7.

A Theil regression was performed with the concentration data as the dependent variable and the year as the independent variable (Theil, 1950). Completeness criteria are provided in Chapter 6. A trend was considered statistically significant at 5% ( $p \leq 0.05$ ), meaning that there was a 95% chance that the slope was not due to random chance. “Trend” is defined as percent change per year (% yr<sup>-1</sup>) and was computed by dividing the slope derived from the Theil regression by the median mass concentration or  $b_{ext}$  value over the period of the trend at a given site, multiplied by 100%. Reporting trends instead of slopes reflects the relative change in concentration or  $b_{ext}$  at a given site. However, trends can be quite large (>100%) when median concentrations or  $b_{ext}$  are very low (e.g., 10<sup>th</sup> percentile).

Trend results were interpolated to provide isopleths to guide the eye Isaaks and Mohan Srivastava, 1989. Positive trends are denoted with an upward-pointing triangle and contoured with warm colors. Negative trends are shown with downward-pointing triangles and contoured with cold colors. Statistically significant trends ( $p \leq 0.05$ ) are denoted with filled triangles. Scales were kept similar for all parameters so that trends can be compared. Only short-term

annual and seasonal mean trends for speciated mass are shown here; for additional results for both long-term and percentile trends for speciated mass and  $b_{ext}$ , see Chapters 6 and 7, respectively.

Short-term, regional mean trends were calculated for ten regions of the United States. Sites were grouped by their state into the following regions: Northeast, Southeast, Midsouth, Central, Southwest, Northwest, California, Alaska, Hawaii, Virgin Islands (see Table 6.0 and Figure 6.0 in Chapter 6) and the continental United States. The Virgin Islands region included one site. Although some names are the same, these regions are broader and do not necessarily correspond to the regions shown in Section S.4 and S.5 or Chapters 3 and 5. The regions were qualitatively determined only as a means for summarizing trends.

### S.6.1 Sulfate Ion Trends

Annual mean short-term sulfate ion trends are shown in Figure S.6.1.1. Sulfate concentrations decreased for all of the short-term sites. The greatest decrease occurred for sites in the Appalachian area where  $\text{SO}_2$  emissions have also dramatically decreased Hand et al., 2020. Sites east of  $-100^{\circ}$  nearly all had concentrations decrease at rates greater than  $-4\% \text{ yr}^{-1}$ , and at sites in the Appalachia and Ohio River valley regions, trends were around  $-7\% \text{ yr}^{-1}$  to  $-10\% \text{ yr}^{-1}$ , corresponding to a 140–200% decrease over the past two decades. A strong spatial gradient in annual mean trends existed between the eastern and western United States, with weaker trends for sites in the West. Trends at sites in the western United States were about  $-2\% \text{ yr}^{-1}$  to  $-4\% \text{ yr}^{-1}$ . Insignificant trends occurred at sites in Hawaii, Alaska, and the Virgin Islands.

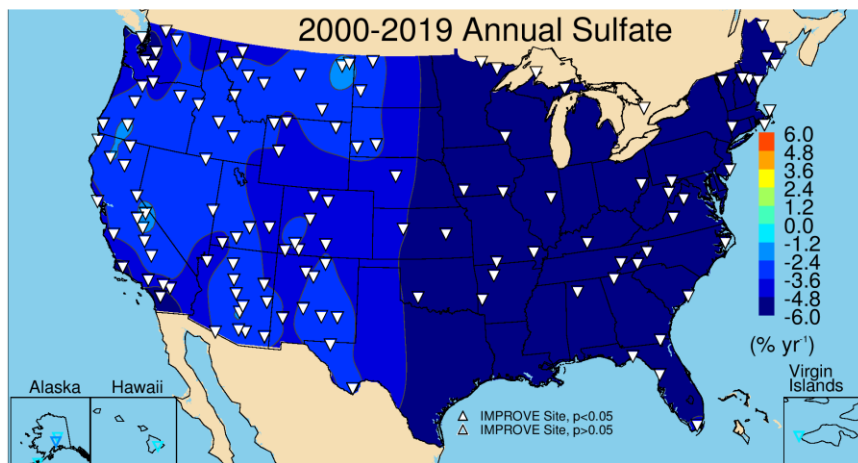


**Figure S.6.1.1.** Short-term (2000–2019) annual mean sulfate ion mass trends ( $\% \text{ yr}^{-1}$ ). Filled triangles correspond to statistically significant trends ( $p \leq 0.05$ ).

The spatial gradients and seasonal distribution in sulfate ion trends are also shown in the regional mean trends presented in Figure S.6.1.2, with regional mean trends ordered from west to east. The largest reductions in seasonal mean sulfate ion concentrations occurred for sites in the Northeast region ( $-10.56\% \text{ yr}^{-1}$  in summer), followed by the Southeast region ( $-9.46\% \text{ yr}^{-1}$  in fall). For the Northeast, Midsouth, and Central regions, the largest decrease in sulfate ion concentrations occurred during summer (in the Southeast decreases in fall were slightly larger), and the lowest decreases occurred during winter. This difference in the seasonal mean trends has led to a decrease in the seasonality of sulfate ion concentrations at eastern regions, as was

discussed in Section S.4.1 and Chapter 3. In regions in the western United States, the rate of decrease was lower, roughly half of the rate of decrease relative to eastern regions. The differences in seasonal mean trends were also smaller, suggesting that sulfate ion concentrations decreased by similar rates across seasons. The exception to this is the Southwest region, where the largest decreases occurred during both winter and fall. Overall, across the United States, sulfate ion concentrations have decreased at a higher rate during summer and fall. Seasonal mean trends at sites in Alaska, Hawaii, and the Virgin Islands were all relatively flat and insignificant.

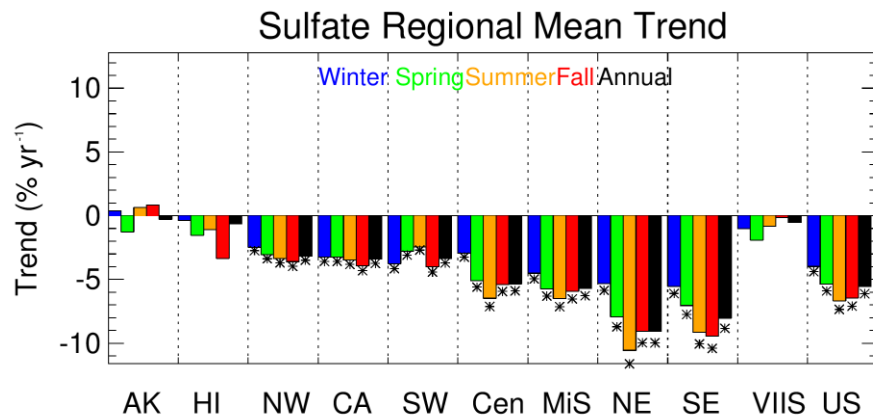


**Figure S.6.1.2.** Short-term (2000–2019) regional seasonal mean sulfate ion trends ( $\% \text{ yr}^{-1}$ ) for major U.S. regions for winter, spring, summer, fall, and annual means. Regions are arranged from western to eastern United States (AK = Alaska, HI = Hawaii, NW = Northwest, CA = California, SW = Southwest, Cen = Central, MiS = Midsouth, NE = Northeast, SE = Southeast, VIIS = Virgin Islands, and US = all sites). Statistically significant trends ( $p \leq 0.05$ ) are denoted with “\*\*”.

## S.6.2 Nitrate Ion Trends

Short-term annual mean nitrate ion trends are shown in Figure S.6.2.1. The largest reductions in the annual mean nitrate ion concentrations occurred at sites in southern California ( $\sim 9\% \text{ yr}^{-1}$ ). Strong reductions in nitrate ion concentrations in California are associated with reduced nitrogen dioxide emissions from vehicles (Krotkov et al., 2016; Hand et al., 2020). The strong east-west gradient observed for sulfate trends did not occur for nitrate trends. Insignificant trends occurred at sites in the northern Great Plains ( $-1\% \text{ yr}^{-1}$  to  $-2\% \text{ yr}^{-1}$ ), likely due to the influence of oil and gas development in the region (Prenni et al., 2016; Evanoski-Cole et al., 2017; Gebhart et al., 2018).

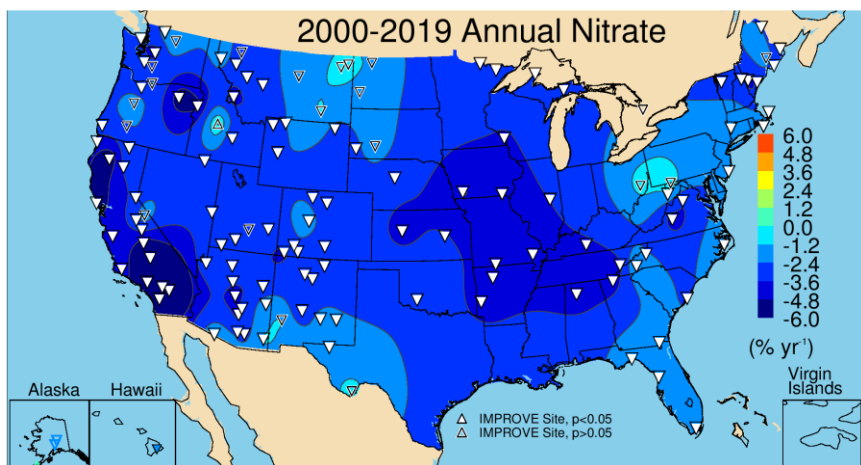


**Figure S.6.2.1.** Short-term (2000–2019) annual mean nitrate ion mass trends ( $\% \text{ yr}^{-1}$ ). Filled triangles correspond to statistically significant trends ( $p \leq 0.05$ ).

Comparisons of short-term regional, seasonal mean nitrate ion concentration trends are shown in Figure S.6.2.2. As seen in Figure S.6.2.1, the strongest reductions occurred in the California region, especially in fall ( $-7.46\% \text{ yr}^{-1}$ ,  $p < 0.001$ ) and spring ( $-7.00\% \text{ yr}^{-1}$ ,  $p < 0.001$ ). In other regions, there were differences in seasonal mean trends. For example, the regions of the Northwest, Southwest, and Southeast followed a similar pattern, with winter trends having the largest reductions, compared to the lowest reductions in summer, and spring and fall were in-between and comparable. This pattern is different from what occurred in the Midsouth region, with the strongest trends in spring, and the Central region, where the fall trends were the strongest and summer trends were lowest and insignificant. In contrast, very little range in seasonal trends occurred in the Northeast region (and winter had the lowest reductions). This range in seasonal mean trends indicates potentially different sources and atmospheric processes affecting nitrate concentrations in these regions.

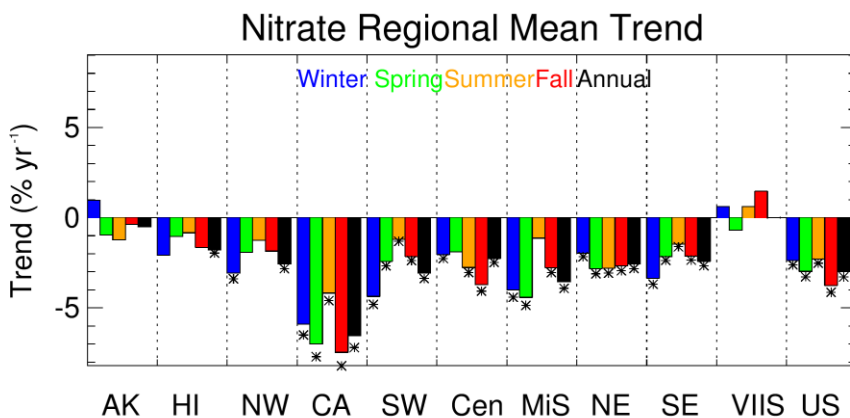


**Figure S.6.2.2.** Short-term (2000–2019) regional seasonal mean nitrate ion trends ( $\% \text{ yr}^{-1}$ ) for major U.S. regions for winter, spring, summer, fall, and annual means. Regions are arranged from western to eastern United States (AK = Alaska, HI = Hawaii, NW = Northwest, CA = California, SW = Southwest, Cen = Central, MiS = Midsouth, NE = Northeast, SE = Southeast, VIIS = Virgin Islands, and US = all sites). Statistically significant trends ( $p \leq 0.05$ ) are denoted with “\*”.

### S.6.3 Organic Carbon Trends

Trends in OC and EC may be affected by changes in analytical methods. A recent review of carbonaceous measurements in the IMPROVE program identified shifts in analytical methods and their impacts on the fraction of EC to total carbon (OC + EC), i.e., EC/TC (Schichtel et al., 2021). Other shifts in EC/TC have also occurred over the history of the program due to new analyzers, new calibrations, and undetermined reasons. These effects have motivated discussions regarding future carbonaceous aerosol measurements within the program (Schichtel et al., 2021).

Annual mean OC trends are shown in Figure S.6.3.1. Relatively strong reductions in annual mean OC occurred at sites in the eastern and northeastern United States. In the western United States, strong reductions also occurred at sites in southern California and parts of Arizona and New Mexico. Insignificant short-term trends occurred at sites in Montana, Idaho, and Washington, where biomass smoke has influenced trends in particulate matter and OC (McClure and Jaffe, 2018). Although insignificant, many of the trends at sites in the northwestern United States were positive.

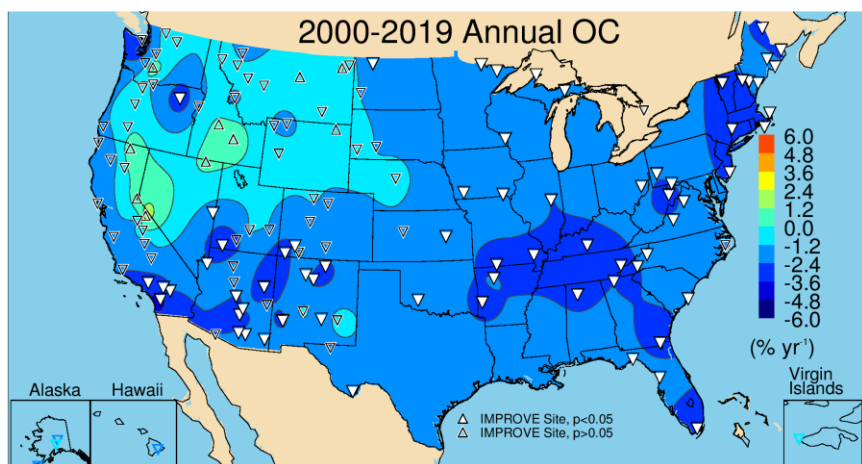
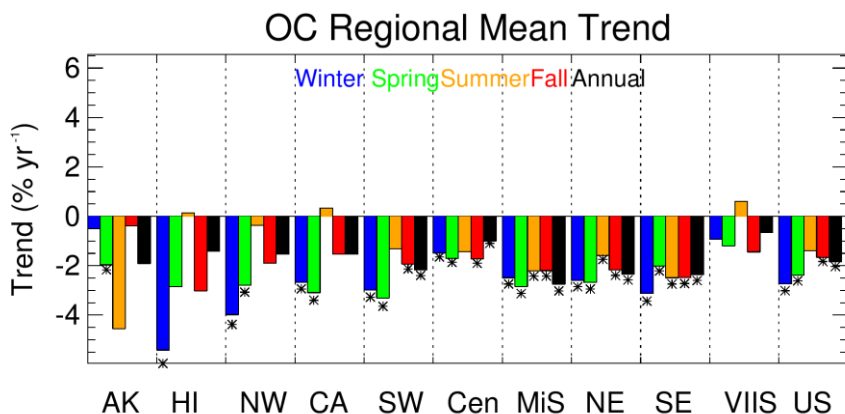


Figure S.6.3.1. Short-term (2000–2019) annual mean organic carbon (OC) mass trends ( $\% \text{ yr}^{-1}$ ). Filled triangles correspond to statistically significant trends ( $p \leq 0.05$ ).

Regional seasonal mean OC trends are shown in Figure S.6.3.2. Statistically significant trends occurred during all seasons in the Southeast, Northeast, and the Midsouth regions, about  $-3\% \text{ yr}^{-1}$ . The strongest reductions in most these regions occurred for winter and spring. Trends in the Central region were lower ( $\sim -2\% \text{ yr}^{-1}$ ) than regions in the East and statistically significant in all seasons except summer. Seasonal mean trends at western regions were more variable than in the East. All of the winter and spring trends were statistically significant, and OC declined more strongly in these months ( $-3\% \text{ yr}^{-1}$  to  $-4\% \text{ yr}^{-1}$ ). Summer and fall trends were insignificant and summer trends were flat in the Northwest and California regions. Trends during these seasons have been influenced by biomass burning emissions.



**Figure S.6.3.2.** Short-term (2000–2019) regional seasonal mean organic carbon (OC) trends ( $\% \text{ yr}^{-1}$ ) for major U.S. regions for winter, spring, summer, fall, and annual means. Regions are arranged from western to eastern United States (AK = Alaska, HI = Hawaii, NW = Northwest, CA = California, SW = Southwest, Cen = Central, MiS = Midsouth, NE = Northeast, SE = Southeast, VIIS = Virgin Islands, and US = all sites). Statistically significant trends ( $p \leq 0.05$ ) are denoted with “\*”.

#### S.6.4 Elemental Carbon Trends

EC trends are affected by hardware and analytic changes, similar to issues that affect OC trends. In addition, Malm et al. (2020) suggested EC may be inadvertently and incorrectly assigned to the OC fraction during the TOA, resulting in an underestimate of true EC concentrations. As discussed by Schichtel et al. (2021), EC concentrations have decreased at rural sites to the point that many sites have concentrations that are below the lower quantifiable limits (LQL, defined as  $3 \times$  minimum detection limit, MDL). From 2017 to 2019, about 30% of all EC concentrations were below the LQL. More sites in the West were below LQL than in the East. These low concentrations make tracking trends difficult, especially for the 10<sup>th</sup> percentile concentrations.

Most of the short-term annual mean EC trends shown in Figure S.6.4.1 were negative and statistically significant. Sites with the strongest reductions ( $-5$  to  $-6\% \text{ yr}^{-1}$ ) were located in southern California, the northwestern United States, and regions of the northeastern United States. Most of the statistically insignificant trends occurred in the West at sites influenced by biomass smoke and in northern Montana and North Dakota, where oil and gas development has been demonstrated to impact EC concentrations (Gebhart et al., 2018).

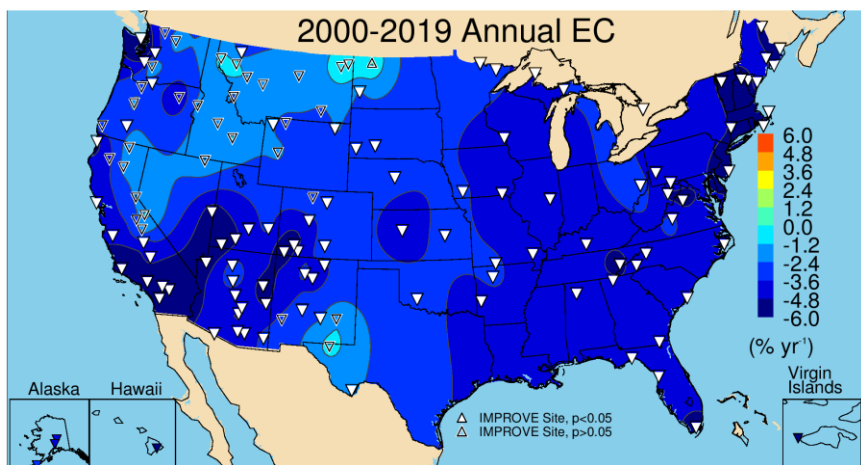


**Figure S.6.4.1.** Short-term (2000–2019) annual mean elemental carbon (EC) mass trends ( $\% \text{ yr}^{-1}$ ). Filled triangles correspond to statistically significant trends ( $p \leq 0.05$ ).

A summary of short-term regional, seasonal mean trends is shown in Figure S.6.4.2. Negative trends occurred for all regions and seasons. In regions in the eastern United States, the largest negative trends occurred during summer. Trends in the Southeast region were somewhat larger than other eastern regions, especially in winter and summer. The lowest negative trends occurred in the Central region, similar to OC trends. In the West, the strongest reductions in EC occurred mainly in winter and spring (e.g., California). Summer trends were weakest, and in the Northwest region were insignificant, likely reflecting the role of biomass smoke on EC concentrations. The difference in seasonal and regional trends implies different sources influencing EC depending on region.

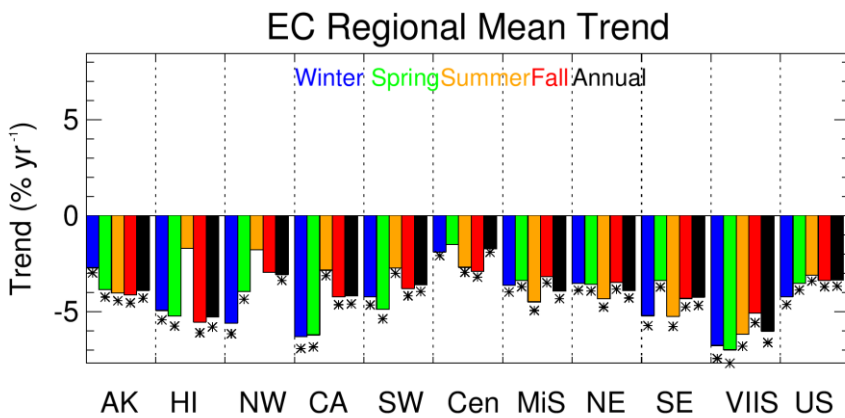


**Figure S.6.4.2.** Short-term (2000–2019) regional seasonal mean elemental carbon (EC) trends ( $\% \text{ yr}^{-1}$ ) for major U.S. regions for winter, spring, summer, fall, and annual means. Regions are arranged from western to eastern United States (AK = Alaska, HI = Hawaii, NW = Northwest, CA = California, SW = Southwest, Cen = Central, MiS = Midsouth, NE = Northeast, SE = Southeast, VIIS = Virgin Islands, and US = all sites). Statistically significant trends ( $p \leq 0.05$ ) are denoted with “\*”.

## S.6.5 Fine Dust Trends

The analytical methods used to determine elemental species used to calculate FD (see Chapter 2) have evolved over time and included PIXE (proton induced X-ray emission) and XRF

(X-ray fluorescence) techniques. The transitions from PIXE to XFR methods, the change in XRF anodes from molybdenum to copper, as well as different calibration procedures affect the data by changing MDLs (Hyslop et al., 2015). In 2011, the analysis method switched to the PANalytical XRF system that resolved issues related to undetected Al with concentrations above the MDL (White, 2006). Before 2011, XRF data below the MDL were replaced by  $0.5 \times \text{MDL}$ . Changes in analytical methods may not equally affect data for each FD species; therefore, the integrated FD concentration may be less susceptible to possible variability introduced by the analytical methods, although this has not been specifically demonstrated.

Annual mean trends in FD for 2000–2019 at sites across the eastern United States were significantly negative, especially at sites in the northeastern United States, and across the Intermountain West and northwestern United States (see Figure S.6.5.1). Many insignificant and positive trends occurred at sites near the Central Valley of California, Oklahoma, Texas, Oregon, and North Dakota. Many of the sites in the southwestern United States had statistically insignificant trends.

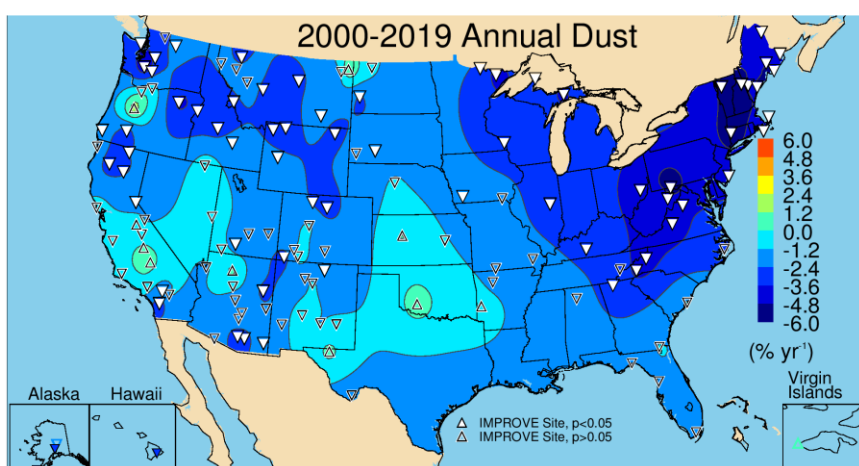


**Figure S.6.5.1.** Short-term (2000–2019) annual mean fine dust (FD) mass trends ( $\% \text{ yr}^{-1}$ ). Filled triangles correspond to statistically significant trends ( $p \leq 0.05$ ).

Compared to other species, trends in FD showed greater seasonal and spatial variability (Figure S.6.5.2). Trends were mostly insignificant and generally not strongly negative as is the case for other species. The Northeast region was the only region with statistically significant trends during all seasons. The Southeast region had statistically significant reductions in FD during all seasons except summer. Similarly, the Midsouth region had insignificant but positive trends during summer; this is the season with impacts from North African dust transport. In the Central region, only winter and spring corresponded to statistically significant negative trends. Across the West, regions were associated with insignificant though negative trends. The California region had insignificant but positive trends during summer, and the summer trends in the Northwest region were flat. FD has not experienced the levels of reduction that have occurred for other species.

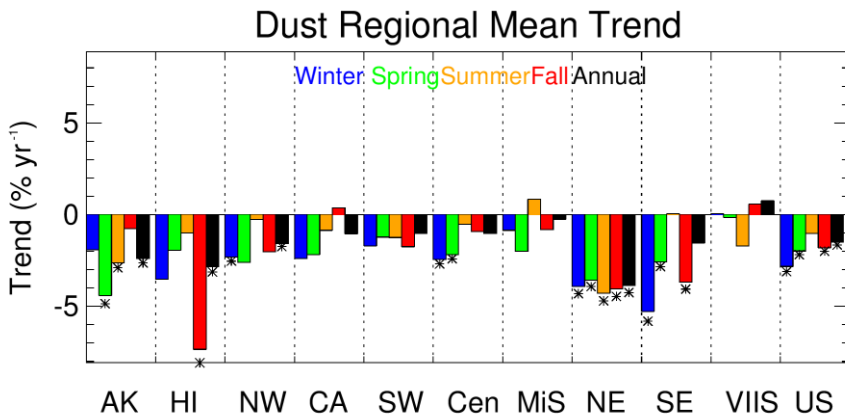


**Figure S.6.5.2.** Short-term (2000–2019) regional seasonal mean fine dust mass trends ( $\% \text{ yr}^{-1}$ ) for major U.S. regions for winter, spring, summer, fall, and annual means. Regions are arranged from western to eastern United States (AK = Alaska, HI = Hawaii, NW = Northwest, CA = California, SW = Southwest, Cen = Central, MiS = Midsouth, NE = Northeast, SE = Southeast, VIIS = Virgin Islands, and US = all sites). Statistically significant trends ( $p \leq 0.05$ ) are denoted with “\*”.

## S.6.6 Gravimetric PM<sub>2.5</sub> Fine Mass Trends

Trends in FM may be driven by trends in a particular species, depending on the degree of its contribution; however, inferring FM trends based on the trends of other species is complicated because of the spatial and seasonal variability of a specific species relative to another. The statistical significance level of trends at a given site differs for each species and for FM trends, complicating comparisons of trends from different species at a specific location. In addition, sampling or analytical artifacts, such as particle bound water, may influence FM trends (see Chapter 1, Section 1.3.1.2). For example, beginning in 2011, higher laboratory relative humidity during weighing resulted in an increase in particle bound water associated with FM data (White, 2016). This issue was resolved in 2019, but it may influence trends in FM (Hand et al., 2019b).

Short-term trends in annual mean FM are shown in Figure S.6.6.1. The strongest trends in FM at sites in the eastern United States was likely associated with sulfate reductions. Of the 134 valid short-term sites, only 78 were associated with statistically significant trends, and nearly all of the insignificant trends occurred at sites in the western United States, especially at sites in the Intermountain West, northwestern United States, and northern California, where OC trends were also insignificant. Sites in southern California had strong negative trends, likely associated with nitrate ion reductions.

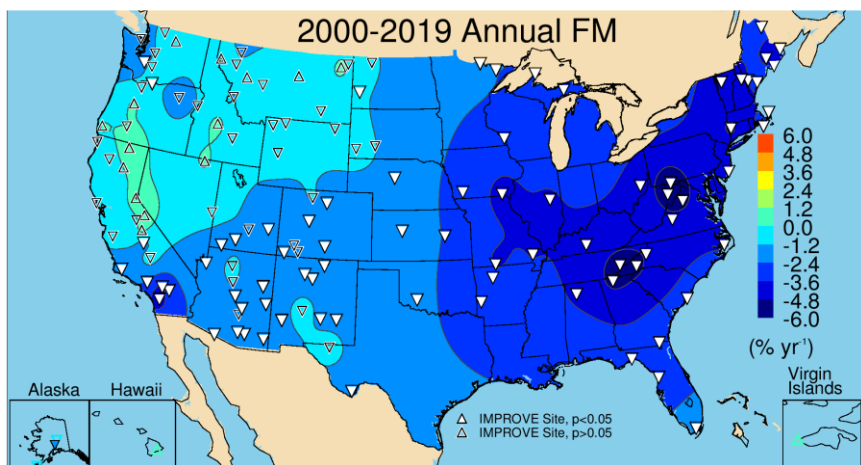


**Figure S.6.6.1.** Short-term (2000–2019) annual mean PM<sub>2.5</sub> gravimetric fine mass (FM) trends (% yr<sup>-1</sup>). Filled triangles correspond to statistically significant trends ( $p \leq 0.05$ ).

The short-term regional, seasonal mean trends in the eastern United States (Figure S.6.6.2) were similar to regional seasonal mean sulfate trends (compare Figure S.6.6.1 to Figure S.6.1.1). The strongest reductions in FM occurred in the Northeast and Southeast regions (-4% yr<sup>-1</sup> to -5% yr<sup>-1</sup>). Trends were weaker moving west, and in regions such as the Northwest and California, FM trends were similar to OC trends. Summer and fall trends in these regions were insignificant and positive, indicating the role of biomass smoke in FM trends. In the Southwest region, all of the seasons except summer had statistically significant reductions in FM. Only summer had an insignificant (negative) trend, similar to both OC and FD trends.

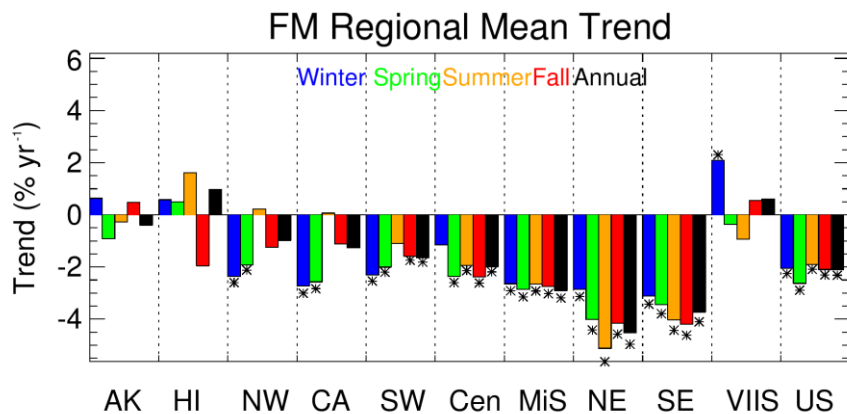


**Figure S.6.6.2.** Short-term (2000–2019) regional seasonal mean gravimetric PM<sub>2.5</sub> fine mass (FM) trends (% yr<sup>-1</sup>) for major U.S. regions for winter, spring, summer, fall, and annual means. Regions are arranged from western to eastern United States (AK = Alaska, HI = Hawaii, NW = Northwest, CA = California, SW = Southwest, Cen = Central, MiS = Midsouth, NE = Northeast, SE = Southeast, VIIS = Virgin Islands, and US = all sites). Statistically significant trends ( $p \leq 0.05$ ) are denoted with “\*\*”.

## S.6.7 Coarse Mass Trends

Short-term annual mean CM trends are shown in Figure S.6.7.1. Unlike trends in FM, only 23 of 131 valid sites had statistically significant trends, suggesting that at most sites, trends were variable. CM declined significantly at some sites, for example, in Colorado, Wyoming, and

Montana, and in Arkansas. Positive trends (mostly insignificant) occurred at 61 sites, with six being statistically significant. The spatial pattern in short-term CM trends was different from FD trends (Figure S.6.6.1), suggesting that different composition or size distribution of coarse-mode aerosols influenced CM trends.

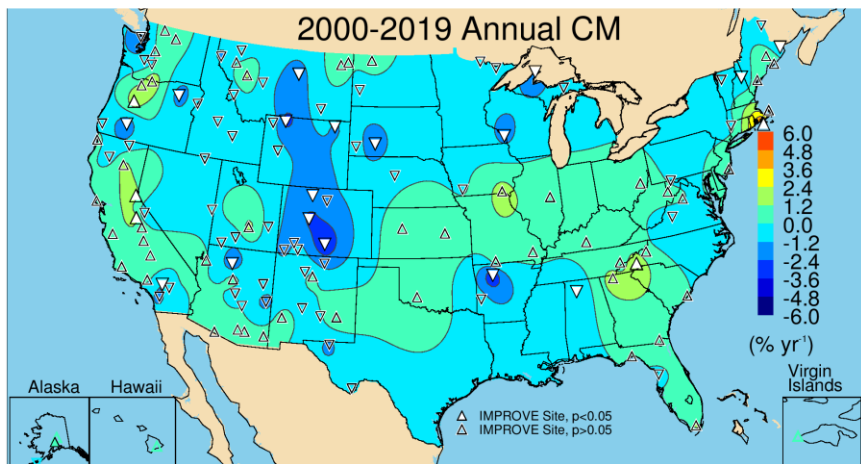


**Figure S.6.7.1** Short-term annual mean (2000–2019) coarse mass (CM) trends ( $\% \text{ yr}^{-1}$ ). Filled triangles correspond to statistically significant trends ( $p \leq 0.05$ ).

Regional seasonal mean trends are shown in Figure S.6.7.2. As suggested in Figure S.6.7.1, nearly all of the regions were associated with insignificant and weak trends, especially relative to other species already discussed. The Northeast region had significant positive trends in summer, as did the Alaska and Hawaii regions. All of the seasonal mean trends in the Central region were positive but insignificant. The Midsouth and Southwest regions had weak but negative and insignificant trends, while the California region had weak, positive insignificant trends in summer and fall but negative, insignificant trends in winter and spring. The Northwest region had statistically significant trends in winter but weak and insignificant trends during other seasons.

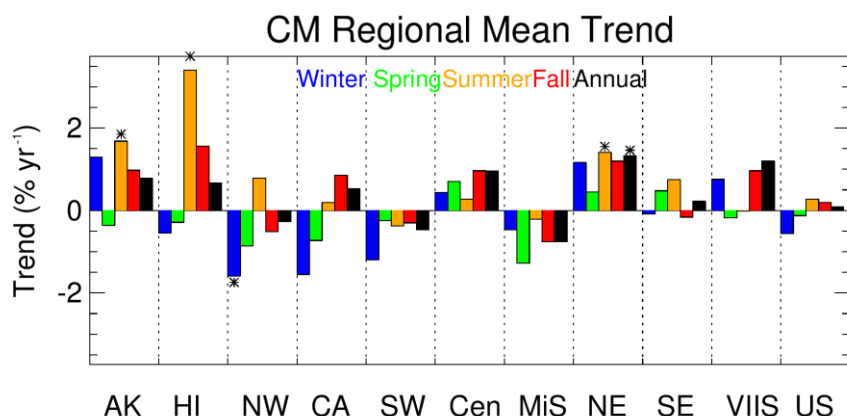


**Figure S.6.7.2.** Short-term (2000–2019) regional seasonal mean coarse mass (CM) trends ( $\% \text{ yr}^{-1}$ ) for major U.S. regions for winter, spring, summer, fall, and annual means. Regions are arranged from western to eastern United States (AK = Alaska, HI = Hawaii, NW = Northwest, CA = California, SW = Southwest, Cen = Central, MiS = Midsouth, NE = Northeast, SE = Southeast, VIIS = Virgin Islands, and US = all sites). Statistically significant trends ( $p \leq 0.05$ ) are denoted with “\*”.

## S.6.8 Discussion

Timelines of regional, annual mean mass concentrations for PM<sub>2.5</sub> sulfate ion, nitrate ion, OC, EC, and FD corresponding to previous trend results are shown in Figure S.6.8 (a-j). Similar timelines for CM concentrations can be found in Chapter 6. These mass concentrations do not include mass correction factors for sulfate, nitrate, or OC (e.g., concentrations are for sulfate ion, not ammonium sulfate); therefore, the sum of individual bars should not be interpreted as RCFM, such as is shown in Chapter 3. However, the basic patterns are similar and reflect both RCFM and FM. It is clear from these timelines and the previous trend discussions that strong reductions in FM have occurred at nearly all remote regions across the United States. These reductions were greatest in the East and driven by strong negative trends in sulfate ion concentrations. Sulfate concentrations have decreased in response to dramatic reductions in SO<sub>2</sub> emissions due to regulatory activity (Hand et al., 2020). In addition, reductions in nitrate ion and OC concentrations (especially in the East) have contributed to reduced FM. Negative trends in nitrate concentrations at sites in southern California occurred where nitrogen dioxide emissions, especially mobile emissions, have declined due to regulatory activity.

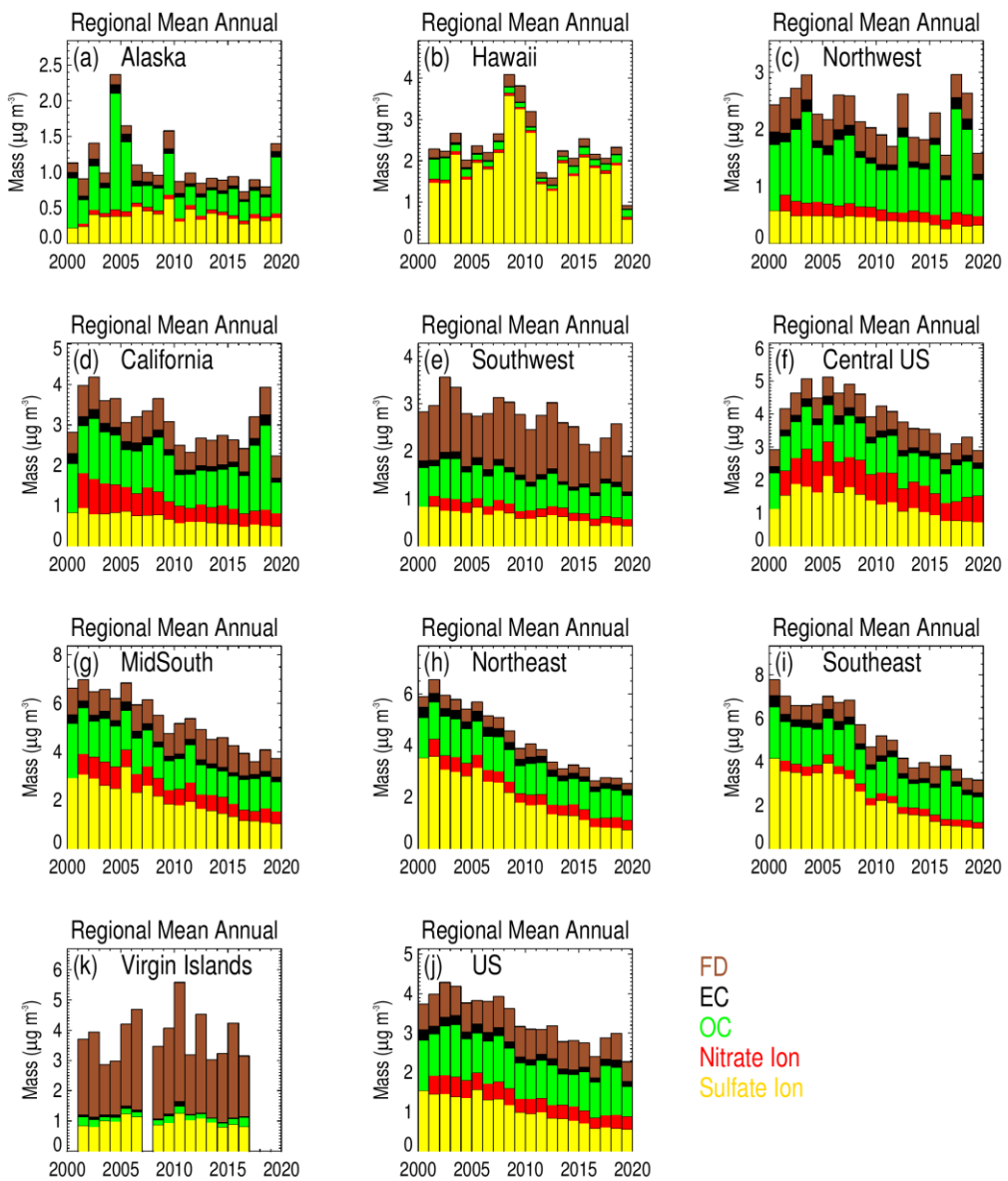


**Figure S.6.8.** Short-term (2001–2019) timelines of IMPROVE regional, annual mean mass concentrations ( $\mu\text{g m}^{-3}$ ) for sulfate ion, nitrate ion, organic carbon (OC), elemental carbon (EC), and fine dust (FD).

At sites in the western United States, especially the Northwest, FM has declined at a weaker rate relative to sites in the East. Comparisons of OC and EC trends suggest that FM is influenced by biomass burning impacts that have led to an increase in OC, or at the very least flat and insignificant trends. OC is a major contributor to FM, especially at western sites, and has influenced FM trends in the region (McClure and Jaffe, 2018).

FM concentrations at sites in the Southwest have decreased (many insignificantly), although to a lower extent relative to sites in the East. The FM budget at these sites includes a significant fraction of FD, and trends in FD were insignificant. OC trends were also insignificant at many southwestern sites, suggesting that the role of FD and OC may have influenced FM trends in the region.

CM trends were notably different from trends in PM<sub>2.5</sub> speciated mass trends in that only a few sites across the United States had statistically significant negative CM trends. Several sites had statistically significant positive trends. Many of these sites did not have positive trends in FD, suggesting that CM may be associated with larger particles or species other than mineral dust.

Regulatory activity has been very successful at reducing pollutant emissions that lead to secondary aerosols, such as sulfate, nitrate, and OC, as well as reductions in primary aerosols such as EC, and some OC, depending on its sources. Reductions in these species have driven negative trends in FM and PM<sub>10</sub> at sites across the United States. However, the role of natural aerosols, such as those derived from biomass smoke and dust storms have not declined and for some sites and seasons have increased. The impact of these positive trends have and likely will continue to impede progress in reducing FM and PM<sub>10</sub> concentrations.

## REFERENCES

- Chow, J. C., Watson, J. G., Pritchett, L. C., Pierson, W. R., Frazier, C. A., and Purcell, R. G. (1993), The DRI thermal/optical reflectance carbon analysis system: description, evaluation and applications in US air quality studies, *Atmospheric Environment. Part A. General Topics*, 27(8), 1185-1201, doi:[https://doi.org/10.1016/0960-1686\(93\)90245-T](https://doi.org/10.1016/0960-1686(93)90245-T).
- Debell, L. J., Gebhart, K., Hand, J. L., Malm, W. C., Pitchford, M. L., Schichtel, B. S., and White, W. H. (2006), IMPROVE (Interagency Monitoring of Protected Visual Environments): Spatial and seasonal patterns and temporal variability of haze and its constituents in the United States: Report IV, *Colorado State University, Fort Collins CO*, 4.
- Evanoski-Cole, A., Gebhart, K., Sive, B., Zhou, Y., Capps, S., Day, D., Prenni, A., Schurman, M., Sullivan, A., and Li, Y. (2017), Composition and sources of winter haze in the Bakken oil and gas extraction region, *Atmospheric Environment*, 156, 77-87, doi:<http://dx.doi.org/10.1016/j.atmosenv.2017.02.019>.
- Gebhart, K. A., Day, D. E., Prenni, A. J., Schichtel, B. A., Hand, J. L., and Evanoski-Cole, A. R. (2018), Visibility impacts at Class I areas near the Bakken oil and gas development, *Journal of the Air & Waste Management Association*, 68(5), 477-493, doi:10.1080/10962247.2018.1429334.
- Gorham, K. A., Raffuse, S. M., Hyslop, N. P., and White, W. H. (2021), Comparison of recent speciated PM<sub>2.5</sub> data from collocated CSN and IMPROVE measurements, *Atmospheric Environment*, 244, 117977, doi:<https://doi.org/10.1016/j.atmosenv.2020.117977>.
- Hand, J. L., Copeland, S., Day, D., Dillner, A., Indresand, H., Malm, W., McDade, C., Moore, C., Pitchford, M., and Schichtel, B. (2011), IMPROVE (Interagency Monitoring of Protected Visual Environments): Spatial and seasonal patterns and temporal variability of haze and its constituents in the United States, *CIRA Report*, 5.
- Hand, J. L., Gill, T., and Schichtel, B. (2017), Spatial and seasonal variability in fine mineral dust and coarse aerosol mass at remote sites across the United States, *Journal of Geophysical Research: Atmospheres*, 122(5), 3080-3097, doi:doi:10.1002/2016JD026290.
- Hand, J. L., Gill, T. E., and Schichtel, B. A. (2019a), Urban and rural coarse aerosol mass across the United States: Spatial and seasonal variability and long-term trends, *Atmospheric Environment*, 218, 117025, doi:doi.org/10.1016/j.atmosenv.2019.117025.
- Hand, J. L., Prenni, A. J., Schichtel, B. A., Malm, W. C., and Chow, J. C. (2019b), Trends in remote PM<sub>2.5</sub> residual mass across the United States: Implications for aerosol mass reconstruction in the IMPROVE network, *Atmospheric Environment*, 203, 141-152, doi:doi:10.1016/j.atmosenv.2019.01.049.
- Hand, J. L., Prenni, A. J., Copeland, S., Schichtel, B. A., and Malm, W. C. (2020), Thirty years of the Clean Air Act Amendments: Impacts on haze in remote regions of the United States

(1990–2018), *Atmospheric Environment*, 243, 117865,  
doi:<https://doi.org/10.1016/j.atmosenv.2020.117865>.

Hyslop, N. P., Trzepla, K., and White, W. H. (2015), Assessing the suitability of historical PM<sub>2.5</sub> element measurements for trend analysis, *Environmental Science & Technology*, 49(15), 9247–9255, doi:DOI: 10.1021/acs.est.5b01572.

Isaaks, E. H., and Mohan Srivastava, R. (1989), *An Introduction to Applied Geostatistics*, Oxford University Press, New York, 978-0195050134.

Krotkov, N. A., McLinden, C. A., Li, C., Lamsal, L. N., Celarier, E. A., Marchenko, S. V., Swartz, W. H., Bucsela, E. J., Joiner, J., Duncan, B. N., Boersma, K. F., Veefkind, J. P., Levelt, P. F., Fioletov, V. E., Dickerson, R. R., He, H., Lu, Z., and Streets, D. G. (2016), Aura OMI observations of regional SO<sub>2</sub> and NO<sub>2</sub> pollution changes from 2005 to 2015, *Atmos. Chem. Phys.*, 16(7), 4605–4629, doi:10.5194/acp-16-4605-2016.

Lambert, A., Hallar, A. G., Garcia, M., Strong, C., Andrews, E., and Hand, J. L. (2020), Dust impacts of rapid agricultural expansion on the Great Plains, *Geophysical Research Letters*, 47(20), e2020GL090347, doi:<https://doi.org/10.1029/2020GL090347>.

Malm, W., Sisler, J. F., Pitchford, M., Scruggs, M., Ames, R. B., Copeland, S., Gebhart, K., and Day, D. (2000), IMPROVE (Interagency Monitoring of Protected Visual Environments): Spatial and seasonal patterns and temporal variability of haze and its constituents in the United States: Report III, *CIRA Report*, 3.

Malm, W., Schichtel, B., Hand, J., and Prenni, A. (2020), Implications of organic mass to carbon ratios increasing over time in the rural United States, *Journal of Geophysical Research: Atmospheres*, 125(5), e2019JD031480.

McClure, C. D., and Jaffe, D. A. (2018), US particulate matter air quality improves except in wildfire-prone areas, *Proceedings of the National Academy of Sciences*, 115(31), 7901–7906, doi:doi:10.1073/pnas.1804353115.

Pitchford, M. L., and Malm, W. C. (1994), Development and applications of a standard visual index, *Atmospheric Environment*, 28(5), 1049–1054, doi:[https://doi.org/10.1016/1352-2310\(94\)90264-X](https://doi.org/10.1016/1352-2310(94)90264-X).

Prenni, A., Day, D., Evanoski-Cole, A., Sive, B., Hecobian, A., Zhou, Y., Gebhart, K., Hand, J., Sullivan, A., and Li, Y. (2016), Oil and gas impacts on air quality in federal lands in the Bakken region: an overview of the Bakken Air Quality Study and first results, *Atmospheric Chemistry and Physics*, 16(3), 1401–1416, doi:doi:10.5194/acp-16-1401-2016.

Schichtel, B. A., Malm, W. C., Beaver, M., Copeland, S., Hand, J. L., Prenni, A. J., Rice, J., and Vimont, J. (2021), The Future of Carbonaceous Aerosol Measurement in the IMPROVE Monitoring Program, [http://vista.cira.colostate.edu/improve/wp-content/uploads/2021/10/041\\_CarbonReport\\_Final.pdf](http://vista.cira.colostate.edu/improve/wp-content/uploads/2021/10/041_CarbonReport_Final.pdf).

Sisler, J. F., Huffman, D., Latimer, D. A., Malm, W. C., and Pitchford, M. (1993), IMPROVE (Interagency Monitoring of Protected Visual Environments): Spatial and Temporal Patterns and the Chemical Composition of the Haze in the United States: An Analysis of Data from the IMPROVE Network, 1988-1991: Report I *Colorado State University, Fort Collins CO*, 1.

Sisler, J. F., Malm, W. C., Gebhart, K., and Pitchford, M. (1996), IMPROVE (Interagency Monitoring of Protected Visual Environments): Spatial and Seasonal Patterns and Long Term Variability of the Composition of the Haze in the United States: An Analysis of Data from the IMPROVE Network, 1996: Report II, *Colorado State University, Fort Collins CO*, 2.

Solomon, P. A., Crumpler, D., Flanagan, J. B., Jayanty, R. K. M., Rickman, E. E., and McDade, C. E. (2014), U.S. National PM<sub>2.5</sub> Chemical speciation monitoring networks—CSN and IMPROVE: Description of networks, *Journal of the Air & Waste Management Association*, 64(12), 1410-1438, doi:doi:10.1080/10962247.2014.956904.

Theil, H. (1950), A rank-invariant method of linear and polynomial regression analysis., *Proc. Kon. Ned. Akad. v Wetensch.*, A(53), 386-392, doi:[https://doi.org/10.1007/978094-011-2546-8\\_20](https://doi.org/10.1007/978094-011-2546-8_20).

White, W. H. (2006), Elemental concentrations above the MDL can go undetected, *IMPROVE Data Advisory* (da0010),  
[http://vista.cira.colostate.edu/improve/Data/QA\\_QC/Advisory/da0010/da0010\\_Almdl.pdf](http://vista.cira.colostate.edu/improve/Data/QA_QC/Advisory/da0010/da0010_Almdl.pdf).

White, W. H. (2016), Increased variation of humidity in the weighing laboratory, *IMPROVE Data Advisory* (da0035),  
[http://vista.cira.colostate.edu/improve/Data/QA\\_QC/Advisory/da0035/da0035\\_IncreasedRH.pdf](http://vista.cira.colostate.edu/improve/Data/QA_QC/Advisory/da0035/da0035_IncreasedRH.pdf).

Zhang, X. (2019), Correction of chloride concentrations for filter blank levels, *IMPROVE Data Advisory* (da0039),  
[http://vista.cira.colostate.edu/improve/Data/QA\\_QC/Advisory/da0039/da0039\\_ChlorideOverCorrection.pdf](http://vista.cira.colostate.edu/improve/Data/QA_QC/Advisory/da0039/da0039_ChlorideOverCorrection.pdf).

# **Chapter 1. Interagency Monitoring of Protected Visual Environments (IMPROVE) Network: Configuration and Measurements**

## **1.1 INTRODUCTION**

The Regional Haze Rule (RHR), promulgated by the U.S. Environmental Protection Agency (EPA) in 1999 (EPA, 1999a), requires monitoring in locations representative of the 156 visibility-protected federal Class I areas (CIAs, see Figure 1.1) in order to track progress toward the goal of returning visibility to natural conditions. Air quality monitoring under the RHR began in 2000. The most recent RHR guidelines stipulate tracking progress using the haze metric in deciview units on the most anthropogenically impaired days (EPA, 2018), calculated from speciated particle composition concentrations. Computing haze metrics from particle speciation data requires sampling and analysis of major aerosol species, using methods employed by the Interagency Monitoring of Protected Visual Environments (IMPROVE) network since 1987 (Joseph et al., 1987; Malm et al., 1994). These methods are consistent with the aerosol monitoring portion of the 1999 Visibility Monitoring Guidance document issued by the EPA (EPA, 1999b).

The IMPROVE program is a cooperative measurement effort designed to

1. establish current visibility and aerosol conditions in mandatory CIAs;
2. identify chemical species and emission sources responsible for existing anthropogenic and natural visibility impairment;
3. document long-term trends for assessing progress toward the national visibility goal;
4. provide regional haze monitoring representing all visibility-protected federal CIAs where practical.

Although the program is focused on visibility objectives, the data acquired and the methodologies developed by the IMPROVE network have been broadly used to address air quality management related to human health, climate change, ecosystem degradation, and material damage.

The program is managed by the IMPROVE steering committee, which consists of representatives from the EPA; the four federal land managers (FLMs): the National Park Service (NPS), U.S. Forest Service (USFS), U.S. Fish and Wildlife Service (FWS), and Bureau of Land Management (BLM); the National Oceanic and Atmospheric Administration (NOAA); four organizations representing state air quality organizations: the National Association of Clean Air Agencies (NACAA), Western States Air Resource Council/Western Regional Air Partnership (WESTAR/WRAP), Northeast States for Coordinated Air Use Management (NESCAUM), and Mid-Atlantic Regional Air Management Association (MARAMA); and three associate members: the State of Arizona Department of Environmental Quality, Environment Canada, and the South Korea Ministry of Environment.

Also included in this report is a summary of monitoring and data from the EPA's Chemical Speciation Network (CSN). This network exists to monitor aerosol speciation data for understanding human exposure in urban and suburban regions. Aggregating data from the CSN

and the IMPROVE network provides a more complete understanding of current and changing conditions in aerosol composition and haze across the United States.



Figure 1.1. Class I areas of the United States. Shading identifies the managing agency of each CIA.

## **1.2 OVERVIEW OF THE IMPROVE MONITORING NETWORK**

### **1.2.1 Site Locations**

The IMPROVE network initially consisted of 30 monitoring sites in CIAs; twenty of these sites began operation in 1987, followed by the others in the early 1990s. An additional ~40 sites, most in remote areas, that used the same instrumentation, monitoring, and analysis protocols (called IMPROVE protocol sites) began operation prior to 2000 and were separately sponsored by individual federal or state organizations, though they were operated identically to other sites in the IMPROVE network. Adjustments to the number of monitoring sites in the network or the suite of measurements collected at an individual site occurred on several occasions, due in some cases to scientific considerations and in others to resource and funding limitations. Several of the sites also included optical monitoring with a nephelometer or a transmissometer and scene monitoring with color photography to document scenic appearance. The current state of optical monitoring is detailed in Section 1.2.3.

In 1998 the EPA increased its support of IMPROVE to expand the network in CIAs to provide the monitoring required under the RHR. Details regarding the selection process of additional sites was provided in IMPROVE report III (Malm et al., 2000). The selection process was completed by the end of 1999 and installations began shortly thereafter. The network consists of 229 sites (159 operating and 70 discontinued), including representative sites for the CIAs, and additional protocol sites to fill in the spatial gaps where CIAs are sparse or absent. The sites are grouped by region, a semiquantitative empirical categorization that regionally organizes sites based on similar aerosol species concentrations and seasonal patterns. There are 36 IMPROVE regions: 29 rural, four urban (including both long-term urban sites and urban quality assurance sites), and three international sites. Some rural regions may have only one site (e.g., Death Valley, Lone Peak, Virgin Islands). A map of the site locations is provided in Figure 1.2, and a list of sampling sites is provided in Table 1.1, which includes the site name, site code, state, latitude, longitude, elevation, and dates of operation. The sites are depicted by their site code and shaded based on their region, as defined in Table 1.1. Blue symbols correspond to sites with data used in the analyses presented in this report. CIAs and their representative sites are listed in Table 1.2.

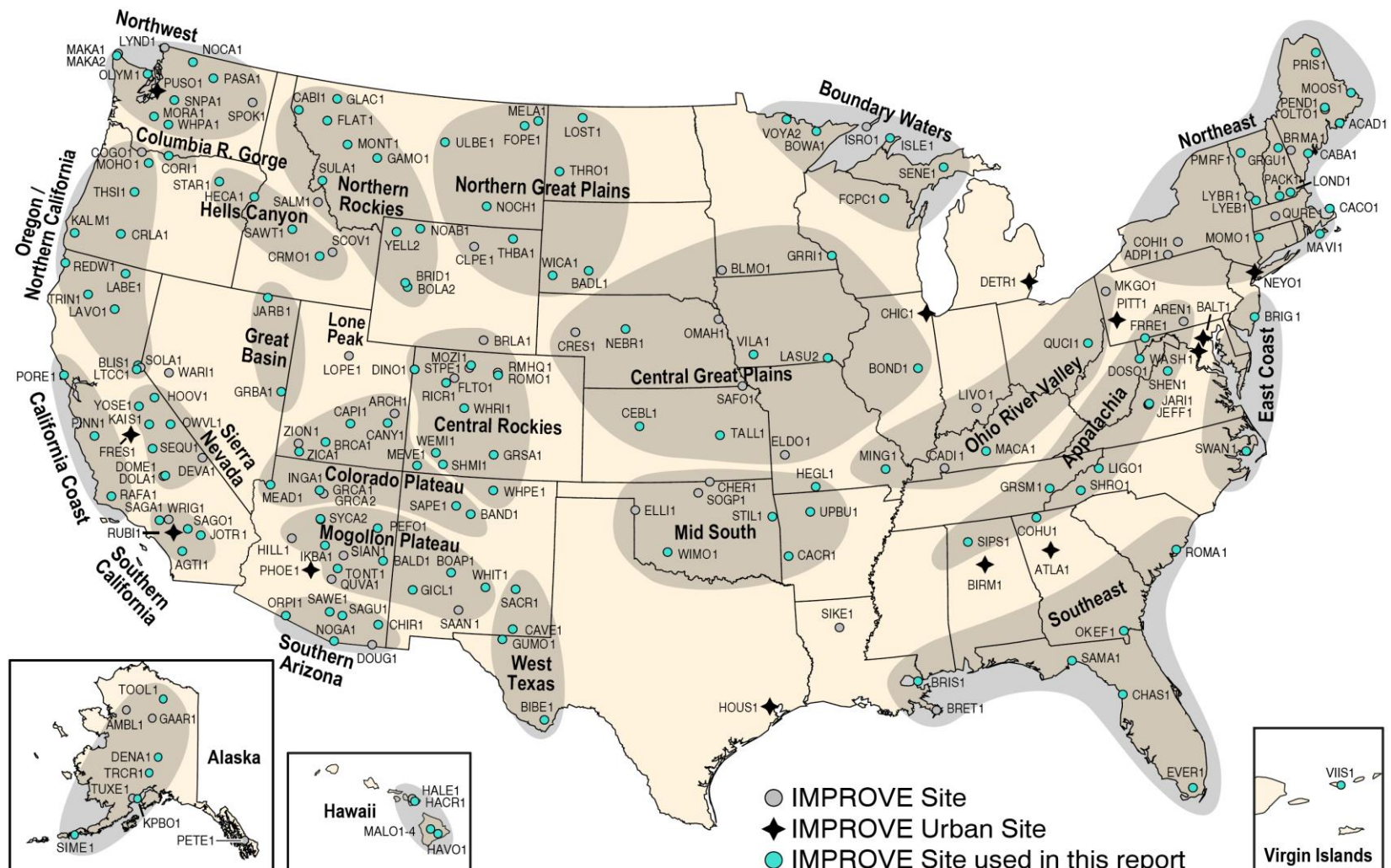


**Figure 1.2. Locations of IMPROVE sites for all discontinued and current sites. IMPROVE regions are indicated by shading and bold text. Urban IMPROVE sites are identified by stars. Blue circles indicate sites with data used in the analyses in this report.**

**Table 1.1. Currently operating and discontinued IMPROVE particulate monitoring sites. Sites are grouped by region, as displayed in Figure 1.2.**

Site Name	Site Code	State	Latitude	Longitude	Elevation (m)	Dates of Operation
<b>Alaska</b>						
Ambler	AMBL1	AK	67.099	-157.863	77	09/03/2003-11/29/2004
Denali NP	DENA1	AK	63.723	-148.968	658	03/02/1988-present
Gates of the Arctic NP	GAAR1	AK	66.903	-151.517	196	11/02/2008-10/30/2015
Kenai Peninsula Borough	KPBO1	AK	60.012	-151.711	5	08/19/2015-present
Petersburg	PETE1	AK	56.611	-132.812	0	07/02/2004-09/28/2009
Simeonof	SIME1	AK	55.325	-160.506	57	09/13/2001-present
Toolik Lake Field Station	TOOL1	AK	68.632	-149.606	740	11/01/2018-present
Trapper Creek	TRCR1	AK	62.315	-150.316	155	09/13/2001-present
Tuxedni	TUXE1	AK	59.992	-152.666	15	12/03/2001-01/12/2015
<b>Alberta</b>						
Barrier Lake	BALA1	AB	51.029	-115.034	1391	01/15/2011-03/29/2017
<b>Appalachia</b>						
Arendtsville	AREN1	PA	39.923	-77.308	267	04/04/2001-12/31/2010
Cohutta	COHU1	GA	34.785	-84.626	735	06/03/2000-present
Dolly Sods WA	DOSO1	WV	39.105	-79.426	1182	09/04/1991-present
Frostburg Reservoir	FRRE1	MD	39.706	-79.012	767	03/01/2004-present
Great Smoky Mountains NP	GRSM1	TN	35.633	-83.942	810	03/02/1988-present
James River Face WA	JARI1	VA	37.627	-79.513	290	06/03/2000-present
Jefferson NF	JEFF1	VA	37.617	-79.483	219	09/1994-02/26/2000
Linville Gorge WA	LIGO1	NC	35.972	-81.933	969	04/01/2000-present
Shenandoah NP	SHEN1	VA	38.523	-78.435	1079	03/02/1988-present
Shining Rock WA	SHRO1	NC	35.394	-82.774	1617	06/01/1994-present
Sipsey WA	SIPS1	AL	34.343	-87.339	286	03/04/1992-present
<b>Boundary Waters</b>						
Boundary Waters Canoe Area WA	BOWA1	MN	47.947	-91.496	527	06/01/1991-present
Forest County Potawatomi Community	FCPC1	WI	45.565	-88.808	564	11/17/2016-present
Isle Royale NP	ISLE1	MI	47.46	-88.149	182	11/17/1999-present
Isle Royale NP	ISRO1	MI	47.917	-89.15	213	06/01/1988-12/29/1999
Seney	SENE1	MI	46.289	-85.95	215	11/17/1999-present
Voyageurs NP #1	VOYA1	MN	48.413	-92.83	426	03/02/1988-12/29/1999
Voyageurs NP #2	VOYA2	MN	48.413	-92.829	429	03/02/1999-present
<b>California Coast</b>						
Pinnacles NP	PINN1	CA	36.483	-121.157	302	03/02/1988-present
Point Reyes NS	PORE1	CA	38.122	-122.909	97	03/02/1988-present
San Rafael WA	RAFA1	CA	34.734	-120.007	956	02/02/2000-present
<b>Central Great Plains</b>						
Blue Mounds	BLMO1	MN	43.716	-96.191	473	06/01/2002-12/29/2015
Bondville	BOND1	IL	40.052	-88.373	263	03/08/2001-present
Cedar Bluff	CEBL1	KS	38.77	-99.763	666	06/01/2002-present
Crescent Lake	CRES1	NE	41.763	-102.434	1207	06/01/2002-12/29/2015
El Dorado Springs	ELDO1	MO	37.701	-94.035	298	03/03/2002-12/29/2015
Great River Bluffs	GRRI1	MN	43.937	-91.405	370	06/01/2002-present

<b>Site Name</b>	<b>Site Code</b>	<b>State</b>	<b>Latitude</b>	<b>Longitude</b>	<b>Elevation (m)</b>	<b>Dates of Operation</b>
Lake Sugema #1	LASU1	IA	40.688	-91.988	210	05/08/2002-11/29/2004
Lake Sugema #2	LASU2	IA	40.693	-92.006	229	12/02/2004-present
Nebraska NF	NEBR1	NE	41.889	-100.339	883	06/01/2002-present
Omaha	OMAH1	NE	42.149	-96.432	430	06/02/2003-08/04/2008
Sac and Fox	SAFO1	KS	39.979	-95.568	293	06/01/2002-06/29/2011
Tallgrass	TALL1	KS	38.434	-96.56	390	09/02/2002-present
Viking Lake	VILA1	IA	40.969	-95.045	371	05/08/2002-present
<b>Central Rocky Mountains</b>						
Brooklyn Lake	BRLA1	WY	41.366	-106.242	3196	07/31/1993-01/31/2004
Dinosaur NM	DINO1	CO	40.25	-108.967	1829	11/01/2018-present
Fort Collins	FOCO1	CO	40.593	-105.143	1572	07/2020-present
Fort Collins	FOCO2	CO	40.593	-105.143	1572	07/2020-present
Flat Tops	FLTO1	CO	39.915	-107.635	2593	10/27/2011-09/28/2021
Great Sand Dunes NP	GRSA1	CO	37.725	-105.519	2498	03/02/1988-present
Mount Zirkel WA	MOZI1	CO	40.538	-106.677	3243	06/01/1994-present
Ripple Creek	RICR1	CO	40.087	-107.314	2934	03/02/2009-10/30/2011
Rocky Mountain NP Headquarters	RMHQ1	CO	40.362	-105.564	2408	03/02/1988-12/29/1999
Rocky Mountain NP	ROMO1	CO	40.278	-105.546	2760	09/01/1990-present
Storm Peak	STPE1	CO	40.445	-106.74	3220	12/01/1993-12/29/1999
Shamrock Mine	SHMI1	CO	37.304	-107.484	2351	08/01/2004-12/27/2021
Wheeler Peak	WHPE1	NM	36.585	-105.452	3366	08/16/2000-present
White River NF	WHRI1	CO	39.154	-106.821	3414	06/02/1993-present
<b>Colorado Plateau</b>						
Arches NP	ARCH1	UT	38.783	-109.583	1722	03/02/1988-12/29/1999
Bandelier NM	BAND1	NM	35.78	-106.266	1988	03/02/1988-present
Bryce Canyon NP	BRCA1	UT	37.618	-112.174	2481	03/02/1988-present
Canyonlands NP	CANY1	UT	38.459	-109.821	1798	03/02/1988-present
Capitol Reef NP	CAPI1	UT	38.302	-111.293	1896	04/19/2000-present
Hopi Point	GRCA1	AZ	36.066	-112.154	2164	03/02/1988-12/29/1999
Hance Camp at Grand Canyon NP	GRCA2	AZ	35.973	-111.984	2267	03/02/1996-present
Indian Gardens	INGA1	AZ	36.078	-112.129	1166	09/02/1989-05/13/2013
Meadview	MEAD1	AZ	36.019	-114.068	902	09/04/1991-02/27/2021
Mesa Verde NP	MEVE1	CO	37.198	-108.491	2172	03/02/1988-present
San Pedro Parks WA	SAPE1	NM	36.014	-106.845	2935	08/16/2000-present
Weminuche WA	WEMI1	CO	37.659	-107.8	2750	03/02/1988-present
Zion Canyon	ZICA1	UT	37.198	-113.151	1215	12/01/2002-present
Zion NP	ZION1	UT	37.459	-113.224	1545	03/25/2000-08/22/2004
<b>Columbia River Gorge</b>						
Columbia Gorge	COGO1	WA	45.569	-122.21	230	09/18/1996-10/30/2011
Columbia River Gorge	CORI1	WA	45.664	-121.001	178	06/02/1993-present
<b>Death Valley</b>						
Death Valley NP	DEVA1	CA	36.509	-116.848	130	09/04/1993-04/28/2013
<b>East Coast</b>						
Brigantine NWR	BRIG1	NJ	39.465	-74.449	5	09/04/1991-present
Swanquarter	SWAN1	NC	35.451	-76.208	-4	06/10/2000-present
<b>Great Basin</b>						
Great Basin NP	GRBA1	NV	39.005	-114.216	2066	03/04/1992-present
Jarbridge WA	JARB1	NV	41.893	-115.426	1869	03/02/1988-present
<b>Hawaii</b>						

<b>Site Name</b>	<b>Site Code</b>	<b>State</b>	<b>Latitude</b>	<b>Longitude</b>	<b>Elevation (m)</b>	<b>Dates of Operation</b>
Haleakala Crater	HACR1	HI	20.759	-156.248	2158	01/24/2007-present
Haleakala NP	HALE1	HI	20.809	-156.282	1153	12/01/1990-05/30/2012
Hawaii Volcanoes NP	HAVO1	HI	19.431	-155.258	1259	03/02/1988-present
Mauna Loa Observatory #1	MALO1	HI	19.536	-155.577	3439	12/02/1992-08/28/2004
Mauna Loa Observatory #2	MALO2	HI	19.536	-155.577	3439	12/02/1992-08/28/2004
Mauna Loa Observatory #3	MALO3	HI	19.539	-155.578	3400	03/06/1996-02/26/2000
Mauna Loa Observatory #4	MALO4	HI	19.539	-155.578	3400	03/02/1996-02/26/2000
<b>Hells Canyon</b>						
Craters of the Moon NM	CRMO1	ID	43.461	-113.555	1818	03/04/1992-present
Hells Canyon	HECA1	OR	44.97	-116.844	655	09/03/2000-present
Sawtooth NF	SAWT1	ID	44.171	-114.927	1990	12/01/1993-present
Scoville	SCOV1	ID	43.65	-113.033	1500	03/04/1992-02/26/2000
Starkey	STAR1	OR	45.225	-118.513	1259	03/15/2000-present
<b>Korea</b>						
Baengnyeong Island	BYIS1		37.966	124.631	100	03/20/2013-present
<b>Lone Peak</b>						
Lone Peak WA	LOPE1	UT	40.445	-111.708	1768	12/01/1993-08/29/2001
<b>Mid South</b>						
Caney Creek	CACR1	AR	34.454	-94.143	683	06/24/2000-present
Cherokee Nation	CHER1	OK	36.956	-97.031	342	09/02/2002-04/20/2010
Ellis	ELLI1	OK	36.085	-99.935	697	03/02/2002-10/18/2015
Hercules-Glades	HEGL1	MO	36.614	-92.922	404	03/02/2001-present
Sikes	SIKE1	LA	32.057	-92.435	45	03/02/2001-12/31/2010
Southern Great Plains	SOGP1	OK	36.605	-97.485	315	10/01/2019-present
Stilwell	STIL1	OK	35.75	-94.67	300	04/23/2010-present
Upper Buffalo WA	UPBU1	AR	35.826	-93.203	723	12/24/1991-present
Wichita Mountains	WIMO1	OK	34.732	-98.713	509	03/02/2001-present
<b>Mogollon Plateau</b>						
Mount Baldy	BALD1	AZ	34.058	-109.441	2509	03/01/2000-present
Bosque del Apache	BOAP1	NM	33.87	-106.852	1390	04/15/2000-present
Gila WA	GICL1	NM	33.22	-108.235	1776	03/02/1994-present
Hillside	HILL1	AZ	34.429	-112.963	1511	04/19/2001-05/31/2005
Ike's Backbone	IKBA1	AZ	34.341	-111.683	1298	03/29/2000-present
Petrified Forest NP	PEFO1	AZ	35.078	-109.769	1766	03/02/1988-present
San Andres	SAAN1	NM	32.687	-106.484	1326	07/30/1997-02/26/2000
Sierra Ancha	SIAN1	AZ	34.091	-110.942	1600	02/09/2000-12/03/2017
Sycamore Canyon #1	SYCA1	AZ	35.141	-111.969	2046	09/04/1991-10/30/2015
Sycamore Canyon #2	SYCA2	AZ	35.164	-111.982	2046	10/24/2015-present
Tonto	TONT1	AZ	33.655	-111.107	775	03/02/1988-present
White Mountain	WHIT1	NM	33.469	-105.535	2064	12/03/2001-present
<b>Northeast</b>						
Acadia NP	ACAD1	ME	44.377	-68.261	157	03/02/1988-present
Addison Pinnacle	ADPI1	NY	42.091	-77.21	512	04/04/2001-06/28/2010
Bridgton	BRMA1	ME	44.107	-70.729	234	03/14/2001-12/29/2015
Casco Bay	CABA1	ME	43.833	-70.064	27	03/14/2001-present
Cape Cod	CACO1	MA	41.976	-70.024	49	04/04/2001-present

<b>Site Name</b>	<b>Site Code</b>	<b>State</b>	<b>Latitude</b>	<b>Longitude</b>	<b>Elevation (m)</b>	<b>Dates of Operation</b>
Connecticut Hill	COHI1	NY	42.401	-76.653	519	04/04/2001-06/25/2006
Great Gulf WA	GRGU1	NH	44.308	-71.218	454	06/03/1995-present
Londonderry	LOND1	NH	42.862	-71.380	124	01/03/2011-present
Lye Brook WA	LYBR1	VT	43.148	-73.127	1015	09/04/1991-09/30/2012
Lye Brook WA	LYEB1	VT	42.956	-72.91	882	01/01/2012-present
Martha's Vineyard	MAVI1	MA	41.331	-70.785	3	12/01/2002-present
Mohawk Mt.	MOMO1	CT	41.821	-73.297	522	09/13/2001-present
Moosehorn NWR	MOOS1	ME	45.126	-67.266	78	12/03/1994-present
Old Town	OLTO1	ME	44.933	-68.646	51	06/27/2001-05/29/2006
Pack Monadnock Summit	PACK1	NH	42.862	-71.879	695	10/03/2007-present
Penobscot	PENO1	ME	44.948	-68.648	45	01/11/2006-present
Proctor Maple Research Facility	PMRF1	VT	44.528	-72.869	401	12/01/1993-present
Presque Isle	PRIS1	ME	46.696	-68.033	166	03/08/2001-present
Quabbin Summit	QURE1	MA	42.298	-72.335	318	04/04/2001-12/29/2015
<b>Northern Great Plains</b>						
Badlands NP	BADL1	SD	43.743	-101.941	736	03/02/1988-present
Cloud Peak	CLPE1	WY	44.334	-106.957	2471	06/01/2002-07/29/2015
Fort Peck	FOPE1	MT	48.308	-105.102	638	06/01/2002-present
Lostwood	LOST1	ND	48.642	-102.402	696	12/15/1999-present
Medicine Lake	MELA1	MT	48.487	-104.476	606	12/15/1999-present
Northern Cheyenne	NOCH1	MT	45.65	-106.557	1283	06/01/2002-present
Thunder Basin	THBA1	WY	44.663	-105.287	1195	06/01/2002-12/29/2019
Theodore Roosevelt NP	THRO1	ND	46.895	-103.378	853	12/15/1999-present
UL Bend	ULBE1	MT	47.582	-108.72	891	01/26/2000-present
Wind Cave NP	WICA1	SD	43.558	-103.484	1296	12/15/1999-present
<b>Northern Rocky Mountains</b>						
Boulder Lake	BOLA1	WY	42.846	-109.640	2296	08/26/2009-present
Bridger WA	BRID1	WY	42.975	-109.758	2627	03/02/1988-present
Cabinet Mountains	CABI1	MT	47.955	-115.671	1441	07/26/2000-present
Flathead	FLAT1	MT	47.773	-114.269	1580	06/01/2002-present
Gates of the Mountains	GAMO1	MT	46.826	-111.711	2387	07/26/2000-present
Glacier NP	GLAC1	MT	48.511	-113.997	975	03/02/1988-present
Monture	MONT1	MT	47.122	-113.154	1282	03/29/2000-present
North Absaroka	NOAB1	WY	44.745	-109.382	2482	01/26/2000-present
Salmon NF	SALM1	ID	45.159	-114.026	2788	12/01/1993-11/05/2000
Sula Peak	SULA1	MT	45.86	-114	1896	06/01/1994-present
Yellowstone NP #1	YELL1	WY	44.565	-110.4	2442	03/09/1988-12/29/1999
Yellowstone NP #2	YELL2	WY	44.565	-110.4	2425	03/02/1988-present
<b>Northwest</b>						
Lynden	LYND1	WA	48.953	-122.559	28	10/16/1996-12/29/1999
Makah Indian Reservation #1	MAKA1	WA	48.372	-124.595	9	09/02/2006-10/29/2010
Makah Indian Reservation #2	MAKA2	WA	48.298	-124.625	480	11/01/2010-present
Mount Rainier NP	MORA1	WA	46.758	-122.124	439	03/02/1988-present
North Cascades	NOCA1	WA	48.732	-121.065	568	07/30/1997-present
Olympic NP	OLYM1	WA	48.007	-122.973	599	07/12/2001-present
Pasayten	PASA1	WA	48.388	-119.928	1627	11/02/2000-present
Snoqualmie Pass	SNPA1	WA	47.422	-121.426	1049	06/02/1993-present

<b>Site Name</b>	<b>Site Code</b>	<b>State</b>	<b>Latitude</b>	<b>Longitude</b>	<b>Elevation (m)</b>	<b>Dates of Operation</b>
Spokane Reservation	SPOK1	WA	47.905	-117.861	552	07/12/2001-06/30/2005
White Pass	WHPA1	WA	46.624	-121.388	1827	02/16/2000-present
<b>Not Assigned</b>						
Walker River Paiute Tribe	WARI1	NV	38.952	-118.815	1250	06/02/2003-10/31/2005
<b>Ohio River Valley</b>						
Cadiz	CADI1	KY	36.784	-87.85	192	03/08/2001-12/31/2010
Livonia	LIVO1	IN	38.535	-86.26	281	03/08/2001-12/31/2010
Mammoth Cave NP	MACA1	KY	37.132	-86.148	235	09/04/1991-present
Mingo	MING1	MO	36.972	-90.143	111	06/03/2000-present
M.K. Goddard	MKGO1	PA	41.427	-80.145	380	04/04/2001-12/31/2010
Quaker City	QUCI1	OH	39.943	-81.338	366	04/04/2001-present
<b>Ontario</b>						
Egbert	EGBE1	ON	44.231	-79.783	251	9/01/2005-present
<b>Oregon and Northern California</b>						
Bliss SP	BLIS1	CA	38.976	-120.103	2131	09/01/1990-present
Crater Lake NP	CRLA1	OR	42.896	-122.136	1996	03/02/1988-present
Kalmiopsis	KALM1	OR	42.552	-124.059	80	03/11/2000-present
Lava Beds NM	LABE1	CA	41.712	-121.507	1460	03/29/2000-present
Lassen Volcanic NP	LAVO1	CA	40.54	-121.577	1733	03/02/1988-present
Lake Tahoe Community College	LTCC1	CA	38.925	-119.98	1935	02/19/2014-present
Mount Hood	MOHO1	OR	45.289	-121.784	1531	03/15/2000-present
Redwood NP	REDW1	CA	41.561	-124.084	244	03/02/1988-present
Three Sisters WA	THSI1	OR	44.291	-122.043	885	06/02/1993-present
Trinity	TRIN1	CA	40.786	-122.805	1014	10/18/2000-present
<b>Phoenix</b>						
Phoenix	PHOE1	AZ	33.504	-112.096	342	04/19/2001-present
Phoenix	PHOE5	AZ	33.504	-112.096	342	01/01/2005-present
<b>Puget Sound</b>						
Puget Sound	PUSO1	WA	47.57	-122.312	98	03/02/1996-present
<b>Sierra Nevada</b>						
Dome Lands WA	DOLA1	CA	35.699	-118.202	914	06/01/1994-12/29/1999
Dome Lands WA	DOME1	CA	35.728	-118.138	927	02/02/2000-present
Hoover	HOOV1	CA	38.088	-119.177	2561	06/06/2001-present
Kaiser	KAIS1	CA	37.221	-119.155	2598	01/26/2000-present
Owens Valley	OWVL1	CA	37.361	-118.331	1234	06/27/2013-present
Sequoia NP	SEQU1	CA	36.489	-118.829	519	03/04/1992-present
South Lake Tahoe	SOLA1	CA	38.933	-119.967	1900	03/01/1989-12/29/1999
Yosemite NP	YOSE1	CA	37.713	-119.706	1603	03/02/1988-present
<b>Southeast</b>						
Breton	BRET1	LA	29.119	-89.207	11	08/16/2000-08/29/2005
Breton Island	BRIS1	LA	30.109	-89.762	-7	01/16/2008-present
Chassahowitzka NWR	CHAS1	FL	28.748	-82.555	4	03/03/1993-present
Everglades NP	EVER1	FL	25.391	-80.681	1	09/03/1988-present
Okefenokee NWR	OKEF1	GA	30.741	-82.128	48	09/04/1991-present
Cape Romain NWR	ROMA1	SC	32.941	-79.657	5	09/03/1994-present
St. Marks NWR	SAMA1	FL	30.093	-84.161	7	08/16/2000-present
<b>Southern Arizona</b>						
Chiricahua NM	CHIR1	AZ	32.009	-109.389	1555	03/02/1988-present
Douglas	DOUG1	AZ	31.349	-109.54	1230	06/02/2004-10/30/2015
Nogales	NOGA1	AZ	31.338	-110.937	1172	10/27/2015-present

<b>Site Name</b>	<b>Site Code</b>	<b>State</b>	<b>Latitude</b>	<b>Longitude</b>	<b>Elevation (m)</b>	<b>Dates of Operation</b>
Organ Pipe	ORPI1	AZ	31.951	-112.802	504	12/01/2002-present
Queen Valley	QUVA1	AZ	33.294	-111.286	661	04/19/2001-12/29/2015
Saguaro NP	SAGU1	AZ	32.175	-110.737	941	06/01/1988-present
Saguaro West	SAWE1	AZ	32.249	-111.218	714	10/31/2001-present
<b>Southern California</b>						
Agua Tibia	AGTI1	CA	33.464	-116.971	508	12/20/2000-present
Joshua Tree NP	JOSH1	CA	34.069	-116.389	1235	02/23/2000-present
Joshua Tree NP	JOTR1	CA	34.069	-116.389	1228	09/04/1991-12/29/1999
San Gabriel	SAGA1	CA	34.297	-118.028	1791	12/03/2001-present
San Gorgonio WA	SAGO1	CA	34.194	-116.913	1726	03/02/1988-present
Wrightwood	WRIG1	CA	34.38	-117.69	2106	10/01/2009-10/15/2012
<b>Urban Quality Assurance Sites</b>						
Atlanta	ATLA1	GA	33.688	-84.29	243	03/01/2004-present
Baltimore	BALT1	MD	39.255	-76.709	78	06/02/2004-12/31/2006
Birmingham	BIRM1	AL	33.553	-86.815	176	03/01/2004-present
Chicago	CHIC1	IL	41.751	-87.713	195	09/03/2003-08/29/2005
Detroit	DETR1	MI	42.229	-83.209	180	09/03/2003-present
Fresno	FRES1	CA	36.782	-119.773	100	09/03/2004-present
Houston	HOUS1	TX	29.67	-95.129	7	03/01/2004-08/29/2005
New York City	NEYO1	NY	40.816	-73.902	45	08/01/2004-06/07/2010
Pittsburgh	PITT1	PA	40.465	-79.961	268	03/01/2004-present
Rubidoux	RUBI1	CA	34.0	-117.416	248	09/03/2004-08/29/2005
<b>Virgin Islands</b>						
Virgin Islands NP	VIIS1	VI	18.336	-64.796	51	09/01/1990-present
<b>Washington D.C.</b>						
Washington D.C.	WASH1	DC	38.876	-77.034	15	03/02/1988-06/08/2015
<b>West Texas</b>						
Big Bend NP	BIBE1	TX	29.303	-103.178	1067	03/02/1988-present
Carlsbad Caverns NP	CAVE1	NM	32.178	-104.444	1355	07/30/2017-present
Guadalupe Mountains NP	GUMO1	TX	31.833	-104.809	1672	03/02/1988-present
Salt Creek	SACR1	NM	33.46	-104.404	1072	04/08/2000-present

NF = National Forest

NM = National Monument

NP = National Park

NS = National Seashore

NWR = National Wildlife Refuge

SP = State Park

WA = Wilderness Area

**Table 1.2. Class I areas and representative monitoring sites.**

<b>Class I Area Name</b>	<b>Site Name</b>	<b>Site Code</b>
Acadia	Acadia NP	ACAD1
Agua Tibia	Agua Tibia	AGTI1
Alpine Lakes	Snoqualmie Pass	SNPA1
Anaconda-Pintler	Sula Peak	SULA1
Ansel Adams	Kaiser	KAIS1
Arches	Canyonlands NP	CANY1
Badlands	Badlands NP	BADL1
Bandelier	Bandelier NM	BAND1
Big Bend	Big Bend NP	BIBE1
Black Canyon of the Gunnison	Weminuche WA	WEMI1
Bob Marshall	Monture	MONT1

<b>Class I Area Name</b>	<b>Site Name</b>	<b>Site Code</b>
Bosque del Apache	Bosque del Apache	BOAP1
Boundary Waters Canoe Area	Boundary Waters Canoe Area WA	BOWA1
Breton	Breton	BRIS1
Bridger	Bridger WA	BRID1
Brigantine	Brigantine NWR	BRIG1
Bryce Canyon	Bryce Canyon NP	BRCA1
Cabinet Mountains	Cabinet Mountains	CABI1
Caney Creek	Caney Creek	CACR1
Canyonlands	Canyonlands NP	CANY1
Cape Romain	Cape Romain NWR	ROMA1
Capitol Reef	Capitol Reef NP	CAPI1
Caribou	Lassen Volcanic NP	LAVO1
Carlsbad Caverns	Guadalupe Mountains NP	GUMO1
Chassahowitzka	Chassahowitzka NWR	CHAS1
Chiricahua NM	Chiricahua NM	CHIR1
Chiricahua W	Chiricahua NM	CHIR1
Cohutta	Cohutta	COHU1
Crater Lake	Crater Lake NP	CRLA1
Craters of the Moon	Craters of the Moon NM	CRMO1
Cucamonga	San Gabriel	SAGA1
Denali	Denali NP	DENA1
Desolation	Bliss SP	BLIS1
Diamond Peak	Crater Lake NP	CRLA1
Dolly Sods	Dolly Sods WA	DOSO1
Dome Land	Dome Lands WA	DOME1
Eagle Cap	Starkey	STAR1
Eagles Nest	White River NF	WHRI1
Emigrant	Yosemite NP	YOSE1
Everglades	Everglades NP	EVER1
Fitzpatrick	Bridger WA	BRID1
Flat Tops	White River NF	WHRI1
Galiuro	Chiricahua NM	CHIR1
Gates of the Mountains	Gates of the Mountains	GAMO1
Gearhart Mountain	Crater Lake NP	CRLA1
Gila	Gila WA	GICL1
Glacier	Glacier NP	GLAC1
Glacier Peak	North Cascades	NOCA1
Goat Rocks	White Pass	WHPA1
Grand Canyon	Hance Camp at Grand Canyon NP	GRCA2
Grand Teton	Yellowstone NP	YELL2
Great Gulf	Great Gulf WA	GRGU1
Great Sand Dunes	Great Sand Dunes NP	GRSA1
Great Smoky Mountains	Great Smoky Mountains NP	GRSM1
Guadalupe Mountains	Guadalupe Mountains NP	GUMO1
Haleakala	Haleakala Crater	HACR1
Hawaii Volcanoes	Hawaii Volcanoes NP	HAVO1
Hells Canyon	Hells Canyon	HECA1
Hercules-Glade	Hercules-Glades	HEGL1
Hoover	Hoover	HOOV1
Isle Royale	Isle Royale NP	ISLE1
James River Face	James River Face WA	JARI1
Jarbridge	Jarbridge WA	JARB1
John Muir	Kaiser	KAIS1
Joshua Tree	Joshua Tree NP	JOSH1

<b>Class I Area Name</b>	<b>Site Name</b>	<b>Site Code</b>
Joyce Kilmer-Slickrock	Great Smoky Mountains NP	GRSM1
Kaiser	Kaiser	KAIS1
Kalmiopsis	Kalmiopsis	KALM1
Kings Canyon	Sequoia NP	SEQU1
La Garita	Weminuche WA	WEMI1
Lassen Volcanic	Lassen Volcanic NP	LAVO1
Lava Beds	Lava Beds NM	LABE1
Linville Gorge	Linville Gorge	LIGO1
Lostwood	Lostwood	LOST1
Lye Brook	Lye Brook WA	LYBR1
Mammoth Cave	Mammoth Cave NP	MACA1
Marble Mountain	Trinity	TRIN1
Maroon Bells-Snowmass	White River NF	WHRI1
Mazatzal	Ike's Backbone	IKBA1
Medicine Lake	Medicine Lake	MELA1
Mesa Verde	Mesa Verde NP	MEVE1
Mingo	Mingo	MING1
Mission Mountains	Monture	MONT1
Mokelumne	Bliss SP	BLIS1
Moosehorn	Moosehorn NWR	MOOS1
Mount Adams	White Pass	WHPA1
Mount Baldy	Mount Baldy	BALD1
Mount Hood	Mount Hood	MOHO1
Mount Jefferson	Three Sisters WA	THSI1
Mount Rainier	Mount Rainier NP	MORA1
Mount Washington	Three Sisters WA	THSI1
Mount Zirkel	Mount Zirkel WA	MOZI1
Mountain Lakes	Crater Lake NP	CRLA1
North Absaroka	North Absaroka	NOAB1
North Cascades	North Cascades	NOCA1
Okefenokee	Okefenokee NWR	OKEF1
Olympic	Olympic	OLYM1
Otter Creek	Dolly Sods WA	DOSO1
Pasayten	Pasayten	PASA1
Pecos	Wheeler Peak	WHPE1
Petrified Forest	Petrified Forest NP	PEFO1
Pine Mountain	Ike's Backbone	IKBA1
Pinnacles	Pinnacles NP	PINN1
Point Reyes	Point Reyes NS	PORE1
Presidential Range-Dry River	Great Gulf WA	GRGU1
Rawah	Mount Zirkel WA	MOZI1
Red Rock Lakes	Yellowstone NP	YELL2
Redwood	Redwood NP	REDW1
Rocky Mountain	Rocky Mountain NP	ROMO1
Roosevelt Campobello	Moosehorn NWR	MOOS1
Saguaro	Saguaro NP	SAGU1
Saint Marks	St. Marks	SAMA1
Salt Creek	Salt Creek	SACR1
San Gabriel	San Gabriel	SAGA1
San Gorgonio	San Gorgonio WA	SAGO1
San Jacinto	San Gorgonio WA	SAGO1
San Pedro Parks	San Pedro Parks	SAPE1
San Rafael	San Rafael	RAFA1
Sawtooth	Sawtooth NF	SAWT1

<b>Class I Area Name</b>	<b>Site Name</b>	<b>Site Code</b>
Scapegoat	Monture	MONT1
Selway-Bitterroot	Sula Peak	SULA1
Seney	Seney	SENE1
Sequoia	Sequoia NP	SEQU1
Shenandoah	Shenandoah NP	SHEN1
Shining Rock	Shining Rock WA	SHRO1
Sierra Ancha	Sierra Ancha	SIAN1
Simeonof	Simeonof	SIME1
Sipsey	Sipsey WA	SIPS1
South Warner	Lava Beds NM	LABE1
Strawberry Mountain	Starkey	STAR1
Superstition	Tonto	TONT1
Swanquarter	Swanquarter	SWAN1
Sycamore Canyon	Sycamore Canyon	SYCA1
Teton	Yellowstone NP	YELL2
Theodore Roosevelt	Theodore Roosevelt NP	THRO1
Thousand Lakes	Lassen Volcanic NP	LAVO1
Three Sisters	Three Sisters WA	THSI1
Tuxedni	Kenai Peninsula Borough	KPBO1
UL Bend	UL Bend	ULBE1
Upper Buffalo	Upper Buffalo WA	UPBU1
Ventana	Pinnacles NP	PENN1
Virgin Islands	Virgin Islands NP	VIIS1
Voyageurs	Voyageurs NP	VOYA2
Washakie	North Absaroka	NOAB1
Weminuche	Weminuche WA	WEMI1
West Elk	White River NF	WHRI1
Wheeler Peak	Wheeler Peak	WHPE1
White Mountain	White Mountain	WHIT1
Wichita Mountains	Wichita Mountains	WIMO1
Wind Cave	Wind Cave	WICA1
Wolf Island	Okefenokee NWR	OKEF1
Yellowstone	Yellowstone NP	YELL2
Yolla Bolly-Middle Eel	Trinity	TRIN1
Yosemite	Yosemite NP	YOSE1
Zion	Zion Canyon	ZICA1

NF = National Forest

NM = National Monument

NP = National Park

NS = National Seashore

NWR = National Wildlife Refuge

SP = State Park

WA = Wilderness Area

## 1.2.2 Aerosol Sampling and Analysis

The current configuration of the IMPROVE monitor collects 24-hour samples every third day from midnight to midnight local standard time and data are reported at local conditions. The samplers have undergone modifications over time (Malm et al., 2000; Debell et al., 2006; Hand et al., 2011). The version II sampler began operating in November 1999 through early 2000 and currently is in use at all IMPROVE sites. The version II sampler was implemented to allow for protocol changes that occurred in 2000 with the expansion of the IMPROVE network and the need for consistency with the EPA's fine mass and fine speciation monitoring network, specifically, the need for consistency with the EPA's sampling schedule. Other sampling configuration changes for IMPROVE occurred to ensure more-consistent data collection protocols (e.g., inlet height, filter collection time after sampling). Details regarding the version I sampler can be found in previous reports (e.g., Malm et al., 2000).

The IMPROVE samplers (versions I and II) consist of four independent modules (A, B, C, and D; see Figure 1.3). Each module incorporates a separate inlet, filter pack, and pump assembly. Modules A, B, and C are equipped with 2.5  $\mu\text{m}$  cyclones that allow for sampling of particles with aerodynamic diameters less than 2.5  $\mu\text{m}$  (PM<sub>2.5</sub>), while module D is fitted with a PM<sub>10</sub> inlet to collect particles with aerodynamic diameters less than 10  $\mu\text{m}$ . Each module contains a filter substrate specific to the analysis planned (Figure 1.3).

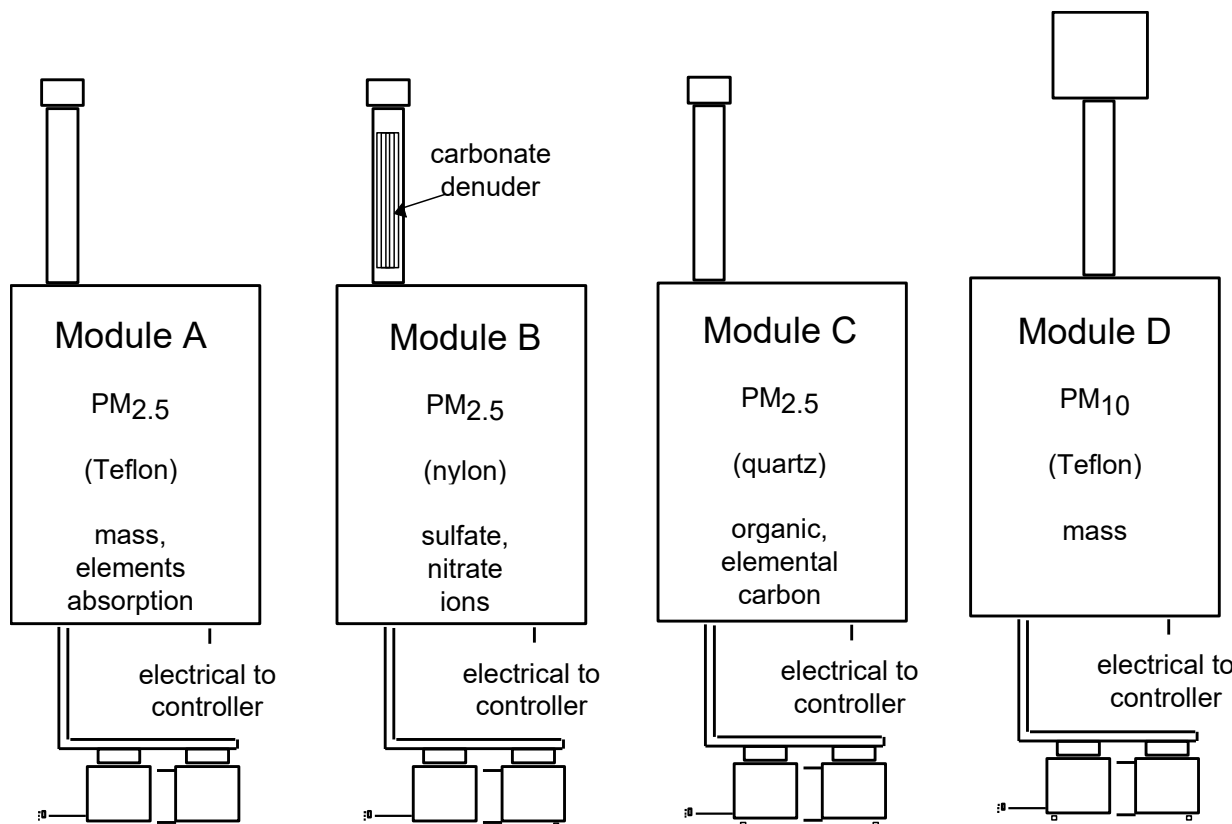


Figure 1.3. IMPROVE sampler showing the four modules with separate inlets and pumps. Substrates with analyses performed for each module are also shown.

To accommodate the every-third-day sampling schedule, the version II sampler has a four-filter manifold for each module. The manifold with solenoid valves sits directly above the

filter cassettes and is raised or lowered as a unit to unload and load the filters. The four filter cassettes are held in a cartridge (shown in Figure 1.4) that is designed to allow only one orientation in the sampler. Date- and site-labeled filter cartridges, along with memory cards, are sent from the analysis laboratory to the site and are returned in special mailing containers. If filter change service is performed on a sample day, the site operator moves the cassette containing that day's filter to the open position in the newly loaded cartridge. The few minutes that it takes to perform this sample change is recorded by the microprocessor on the memory card so that the correct air volume is used to calculate concentrations.

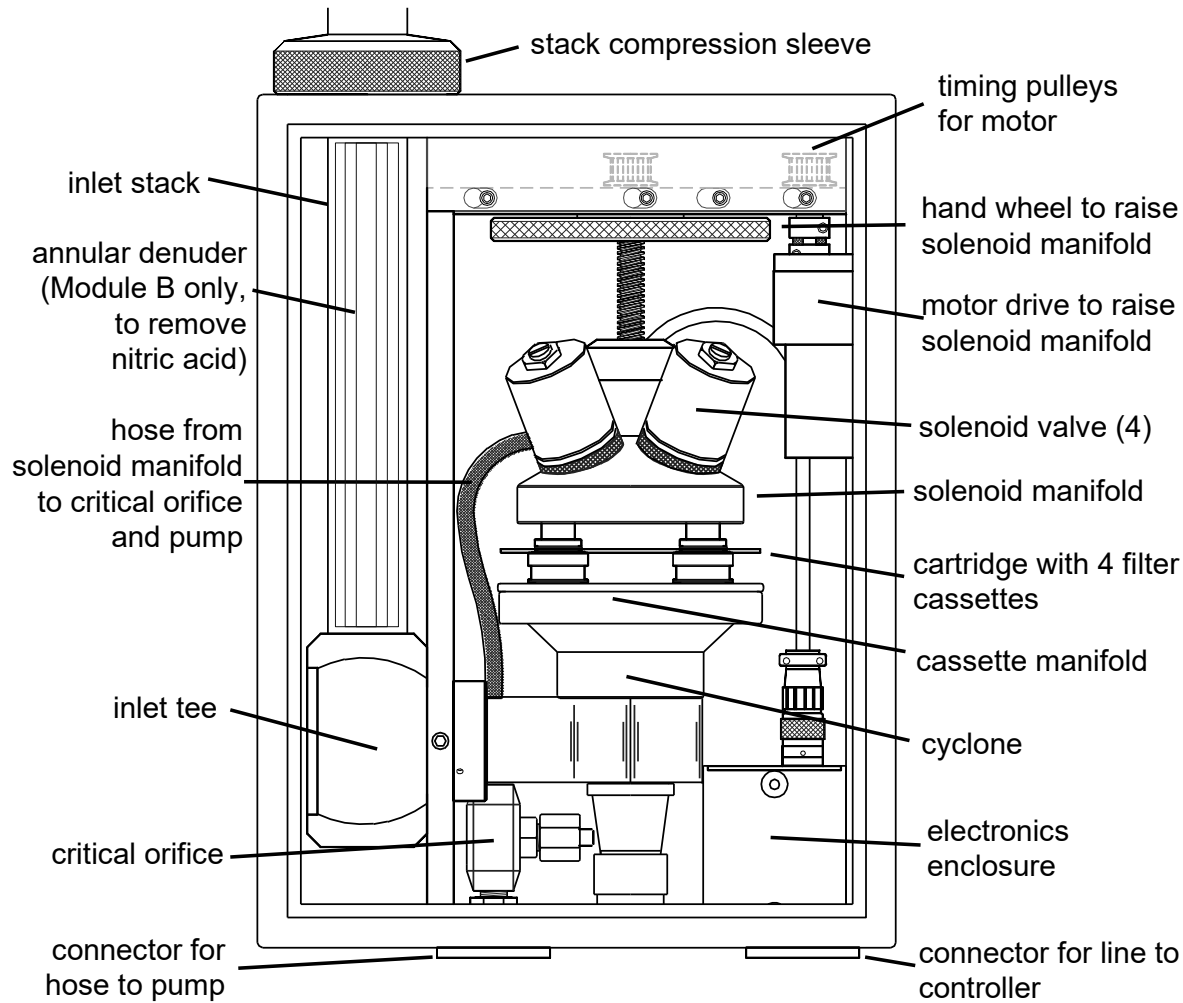


Figure 1.4. Version II IMPROVE sampler PM<sub>2.5</sub> module.

The version II sampler electronics became obsolete around 2011, and thus it became harder to maintain, repair, and obtain replacement parts. In 2018 and 2019, the version II sampler electronics were upgraded throughout the network and are referred to as version 4. The version 4 controller uses a Beaglebone Black development platform along with custom-designed electronics boards to manage all the sampler operations. The version 4 controller also includes an LCD color display that provides comprehensive instructions on how to operate the sampler, including diagrams and videos to assist the operator. Flow rate, sample temperature, and other operating parameters are recorded throughout the sample period on a secure digital (SD) card. In

addition, the data are uploaded to the University of California, Davis (UC Davis),<sup>1</sup> on a nightly basis. Internet connections using mobile carriers or nearby Wi-Fi connections were established at all the sites when the new controllers were installed. The controllers can be accessed remotely to diagnose and troubleshoot problems, operate the hardware (e.g., turn on/off pumps, lower the sampling manifold, turn on/off solenoids), and upgrade the software. Data received from the sampler are reviewed on a daily basis, allowing equipment problems to be quickly identified and resolved. Several new software tools have been developed to process and display this new data stream.

At some IMPROVE sites, a fifth module is added to accommodate replicate sampling and analysis for mass and composition. This quality assurance module is operated for each sampling period and collects a replicate sample for one of the four modules so that, over time, relative precision information can be developed for each parameter. Starting in 2003, collocated modules were installed at 25 sites across the network, providing ~4% replication for each of the four modules. Sites with only one additional module include four collocated A modules, three collocated B modules, three collocated C modules, and two collocated D modules. In addition, the Phoenix site (PHOE5) has a complete collocated sampler with all four modules (Table 1.3).

---

<sup>1</sup> UC Davis is the National Park Service contractor during the period of this report.

**Table 1.3. Sites with a fifth collocated module.**

<b>Site Name</b>	<b>Site</b>	<b>A</b>	<b>B</b>	<b>C</b>	<b>D</b>	<b>Date of Operation</b>
Mesa Verde NP	MEVE1	X				08/13/2003-present
Olympic NP	OLYMI1	X				11/08/2003-05/14/2013
Proctor Maple Research Facility	PMRF1	X				09/03/2003-present
Sac and Fox	SAFO1	X				11/20/2003-07/01/2011
St. Marks NWR	SAMA1	X				11/18/2004-present
Trapper Creek	TRCR1	X				06/22/2004-06/25/2013
Yosemite NP	YOSE1	X				10/24/2012-present
Big Bend NP	BIBE1		X			08/30/2003-05/20/2013
Blue Mounds	BLMO1		X			09/16/2004-present
Frostburg	FRRE1		X			04/15/2004-present
Gates of the Mountains	GAMO1		X			09/23/2003-05/14/2013
Lassen Volcanic NP	LAVO1		X			04/18/2003-05/14/2013
Mammoth Cave NP	MACA1		X			05/12/2003-present
San Gabriel	SAGA1		X			11/20/2018- present
Everglades NP	EVER1			X		07/11/2003-12/15/2017
Hercules-Glades	HEGL1			X		08/24/2004-present
Hoover	HOOV1			X		08/13/2003-05/14/2013
Medicine Lake	MELA1			X		09/25/2003-present
Saguaro West NP	SAWE1			X		03/25/2004-05/20/2013
Seney	SENE1			X		08/10/2003-05/14/2013
Everglades NP	EVER1			X		06/02/2003-present
Houston	HOUS1				X	04/30/2004-09/01/2005
Jarbridge WA	JARB1				X	06/30/2004-05/14/2013
Joshua Tree NP	JOSH1				X	08/07/2003-05/14/2013
Quabbin Summit	QURE1				X	09/04/2003-05/20/2013
Swanquarter	SWAN1				X	11/09/2004-present
Wind Cave NP	WICA1				X	09/17/2004-present
Breton	BRIS1				X	01/28/2008-05/20/2013
Phoenix	PHOE5	X	X	X	X	03/01/2004-present

NP = National Park

NWR = National Wildlife Refuge

WA = Wilderness Area

The laboratory at UC Davis prepares the sample cartridges for the IMPROVE sites. Every three weeks, UC Davis sends containers with the necessary sampling supplies to each site. The containers are typically received 10 days before the first sample-change day of the next three-week cycle. Often there will be two containers at a site, one in current use and the second ready for the next period or ready to be shipped back to UC Davis. The site operators send the container with the exposed filters back to UC Davis within one to two days following the completion of each three-week cycle. All shipments, to and from the field, are sent by second-day express delivery. Thus, a sample container typically spends a little over a month between shipment from and delivery to UC Davis, with the filters installed in the sampler during one week of that period.

As these filters arrive at UC Davis from the field sites, they are placed in Petri dishes and accumulate until a shipping tray has been filled, usually 400 filters. Nylon filters are sent to the Research Triangle Institute (RTI)<sup>2</sup> for ion analysis, and quartz filters are sent to the Desert

---

<sup>2</sup> RTI is the NPS contractor for the ion analyses during the period of this report.

Research Institute (DRI)<sup>3</sup> for carbon analysis. Full trays of each type are sent to RTI and DRI approximately once a week by overnight express.

Module A is equipped with a PTFE (polytetrafluoroethylene) Teflon® (referred to as “Teflon”) filter that is analyzed for PM<sub>2.5</sub> gravimetric fine mass (also referred to as fine mass, FM), elemental analysis, and filter light absorption. Samples are pre- and post-weighed to gravimetrically determine PM<sub>2.5</sub> fine mass using an electro-microbalance, after equilibrating for four hours at 30–40% relative humidity (RH) and 20–30° C. This procedure for determining gravimetric fine mass is associated with both positive and negative artifacts. Negative artifacts include loss of semivolatile species such as ammonium nitrate (AN) and some organic species from the Teflon filter during sampling. Positive artifacts include particle-bound water associated with hygroscopic aerosol species such as sulfates, nitrates, sea salt, and some organic species. Reactions with atmospheric gases may also contribute to positive artifacts. Storage conditions and shipping conditions may also contribute to artifacts. Beginning with samples and field blanks collected in October 2018, the gravimetric measurements are performed in the Measurement Technology Laboratories (MTL) AH500E climate-controlled, automated weighing system. Modules A and D Teflon filters are weighed in the MTL chambers with strict environmental controls, with the temperature set to 21.5 °C ± 1.0 °C and RH set to 39% ± 2.0%.

Elemental analysis is performed on the module A Teflon filters for elements with atomic number greater than 11 (Na) and less than 82 (Pb) by X-ray fluorescence (XRF), with a subset of elements reported. The techniques used for elemental analysis for the IMPROVE network have included proton elastic scattering analysis (PESA), proton induced X-ray emission (PIXE), and XRF. Elemental hydrogen was quantified using PESA. PIXE was used for quantifying nearly all elements with atomic number greater than 11 and less than 82, although not all were reported. Beginning in 1992, however, analysis of heavier elements with atomic weights from 26 (Fe) to 82 (Pb) switched to XRF with a molybdenum (Mo) anode source. PIXE was discontinued in late 2001 and analysis of the lighter elements with atomic numbers from 11 (Na) to 25 (Mn) was changed from PIXE to XRF using a copper (Cu) anode source. Also, in late 2001, the analysis of Fe was changed from Mo anode XRF to Cu anode XRF. In both cases the change from PIXE to XRF provided lower minimum detection limits (MDLs) for most elements of interest, as well as better sample preservation for reanalysis. The exceptions were Na, Mg, Al, and to a lesser extent Si, where the change to Cu XRF resulted in significantly increased MDL and uncertainty. The details on the transitions from PIXE to XRF are provided in Section 1.3.1.3. Starting in 2011 the XRF analysis has been performed with Malvern PANalytical Epsilon 5 XRF instruments as described in Section 1.3.1.3.

Field blanks are collected to determine positive artifacts that are used to correct concentrations of all the reported elements. A field blank filter is placed in an unused port in the filter cassette where it is exposed to all aspects of the filter handling process, with the exception of sample air drawn being through it. Artifact corrections are performed by subtracting the median field blank from the same filter lot as that of the sample filters. The field blank correction is specific to each filter lot, and a minimum of 35 field blanks are required for a median to be calculated, which may require including field blanks from the previous month (SOP 351 Data Processing and Validation, <http://vista.cira.colostate.edu/Improve/particulate->

---

<sup>3</sup> DRI is the NPS contractor for the carbon analyses during the period of this report.

[monitoring-network/](#)). Figure 1.5 presents field blank values for elements measured with XRF from January 2019 to January 2020.

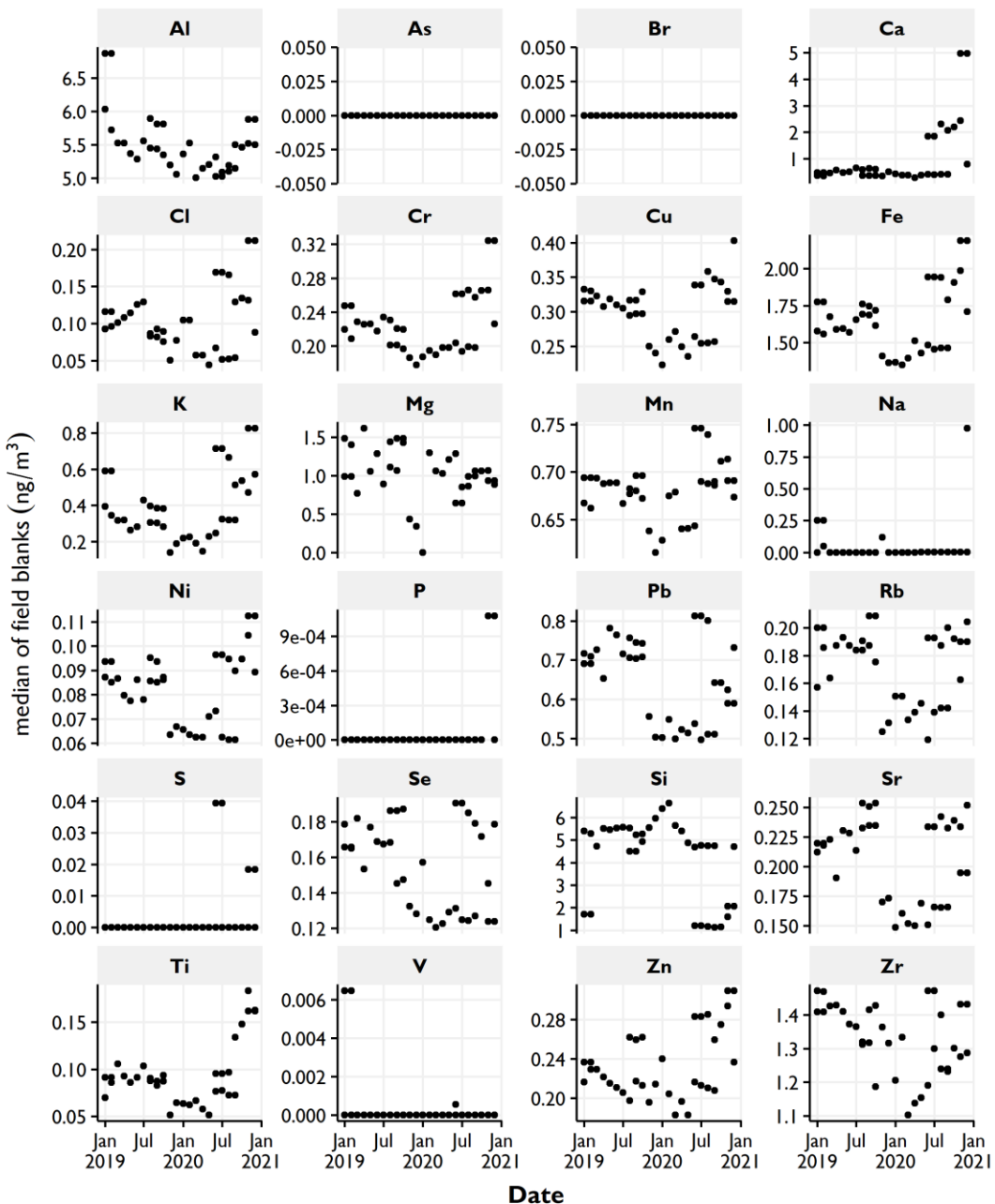


**Figure 1.5. IMPROVE XRF field blank concentrations ( $\text{ng m}^{-3}$ ) for elemental species from January 2019 to January 2021.**

The filter light absorption coefficient ( $f_{\text{abs}}$ ,  $\text{Mm}^{-1}$ ) is determined from the channel A Teflon filter using a hybrid integrating plate/sphere system (HIPS) that shines a laser light (wavelength of 633 nm) on the backside of filter and measures reflected and transmitted light to determine the light absorption by the  $\text{PM}_{2.5}$  sample. Field blank samples are used to calibrate the HIPS system to zero absorption. Prior to 1 March 1994, a laser integrating plate method (LIPM)

was used that did not include measurement of the reflection. Additional discussion of  $f_{abs}$  calibration is in Section 1.3.1.4.

Module B is fitted with a sodium carbonate denuder tube in the inlet to remove gaseous nitric acid in the air sample, followed by a Nylasorb (nylon) filter as the collection substrate. The material collected on the nylon filter is extracted ultrasonically in an aqueous solution that is subsequently analyzed for the anions sulfate, nitrate, nitrite, and chloride using ion chromatography (IC). The negative artifact associated with the loss of nitrate on Teflon filters is not as critical for nylon filters, as they have been shown to be more effective at capturing and retaining nitrate from semivolatile AN than Teflon filters (Yu et al., 2005).

Field blanks for the B module are collected to determine positive artifacts that are used to correct concentrations of all the reported anions. Field blanks are collected randomly at all sites on a periodic basis. When there are more than 50 field blanks in a month, the artifact is calculated as the median loading measured on the field blanks. Otherwise, values from the previous month are included until at least 50 field blanks are available. Artifact corrections are subtracted from ambient concentrations for the corresponding month. A single artifact correction is applied for each species for every site in the network for the period being processed. Monthly median field blanks for measured ions are shown in Figure 1.6 for 2016 through 2020.

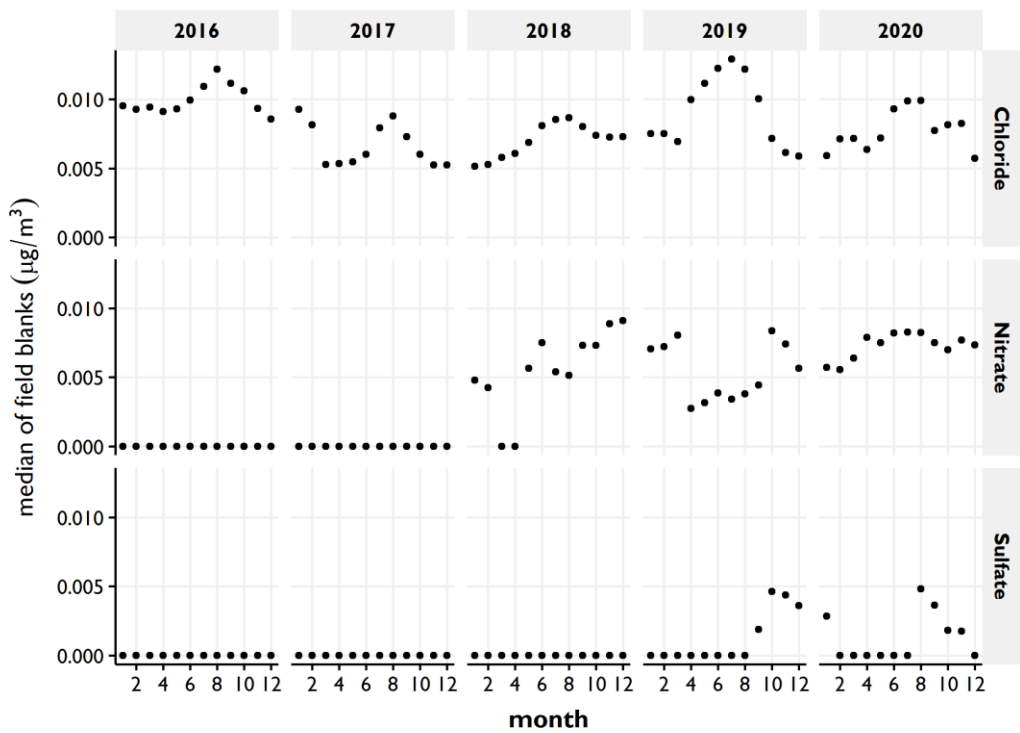


**Figure 1.6. IMPROVE monthly median field blank concentrations ( $\mu\text{g m}^{-3}$ ) for ions for 2016 through 2020.**

Module C uses quartz fiber filters that are analyzed by thermal optical reflectance (TOR) for particulate organic and elemental carbon (OC and EC, respectively) (Chow et al., 1993). The fraction of carbonaceous aerosols evolving at high temperature during TOR is referred to in this report as “elemental carbon” following its operational definition and the recommendation by Petzold et al. (2013) that reflects the measurement technique and associated scientific literature.

However, “light absorbing carbon” is likely a more inclusive description of this carbonaceous aerosol fraction because particles evolving at high temperature may not be graphitic.

Thermally derived carbon fractions, including OC and EC, have been measured since 2016 using the DRI Model 2015 multiwavelength carbon analyzer (Chen et al., 2015; Chow et al., 2015a). As discussed in Section 1.3.1.1, measurements prior to this were made with different instruments, but equivalence among the carbon fractions was demonstrated by replicate measurements with the old and new instruments to assure long-term consistency. In this method, reflectance (R) from and transmittance (T) through a punch from the quartz filter are monitored continuously as the temperature is ramped through different steps that define the fractions. The evolved carbon at each temperature step is oxidized to carbon dioxide and quantified with a nondispersive infrared detector. R and T are monitored at 405, 445, 532, 635, 780, 808, and 980 nm wavelengths throughout the analysis to detect OC charring to EC of the aerosol deposit and organic vapors adsorbed throughout the quartz filter (Chow et al., 2001; Chow et al., 2004). Carbon that evolves after R returns to its initial value for the 635 nm wavelength in a 98% He/2% O<sub>2</sub> carrier gas is classified as EC in the aerosol deposit. EC by transmittance (ECT) is usually less than EC by reflectance (ECR), as T is dominated by the filter-adsorbed gases owing to charring of organic vapors adsorbed within the quartz-fiber filter (Chow et al., 2004; Chow et al., 2010; Watson et al., 2009). The amount of carbon associated with charring during the process is referred to as OP. When the reflected or transmitted light returns to its original intensity, the pyrolyzed (charred) OP is assumed to have been removed. Temperature-defined fractions are 1) OC1, OC2, OC3, and OC4 that evolve in a pure He [>99.999%] atmosphere at 140, 280, 480, and 580 °C, respectively; and 2) EC1, EC2, and EC3 that evolve in a 98% He/2% O<sub>2</sub> atmosphere at 580, 740, and 840 °C, respectively). The analysis temperature stays constant until each fraction is fully evolved, and total analysis times are longer for more heavily loaded samples. In addition to the carbon fractions, the following categories and their analytical uncertainties are reported: 1) total organic carbon by reflectance (OC; OC1 + OC2 + OC3 + OC4 + OP); 2) total elemental carbon by reflectance (EC; EC1 + EC2 + EC3 - OP); 3) total carbon (TC): all carbon evolved from the filter punch between ambient (~25 °C) and 840 °C during analysis; and 4) laser signals, including initial, minimum, and final laser reflectance and transmittance value counts for each wavelength. Analytical precisions for each batch of measurements are calculated from replicate analyses, MDLs are determined from laboratory blanks, and lower quantifiable limits (LQLs) are determined by the variability of passive field blanks (Watson et al., 2001).

Organic carbon concentrations reported by IMPROVE are corrected for an approximate positive artifact (Dillner et al., 2009). Positive artifact corrections account for contamination by the filter medium, handing the cassettes, or adsorption by gases during collection that are erroneously measured as particles. Field blanks are handled as normal filters (loaded into cassettes and cartridges, shipped to and from the field, and left in the sampler for a week) except no air is drawn through them. Field blanks are collected randomly at all sites on a periodic basis. When there are greater than 50 field blanks in a month, the artifact corrections are calculated as the monthly medians and subtracted from ambient concentrations for the corresponding month (IMPROVE Standard Operating Procedure #351, <http://vista.cira.colostate.edu/Improve/particulate-monitoring-network/>). Monthly median carbon fraction field blanks are shown in Figure 1.7 for 2016 through 2020.

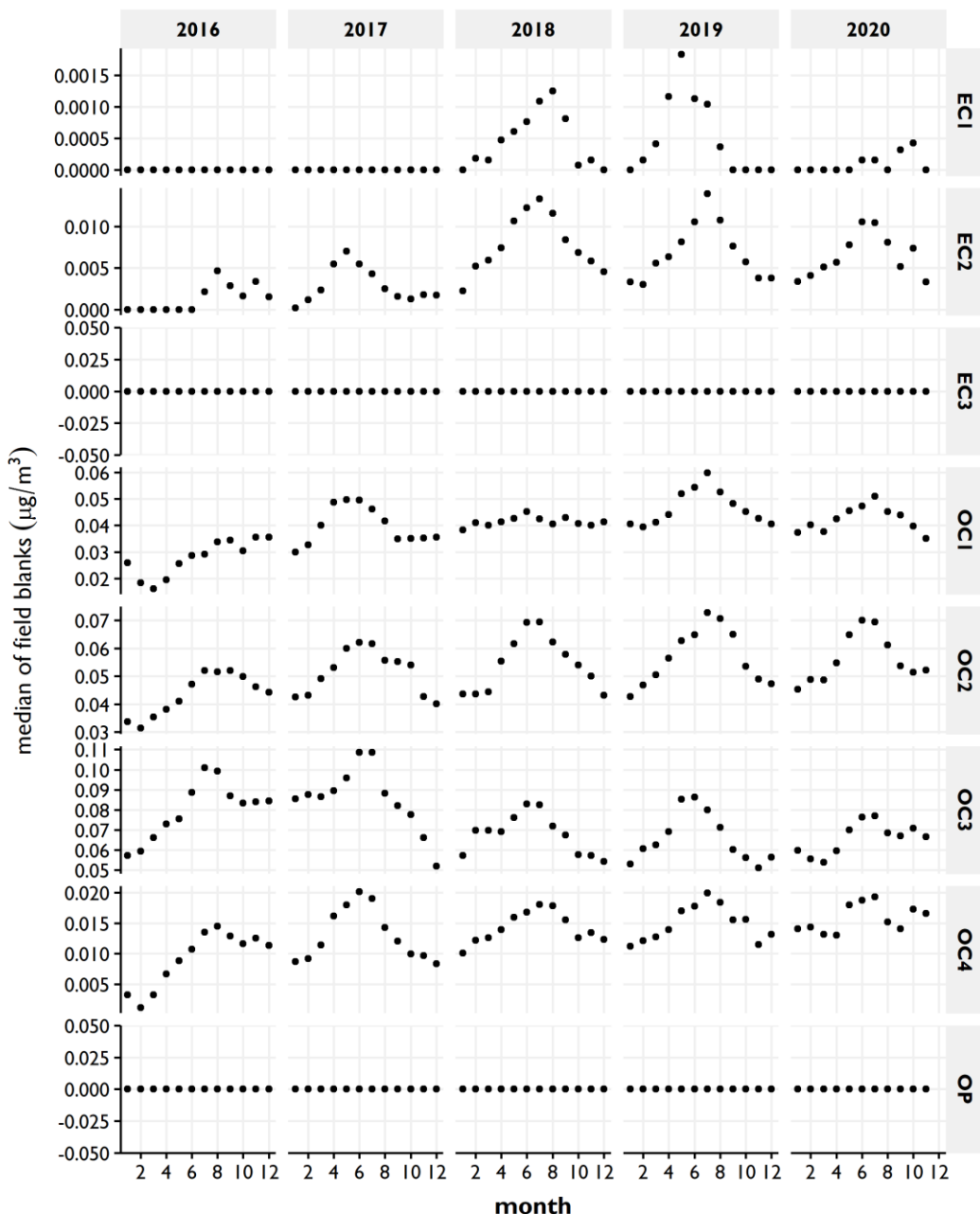


**Figure 1.7. IMPROVE carbon fraction monthly median field blank concentrations ( $\mu\text{g m}^{-3}$ ) from 2016 through 2020.**

Negative artifacts due to the volatilization of particulate organics are not accounted for because they are thought to be small (Turpin et al., 2000), although some studies suggest they could be important. Changes in analytical methods due to hardware upgrades on 1 January 2005 resulted in changes in the split between OC and EC (Chow et al., 2007; White, 2007)). Higher EC/TC ratios were reported after the change in analytical methods, but no changes in TC were detected (White, 2007; see Section 1.3.1.1). Additional discussion of OC and EC concentrations can be found in Schichtel et al., 2021.

While OC and EC at 635 nm are used for estimating reconstructed mass (Chow et al., 2015b) and chemical extinction (Pitchford et al., 2007), the carbon fractions have been found useful for emissions characterization (Dewangan et al., 2016; Shibata et al., 2019), source apportionment (Kim and Hopke, 2004; Kim et al., 2004), and health studies (Wagner et al., 2014). The multiwavelength measurements are being used to determine the brown carbon (BrC) in source and ambient emissions and its effect on visibility and climate (Chen et al., 2021; Chow et al., 2018; Chow et al., 2021; June et al., 2020; Li et al., 2018; Shen et al., 2017).

Finally, module D is fitted with a PM<sub>10</sub> inlet and uses a Teflon filter. PM<sub>10</sub> aerosol mass concentrations are determined gravimetrically, following a similar protocol as PM<sub>2.5</sub> gravimetric mass measurements.

All IMPROVE data are available for download from the Federal Land Manager Environmental Database (FED: <http://views.cira.colostate.edu/fed/>).

All standard operating procedures (SOPs) are available online (<https://airquality.ucdavis.edu/improve-documentation>).

### 1.2.3 Optical Monitoring and Analysis

Routine optical monitoring includes light scattering coefficients as measured by nephelometers at a subset of IMPROVE monitoring sites. The number of nephelometer sites has decreased significantly due to budgetary constraints. Transmissometers, which were used to measure light extinction coefficients, are no longer operated at any IMPROVE site (Hand et al., 2011). Optical scenes are monitored using the NPS web camera network. A map of current nephelometer and web camera sites is shown in Figure 1.8.

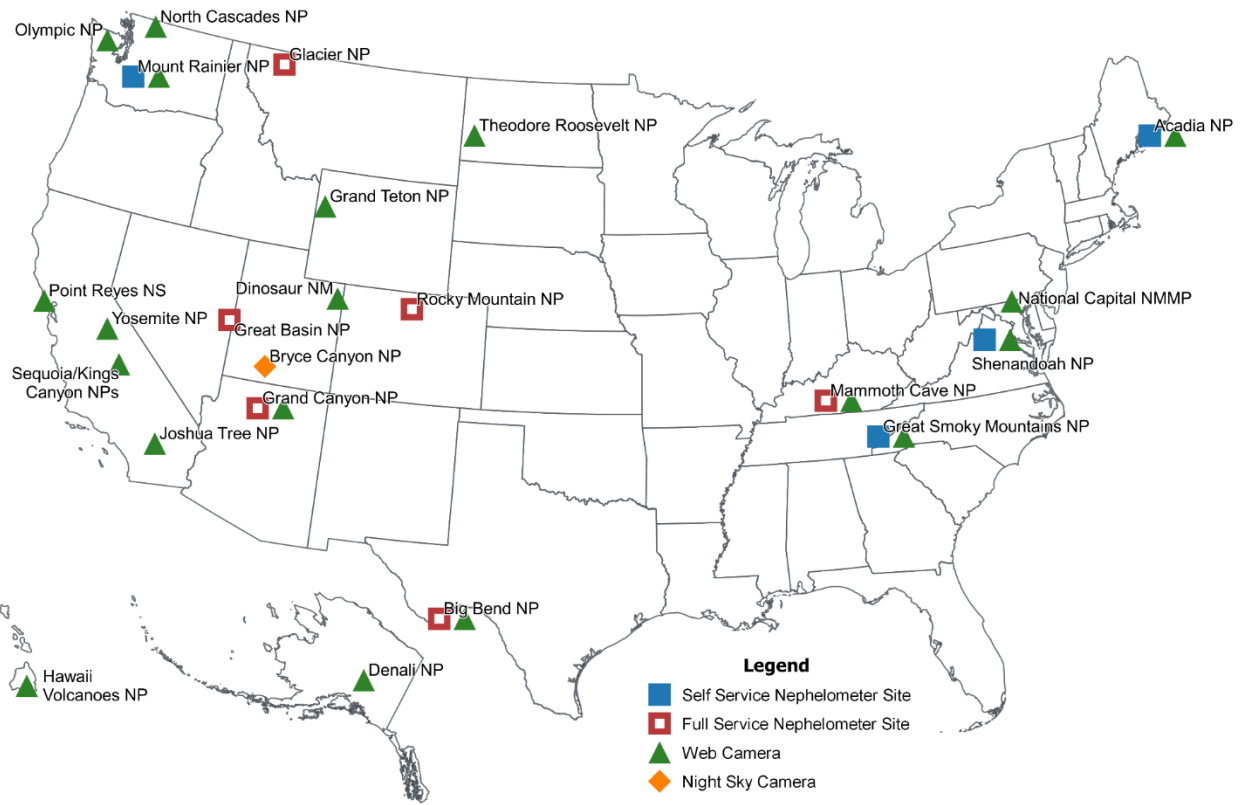


**Figure 1.8. Locations of nephelometers and web cameras.**

The Optec NGN-2 open air nephelometer measures total ambient light scattering coefficients for all particles sizes at an effective wavelength of 550 nm (Molenar et al., 1989). The instrument's open-air design has minimal heating and allows a larger distribution of particle sizes to pass through it. It was designed with solid-state electronics that are very stable over a wide temperature and humidity range. It has an inherent limitation of an abbreviated acceptance angle in that it only samples light scattered between 5° and 175°, and the cut point of the instrument has not been characterized. Calibration of the instrument and data validation and processing algorithms are discussed in detail in Molenar and Malm (1992). Uncertainties in nephelometer calibration lead to multiplicative errors in measured scattering coefficients. Typical uncertainties for the Optec NGN-2 are on the order of 5–10% (Molenar and Malm, 1992).

During high humidity and precipitation events, the nephelometer can report erroneously high scattering coefficients. This is due to water condensing on the walls of the nephelometer and spray from raindrops impacting the screen on the nephelometer inlet. This water collects in the light trap and reflects light directly into the scattered-light detector, causing extremely high readings. In order to minimize this problem, the door of the nephelometer closes during heavy precipitation events, and a wick was added to the light trap to facilitate the removal of any collected water. A list of past and current nephelometer sites is provided in Table 1.4. Ten nephelometers are currently in operation. Data can be downloaded from the FED website (<http://views.cira.colostate.edu/fed/>).

**Table 1.4. IMPROVE nephelometer network site locations.**

Site	Code	State	Latitude	Longitude	Elevation (m)	Dates of Operation
Acadia NP	ACAD1	ME	44.38	-68.26	122	06/10/1993-12/01/1997
Acadia NP	ACAD2	ME	44.38	-68.26	157	04/01/1993-present
Big Bend NP	BIBE1	TX	29.30	-103.18	1067	01/01/1998-present
Bliss SP	BLIS1	CA	38.98	-120.11	2131	07/01/1996-03/31/2006
Boundary Waters Canoe Area WA	BOWA1	MN	47.95	-91.50	527	04/01/1993-12/31/1997
Brigantine NWR	BRIG1	NJ	39.47	-74.45	5	04/01/1993-06/30/1994
Cedar Bluff SP	CEBL1	KS	38.77	-99.76	666	07/01/2004-09/30/2007
Chiricahua NM	CHIR1	AZ	32.01	-109.39	243	10/01/2003-06/30/2010
Children's Park-Tucson	CHPA1	AZ	32.30	-110.98	704	04/01/2003-09/30/2010
Columbia River Gorge NSA	COGO2	WA	45.57	-122.21	243	04/01/2001-03/31/2005
Cohutta WA	COHU1	GA	34.79	-84.63	743	01/01/2004-03/31/2007
Columbia River Gorge NSA	CORI1	WA	45.66	-121.00	179	07/01/1993-03/31/2005
Tucson	CRAY1	AZ	32.20	-110.88	1707	01/01/2001-09/30/2010
Dolly Sods WA	DOSO1	WV	39.11	-79.43	1182	04/01/1993-12/31/2006
Phoenix	DYRT1	AZ	33.64	-112.34	364	07/01/2003-06/30/2016
Phoenix	ESTR1	AZ	33.38	-112.38	290	01/01/2003-06/30/2016
Gila WA	GICL1	NM	33.22	-108.24	1776	04/01/1994-12/31/2003
Glacier NP	GLAC2	MT	48.51	-114.00	939	10/01/2007-present
Great Basin NP	GRBA2	NV	39.01	-114.22	2066	01/01/2008-present
Grand Canyon NP	GRCA2	AZ	35.97	-111.98	2267	10/01/1997-present
Mount Baldy WA (Greer, AZ)	GRER1	AZ	34.07	-109.44	2513	04/01/2001-06/30/2010

<b>Site</b>	<b>Code</b>	<b>State</b>	<b>Latitude</b>	<b>Longitude</b>	<b>Elevation (m)</b>	<b>Dates of Operation</b>
Great Gulf WA	GRGU1	NH	44.31	-71.22	454	04/01/1995-03/31/2005
Great Smoky Mountains NP	GRSM1	TN	35.63	-83.94	811	04/01/1993-present
Green River Basin	GRVS1	WY	41.84	-109.61	1950	07/01/1996-12/31/2000
Pine Mountain WA (Humble Mountain)	HUMB1	AZ	33.98	-111.78	1586	01/01/1997-12/31/2003
Mazatzal WA (Ike's Backbone)	IKBA1	AZ	34.34	-111.68	1298	04/01/2001-06/30/2010
Grand Canyon NP (Indian Gardens)	INGA1	AZ	36.08	-112.13	1166	04/01/2004-09/30/2013
Jarbridge WA	JARB1	NV	41.89	-115.43	1869	04/01/1993-12/31/1997
James River Face WA	JARI1	VA	37.63	-79.51	290	10/01/2000-12/31/2003
Lone Peak WA	LOPE1	UT	40.44	-111.71	1768	10/01/1993-09/30/2001
South Lake Tahoe	LTBV1	CA	38.95	-119.96	1902	01/01/1996-09/30/2004
South Lake Tahoe	LTBV2	CA	38.93	-119.96	1904	10/01/2005-03/31/2006
Lye Brook WA	LYBR1	VT	43.15	-73.13	1015	07/01/1993-12/31/2003
Mammoth Cave NP	MACA1	KY	37.13	-86.15	235	01/01/1993-present
Mayville	MAYV1	WI	43.44	-88.53	306	10/01/2000-12/31/2006
Mazatzal WA	MAZA1	AZ	33.91	-111.43	2164	01/01/1997-09/30/2000
Sierra Ancha WA (McFadden Peak)	MCFD1	AZ	34.0	-111.0	2175	10/01/1997-03/31/2000
Milwaukee	MILW1	WI	43.00	-87.89	193	04/01/2004-06/30/2006
Mount Rainier NP	MORA1	WA	46.76	-122.12	439	01/01/1993-present
Mount Zirkel WA	MOZI2	CO	40.54	-106.68	3243	10/01/1993-09/30/2009
Galiuro WA (Muleshoe Ranch)	MUSR1	AZ	32.35	-110.23	1402	07/01/1997-06/30/2005
National Capitol - Central	NACA1	DC	38.9	-77.04	514	04/01/2003-03/31/2016
Nebraska National Forest	NEBR1	NE	41.89	-100.34	883	07/01/2005-09/30/2007
Okefenokee NWR	OKEF1	GA	30.74	-82.13	48	01/01/1993-06/30/1997
Organ Pipe NM	ORPI1	AZ	31.95	-112.80	366	04/01/2003-06/30/2010
Petrified Forest NP	PEFO3	AZ	34.91	-109.8	1690	10/01/2003-06/30/2010
Phoenix	PHON1	AZ	33.50	-112.10	372	04/01/1997-06/30/2018
Quaker City	QUAK1	OH	39.94	-81.34	372	04/01/2002-03/31/2004
Superstition WA (Queen Valley)	QUVA1	AZ	33.29	-111.29	668	04/01/2003-06/30/2010
Cape Romain NWR	ROMA1	SC	32.94	-79.66	5	01/01/2004-12/31/2012
Rocky Mountain NP	ROMO3	CO	40.28	-105.55	2760	01/01/2008-present
Chiricahua WA (Rucard Canyon)	RUCA1	AZ	31.78	-109.30	1637	10/01/1997-06/30/2001
Seney NWR	SENY1	MI	46.29	-85.95	216	01/01/2002-06/30/2006
Shenandoah NP	SHEN1	VA	38.52	-78.43	1079	07/01/1996-present
Shining Rock WA	SHRO1	NC	35.39	-82.77	1617	04/01/1994-09/30/1999
Sierra Ancha WA	SIAN1	AZ	34.09	-110.94	1600	07/01/2000-06/30/2010
Alpine Lakes WA	SNPA1	WA	47.42	-121.43	1049	07/01/1993-06/30/2001
Sycamore Canyon WA	SYCA1	AZ	35.14	-111.97	2046	07/01/1998-06/30/2010
Three Sisters WA	THSI1	OR	44.29	-122.04	885	07/01/1993-present
Tucson	TUCN1	AZ	32.24	-110.96	745	04/01/1997-06/30/2001
Saguaro NP (Tucson Mountain)	TUMO1	AZ	32.28	-111.17	754	10/01/1996-12/31/2001

<b>Site</b>	<b>Code</b>	<b>State</b>	<b>Latitude</b>	<b>Longitude</b>	<b>Elevation (m)</b>	<b>Dates of Operation</b>
Saguaro NP (Tucson Mountain)	TUMO2	AZ	32.25	-111.22	754	10/01/2001-06/30/2010
Upper Buffalo WA	UPBU1	AR	35.83	-93.20	722	01/01/1993-09/30/2009
Phoenix (Vehicle Emissions)	VEIX1	AZ	33.46	-112.00	345	04/01/2003-06/30/2016
Virgin Islands NP	VIIS1	VI	18.34	-64.80	51	04/23/1998-09/30/2005
Wichita Mountains NWR	WIMO1	OK	34.73	-98.71	509	07/01/2004-09/30/2007

NM = National Monument

NP = National Park

NWR = National Wildlife Refuge

NSA = National Scenic Area

SP = State Park

WA = Wilderness Area

Monitoring of scenic views is accomplished using digital cameras to document the visual impact of regional and layered hazes as a function of aerosol concentrations. Scene monitoring has the added benefit of displaying real-time park imagery to the public through the NPS Air Resources Division (ARD) website (<https://www.nps.gov/subjects/air/webcams.htm>). Images are provided in two sizes, and archived images are available online (<https://www.nps.gov/AirWebCams/>). Scene monitoring is more in line with the simple definition of visibility; scene characteristics include observer visual range, scene contrast, color, texture, and clarity and have the distinction that they are also dependent on scene and lighting conditions.

Early scene monitoring was accomplished using automated 35-mm camera systems. At each camera site, a spectrum of images associated with varying haze levels have been digitized and are available from the IMPROVE website (<http://vista.cira.colostate.edu/IMPROVE/>). These early camera systems have been replaced with webcams that take still photographs and upload images to the NPS Air Resources Division web page every 15 minutes at 22 locations in national parks across the country (<https://www.nps.gov/features/ard/webcams/webcams.htm>). A list of currently operated webcams is provided in Table 1.5.

**Table 1.5 Web camera network site locations.**

<b>Site</b>	<b>Code</b>	<b>Latitude</b>	<b>Longitude</b>	<b>Elevation (m)</b>	<b>Start Date</b>
Acadia NP	ACAD	44.38	-68.26	158	06/1/1999
Big Bend NP	BIBE	29.33	-103.21	1170	08/1/2001
Bryce Canyon NP	BRCA	37.48	-112.24	2766	09/1/2013
Denali NP	DENA	63.47	-150.84	694	07/1/2004
Dinosaur NM	DINO	40.44	-109.31	1549	10/31/2018
Grand Canyon NP	GRCA	36.06	-112.12	2150	11/1/2001
Great Smoky Mountains NP - Clingmans Dome	GRSM-CD	35.56	-83.50	1935	05/1/2018
Great Smoky Mountains NP - Look Rock	GRSM-LR	35.63	-83.94	793	04/1/1998
Great Smoky Mountains NP - Purchase Knob	GRSM-PK	35.59	-83.07	1500	08/19/2003
Grand Teton NP	GRTE	43.67	-110.60	2307	08/30/2011
Hawaii Volcanoes NP	HAVO	19.43	-155.26	1213	01/6/2011

Site	Code	Latitude	Longitude	Elevation (m)	Start Date
Joshua Tree NP	JOTR	34.00	-116.00	1265	11/1/2001
Mammoth Cave NP	MACA	37.19	-86.10	226	12/1/2001
Mount Rainier NP	MORA	46.79	-121.73	1650	07/1/2003
National Capital NMMP	NACA	38.89	-77.07	60	07/1/2003
North Cascades NP	NOCA	48.67	-121.27	163	07/16/2014
Olympic NP	OLYM	48.09	-123.80	191	07/1/2003
Point Reyes NS	PORE	38.00	-123.02	30	01/1/2004
Sequoia/Kings Canyon NP	SEKI	36.57	-118.78	1927	10/1/2002
Shenandoah NP	SHEN	38.62	-78.32	1015	01/19/2011
Theodore Roosevelt NP	THRO	46.90	-103.38	966	08/1/2002
Yosemite NP	YOSE	37.71	-119.71	1606	10/25/2005

NMMP = National Mall and Memorial Parks

NP = National Park

NM = National Monument

NS = National Seashore

## 1.3 PROTOCOL AND EQUIPMENT CHANGES

While consistency through time is critical to a monitoring program that tracks trends, significant changes in sampling, analysis, and data processing have occurred in the history of the IMPROVE network. Most of the changes were implemented to improve the quality or usefulness of the IMPROVE dataset or to increase the overall effectiveness of the network within available resources. Evaluations were conducted prior to many of the changes to assess and, where possible, identify approaches that would minimize the effects of changes on the dataset. In addition, IMPROVE routinely conducts data consistency assessments, specifically designed to identify and attempt to explain data discontinuities and trends that are not thought to be associated with changes in atmospheric conditions. The results of these assessments are used to inform decisions concerning the operation of IMPROVE and to alert data users via data advisories posted on the IMPROVE website. This section encompasses changes that have occurred since IMPROVE report V. Many of the summaries in this section reference data advisories on the IMPROVE website that provide additional information, including data plots and useful graphics (<http://vista.cira.colostate.edu/Improve/data-advisories/>).

### 1.3.1 Analytical Changes

#### 1.3.1.1 Carbon Analyzer Replacements

OC and EC on quartz filters have been measured by DRI since 1987, starting with laboratory analyzers developed at the Oregon Graduate Institute (OGI, now part of the Oregon Health and Science University).

By the late 1990s it was evident that the DRI/OGI analyzers were deteriorating. Some components were no longer manufactured, and the data acquisition system was antiquated. The Model 2001 (Atmoslytic Inc., Calabasas, CA) analyzer was developed and made commercially available as a replacement. It introduced a number of enhancements, including better characterization of sample temperature and sample atmosphere, automatic sample positioning, more rapid temperature response, improved seals and flow control, greater heating capacity, advanced electronics, modern data acquisition, the potential for an automated sample changer,

and the ability to simultaneously measure reflectance and transmittance. Concurrent with the hardware modifications was the application of a new TOR protocol, named IMPROVE\_A, designed to reflect the more accurate and less variable temperature and sample atmosphere conditions provided by the new instruments.

The Model 2001 analyzer was used for routine analysis of IMPROVE samples collected on or after 1 January 2005. Extensive testing prior to deployment had suggested that observable differences in the data record would be minimal (Chow et al., 2005). However, subsequent examination of data from the first two years of analysis (2005 and 2006) revealed unforeseen differences between data from the old and new instruments (White, 2007). The differences vary as a function of site, but the new data generally identify a higher proportion of TC as EC and a lower proportion as OC than were observed in the final years of the old instruments. The EC/OC distinction is operationally defined, and the differences are not fully understood (White, 2007).

Samples acquired after 1 January 2016 have been analyzed with the Model 2015 multiwavelength carbon analyzer (McGee Scientific Instruments, Berkeley, CA) as described in Section 1.2.2.

### ***1.3.1.2 Environmentally Controlled Chamber Measurements of PM<sub>2.5</sub> and PM<sub>10</sub> Gravimetric Mass***

From December 2010 through September 2018, IMPROVE PM<sub>2.5</sub> and PM<sub>10</sub> gravimetric mass measurements were performed manually in a temperature-controlled laboratory using Mettler-Toledo XP6 microbalances. Prior to 2011, periodic laboratory measurements suggested that RH was typically below 50%; however, a laboratory relocation in 2011 resulted in highly variable RH conditions in the weighing laboratory. Laboratory RH was not continuously recorded, but available data suggested that RH varied significantly during weighing and since 2011 exceeded 40% for almost half of the analyses, occasionally exceeding 60% (White, 2016). Thus, from 2011 to 2018, gravimetric mass data were potentially subject to high RH conditions and likely contained particle-bound water (Hand et al., 2019).

Beginning with samples and field blanks collected in October 2018, UC Davis transitioned from manual weighing to the Measurement Technology Laboratories (MTL) AH500E climate-controlled automated weighing system. The MTL AH500E system was used for the vast majority of the mass measurements from 2019 through 2020, although occasionally the system failed and the samples had to be weighed manually as shown in Figure 1.9.

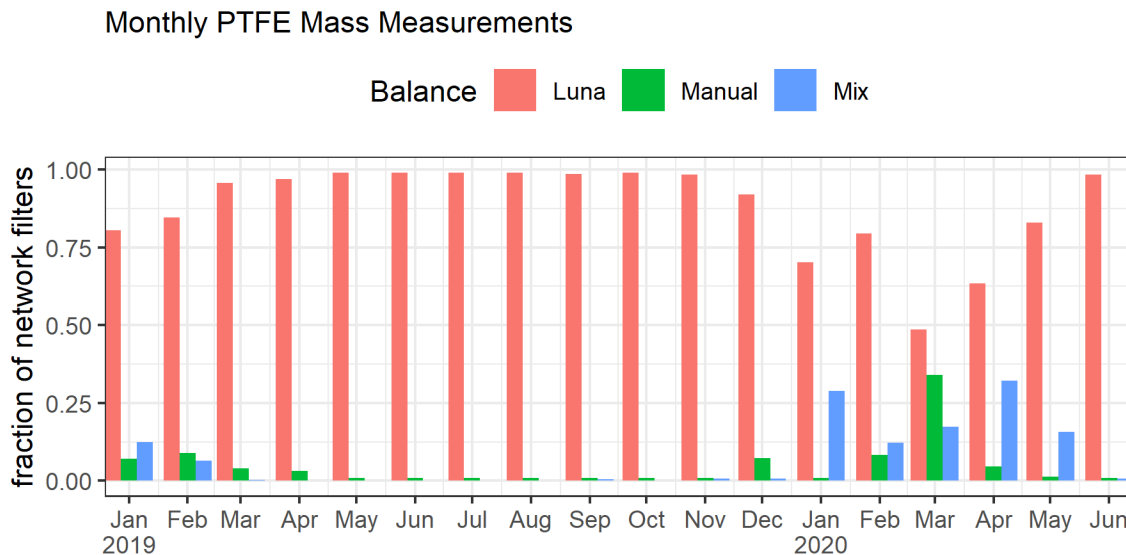


**Figure 1.9. Fraction of IMPROVE network samples from January 2019 through June 2020 weighed on the MTL automated weighing system (Luna), the manual balance, or a mix of the two (e.g., pre-sampling mass from MTL automated weighing system and post-sampling mass from manual balance).**

### 1.3.1.3 Transition from Custom-built XRF Instruments to PANalytical Epsilon 5 Instruments

A timeline of the elemental analysis methods employed at UC Davis is shown in Figure 1.10. PIXE analysis with the Crocker Nuclear Laboratory (CNL) cyclotron at UC Davis was originally used for all of the elements. From 1992 through 2010, IMPROVE samples were analyzed on two XRF instruments that employed copper (Cu) and molybdenum (Mo) X-ray sources, collectively referred to as the CuMo systems. These instruments were fabricated and used by CNL. The Cu XRF system initially operated in a helium environment, which simulates a vacuum photon path length with less sealing requirements. In 2005, the Cu XRF system was converted to vacuum to improve sensitivity for light elements. The Mo XRF system always operated in air since the interferences are low energy (e.g., argon K $\alpha$  peak occurs at 2.96 KeV), and this instrument only quantified elements with an atomic number (Z) of 26 and higher ( $\geq 6.40$  KeV). New XRF instruments (Malvern PANalytical Epsilon 5, abbreviated E5, Armelo, The Netherlands) were introduced for analysis of all IMPROVE samples starting 1 January 2011 to replace the aging systems.

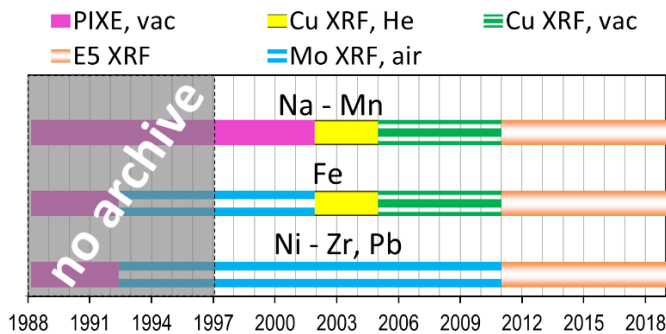


**Figure 1.10. Timeline of elemental characterization methods used to analyze IMPROVE samples at UC Davis. PANalytical XRF is abbreviated “E5”.**

To evaluate the performance of these new instruments, archived IMPROVE filters were analyzed both on the Cu- and Mo-anode XRF instruments and the PANalytical Epsilon 5 (E5) instrument. The archived filters for Great Smoky Mountains NP (GRSM1), Point Reyes NS (PORE1), and Mount Rainier NP (MORA1) were retrieved and inspected. The filters from each site were then assembled into a queue for analysis on the same instruments. The Cu-anode XRF in vacuum was used for the light elements and the Mo-anode XRF in air was used for the heavier elements in 2011. A subset of the archived filters from GRSM1, PORE1, and MORA1 were analyzed on the E5 XRF instruments for comparison. Figure 1.11 shows the results from the two instruments; five elements (P, Cr, As, Sr, and Zr) were excluded due to low numbers of pairs above the detection limits. Clustering around the dashed 1:1 line is observed for all elements shown, indicating generally good agreement between the two measurements. However, deviations from this line are observed, particularly for low-Z elements (Na, Mg, Al, and Si) as well as the halogens Cl and Br as concentrations increase. Na, Mg, and Cl agree at lower concentrations but show distinct deviations in the 1:1 agreement at higher concentrations, with CuMo XRF reporting much higher concentrations than E5 XRF.

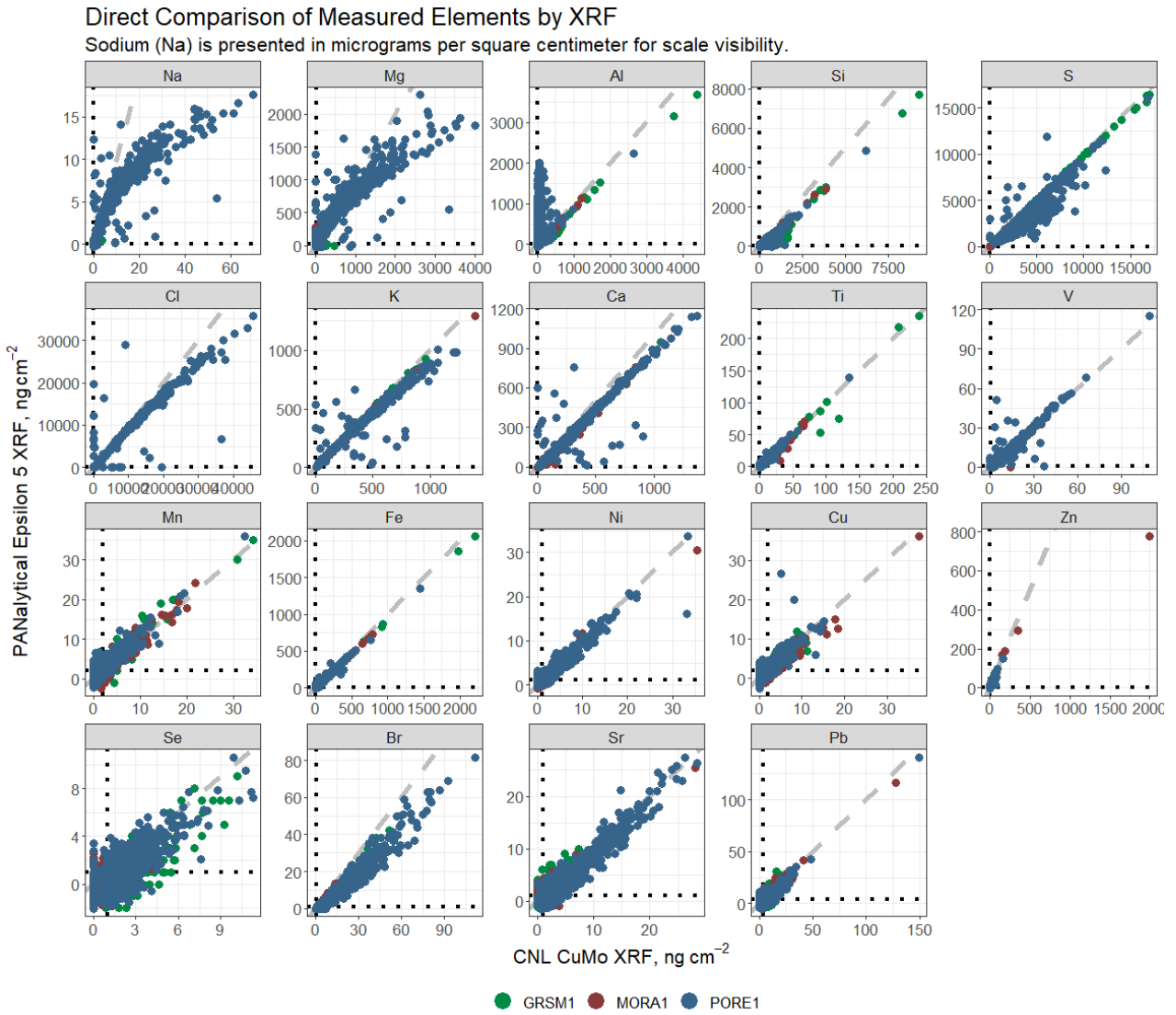


**Figure 1.11. Scatterplots showing the agreement between XRF analytical instruments for elements routinely measured above 3 times the reported MDLs. Black dotted lines show the reported MDLs for each element and instrument while gray dashed lines show a 1:1 agreement, not a regression line. Data are for three sites (GRSM1, MORA1, and PORE1).**

#### 1.3.1.4 Changes to Filter Light Absorption Measurement ( $f_{abs}$ )

Filter light absorption is quantified from HIPS measurements of transmittance ( $t$ ) and reflectance ( $r$ ) off the backside of a PM<sub>2.5</sub> Teflon filter since 1994. White et al. (2016) developed a calibration method based on fundamental principles where the HIPS  $t$  and  $r$  are calibrated such that  $r + t = 1$  for clean filters. Unexposed field and lab blanks are used for the clean filters. Filter absorption ( $f_{abs}$ ) is calculated with equation (1.1),

$$f_{abs} = \frac{f}{V} \times \tau_{abs} = \frac{f}{V} \ln \left( \frac{1-r}{t} \right) \quad (1.1)$$

where  $f$  is the area of the sample deposit,  $V$  is the volume of air sampled, and  $\tau_{abs}$  is the absorption optical depth. The  $f_{abs}$  measurements are not equivalent to ambient absorption ( $b_{abs}$ ), due in part to the potential for changes in aerosol absorbing properties as they are deposited on the filter. Also, the illumination of the aerosol in the atmosphere is columnar, while the HIPS calibration model approximated the illumination as diffuse, which would yield twice the effective path length and resulting optical depth. Actual sample illumination is anisotropic and  $1 \leq f_{abs}/b_{abs} \leq 2$ . Calibrating the system to blank filters has the advantage that the system is demonstrably well calibrated at zero absorption and should not suffer from biases at low values. The measurement of both  $r$  and  $t$  accounts for changes in filter scattering properties. However, it was found that filters with significantly different light scattering properties require a separate calibration. Consequently, filter acceptance testing is important to ensure the calibration is applicable to a given filter batch. HIPS is not a fully calibrated system since reference standards with known absorbing properties are not used in the calibration. However, there has been adequate theoretical and empirical evidence for the linearity of the response of HIPS to absorbing particulate matter in lightly loaded samples (White et al., 2016). Retrospective analyses of 15 years of IMPROVE samples have demonstrated that HIPS  $f_{abs}$  measurements are stable and reproducible.

Multiple changes and updates have been made to the UC Davis HIPS system. In April 2018 the HIPS integrating sphere was changed from the legacy 2-inch Spectrareflect-coated sphere described in White et al. (2016) to a newer 4-inch Spectralon sphere from the same manufacturer, and the laser was replaced. A calibration was performed following the April 2018 instrument upgrades; samples were analyzed under this calibration beginning with those collected January 2017. Additionally, in November 2018 new detectors were installed and the instrument was subsequently recalibrated; samples collected beginning March 2018 were analyzed under this calibration. The possible effects on the data due to modifications and new calibrations will be evaluated and reported in an upcoming data advisory.

**Table 1.6. Changes and updates made to the UC Davis HIPS system.**

Lab Date	Change	Reason	Comments
05/09/2017	HIPS moved to new laboratory	Instrument moved to new lab to help with environmental light and vibration issues.	
~10/1/2017	Change of the laser in the system.	The old HeNe laser lost power output and a new HeNe laser was purchased and installed.	New laser is Thor Labs model HNL050R, 5 mW 632.8 nm.
03/07/2018	Replacement of old 2-inch integrating sphere with newer 4-inch sphere.	Old sphere was dirty and it was thought better consistency would be gained with the larger sphere.	Old sphere was a 2-inch Labsphere Spectrareflect model. The new sphere is a 4-inch Labsphere Spectralon model.
03/26/2018	Removed the black pipe between laser and integrating sphere.	The pipe was used to house a diffuser and optics which are no longer used. The assembly was removed to address light leakage and alignment issues.	

<b>Lab Date</b>	<b>Change</b>	<b>Reason</b>	<b>Comments</b>
8/24/2018	Replaced reflectance and transmittance detectors and their power meters.	Detectors were over 30 years old, and the transmittance detector was losing stability.	New power meter is a dual input Newport 2936-R. Reflectance detector is a Si photodiode with a built in OD 3 neutral density filter, Newport 918D-SL-OD3R. Transmittance detector is the same but with an OD2 filter, Newport 918D-SL-OD2R.
8/24/2018 – 10/22/2018	Tested various iterations of neutral density filters and diffusers for the integrating plate.	Old plate optics (neutral density filter and opal glass diffuser) did not fit the lens tube for the new transmittance detector. They were replaced with 2-inch optics which fit the new lens tube.	Final plate optics arrangement is a 0.6 OD neutral density filter at the end of the lens tube closest to the sample filter with an opal glass diffuser directly behind it. Both mounted on a 0.5-inch long, 2-inch diameter lens tube connected to the detector via a short adapter.
11/08/2018	Start routine use of new detectors and integrating plate.	Testing complete and routine sample analysis began.	

For sample dates from January 2003 through December 2016 (HIPS analysis dates prior to April 2017), HIPS data calibration and operation are as described in White et al. (2016). For sample dates from January 2017 through February 2018 (HIPS analysis dates 12 April 2018 to 17 August 2018), the data are reported with a new calibration that reflects the installation of the 4-inch sphere and removal of the diffuser tube assembly. For samples dates from March 2018 through present (HIPS analysis dates of 16 November 2018 to present), data are reported after recalibration for the new detectors and integrating plate optics.

In addition to the abovementioned changes, in April 2020, the control software for the HIPS instrument was upgraded from a combination of Excel macros and a data acquisition card to LabVIEW control software that pulls digital data directly off the new detector controller that was installed in November 2018. The new LabVIEW control software provides an intuitive user interface to the instrument and automates more of the measurement process including writing instrument results directly to the database.

### ***1.3.1.5 Fourier Transform-Infrared Spectroscopy (FT-IR)***

For the last decade, Fourier transform-infrared (FT-IR) spectroscopy has been explored to cost-effectively reproduce existing IMPROVE speciation data and to measure additional speciation data in the form of organic functional groups. FT-IR spectra are measured from IMPROVE PM<sub>2.5</sub> Teflon filters with a nondestructive 5-minute analysis per sample.

A multitude of compositional data can be obtained from FT-IR analysis because many aerosol constituents have bonds that absorb infrared light. Proof-of-concept work began with efforts to reproduce TOR OC and EC data at the seven collocated module A sites in 2011 (Dillner and Takahama, 2015a; Dillner and Takahama, 2015b) and were extended to 11 additional sites in 2013 (Reggente et al., 2016). A select group of spectra was calibrated to TOR OC and EC data to accurately predict FT-IR OC and EC concentrations in all other samples, as

long as the mass range and chemical composition of samples in the calibration set were similar to the samples to be measured. In addition, samples from one year were used to predict samples in another year. Analysis on multiple FT-IR instruments suggested that several instruments could be used interchangeably as long as environmental conditions for the filters and the instruments were maintained over time (Debus et al., 2019), resulting in calibration for all instruments rather than a single calibration for each instrument. Applying calibrations networkwide to measure FT-IR OC and EC includes the need for one calibration per constituent measured (e.g., TC = OC + EC) due to the large variability in samples across the network. For example, samples influenced by forest fires or prescribed burns and those more typical of rural samples may require different calibrations in order to reproduce OC and EC from TOR (Takahama et al., 2019). This calibration method is conceptually different from calibrations with laboratory standards. However, the complexities of the carbonaceous fraction are not rivaled by other constituents (ions and elements), and calibration to ambient standards analyzed continuously provides a robust means of spanning the mass loadings, composition, and interferents as well as predicting operationally defined constituents for which there are no agreed upon standards.

Using networkwide data from 2015 through 2017, calibration methods and measurements of FT-IR OC, EC, and TC as well as inorganic ions (sulfate and nitrate) and dust elements (Si, Al, Ca, Ti, Fe), light absorption, and PM<sub>2.5</sub> mass were made for all continental U.S. sites (Debus et al., submitted). FT-IR measured concentrations were compared to routine IMPROVE data for all constituents. Reliably predicted concentrations were obtained for a broad range of atmospheric constituents with detectable infrared signatures such as OC, EC, TC, sulfate, dust elements, light absorption, and PM<sub>2.5</sub> mass. Due to volatilization off the Teflon filter, nitrate measurements were found to be unsatisfactory. To make this procedure operationally practical, select IMPROVE sites were used for calibration and the remainder of the sites were predicted using FT-IR spectra. The calibration sites were selected to represent the diversity of PM<sub>2.5</sub> concentrations and composition across the IMPROVE network. Strengths of the method include that it has nondestructive analysis, it has no gas-phase adsorption onto the Teflon filter (sampling artifact), it provides a new data stream of functional groups and most of the current suite of composition data, and it has a lower cost. Limitations of the FT-IR analysis include the use of the inconsistent Teflon filters with variable scattering and absorption that interferes with some peaks useful for measuring carbonaceous components, the lack of strong and unique absorptions related to EC, and the complexity of the spectra requiring advanced mathematical tools. A detailed description of FT-IR analysis, studies, and results can be found in Appendix 1.1.

#### **1.3.1.6 Summary of Data Advisories**

Data advisories are regularly posted to the IMPROVE website to inform users about events or measurement interferences that might affect the data (<http://vista.cira.colostate.edu/Improve/data-advisories/>). These events include both intentional and unintentional changes to instrumentation, procedures, or sampling media. Summaries of the data advisories that affected all sites were posted from 2011 through 2021 and are listed below.

- *Changes in Data Redelivery of 1/2005 through 5/2014 Data*

Several changes were applied to the data from January 2005 through May 2014. Data downloaded before 20 April 2015 may not have these changes applied. The data advisory describes several changes, including carbon concentrations, MDLs, and uncertainties;

HIPS measurements, MDLs, and uncertainties; ion MDLs and uncertainties; updated flow rates; updated sample status flags; and XRF concentrations, MDLs, and uncertainties (Cheng, 2015).

- *Change to OC Artifact Correction Method for OC Carbon Fractions*

OC carbon fractions are artifact-corrected to account for gas-phase adsorption of OC onto quartz filters. For data downloaded before May 2015, OC fractions were artifact-corrected using monthly median OC fractions from back-up quartz filters, located downstream the primary quartz filter at a few sites. The revised artifact correction method utilizes the monthly median blank filters collected at a few sites in the network. Blank filters have no air pulled through them but are loaded in the filter cassette and remain in the sampler for the same length of time as the sample filters (~7 days) (Dillner, 2015).

- *Change in Reporting of Filter Light Absorption*

Light absorption by the module A Teflon filter has been monitored using a He-Ne laser operating at 633 nm. From 1988 through February 1994, filters were analyzed with a LIPM method. Samples collected since March 1994 have been analyzed with HIPS. In 2015 the HIPS calibration was improved and data were reprocessed back to 2003. The revised data are identified as  $f_{abs}$  (White, 2015a).

- *Bias in Masked and Unmasked Filter Light Absorption Measurements*

Masks were historically used at many sites to reduce the collection area of module A filters from  $3.53\text{ cm}^2$  to  $2.20\text{ cm}^2$ . As recently as 2003, masks were employed at approximately half of all sites; by the end of 2007, all masks were removed. An inequivalence in  $f_{abs}$  was noted between masked and unmasked samples (White, 2015b).

- *Increased Variation of Humidity in the Weighing Laboratory*

IMPROVE gravimetric measurements have never been in compliance with EPA requirements regarding Federal Reference Method (FRM) determination of PM<sub>2.5</sub> mass. Starting with samples in 2011, IMPROVE filter handling and weighing operations were relocated to a different laboratory at UC Davis. The new laboratory did not have regulated RH capabilities. Additional analyses suggested that PM<sub>2.5</sub> gravimetric mass could be influenced by particle-bound water associated with hygroscopic species on the filters, especially during periods with higher laboratory RH (White, 2016; Hand et al., 2019).

- *Negative Chloride Concentrations at Salt-poor Sites*

At coastal sites influenced by marine aerosols, the module B chloride ion measurement has been indicative of fresh sea salt. Chloride is a less reliable tracer farther inland due to atmospheric reactions that deplete it. From 2000 through 2003, samples at many interior sites were associated with strictly negative concentrations. These negative concentrations were due to excessive chloride backgrounds on 37-mm nylon filters used during that period. This problem was addressed by switching suppliers of nylon filters with much lower backgrounds for 2004 and onward (White, 2017a).

- *Over-reporting of Sodium in Salt-rich Samples*

Elemental concentrations in samples analyzed with the legacy PIXE and XRF systems were reported with a semi-empirical correction for the attenuation of X-rays within the sample deposit. Attenuation increases as the element's atomic number decreases and is

strongest for Na, the lightest element reported. Samples collected since the beginning of 2011 have been analyzed with the Epsilon 5 PANalytical XRF. Results from this system do not include an adjustment for sample thickness (White, 2017b).

- *Calibration Bias in Reported Vanadium Concentrations*

Elemental concentrations from XRF analysis are based on linear calibrations of the instruments. Since the 2011 sample year, two thin-film standards certified by a commercial manufacturer have underpinned the vanadium (V) calibration. These standards were returned in 2017 to the original manufacturer for recertification. The V loadings reported in 2017 were lower than previously certified values by a factor of about 1/1.3. The XRF systems have been recalibrated using the newly certified V loadings of the same two original standards. The updated calibration yields XRF values consistent with quoted loadings for four new V standards purchased from the same manufacturer in 2017. V concentrations in samples collected starting in November 2017 are being reported with the new XRF calibration. Retrospective application of the 2017 recalibration back to 2011 assumes that the standards themselves did not change between their 2011 and 2017 certifications, and annual calibration records provide evidence of this stability (Trzepla, 2018).

- *Correction of Chloride Concentrations for Filter Blank Levels*

This data advisory serves as an update on a 2009 data advisory (White, 2009). Elevated chloride mass loadings on nylon filter field blanks were observed between mid-2007 and early 2011. During this period, chloride blank values started climbing within the consumption of a single manufacturing lot, the reason for which was later found to be adsorption by unsampled nylon filters from their packaging. The problem was eliminated by new storage procedures for the next manufacturing lot, introduced with the February 2011 samples. To account for the elevated and varying chloride blank values, monthly blank correction was implemented in 2009 and applied retroactively to the post-2005 ion data. Later analyses, reported in a 2017 data advisory, suggest that unknown and variable portions of the contaminant (blank) chloride initially present in affected filters may have been lost during the subsequent active sampling. The blank corrections made to sample values may thus have been excessive; consistent with this hypothesis, recent analysis of chloride long-term trends revealed a small step increase in network-median ambient chloride concentrations when the improved storage procedures eliminated most of the contamination. Thus, it is advisable to use the chloride ion data between mid-2007 and early 2011 with caution (Zhang, 2019).

- *Updated Data for Carbon*

Starting with January 2016 sample dates, DRI switched from Model 2001 to Model 2015 carbon analyzers for module C quartz filters. The Model 2015 analyzers directly measure carbon dioxide with a nondispersive infrared (NDIR) detector, where the earlier Model 2001 analyzers directly measured methane with a flame ionization detector (FID). Following quality assurance analyses, DRI determined that the software's initial threshold for peak integration was not appropriate for the new NDIR carbon signal. Carbon data from 2016 and early 2017 were reprocessed and redelivered (Schichtel, 2019).

- *Changes to HIPS System*

The HIPS instrument for measuring light absorption was completely refurbished in 2018. Details are provided in the data advisory (Trzepla and Giacomo, 2019).

- *Method Change for Calibrating Flow Rate Transfer Standards*

The flow calibration procedure prior to 2014 was creating a bias in the sampler flow rate calibrations, which led to low nominal flow rates at the IMPROVE sites. In November 2014, the method for calibrating each transfer standard against a primary standard was adjusted to avoid placing the two devices in series. A range of flowrates are now generated using a standard IMPROVE controller with a calibration cartridge that includes four different flow restrictions and are measured with 1) only the primary standard placed at the inlet to establish the reference flow rates and 2) only the transfer standard at the inlet. The calibration is now performed with three different calibration cartridges for a 12-point calibration, whereas the old calibration was only performed at four flow rates set using a needle valve. Evaluation of system pressure at the ORI (Open on Rise of Inlet) pressure tap indicated a negligible change in flow when switching between the two configurations. A comparison of transfer standard calibrations using the new method to previous calibrations of the same devices using the old method of devices in series shows that the new method results in a transfer standard calibration that is typically 2–3% lower on average at nominal sampler flow. The direction of this shift is consistent with expectations from the change in calibration method (Wallis, 2019a).

- *Change in Analytical Protocol for XRF Analysis*

The element content of collected IMPROVE samples is quantified by energy-dispersive X-ray fluorescence (EDXRF) analysis. The PANalytical Epsilon 5 instruments used since the 2011 sample year employ a primary X-ray tube to excite a sequence of secondary targets, whose secondary excitation spectra in turn irradiate the sample. In order to improve detection of lead and some other elements, the analytical protocol for XRF analysis was slightly modified starting with samples collected in October 2018. The KBr secondary target, previously included to highlight arsenic, was dropped to allow more time for some of the other targets in the sequence. Longer target irradiation generally improves sensitivities for the elements reported from that target. The effects on data quality are expected to be small, detectable only after a sufficient record has been acquired with the new protocol. The XRF analyzers have now been recalibrated with the modified protocol, and all IMPROVE samples starting October 2018 are being reported with the new calibration and new analytical protocol (Trzepla, 2019).

- *Universal Calibration Constants for Flow Rate Calculation*

In the past, the flow-rate calibration constants needed to be both site- and module-specific because the controller's pressure transducers were not calibrated to measure pressure in absolute units. Improvements in electronics now allow the use of universal constants for the entire network. The version 4 electronics are digital, and the pressure transducers provide absolute measures of pressure in inches of water for the cyclone transducer and pounds per square inch absolute (PSIA) for the orifice transducer. Quality control testing prior to deployment shows that the transducers are very consistent, with a full-scale, best-fit, straight-line accuracy of 0.25% and a maximum total error band of  $\pm 2\%$  full scale. Therefore, universal flow rate constants were implemented throughout the network. In 2018 and 2019, field calibrations from the 128 IMPROVE sites equipped with version 4

electronics were used to determine universal flow rate constants for the PM<sub>2.5</sub> and PM<sub>10</sub> modules. The universal constants determined are intended to characterize the entire network, provided that standard equipment is used at each site. Flow constants will not change with each site maintenance visit; rather, equipment will be checked during maintenance to ensure that flow calculation is within specifications. If outside of specifications, the maintenance team will seek to determine the cause of the discrepancy and make repairs as necessary (Wallis, 2019b).

#### ***1.3.1.7 Quality Assurance Reports***

Both UC Davis and RTI routinely review quality assurance (QA) activities, and reports are delivered semiannually (<http://vista.cira.colostate.edu/Improve/quality-assurance/>). The UC Davis report summarizes laboratory and data quality issues as well as analytical and data processing changes during the review period. The primary objectives of the report series are to

- provide graphics illustrating some of the comparisons used to evaluate the quality and consistency of measurements within the network;
- highlight observations that may give early indications of emerging trends, whether in atmospheric composition or measurement quality; and
- serve as a record and tool for ongoing QA efforts.

### **1.3.2 Sampling Equipment Changes**

#### ***1.3.2.1 New Sampler Controller***

UC Davis has developed new sampler controllers (V4 controller) and is currently updating new Ebox firmware to version 1.3. As of 30 June 2020, V4 controllers had been installed at all IMPROVE sites across the network in the United States and Canada. As of the same date, internet connections to all IMPROVE sites had been established except for Simeonof (SIME1) in Alaska and Baengnyeong Island (BYIS1) in South Korea. Sites with V4 controllers and internet connections are monitored in real time by UC Davis technicians, allowing faster follow up and recovery in cases where samples are being lost or equipment has failed.

#### ***1.3.2.2 Teflon Manufacturer Change***

Beginning with samples and field blanks collected mid-October 2018, UC Davis transitioned to using Teflon filters made by MTL (Measurement Technology Laboratories) instead of Pall Corporation. Teflon filter field blanks from the A-module (PM<sub>2.5</sub>; Figure 1.12) and D-module (PM<sub>10</sub>; Figure 1.13) were gravimetrically analyzed to monitor contamination levels and balance stability. As seen in Figure 1.12 and Figure 1.13, there was a step increase in PM<sub>2.5</sub> and PM<sub>10</sub> concentrations, respectively, measured from field blanks corresponding with the transition, indicating that the filters gained mass between pre- and post-weight measurements. Experiments conducted confirmed that the mass gain was connected to the filters themselves, not the weighing chamber. It was unclear what part of the filters was gaining mass (either the filter ring or the Teflon film) and if the gain was from water or potentially volatile organic carbon. UC Davis has continued working with both Pall Corporation and MTL to acquire Teflon filters that meet all quality specifications.

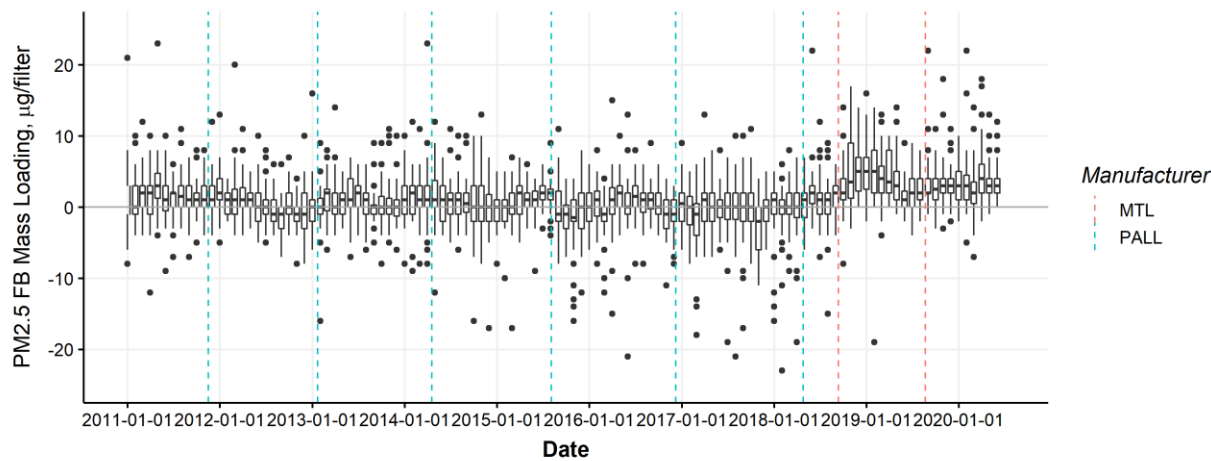


**Figure 1.12.** Time series of PM<sub>2.5</sub> ( $\mu\text{g}/\text{filter}$ ) on Teflon filter field blanks (1 January 2011 through 30 June 2020). Blue vertical lines indicate manufacturer lot transition, where Pall Corporation is the manufacturer. Red vertical line indicates manufacturer transition to Measurement Technology Laboratories (MTL) as manufacturer.

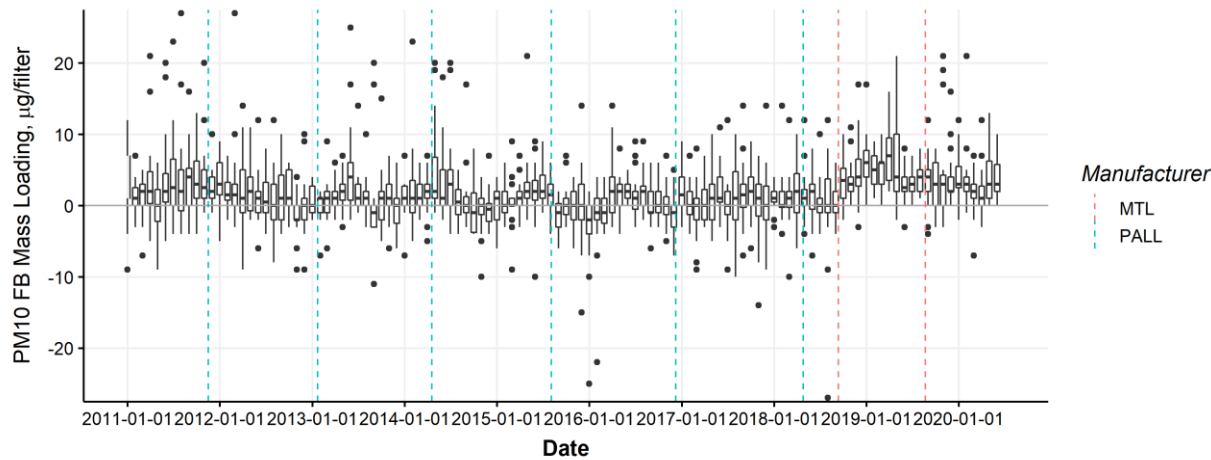


**Figure 1.13.** Time series of PM<sub>10</sub> ( $\mu\text{g}/\text{filter}$ ) on Teflon filter field blanks (1 January 2011 through 30 June 2020). Blue vertical lines indicate manufacturer lot transition, where Pall Corporation is the manufacturer. Red vertical line indicates manufacturer transition to Measurement Technology Laboratories (MTL) as manufacturer.

### 1.3.3 Data Processing Changes

During 2018 through 2020, IMPROVE data processing was modified to standardize field blank processing, uncertainty calculation, and MDL calculation across all analyses: gravimetric mass, XRF, IC, and thermal optical analysis (TOA) for OC and EC. Field blanks are used to calculate representative networkwide statistics that are used to perform artifact correction, estimate uncertainty, and calculate MDL. Prior to this period, the particulars of these estimates varied by analysis. There are now two standard calculation paths, one that is filter lot specific for analyses that are more dependent on filter lot variability and one that is independent of filter lot.

The lot-specific analyses are XRF and HIPS, while gravimetric mass, IC, and TOA are lot independent.

Artifact correction and MDL estimates are based on monthly field blank statistics, and reported uncertainty depends partly on the MDL estimate. For lot-independent analyses, a minimum of 50 field blanks is required to calculate the statistics, and a minimum of 35 field blanks is required for lot-specific analyses. In most cases, there are enough field blanks of each lot within a month to meet these minimum requirements. However, if there are not, the algorithm includes field blanks from prior and/or subsequent months until the minimum threshold is reached. The two statistics calculated are median and 95<sup>th</sup> percentile.

Concentrations are calculated with equation (1.2), where C is the ambient concentration (ng/m<sup>3</sup>) and A is the mass measured on the filter (ng). The artifact mass, B (ng), is the field blank median for IC, TOA, and XRF, and zero for gravimetric mass and HIPS. The sample of air volume is given as V (m<sup>3</sup>).

$$C = \frac{A-B}{V} \quad (1.2)$$

The reported MDL (ng/m<sup>3</sup>) is calculated with equation (1.3):

$$MDL = \frac{\max(P95-B, MDL_a)}{V} \quad (1.3)$$

where P95 is the 95<sup>th</sup> percentile of field blank mass (ng) and MDL<sub>a</sub> is the analytical MDL determined and reported by the laboratory (ng). Concentration uncertainty ( $\sigma(c)$ , ng/m<sup>3</sup>) is calculated with equation (1.4),

$$\sigma(c) = \sqrt{[fC]^2 + \left[ \frac{0.608 * \max(P95-B, MDL_a)}{V} \right]^2} \quad (1.4)$$

where f is the fractional uncertainty. This term results from various sources of proportional uncertainties, such as analytical calibration and flow-rate measurements. Beginning with data from samples collected in January 2018, f is determined using the most recent two years of data from collocated measurements. If the count of collocated pairs over the two-year period is less than 60, a value of 0.25 is adopted as f.

The standardization of these calculations occurred in stages, outlined below.

- January 2018: Updated IC and TOA MDL

Prior to sample day 1 January 2018, IC and TOA species MDLs were calculated using 3 × the standard deviation of each field blank set, rather than the 95<sup>th</sup> percentile now used. For most months, these calculations are similar; however, high outliers can make the standard deviation calculation significantly higher. This can occur, for example, when an intended field blank is accidentally sampled. The switch to 95<sup>th</sup> percentile provides a more stable estimate of MDL that is more robust against outliers. In addition, prior to sample day 1 January 2018, IC and TOA field blank statistics required a minimum of

three monthly field blanks instead of the 50 now required. There are routinely >50 field blanks each month, so this change has little impact.

- October 2018: Updated XRF processing

The IMPROVE program uses three PANalytical Epsilon 5 XRF instruments. Prior to October 2018, XRF field blank analyses were aggregated by instrument used and instrument analysis date. There was no check to see if the field blanks were from the same sample collection period as the samples. As of October 2018, field blanks are aggregated using the universal methods described above, independent of instrument and separated by filter lot. This timing coincides with the change in analytical protocol described in the Section 1.3.1.6.

- January 2019: Update gravimetric mass and HIPS MDL

Prior to data collected 1 January 2019, gravimetric mass and HIPS absorption were assigned static MDL values. Assuming nominal flow, the resultant reported MDLs were approximately 300 ng/m<sup>3</sup> for PM<sub>2.5</sub> mass, 400 ng/m<sup>3</sup> for PM<sub>10</sub> mass, and 0.35 Mm<sup>-1</sup> for filter absorption. As of January 2019 sample data, MDLs for all these parameters are calculated using the universal methods described above.

### 1.3.4 Summary of Changes

A summary of changes to the network since 2011 is listed in Table 1.7.

**Table 1.7. Major network wide changes in sampling, analysis, and data reporting affecting samples collected January 2011 and later.**

Change Date	Change Description
01/01/2011 (sampling date)	Introduced PANalytical XRF instruments for element analysis
02/01/2011	Transitioned from Cahn Microbalances to Mettler Toledo XP6 Microbalances
10/01/2012	New loose-screen sample cassettes deployed in network
09/29/2014	New sample handling laboratory software system deployed
11/01/2014	Changed method for calibrating flow rate transfer standards
01/01/2015	HIPS light absorption data ( $f_{abs}$ ) between 2003 and 2015 reprocessed using new 2015 calibration and updated in FED database
04/20/2015	Changed duration criteria for clogged and clogging filters during redelivery of 1/2005-5/2014 data
04/20/2015	Changed temperature equation used in flow rate calculation during redelivery of 01/01/2005-05/01/2014 data
04/20/2015	Changed OC artifact correction from using back-up quartz filters to using monthly median blanks during redelivery of 1/2005-5/2014 data
2015-2016	Installed precision ruby orifices in PM <sub>10</sub> modules to improve flow rate measurement
01/01/2016 (sampling date)	TOA carbon analysis transitioned from using DRI 2001 carbon analyzer to DRI 2015 multi-wavelength carbon analyzer
08/31/2017	Started delivery of IMPROVE semi-annual QA report
2018-2019	Deployed new sampler controller (V4 controller) including new Ebox with digital pressure transducers and internet connectivity throughout the network

<b>Change Date</b>	<b>Change Description</b>
01/01/2018 (sampling date)	Changed flow rate calculation to using universal flow constants for sites with V4 sampler controlled installed
10/01/2018 (sampling date)	Teflon filter manufacturer changed from Pall to MTL
10/01/2018	Modified XRF analytical application by removing KBr secondary target to improve sensitivity for selected elements
10/01/2018 (sampling date)	Introduced MTL weighing chamber for gravimetric analysis
2017	Implemented multiple changes to the HIPS system and data processing for filter light absorption measurement
2018	Standardized blank processing and MDL estimation for XRF, HIPS, gravimetric, IC and TOA analysis
02/01/2021 (deployment date)	Second MTL weighing chamber deployed. Mettler Toledo balance in both MTL weighing chambers upgraded to XPR6UD5 ultrabalances

### 1.3.5 IMPROVE Technical System Audits

Technical System Audits (TSA) of field operations are conducted to assess whether the IMPROVE sampling sites are in compliance with the IMPROVE Quality Assurance Project Plan (QAPP, [http://vista.cira.colostate.edu/improve/wp-content/uploads/2020/02/IMPROVE-QAPP-Signed\\_3\\_2016\\_updated.pdf](http://vista.cira.colostate.edu/improve/wp-content/uploads/2020/02/IMPROVE-QAPP-Signed_3_2016_updated.pdf)). TSAs focus primarily on evaluating the sampling sites and the particle samplers in the field. In conducting a TSA, the auditor

1. assesses whether the sampling site meets siting criteria for an IMPROVE sampler;
2. evaluates the integrity of the sampling structure;
3. checks the flow rate of each sampling module using a NIST (National Institute of Standards and Technology) certified flow meter;
4. observes the technique of the site operator (when possible);
5. asks the site operator to complete a questionnaire to ensure that (s)he has adequate sampler and sample change knowledge, that all safety concerns have been addressed, and that the current IMPROVE Operations Contractor is providing adequate support to run the sites.

From 2016 through 2022 nearly all of the IMPROVE sites have been audited, with the goal to complete TSAs at all sites within a ten year period. Figure 1.14 shows the locations of IMPROVE sites, with the symbol color denoting whether the site has been audited. Minor problems discovered during the audits are addressed by the Operation Contractor (currently UC Davis); major problems are addressed by a joint committee, including the principal investigator of the Operations Contractor, the Steering Committee Chair, and the contracting officer representative at NPS. Audit results are provided in annual TSA reports (<http://vista.cira.colostate.edu/Improve/technical-system-audits/>).

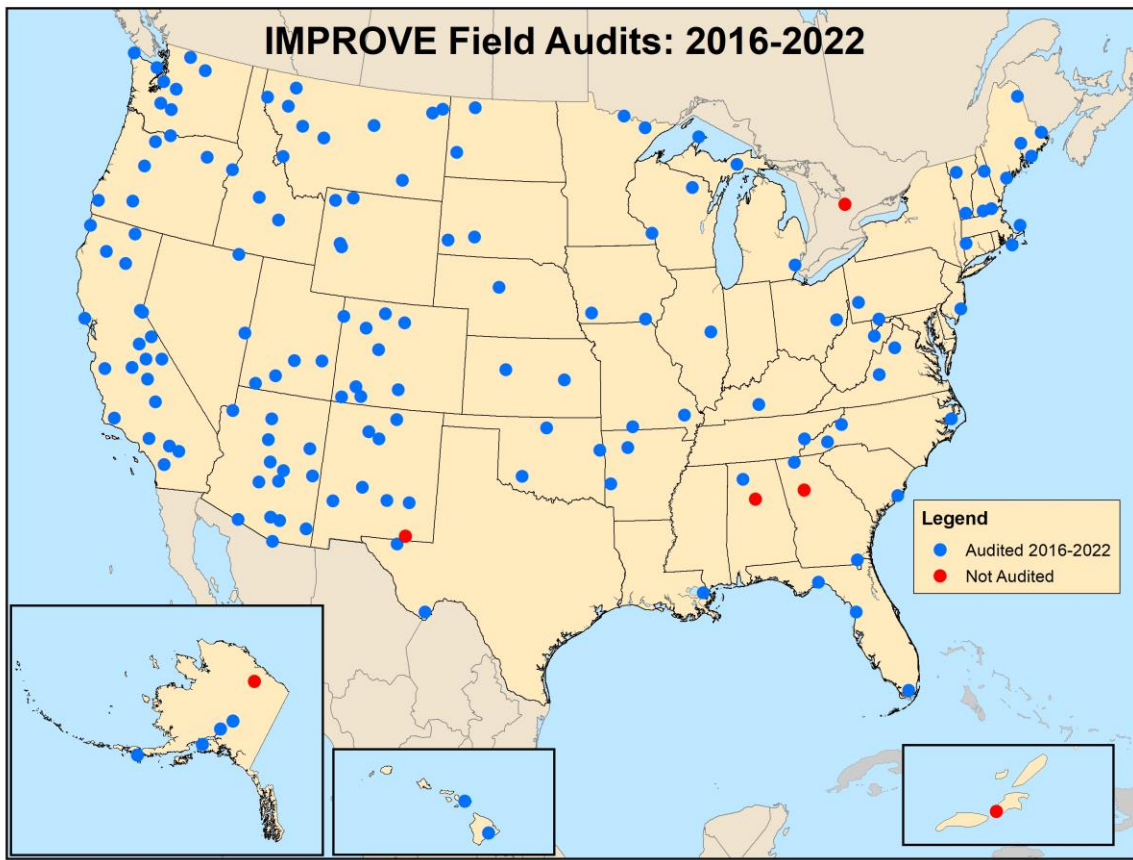


**Figure 1.14 IMPROVE field site audits from 2016-2022. Blue symbols correspond to audited sites; red symbols are sites yet to have a technical system audit.**

#### 1.4 CHEMICAL SPECIATION NETWORK

The objectives of the EPA's Chemical Speciation Network (CSN) are to track progress of emission reduction strategies through the characterization of trends, validation of air quality modeling and source apportionment activities, and support of health effects and exposure studies. The CSN comprises approximately nearly 150 sites operated by state, local, and tribal agencies, primarily in urban/suburban settings.

The EPA's PM<sub>2.5</sub> speciation program was established in 1997 as a complement to the PM<sub>2.5</sub> Federal Reference Method (FRM) mass network. The pilot phase of the program included thirteen sites that operated from February through July 2000. The Speciated Trends Network (now referred to as the CSN) was deployed in the fall of 2000 (EPA, 2004). Historically, the CSN utilized several types of samplers, including the Thermo Andersen RAAS, Met One SASS, and the URG MASS (Solomon et al., 2014). The specific sampler employed at a given site was chosen by the state, local, or tribal agency. Currently, each site operates two samplers: a Met One SASS or SuperSASS for collection of Teflon (for elemental concentration using XRF) or nylon filters for ion concentration using IC. A URG 3000N sampler is used for collection of quartz filters for TOA. All samplers use a PM<sub>2.5</sub> inlet. Samplers operate on a 24-hour schedule from

midnight to midnight every third or every sixth day, and data are reported at local conditions. A detailed description of network operation and sampling details is provided in Solomon et al. (2014). In 2014, budget considerations led to changes in CSN operations, resulting in the elimination of the PM<sub>2.5</sub> mass measurement and defunding of 38 sites. Sample frequency was also reduced from every third day to every sixth day at a small number of CSN sites (<https://ha.battelle.org/CSNAssessment/html/Default.html>).

Historically, the RTI International Laboratory held the EPA CSN contract for filter shipping, handling, laboratory analysis (except for carbon analysis, which was subcontracted to DRI in 2007), and data reporting. In November 2015 the laboratory analysis and data processing activities were awarded to UC Davis, with ion and carbon analysis subcontracted to DRI. The filter shipping and handling was awarded separately to Wood PLC. A number of shifts in laboratory analysis and data processing methods also occurred. XRF laboratory analysis shifted from RTI to UC Davis starting with 20 November 2015 samples. IC laboratory analysis was subcontracted to DRI and then to RTI after 1 October 2018. Carbon laboratory analysis switched to UC Davis on 1 October 2018. A number of other changes occurred to methods for determining and applying blank corrections and reporting data with these contract changes; these are discussed in detail in the CSN data advisory in Appendix 1.2.

CSN carbon analysis was historically performed using thermal optical transmittance (TOT) using a NIOSH (National Institute for Occupational Safety and Health)-type protocol. The recognition that IMPROVE samplers and TOR analysis produce different OC and EC concentrations than CSN samplers and TOT analysis motivated the CSN transition to TOR analysis for consistency with the IMPROVE network and to the URG 3000N sampler. The conversion began in May 2007 with 56 sites, followed by another 63 sites in April 2009 and 78 additional sites in October 2009 (EPA, 2009). A discussion of the adjustments applied to CSN carbon data collected prior to the transition to the new analyses and monitors is provided by Malm et al. (2011). After 2009, carbon data from CSN and the IMPROVE network should be directly comparable, with the exception of blank corrections.

Starting 20 November 2015, concentration data for ions and carbon are reported with blank corrections (positive sampling artifacts). Prior to this date, only elements were blank corrected using filter lot-specific background levels. For samples collected between 20 November 2015 and 31 January 2017, elemental measurements were corrected using the laboratory filter blank median areal density from each manufacturer filter lot. Beginning in February 2017, elemental blank corrections used the monthly median of field blanks, consistent with other corrections. Blank corrections for ion data began with samples collected in January 2016, using monthly median data for the corresponding sample month. Carbon blank corrections are applied for each thermal subfraction of the thermal optical analysis, using the corresponding median value from the quartz field blanks during the sample month. Both corrected and uncorrected carbon data are reported to EPA's Air Quality System (AQS) database.

A map of 372 current and discontinued CSN sites is provided in Figure 1.15, with the general regions depicted. Twenty-nine regions for the CSN sites were empirically defined based on seasonal distribution of aerosol concentrations and site locations (Hand et al., 2011; Hand et al., 2012). For comparison purposes, sites were grouped into similar regions to those defined for the IMPROVE network. Of the 29 regions, eleven had only one site per region. A list of the 136

sites that met the completeness criteria (outlined in Chapter 2) is provided in Table 1.8, including site location, region, and setting (urban, suburban, or rural). The sites used in this report are shown as orange circles in Figure 1.15. CSN data can be downloaded from <http://views.cira.colostate.edu/fed/> or <http://www.epa.gov/ttn/airs/airsaqs/>.

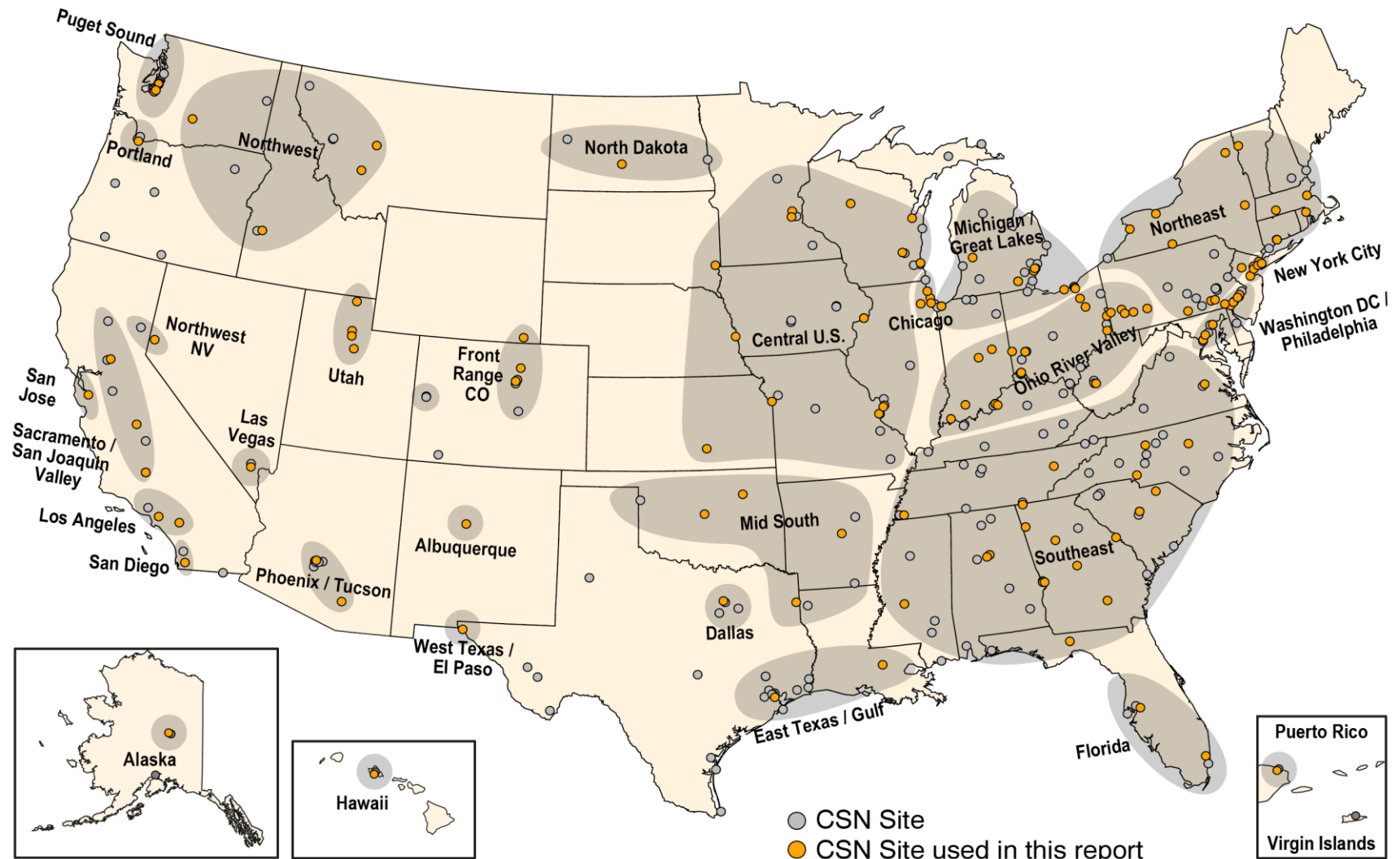


Figure 1.15. Current and discontinued Chemical Speciation Network (CSN) sites operated by the Environmental Protection Agency. Regions are shown as shaded areas and bold text. Sites included in the analyses in this report are shown as orange circles.

**Table 1.8. Chemical Speciation Network (CSN) site location, elevation, setting and region.**

Site	City	State	Region	Latitude	Longitude	Elevation (m)	Setting
				(deg)	(deg)		
10730023	Birmingham	AL	Southeast	33.553	-86.815	177	urban
10732003	Birmingham	AL	Southeast	33.5	-86.924	180	suburban
11130003	Phenix City	AL	Southeast	32.437	-84.999	25	urban
20900034	Fairbanks/NCORE	AK	Alaska	64.846	-147.727	132	urban
40139997	Phoenix	AZ	Phoenix/Tucson	33.504	-112.095	355	urban
40191028	Tucson	AZ	Phoenix/Tucson	32.295	-110.982	710	urban
51190007	Little Rock	AR	Midsouth	34.756	-92.276	77	urban
60190011	Fresno	CA	Sacramento/San Joaquin Valley	36.785	-119.773	96	suburban
60290014	Bakersfield	CA	Sacramento/San Joaquin Valley	35.356	-119.04	118	urban
60371103	Los Angeles	CA	Los Angeles	34.067	-118.227	126	urban
60658001	Rubidoux	CA	Los Angeles	34	-117.416	250	suburban
60670006	Sacramento	CA	Sacramento/San Joaquin Valley	38.614	-121.367	19	suburban
60731022	El Cajon	CA	San Diego	32.79	-116.944	141	suburban
60850005	San Jose	CA	San Francisco	37.349	-121.895	21	urban
80010008	Commerce City	CO	Front Range CO	39.828	-104.938	1574	urban
80310026	Denver	CO	Front Range CO	39.779	-105.005	1602	urban
81230008	Platteville	CO	Front Range CO	40.209	-104.823	1464	rural
90090027	New Haven	CT	Northeast	41.301	-72.903	5	urban
100032004	Wilmington	DE	Washington D.C./Philadelphia Corridor	39.739	-75.558	31	urban
110010043	Washington D.C.	DC	Washington D.C./Philadelphia Corridor	38.919	-77.013	31	suburban
120110034	Davie	FL	Florida	26.054	-80.257	2	suburban
120573002	Valrico	FL	Florida	27.966	-82.23	28	rural
120730012	Tallahassee	FL	East Texas/Gulf	30.44	-84.348	16	suburban
130210007	Macon	GA	Southeast	32.777	-83.641	103	suburban
130690002	Douglas	GA	Southeast	31.513	-82.75	64	rural
130890002	Panthersville	GA	Southeast	33.688	-84.29	244	suburban
131150003	Rome	GA	Southeast	34.261	-85.323	196	suburban
132150011	Columbus	GA	Southeast	32.431	-84.932	78	suburban
132450091	Augusta	GA	Southeast	33.434	-82.022	57	suburban
132950002	Rossville	GA	Southeast	34.978	-85.301	200	suburban
150030010	Kapolei	HI	Hawaii	21.324	-158.089	17	suburban
160010010	Meridian	ID	Northwest	43.601	-116.348	826	urban
170310057	Chicago	IL	Chicago	41.915	-87.723	185	suburban
170310076	Chicago	IL	Chicago	41.751	-87.714	188	suburban
170314201	Northbrook	IL	Chicago	42.14	-87.799	194	suburban
170434002	Naperville	IL	Chicago	41.771	-88.153	213	urban
171190024	Granite City	IL	Central U.S.	38.701	-90.145	128	urban
180190006	Jefferson	IN	Ohio River Valley	38.278	-85.74	137	urban
180372001	Jasper	IN	Ohio River Valley	38.391	-86.929	139	urban
180650003	Middleton	IN	Ohio River Valley	40.012	-85.524	309	rural
180890022	Gary	IN	Michigan/Great Lakes	41.607	-87.305	179	urban
180970078	Indianapolis	IN	Ohio River Valley	39.811	-86.115	240	suburban
181630021	Evansville	IN	Ohio River Valley	38.013	-87.577	116	urban

Site	City	State	Region	Latitude	Longitude	Elevation (m)	Setting
191630015	Davenport	IA	Central U.S.	41.53	-90.588	212	urban
201730010	Wichita	KS	Central U.S.	37.701	-97.314	405	urban
202090021	Kansas City	KS	Central U.S.	39.118	-94.636	269	urban
211110067	Louisville	KY	Ohio River Valley	38.229	-85.654	127	suburban
220330009	Baton Rouge	LA	East Texas/Gulf	30.461	-91.177	16	urban
240053001	Essex	MD	Washington D.C./Philadelphia Corridor	39.311	-76.474	10	suburban
240330030	Beltsville	MD	Washington D.C./Philadelphia Corridor	39.055	-76.878	47	suburban
250130008	Westover AFB	MA	Northeast	42.195	-72.556	60	suburban
250250042	Boston	MA	Northeast	42.329	-71.083	5	urban
260810020	Grand Rapids	MI	Michigan/Great Lakes	42.984	-85.671	190	urban
260910007	Tecumseh	MI	Michigan/Great Lakes	41.996	-83.947	0	suburban
261630001	Allen Park	MI	Michigan/Great Lakes	42.229	-83.208	182	suburban
261630015	Detroit	MI	Michigan/Great Lakes	42.303	-83.107	180	urban
261630033	Detroit	MI	Michigan/Great Lakes	42.307	-83.149	179	suburban
270031002	Blaine	MN	Central U.S.	45.138	-93.208	280	suburban
270530963	Minneapolis	MN	Central U.S.	44.955	-93.258	265	urban
280490020	Jackson	MS	Southeast	32.329	-90.183	106	urban
290990019	Arnold	MO	Central U.S.	38.449	-90.396	195	suburban
295100085	St. Louis	MO	Central U.S.	38.656	-90.198	144	urban
300490004	Helena	MT	Northwest	46.851	-111.987	1194	rural
300930005	Butte	MT	Northwest	46.003	-112.501	1682	urban
310550019	Omaha	NE	Central U.S.	41.247	-95.976	347	suburban
320030540	Las Vegas	NV	Las Vegas	36.412	-115.079	610	urban
320310016	Reno	NV	Northwest Nevada	39.525	-119.808	1403	urban
340070002	Camden	NJ	Northeast	39.934	-75.125	4	urban
340130003	Newark	NJ	Northeast	40.721	-74.193	27	urban
340230011	Rutgers	NJ	Northeast	40.462	-74.429	19	rural
340273001	Chester	NJ	Northeast	40.788	-74.676	256	rural
340390004	Elizabeth	NJ	Northeast	40.641	-74.208	3	suburban
350010023	Albuquerque	NM	Albuquerque	35.134	-106.586	1578	urban
360010005	Albany	NY	Northeast	42.642	-73.755	7	urban
360050110	Bronx	NY	New York City	40.816	-73.902	14	urban
360290005	Buffalo	NY	Northeast	42.877	-78.81	186	urban
360310003	Wilmington	NY	Northeast	44.393	-73.859	584	rural
360551007	Rochester	NY	Northeast	43.146	-77.548	146	urban
360610134	New York City	NY	New York City	40.714	-73.996	5	urban
360810124	Queens	NY	New York City	40.736	-73.823	13	suburban
361010003	Addison	NY	Northeast	42.091	-77.21	490	rural
370670022	Winston-Salem	NC	Southeast	36.111	-80.227	279	urban
371190041	Charlotte	NC	Southeast	35.24	-80.786	223	urban
371830014	Raleigh	NC	Southeast	35.856	-78.574	92	suburban
380150003	Bismarck	ND	North Dakota	46.825	-100.768	548	suburban
390350038	Cleveland	OH	Ohio River Valley	41.477	-81.682	186	urban
390350060	Cleveland	OH	Michigan/Great Lakes	41.494	-81.679	197	urban

Site	City	State	Region	Latitude	Longitude	Elevation (m)	Setting
390350065	Newburgh Heights	OH	Ohio River Valley	41.447	-81.662	210	urban
390350076	Cuyahoga Heights	OH	Ohio River Valley	41.424	-81.648	182	urban
390610040	Cincinnati	OH	Ohio River Valley	39.129	-84.504	213	urban
390810017	Stuebenville	OH	Ohio River Valley	40.366	-80.616	222	urban
390933002	Sheffield	OH	Michigan/Great Lakes	41.463	-82.114	182	suburban
391130038	Sinclair	OH	Ohio River Valley	39.756	-84.199	220	urban
391351001	New Paris	OH	Ohio River Valley	39.836	-84.721	357	rural
391510017	Canton	OH	Ohio River Valley	40.787	-81.394	334	urban
391530023	Akron	OH	Ohio River Valley	41.088	-81.542	313	urban
401091037	Edmond	OK	Midsouth	35.614	-97.475	344	suburban
401431127	Tulsa	OK	Midsouth	36.205	-95.977	193	urban
410510080	Portland	OR	Oregon	45.497	-122.602	86	suburban
420010001	Arendtsville	PA	Northeast	39.92	-77.31	241	rural
420030008	Pittsburgh	PA	Ohio River Valley	40.466	-79.961	312	suburban
420030064	Liberty	PA	Ohio River Valley	40.324	-79.868	279	suburban
420210011	Johnstown	PA	Ohio River Valley	40.31	-78.915	361	urban
420290100	Toughkenamon	PA	Washington D.C./Philadelphia Corridor	39.834	-75.769	91	rural
420450002	Chester	PA	Washington D.C./Philadelphia Corridor	39.836	-75.373	3	urban
420450109	Marcus Hook	PA	Washington D.C./Philadelphia Corridor	39.819	-75.414	0	urban
420710007	Lancaster	PA	Northeast	40.047	-76.283	99	suburban
420710012	Intercourse	PA	Northeast	40.044	-76.112	116	suburban
421010048	Philadelphia	PA	Washington D.C./Philadelphia Corridor	39.923	-75.098	25	urban
421010055	Philadelphia	PA	Washington D.C./Philadelphia Corridor	39.923	-75.187	3	urban
421255001	Burgettstown	PA	Ohio River Valley	40.445	-80.421	344	rural
421290008	Greensburg	PA	Ohio River Valley	40.305	-79.506	378	suburban
440071010	Rumford	RI	Northeast	41.841	-71.361	15	suburban
460990008	Sioux Falls	SD	Central U.S.	43.548	-96.701	451	urban
470931020	Knoxville	TN	Southeast	36.019	-83.874	309	suburban
471570075	Memphis	TN	Southeast	35.152	-89.85	87	suburban
481130069	Dallas	TX	Dallas	32.82	-96.86	132	urban
481410044	El Paso	TX	West Texas/El Paso	31.766	-106.455	1122	urban
482011039	Deer Park	TX	East Texas/Gulf	29.67	-95.129	9	suburban
482030002	Karnack	TX	Midsouth	32.669	-94.168	72	rural
490110004	Bountiful	UT	Utah	40.903	-111.885	1307	suburban
490353006	Salt Lake City	UT	Utah	40.736	-111.872	1309	suburban
490494001	Lindon	UT	Utah	40.341	-111.714	1456	suburban
500070012	Burlington	VT	Northeast	44.48	-73.214	42	urban
510870014	Richmond	VA	Southeast	37.558	-77.4	34	suburban
530330030	Seattle	WA	Puget Sound	47.597	-122.32	15	urban
530330080	Seattle	WA	Puget Sound	47.57	-122.309	58	urban
530530029	Tacoma	WA	Puget Sound	47.186	-122.452	97	suburban
530770009	Yakima	WA	Northwest	46.598	-120.499	326	urban
540390020	Charleston	WV	Ohio River Valley	38.346	-81.621	223	urban
540511002	Moundsville	WV	Ohio River Valley	39.916	-80.734	245	suburban

Site	City	State	Region	Latitude	Longitude	Elevation (m)	Setting
550090005	Green Bay	WI	Central U.S.	44.507	-87.993	184	urban
550270001	Horicon	WI	Central U.S.	43.466	-88.621	287	rural
550790026	Milwaukee	WI	Central U.S.	43.061	-87.913	216	urban
551198001	Perkinstown	WI	Central U.S.	45.204	-90.6	449	rural
560210100	Cheyenne	WY	Front Range CO	41.182	-104.778	15	suburban

The IMPROVE and CSN networks operate collocated samplers in several urban/suburban sites. Collocated sites with data that met the completeness criteria outlined in Chapter 2 were compared to identify relative biases between IMPROVE and CSN speciated aerosol concentrations. Monthly mean data from Birmingham, Alabama; Fresno, California; Phoenix, Arizona; and Puget Sound, Washington, for 2016–2019 were compared for ammonium sulfate (AS), AN, OC, EC, fine dust, sea salt (SS), PM<sub>2.5</sub> gravimetric fine mass (FM), and reconstructed fine mass (RCFM). Descriptions of species mass concentrations calculations are listed in Table 2.1 in Chapter 2.

Scatter plots of comparisons between IMPROVE and CSN species mass concentrations are presented in Figure 1.16. A summary of results is provided in Table 1.9. Errors were less than 20% for most species, with the exception of fine dust (21%) and sea salt (85%). IMPROVE SS concentrations were computed using chloride ion concentrations ( $1.8 \times \text{Cl}^-$ ), whereas CSN SS concentrations were computed using chlorine concentrations ( $1.8 \times \text{Cl}$ ) from XRF analysis. (CSN began reporting chloride concentrations in February 2017). Errors for EC were 19%, in part due to TOR hardware changes for CSN. Biases were typically within  $\pm 15\%$ , except for a -20% bias in fine dust (IMPROVE higher), -81% bias in SS (IMPROVE higher), and 21% bias in EC (CSN higher). Higher biases and errors associated with coarse-mode species may be due in part to differences in the sharpness of the cut points between IMPROVE and CSN samplers, with sharper CSN cut points resulting in lower concentrations, because less of the tail of the coarse-mode species is collected by the PM<sub>2.5</sub> filter. Additional comparisons between IMPROVE and CSN data are described in Gorham et al. (2021).

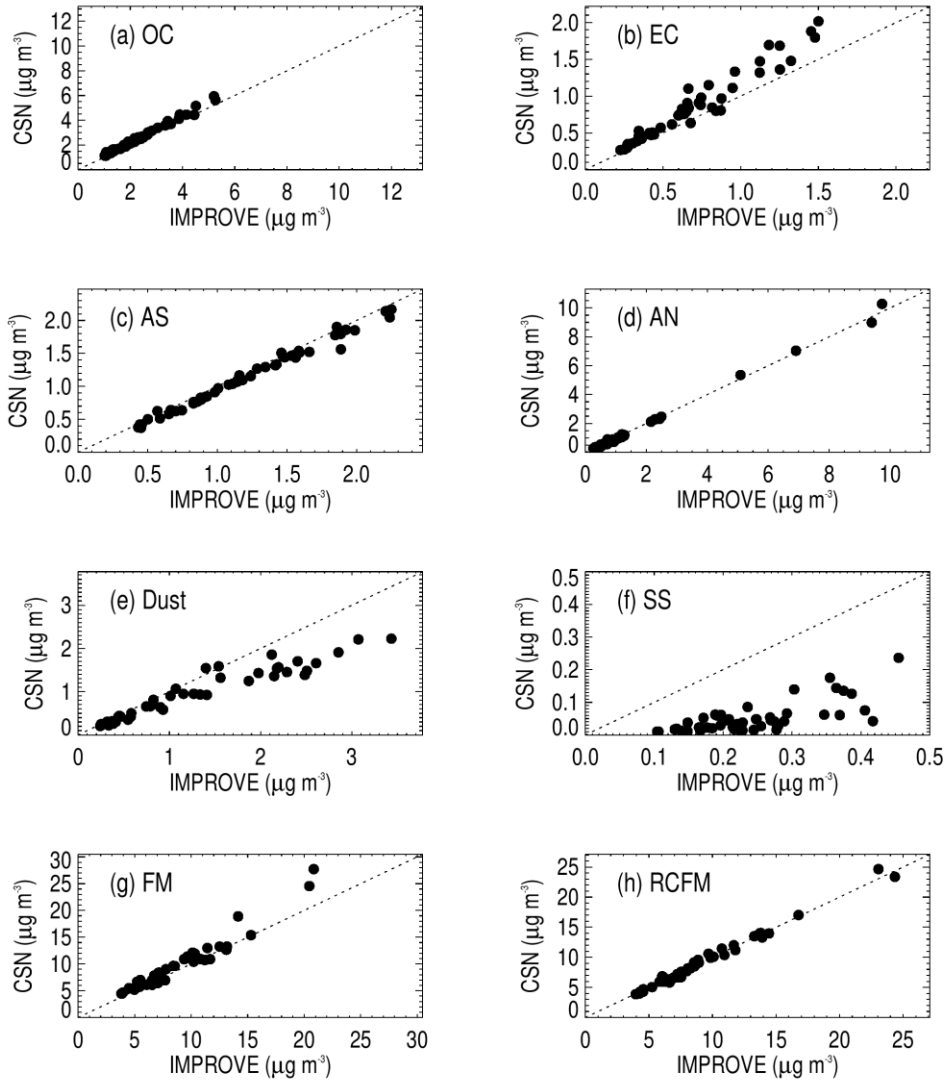


**Figure 1.16. Comparisons of monthly mean 2016–2019 PM<sub>2.5</sub> aerosol mass concentration data ( $\mu\text{g m}^{-3}$ ) for four collocated IMPROVE and CSN sites (see text) for (a) organic carbon (OC), (b) elemental carbon (EC), (c) ammonium sulfate (AS), (d) ammonium nitrate (AN), (e) fine dust, (f) sea salt (SS), (g) PM<sub>2.5</sub> gravimetric fine mass (FM), and (h) reconstructed fine mass (RCFM).**

**Table 1.9. Comparisons between monthly mean data at collocated IMPROVE and CSN sites from 2016 through 2019. Species include organic carbon (OC), elemental carbon (EC), ammonium sulfate (AS), ammonium nitrate (AN), fine dust (FD), sea salt (SS), PM<sub>2.5</sub> gravimetric fine mass (FM), and PM<sub>2.5</sub> reconstructed fine mass (RCFM). Positive biases correspond to higher CSN concentrations.**

Statistic	OC	EC	AS <sup>3</sup>	AN <sup>4</sup>	Dust	Sea salt <sup>5</sup>	FM	RCFM
Average IMPROVE ( $\mu\text{g m}^{-3}$ )	2.36	0.69	1.21	1.44	1.21	0.24	8.58	9.04
Average CSN ( $\mu\text{g m}^{-3}$ )	2.59	0.84	1.15	1.40	0.90	0.05	9.42	9.01
Bias <sup>1</sup> (%)	11	21	-6	-6	-20	-81	9	-1
Error <sup>2</sup> (%)	11	19	6	8	21	85	10	4
r	0.99	0.97	0.99	1.00	0.96	0.71	0.97	0.99
IMP/CSN	0.91	0.82	1.06	1.03	1.34	4.75	0.91	1.00

$$^1 \text{Error} = \text{median} \left( \left| \frac{\bar{X}_i - \bar{Y}_i}{\bar{Y}_i} \right| \right)$$

<sup>2</sup>Bias =  $\frac{1}{N} \sum_i \frac{\bar{X}_i - \bar{Y}_i}{\bar{Y}_i}$ ;  $\bar{X}_i$  and  $\bar{Y}_i$  are the daily data for CSN and IMPROVE concentrations, respectively. N gives

the number of data points.

<sup>3</sup>AS = 1.375×[sulfate ion]

<sup>4</sup>AN = 1.29×[nitrate ion]

<sup>5</sup>Sea salt = 1.8×[chloride ion] for IMPROVE and 1.8×[chlorine] for CSN.

## REFERENCES

- Chen, L.-W., Chow, J., Wang, X., Robles, J., Sumlin, B., Lowenthal, D., Zimmermann, R., and Watson, J. (2015), Multi-wavelength optical measurement to enhance thermal/optical analysis for carbonaceous aerosol, *Atmospheric Measurement Techniques*, 8(1), 451-461, doi:doi:10.5194/amt-8-451-2015.
- Chen, L.-W. A., Chow, J. C., Wang, X., Cao, J., Mao, J., and Watson, J. G. (2021), Brownness of organic aerosol over the United States: Evidence for seasonal biomass burning and photobleaching effects, *Environmental Science & Technology*, 55(13), 8561-8572, doi:10.1021/acs.est.0c08706.
- Cheng, X. (2015), Changes in redelivery of 1/2005 through 5/2014 data, *IMPROVE Data Advisory*(da0031), [http://vista.cira.colostate.edu/improve/Data/QA\\_QC/Advisory/da0031/da0031\\_2010to2014Redelivery.pdf](http://vista.cira.colostate.edu/improve/Data/QA_QC/Advisory/da0031/da0031_2010to2014Redelivery.pdf).
- Chow, J. C., Watson, J. G., Pritchett, L. C., Pierson, W. R., Frazier, C. A., and Purcell, R. G. (1993), The DRI thermal/optical reflectance carbon analysis system: description, evaluation and applications in US air quality studies, *Atmospheric Environment. Part A. General Topics*, 27(8), 1185-1201, [https://doi.org/10.1016/0960-1686\(93\)90245-T](https://doi.org/10.1016/0960-1686(93)90245-T).
- Chow, J. C., Watson, J. G., Crow, D., Lowenthal, D. H., and Merrifield, T. (2001), Comparison of IMPROVE and NIOSH carbon measurements, *Aerosol Science & Technology*, 34(1), 23-34, doi:10.1080/02786820600623711.
- Chow, J. C., Watson, J. G., Chen, L.-W. A., Arnott, W. P., Moosmüller, H., and Fung, K. (2004), Equivalence of elemental carbon by thermal/optical reflectance and transmittance with different temperature protocols, *Environmental Science & Technology*, 38(16), 4414-4422, doi:10.1021/es034936u.
- Chow, J. C., Watson, J. G., Chen, L.-W. A., Chang, M., and Paredes-Miranda, G. (2005), Comparison of the DRI/OGC and Model 2001 thermal/optical carbon analyzers, *Prepared for IMPROVE Steering Committee, Fort Collins, CO, by Desert Research Institute, Reno, NV*, [http://vista.cira.colostate.edu/improve/Publications/GrayLit/013\\_CarbonAnalyzer/IMPROVECarbonAnalyzerAssessment.pdf](http://vista.cira.colostate.edu/improve/Publications/GrayLit/013_CarbonAnalyzer/IMPROVECarbonAnalyzerAssessment.pdf).
- Chow, J. C., Watson, J. G., Chen, L.-W. A., Chang, M. O., Robinson, N. F., Trimble, D., and Kohl, S. (2007), The IMPROVE\_A temperature protocol for thermal/optical carbon analysis: maintaining consistency with a long-term database, *Journal of the Air & Waste Management Association*, 57(9), 1014-1023, <https://doi.org/10.3155/1047-3289.57.9.1014>.
- Chow, J., Watson, J., Chen, L.-W., Rice, J., and Frank, N. (2010), Quantification of PM 2.5 organic carbon sampling artifacts in US networks, *Atmospheric Chemistry and Physics*, 10(12), 5223-5239, doi:<https://doi.org/10.5194/acp-10-5223-2010>.
- Chow, J. C., Wang, X., Sumlin, B. J., Gronstal, S. B., Chen, L.-W. A., Trimble, D. L., Kohl, S. D., Mayorga, S. R., Riggio, G., and Hurbain, P. R. (2015a), Optical calibration and equivalence of a multiwavelength thermal/optical carbon analyzer, *Aerosol and Air Quality Research*, 15(4), 1145-1159, doi:10.4209/aaqr.2015.02.0106.

Chow, J. C., Lowenthal, D. H., Chen, L.-W. A., Wang, X., and Watson, J. G. (2015b), Mass reconstruction methods for PM<sub>2.5</sub>: a review, *Air Quality, Atmosphere & Health*, 8(3), 243-263, doi:10.1007/s11869-015-0338-3.

Chow, J. C., Watson, J. G., Green, M. C., Wang, X., Chen, L.-W. A., Trimble, D. L., Cropper, P. M., Kohl, S. D., and Gronstal, S. B. (2018), Separation of brown carbon from black carbon for IMPROVE and Chemical Speciation Network PM<sub>2.5</sub> samples, *Journal of the Air & Waste Management Association*, 68(5), 494-510, doi:<https://doi.org/10.1080/10962247.2018.1426653>.

Chow, J. C., Chen, L.-W. A., Wang, X., Green, M. C., and Watson, J. G. (2021), Improved estimation of PM<sub>2.5</sub> brown carbon contributions to filter light attenuation, *Particuology*, 56, 1-9, doi:10.1016/j.partic.2021.01.001.

Debell, L. J., Gebhart, K., Hand, J. L., Malm, W. C., Pitchford, M. L., Schichtel, B. S., and White, W. H. (2006), IMPROVE (Interagency Monitoring of Protected Visual Environments): Spatial and seasonal patterns and temporal variability of haze and its constituents in the United States: Report IV, Colorado State University, Fort Collins CO, ISSN 0737-5352-74.

Debus, B., Takahama, S., Weakley, A. T., Seibert, K., and Dillner, A. M. (2019), Long-term strategy for assessing carbonaceous particulate matter concentrations from multiple Fourier transform infrared (FT-IR) instruments: influence of spectral dissimilarities on multivariate calibration performance, *Applied Spectroscopy*, 73(3), 271-283.

Debus, B., Weakley, A. T., Takahama, S., George, K. M., Schichtel, B. A., Copeland, S., Wexler, A. S., and Dillner, A. M. (submitted), Quantification of major particulate matter species from a single filter type using infrared spectroscopy – Application to a large-scale monitoring network, *Atmospheric Measurement Techniques Discussion*.

Dewangan, S., Pervez, S., Chakrabarty, R., Watson, J. G., Chow, J. C., Pervez, Y., Tiwari, S., and Rai, J. (2016), Study of carbonaceous fractions associated with indoor PM<sub>2.5</sub>/PM10 during Asian cultural and ritual burning practices, *Building and Environment*, 106, 229-236, <https://doi.org/10.1016/j.buildenv.2016.06.006>.

Dillner, A. M., Phuah, C. H., and Turner, J. R. (2009), Effects of post-sampling conditions on ambient carbon aerosol filter measurements, *Atmospheric Environment*, 43(37), 5937-5943, <https://doi.org/10.1016/j.atmosenv.2009.08.009>.

Dillner, A. (2015), Change to artifact correction method for OC carbon fractions, *IMPROVE Data Advisory* (da0032), [http://vista.cira.colostate.edu/improve/Data/QA\\_QC/Advisory/da0032/da0032\\_OC\\_artifact.pdf](http://vista.cira.colostate.edu/improve/Data/QA_QC/Advisory/da0032/da0032_OC_artifact.pdf).

Dillner, A. M., and Takahama, S. (2015a), Predicting ambient aerosol thermal-optical reflectance (TOR) measurements from infrared spectra: organic carbon, *Atmos. Meas. Tech.*, 8(3), 1097-1109, doi:10.5194/amt-8-1097-2015.

Dillner, A. M., and Takahama, S. (2015b), Predicting ambient aerosol thermal-optical reflectance measurements from infrared spectra: elemental carbon, *Atmos. Meas. Tech.*, 8(10), 4013-4023, doi:10.5194/amt-8-4013-2015.

EPA, U. S. (1999a), U.S. Environmental Protection Agency, Regional Haze Rule regulations, *Final Rule*, 40 CFR 51(Federal Register, 64), 35714-35774, <https://www.govinfo.gov/content/pkg/FR-1999-07-01/pdf/99-13941.pdf>.

EPA, U. S. (1999b), U.S. Environmental Protection Agency, Visibility Monitoring Guidance, *EPA-454/R-99-003*.

EPA, U. S. (2004), U.S. Environmental Protection Agency, PM2.5 Speciation Network Newsletter, 1(1), <https://www3.epa.gov/ttnamti1/files/ambient/pm25/spec/spnews1.pdf>.

EPA, U. S. (2009), U.S. Environmental Protection Agency, PM2.5 Speciation Network Newsletter, 1(6), <https://www3.epa.gov/ttnamti1/files/ambient/pm25/spec/spnews6.pdf>.

EPA, U. S. (2018), U.S. Environmental Protection Agency, Technical guidance on tracking visibility progress for the second implementation period of the Regional Haze program, *EPA-454/R-18-010*.

Gorham, K. A., Raffuse, S. M., Hyslop, N. P., and White, W. H. (2021), Comparison of recent speciated PM<sub>2.5</sub> data from collocated CSN and IMPROVE measurements, *Atmospheric Environment*, 244, 117977, <https://doi.org/10.1016/j.atmosenv.2020.117977>.

Hand, J. L., Copeland, S., Day, D., Dillner, A., Indresand, H., Malm, W., McDade, C., Moore, C., Pitchford, M., and Schichtel, B. (2011), IMPROVE (Interagency Monitoring of Protected Visual Environments): Spatial and seasonal patterns and temporal variability of haze and its constituents in the United States, Report V, Colorado State University, Fort Collins, CO.

Hand, J. L., Schichtel, B. A., Pitchford, M., Malm, W. C., and Frank, N. H. (2012), Seasonal composition of remote and urban fine particulate matter in the United States, *Journal of Geophysical Research: Atmospheres*, 117(D5), D05209, doi:10.1029/2011jd017122.

Hand, J. L., Prenni, A. J., Schichtel, B. A., Malm, W. C., and Chow, J. C. (2019), Trends in remote PM<sub>2.5</sub> residual mass across the United States: Implications for aerosol mass reconstruction in the IMPROVE network, *Atmospheric Environment*, 203, 141-152, doi:[10.1016/j.atmosenv.2019.01.049](https://doi.org/10.1016/j.atmosenv.2019.01.049).

Joseph, D., Metsa, J., Malm, W. C., and Pitchford, M. (1987), Plans for IMPROVE: A federal program to monitor visibility in class I areas, in *Visibility Protection: Research and Policy Aspects*, Bhardwaja, P. S. (ed), APC, Pittsburgh, PA.

June, N. A., Wang, X., Chen, L. W. A., Chow, J. C., Watson, J. G., Wang, X., Henderson, B. H., Zheng, Y., and Mao, J. (2020), Spatial and temporal variability of brown carbon in the United States: Implications for direct radiative effects, *Geophysical Research Letters*, 47(23), e2020GL090332, doi:10.1029/2020GL090332.

Kim, E., and Hopke, P. K. (2004), Comparison between conditional probability function and nonparametric regression for fine particle source directions, *Atmospheric Environment*, 38(28), 4667-4673, <https://doi.org/10.1016/j.atmosenv.2004.05.035>.

Kim, E., Hopke, P. K., Larson, T. V., Maykut, N. N., and Lewtas, J. (2004), Factor analysis of Seattle fine particles, *Aerosol Science and Technology*, 38(7), 724-738, <https://doi.org/10.1080/02786820490490119>.

Li, S., Zhu, M., Yang, W., Tang, M., Huang, X., Yu, Y., Fang, H., Yu, X., Yu, Q., and Fu, X. (2018), Filter-based measurement of light absorption by brown carbon in PM<sub>2.5</sub> in a megacity in South China, *Science of The Total Environment*, 633, 1360-1369, doi:10.1016/j.scitotenv.2018.03.235.

Malm, W. C., Sisler, J. F., Huffman, D., Eldred, R. A., and Cahill, T. A. (1994), Spatial and seasonal trends in particle concentration and optical extinction in the United States, *Journal of Geophysical Research: Atmospheres*, 99(D1), 1347-1370, <https://doi.org/10.1029/93JD02916>.

Malm, W., Sisler, J. F., Pitchford, M., Scruggs, M., Ames, R. B., Copeland, S., Gebhart, K., and Day, D. (2000), IMPROVE (Interagency Monitoring of Protected Visual Environments): Spatial and seasonal patterns and temporal variability of haze and its constituents in the United States: Report III, Colorado State University, Fort Collins, CO, ISSN 0737-5352-47.

Malm, W. C., Schichtel, B. A., and Pitchford, M. L. (2011), Uncertainties in PM<sub>2.5</sub> gravimetric and speciation measurements and what we can learn from them, *Journal of the Air & Waste Management Association*, 61(11), 1131-1149, doi:10.1080/10473289.2011.603998.

Molenar, J. V., Dietrich, D. L., and Tree, R. M. (1989), Application of a long-range transmissometer to measure the ambient atmospheric extinction coefficient in remote pristine environments, in *Visibility and Fine Particles*, Mathai, C. V. (ed), 374-383, A&WMA, Pittsburgh, PA.

Molenar, J., and Malm, W. (1992), Ambient optical monitoring techniques, in *Proceedings of Conference on Visibility and Fine Particles*, Vienna.

Petzold, A., Ogren, J. A., Fiebig, M., Laj, P., Li, S. M., Baltensperger, U., Holzer-Popp, T., Kinne, S., Pappalardo, G., Sugimoto, N., Wehrli, C., Wiedensohler, A., and Zhang, X. Y. (2013), Recommendations for reporting "black carbon" measurements, *Atmos. Chem. Phys.*, 13(16), 8365-8379, doi:10.5194/acp-13-8365-2013.

Pitchford, M., Malm, W. C., Schichtel, B. A., Kumar, N., Lowenthal, D., and Hand, J. L. (2007), Revised algorithm for estimating light extinction from IMPROVE particle speciation data, *Journal of the Air & Waste Management Association*, 57(11), 1326-1336, doi:10.3155/1047-3289.57.11.1326.

Reggente, M., Dillner, A. M., and Takahama, S. (2016), Predicting ambient aerosol thermal-optical reflectance (TOR) measurements from infrared spectra: Extending the predictions to different years and different sites, *Atmos. Meas. Tech.*, 9(2), 441-454, doi:10.5194/amt-9-441-2016.

Schichtel, B. A. (2019), Updated data for carbon, *IMPROVE Data Advisory* (da0040), [http://vista.cira.colostate.edu/improve/Data/QA\\_QC/Advisory/da0040/da0040\\_TOR\\_integration.pdf](http://vista.cira.colostate.edu/improve/Data/QA_QC/Advisory/da0040/da0040_TOR_integration.pdf).

Schichtel, B. A., Malm, W. C., Beaver, M., Copeland, S., Hand, J. L., Prenni, A. J., Rice, J., and Vimont, J. (2021), The Future of Carbonaceous Aerosol Measurement in the IMPROVE Monitoring Program, [http://vista.cira.colostate.edu/improve/wp-content/uploads/2021/10/041\\_CarbonReport\\_Final.pdf](http://vista.cira.colostate.edu/improve/wp-content/uploads/2021/10/041_CarbonReport_Final.pdf).

Shen, Z., Lei, Y., Zhang, L., Zhang, Q., Zeng, Y., Tao, J., Zhu, C., Cao, J., Xu, H., and Liu, S. (2017), Methanol extracted brown carbon in PM<sub>2.5</sub> over Xi'an, China: Seasonal variation of optical properties and sources identification, *Aerosol Science and Engineering*, 1(2), 57-65, doi:10.1007/s41810-017-0007-z.

Shibata, K., Enya, K., Ishikawa, N., and Sakamoto, K. (2019), EC/OC and PAHs emissions from a modern diesel engine with DPF regeneration fueled by 10% RME biodiesel, *Aerosol and Air Quality Research*, 19(8), 1765-1774, doi:10.4209/aaqr.2018.12.0476.

Solomon, P. A., Crumpler, D., Flanagan, J. B., Jayanty, R. K. M., Rickman, E. E., and McDade, C. E. (2014), U.S. national PM2.5 chemical speciation monitoring networks—CSN and IMPROVE: Description of networks, *Journal of the Air & Waste Management Association*, 64(12), 1410-1438, doi:10.1080/10962247.2014.956904.

Takahama, S., Dillner, A. M., Weakley, A. T., Reggente, M., Bürki, C., Lbadaoui-Darvas, M., Debus, B., Kuzmiakova, A., and Wexler, A. S. (2019), Atmospheric particulate matter characterization by Fourier transform infrared spectroscopy: a review of statistical calibration strategies for carbonaceous aerosol quantification in US measurement networks, *Atmospheric Measurement Techniques*, 12(1), 525-567, <https://doi.org/10.5194/amt-12-525-2019>.

Trzepla, K. (2018), Calibration bias in reported vanadium concentrations, *IMPROVE Data Advisory* (da0038),  
[http://vista.cira.colostate.edu/improve/Data/QA\\_QC/Advisory/da0038/da0038\\_V\\_advisory.pdf](http://vista.cira.colostate.edu/improve/Data/QA_QC/Advisory/da0038/da0038_V_advisory.pdf).

Trzepla, K. (2019), Change in the analytical protocol for XRF analysis, *IMPROVE Data Advisory* (da0043),  
[http://vista.cira.colostate.edu/improve/Data/QA\\_QC/Advisory/da0043/da0043\\_XRFprotocolChange2019.pdf](http://vista.cira.colostate.edu/improve/Data/QA_QC/Advisory/da0043/da0043_XRFprotocolChange2019.pdf).

Trzepla, K., and Giacomo, J. (2019), Changes/upgrades in HIPS system resulting in calibration changes, *IMPROVE Data Advisory* (da0041),  
[http://vista.cira.colostate.edu/improve/Data/QA\\_QC/Advisory/da0041/da0041\\_HIPSmodifications.pdf](http://vista.cira.colostate.edu/improve/Data/QA_QC/Advisory/da0041/da0041_HIPSmodifications.pdf).

Turpin, B. J., Saxena, P., and Andrews, E. (2000), Measuring and simulating particulate organics in the atmosphere: problems and prospects, *Atmospheric Environment*, 34(18), 2983-3013, [https://doi.org/10.1016/S1352-2310\(99\)00501-4](https://doi.org/10.1016/S1352-2310(99)00501-4).

Wagner, J. G., Kamal, A. S., Morishita, M., Dvonch, J. T., Harkema, J. R., and Rohr, A. C. (2014), PM2.5-induced cardiovascular dysregulation in rats is associated with elemental carbon and temperature-resolved carbon subfractions, *Particle and Fibre Toxicology*, 11(1), 25, doi:10.1186/1743-8977-11-25.

Wallis, C. (2019a), Method change for calibrating flow rate transfer standards, *IMPROVE Data Advisory* (da0042),  
[http://vista.cira.colostate.edu/improve/Data/QA\\_QC/Advisory/da0042/da0042\\_FlowrateTransferStandardCalibrationProtocol.pdf](http://vista.cira.colostate.edu/improve/Data/QA_QC/Advisory/da0042/da0042_FlowrateTransferStandardCalibrationProtocol.pdf).

Wallis, C. (2019b), Universal calibration constants for flow rate calculation, *IMPROVE Data Advisory* (da0044),  
[http://vista.cira.colostate.edu/improve/Data/QA\\_QC/Advisory/da0044/da0044\\_UniversalFlowRateCalibrationConstants.pdf](http://vista.cira.colostate.edu/improve/Data/QA_QC/Advisory/da0044/da0044_UniversalFlowRateCalibrationConstants.pdf).

Watson, J., Lioy, P., and Mueller, P. (2001), The measurement process: Precision, accuracy, and validity, *Air sampling instruments for evaluation of atmospheric contaminants*, 8.

Watson, J. G., Chow, J. C., Chen, L.-W. A., and Frank, N. H. (2009), Methods to assess carbonaceous aerosol sampling artifacts for IMPROVE and other long-term networks, *Journal of the Air & Waste Management Association*, 59(8), 898-911, <https://doi.org/10.3155/1047-3289.59.8.898>.

White, W. H. (2007), Shift in EC/OC split with 1 January 2005 TOR hardware upgrade, *IMPROVE Data Advisory* (da0016),  
[http://vista.cira.colostate.edu/improve/Data/QA\\_QC/Advisory/da0016/da0016\\_TOR2005.pdf](http://vista.cira.colostate.edu/improve/Data/QA_QC/Advisory/da0016/da0016_TOR2005.pdf).

White, W. H. (2009), Under-correction of chloride concentrations for filter blank levels, *IMPROVE Data Advisory* (da0024),  
[http://vista.cira.colostate.edu/improve/Data/QA\\_QC/Advisory/da0024/da0024\\_HDA\\_Chloride.pdf](http://vista.cira.colostate.edu/improve/Data/QA_QC/Advisory/da0024/da0024_HDA_Chloride.pdf).

White, W. H. (2015a), Changed reporting of light absorption, *IMPROVE Data Advisory* (da0033),  
[http://vista.cira.colostate.edu/improve/Data/QA\\_QC/Advisory/da0033/da0033\\_Fabs.pdf](http://vista.cira.colostate.edu/improve/Data/QA_QC/Advisory/da0033/da0033_Fabs.pdf).

White, W. H. (2015b), Bias between masked and unmasked light absorption measurements, *IMPROVE Data Advisory* (da0034),  
[http://vista.cira.colostate.edu/improve/Data/QA\\_QC/Advisory/da0034/da0034\\_update-mask-Fabs.pdf](http://vista.cira.colostate.edu/improve/Data/QA_QC/Advisory/da0034/da0034_update-mask-Fabs.pdf).

White, W. H. (2016), Increased variation of humidity in the weighing laboratory, *IMPROVE Data Advisory* (da0035),  
[http://vista.cira.colostate.edu/improve/Data/QA\\_QC/Advisory/da0035/da0035\\_IncreasedRH.pdf](http://vista.cira.colostate.edu/improve/Data/QA_QC/Advisory/da0035/da0035_IncreasedRH.pdf).

White, W. H., Trzepla, K., Hyslop, N. P., and Schichtel, B. A. (2016), A critical review of filter transmittance measurements for aerosol light absorption, and de novo calibration for a decade of monitoring on PTFE membranes, *Aerosol Science and Technology*, 50(9), 984-1002,  
<http://dx.doi.org/10.1080/02786826.2016.1211615>.

White, W. H. (2017a), Negative chloride concentrations at salt-poor sites, *IMPROVE Data Advisory* (da0036),  
[http://vista.cira.colostate.edu/improve/Data/QA\\_QC/Advisory/da0036/da0036\\_chloride\\_loss.pdf](http://vista.cira.colostate.edu/improve/Data/QA_QC/Advisory/da0036/da0036_chloride_loss.pdf)

White, W. H. (2017b), Over-reporting of sodium in salt-rich samples, *IMPROVE Data Advisory* (da0037),  
[http://vista.cira.colostate.edu/improve/Data/QA\\_QC/Advisory/da0037/da0037\\_Na\\_matrix.pdf](http://vista.cira.colostate.edu/improve/Data/QA_QC/Advisory/da0037/da0037_Na_matrix.pdf).

Yu, X.-Y., Lee, T., Ayres, B., Kreidenweis, S. M., Collett Jr, J. L., and Malm, W. (2005), Particulate nitrate measurement using nylon filters, *Journal of the Air & Waste Management Association*, 55(8), 1100-1110, <https://doi.org/10.1080/10473289.2005.10464721>.

Zhang, X. (2019), Correction of chloride concentrations for filter blank levels, *IMPROVE Data Advisory* (da0039),  
[http://vista.cira.colostate.edu/improve/Data/QA\\_QC/Advisory/da0039/da0039\\_ChlorideOverCorrection.pdf](http://vista.cira.colostate.edu/improve/Data/QA_QC/Advisory/da0039/da0039_ChlorideOverCorrection.pdf).

## Chapter 2. Spatial Patterns of Speciated PM<sub>2.5</sub> Aerosol Mass Concentrations

Characterizing the contributions of major aerosol species to PM<sub>2.5</sub> gravimetric mass (mass of particles with aerodynamic diameters less than 2.5  $\mu\text{m}$ ) is essential for estimating visibility degradation, and analyzing the spatial variability of these species is critical for understanding their sources and local and regional impacts. Data from the IMPROVE network are particularly useful for these types of analyses, given the spatial distribution of sites and the long temporal record of the network. In addition to the mostly remote/rural sites operated by IMPROVE, the Environmental Protection Agency's (EPA) Chemical Speciation Network (CSN) collects PM<sub>2.5</sub> speciated aerosol data at approximately 150 urban/suburban monitoring sites. Data from the IMPROVE and CSN networks are useful independently, but by combining data from the two networks, a more complete spatial analysis of key aerosol species can be explored as a function of geographical region by specifically exploring the differences in urban and rural aerosol signatures. The 2016–2019 annual mean mass concentrations of ammonium sulfate (AS), ammonium nitrate (AN), particulate organic matter (POM), elemental carbon (EC), fine dust (FD), sea salt (SS), and PM<sub>2.5</sub> gravimetric fine mass (FM; PM<sub>2.5</sub> gravimetric mass and fine mass are used interchangeably in this report), reconstructed fine mass (RCFM, the sum of the above-listed major PM<sub>2.5</sub> aerosol species), and the fine mass residual (FM - RCFM) are examined. POM is calculated using organic carbon (OC) and an assumed organic carbon to organic mass ratio (OM/OC; POM = (OM/OC)  $\times$  OC). Annual mean PM<sub>10</sub> gravimetric mass (mass of particles with aerodynamic diameters less than 10  $\mu\text{m}$ ), and coarse mass (CM; the difference between PM<sub>10</sub> and PM<sub>2.5</sub>) are also presented in this chapter. PM<sub>10</sub> measurements are not available at CSN sites, therefore data from the EPA PM<sub>10</sub> FRM (Federal Reference Method) network were used (Hand et al., 2019a). Finally, the fractional contributions of major aerosol species to RCFM are presented.

Data aggregated over a 4-year period (2016–2019) are presented. To ensure that the data are representative of the entire period, completeness criteria were applied. Fifty percent completeness of the data (two years of valid monthly mean data) for a given site was required to be included in the analysis. Half of the total observations in a given month had to be valid for a monthly mean. In addition, 66% of each 3-month season was required for an annual mean (Debell et al., 2006; Hand et al., 2011). Seasons correspond to winter (December, January, February), spring (March, April, May), summer (June, July, August), and fall (September, October, November). These criteria were applied for each species separately. Data from the CSN were handled similarly. Values below the minimum detection limit (MDL) were handled according to how they were reported by each network, i.e., no additional substitutions were made for values below MDLs. Average reconstructed mass calculations were performed by summing the averages of individual species; for example, average concentrations of each species were computed and summed to obtain an average RCFM (Debell et al., 2006; Hand et al., 2011). Valid data for all of the species were required to compute monthly mean RCFM. This approach was used to avoid small sample sizes and provide a more accurate representation of average conditions. Applying the completeness criteria resulted in 153 IMPROVE sites and 136 CSN sites used in the analyses.

Annual mean concentration maps were created for each species from sites that met the completeness criteria. A Kriging algorithm was used to interpolate concentrations between site locations in order to create concentration isopleths (Isaaks and Mohan Srivastava, 1989). Maps

based on interpolation schemes should be viewed and interpreted with caution. The maps only are intended to help visualize the data and identify large spatial patterns. The density of site locations affects the interpolated fields, and neither the IMPROVE nor CSN networks have uniformly distributed site locations. Given these caveats, there is still interesting and useful information that can be gained from these maps, especially by examining the differences that occur when maps based only on the rural/remote IMPROVE sites are compared to those created when integrating the urban/suburban CSN and IMPROVE data. The following sections include discussions of spatial patterns for annual mean concentrations of AS, AN, POM, EC, FD, SS, FM, RCFM, the FM residual, PM<sub>10</sub> mass, and CM. The top number in the scale shown on each contour map corresponds to the maximum concentrations for all sites; the contour levels themselves were created with the highest level corresponding to the 95<sup>th</sup> percentile in mass concentration and 5<sup>th</sup> and 95<sup>th</sup> percentile for the residual. Maps of species mass fractions are also included.

## 2.1 AEROSOL SPECIES COMPOSITION

Reconstructing PM<sub>2.5</sub> mass concentrations requires assumptions about the molecular form of assumed species. Table 2.1 presents the assumptions used in this report. More detail regarding each species will be presented in the following sections. Similar assumptions were made for IMPROVE and CSN unless otherwise noted in Table 2.1.

**Table 2.1. Form of molecular species assumed in this report. Units in  $\mu\text{g m}^{-3}$  unless otherwise noted.**

PM <sub>2.5</sub> Aerosol Species	This Report	Assumptions
Ammonium Sulfate (AS = (NH <sub>4</sub> ) <sub>2</sub> SO <sub>4</sub> )	$1.375 \times [\text{SO}_4^{2-}]$	Sulfate [SO <sub>4</sub> <sup>2-</sup> ] is assumed to be fully neutralized.
Ammonium Nitrate (AN = NH <sub>4</sub> NO <sub>3</sub> )	$1.29 \times [\text{NO}_3^-]$	Nitrate [NO <sub>3</sub> <sup>-</sup> ] is assumed to be ammonium nitrate.
Particulate Organic Matter (POM)	(OM/OC) × [OC]	OM/OC ratios account for additional species included in organic mass. A monthly-varying value was used for IMPROVE; seasonal-varying values were used for CSN (see below). OC is the sum of the subfractions from TOR analysis: OC = OC1 + OC2 + OC3 + OC4 + OP (see Section 1.2.2)
Elemental Carbon (EC)	EC	Also referred to as light absorbing carbon (LAC). EC is sum of subfractions from the TOR analysis: EC = EC1 + EC2 + EC3 – OP (see Section 1.2.2)
Filter light absorption ( $f_{\text{abs}}$ )	$f_{\text{abs}}$	Hybrid integrating plate and sphere (HIPS) filter light absorption ( $\text{Mm}^{-1}$ )
IMPROVE Fine Dust (FD)	$1.15 \times$ $(2.2 \times [\text{Al}] +$ $2.49 \times [\text{Si}] +$ $1.63 \times [\text{Ca}] +$ $2.42 \times [\text{Fe}] +$ $1.94 \times [\text{Ti}]$ )	Soil potassium = $0.6 \times [\text{Fe}]$ . Fe and Fe <sub>2</sub> O <sub>3</sub> are equally abundant. A factor of 1.16 is used to account for other compounds such as MgO, Na <sub>2</sub> O, H <sub>2</sub> O and CO <sub>3</sub> (Malm et al., 1994). FD concentrations are multiplied by 1.15 based on multiple linear regression analyses (Hand et al., 2019b; see below).

PM <sub>2.5</sub> Aerosol Species	This Report	Assumptions
CSN Fine Dust (FD)	$2.2 \times [\text{Al}] + 2.49 \times [\text{Si}] + 1.63 \times [\text{Ca}] + 2.42 \times [\text{Fe}] + 1.94 \times [\text{Ti}]$	Soil potassium = $0.6 \times [\text{Fe}]$ . Fe and Fe <sub>2</sub> O <sub>3</sub> are equally abundant. A factor of 1.16 is used to account for other compounds such as MgO, Na <sub>2</sub> O, H <sub>2</sub> O and CO <sub>3</sub> .
Sea Salt (SS)	$1.8 \times [\text{Cl}^-]$	Sea salt is 55% chloride ion by weight.
CSN Sea Salt (SS)	$1.8 \times [\text{Cl}]$	Sea salt is derived using chlorine concentrations from XRF.
IMPROVE Gravimetric PM <sub>2.5</sub> Mass (FM)	PM <sub>2.5</sub>	Mass of particles with aerodynamic diameters less than 2.5 μm.
CSN Gravimetric PM <sub>2.5</sub> Mass (FM)	PM <sub>2.5</sub>	Mass of particles with aerodynamic diameters less than 2.5 μm using data from collocated EPA Federal Reference Method (FRM) network.
IMPROVE Gravimetric PM <sub>10</sub> Mass	PM <sub>10</sub>	Mass of particles with aerodynamic diameters less than 10 μm.
EPA PM <sub>10</sub>	PM <sub>10</sub>	Mass of particles with aerodynamic diameters less than 10 μm. Data from EPA's Federal Reference Method (FRM) network.
IMPROVE Coarse Mass (CM)	PM <sub>10</sub> - PM <sub>2.5</sub>	Difference in PM <sub>10</sub> and PM <sub>2.5</sub> .
EPA Coarse Mass (CM)	PM <sub>10</sub> - PM <sub>2.5</sub>	Difference in PM <sub>10</sub> and PM <sub>2.5</sub> using collocated data from EPA's Federal Reference Method (FRM) network.
Reconstructed Fine Mass (RCFM)	AS + AN + POM + EC + FD + SS	Reconstructed fine mass algorithm represents PM <sub>2.5</sub> aerosol mass.
Fine Mass Residual	FM - RCFM	Difference in PM <sub>2.5</sub> gravimetric mass (FM) and reconstructed fine mass (RCFM).

Two changes from previous reports for estimating species mass include the calculation of POM and FD. Previous analyses of the fine mass residual identified increased biases over time that affected the agreement between gravimetric PM<sub>2.5</sub> mass and RCFM (Hand et al., 2019b). Results from a multilinear regression (MLR) analysis suggested that the constant OM/OC ratio of 1.8 that was previously applied in the RCFM algorithm was contributing to the bias. Applying a monthly varying value resulted in lower residuals and better agreement, especially in summer. The values applied are shown in Table 2.2. Seasonal values were assumed for the CSN based on Philip et al. (2014). IMPROVE FD concentrations were also determined to be low based on the MLR analysis and therefore were increased across the network and year by increasing the concentrations by 15%. A full discussion of these changes can be found in Appendix 2.1.

**Table 2.2. OM/OC ratios used to calculate POM and applied in the reconstructed mass algorithm for the CSN and IMPROVE networks.**

Month	IMPROVE	CSN
Jan	1.5	1.6
Feb	1.5	1.6
Mar	1.5	1.6
Apr	1.6	1.6
May	1.7	1.6
Jun	1.9	1.8

Month	IMPROVE	CSN
Jul	2.0	1.8
Aug	2.1	1.8
Sept	2.0	1.8
Oct	1.7	1.8
Nov	1.7	1.8
Dec	1.7	1.8

## 2.2 SPATIAL PATTERNS IN ANNUAL MEAN MASS CONCENTRATIONS

### 2.2.1 PM<sub>2.5</sub> Ammonium Sulfate Mass

The majority of sulfate in the atmosphere is produced through chemical reactions of sulfur dioxide (SO<sub>2</sub>). Anthropogenic SO<sub>2</sub> is emitted through industrial activities such as coal and diesel fuel combustion. Regions that host electric utilities and industrial boilers (such as the eastern United States) are sources of SO<sub>2</sub> emissions that, combined with the elevated relative humidity or other aqueous pathways, create the most efficient conditions for sulfate production. The degree of acidity of sulfate (from acidic sulfuric acid to fully neutralized AS) depends on the availability of ammonia to neutralize the sulfuric acid formed from SO<sub>2</sub>. Sulfate acidity can vary spatially and temporally (e.g., Lawal et al., 2018). In fact, recent studies have suggested that especially in the East, sulfate is in a more acidic form (Hidy et al., 2014; Kim et al., 2015; Lowenthal et al., 2015; Weber et al., 2016; Silvern et al., 2017; Lawal et al., 2018; Chen et al., 2019). However, without additional measurements of ammonium ion concentrations at IMPROVE sites, the degree of neutralization is unknown. A recent study suggests that potential biases associated with the assumed form of sulfate are relatively low (Hand et al., 2019b). These results are described in more detail in Appendix 2.1. For this report, sulfate is assumed to be in the form of fully neutralized AS (see Table 2.1), an upper bound of mass associated with dry sulfate.

The rural 2016–2019 IMPROVE annual mean AS concentrations ranged from 0.27 µg m<sup>-3</sup> in White Pass, Washington (WHPA1), to 2.03 µg m<sup>-3</sup> in Hawaii Volcanoes National Park (NP), Hawaii (HAVO1). The highest concentrations in the continental United States centered around the Ohio River valley and the Midsouth (1.5–2 µg m<sup>-3</sup>) (see Figure 2.2.1a). The concentrations of AS decreased sharply toward the western United States, where concentrations were less than 1.0 µg m<sup>-3</sup>, with the lowest concentrations at sites in the Northwest, Montana, and Idaho. Lower concentrations in the West reflected lower SO<sub>2</sub> emissions that lead to secondary particulate AS (Hand et al., 2020).

The regional nature of AS concentrations were evidenced by the similar concentrations of annual mean AS at the urban CSN sites (Figure 2.2.1b) and similar spatial variability in the two networks. A maximum annual mean CSN concentration of 3.23 µg m<sup>-3</sup> occurred in southwestern Pennsylvania (Liberty, 420030064), somewhat higher than the maximum concentration observed in the IMPROVE network. The lowest concentration (0.37 µg m<sup>-3</sup>) occurred at Butte, Montana (300930005). The addition of urban sites in the Ohio River valley, eastern Texas, and the Central Valley of California provided some additional structure in the isopleths in Figure 2.2.1b but did not alter the overall spatial pattern presented in Figure 2.2.1a.

AS contributed roughly a third of RCFM at rural sites in the eastern United States on an annual mean basis (see Figure 2.2.1c). Higher AS mass fractions (~0.30) stretched from sites in the Northeast, south toward western Texas. A transition to lower mass fractions occurred in the Intermountain West, with the lowest mass fractions occurring in the Northwest (<0.10). The highest IMPROVE AS mass fraction occurred in Hawaii Volcanoes NP (HAVO1, 0.70) where the highest AS annual mean concentrations occurred, most likely due to the high levels of volcanic emissions of SO<sub>2</sub>. The lowest annual mean fraction occurred in Monture, Montana (MONT1, 0.06).

The spatial pattern of AS mass fraction for the combined rural and urban sites was similar to the rural-only distribution (Figure 2.2.1d), especially with respect to the large-scale spatial gradients. The highest urban fraction (0.37) also occurred in Hawaii (Kapolei, 150030010), although a much lower contribution than at the IMPROVE HAVO1 site. The lowest mass fraction (0.05) also occurred in Montana (Butte, 300930005). The combined urban and rural data demonstrated areas of relatively lower mass fractions in parts of the eastern United States, especially in the Southeast and Northeast, with fractions near 0.20. Other urban sites also had lower mass fractions, such as sites in the Front Range of Colorado; Salt Lake City, Utah; and Central Valley of California. Overall, the similarity in the urban and rural AS concentrations and fractions demonstrated the regional impact of the sources and atmospheric processes that lead to AS in the atmosphere.

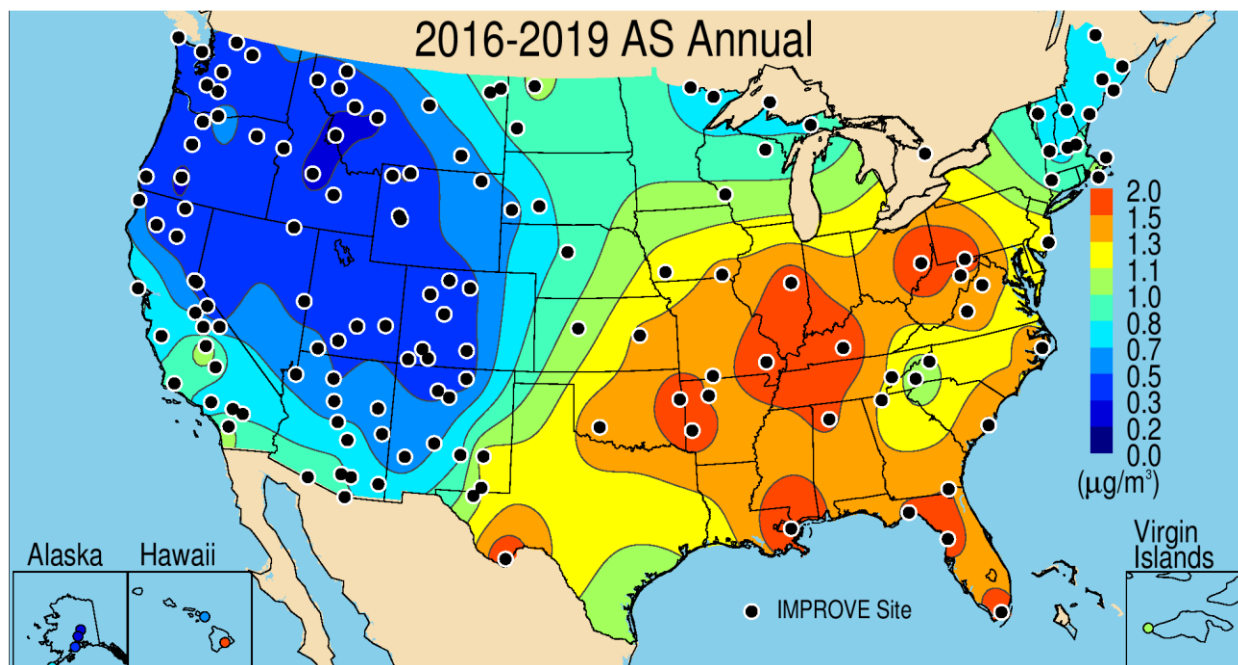


**Figure 2.2.1a. IMPROVE 2016–2019 PM<sub>2.5</sub> ammonium sulfate (AS) annual mean mass concentrations ( $\mu\text{g m}^{-3}$ ).**

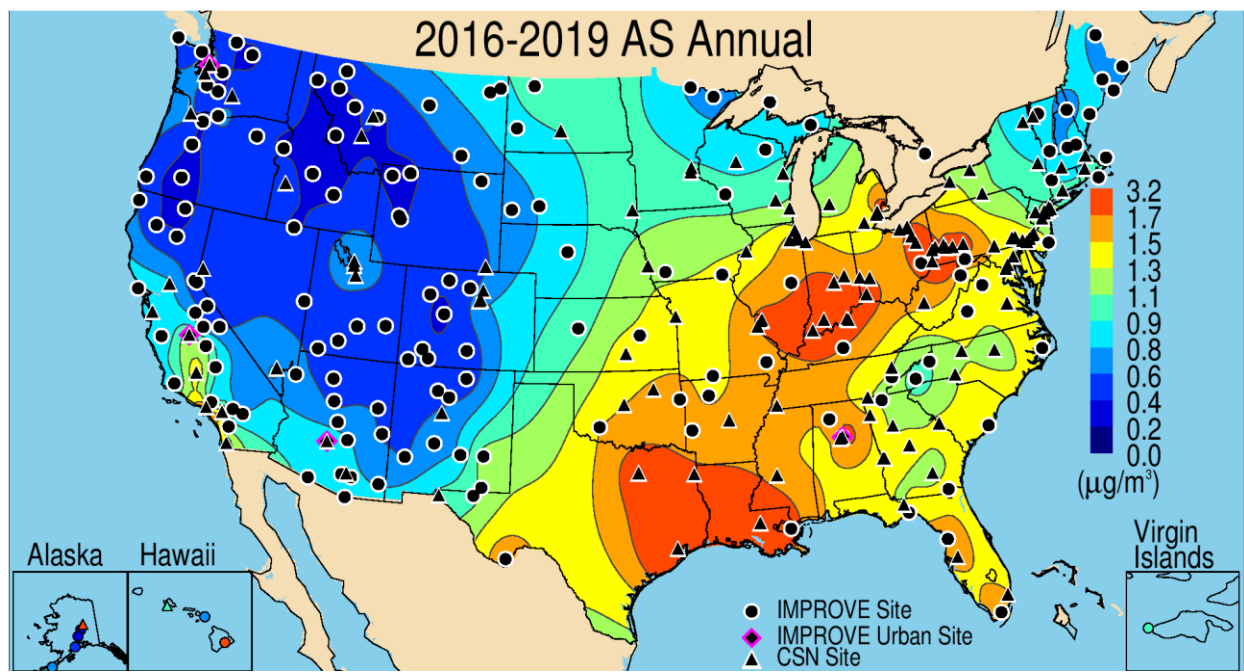


**Figure 2.2.1b.** IMPROVE and CSN 2016–2019 PM<sub>2.5</sub> ammonium sulfate (AS) annual mean mass concentrations ( $\mu\text{g m}^{-3}$ ).

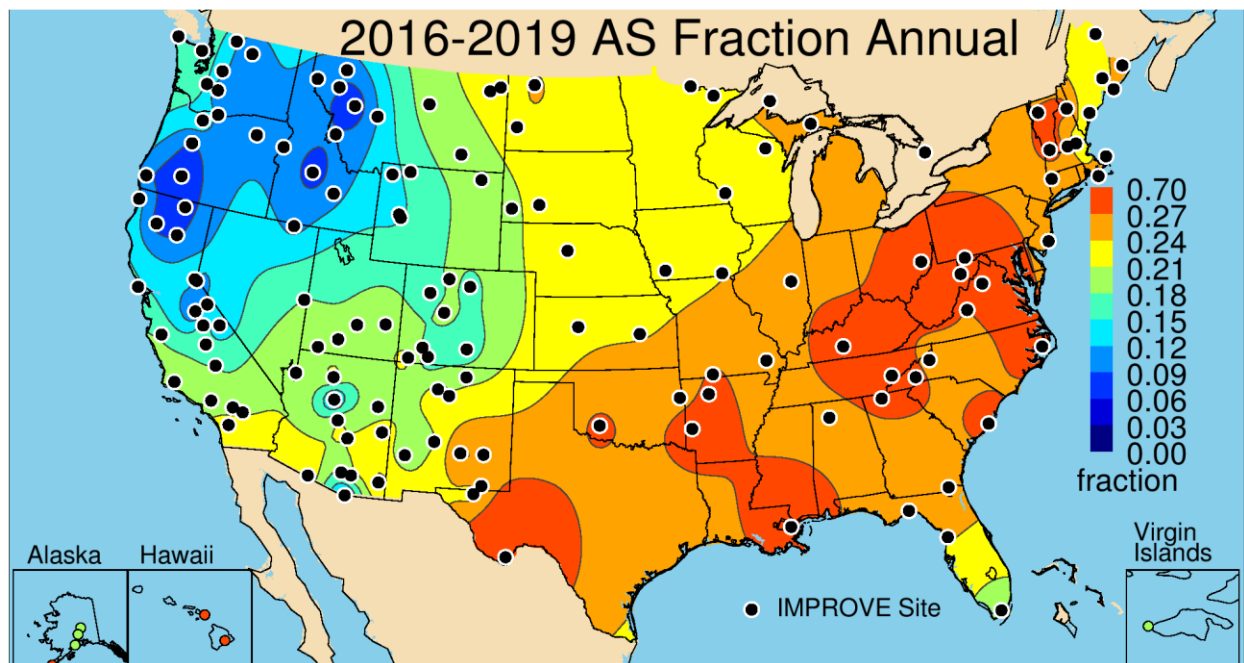


**Figure 2.2.1c.** IMPROVE 2016–2019 annual mean fraction contributions of ammonium sulfate (AS) to PM<sub>2.5</sub> reconstructed fine mass (RCFM).

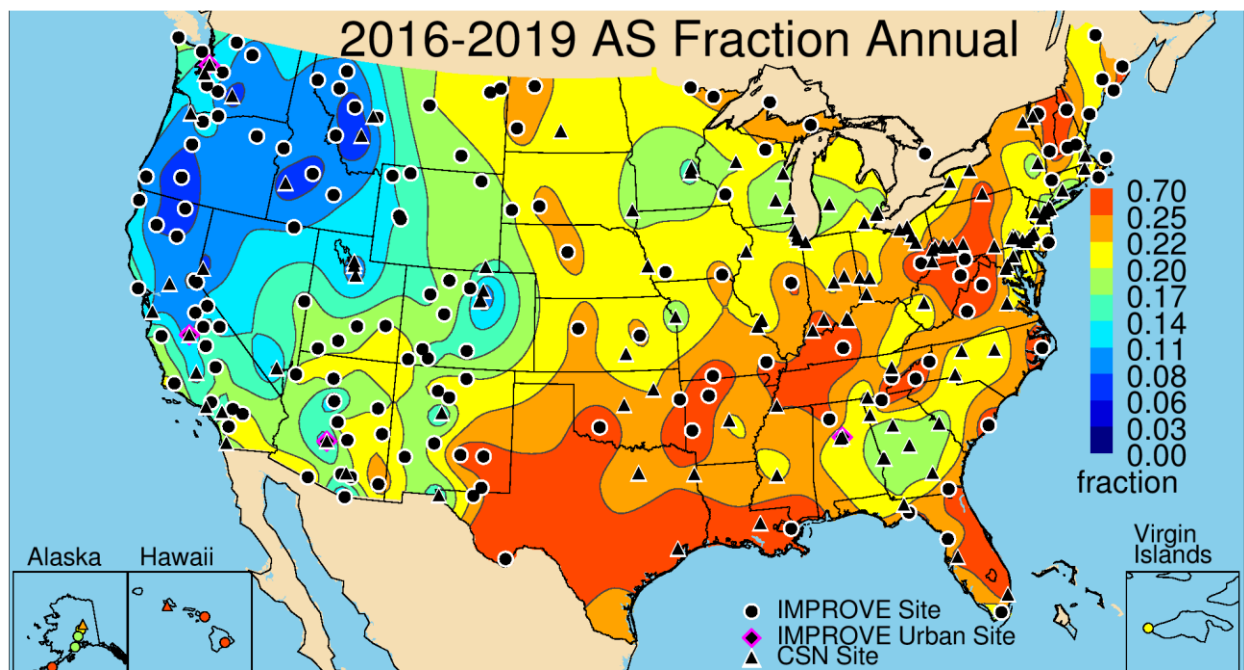


**Figure 2.2.1d. IMPROVE and CSN 2016–2019 annual mean fraction contributions of ammonium sulfate (AS) to PM<sub>2.5</sub> reconstructed fine mass (RCFM).**

## 2.2.2 PM<sub>2.5</sub> Ammonium Nitrate Mass

AN forms from the reversible reaction of gas-phase ammonia and nitric acid. Sources of oxidized nitrogen include combustion of fossil fuels from point sources such as coal-fired powered plants, on-road mobile sources, and non-road mobile sources. Other high-temperature processes such as biomass burning also contribute oxidized nitrogen, as do biogenic sources such as soil emissions (Vitousek et al., 1997). Sources of ammonia include agricultural activities, including animal husbandry, as well as mobile sources and natural emissions. The equilibrium reactions producing particle-phase AN are sensitive to small changes in temperature and relative humidity that can shift the equilibrium between the particle and gas phase. Lower temperatures and higher relative humidity favor particulate AN, while higher temperatures and lower relative humidity favor the gas phase. Nitrate (as AN) is often assumed to be in the fine mode, and this is probably a reasonable assumption in regions with high ammonia and nitric acid concentrations and low sulfate concentrations (Lee et al., 2008). The central United States is an area of high agricultural activity and is associated with high nitrate and ammonium concentrations that can lead to elevated fine-mode AN concentrations (Pitchford et al., 2009; Heald et al., 2012; Warner et al., 2017; Hu et al., 2020). Using data reported by Lee et al. (2008), Hand and Malm (2006) found that when fine-mode nitrate concentrations were greater than 0.5  $\mu\text{g m}^{-3}$ , AN contributed over 70% of the observed total nitrate in the fine mode at certain locations. However, Lee et al. (2008) showed that in many locations nitrate is associated with the coarse mode from reactions of gas-phase nitric acid with sea salt or calcium carbonate. Allen et al. (2015) reported similar results during the 2013 Southern Oxidant and Aerosol Study in the Southeast, and Malm et al. (2007) reported regions and seasons with high nitrate concentrations in the coarse mode at a subset of IMPROVE sites. For the purposes of reconstructing fine mass and light extinction coefficients, and because the necessary measurements to determine the form of nitrate are not regularly available, nitrate is assumed to be in the form of AN.

The area of high annual mean AN concentrations in the central United States (Figure 2.2.2a) is associated with agricultural activity in the region. The maximum IMPROVE 2016–2019 rural AN annual mean concentration of  $1.92 \mu\text{g m}^{-3}$  occurred at Bondville, Illinois (BOND1), a site located in the agricultural Midwest. Sites in central and southern California were also associated with higher AN concentrations, as were sites in northern North Dakota, with concentrations near  $1.0 \mu\text{g m}^{-3}$ . High concentrations at sites in North Dakota may be associated with oil and gas energy development (Prenni et al., 2016; Evanoski-Cole et al., 2017; Gebhart et al., 2018). Concentrations were much lower outside of the central United States, especially at sites in the Intermountain West and Northwest, with concentrations less than  $0.5 \mu\text{g m}^{-3}$ . Similarly low annual mean concentrations were observed in the Southeast and Northeast. The lowest rural concentration occurred in Denali NP, Alaska ( $0.05 \mu\text{g m}^{-3}$ , DENA1).

The inclusion of CSN sites provided more spatial resolution to the rural AN spatial pattern and showed the impact of urban AN concentrations on surrounding areas (Figure 2.2.2b). High AN was associated with sites surrounding Lake Michigan, and other hot spots occurred near Denver, Colorado and Salt Lake City, Utah. The highest urban annual mean AN concentration ( $4.5 \mu\text{g m}^{-3}$ ) occurred at Bakersfield, California, (060290014) and other urban sites in the Central Valley. The lowest CSN AN concentration occurred at Kapolei, Hawaii ( $0.18 \mu\text{g m}^{-3}$ , 150030010). Generally, urban concentrations of AN were considerably higher than rural concentrations.

Sites with high contributions of AN to RCFM were similar to those with high annual mean AN concentrations. The central United States, northern North Dakota, and California sites are examples, with annual mean AN RCFM fractions near 0.25–0.30 (Figure 2.2.2c). The rural IMPROVE site at Great River Bluffs, Minnesota (GRRI1), had the highest annual contribution of AN to RCFM (0.31), compared to the lowest at Monture, Montana (0.02, MONT1). In general, most rural IMPROVE sites were not highly influenced by AN contributions to RCFM on an annual mean basis. Lower contributions (~0.05) of AN to RCFM occurred at sites in the Southeast and across the Intermountain West. With the addition of the urban CSN sites, the influence of the contribution of AN to RCFM extended farther west from the central United States (Figure 2.2.2d), where AN contributed over a quarter of RCFM at sites in Colorado and central California, and the maximum contribution occurred at Bountiful, Utah (0.34, 490110004). The lowest urban CSN fraction (0.04) occurred in the southern Georgia city of Douglas (130690002).

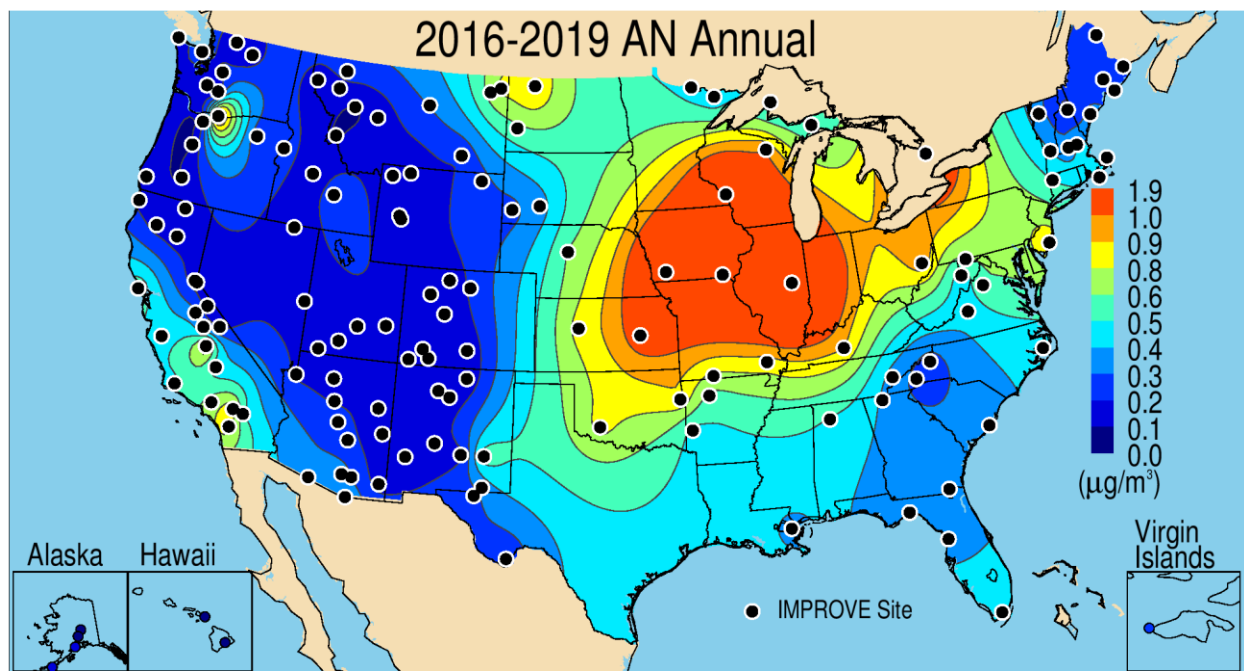


Figure 2.2.2a. IMPROVE 2016–2019 PM<sub>2.5</sub> ammonium nitrate (AN) annual mean mass concentrations ( $\mu\text{g m}^{-3}$ ).

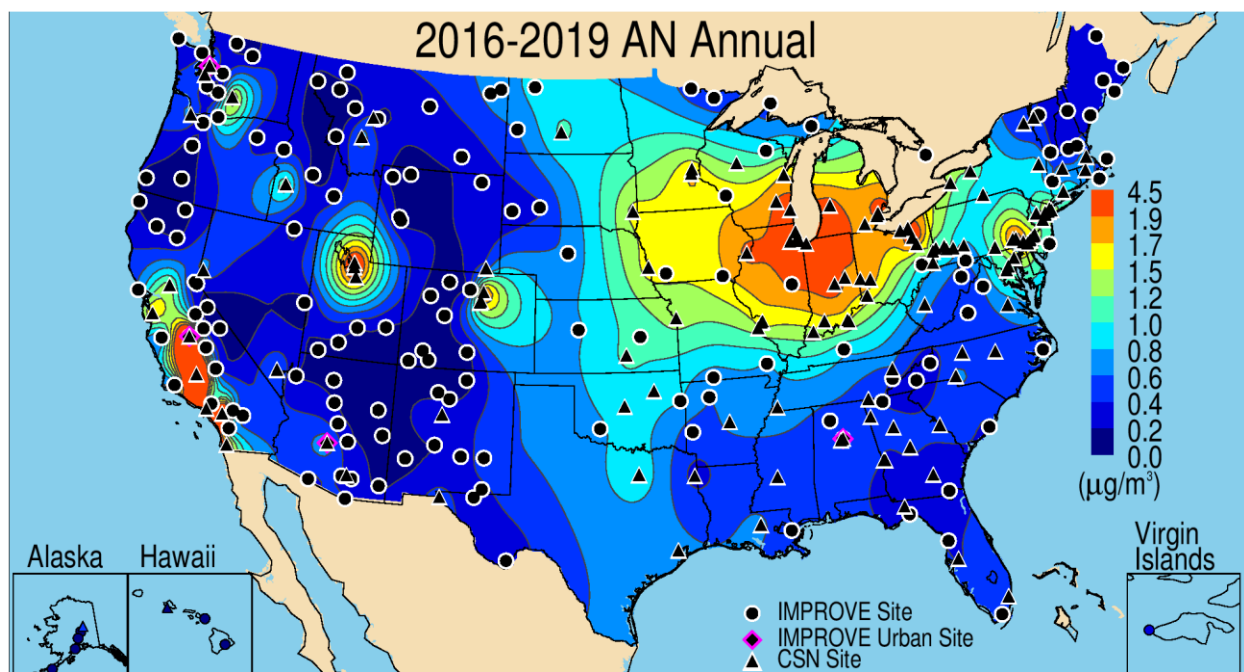


Figure 2.2.2b. IMPROVE and CSN 2016–2019 PM<sub>2.5</sub> ammonium nitrate (AN) annual mean mass concentrations ( $\mu\text{g m}^{-3}$ ).

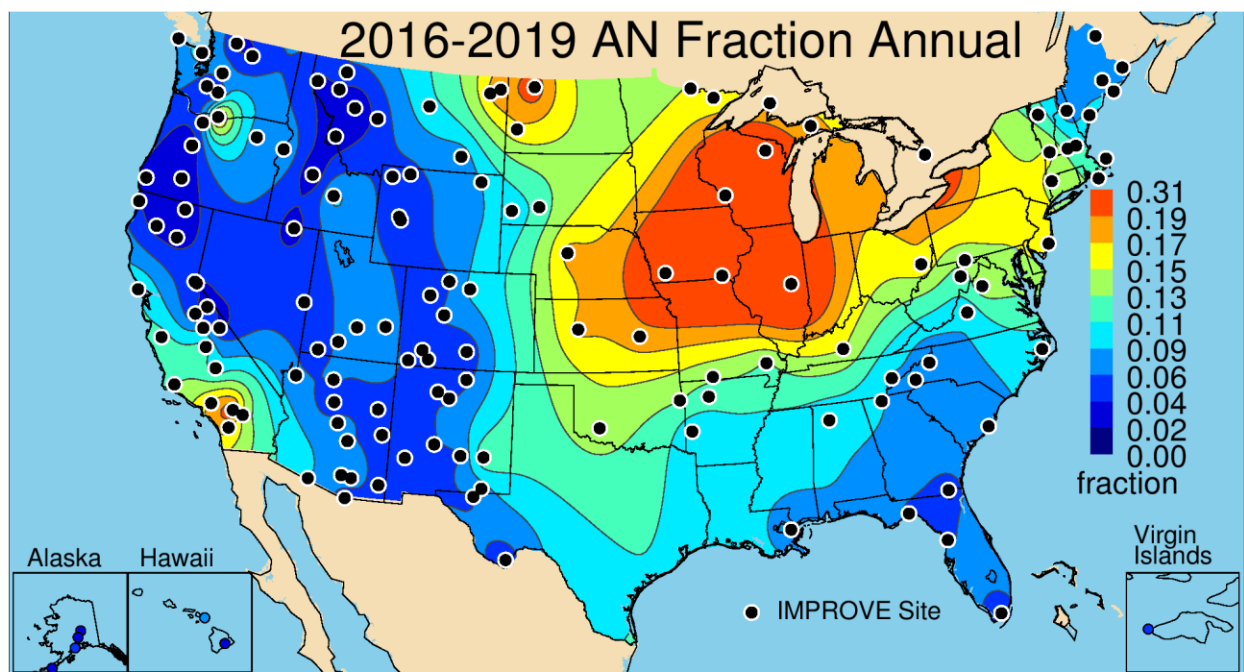


Figure 2.2.2c. IMPROVE 2016–2019 annual mean fraction contributions of ammonium nitrate (AN) to PM<sub>2.5</sub> reconstructed fine mass (RCFM).

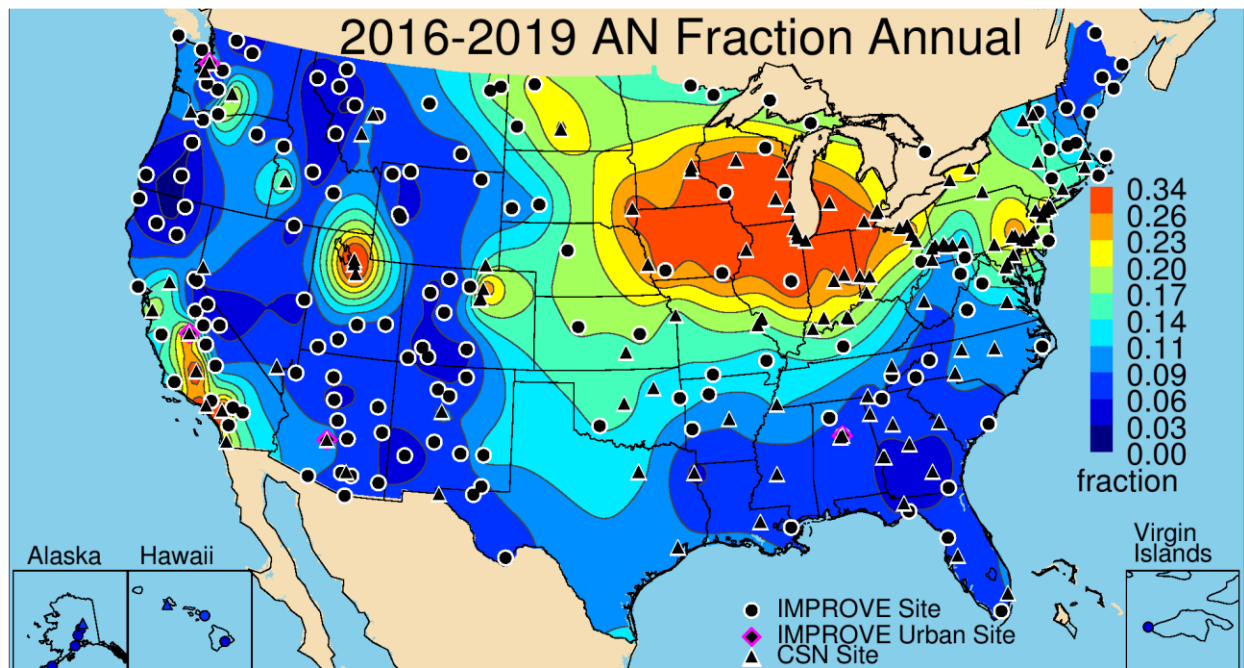


Figure 2.2.2d. IMPROVE and CSN 2016–2019 annual mean fractions of ammonium nitrate (AN) to PM<sub>2.5</sub> reconstructed fine mass (RCFM).

## 2.2.3 PM<sub>2.5</sub> Particulate Organic Matter Mass

The sources of POM in the atmosphere are both primary emissions and secondary formation. Primary emissions include particle mass emitted directly from combustion of fossil fuels or biomass. Secondary organic aerosol formation results from the oxidation of gas-phase precursors from both anthropogenic and biogenic sources. Accurate estimates of POM from OC

are required in order to compute RCFM and to estimate optical properties such as light scattering coefficients. The OM/OC ratio used to estimate POM takes into account contributions from other elements associated with the organic matter, such as nitrogen, oxygen, and hydrogen. It is spatially and temporally variable. Typical values range from 1.2 to 2.6. It is impossible to determine which and how many elements are associated with POM without knowing the chemical formula of the organic compound, and it is common for a significant portion of organic aerosol mass to remain unidentified (Turpin and Lim, 2001; Jimenez et al., 2009; Heald and Kroll, 2020). Because the organic compounds that compose POM are typically unknown, the approach for taking into account other elements in POM mass has been to apply an average OM/OC ratio. However, recent measurements and statistical studies have indicated the seasonal and regional variability in OM/OC. For example, values in warm months tend to be higher than cold months, and values in rural areas tend to be higher than in urban areas (e.g., Bae et al., 2006; Aiken et al., 2008; Polidori et al., 2008; El-Zanan et al., 2005; 2009; Lowenthal et al., 2009; Malm et al., 2011; Simon et al., 2011; Hallar et al., 2013; Philip et al., 2014; Ruthenburg et al., 2014; Lowenthal et al., 2015; Blanchard et al., 2016; Hand et al., 2019b; Malm et al., 2020). Following the methods in Hand et al. (2019b), a multiple linear regression was performed with monthly resolution using IMPROVE data from 2016 through 2019. Results suggested that the monthly variability in OM/OC ratios was consistent with other studies in rural areas, therefore these values were used to compute POM for the IMPROVE network (Table 2.2) to be more consistent with recent literature and to address issues related to biases in the fine mass residual (see Appendix 2.1). To compute POM using CSN data, estimates from Philip et al. (2014) were applied on a seasonal basis (Table 2.2).

The highest 2016–2019 annual mean rural IMPROVE POM concentrations occurred in southern Florida, the northwestern United States, and central and northern California due to the influence of biomass burning (Figure 2.2.3a). The highest concentrations occurred in Yosemite NP, California ( $6.8 \mu\text{g m}^{-3}$ , YOSE1). Elevated levels of POM ( $\sim 3.0 \mu\text{g m}^{-3}$ ) also occurred at sites in the Southeast, as well as at sites in the Northwest and California. The 2016–2019 period was associated with high fire activity, especially 2017 and 2018 in the Northwest, and 2016 in the Southeast. The lowest annual mean concentrations occurred in Haleakala Crater NP, Hawaii ( $0.15 \mu\text{g m}^{-3}$ , HACR1). Annual mean concentrations in western Colorado, portions of Wyoming and New Mexico, and the Four Corners region were less than  $1 \mu\text{g m}^{-3}$ .

The combined urban and rural POM concentrations demonstrated the influence of urban POM sources, with higher concentrations at sites in the Southeast and along the Central Valley of California (Figure 2.2.3b). Sites in Alabama, Georgia, South Carolina, and North Carolina had POM concentrations greater than  $4.0 \mu\text{g m}^{-3}$ . The highest annual mean CSN POM concentration occurred at Fresno, California ( $6.01 \mu\text{g m}^{-3}$ , 060190011). Similar maximum annual mean rural and urban POM concentrations demonstrated the influence of biomass burning on rural POM concentrations. As in the IMPROVE network, the lowest annual mean CSN POM concentration occurred in Hawaii ( $0.42 \mu\text{g m}^{-3}$ , Kapolei, 150030010).

The IMPROVE sites with the highest contributions ( $>0.7$ ) of POM to RCFM occurred in the northwestern United States, in regions influenced by biomass smoke emissions (see Figure 2.2.3c). The highest fraction occurred in Crater Lake NP, Oregon (0.79, CRLA1). At sites cross most of the United States, annual mean POM fractions were around 0.5, with somewhat higher fractions (0.55–0.60) occurring at sites in the Southeast and Northeast. The lowest rural fractions

in the continental United States occurred in the Southwest, and the lowest fraction of all rural sites occurred in Hawaii Volcanoes NP, Hawaii (0.09, HAVO1). The general spatial pattern did not change with the addition of CSN sites (Figure 2.2.3d), with higher contributions at sites in the Northwest. The highest CSN annual mean POM fraction (0.65) occurred at Butte, Montana (300930005). Similar to rural sites, urban POM fractions were generally high at sites in the Southeast, including several urban sites in Georgia with fractions greater than 0.65.

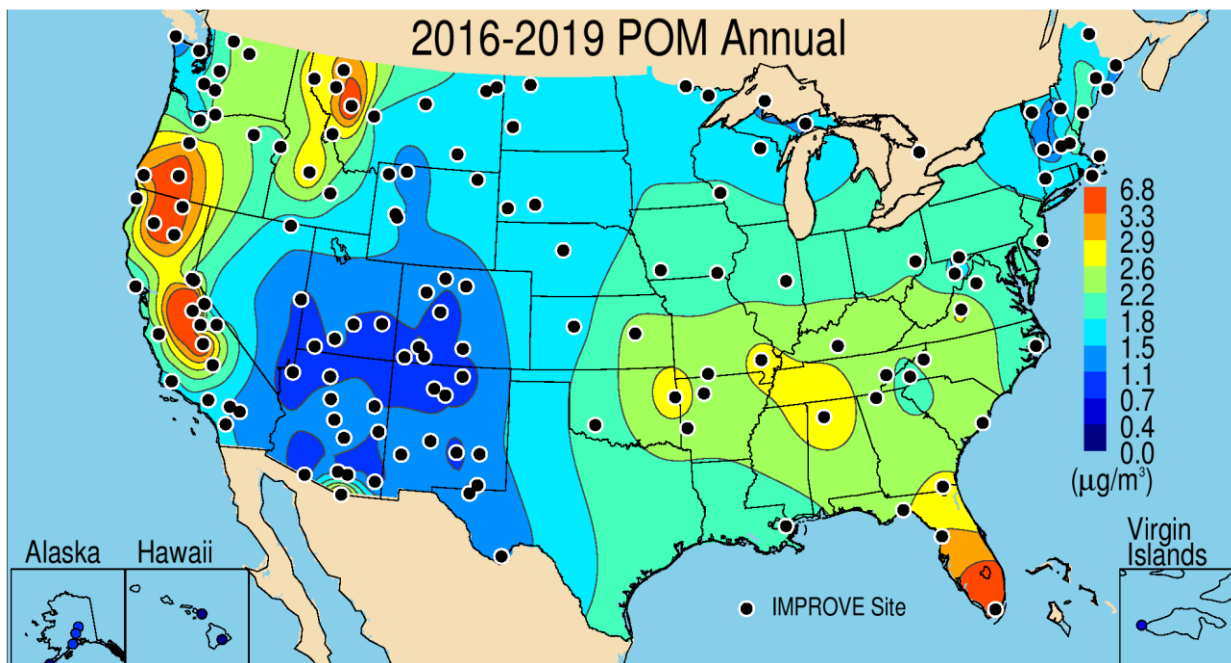


**Figure 2.2.3a.** IMPROVE 2016–2019 PM<sub>2.5</sub> particulate organic matter (POM) annual mean mass concentrations ( $\mu\text{g m}^{-3}$ ).

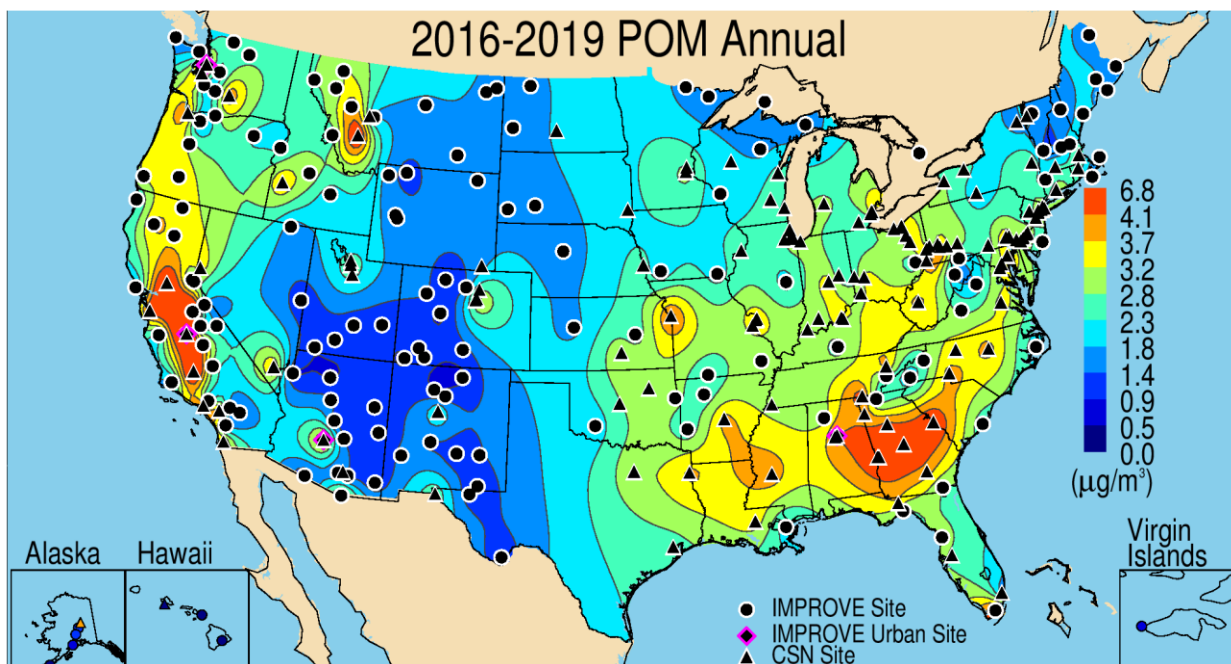


**Figure 2.2.3b.** IMPROVE and CSN 2016–2019 PM<sub>2.5</sub> particulate organic matter (POM) annual mean mass concentrations ( $\mu\text{g m}^{-3}$ ).

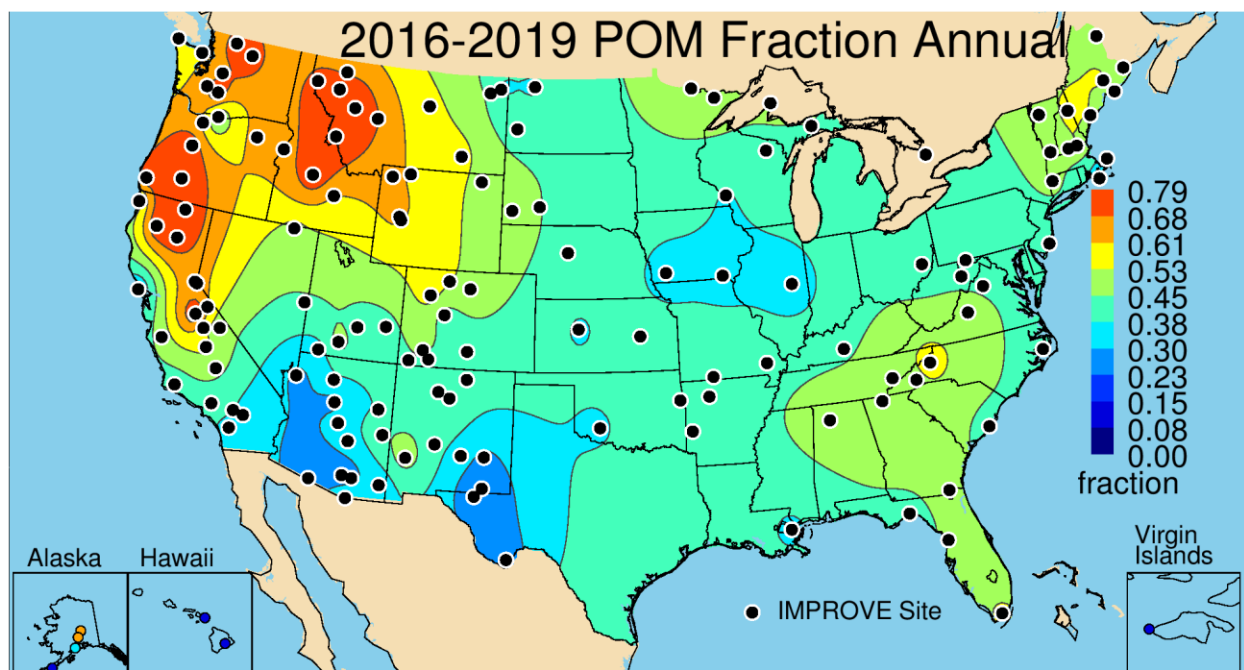


Figure 2.2.3c. IMPROVE 2016–2019 annual mean fraction contributions of particulate organic matter (POM) to PM<sub>2.5</sub> reconstructed fine mass (RCFM).

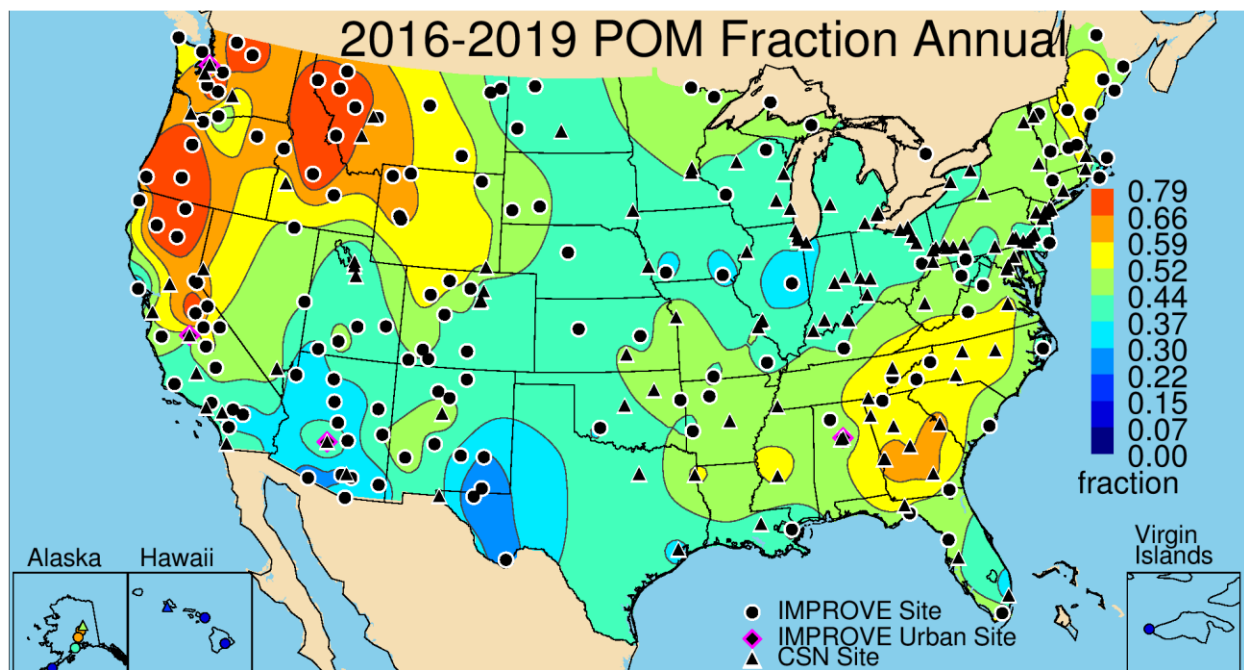


Figure 2.2.3d. IMPROVE and CSN 2016–2019 annual mean fraction contributions of particulate organic matter (POM) to PM<sub>2.5</sub> reconstructed fine mass (RCFM).

## 2.2.4 PM<sub>2.5</sub> Elemental Carbon Mass

EC, also referred to as light absorbing carbon or black carbon depending on the measurement method, is emitted directly from incomplete combustion of fossil fuels or biomass (e.g., Bond et al., 2013). EC as reported here is determined through thermal optical analysis (see Section 1.2.2), and Malm et al. (2020) (and references therein) indicated that the analysis can

inadvertently apportion some of the EC to OC, leading to underestimations of EC, depending on analysis conditions.

The IMPROVE rural 2016–2019 annual mean EC concentrations ranged from  $0.02 \mu\text{g m}^{-3}$  in Haleakala Crater NP, Hawaii (HACR1), to  $0.89 \mu\text{g m}^{-3}$  in Nogales, Arizona (NOGA1). The high annual mean concentration at Nogales was an outlier relative to sites in the rest of the Southwest and Intermountain West, where concentrations were typically around  $0.1 \mu\text{g m}^{-3}$ . The IMPROVE site in Nogales is located on the edge of town near the border with Mexico and may experience impacts from Mexico. The EC seasonal pattern in Nogales reflects urban sources that typically peak in winter, and therefore the site may not represent typical rural EC seasonality and sources. The next-highest annual mean concentration occurred at Chassahowitzka National Wildlife Refuge (NWR) in Florida ( $0.34 \mu\text{g m}^{-3}$ , CHAS1), likely due to fire impacts. Farther west, EC concentrations were higher at sites in California and the Northwest ( $\sim 0.25 \mu\text{g m}^{-3}$ ). Most of the central and eastern United States also had higher annual mean concentrations ( $> 0.25 \mu\text{g m}^{-3}$ ; see Figure 2.2.4a).

Urban CSN EC concentrations were generally higher than at IMPROVE sites (maximum of  $1.43 \mu\text{g m}^{-3}$  in Liberty, Pennsylvania, 420030064). Regionally, urban EC concentrations were highest at sites in the East; however, most impacts of EC were local in extent. Several hot spots occurred in major urban areas, for example, near Denver, Colorado; Butte, Montana; Las Vegas, Nevada, and several sites in the Central Valley of California (Figure 2.2.4b). The urban hotspots were indicative of local urban EC emissions (e.g., mobile sources or local residential wood burning) rather than regional sources like biomass combustion from controlled or wild fires. The steep spatial gradient surrounding the hotspots of EC in Figure 2.2.4b indicated that the spatial extent of the impact was small with low regional impacts.

EC was a minor contributor to RCFM at most IMPROVE sites around the United States (Figure 2.2.4c). The highest EC fractions occurred at sites in the Northwest and Northeast (0.05–0.09), with the maximum of 0.09 at Nogales, Arizona (NOGA1), where the highest annual mean concentrations also occurred in the IMPROVE network. The Nogales site was an outlier in the region where most sites had EC fractions of 0.03–0.04. The second-highest EC mass fraction occurred at Londonderry, New Hampshire (LOND1, 0.07). The lowest contributions occurred at Virgin Islands NP (0.01, VIIS1).

Many of the urban CSN sites that had elevated annual mean EC concentrations also had higher EC fractions ( $> 0.10$ ; see Figure 2.2.4.d). The highest urban EC fraction (0.16) occurred at Charleston, West Virginia (540390020) and the lowest (0.04) occurred at Kapolei, Hawaii (150030010). In general, urban sites had higher EC fractions, and this influence appeared to be fairly localized.

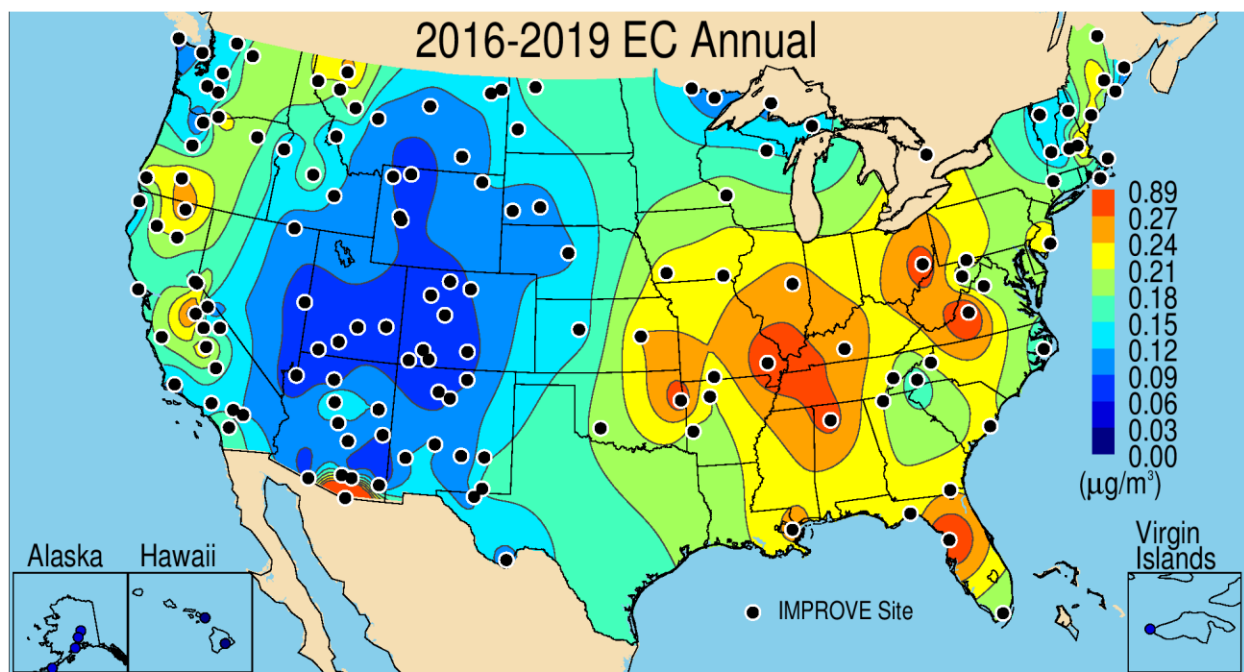


Figure 2.2.4a. IMPROVE 2016–2019 PM<sub>2.5</sub> elemental carbon (EC) annual mean mass concentrations ( $\mu\text{g m}^{-3}$ ).

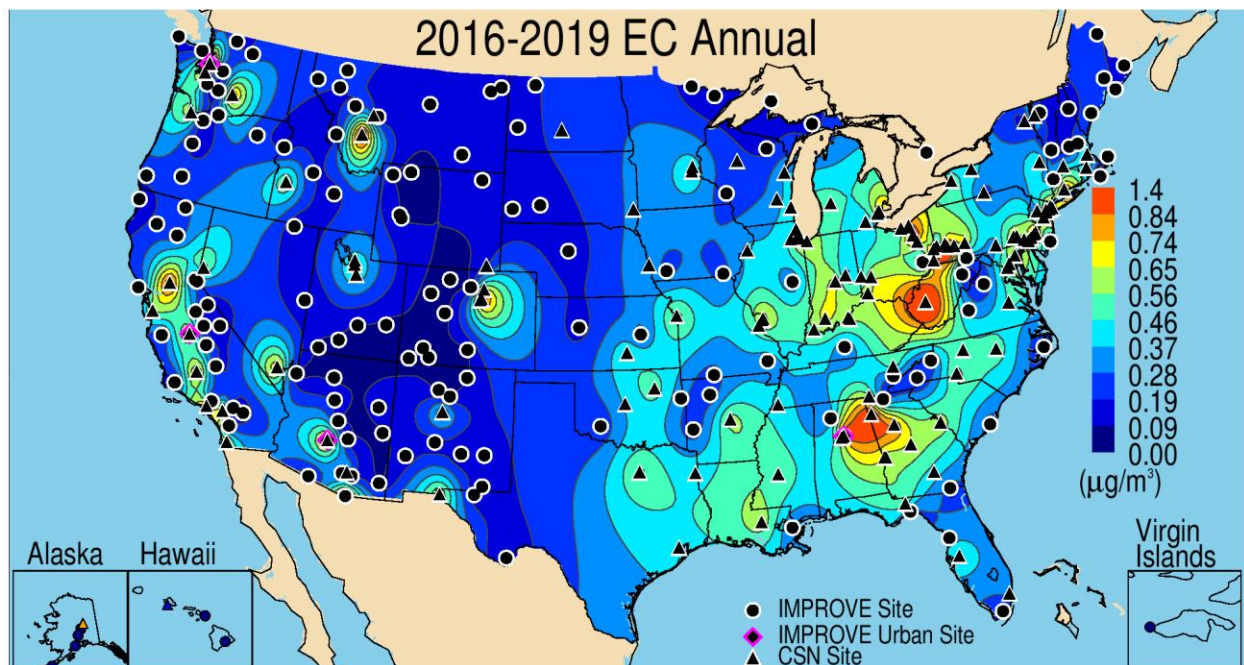


Figure 2.2.4b. IMPROVE and CSN 2016–2019 PM<sub>2.5</sub> elemental carbon (EC) annual mean mass concentrations ( $\mu\text{g m}^{-3}$ ).

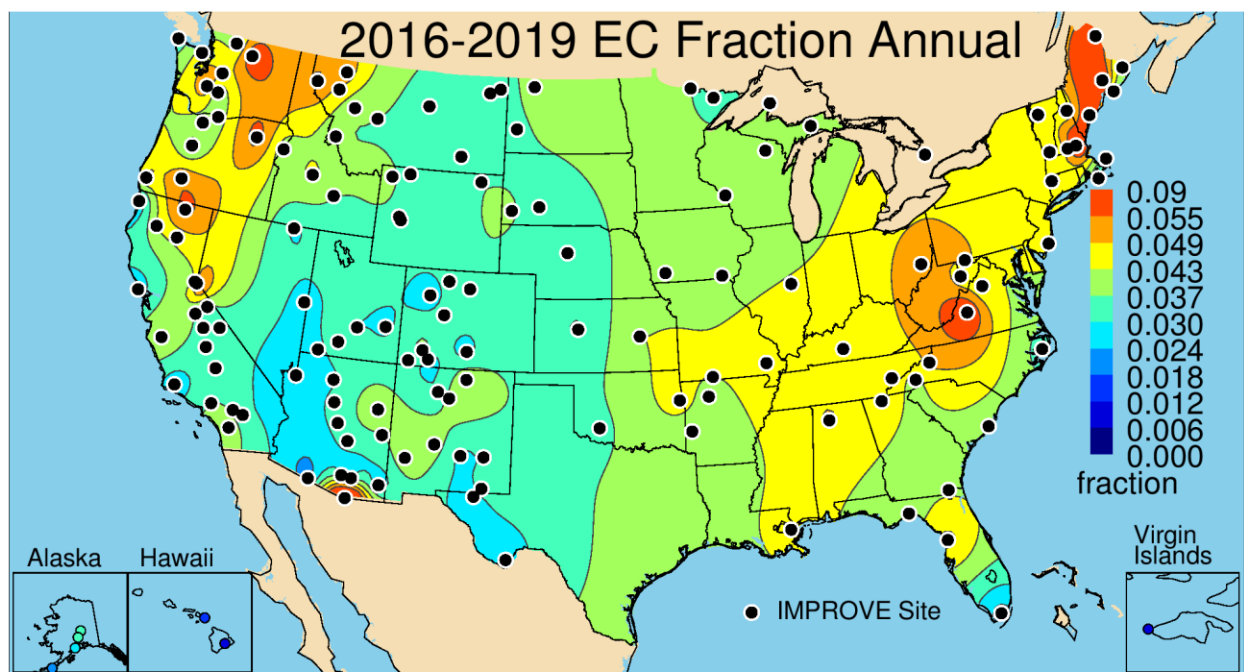


Figure 2.2.4c. IMPROVE 2016–2019 annual mean fraction contributions of elemental carbon (EC) to PM<sub>2.5</sub> reconstructed fine mass (RCFM).

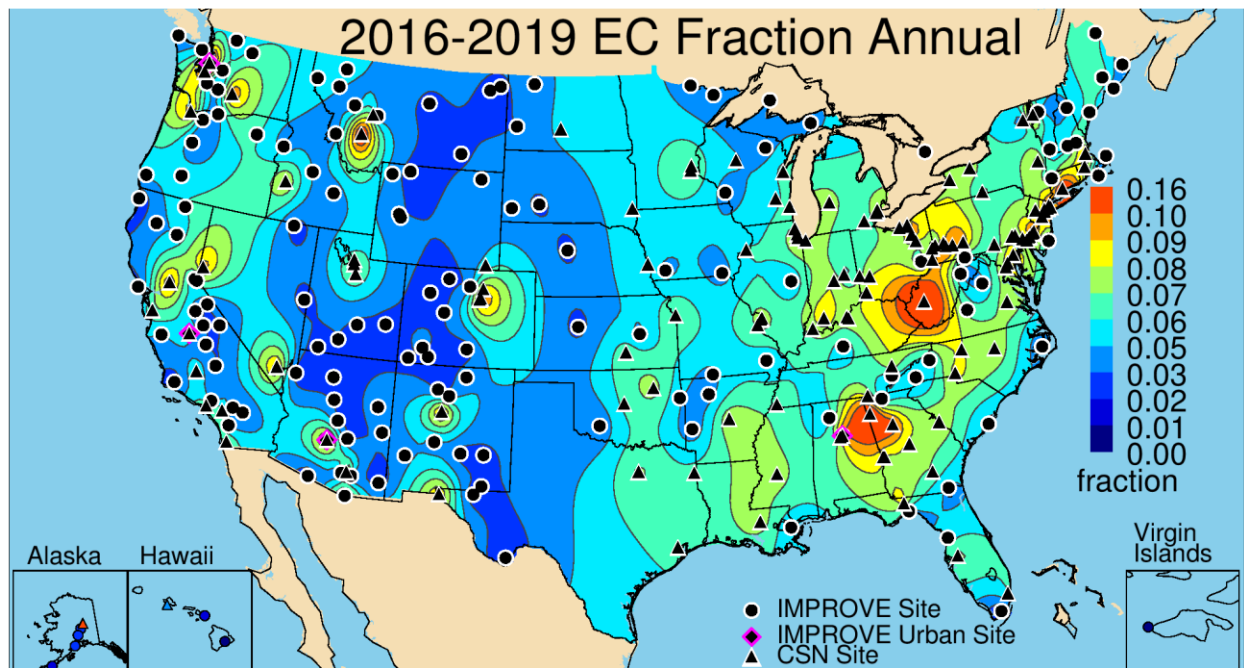


Figure 2.2.4d. IMPROVE and CSN 2016–2019 annual mean fraction contributions of elemental carbon (EC) to PM<sub>2.5</sub> reconstructed fine mass (RCFM).

## 2.2.5 Filter Light Absorption ( $f_{abs}$ )

Black carbon strongly absorbs visible light (Moosmüller et al., 2009; Bond et al., 2013) and although  $f_{abs}$  is a measure of all light absorbing particles on the PM<sub>2.5</sub> Teflon filter, black carbon is likely the main contributor given its strong absorbing properties. However, fine mineral dust containing iron oxides is known to absorb in the visible spectrum, (Moosmüller et al., 2012;

White et al., 2016); therefore it is expected that absorption from iron oxides will also contribute to  $f_{abs}$ . Measurements of  $f_{abs}$  are currently available only for the IMPROVE network and only on PM<sub>2.5</sub> filters.

The 2016–2019 annual mean  $f_{abs}$  tends to follow EC spatial patterns since most of the filter absorption is likely due to EC (Figure 2.2.5). The highest annual mean  $f_{abs}$  occurred in Nogales, Arizona (10.5 Mm<sup>-1</sup>, NOGA1) and the lowest occurred in Hawaii Volcanoes NP, Hawaii (0.21 Mm<sup>-1</sup>, HAVO1). The highest EC concentration also occurred at Nogales and the lowest EC concentration occurred in Hawaii (Haleakala NP). The second-highest annual mean  $f_{abs}$  occurred at Chassahowitzka NWR in Florida (CHAS1, 4.1 Mm<sup>-1</sup>), likely due to impacts from biomass smoke. Biomass smoke also likely influenced higher  $f_{abs}$  at sites along the West Coast. Somewhat elevated  $f_{abs}$  occurred in the Southwest, perhaps due to the role of iron absorption in dust. The eastern United States was associated with elevated  $f_{abs}$  across large regions, very similar to the observed EC pattern.

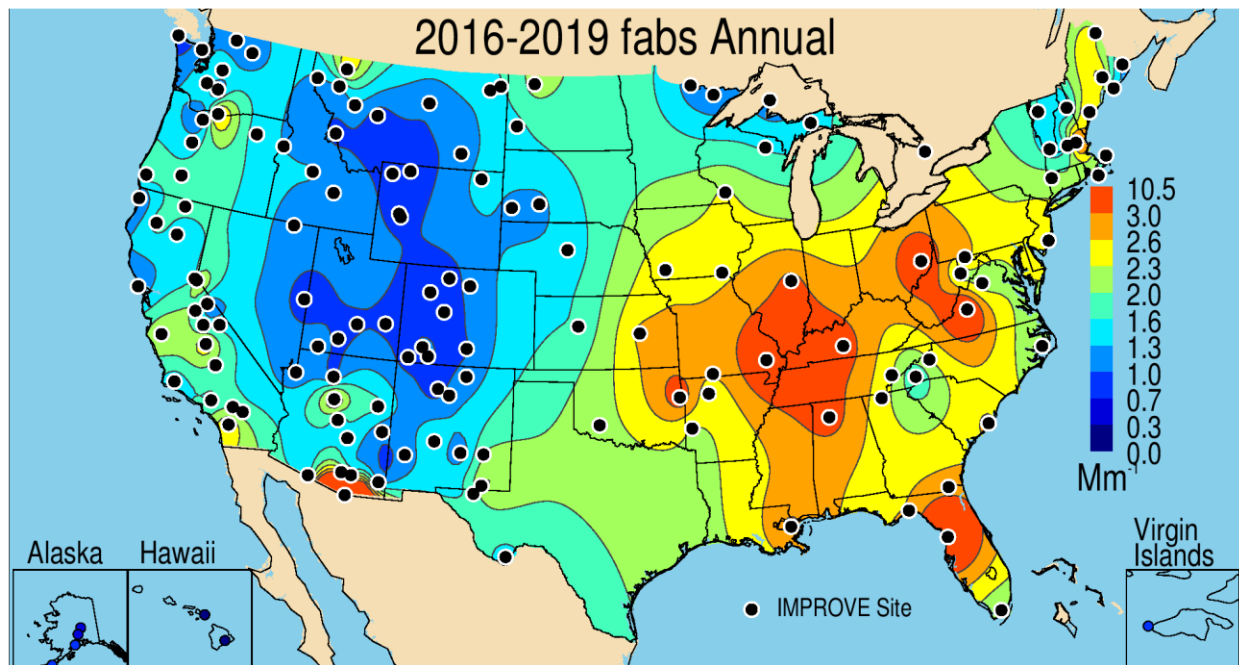


Figure 2.2.5. IMPROVE 2016–2019 PM<sub>2.5</sub> annual mean filter absorption ( $f_{abs}$ ) (Mm<sup>-1</sup>).

## 2.2.6 PM<sub>2.5</sub> Fine Dust Mass

Sources of mineral dust in the atmosphere include entrainment from deserts, paved and unpaved roads, agricultural activity, construction, and fire. Deposition of dust usually corresponds to large particles that settle near their source regions, although there are many exceptions. The seasonal and spatial variability of dust in the United States is influenced by both local, regional, and long-range transport. Several studies have shown that contributions of Asian dust to U.S. fine dust concentrations can be significant episodically, affecting aerosol concentrations and mineralogy across the United States, typically in the spring (e.g., Husar et al., 2001; Prospero et al., 2002; Creamean et al., 2014; Hand et al., 2017; Kim et al., 2021). Transport of North African dust to the United States occurs regularly in summer, affecting aerosol concentrations in the Virgin Islands, the eastern and southeastern United States (Perry et

al., 1997; Hand et al., 2017; Bozlaker et al., 2019; Prospero et al., 2021), and even as far west as Big Bend NP, Texas (Hand et al., 2002). Dust concentrations in desert regions of the Southwest are expected to be higher due to the impacts of local sources as well as transboundary transport from the Chihuahuan desert in Mexico, especially in winter and spring (Rivera et al., 2009; Tong et al., 2012; Hand et al., 2016; 2017). Dust in the central United States is influenced by agricultural activity (Hand et al., 2017; Pu and Ginoux, 2018; Lambert et al., 2020).

FD as characterized by PM<sub>2.5</sub> samplers most likely corresponds to the fine tail of the coarse mode. Variability in dust concentrations could be due to changes in the magnitudes of mass concentrations for a given size mode or to a shifting size distribution that results in more or less mass available in the fine-mode size range. Due to the spatial and temporal variability in dust sources, it is very difficult to characterize an appropriate aerosol dust composition for each measurement site. FD mass concentrations are therefore estimated by a general method that sums the oxides of elements that are typically associated with soil (Al<sub>2</sub>O<sub>3</sub>, SiO<sub>2</sub>, CaO, K<sub>2</sub>O, FeO, Fe<sub>2</sub>O<sub>3</sub>, TiO<sub>2</sub>), with a correction for other compounds such as MgO, Na<sub>2</sub>O, H<sub>2</sub>O, and carbonates (Malm et al., 1994). Elemental concentrations are multiplied by factors that represent the mass concentrations of the oxide forms. Several corrections are also made. Molar concentrations of iron are assumed to be equally abundant in the forms of FeO and Fe<sub>2</sub>O<sub>3</sub>. Potassium has a nonsoil contribution from biomass smoke, so the soil potassium is estimated by using Fe as a surrogate, or [K] = 0.6×[Fe]. The original formula for computing FD concentrations included a multiplier of 1.16 to account for missing compounds (Table 2.1). As discussed in Section 2.1, IMPROVE FD concentrations in this report are derived from the original formula and multiplied by 1.15 to reflect an underestimation of FD identified by multiple linear regression analyses (see Appendix 2.1). CSN FD concentrations are not multiplied by this factor; however, recall that comparisons of IMPROVE and CSN data at collocated sites suggested that relative biases of 20% in FD concentrations existed, with higher IMPROVE concentrations. This bias is likely due to the differences in the sharpness of size cut points of the samplers. Given these uncertainties, the aggregation of IMPROVE and CSN FD concentrations should be interpreted as semiquantitative.

The patterns observed in the 2016–2019 annual mean rural IMPROVE FD concentrations were reflective of dominant seasons of elevated dust concentrations, namely the Southwest during spring and the Southeast during summer (Hand et al., 2017). The highest annual mean concentrations occurred at sites in the Southwest, with the highest at Nogales, Arizona (3.11 µg m<sup>-3</sup>, NOGA1), and followed a lobed spatial pattern determined by the terrain of the Mogollon Plateau. Concentrations at other sites in Arizona ranged from 1.3 to 3.1 µg m<sup>-3</sup>. The second-highest annual mean FD concentration occurred at Sycamore Canyon, Arizona (3.10 µg m<sup>-3</sup>, SYCA2). Sites around the Colorado Plateau as well as sites in southern New Mexico and western Texas had concentrations near 1 µg m<sup>-3</sup> (see Figure 2.2.6a). Unlike other species with spatial gradients along the east/west orientation, FD gradients extended north/south. The concentrations at northern sites tended to be lower (~0.5 µg m<sup>-3</sup>), and the lowest rural annual mean FD concentration occurred at the Makah Tribe site in Washington (0.07 µg m<sup>-3</sup>, MAK1).

Although the CSN FD concentrations were biased low relative to IMPROVE concentrations, the spatial patterns in combined urban and rural FD generally agreed, with higher concentrations at sites in the Southwest (Figure 2.2.6b). There were several urban hot spots with elevated FD concentrations. For example, the CSN sites at Denver, Colorado; Las Vegas, Nevada; St. Louis, Missouri; Dallas, Texas; and sites in the Central Valley of California had

higher FD concentrations relative to surrounding areas. The highest annual mean FD concentration ( $2.07 \mu\text{g m}^{-3}$ ) occurred at El Paso, Texas (481410044), and the lowest concentration in the CSN network was measured in northeastern New York ( $0.17 \mu\text{g m}^{-3}$ , Wilmington, 360310003).

FD contributed a substantial fraction of RCFM at rural sites in the western United States (Figure 2.2.6c), where annual mean fractions ranged from 0.25 to 0.55. The highest fraction (0.55) occurred at Sycamore Canyon, Arizona (0.55, SYCA2). At sites across the Northwest and the eastern United States, annual mean FD contributions were typically  $<0.15$ . The lowest annual mean FD fractional contribution occurred at Redwood NP, California (0.03, REDW1). The combined IMPROVE and CSN annual mean FD fraction spatial pattern was very similar to that of IMPROVE alone, with higher contributions in the Southwest (Figure 2.2.6d). At sites across the Northwest and eastern United States, the urban FD fraction was typically  $<0.1$ . The highest CSN annual mean FD fraction occurred in El Paso, Texas (0.29, 481410044), similar to the highest CSN FD concentration. The lowest fraction occurred at Tacoma, Washington (0.04, 530530029).

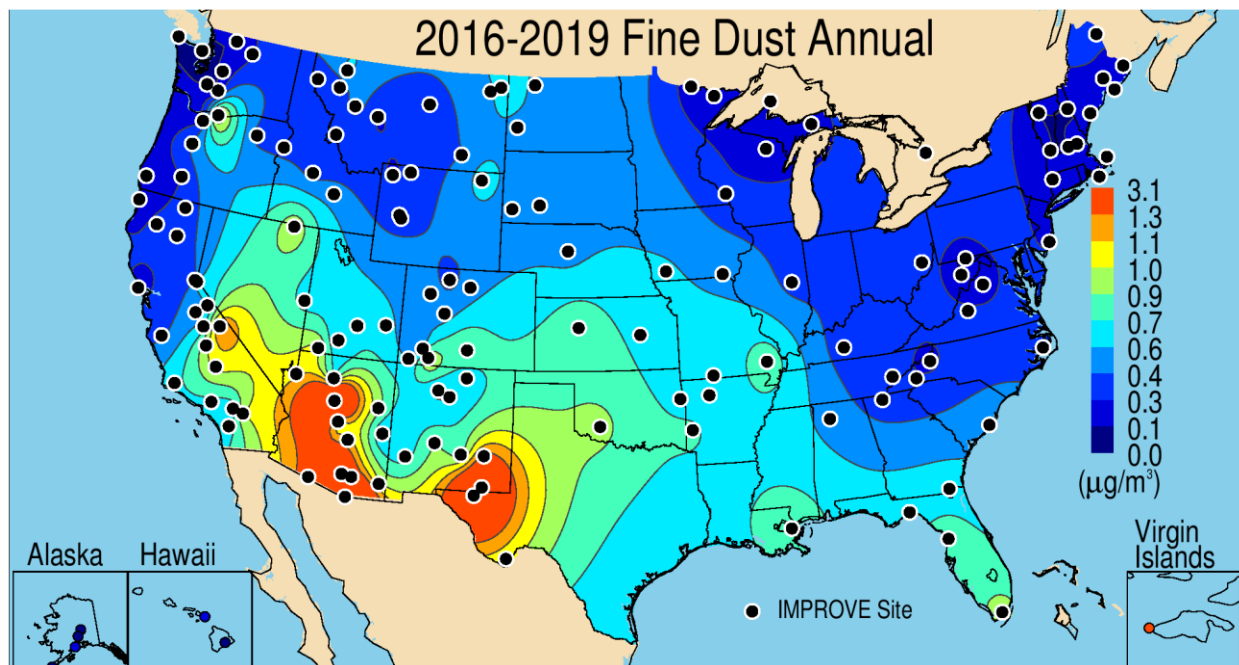


Figure 2.2.6a. IMPROVE 2016–2019 PM<sub>2.5</sub> fine dust annual mean mass concentrations ( $\mu\text{g m}^{-3}$ ).

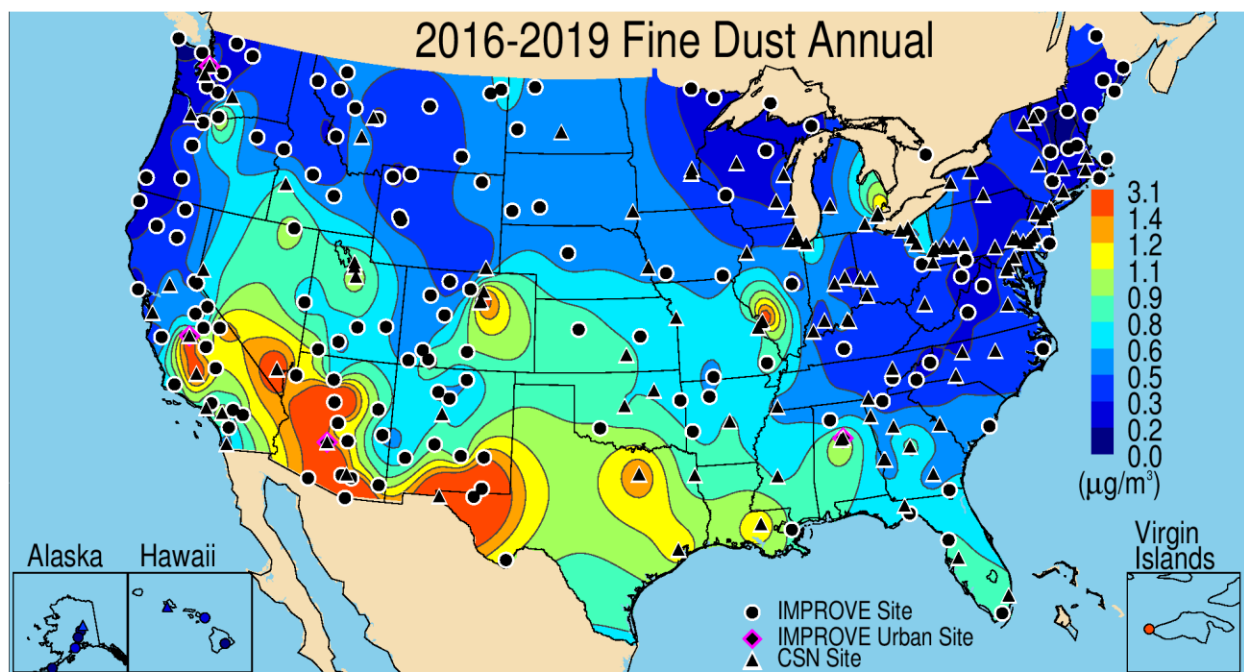


Figure 2.2.6b. IMPROVE and CSN 2016–2019 PM<sub>2.5</sub> fine dust annual mean mass concentrations ( $\mu\text{g m}^{-3}$ ).

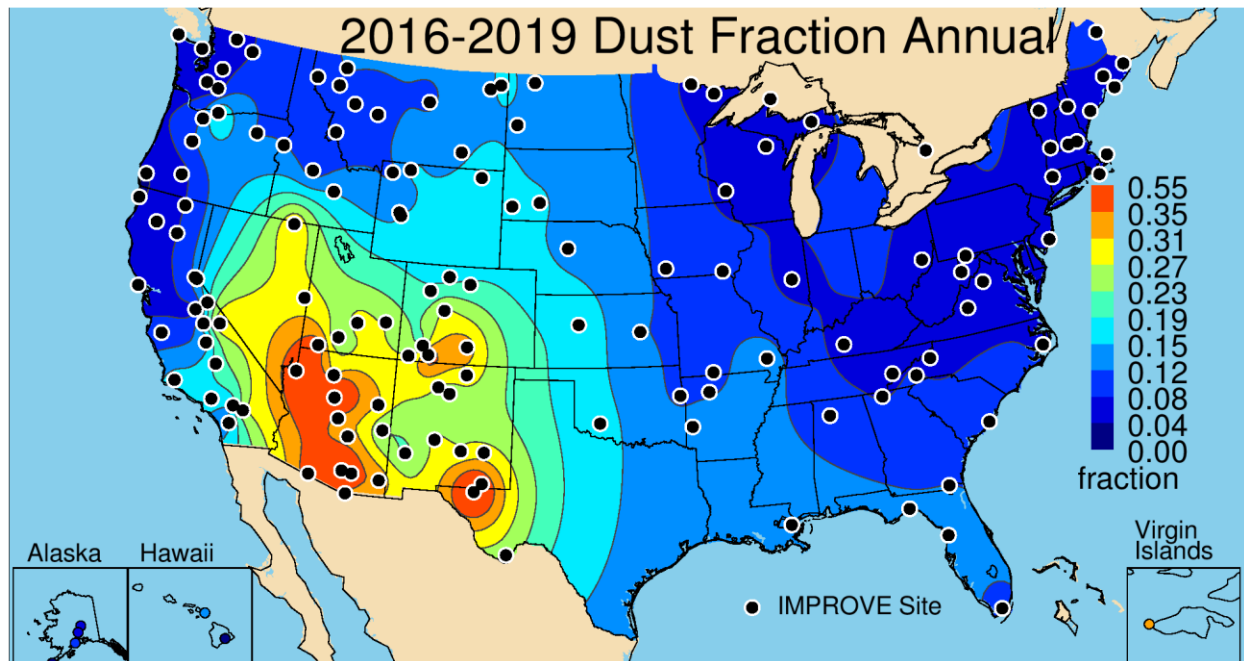
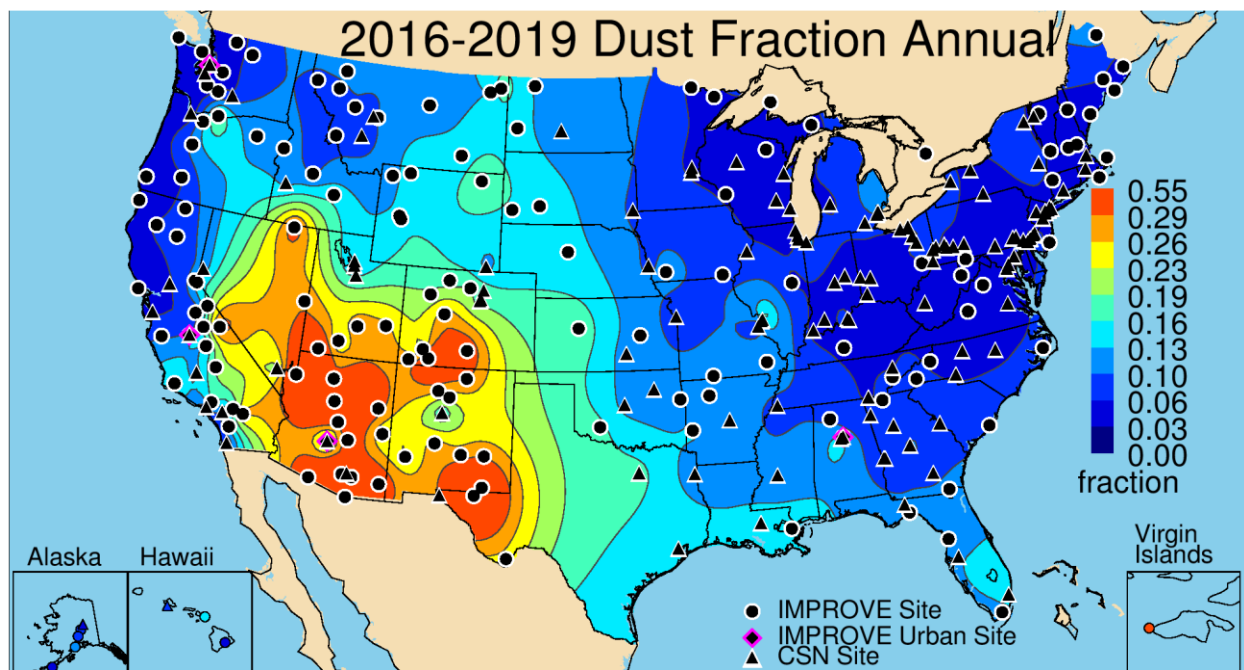


Figure 2.2.6c. IMPROVE 2016–2019 annual mean fraction contributions of fine dust to PM<sub>2.5</sub> reconstructed fine mass (RCFM).



**Figure 2.2.6d. IMPROVE and CSN 2016–2019 annual mean fraction contributions of fine dust to PM<sub>2.5</sub> reconstructed fine mass (RCFM).**

## 2.2.7 PM<sub>2.5</sub> Sea Salt Mass

SS can be a significant fraction of the RCFM at many coastal locations, as well as contribute significantly to light scattering (e.g., Lowenthal and Kumar, 2006; Murphy et al., 2019). SS concentrations are typically computed from SS markers like sodium ion, chloride ion, or combination of ions (White, 2008). Difficulties in computing SS from data from the IMPROVE network arise because positive ions are not analyzed; therefore sodium ion data (the strongest indicator of SS) are not available. Elemental sodium data are available from X-ray fluorescence (XRF) analyses; however, sensitivity issues regarding poor detection of Na result in large uncertainties (White, 2008). Issues also arise when using the chloride ion or chlorine to estimate SS, because the reaction of gaseous nitric acid with SS produces sodium nitrate particles and the release of gaseous hydrochloric acid. The depletion of chloride during this reaction results in an underestimation of SS when using chloride to compute it. However, given these limitations, it was proposed by Pitchford et al. (2007) that calculations for reconstructing mass in the IMPROVE algorithm include SS by multiplying the chloride ion (Cl<sup>-</sup>) by 1.8 (SS is 55% Cl by weight as defined by the composition of seawater). Because the chloride ion only began being reported for the CSN in February 2017, SS is computed using a 1.8 factor multiplied by chlorine as measured by XRF. Comparisons of SS concentrations between collocated CSN and IMPROVE sites (see Section 1.4) suggested that IMPROVE concentrations were up to three times higher on average compared to CSN, with a relative bias of 63%. Given these disparities in concentrations, the integration of CSN and IMPROVE SS data should be interpreted with caution.

The IMPROVE sites with the highest 2016–2019 annual mean SS concentrations were along coastal regions (Figure 2.2.7a). Concentrations at rural IMPROVE sites ranged from 0.01 µg m<sup>-3</sup> at North Absaroka, Wyoming (NOAB1), to 2.29 µg m<sup>-3</sup> at Point Reyes National Seashore

(NS), California (PORE1). Outside of coastal regions, SS concentrations were low ( $<0.10 \mu\text{g m}^{-3}$ ). The spatial patterns were generally similar when aggregating IMPROVE and CSN data (Figure 2.2.7b). The minimum annual mean concentration was essentially zero ( $-0.0004 \mu\text{g m}^{-3}$ ) at Cheyenne, Wyoming (560210100), and the maximum SS concentration of  $0.83 \mu\text{g m}^{-3}$  occurred in Kapolei, Hawaii (150030010).

At the IMPROVE site at Simeonof, Alaska (SIME1), SS fractional contributions to RCFM was 0.49, compared to the minimum contribution at Monture, Montana (0.02, MONT1) (Figure 2.2.7c). Similar to the spatial distribution of SS concentrations, fractional contributions were highest at coastal sites and at sites in Hawaii, Alaska, and the Virgin Islands. These spatial patterns also held for combined IMPROVE and CSN fraction contributions (Figure 2.2.7d). The highest annual mean SS contribution (0.30) at CSN sites occurred at Kapolei, Hawaii (150032010), where the highest concentration was observed. The lowest contribution (zero) also occurred at Cheyenne, Wyoming (560210100).

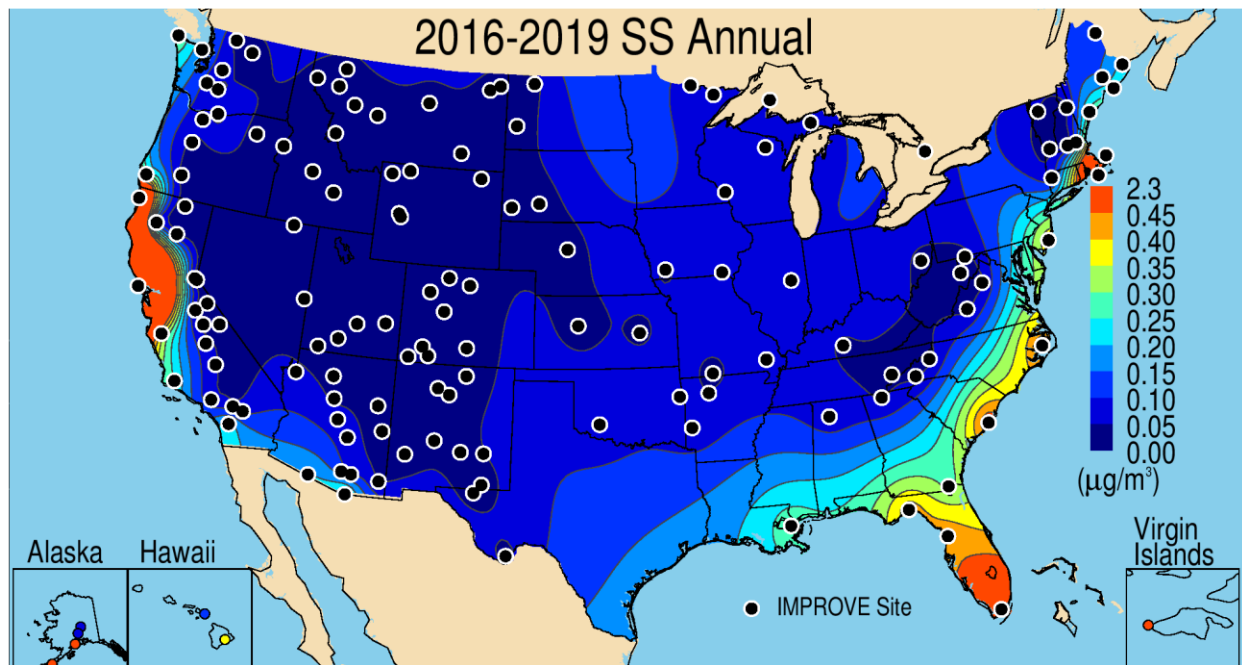


Figure 2.2.7a. IMPROVE 2016–2019 PM<sub>2.5</sub> sea salt (SS) annual mean mass concentrations ( $\mu\text{g m}^{-3}$ ).

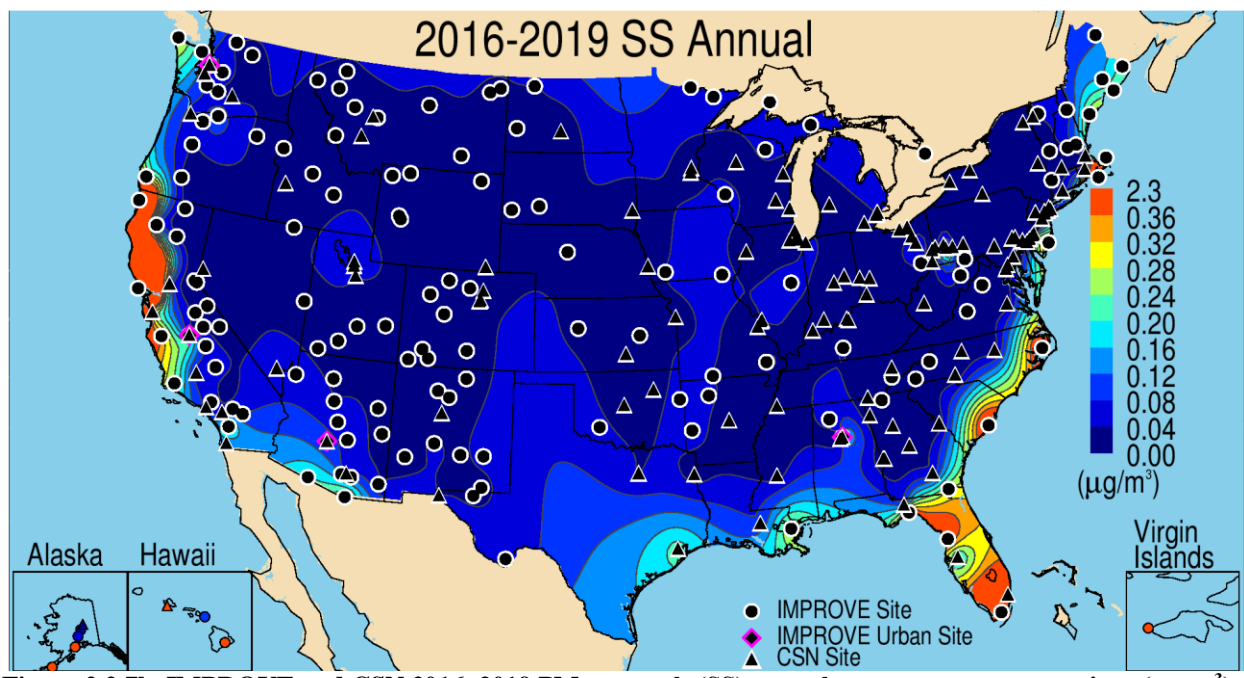


Figure 2.2.7b. IMPROVE and CSN 2016–2019 PM<sub>2.5</sub> sea salt (SS) annual mean mass concentrations ( $\mu\text{g m}^{-3}$ ).

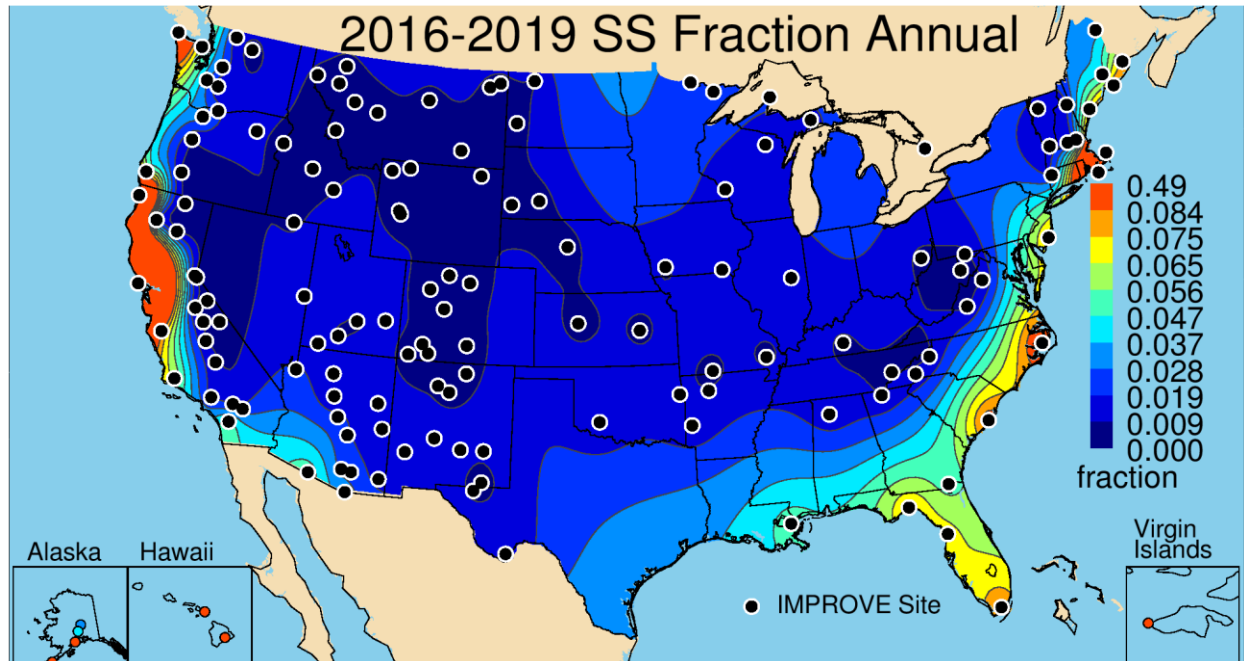
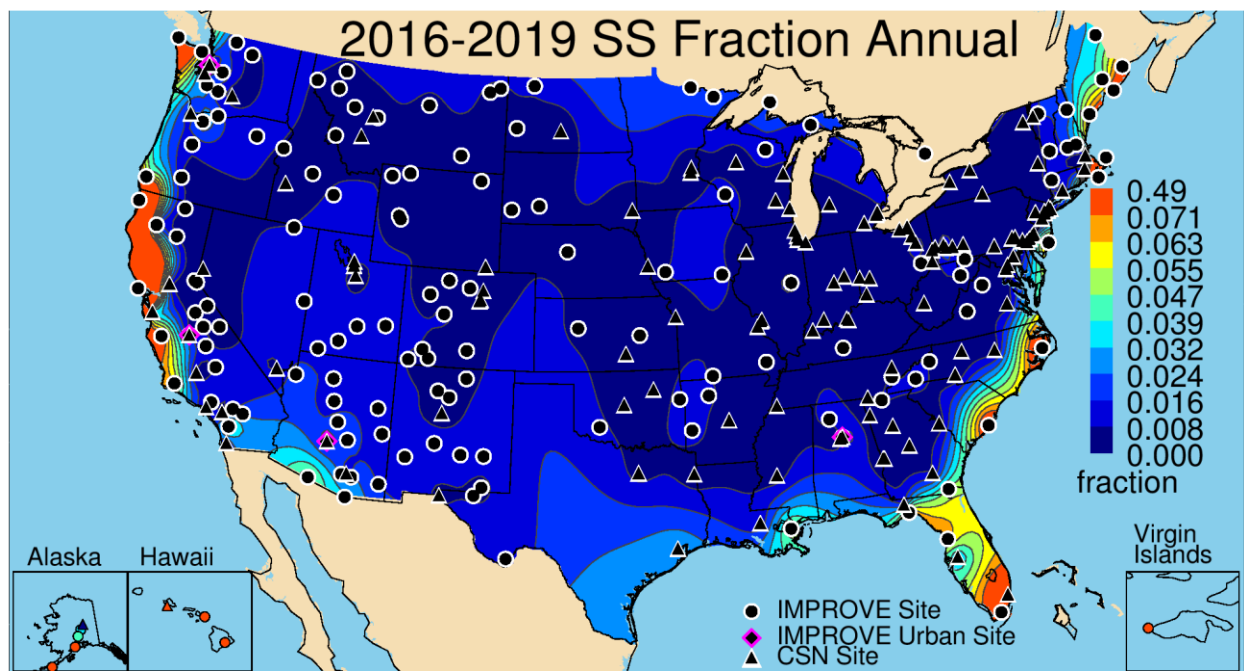


Figure 2.2.7c. IMPROVE 2016–2019 annual mean fraction contributions of sea salt to PM<sub>2.5</sub> reconstructed fine mass (RCFM).



**Figure 2.2.7d. IMPROVE and CSN 2016–2019 annual mean fraction contributions of sea salt (SS) to PM<sub>2.5</sub> reconstructed fine mass (RCFM).**

## 2.2.8 PM<sub>2.5</sub> Gravimetric Fine Mass

Gravimetric PM<sub>2.5</sub> mass concentrations (FM) are determined by pre- and post-weighing of Teflon filters. Teflon filters have known sampling artifacts. For example, nitrate loss and volatilization of some organic species contribute to negative artifacts (e.g., Hering and Cass, 1999; Chow et al., 2005; Watson et al., 2009; Chow et al., 2010), while positive artifacts correspond to retention of water associated with hygroscopic species (Frank, 2006; Hand et al., 2019b). Due to budget considerations, at the end of 2014, gravimetric analysis was no longer performed on CSN filters. Instead, gravimetric PM<sub>2.5</sub> data from the EPA's FRM samplers at collocated CSN sites were used.

The spatial pattern of 2016–2019 annual mean IMPROVE FM concentrations reflected the combined patterns of annual mean concentrations of AS, AN, and POM (see Figure 2.2.8a). The highest IMPROVE annual mean FM concentrations occurred in Nogales, Arizona ( $8.55 \mu\text{g m}^{-3}$ , NOGA1), where the maximum  $f_{\text{abs}}$ , EC, and FD concentrations occurred. The second-highest annual mean FM occurred at Sequoia NP, California ( $7.52 \mu\text{g m}^{-3}$ , SEQU1). Sites in the central and eastern United States also had relatively high annual mean FM concentrations ( $>5.6 \mu\text{g m}^{-3}$ ). In addition, sites in California's Central Valley had higher concentrations. The lowest FM concentrations occurred in the Intermountain West, and the lowest annual mean concentration occurred in Denali NP, Alaska ( $1.24 \mu\text{g m}^{-3}$ , DENA1).

The urban FM concentrations measured by the CSN network were somewhat higher than the IMPROVE concentrations, especially at sites in the central and eastern United States (Figure 2.2.8b). High annual mean urban FM was also observed at sites in the Central Valley of California, where the highest urban annual mean FM ( $13.57 \mu\text{g m}^{-3}$ ) occurred at Fresno (060190011). Several hot spots of annual mean FM occurred at urban sites across the West, such

as Denver, Colorado; El Paso, Texas; Salt Lake City, Utah; Butte, Montana; and Yakima, Washington. The lowest CSN annual mean FM concentration ( $3.43 \mu\text{g m}^{-3}$ ) occurred at White Face, New York (360310003).

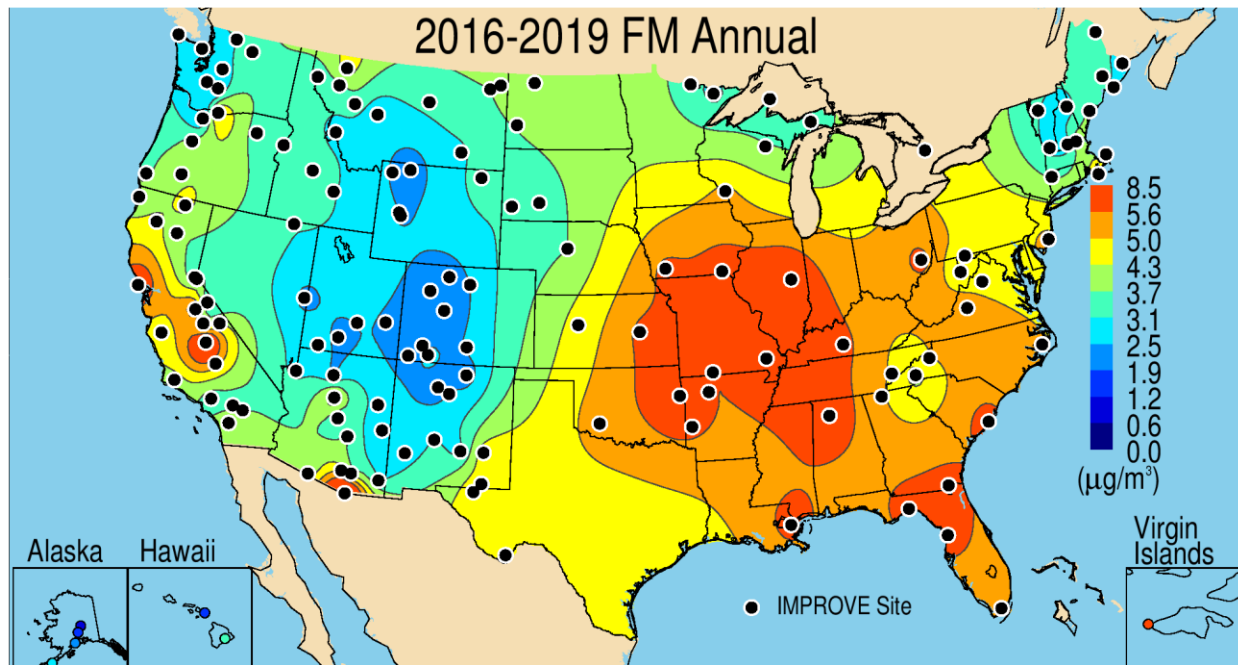


Figure 2.2.8a. IMPROVE 2016–2019 PM<sub>2.5</sub> annual mean gravimetric fine mass (FM) concentrations ( $\mu\text{g m}^{-3}$ ).

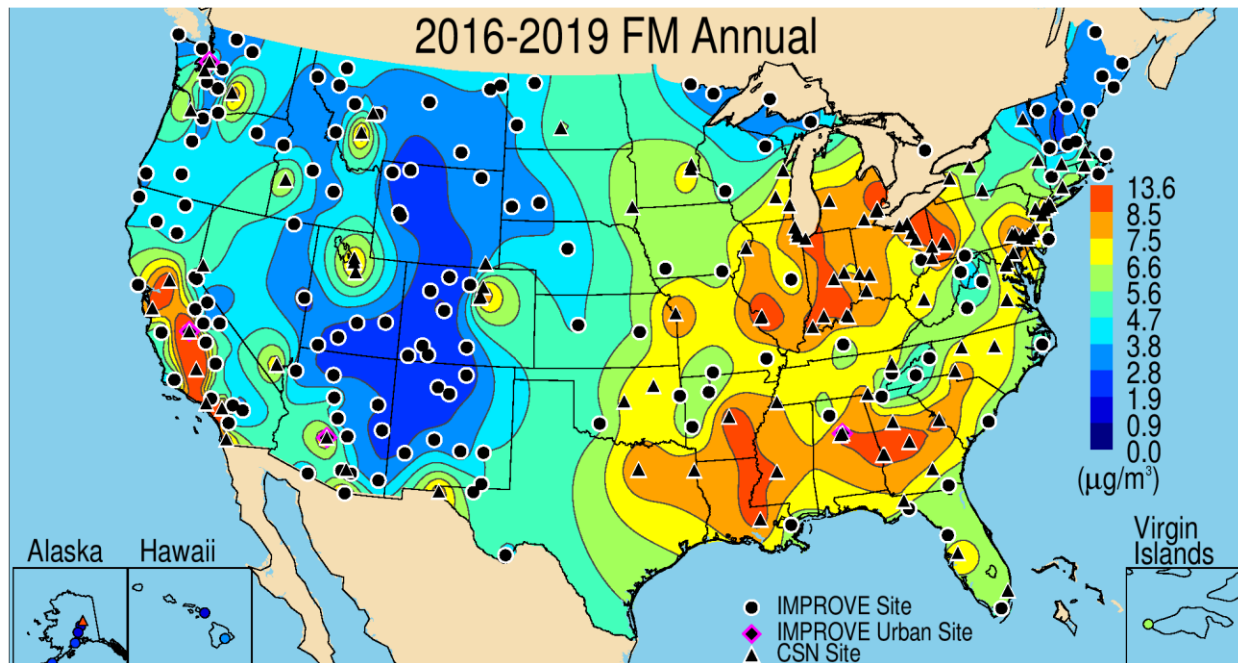


Figure 2.2.8b. IMPROVE and CSN 2016–2019 PM<sub>2.5</sub> annual mean gravimetric fine mass (FM) concentrations ( $\mu\text{g m}^{-3}$ ).

## 2.2.9 PM<sub>2.5</sub> Reconstructed Fine Mass

RCFM is the sum of AS, AN, POM, EC, FD, and SS. RCFM should equal FM if the assumptions regarding molecular forms of species are appropriate and if there are minimal biases associated with the measurements.

The spatial patterns of annual mean RCFM generally followed those of FM patterns, although different scales may affect the appearance (Figure 2.2.9a). For example, sites with highest annual mean RCFM were in the central United States and along the Central Valley of California. The maximum annual mean RCFM also occurred in Nogales, Arizona ( $9.34 \mu\text{g m}^{-3}$ ), as did the maximum for FM. The second-highest RCFM occurred at Everglades NP, Florida ( $8.7 \mu\text{g m}^{-3}$ , EVER1). In the continental United States, sites in the Intermountain West had the lowest annual mean RCFM. The minimum annual mean RCFM occurred in Haleakala Crater NP, Hawaii ( $1.15 \mu\text{g m}^{-3}$ , HACR1). The urban CSN annual mean RCFM ranged from  $2.75 \mu\text{g m}^{-3}$  at Kapolei, Hawaii (150030010), to  $14.21 \mu\text{g m}^{-3}$  at Bakersfield in California's Central Valley (060290014) (Figure 2.2.9b).

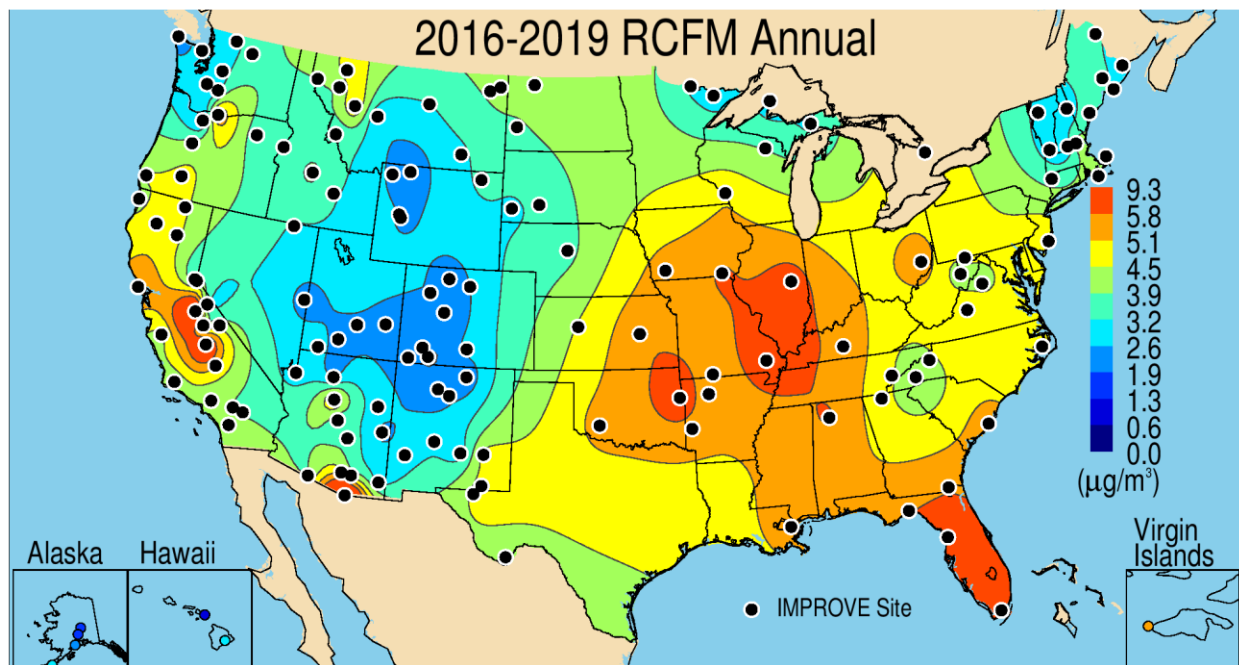
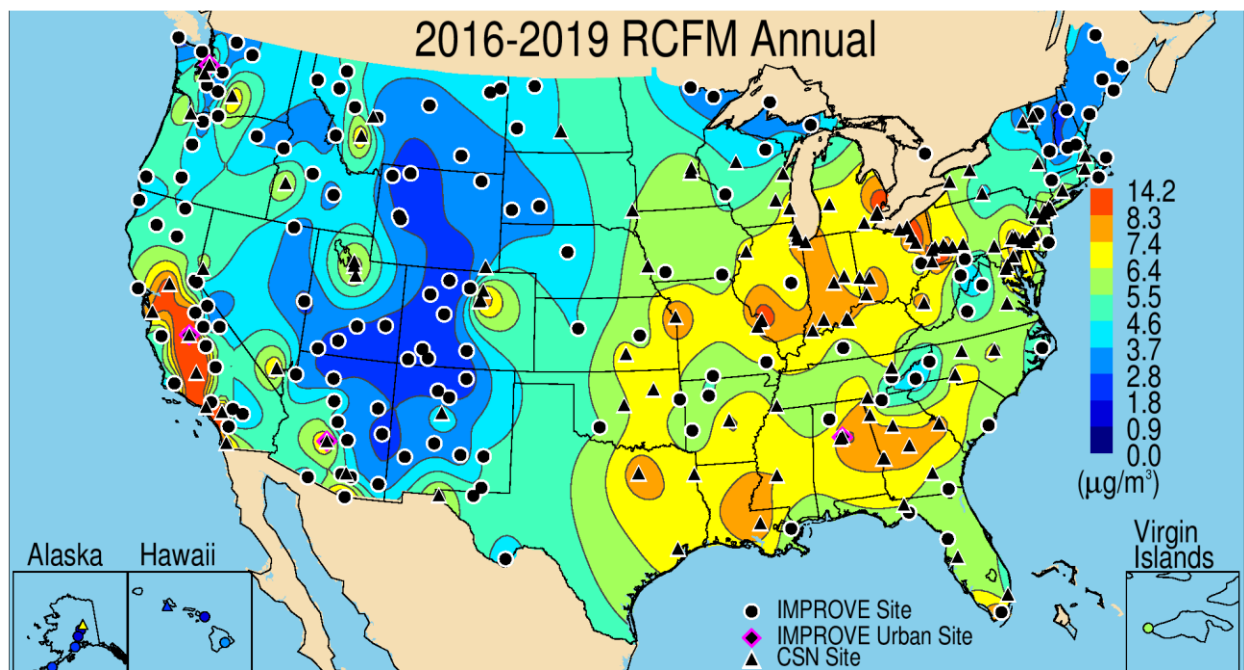


Figure 2.2.9a. IMPROVE 2016–2019 PM<sub>2.5</sub> annual mean reconstructed fine mass (RCFM) concentrations ( $\mu\text{g m}^{-3}$ ).



**Figure 2.2.9b. IMPROVE and CSN 2016–2019 PM<sub>2.5</sub> annual mean reconstructed fine mass (RCFM) concentrations ( $\mu\text{g m}^{-3}$ ).**

## 2.2.10 PM<sub>2.5</sub> Residual

The residual in fine mass (FM - RCFM) was computed to investigate the level of agreement between RCFM and measured FM concentrations. Differences may be related to the sampling artifacts associated with FM as discussed earlier, such as loss of volatile species or retained water on the filter. Biases could be related to inappropriate molecular forms of assumed species applied in the RCFM algorithm. For example, sulfate could be in a more acidic form, nitrate could be associated with coarse mode species, and OM/OC ratios used to derive POM could be inappropriate, as could the FD algorithm. A detailed investigation into biases associated with FM measurements is presented in Appendix 2.1 and by Hand et al. (2019b). The results from this study informed the changes in the RCFM algorithm included in Table 2.1, specifically regarding calculations of POM and FD.

The residual for most of the rural IMPROVE sites (Figure 2.2.10a) ranged from -3.27 µg m<sup>-3</sup> at Everglades NP, Florida (EVER1), to 0.78 µg m<sup>-3</sup> at Point Reyes NP, California (PORE1). The estimated uncertainty in the residual is 0.1 µg m<sup>-3</sup> (Hand et al., 2019b) based on uncertainty estimates reported in Hyslop and White (2008). The highest annual mean residuals that occurred at sites in the eastern United States may be associated with particle bound water on filters laden with AS (Hand et al., 2019b). Some of the most-negative residuals occurred in the Northwest regions that were influenced by biomass smoke during this period. It is possible that the OM/OC ratio used to compute POM were too low for the smoke conditions at these sites. Negative residuals at sites in southern and central California may also be associated with losses of nitrate from the Teflon filters used to measure gravimetric mass.

Interpretation of the residual for CSN has the added complication of different samplers used to collect filters for gravimetric weighing and for speciated analyses, which could introduce

additional sampling biases and contribute to larger residuals. The annual mean residual at CSN sites ranged from  $-2.05 \mu\text{g m}^{-3}$  at Five Points, Ohio (391530023), to  $1.78 \mu\text{g m}^{-3}$  at Parr, Arkansas (051190007). The general spatial pattern in the annual mean residual of the combined IMPROVE-CSN data was similar to IMPROVE-only, with higher residuals at sites in the East and lower residuals at sites in the West (Figure 2.2.10b). Urban sites in the West associated with positive residuals corresponded to Salt Lake City, Utah; Butte, Montana; and Yakima, Washington.

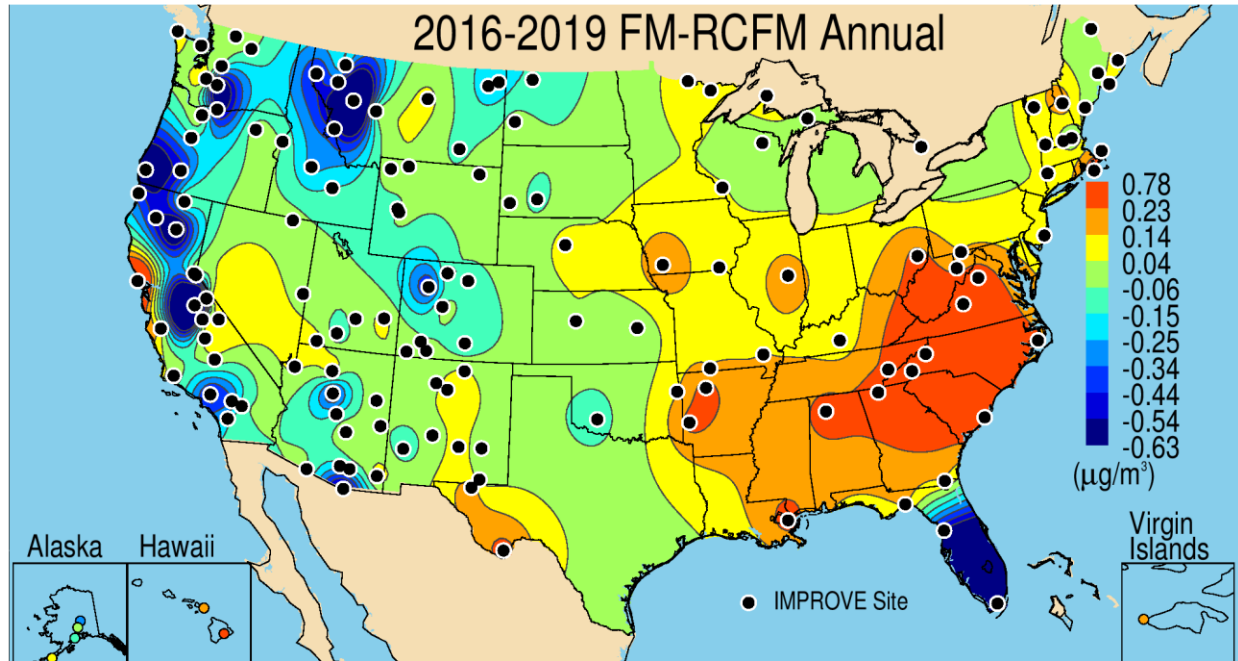
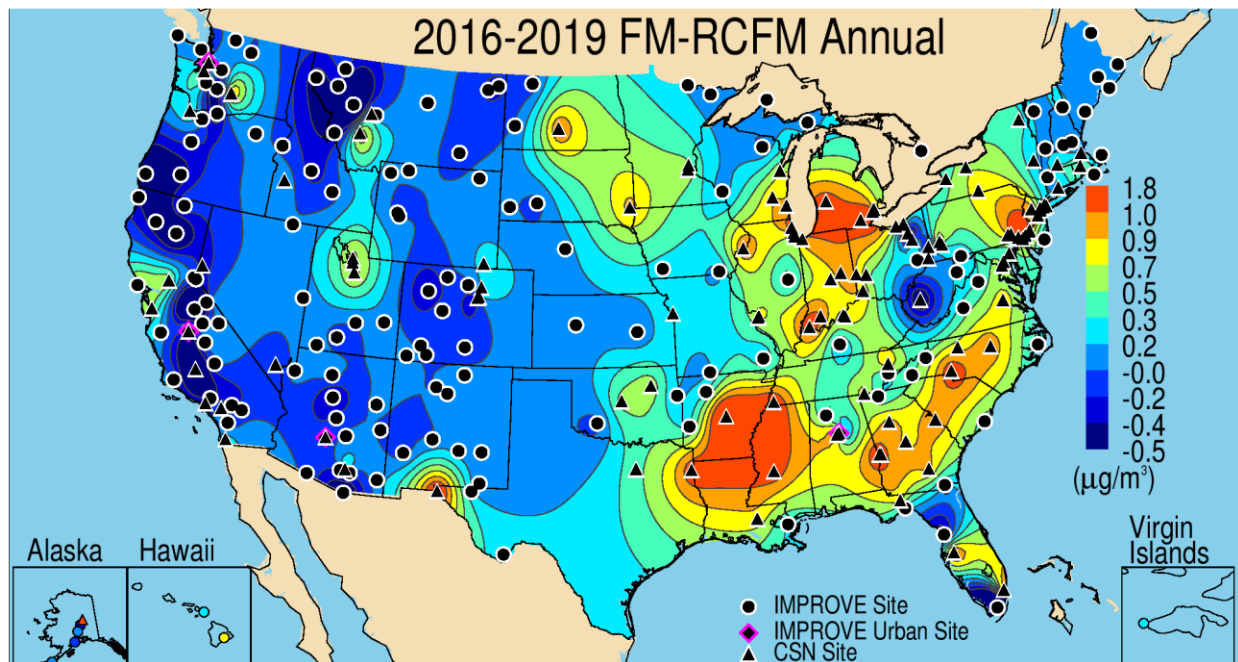


Figure 2.2.10a. IMPROVE 2016–2019 annual mean PM<sub>2.5</sub> residuals (FM - RCFM) between PM<sub>2.5</sub> gravimetric fine mass (FM) and reconstructed fine mass (RCFM) ( $\mu\text{g m}^{-3}$ ).



**Figure 2.2.10b. IMPROVE and CSN 2016–2019 annual mean PM<sub>2.5</sub> residuals (FM - RCFM) between PM<sub>2.5</sub> gravimetric fine mass (FM) and reconstructed fine mass (RCFM) ( $\mu\text{g m}^{-3}$ ).**

## 2.2.11 PM<sub>10</sub> Mass

PM<sub>10</sub> concentrations are not routinely measured at CSN sites; therefore EPA's FRM PM<sub>10</sub> samplers were used for urban PM<sub>10</sub> concentrations. These data are reported at standard pressure and temperature (STP) and therefore were adjusted to local conditions for comparison with IMPROVE PM<sub>10</sub> data (see Hand et al., 2019b). Completeness criteria were applied following the description given above for speciated data, resulting in 399 PM<sub>10</sub> sites. PM<sub>10</sub> concentrations include contributions from PM<sub>2.5</sub> species, in addition to contributions from coarse mode species. Therefore, spatial patterns may be similar to the PM<sub>2.5</sub> concentrations depending on location and sources but may differ in locations where coarse mode contributions are significant.

The spatial pattern of 2016–2019 IMPROVE annual mean PM<sub>10</sub> mass concentrations are shown in Figure 2.2.11a. The highest annual mean concentrations occurred at sites in the central United States, along the southwest border with Mexico, and the Central Valley of California. The highest IMPROVE annual mean PM<sub>10</sub> concentration occurred at Nogales, Arizona ( $28.68 \mu\text{g m}^{-3}$ , NOGA1), and the second highest PM<sub>10</sub> concentration occurred at Virgin Islands NP ( $18.68 \mu\text{g m}^{-3}$ , VIIS1), likely due to high SS and FD contributions. The lowest annual mean IMPROVE PM<sub>10</sub> concentration occurred at Haleakala Crater NP, Hawaii ( $1.15 \mu\text{g m}^{-3}$ , HACR1). The spatial pattern of rural PM<sub>10</sub> concentrations generally followed the patterns of PM<sub>2.5</sub> concentrations, with higher values at sites in the eastern half of the United States, relatively low values at sites in the Intermountain/Southwest and Northwest, and increased values at sites in California. However, there are some important differences. Sites in the central United States had high PM<sub>10</sub> concentrations, suggesting additional coarse mass contributions in that region.

The combined IMPROVE and EPA PM<sub>10</sub> mass concentrations (Figure 2.2.11b) demonstrated higher spatial variability compared to the IMPROVE-only map, in part because of the higher EPA PM<sub>10</sub> site density. An overall similar pattern existed, with higher PM<sub>10</sub> concentrations at sites in the central United States, lower concentrations at sites in the Intermountain/Southwest and Northwest, and higher concentrations at sites along the U.S.–Mexico border and the Central Valley of California. Additional hot spots of high annual mean PM<sub>10</sub> concentrations also occurred near Denver, Colorado; El Paso, Texas; Mission and Edinburg, Texas; St. Louis, Missouri; and Minneapolis, Minnesota. The PM<sub>10</sub> concentrations were also much higher at the EPA sites, suggesting local sources. The urban PM<sub>10</sub> annual mean concentrations ranged from  $3.04 \mu\text{g m}^{-3}$  at Cornwall, Connecticut (090050005), to  $49.50 \mu\text{g m}^{-3}$  in Bakersfield, California (060290010).

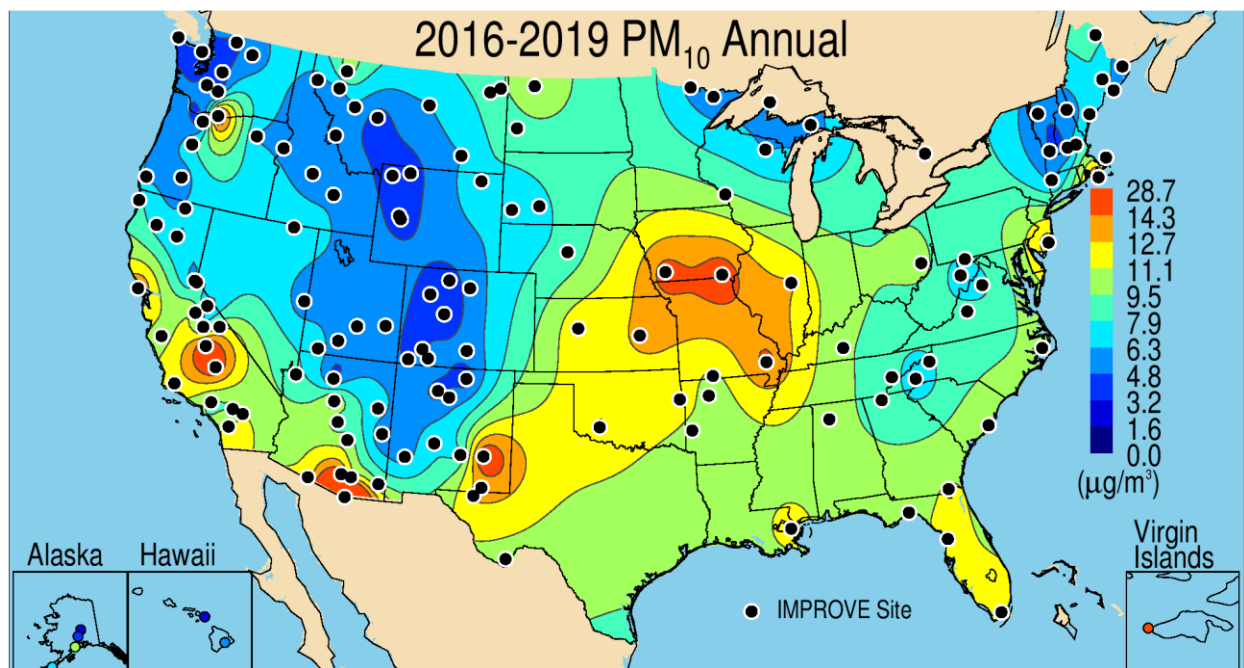


Figure 2.2.11a. IMPROVE 2016–2019 annual mean PM<sub>10</sub> mass ( $\mu\text{g m}^{-3}$ ).

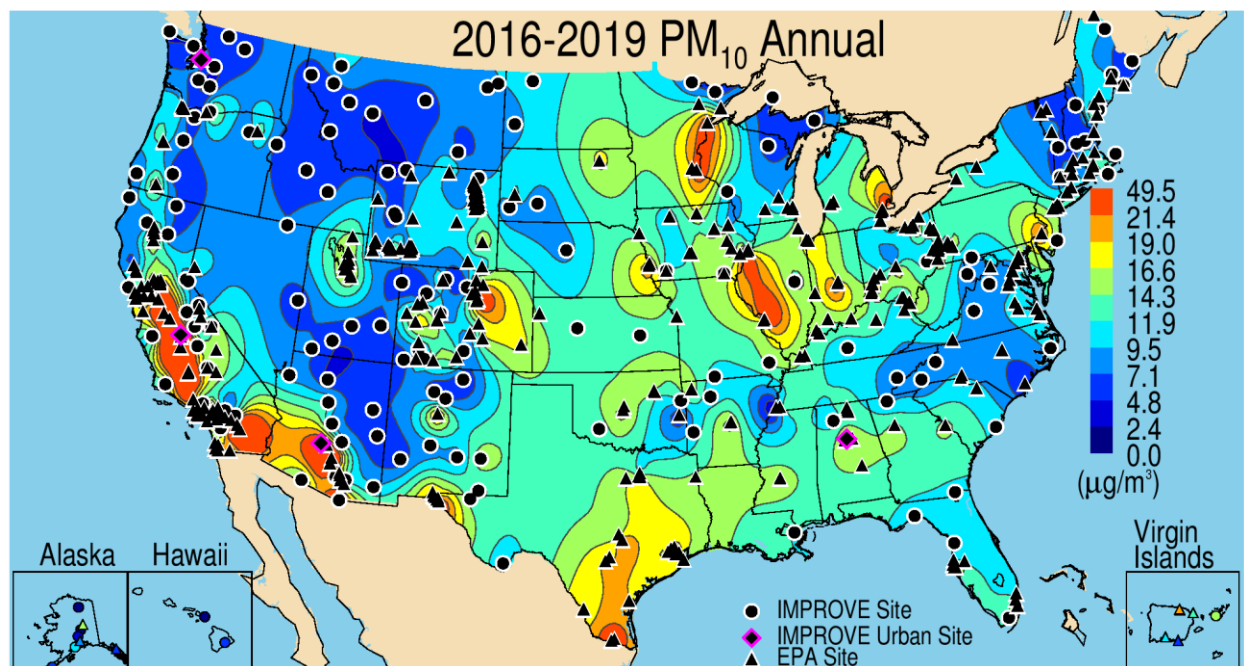


Figure 2.2.11b. IMPROVE and EPA 2016–2019 annual mean PM<sub>10</sub> mass ( $\mu\text{g m}^{-3}$ ).

## 2.2.12 Coarse Mass

CM concentrations are calculated as the difference between gravimetric PM<sub>10</sub> and PM<sub>2.5</sub> mass concentrations (PM<sub>10</sub> - PM<sub>2.5</sub>). Since PM<sub>10</sub> filters are not routinely analyzed for speciation, CM concentrations are also not speciated. CM concentrations were calculated at IMPROVE sites and at collocated urban/suburban EPA FRM PM<sub>2.5</sub> (not just CSN locations) and PM<sub>10</sub> sites, resulting in 198 EPA sites. CM is often assumed to be associated with mineral dust, although

other studies have shown it also could include ionic species such as sodium or nitrate, or organic carbon (e.g., Malm et al., 2007; Lee et al., 2008; Allen et al., 2015; Bondy et al., 2018; Hand et al., 2019b), with sources such as sea salt or biological particles.

The 2016–2019 annual mean rural CM concentrations ranged from  $0.97 \mu\text{g m}^{-3}$  in Haleakala Crater NP, Hawaii (HACR1), to  $20.09 \mu\text{g m}^{-3}$  in Nogales, Arizona (NOGA1) (Figure 2.2.12a), where the highest annual mean FD concentrations also occurred. The second-highest CM occurred at the Virgin Islands NP ( $13.12 \mu\text{g m}^{-3}$ , VIIS1). The spatial patterns of CM in the Southwest were similar to those of FD and suggest similar sources (Hand et al., 2017). Higher concentrations also occurred at sites in the California’s Central Valley. At sites in the central United States, higher concentrations most likely corresponded to agricultural activity and fugitive dust sources (Hand et al., 2019a; Lambert et al., 2020). Lower annual mean CM concentrations occurred at sites across the Intermountain West, the Northwest, and along the eastern United States into the Northeast.

The overall spatial patterns in urban annual mean CM concentrations (Figure 2.2.12b) were similar to those at rural sites, with higher values at sites in the central United States and along the U.S.–Mexico border and California’s Central Valley. Hot spots of CM concentrations were similar to hot spots in  $\text{PM}_{10}$  concentrations, such as at Salt Lake City, Utah; Denver, Colorado; and St. Louis, Missouri. The highest annual mean urban CM concentration ( $34.76 \mu\text{g m}^{-3}$ ) occurred at Bakersfield, California (060290010) and the lowest annual mean CM concentration ( $0.51 \mu\text{g m}^{-3}$ ) occurred at Castle Hayne, North Carolina (371290002), near Wilmington.

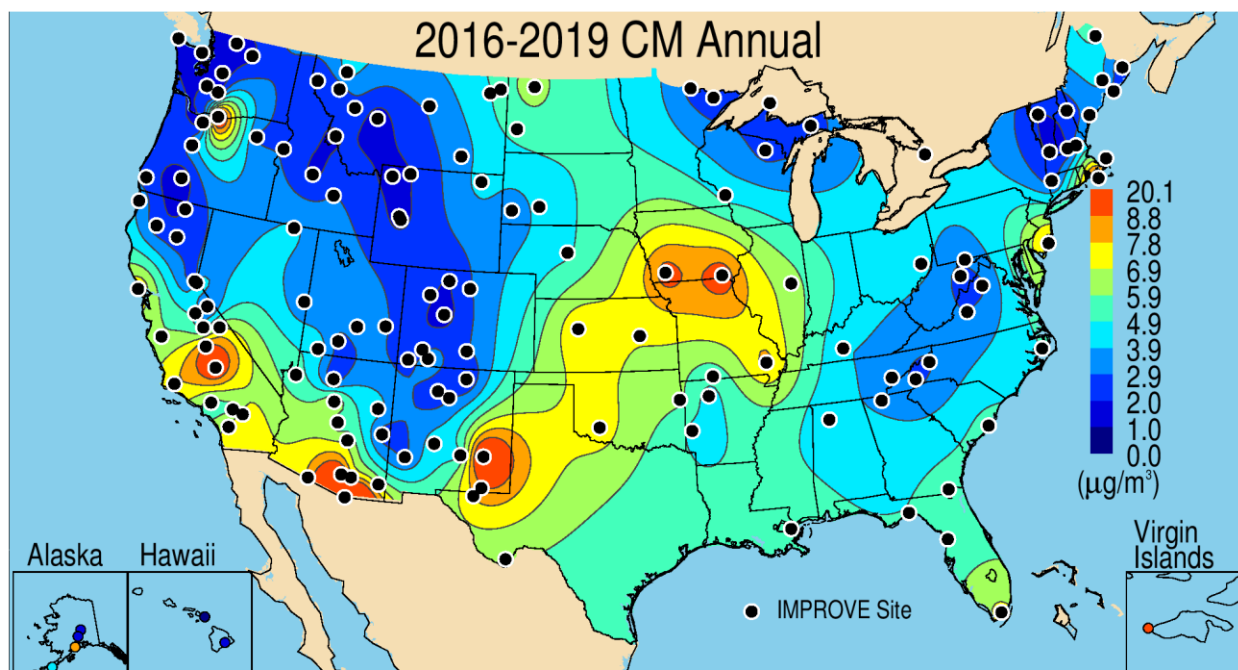
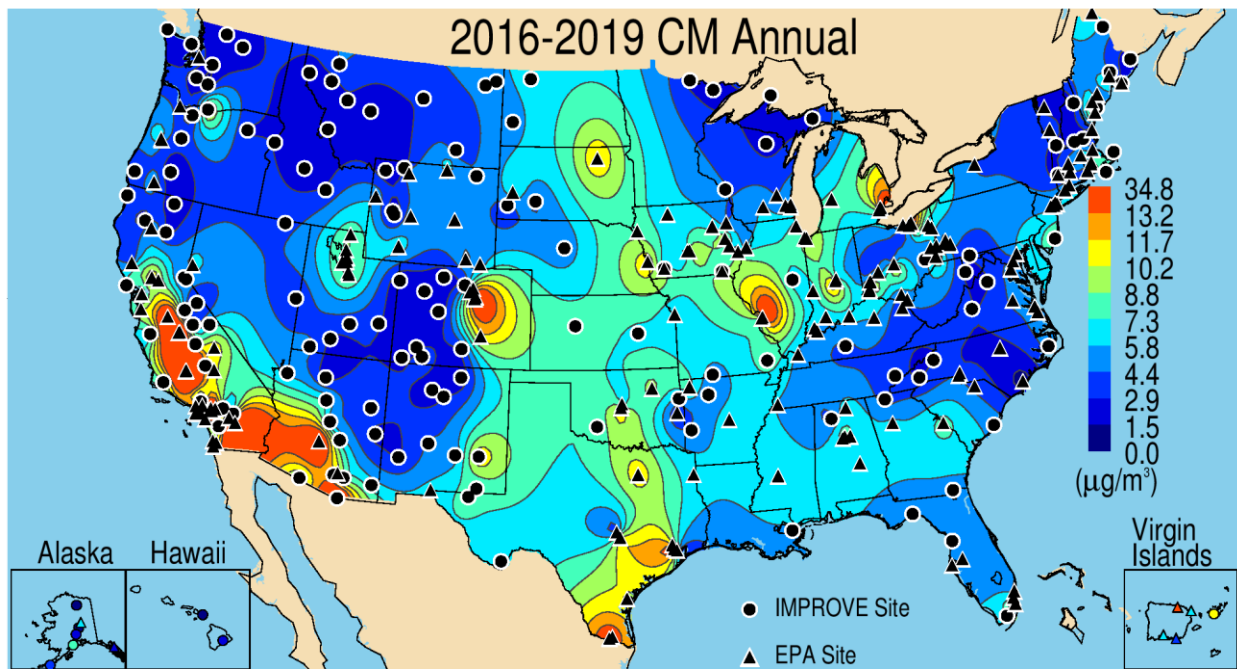


Figure 2.2.12a. IMPROVE 2016–2019 annual mean coarse mass (CM =  $\text{PM}_{10}$  -  $\text{PM}_{2.5}$ ) ( $\mu\text{g m}^{-3}$ ).



**Figure 2.2.12b. IMPROVE and EPA 2016–2019 annual mean coarse mass (CM =  $\text{PM}_{10}$  -  $\text{PM}_{2.5}$ ) ( $\mu\text{g m}^{-3}$ ).**

The fractional contribution of annual mean CM to  $\text{PM}_{10}$  ( $\text{CM}/\text{PM}_{10}$ ) shown in Figure 2.2.12c demonstrated the importance of CM to  $\text{PM}_{10}$  concentrations at rural sites, especially at sites in the central and southwestern United States. Over half of annual mean  $\text{PM}_{10}$  concentrations were due to CM for most of the sites in the central United States and for sites in portions of the Intermountain West. Sites in the Southwest had higher contributions, ranging from ~0.6 to 0.8. Contributions were lower at sites in the East and Northwest, with values around 0.3 to 0.4. The highest rural CM fraction (0.83) occurred at Kenai Peninsula Borough, Alaska (KPBO1), and the lowest contribution (0.2) occurred at Crater Lake NP, Oregon (CRLA1).

At urban EPA sites, the spatial variability of annual mean  $\text{CM}/\text{PM}_{10}$  was very similar to rural sites, with higher values at sites in the central United States and Southwest (Figure 2.2.12d). The addition of urban sites provided more spatial detail, especially in the East. The lowest annual mean contribution (0.18) occurred at Castle Hayne, North Carolina (371290002), near Wilmington, similar to the lowest annual mean urban CM concentration. The largest contribution (0.78) occurred at Indio, California (060652002), near the Salton Sea.

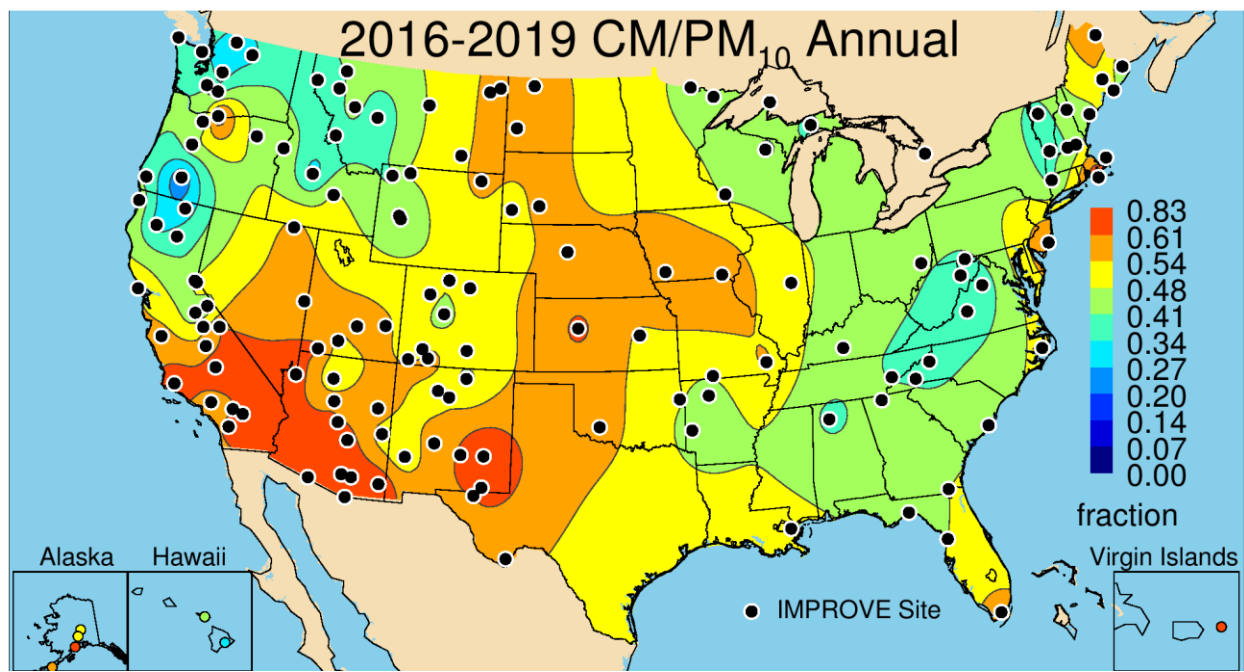


Figure 2.2.12c. IMPROVE 2016–2019 annual mean fraction contributions of CM to PM<sub>10</sub> gravimetric mass.

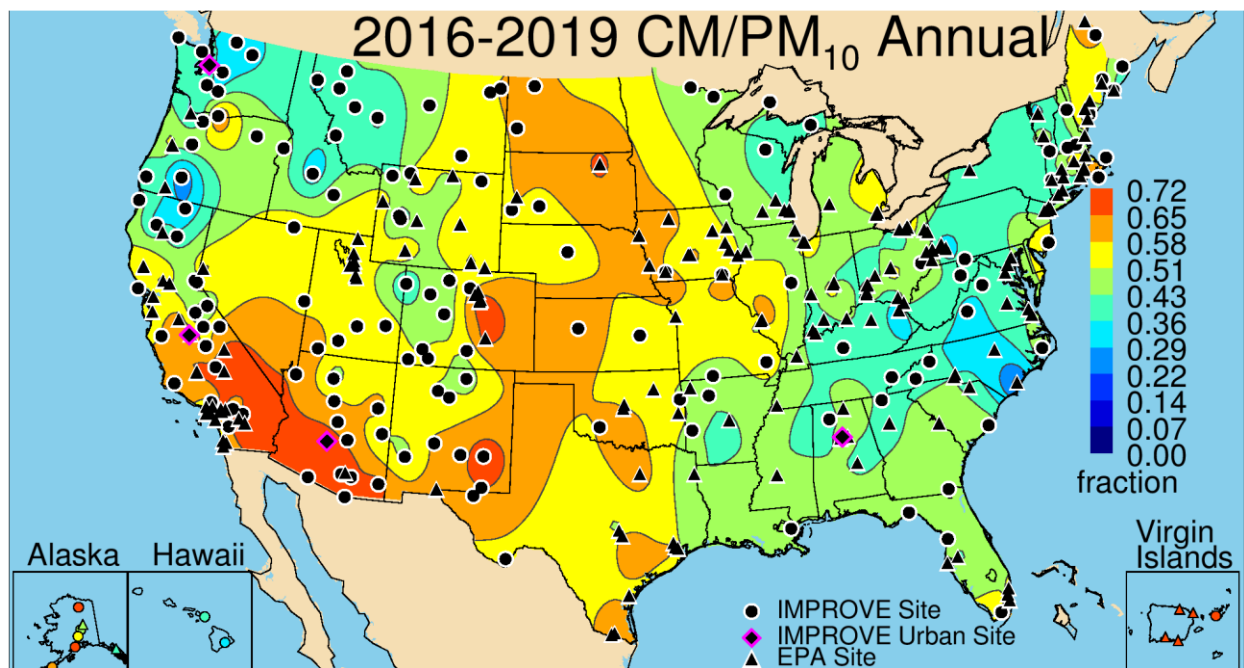


Figure 2.2.12d. IMPROVE and EPA 2016–2019 annual mean fraction contributions of CM to PM<sub>10</sub> gravimetric mass.

## 2.2.13 Summary

The spatial variability of FM depends on sources, sinks, and transport of speciated aerosols. A strong spatial gradient in FM was observed, with higher concentrations at sites in the eastern United States. FM decreased rapidly moving westward, with concentrations that were half of those at sites in the East, especially for sites in the Intermountain West. Higher concentrations occurred at sites in California and sites in Oregon and Washington. The spatial

patterns did not change significantly with the addition of urban sites, although urban concentrations were higher, including several hot spots at sites in the West, and at sites in the Central Valley of California. The lowest concentrations of annual mean FM occurred at sites in the Intermountain West and Southwest and at sites in the Northeast. FM and PM<sub>10</sub> had similar spatial variability, except that rural PM<sub>10</sub> concentrations were highest at sites in the central United States, rather than for sites throughout the East. The addition of urban PM<sub>10</sub> sites suggested additional urban sources, with much higher annual mean PM<sub>10</sub> concentrations at sites in the central United States, southern Arizona, southern Texas, the Front Range of Colorado, southern California, and the Central Valley of California.

The spatial patterns of FM reflected the combined patterns of AS, AN, and POM. AS concentrations were highest in the eastern United States, where SO<sub>2</sub> emissions were highest, and AS contributed significantly to FM in those regions (~0.3). Rural AN concentrations were highest at sites in the central United States and contributed to high FM at sites in that region (0.2–0.3). Additional urban sources influenced urban FM sites at regions in the Central Valley of California, as well as other urban hot spots in the West.

Rural POM concentrations were highest at sites in the northwestern United States, where biomass smoke impacts influenced concentrations, and at sites in the eastern United States, due to biogenic emissions and biomass smoke. The lowest annual mean POM concentrations occurred at sites in the Intermountain West and Southwest. The general spatial patterns of urban and rural POM concentration were similar to rural-only patterns, although higher urban concentrations occurred at sites in Southeast and Central Valley. Contributions of POM to RCFM were significant at sites in the western United States, around 0.7 or greater, and this fraction was similar for CSN sites. At sites in the eastern United States, contributions at CSN sites was around 0.6 or greater, while for rural sites it was around 0.5. Annual mean EC concentrations followed similar patterns to those of POM concentrations at rural sites, with higher concentrations at sites both in the eastern and western United States. Urban EC concentrations were considerably higher than at rural sites, indicating the importance of localized urban sources. Contributions of EC to RCFM at urban sites were roughly double relative to at rural sites (~0.1 relative to ~0.05). Filter light absorption ( $f_{abs}$ ) was also higher at sites with elevated EC concentrations, suggesting that most of the PM<sub>2.5</sub> absorption was due to EC, although it was somewhat elevated at sites in the Southwest, perhaps due to the role of iron absorption in dust.

The spatial pattern of FD mass reflected its source areas, with high concentrations at both rural and urban sites in the Southwest, where local and regional sources affect FD concentrations. Sites in the Central Valley also had high FD concentrations, especially for urban sites. Higher annual mean FD at sites in the Southeast reflected the influence of North African dust transport to that area, both for rural and urban sites. FD contributions to RCFM at sites in the Southwest were over 0.5 for many sites in the region. The spatial variability in annual mean CM was similar to FD, especially for sites in the Southwest, suggesting similar sources. However, higher annual mean CM at sites in the central United States, relative to FD patterns, suggested additional sources of coarse-mode aerosol or larger size distributions of dust relative to sources in the Southwest. Urban sites with high CM concentrations occurred in the Central Valley and southern Arizona. CM contributed significantly to PM<sub>10</sub>, especially at sites in the western United States, where annual mean contributions were over 0.6. For sites in the eastern

United States, the contribution of CM to PM<sub>10</sub> was ~0.3–0.4. Similar contributions occurred for sites in the Northwest.

SS concentrations, while likely underestimated, also followed suspected marine sources, with higher values along coastal areas for both IMPROVE and CSN sites. SS contributions could be significant (>0.1) at some sites, especially in Alaska and Hawaii, and along the coasts.

The spatial pattern in the annual mean fine mass residuals indicated potential biases associated with the measurements or reconstruction algorithms. Positive residuals at sites in the eastern United States were likely associated with the influence of particle bound water on gravimetric mass measurements from hygroscopic species. In the northwestern United States, sites with negative residuals likely reflected the impact of biomass burning on POM, indicating that the assumed OM/OC ratio may have been too low to account for the wildfire smoke sources of POM.

Tables listing 2016–2019 annual mean concentrations for each site for the IMPROVE network and the CSN are provided in Appendix 2.2. Annual mean PM<sub>2.5</sub> mass fractions are listed according to site for the IMPROVE network and the CSN in Appendix 2.3.

## REFERENCES

- Aiken, A. C., Decarlo, P. F., Kroll, J. H., Worsnop, D. R., Huffman, J. A., Docherty, K. S., Ulbrich, I. M., Mohr, C., Kimmel, J. R., and Sueper, D. (2008), O/C and OM/OC ratios of primary, secondary, and ambient organic aerosols with high-resolution time-of-flight aerosol mass spectrometry, *Environmental Science & Technology*, 42(12), 4478-4485, doi:10.1021/es703009q.
- Allen, H. M., Draper, D. C., Ayres, B. R., Ault, A., Bondy, A., Takahama, S., Modini, R. L., Baumann, K., Edgerton, E., Knote, C., Laskin, A., Wang, B., and Fry, J. L. (2015), Influence of crustal dust and sea spray supermicron particle concentrations and acidity on inorganic NO<sub>3</sub>- aerosol during the 2013 Southern Oxidant and Aerosol Study, *Atmospheric Chemistry and Physics*, 15(18), 10669-10685, doi:10.5194/acp-15-10669-2015.
- Bae, M.-S., Demerjian, K. L., and Schwab, J. J. (2006), Seasonal estimation of organic mass to organic carbon in PM2. 5 at rural and urban locations in New York state, *Atmospheric Environment*, 40(39), 7467-7479, <https://doi.org/10.1016/j.atmosenv.2006.07.008>.
- Blanchard, C., Hidy, G., Shaw, S., Baumann, K., and Edgerton, E. (2016), Effects of emission reductions on organic aerosol in the southeastern United States, *Atmospheric Chemistry and Physics*, 16(1), 215-238, doi:10.5194/acp-16-215-2016.
- Bond, T. C., Doherty, S. J., Fahey, D. W., Forster, P. M., Berntsen, T., DeAngelo, B. J., Flanner, M. G., Ghan, S., Kärcher, B., and Koch, D. (2013), Bounding the role of black carbon in the climate system: A scientific assessment, *Journal of Geophysical Research: Atmospheres*, 118(11), 5380-5552, doi:10.1002/jgrd.50171.
- Bondy, A. L., Bonanno, D., Moffet, R. C., Wang, B., Laskin, A., and Ault, A. P. (2018), The diverse chemical mixing state of aerosol particles in the southeastern United States, *Atmospheric Chemistry and Physics*, 18(16), 12595-12612, doi:10.5194/acp-18-12595-2018.
- Bozlaker, A., Prospero, J. M., Price, J., and Chellam, S. (2019), Identifying and quantifying the impacts of advected North African dust on the concentration and composition of airborne fine particulate matter in Houston and Galveston, Texas, *Journal of Geophysical Research: Atmospheres*, 124(22), 12282-12300, doi:<https://doi.org/10.1029/2019JD030792>.
- Chen, Y., Shen, H., and Russell, A. G. (2019), Current and future responses of aerosol ph and composition in the US to declining SO<sub>2</sub> emissions and increasing NH<sub>3</sub> emissions, *Environmental Science & Technology*, 53(16), 9646-9655, doi:10.1021/acs.est.9b02005.
- Chow, J. C., Watson, J. G., Lowenthal, D. H., and Magliano, K. L. (2005), Loss of PM2.5 nitrate from filter samples in central California, *Journal of the Air & Waste Management Association*, 55(8), 1158-1168, doi:10.1080/10473289.2005.10464704.
- Chow, J., Watson, J., Chen, L.-W., Rice, J., and Frank, N. (2010), Quantification of PM 2.5 organic carbon sampling artifacts in US networks, *Atmospheric Chemistry and Physics*, 10(12), 5223-5239, doi:<https://doi.org/10.5194/acp-10-5223-2010>.
- Creamean, J. M., Spackman, J. R., Davis, S. M., and White, A. B. (2014), Climatology of long-range transported Asian dust along the West Coast of the United States, *Journal of Geophysical Research: Atmospheres*, 119(21), 12,171-112,185, doi:10.1002/2014JD021694.

Debell, L. J., Gebhart, K., Hand, J. L., Malm, W. C., Pitchford, M. L., Schichtel, B. S., and White, W. H. (2006), IMPROVE (Interagency Monitoring of Protected Visual Environments): Spatial and seasonal patterns and temporal variability of haze and its constituents in the United States: Report IV, Colorado State University, Fort Collins CO, ISSN 0737-5352-74.

El-Zanan, H. S., Lowenthal, D. H., Zielinska, B., Chow, J. C., and Kumar, N. (2005), Determination of the organic aerosol mass to organic carbon ratio in IMPROVE samples, *Chemosphere*, 60(4), 485-496, doi:10.1016/j.chemosphere.2005.01.005.

El-Zanan, H. S., Zielinska, B., Mazzoleni, L. R., and Hansen, D. A. (2009), Analytical determination of the aerosol organic mass-to-organic carbon ratio, *Journal of the Air & Waste Management Association*, 59(1), 58-69, doi: 10.3155/1047-3289.59.1.58.

Evanoski-Cole, A., Gebhart, K., Sive, B., Zhou, Y., Capps, S., Day, D., Prenni, A., Schurman, M., Sullivan, A., and Li, Y. (2017), Composition and sources of winter haze in the Bakken oil and gas extraction region, *Atmospheric Environment*, 156, 77-87, <http://dx.doi.org/10.1016/j.atmosenv.2017.02.019>.

Frank, N. H. (2006), Retained nitrate, hydrated sulfates, and carbonaceous mass in federal reference method fine particulate matter for six eastern US cities, *Journal of the Air & Waste Management Association*, 56(4), 500-511, <https://doi.org/10.1080/10473289.2006.10464517>.

Gebhart, K. A., Day, D. E., Prenni, A. J., Schichtel, B. A., Hand, J. L., and Evanoski-Cole, A. R. (2018), Visibility impacts at Class I areas near the Bakken oil and gas development, *Journal of the Air & Waste Management Association*, 68(5), 477-493, doi:10.1080/10962247.2018.1429334.

Hallar, A. G., Lowenthal, D. H., Clegg, S. L., Samburova, V., Taylor, N., Mazzoleni, L. R., Zielinska, B. K., Kristensen, T. B., Chirokova, G., and McCubbin, I. B. (2013), Chemical and hygroscopic properties of aerosol organics at Storm Peak Laboratory, *Journal of Geophysical Research: Atmospheres*, 118(10), 4767-4779, doi:10.1002/jgrd.50373.

Hand, J., Kreidenweis, S., Sherman, D. E., Collett Jr, J., Hering, S., Day, D., and Malm, W. (2002), Aerosol size distributions and visibility estimates during the Big Bend regional aerosol and visibility observational (BRAVO) study, *Atmospheric Environment*, 36(32), 5043-5055, [https://doi.org/10.1016/S1352-2310\(02\)00568-X](https://doi.org/10.1016/S1352-2310(02)00568-X).

Hand, J. L., and Malm, W. C. (2006), Review of the IMPROVE equation for estimating ambient light extinction coefficients, Colorado State University, Fort Collins, CO, ISSN 0737-5352-71.

Hand, J. L., Copeland, S., Day, D., Dillner, A., Indresand, H., Malm, W., McDade, C., Moore, C., Pitchford, M., and Schichtel, B. (2011), IMPROVE (Interagency Monitoring of Protected Visual Environments): Spatial and seasonal patterns and temporal variability of haze and its constituents in the United States, Report V, Colorado State University, Fort Collins, CO.

Hand, J. L., White, W., Gebhart, K., Hyslop, N., Gill, T., and Schichtel, B. (2016), Earlier onset of the spring fine dust season in the southwestern United States, *Geophysical Research Letters*, 43(8), 4001-4009, doi:10.1002/2016GL068519.

Hand, J. L., Gill, T., and Schichtel, B. (2017), Spatial and seasonal variability in fine mineral dust and coarse aerosol mass at remote sites across the United States, *Journal of Geophysical Research: Atmospheres*, 122(5), 3080-3097, doi:10.1002/2016JD026290.

Hand, J. L., Gill, T. E., and Schichtel, B. A. (2019a), Urban and rural coarse aerosol mass across the United States: Spatial and seasonal variability and long-term trends, *Atmospheric Environment*, 218, 117025, doi.org/10.1016/j.atmosenv.2019.117025.

Hand, J. L., Prenni, A. J., Schichtel, B. A., Malm, W. C., and Chow, J. C. (2019b), Trends in remote PM<sub>2.5</sub> residual mass across the United States: Implications for aerosol mass reconstruction in the IMPROVE network, *Atmospheric Environment*, 203, 141-152, doi:doi:10.1016/j.atmosenv.2019.01.049.

Hand, J. L., Prenni, A. J., Copeland, S., Schichtel, B. A., and Malm, W. C. (2020), Thirty years of the Clean Air Act Amendments: Impacts on haze in remote regions of the United States (1990–2018), *Atmospheric Environment*, 243, 117865, <https://doi.org/10.1016/j.atmosenv.2020.117865>.

Heald, C. L., Collett Jr, J., Lee, T., Benedict, K., Schwandner, F., Li, Y., Clarisse, L., Hurtmans, D., Van Damme, M., and Clerbaux, C. (2012), Atmospheric ammonia and particulate inorganic nitrogen over the United States, *Atmospheric Chemistry and Physics*, 12, 10295-10312, doi:10.5194/acp-12-10295-2012.

Heald, C. L., and Kroll, J. (2020), The fuel of atmospheric chemistry: Toward a complete description of reactive organic carbon, *Science Advances*, 6(6), eaay8967, doi:10.1126/sciadv.aay8967.

Hering, S., and Cass, G. (1999), The magnitude of bias in the measurement of PM<sub>2.5</sub> arising from volatilization of particulate nitrate from Teflon filters, *Journal of the Air & Waste Management Association*, 49(6), 725-733, doi:10.1080/10473289.1999.10463843.

Hidy, G., Blanchard, C., Baumann, K., Edgerton, E., Tanenbaum, S., Shaw, S., Knipping, E., Tombach, I., Jansen, J., and Walters, J. (2014), Chemical climatology of the southeastern United States, 1999–2013, *Atmospheric Chemistry and Physics*, 14(21), 11893-11914, doi:10.5194/acp-14-11893-2014.

Hu, C., Griffis, T. J., Baker, J. M., Wood, J. D., Millet, D. B., Yu, Z., and Lee, X. (2020), Modeling the sources and transport processes during extreme ammonia episodes in the US corn belt, *Journal of Geophysical Research: Atmospheres*, 125, e2019JD031207, <http://doi.org/10.1029/2019JD031207>.

Husar, R. B., Tratt, D., Schichtel, B. A., Falke, S., Li, F., Jaffe, D., Gasso, S., Gill, T., Laulainen, N. S., and Lu, F. (2001), Asian dust events of April 1998, *Journal of Geophysical Research: Atmospheres*, 106(D16), 18317-18330.

Hyslop, N. P., and White, W. H. (2008), An evaluation of interagency monitoring of protected visual environments (IMPROVE) collocated precision and uncertainty estimates, *Atmospheric Environment*, 42(11), 2691-2705, doi:10.1016/j.atmosenv.2007.06.053.

Isaaks, E. H., and Mohan Srivastava, R. (1989), *An Introduction to Applied Geostatistics*, Oxford University Press, New York, ISBN 978-0195050134.

Jimenez, J. L., Canagaratna, M., Donahue, N., Prevot, A., Zhang, Q., Kroll, J. H., DeCarlo, P. F., Allan, J. D., Coe, H., and Ng, N. (2009), Evolution of organic aerosols in the atmosphere, *Science*, 326(5959), 1525-1529, doi:10.1126/science.1180353.

Kim, P. S., Jacob, D. J., Fisher, J. A., Travis, K., Yu, K., Zhu, L., Yantosca, R. M., Sulprizio, M., Jimenez, J. L., and Campuzano-Jost, P. (2015), Sources, seasonality, and trends of southeast US aerosol: an integrated analysis of surface, aircraft, and satellite observations with the GEOS-Chem chemical transport model, *Atmospheric Chemistry and Physics*, 15(18), 10411-10433, doi: 10.5194/acp-15-10411-2015.

Kim, D., Chin, M., Cruz, C. A., Tong, D., and Yu, H. (2021), Spring dust in western North America and its interannual variability—understanding the role of local and transported dust, *Journal of Geophysical Research: Atmospheres*, 126(22), e2021JD035383, <https://doi.org/10.1029/2021JD035383>.

Lambert, A., Hallar, A. G., Garcia, M., Strong, C., Andrews, E., and Hand, J. L. (2020), Dust impacts of rapid agricultural expansion on the Great Plains, *Geophysical Research Letters*, 47(20), e2020GL090347, <https://doi.org/10.1029/2020GL090347>.

Lawal, A. S., Guan, X., Liu, C., Henneman, L. R., Vasilakos, P., Bhogineni, V., Weber, R. J., Nenes, A., and Russell, A. G. (2018), Linked response of aerosol acidity and ammonia to SO<sub>2</sub> and NO<sub>x</sub> emissions reductions in the United States, *Environmental Science & Technology*, 52(17), 9861-9873, doi: 10.1021/acs.est.8b00711.

Lee, T., Yu, X.-Y., Ayres, B., Kreidenweis, S. M., Malm, W. C., and Collett Jr, J. L. (2008), Observations of fine and coarse particle nitrate at several rural locations in the United States, *Atmospheric Environment*, 42(11), 2720-2732, doi: 10.1016/j.atmosenv.2007.05.016.

Lowenthal, D., and Kumar, N. (2006), Light scattering from sea-salt aerosols at Interagency Monitoring of Protected Visual Environments (IMPROVE) sites, *Journal of the Air & Waste Management Association*, 56(5), 636-642, <https://doi.org/10.1080/10473289.2006.10464478>.

Lowenthal, D., Zielinska, B., Mason, B., Samy, S., Samburova, V., Collins, D., Spencer, C., Taylor, N., Allen, J., and Kumar, N. (2009), Aerosol characterization studies at Great Smoky Mountains National Park, summer 2006, *Journal of Geophysical Research: Atmospheres*, 114(D8), doi: 10.1029/2008JD011274.

Lowenthal, D., Zielinska, B., Samburova, V., Collins, D., Taylor, N., and Kumar, N. (2015), Evaluation of assumptions for estimating chemical light extinction at US national parks, *Journal of the Air & Waste Management Association*, 65(3), 249-260, doi:10.1080/10962247.2014.986307.

Malm, W. C., Sisler, J. F., Huffman, D., Eldred, R. A., and Cahill, T. A. (1994), Spatial and seasonal trends in particle concentration and optical extinction in the United States, *Journal of Geophysical Research: Atmospheres*, 99(D1), 1347-1370, <https://doi.org/10.1029/93JD02916>.

Malm, W. C., Pitchford, M. L., McDade, C., and Ashbaugh, L. L. (2007), Coarse particle speciation at selected locations in the rural continental United States, *Atmospheric Environment*, 41(10), 2225-2239, doi:10.1016/j.atmosenv.2006.10.077.

Malm, W. C., Schichtel, B. A., and Pitchford, M. L. (2011), Uncertainties in PM<sub>2.5</sub> gravimetric and speciation measurements and what we can learn from them, *Journal of the Air & Waste Management Association*, 61(11), 1131-1149, doi: 10.1080/10473289.2011.603998.

Malm, W., Schichtel, B., Hand, J., and Prenni, A. (2020), Implications of organic mass to carbon ratios increasing over time in the rural United States, *Journal of Geophysical Research: Atmospheres*, 125(5), e2019JD031480.

Moosmüller, H., Chakrabarty, R., and Arnott, W. (2009), Aerosol light absorption and its measurement: A review, *Journal of Quantitative Spectroscopy and Radiative Transfer*, 110(11), 844-878, doi:10.1016/j.jqsrt.2009.02.035.

Moosmüller, H., Engelbrecht, J. P., Skiba, M., Frey, G., Chakrabarty, R. K., and Arnott, W. P. (2012), Single scattering albedo of fine mineral dust aerosols controlled by iron concentration, *Journal of Geophysical Research: Atmospheres*, 117(D11), doi:10.1029/2011JD016909.

Murphy, D. M., Froyd, K. D., Bian, H., Brock, C. A., Dibb, J. E., DiGangi, J. P., Diskin, G., Dollner, M., Kupc, A., Scheuer, E. M., Schill, G. P., Weinzierl, B., Williamson, C. J., and Yu, P. (2019), The distribution of sea-salt aerosol in the global troposphere, *Atmos. Chem. Phys.*, 19(6), 4093-4104, doi:10.5194/acp-19-4093-2019.

Perry, K. D., Cahill, T. A., Eldred, R. A., Dutcher, D. D., and Gill, T. E. (1997), Long-range transport of North African dust to the eastern United States, *Journal of Geophysical Research: Atmospheres*, 102(D10), 11225-11238, <https://doi.org/10.1029/97JD00260>.

Philip, S., Martin, R., Pierce, J., Jimenez, J.-L., Zhang, Q., Canagaratna, M., Spracklen, D., Nowlan, C., Lamsal, L., and Cooper, M. (2014), Spatially and seasonally resolved estimate of the ratio of organic mass to organic carbon, *Atmospheric Environment*, 87, 34-40, <http://dx.doi.org/10.1016/j.atmosenv.2013.11.065>.

Pitchford, M., Malm, W. C., Schichtel, B. A., Kumar, N., Lowenthal, D., and Hand, J. L. (2007), Revised algorithm for estimating light extinction from IMPROVE particle speciation data, *Journal of the Air & Waste Management Association*, 57(11), 1326-1336, doi:10.3155/1047-3289.57.11.1326.

Pitchford, M., Poirot, R., Schichtel, B. A., and Malm, W. C. (2009), Characterization of the winter midwestern particulate nitrate bulge, *Journal of the Air & Waste Management Association*, 59(9), 1061-1069, doi:10.3155/1047-3289.59.9.1061.

Polidori, A., Turpin, B. J., Davidson, C. I., Rodenburg, L. A., and Maimone, F. (2008), Organic PM 2.5: Fractionation by polarity, FTIR spectroscopy, and OM/OC ratio for the Pittsburgh aerosol, *Aerosol Science and Technology*, 42(3), 233-246, <https://doi.org/10.1080/02786820801958767>.

Prenni, A., Day, D., Evanisko-Cole, A., Sive, B., Hecobian, A., Zhou, Y., Gebhart, K., Hand, J., Sullivan, A., and Li, Y. (2016), Oil and gas impacts on air quality in federal lands in the Bakken region: an overview of the Bakken Air Quality Study and first results, *Atmospheric Chemistry and Physics*, 16(3), 1401-1416, doi:10.5194/acp-16-1401-2016.

Prospero, J. M., Ginoux, P., Torres, O., Nicholson, S. E., and Gill, T. E. (2002), Environmental characterization of global sources of atmospheric soil dust identified with the Nimbus 7 Total Ozone Mapping Spectrometer (TOMS) absorbing aerosol product, *Reviews of geophysics*, 40(1), 2-1-2-31, doi:10.1029/2000RG000095.

Prospero, J. M., Delany, A. C., Delany, A. C., and Carlson, T. N. (2021), The discovery of African dust transport to the Western Hemisphere and the Saharan air layer: A history, *Bulletin of the American Meteorological Society*, 102(6), E1239-E1260, <https://doi.org/10.1175/BAMS-D-19-0309.1>.

- Pu, B., and Ginoux, P. (2018), Climatic factors contributing to long-term variations in surface fine dust concentration in the United States, *Atmospheric Chemistry and Physics*, 18(6), 4201-4215, <https://doi.org/10.5194/acp-18-4201-2018>.
- Rivera, N. I. R., Gill, T. E., Gebhart, K. A., Hand, J. L., Bleiweiss, M. P., and Fitzgerald, R. M. (2009), Wind modeling of Chihuahuan Desert dust outbreaks, *Atmospheric Environment*, 43(2), 347-354, doi:10.1016/j.atmosenv.2008.09.069.
- Ruthenburg, T. C., Perlin, P. C., Liu, V., McDade, C. E., and Dillner, A. M. (2014), Determination of organic matter and organic matter to organic carbon ratios by infrared spectroscopy with application to selected sites in the IMPROVE network, *Atmospheric Environment*, 86, 47-57, <http://dx.doi.org/10.1016/j.atmosenv.2013.12.034>.
- Silvern, R. F., Jacob, D. J., Kim, P. S., Marais, E. A., Turner, J. R., Campuzano-Jost, P., and Jimenez, J. L. (2017), Inconsistency of ammonium–sulfate aerosol ratios with thermodynamic models in the eastern US: a possible role of organic aerosol, *Atmospheric Chemistry and Physics*, 17(8), 5107-5118, doi:10.5194/acp-17-5107-2017.
- Simon, H., Bhave, P., Swall, J., Frank, N., and Malm, W. (2011), Determining the spatial and seasonal variability in OM/OC ratios across the US using multiple regression, *Atmospheric Chemistry and Physics*, 11(6), 2933-2949, <https://doi.org/10.5194/acp-11-2933-2011>.
- Tong, D., Dan, M., Wang, T., and Lee, P. (2012), Long-term dust climatology in the western United States reconstructed from routine aerosol ground monitoring, *Atmospheric Chemistry and Physics*, 12(11), 5189-5205, doi:10.5194/acp-12-5189-2012.
- Turpin, B. J., and Lim, H.-J. (2001), Species contributions to PM<sub>2.5</sub> mass concentrations: Revisiting common assumptions for estimating organic mass, *Aerosol Science & Technology*, 35(1), 602-610, doi:10.1080/02786820119445.
- Vitousek, P. M., Aber, J. D., Howarth, R. W., Likens, G. E., Matson, P. A., Schindler, D. W., Schlesinger, W. H., and Tilman, D. G. (1997), Human alteration of the global nitrogen cycle: sources and consequences, *Ecological applications*, 7(3), 737-750, [https://doi.org/10.1890/1051-0761\(1997\)007\[0737:HAOTGN\]2.0.CO;2](https://doi.org/10.1890/1051-0761(1997)007[0737:HAOTGN]2.0.CO;2).
- Warner, J., Dickerson, R., Wei, Z., Strow, L., Wang, Y., and Liang, Q. (2017), Increased atmospheric ammonia over the world's major agricultural areas detected from space, *Geophysical Research Letters*, 44, 2875-2884, doi:10.1002/2016GL072305.
- Watson, J. G., Chow, J. C., Chen, L.-W. A., and Frank, N. H. (2009), Methods to assess carbonaceous aerosol sampling artifacts for IMPROVE and other long-term networks, *Journal of the Air & Waste Management Association*, 59(8), 898-911, <https://doi.org/10.3155/1047-3289.59.8.898>.
- Weber, R. J., Guo, H., Russell, A. G., and Nenes, A. (2016), High aerosol acidity despite declining atmospheric sulfate concentrations over the past 15 years, *Nature Geoscience*, 9(4), 282-285, doi:10.1038/Ngeo2665.
- White, W. H. (2008), Chemical markers for sea salt in IMPROVE aerosol data, *Atmospheric Environment*, 42(2), 261-274, doi:10.1016/j.atmosenv.2007.09.040.
- White, W. H., Trzepla, K., Hyslop, N. P., and Schichtel, B. A. (2016), A critical review of filter transmittance measurements for aerosol light absorption, and de novo calibration for a decade of

monitoring on PTFE membranes, *Aerosol Science and Technology*, 50(9), 984-1002,  
<http://dx.doi.org/10.1080/02786826.2016.1211615>.

## Chapter 3. Seasonal Distributions of PM<sub>2.5</sub> Aerosol Mass

The seasonality of aerosol concentrations can be significant depending on species and region and is a function of the source emissions, meteorological parameters, and local and long-range transport. Examining aerosol concentrations on a regional basis, rather than a site-specific basis, can lead to insights regarding air quality issues on regional scales. In this chapter, the differences in the regional seasonal patterns of major aerosol species and their contributions to reconstructed fine mass are examined for rural and urban regions.

IMPROVE and CSN data were aggregated according to semi-empirically defined regions. When a specific region is used in this report, it refers to an IMPROVE or CSN region as defined in Figure 1.2 or Figure 1.15, respectively (Chapter 1), not a commonly-used geographical region. For example, the IMPROVE “Northwest” region refers to a specific group of IMPROVE sites, not to the geographical area typically considered as “northwestern United States”. There are 36 IMPROVE regions, 29 of which are rural, four that are urban (including both long-term urban sites and urban quality assurance sites), and three that are international sites (see Table 1.1 in Chapter 1). Some rural regions may have only one site (e.g., Death Valley, Lone Peak, Virgin Islands). The IMPROVE regions were defined based on site location and the seasonal distribution of aerosol concentrations for major species (e.g., Malm et al., 2000; Debell et al., 2006; Hand et al., 2011). The variability in the species composition between sites in a given region were not investigated, nor were differences in elevation accounted for.

A similar semi-empirical method for grouping sites was used for the CSN network, resulting in 29 regions (Hand et al., 2011; Hand et al., 2012). Eleven regions had only one site per region. A list of the 136 sites that met the completeness criteria (outlined in Chapter 2) is provided in Table 1.8 in Chapter 1, including site location, region, and setting (urban, suburban, or rural).

The monthly and annual mean concentrations of PM<sub>2.5</sub> ammonium sulfate (AS), ammonium nitrate (AN), particulate organic matter (POM), elemental carbon (EC), fine dust (FD), sea salt (SS), coarse mass (CM), and reconstructed fine mass (RCFM) were analyzed. The fractional contribution of an individual species mass to RCFM was also determined. Evaluation of the seasonal distributions of both absolute and relative concentrations highlights the relative importance of each species to the PM<sub>2.5</sub> mass budget throughout the year.

The monthly mean IMPROVE and CSN regional data are presented as stacked bar charts. Monthly mean concentrations are depicted with the first letter of the month followed by an “A” for annual mean. Stacked bar charts for monthly mean concentrations are grouped into figures corresponding to three sections of the country: eastern, northwestern, and southwestern United States. Stacked bar charts for monthly mean mass fractions are also provided. Scales vary for each regional bar plot. The following sections are organized by species and include discussions for both IMPROVE and CSN.

## **3.1 PM<sub>2.5</sub> AMMONIUM SULFATE**

### **3.1.1 IMPROVE**

The majority of sulfate in the atmosphere is produced through chemical reactions of sulfur dioxide (SO<sub>2</sub>). Anthropogenic sources of SO<sub>2</sub> include industrial activities, such as coal and diesel fuel combustion, and emissions of SO<sub>2</sub> are highest in the eastern United States. Elevated relative humidity or other aqueous pathways create the most efficient conditions for sulfate production and, along with transport, lead to regional impacts of sulfate aerosols on PM<sub>2.5</sub>. The maximum 2016–2019 regional monthly mean AS concentration of 2.77 µg m<sup>-3</sup> occurred in Hawaii in March due to volcanic emissions of SO<sub>2</sub>. The maximum CONUS (continental United States) monthly mean concentration occurred in the Ohio River Valley region in July (2.25 µg m<sup>-3</sup>), followed by the Midsouth region in September (2.10 µg m<sup>-3</sup>). The minimum regional monthly mean AS concentration occurred in both the Northwest and Oregon/Northern California regions in January (0.13 µg m<sup>-3</sup>). In most of the regions in the eastern United States, regional mean AS concentrations rarely exceeded 2 µg m<sup>-3</sup> year round (Figure 3.1.1). Monthly mean AS in regions farther north, such as the Boundary Waters and Northeast regions, were 1 µg m<sup>-3</sup> or less year round. In addition, the monthly variability of AS was flat, with a small increase in summer months in some regions (e.g., MidSouth and East Coast). Monthly mean concentrations in regions in the northwestern United States were lower than in the eastern United States (typically <1 µg m<sup>-3</sup>) and had little seasonal variability (see Figure 3.1.2). The highest mean AS concentrations in regions in the northwestern United States occurred in the Northern Great Plains and Columbia River Gorge regions, where concentrations approached 1 µg m<sup>-3</sup>. AS concentrations in the regions of the southwestern United States (Figure 3.1.3) were generally <2 µg m<sup>-3</sup> and demonstrated more of a summer peak (e.g., Southern California, Southern Arizona, and West Texas regions). Low monthly mean concentrations (<1 µg m<sup>-3</sup>) were observed in the Great Basin, Colorado Plateau, and Central Rockies regions. In the Hawaii region, monthly mean AS concentrations were >1 µg m<sup>-3</sup> for most months of the year.

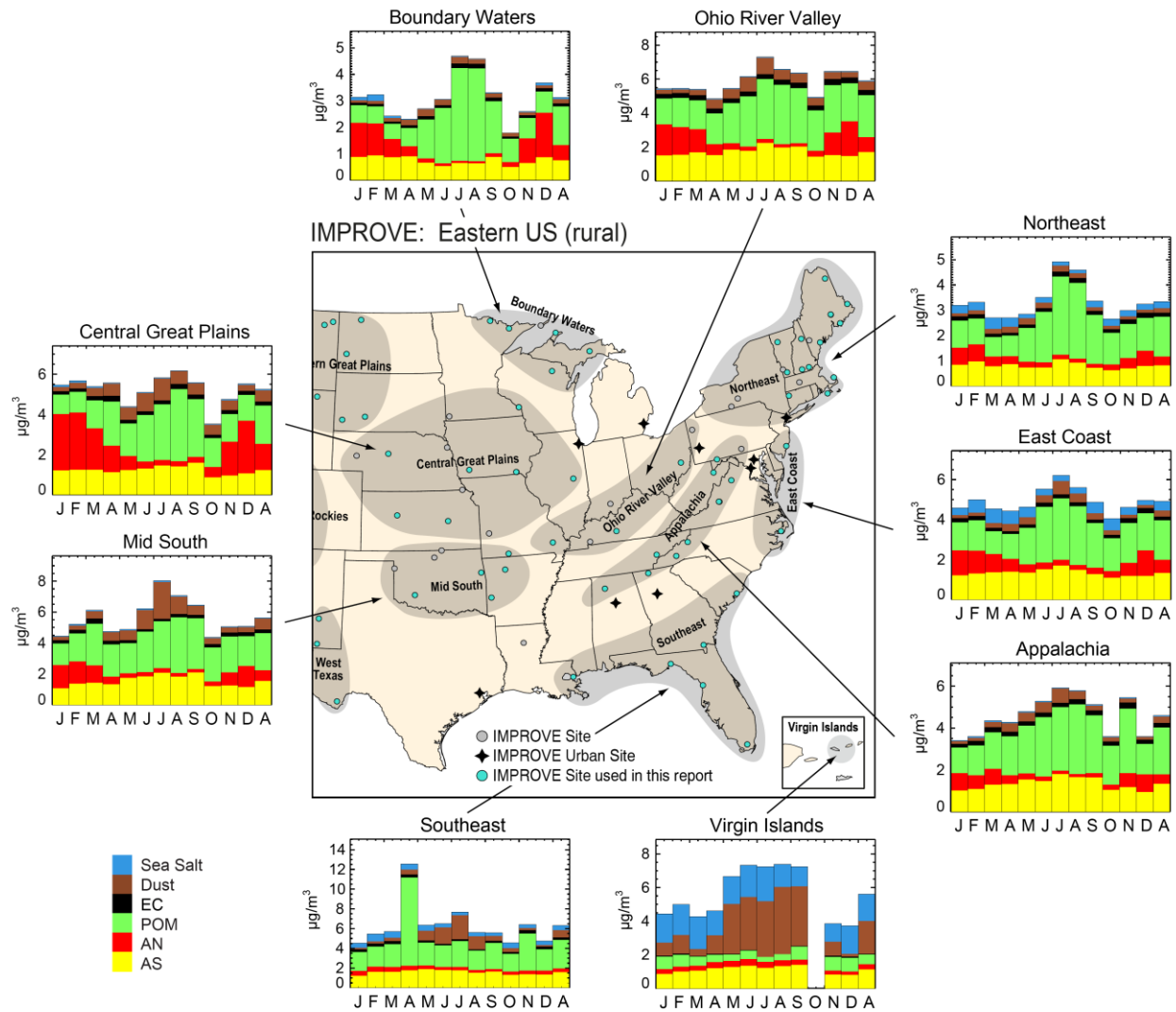


**Figure 3.1.1. IMPROVE 2016–2019 regional monthly mean PM<sub>2.5</sub> mass concentrations (µg m<sup>-3</sup>) for the eastern United States. Letters on the x-axis correspond to month and “A” corresponds to annual mean. Shaded areas in the map correspond to regions that include the sites used in the analysis, shown as blue dots.**

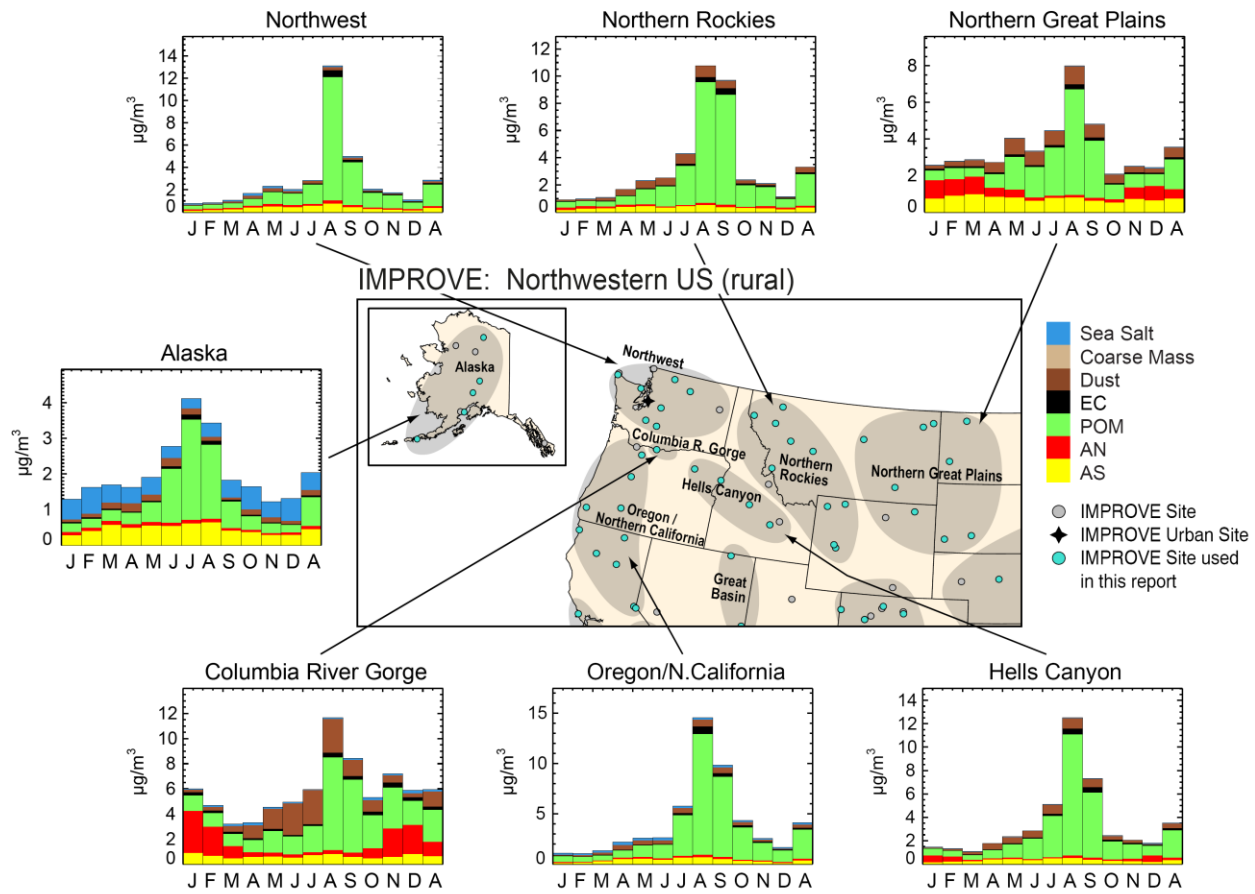


**Figure 3.1.2. IMPROVE 2016–2019 regional monthly mean PM<sub>2.5</sub> mass concentrations (µg m<sup>-3</sup>) for the northwestern United States. Letters on the x-axis correspond to month and “A” corresponds to annual mean. Shaded areas in the map correspond to regions that include the sites used in the analysis, shown as blue dots.**

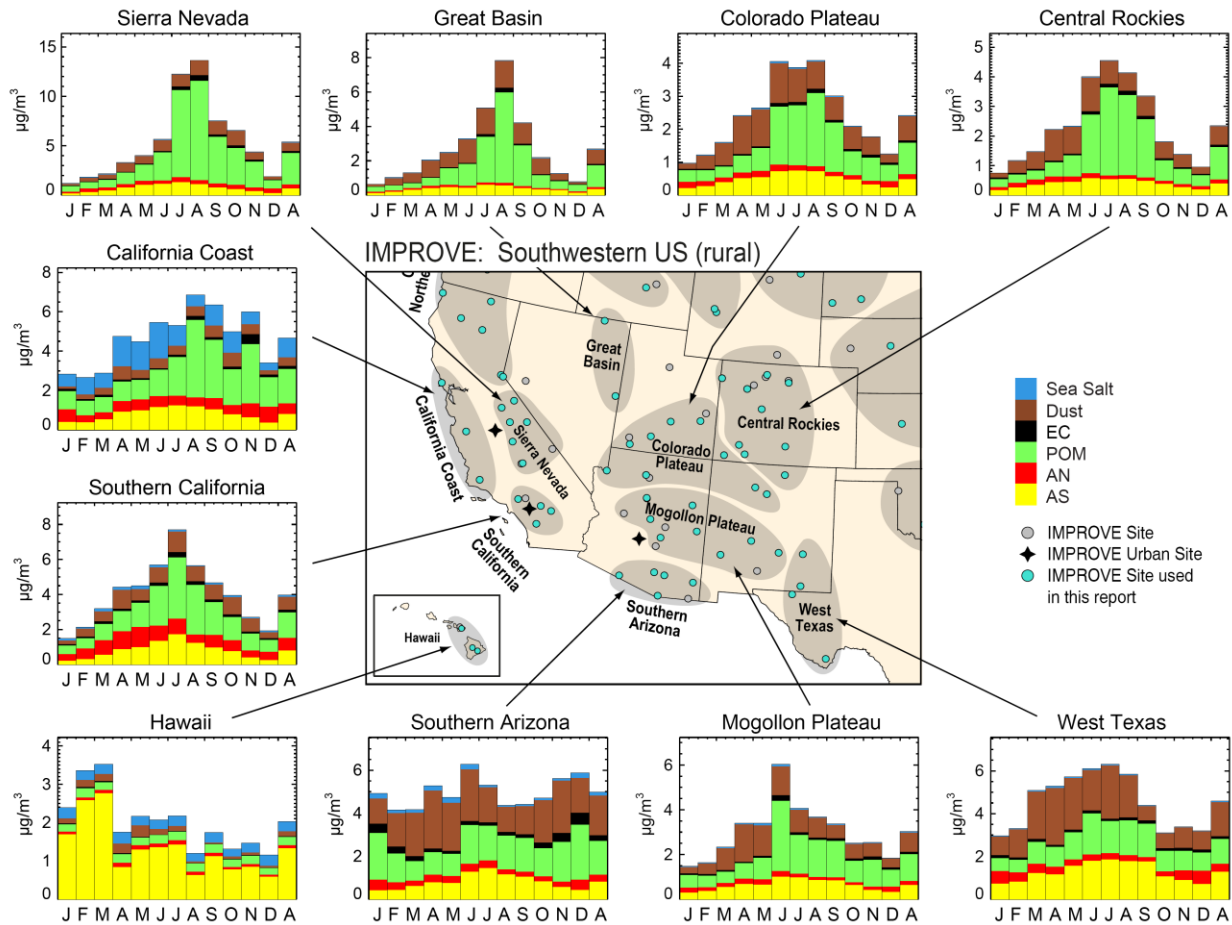


**Figure 3.1.3. IMPROVE 2016–2019 regional monthly mean PM<sub>2.5</sub> mass concentrations ( $\mu\text{g m}^{-3}$ ) for the southwestern United States. Letters on the x-axis correspond to month and “A” corresponds to annual mean. Shaded areas in the map correspond to regions that include the sites used in the analysis, shown as blue dots.**

The maximum IMPROVE regional monthly mean fractional contributions of AS to RCFM of 0.787 occurred in the Hawaii region in March, where maximum AS concentrations also occurred. The Hawaii region had monthly mean contributions from over 0.5 to near 0.8 year round. The minimum contribution of 0.038 occurred in the Northern Rockies region in September. Low contributions also occurred in August in the Hells Canyon region (0.044) and the Oregon/Northern California region (0.047). The CONUS regional mean maximum contributions occurred in the West Texas region (0.404) in September and in the Boundary Waters region (0.392) in April. Regions in the eastern United States typically had AS contributions between 0.2 and 0.3 year round (Figure 3.1.4) with no strong seasonal maxima, except in the Boundary Waters region, which experienced higher contributions in spring and fall. In the northwestern United States, contributions from AS to RCFM of around 0.2 occurred during spring months for many regions. (Figure 3.1.5). Much of the seasonal variability in AS contributions in the northwestern United States was due to the contributions of other species, such as POM in summer. In the southwestern United States (Figure 3.1.6), the regional mean contributions were around 0.20 or less. Seasonal variability of regions farther north indicated larger contributions in spring and fall (e.g., Sierra Nevada and Great Basin regions), in part due to strong contributions of POM in summer. Farther south, seasonal maxima occurred in summer

in the Southern Arizona region, but other regions showed little seasonal variability in AS contributions (e.g., Mogollon Plateau and Colorado Plateau regions).

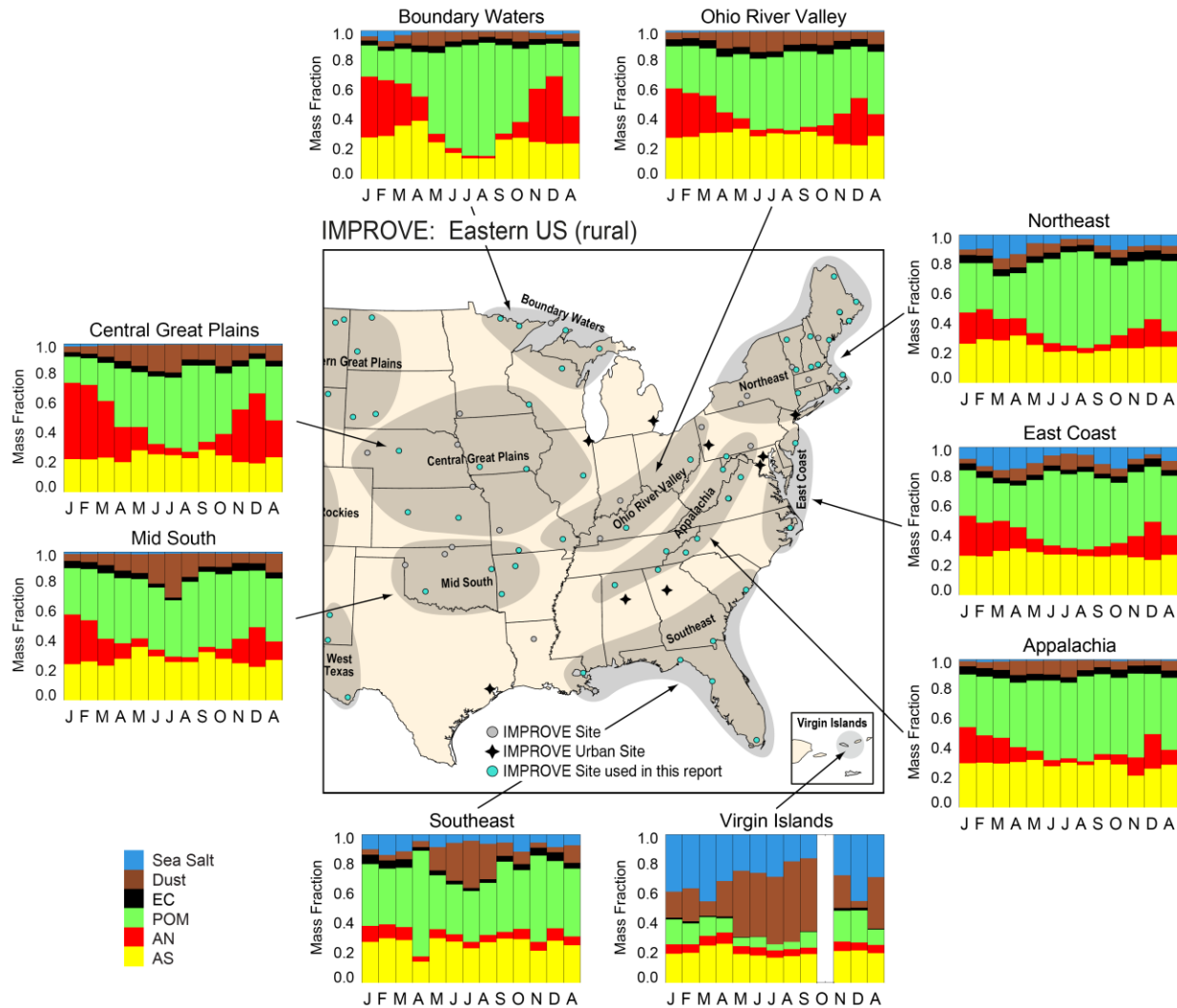


**Figure 3.1.4. IMPROVE 2016–2019 regional monthly mean PM<sub>2.5</sub> reconstructed fine mass fractions for the eastern United States. Letters on the x-axis correspond to month and “A” corresponds to annual mean. Shaded areas in the map correspond to regions that include the sites used in the analysis, shown as blue dots.**

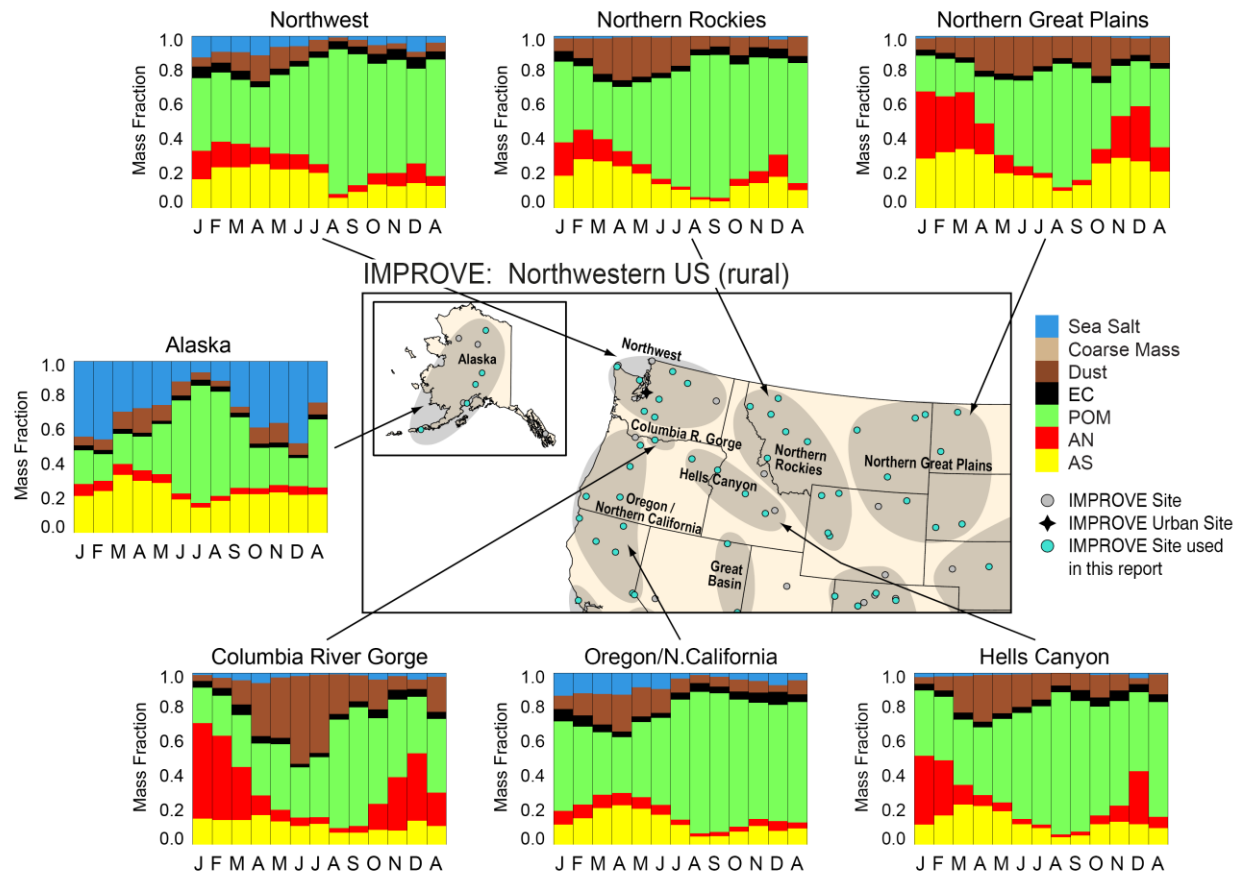


**Figure 3.1.5. IMPROVE 2016–2019 regional monthly mean PM<sub>2.5</sub> reconstructed fine mass fractions for the northwestern United States. Letters on the x-axis correspond to month and “A” corresponds to annual mean. Shaded areas in the map correspond to regions that include the sites used in the analysis, shown as blue dots.**

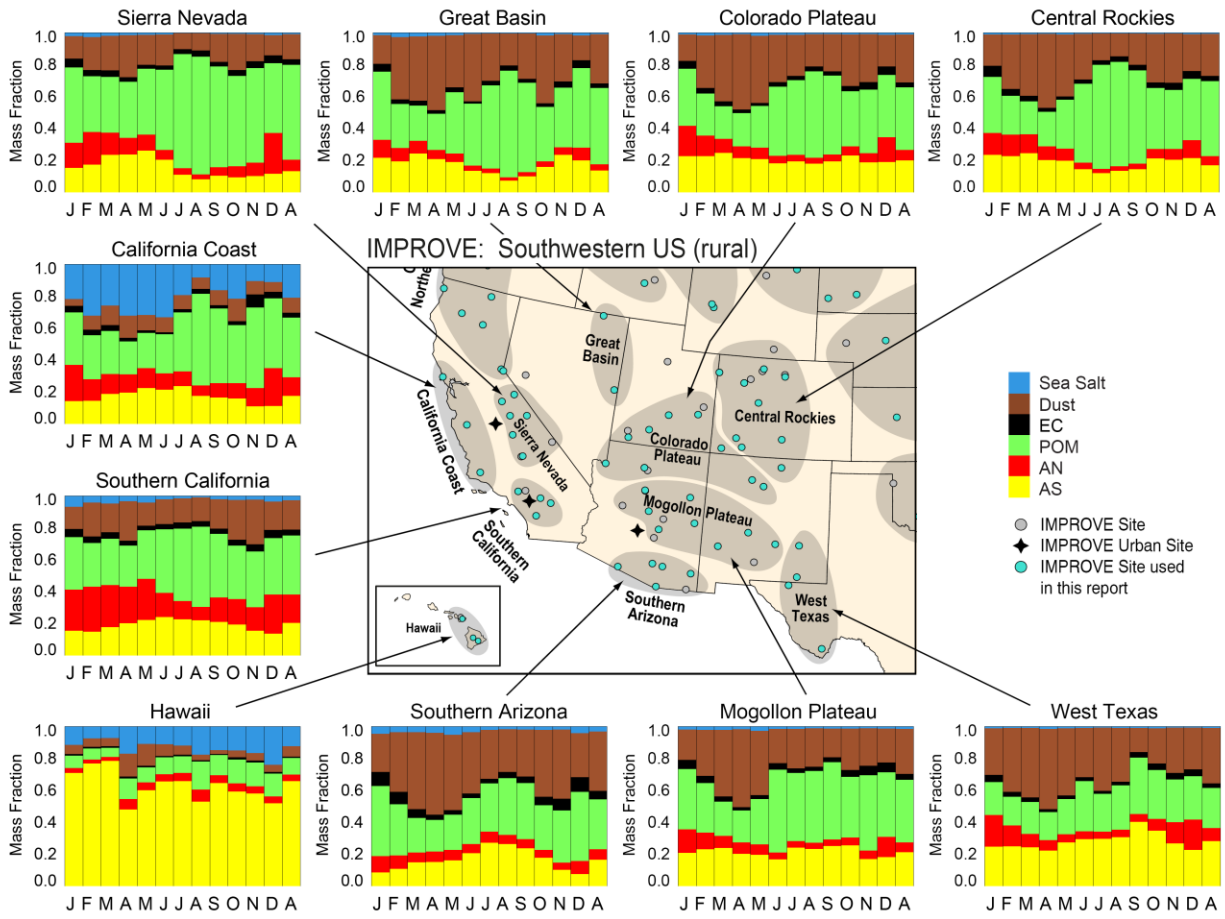


**Figure 3.1.6. IMPROVE 2016–2019 regional monthly mean  $\text{PM}_{2.5}$  reconstructed fine mass fractions for the southwestern United States. Letters on the x-axis correspond to month and “A” corresponds to annual mean. Shaded areas in the map correspond to regions that include the sites used in the analysis, shown as blue dots.**

### 3.1.2 CSN

The CSN maximum regional monthly mean AS concentration was  $4.76 \mu\text{g m}^{-3}$  in the Alaska region in January, followed by the CONUS maximum of  $3.61 \mu\text{g m}^{-3}$  in the Los Angeles region in July. The regional minimum mean AS concentration ( $0.29 \mu\text{g m}^{-3}$ ) occurred in the Northwest region in March. Similar to the IMPROVE regions, in CSN regions AS monthly mean concentrations in the eastern United States rarely reached above  $2 \mu\text{g m}^{-3}$  (see Figure 3.1.7). The similarity in seasonal patterns of AS concentrations in the eastern United States pointed to regional sources of AS that impact urban and rural regions alike (compare Figures 3.1.1 and 3.1.7). In addition, the seasonal variability was quite low, with mostly flat monthly mean concentrations year round. Monthly mean AS concentrations were generally quite low ( $<1.5 \mu\text{g m}^{-3}$ ) for regions in the northwestern United States (Figure 3.1.8) and were seasonally flat, similar to IMPROVE monthly mean concentrations (see Figure 3.1.2). The exception was the Alaska region, with maximum monthly mean concentrations during cold months. The regional monthly mean AS concentrations in the southwestern United States were generally low ( $<2.0 \mu\text{g m}^{-3}$ ) in most regions but with more seasonal variability than in the eastern United States (Figure 3.1.9). Summer maxima were observed for many regions, such as in the Phoenix/Tucson, Albuquerque, Las Vegas, and West Texas regions. The strongest seasonal variability occurred in the Los

Angeles and San Diego regions with summer maxima. These patterns also occurred for IMPROVE regions. The Hawaii region experienced some seasonal variability with winter maxima.

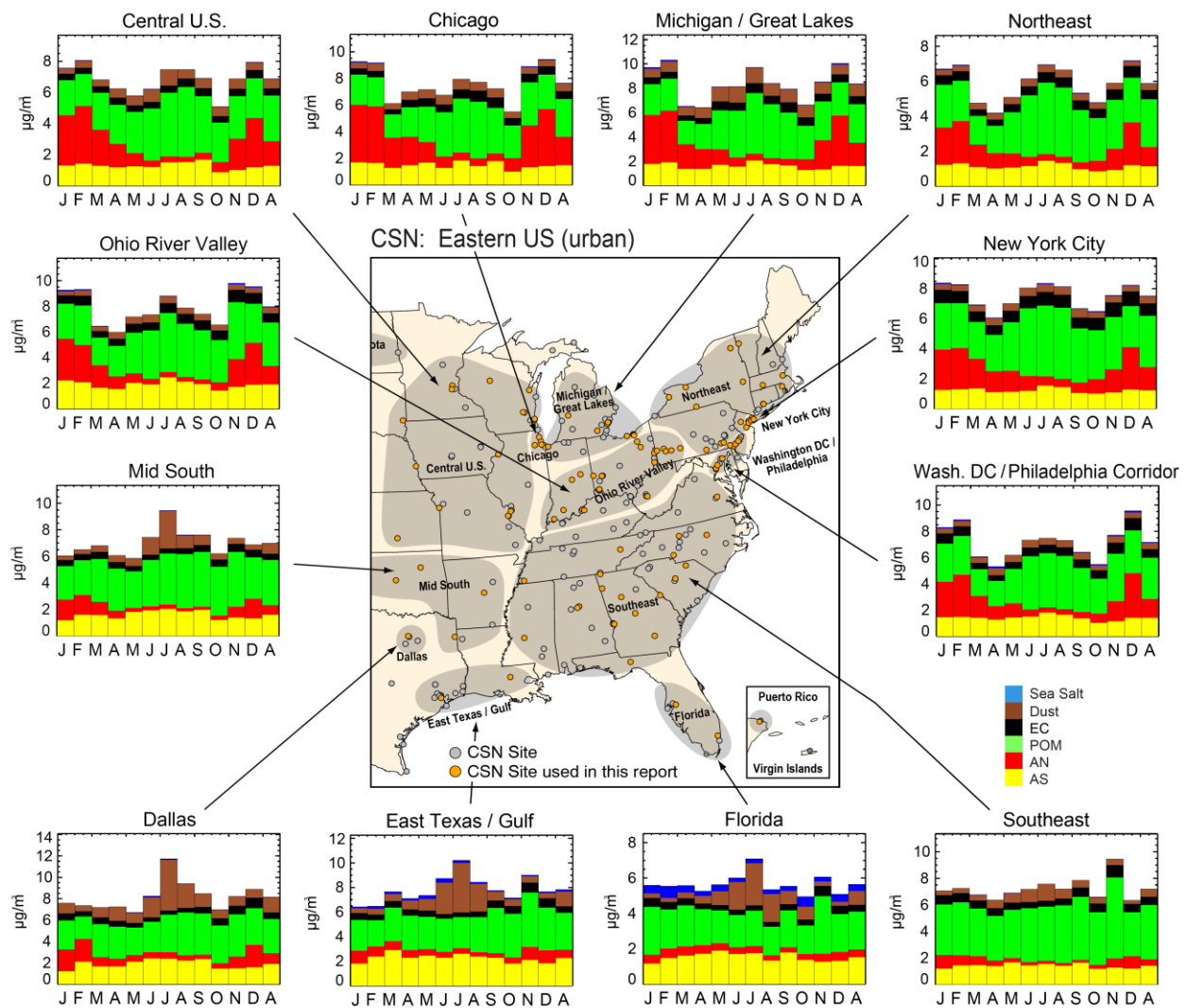


**Figure 3.1.7. CSN 2016–2019 regional monthly mean PM<sub>2.5</sub> mass concentrations (µg m<sup>-3</sup>) for the eastern United States. Letters on the x-axis correspond to month and “A” corresponds to annual mean. Shaded areas in the map correspond to regions that include the sites used in the analysis, shown as orange dots.**

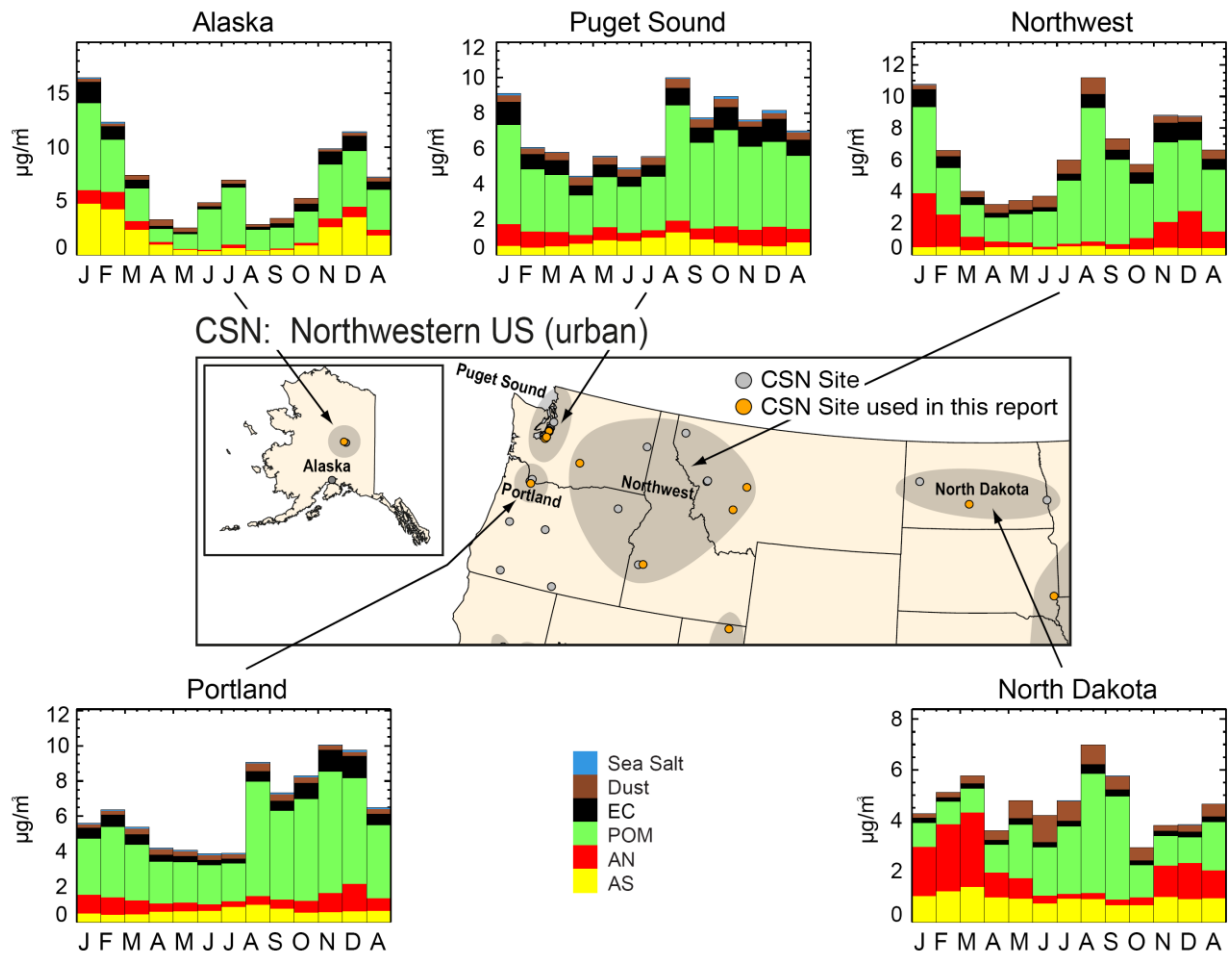


**Figure 3.1.8. CSN 2016–2019 regional monthly mean PM<sub>2.5</sub> mass concentrations ( $\mu\text{g m}^{-3}$ ) for the northwestern United States. Letters on the x-axis correspond to month and “A” corresponds to annual mean. Shaded areas in the map correspond to regions that include the sites used in the analysis, shown as orange dots.**

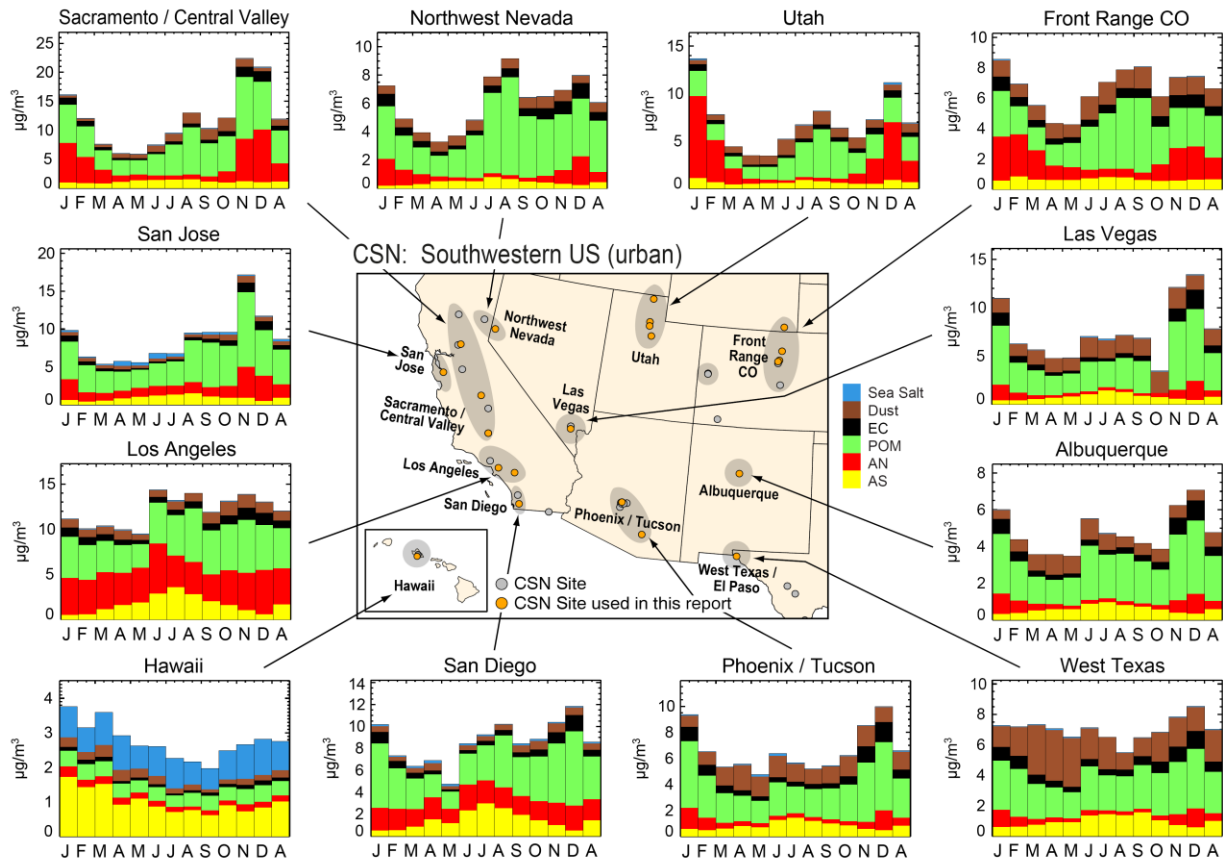


**Figure 3.1.9. CSN 2016–2019 regional monthly mean PM<sub>2.5</sub> mass concentrations (µg m<sup>-3</sup>) for the northwestern United States. Letters on the x-axis correspond to month and “A” corresponds to annual mean. Shaded areas in the map correspond to regions that include the sites used in the analysis, shown as orange dots.**

The CSN AS regional fractional contribution to RCFM ranged from 0.027 in the Northwest Nevada region in January to 0.460 in the Hawaii region in January and 0.381 in the CONUS region of East Texas/Gulf in March. With the exception of the East Texas/Gulf and Florida regions, the monthly mean AS fractional contribution to RCFM was rarely above 0.3 in regions across the United States. In many regions in the eastern United States, the fractional contribution did not vary much seasonally, averaging around 0.2, with the exception of the Midsouth region that demonstrated a small summer peak that reached ~ 0.3 (Figure 3.1.10). Generally, regions in the northwestern United States had lower AS contributions, typically <0.2 (Figure 3.1.11). The Alaska region had higher contributions in cold months, but CONUS regions displayed different seasonal variability, with spring maxima in the Puget Sound and Northwest regions and summer maxima in the Portland region. More seasonal variability was observed in regions in the southwestern United States (Figure 3.1.12), with summer maxima in urban regions farther south, such as many of the regions in California, as well as the Phoenix/Tucson region in Arizona. The Sacramento/Central Valley and Northwest Nevada regions experienced spring maxima. Like the Northwest region, contributions of AS to RCFM were around 0.2 or less. Contributions in the Hawaii region were near 0.4 or less but with low seasonal variability.

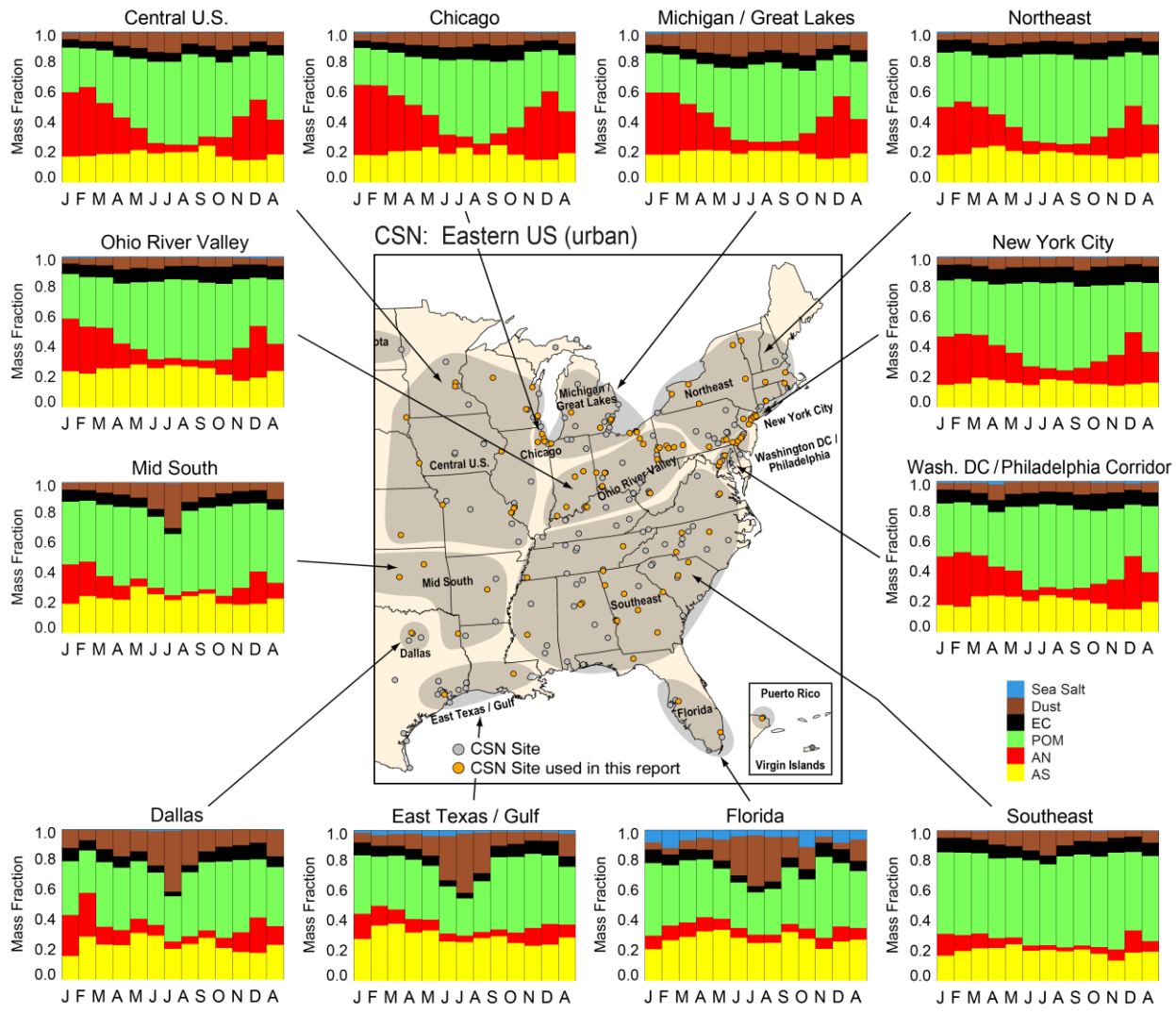


**Figure 3.1.10. CSN 2016–2019 regional monthly mean PM<sub>2.5</sub> reconstructed fine mass fractions for the eastern United States. Letters on the x-axis correspond to month and “A” corresponds to annual mean. Shaded areas in the map correspond to regions that include the sites used in the analysis, shown as orange dots.**

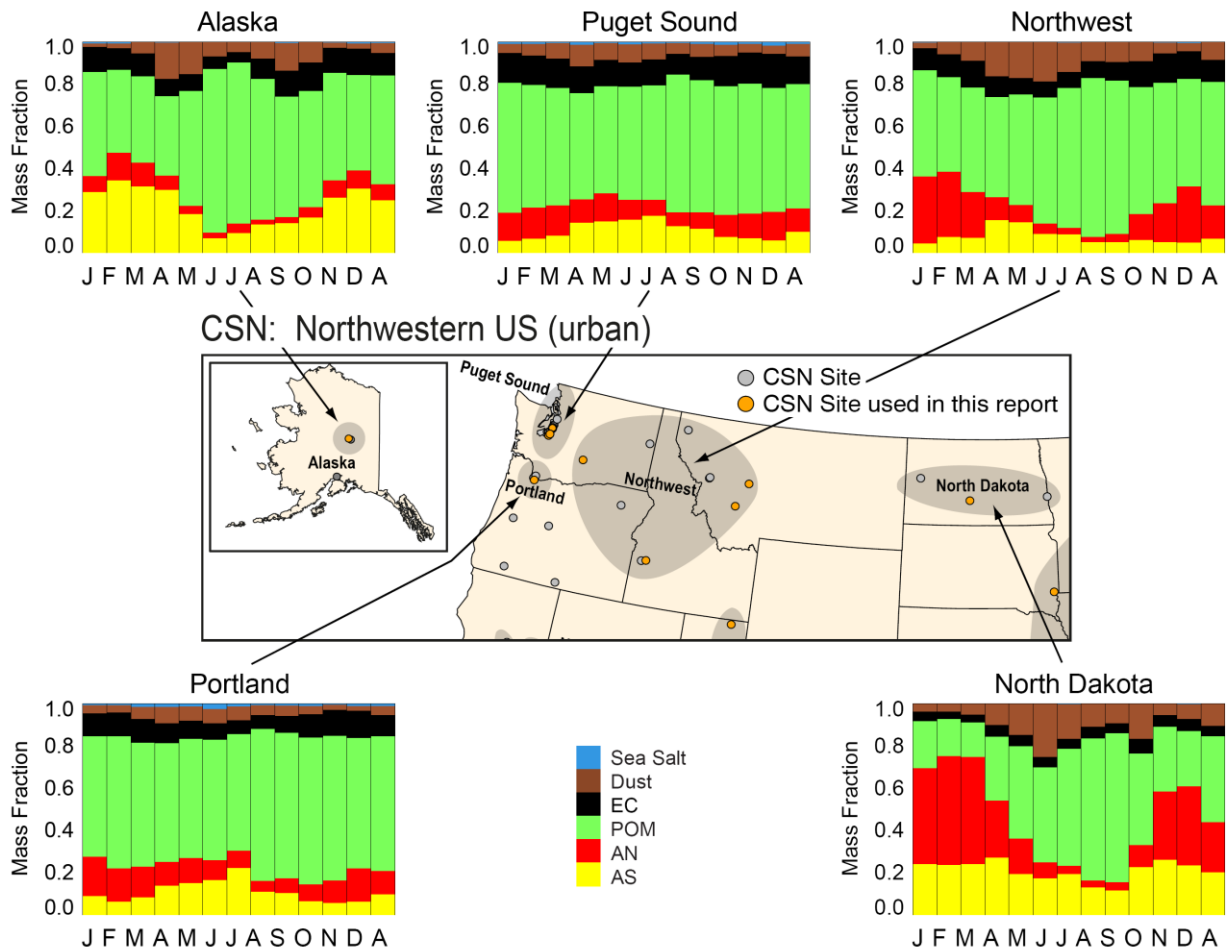


**Figure 3.1.11. CSN 2016–2019 regional monthly mean PM<sub>2.5</sub> reconstructed fine mass fractions for the northwestern United States. Letters on the x-axis correspond to month and “A” corresponds to annual mean. Shaded areas in the map correspond to regions that include the sites used in the analysis, shown as orange dots.**

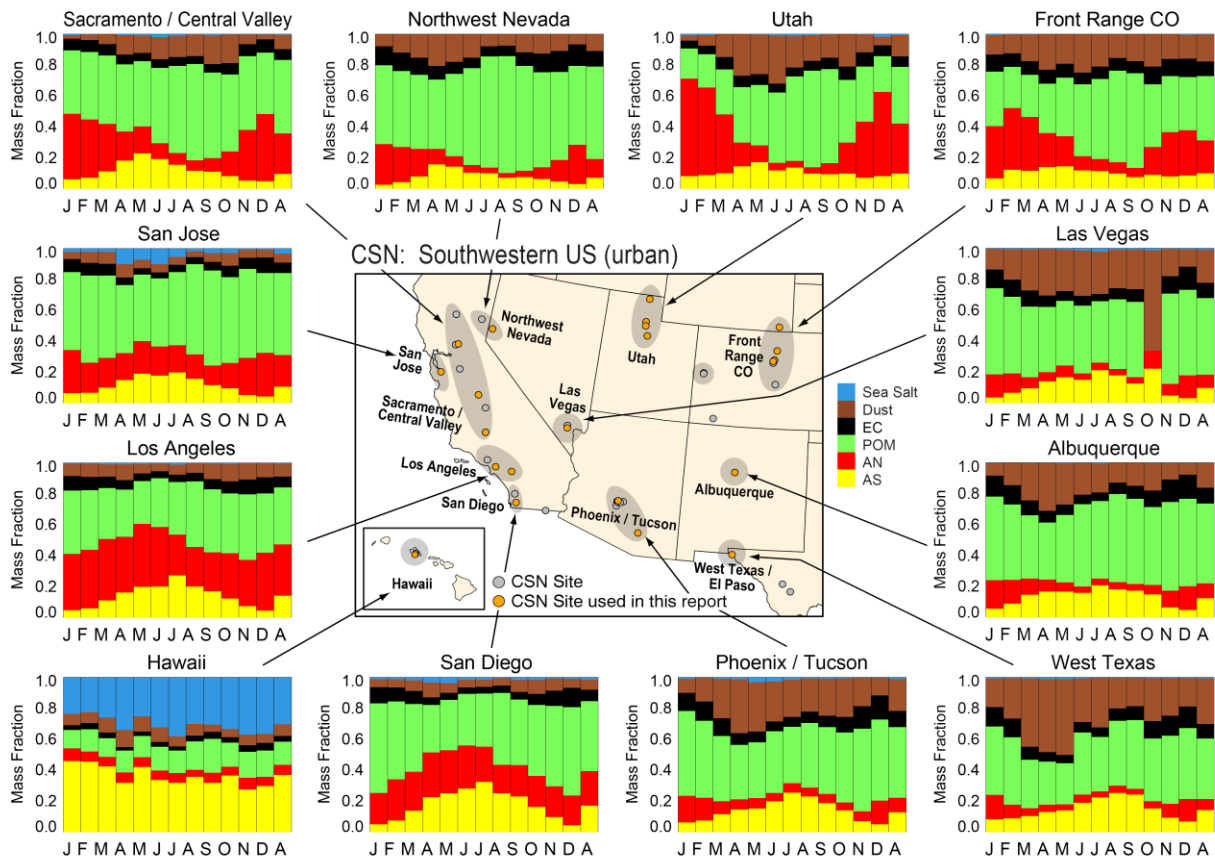


**Figure 3.1.12.** CSN 2016–2019 regional monthly mean PM<sub>2.5</sub> reconstructed fine mass fractions for the southwestern United States. Letters on the x-axis correspond to the month and “A” corresponds to annual mean. Shaded areas in the map correspond to regions that include the sites used in the analysis, shown as orange dots.

## 3.2 PM<sub>2.5</sub> AMMONIUM NITRATE

### 3.2.1 IMPROVE

Recall from Chapter 2 that AN forms from the reversible reaction of gas-phase ammonia and nitric acid, a form of oxidized nitrogen. Sources of oxidized nitrogen include combustion of fossil fuels and biomass. Sources of ammonia include agricultural activities, mobile sources, and natural emissions. Lower temperatures and higher relative humidity favor particulate AN. Regions with oxidized nitrogen and ammonia emissions, as well as locations and seasons that favor AN formation, will likely be associated with higher AN concentrations. The IMPROVE 2016–2019 regional maximum monthly mean ammonium nitrate (AN) mass concentration (3.35  $\mu\text{g m}^{-3}$ ) occurred in the Columbia River Gorge region in January. A minimum regional monthly mean concentration of 0.05  $\mu\text{g m}^{-3}$  was observed both in the Alaska region in October and the Hawaii region in December. The minimum CONUS monthly mean concentration of 0.06  $\mu\text{g m}^{-3}$  occurred in the Great Basin region in November. In the eastern United States, the highest AN monthly mean concentrations occurred during winter months in the Central Great Plains region, near 3  $\mu\text{g m}^{-3}$  (Figure 3.1.1). Along with the Central Great Plains region, winter monthly mean concentrations were generally higher for regions farther north, such as the Boundary Waters and

Ohio River Valley regions, with mean concentrations nearing  $2 \mu\text{g m}^{-3}$ . Farther south, such as the Southeast and Appalachia regions, mean concentrations were much lower ( $<1 \mu\text{g m}^{-3}$  year round). In the northwestern United States, the highest monthly mean concentrations occurred during winter months in the Columbia River Gorge and Northern Great Plains regions (Figure 3.1.2). Other regions in the northwestern United States experienced relatively low concentrations year round ( $<0.3 \mu\text{g m}^{-3}$ ). Regions in the southwestern United States also had low concentrations (Figure 3.1.3). The exceptions were the California Coast and Southern California regions, where concentrations were higher ( $<1 \mu\text{g m}^{-3}$ ). Unlike regions in the eastern United States, regions in the northwestern and southwestern United States had low monthly variability, and, interestingly, the AN monthly mean concentrations in the Southern California region peaked in spring.

Rural IMPROVE monthly mean mass fractions for AN ranged from 0.014 in the Northern Rockies region in August to 0.557 in the Columbia River Gorge region in January. In regions farther north in the eastern United States, mass fractions reached 0.5 or higher during winter, such as in the Boundary Waters and Central Great Plains regions (Figure 3.1.4). Regions such as the East Coast and Appalachia regions also had higher mass fractions in the winter, from 0.2 to 0.3. The Southeast region experienced the lowest mass fractions, near 0.1 or less. The highest AN monthly mean mass fractions in the northwestern United States occurred in the Columbia River Gorge, Northern Great Plains, and Hells Canyon regions, with mass fractions greater than 0.4 in winter (Figure 3.1.5). The mass fractions in the Northwest, Northern Rockies, and the Oregon/Northern California regions were  $<0.2$ . Across the southwestern United States, most regions experienced relatively low AN monthly mean mass fractions, typically  $<0.2$  (Figure 3.1.6). The exception was the Southern California region, where mass fractions were closer to 0.25–0.3 and higher during spring months.

### 3.2.2 CSN

The maximum CSN regional monthly mean concentration ( $9.10 \mu\text{g m}^{-3}$ ) occurred in the Sacramento/Central Valley region in December, and the minimum concentration occurred in the Alaska ( $0.07 \mu\text{g m}^{-3}$ ) and Hawaii ( $0.10 \mu\text{g m}^{-3}$ ) regions, both in August, and in the CONUS region of Albuquerque in September ( $0.17 \mu\text{g m}^{-3}$ ). In the eastern United States, a strong seasonal pattern was observed with peaks in winter months, especially for regions farther north (Figure 3.1.7). High concentrations ( $\sim 4 \mu\text{g m}^{-3}$ ) occurred in winter months in the Central U.S. and Michigan/Great Lake regions. Concentrations decreased for regions farther south, such as the East Texas/Gulf, Florida, and Southeast regions, with lower monthly variability. A similar spatial pattern was observed for IMPROVE regions. Concentrations were generally lower for regions in the northwestern United States (Figure 3.1.8). The Northwest and North Dakota regions had the highest monthly mean concentrations near  $3 \mu\text{g m}^{-3}$  during winter months. Farther west, concentrations decreased, but a seasonal pattern with higher winter concentrations was observed. Regions in the southwestern United States experienced the highest monthly mean concentrations (see Figure 3.1.9). The maximum monthly concentrations in Sacramento/Central Valley region were only slightly higher than those observed in the Utah region in December ( $8.62 \mu\text{g m}^{-3}$ ). Mean concentrations decreased in regions farther south, such as in the Las Vegas, Albuquerque, West Texas, and Phoenix/Tucson regions, although maxima still occurred in winter months. In contrast, regions in southern California, such as Los Angeles and San Diego, experienced higher concentrations year round.

CSN regional monthly mean AN fractional contributions to RCFM ranged from 0.024 in both the Alaska and the Northwest regions in August to 0.631 in the Utah region in January. In the eastern United States, the contribution of AN to RCFM was considerable (near 0.5) in regions farther north, such as the Central U.S., Chicago, and the Michigan/Great Lakes regions (Figure 3.1.10). Similar to IMPROVE regions in the eastern United States, contributions decreased farther south, such as the Southeast, Florida, and East Texas/Gulf regions (<0.15). In the northwestern United States, the contributions reached 0.5 in the North Dakota region and 0.3 in the Northwest region, both during winter months (Figure 3.1.11). Other regions in the northwestern United States had lower contributions and lower monthly variability. Strong seasonal patterns in the contributions of AN to RCFM were observed in the Utah and Front Range CO regions in the southwestern United States (Figure 3.1.12). However, farther south, the contributions decreased as did the monthly variability. In the San Diego, Los Angeles, and San Jose regions, the contributions ranged between ~0.2–0.4 and were nearly constant year round. Monthly mean contributions in the Hawaii region were <0.1 year round.

### 3.3 PM<sub>2.5</sub> PARTICULATE ORGANIC MATTER

#### 3.3.1 IMPROVE

The sources of POM in the atmosphere are both primary emissions and secondary formation. Primary emissions are emitted directly into the atmosphere and include particles from combustion of fossil fuels and biomass. Secondary organic aerosols form from the oxidation of gas-phase organic precursors from both anthropogenic and biogenic sources. IMPROVE 2016–2019 regional monthly mean POM concentrations ranged from 0.17 µg m<sup>-3</sup> in the Hawaii region in December and 0.27 µg m<sup>-3</sup> in both of the CONUS regions of the Central Rockies and Great Basin, both in January, to a maximum monthly mean POM concentration of 12.0 µg m<sup>-3</sup> in the Oregon/Northern California region in August. In the eastern United States, POM concentrations were highly seasonal, with peaks in summer months (Figure 3.1.1). During July and August, concentrations reached over 3 µg m<sup>-3</sup> in most regions, such as the Boundary Waters, Ohio River Valley, Central Great Plains, Northeast, Appalachia, and East Coast regions. The strong peak in POM in April in the Southeast region was due to the influence of biomass smoke. The Virgin Islands region had relatively low concentrations (<1 µg m<sup>-3</sup>). The largest POM concentrations occurred in the northwestern United States (Figure 3.1.2) where peak concentrations ranged from 5 to 12 µg m<sup>-3</sup>, mainly in August and September due to biomass smoke influence. A strong seasonal pattern in POM was observed at these regions, with relatively low concentrations during winter months (<1 µg m<sup>-3</sup>). This pattern was also observed for more-northerly regions in the southwestern United States (Figure 3.1.3), but the magnitude of the concentrations and degree of seasonality decreased farther south (e.g., Southern Arizona and West Texas).

The lowest IMPROVE regional monthly mean POM mass fraction occurred in the Virgin Islands region in July (0.040) and the CONUS region of Northern Great Plains in March (0.171), compared to the highest fraction (0.843) in the Northwest region in August. In the eastern United States, POM monthly mean contributions to RCFM were >0.5 during summer months in all of the CONUS regions and reached 0.765 in the Boundary Waters region in August and 0.713 in the Southeast region in April (Figure 3.1.4). Contributions during colder months were typically above 0.3. In the northwestern United States, POM contributions dominated the RCFM. Contributions were typically 0.4–0.6 and generally higher in summer (see Figure 3.1.5).

Contributions were often lowest for winter months, increased in summer, and remained high throughout the end of the year, such as in the Oregon/Northern California, Northwest, and Northern Rockies regions. In the southwestern United States, the magnitude and seasonality of POM contributions decreased (Figure 3.1.6). Contributions were still highest in summer and reached above 0.7, such as in the Sierra Nevada region, but farther south contributions decreased. For example, in the Southern Arizona region, monthly mean contributions were <0.5 year round, and peaked in both winter and summer. A similar pattern was observed in the Mogollon Plateau region. Contributions in the Hawaii region were quite low (<0.2).

### 3.3.2 CSN

The CSN POM regional monthly mean mass concentrations ranged from  $0.33 \mu\text{g m}^{-3}$  in the Hawaii region in July and  $0.89 \mu\text{g m}^{-3}$  in the CONUS region of North Dakota in February to  $10.67 \mu\text{g m}^{-3}$  in the Sacramento/Central Valley region in November. POM monthly mean concentrations in regions in the eastern United States ranged from 2 to  $5 \mu\text{g m}^{-3}$  and peaked during summer months in many regions farther north, such as the Chicago, Michigan/Great Lakes, Northeast, New York City, and Washington/Philadelphia Corridor regions (Figure 3.1.7). Toward the south, regions had less seasonal variability (e.g., Southeast region); however, magnitudes of POM were similar. Higher concentrations were observed in regions in the northwestern United States, likely associated with biomass smoke impacts. The Northwest, Portland, and North Dakota regions experienced monthly mean concentrations of  $6\text{--}8 \mu\text{g m}^{-3}$ , especially during summer and fall months (Figure 3.1.8). The Alaska region had higher POM concentrations during cold months. In the southwestern United States, regions toward the north also experienced high POM concentrations during summer and fall, such as the Northwest Nevada, Sacramento/Central Valley, San Jose, and Front Range CO regions (Figure 3.1.9). Farther south, POM concentrations peaked during winter months, such as in the Albuquerque, Phoenix/Tucson, and West Texas regions. Relatively low monthly mean POM concentrations ( $<0.5 \mu\text{g m}^{-3}$ ) were observed in the Hawaii region year round.

The maximum CSN monthly mean POM mass fraction of 0.776 occurred in the Alaska region in June and 0.755 in the CONUS region of Northwest Nevada in August. The minimum mass fraction of 0.120 occurred in the Hawaii region in January and in March for the North Dakota region (0.164). The monthly mean contribution of POM to RCFM in northern regions in the eastern United States were around 0.2–0.3 in cold months and over 0.5 in summer months (e.g., Chicago, Michigan/Great Lakes, and Northeast regions). For many regions farther south, the seasonal variability decreased and winter contributions were much higher. Year-round monthly mean contributions ranged from 0.4 to over 0.5, such as in the Southeast region (Figure 3.1.10). In the northwestern United States, POM contributions dominated RCFM with monthly mean contributions of 0.5 in winter months and over 0.7 in summer and fall months. The exception was the North Dakota region, with lower winter contributions due to the higher AN contributions (Figure 3.1.11). Contributions in the southwestern United States were also considerable in regions farther north, such as the Northwest Nevada region, where mass fractions over 0.7 occurred in summer months (Figure 3.1.12). In some regions large winter AN contributions led to more seasonal variability in POM contributions, with higher fractions during summer months and lower fractions in winter months, such as in the Sacramento/Central Valley, Utah, and Front Range CO regions. In regions farther south, such as the Phoenix/Tucson and San

Diego regions, contributions were higher during winter. In the Hawaii region, the monthly mean contributions from POM to RCFM were 0.2 or less year round.

### **3.4 PM<sub>2.5</sub> ELEMENTAL CARBON**

#### **3.4.1 IMPROVE**

EC is emitted directly through emissions from incomplete combustion of fossil fuels or biomass. The maximum regional monthly mean EC mass concentration of  $0.74 \mu\text{g m}^{-3}$  occurred in the Oregon/Northern California region in August. The minimum regional monthly mean mass concentration occurred in the Hawaii region in August ( $0.010 \mu\text{g m}^{-3}$ ) and in the CONUS region of Great Basin in February ( $0.03 \mu\text{g m}^{-3}$ ). EC concentrations are difficult to discern on the bar charts because they are low relative to other aerosol species. In the eastern United States, concentrations rarely exceeded  $0.3 \mu\text{g m}^{-3}$  (Figure 3.1.1). Unlike other species, the monthly variability of EC was highly spatially variable. The Boundary Waters region peaked during summer months, Central Great Plains during spring months, Ohio River Valley during fall and winter months, Appalachia during fall months, and in the Southeast during spring and fall months. In the Virgin Islands region, monthly mean concentrations were below  $0.1 \mu\text{g m}^{-3}$  year round. The monthly mean seasonal and spatial variability suggests localized impacts of sources in regions in the eastern United States. In contrast, monthly mean concentrations in regions in the northwestern United States peaked in late summer and/or early fall for all of the regions (Figure 3.1.2). Concentrations were  $>0.5 \mu\text{g m}^{-3}$  in the Hells Canyon, Northern Rockies, Northwest, and Oregon/Northern California regions in August or September, indicating the important role of biomass burning in the area. Lower monthly mean EC concentrations were also observed in regions in the southwestern United States (Figure 3.1.3) in summer, except in the Sierra Nevada region in August ( $\sim 0.5 \mu\text{g m}^{-3}$ ) and in the California Coast region in November ( $\sim 0.5 \mu\text{g m}^{-3}$ ). Farther south, concentrations peaked during winter months in the Southern Arizona region ( $\sim 0.5 \mu\text{g m}^{-3}$  in December). Otherwise, monthly mean concentrations in most regions rarely exceeded  $0.2 \mu\text{g m}^{-3}$ . In the Hawaii region, monthly mean concentration were  $<0.04 \mu\text{g m}^{-3}$  year round.

The minimum monthly mean contribution of EC to RCFM occurred in the Virgin Islands region (0.0016) in July and the CONUS region of the California Coast in June (0.0128). The maximum contribution occurred in the Southern Arizona region in December (0.093) and in the California Coast region in November (0.083). Contributions in regions in the eastern United States were nearly all near or below 0.05 (Figure 3.1.4). Contributions were similar in magnitude at regions in the northwestern United States, with the exception of the Northwest and Oregon/Northern California regions where contributions reached 0.07 during cold months (Figure 3.1.5). Relative contributions of EC were around 0.02-0.03 in many regions in the southwestern United States (Figure 3.1.6), with the exception of the California Coast region in November, Southern Arizona region in winter months, Mogollon Plateau region in fall and winter months, and the Central Rockies and Southern California regions, where contributions reached up to 0.09. Monthly mean contributions in the Hawaii region were near or  $<0.01$  year round.

### **3.4.2 CSN**

The CSN minimum regional monthly mean EC concentrations ranged from  $0.06 \mu\text{g m}^{-3}$  in the Hawaii region in July and  $0.18 \mu\text{g m}^{-3}$  in the CONUS North Dakota region in February to a maximum concentration of  $2.01 \mu\text{g m}^{-3}$  in the Las Vegas region in December. EC monthly mean concentrations in the eastern United States peaked between  $0.5$  and  $1.0 \mu\text{g m}^{-3}$  and were higher in regions such as the Ohio River Valley, Chicago, and New York City regions (Figure 3.1.7). Concentrations were generally low in regions farther south, with the exception of the Dallas and Southeast regions, where concentrations almost reached  $1 \mu\text{g m}^{-3}$  during cold months. Monthly mean concentrations were generally higher in regions in the northwestern United States than in the eastern United States. Concentrations reached over  $1.0 \mu\text{g m}^{-3}$  during fall and winter months, such as in the Puget Sound, Northwest, and Portland regions (Figure 3.1.8). Concentrations in the Alaska region were also near  $2.0 \mu\text{g m}^{-3}$  during winter months. In some southwestern regions, monthly mean concentrations also reached values over  $1.0 \mu\text{g m}^{-3}$ , such as the Sacramento/Central Valley, San Diego, Los Angeles, Northwest Nevada, Phoenix/Tucson, and Albuquerque regions, often during late fall (Figure 3.1.9). EC monthly mean concentrations in the Hawaii region were relatively low, around  $0.1 \mu\text{g m}^{-3}$  or less.

CSN regional mean mass fractions ranged from 0.023 in the Hawaii region in April and 0.032 in the Dallas region in July to 0.160 in the Puget Sound region in December. Regional monthly mean EC mass fractions generally were  $<0.10$  in many regions in the eastern United States (Figure 3.1.10), except the Chicago, Michigan/Great Lakes, Ohio River Valley, and Northeast regions. In the New York City region, EC monthly mean mass fractions were 0.1 or greater year round. Contributions from EC to RCFM were higher in the northwestern United States (Figure 3.1.11). The highest monthly mean EC mass fractions occurred in the Puget Sound region, where fractions over 0.1 occurred during all months. The Northwest and Portland regions experienced higher EC mass fractions during cold months, as did the Alaska region. EC mass fractions were generally lower ( $<0.1$ ) for many regions in the southwestern United States (Figure 3.1.12). The exceptions occurred in the Northwest Nevada, Front Range CO, Las Vegas, Albuquerque and Phoenix/Tucson regions where mass fractions reached over 0.1, especially during cold months. In the Hawaii region, EC monthly mean mass fractions were  $<0.05$  year round.

## **3.5 PM<sub>2.5</sub> FINE DUST MASS**

### **3.5.1 IMPROVE**

Sources of mineral dust in the atmosphere include entrainment from deserts, paved and unpaved roads, agricultural activity, construction, and fire. The seasonal and spatial variability of FD in the United States is influenced by local, regional, and long-range transport. A maximum 2016–2019 regional monthly mean IMPROVE FD mass concentration of  $4.01 \mu\text{g m}^{-3}$  was observed in August in the Virgin Islands region, a site known to have impacts from North African dust transport, especially during summer. The maximum CONUS region concentrations occurred in the Columbia River Gorge region in July ( $2.72 \mu\text{g m}^{-3}$ ) and the Southern Arizona region in April ( $2.70 \mu\text{g m}^{-3}$ ). The minimum concentration was observed in the Northwest region in December ( $0.03 \mu\text{g m}^{-3}$ ) (see Figure 3.1.1). In the eastern United States, the highest FD

concentration occurred during summer months, especially at regions farther south, such as the Southeast and Midsouth regions ( $>2.0 \mu\text{g m}^{-3}$ ). However, increased concentrations during summer months also occurred in the East Coast, Appalachia, and Ohio River Valley regions. These regions are known to be influenced by the transport of North African FD during summer (Hand et al., 2017). Concentrations during winter months were relatively low ( $0.1\text{--}0.3 \mu\text{g m}^{-3}$ ). Monthly mean FD concentrations in the Virgin Islands region were high from late spring through summer ( $3\text{--}4 \mu\text{g m}^{-3}$ ). Monthly mean FD concentrations in the northwestern United States were highest in the Columbia River Gorge region in summer (Figure 3.1.2). Monthly mean concentrations in other regions were relatively low ( $<1 \mu\text{g m}^{-3}$ ) but also peaked during summer months. Regional mean concentrations in the southwestern United States were highest ( $2\text{--}3 \mu\text{g m}^{-3}$ ) for regions farther south (Figure 3.1.3) and peaked in spring and early summer months. Regions farther north, such as the Sierra Nevada and Great Basin regions, had higher concentrations during summer and fall months.

FD monthly mean contributions to RCFM ranged from 0.023 in the Northwest region in August to 0.543 in the Virgin Islands region in August, 0.513 in the Southern Arizona region in April, and 0.511 in the Columbia River Gorge region in June. In regions in the eastern United States, FD mass fractions were near 0.3 during July in the Midsouth and Southeast regions (Figure 3.1.4). In the Central Great Plains region, the mass fraction nearly reached 0.2 during July. In regions farther north, the monthly mean mass fractions were lower ( $<0.1$ ). FD mass fractions in the Virgin Islands region were near 0.5 from late spring through early fall months. The largest mass fractions of FD in the northwestern United States occurred in the Columbia River Gorge region (Figure 3.1.5). In most other regions, the fractions were between 0.2 and 0.3 during late spring and early summer months. The highest FD fractions in the Northwest region occurred in April and May ( $\sim 0.15$ ), and the highest fraction in the Alaska region also occurred in April ( $\sim 0.15$ ). Spring maxima in FD mass fractions also occurred in regions in the southwestern United States (Figure 3.1.6), and the fractions were higher than in the northwestern U.S. regions. For most regions, the maximum fraction ( $\sim 0.5$ ) occurred in April. The exceptions were in the Sierra Nevada, California Coast, and Southern California regions, where the FD fractions were lower ( $<0.3$ ) and exhibited less seasonal variability than other regions.

### 3.5.2 CSN

Regional monthly mean FD concentrations ranged from  $0.09 \mu\text{g m}^{-3}$  in the Hawaii region in September and  $0.15 \mu\text{g m}^{-3}$  in the North Dakota region in January to  $4.75 \mu\text{g m}^{-3}$  in the Dallas region in July. Regions farther south in the eastern United States had higher FD concentrations in summer months, such as in the Dallas and East Texas/Gulf regions ( $4\text{--}5 \mu\text{g m}^{-3}$  in July) and the Midsouth and Florida regions ( $2\text{--}3 \mu\text{g m}^{-3}$  in July), likely influenced by long-range transport of dust from North Africa. Monthly mean concentrations in other regions ranged between  $0.5$  and  $1.0 \mu\text{g m}^{-3}$  (Figure 3.1.7). In the northwestern United States, monthly mean concentrations were typically  $<0.5 \mu\text{g m}^{-3}$  in most regions year round. The exception was in the Northwest region, where concentrations reached over  $1.0 \mu\text{g m}^{-3}$  in August, and the North Dakota region in June (Figure 3.1.8). In the Alaska region, the monthly mean FD concentrations reached  $\sim 0.5 \mu\text{g m}^{-3}$  in April and October. Relatively high concentrations were observed in many regions in the southwestern United States (Figure 3.1.9). In the Phoenix/Tucson region, monthly mean concentration were between  $1$  and  $2 \mu\text{g m}^{-3}$  most of the year, and the West Texas region had

monthly mean concentrations during spring months over  $3 \mu\text{g m}^{-3}$ . Other regions (Front Range CO, Las Vegas, Albuquerque, and Utah) experienced monthly mean concentrations over  $1 \mu\text{g m}^{-3}$  during most months. Monthly mean concentrations in the Sacramento/Central Valley region reached over  $2 \mu\text{g m}^{-3}$  during fall months, and in the Los Angeles region monthly mean concentrations were over  $1 \mu\text{g m}^{-3}$  during April and fall months. Monthly mean concentrations in the Hawaii region were  $<0.4 \mu\text{g m}^{-3}$  year round but peaked in March and April.

The maximum CSN urban FD mass fraction (0.492) occurred in the West Texas region in May, and the minimum mass fraction occurred in the Alaska region in January (0.018) and the Portland region in December (0.022). In the eastern United States, mass fractions of FD were highly seasonal and reached 0.4 in the East Texas/Gulf and Dallas regions in July and 0.34 in the Florida region in July. Mass fractions in regions farther north were typically  $<0.15$  and for most regions ranged around 0.05–0.08 (Figure 3.1.10) with less monthly variability than regions farther south. Similar FD mass fractions were observed in regions in the northwestern United States (Figure 3.1.11). The exceptions occurred in the Northwest and North Dakota regions, where monthly mean FD fractions reached 0.25 in late spring and summer months. Mass fractions were higher for many regions in the southwestern United States (Figure 3.1.12). The Phoenix/Tucson, Albuquerque, and Las Vegas regions experienced mass fractions over 0.3 in spring, especially April. Mass fractions in the West Texas region ranged between 0.4 and 0.5 during spring months. Regions farther west had lower mass fractions, such as the San Jose and Los Angeles regions, where mass fractions were 0.1 or less year round. Monthly mean mass fractions in the Hawaii region were also  $<0.1$  year round.

## 3.6 PM<sub>2.5</sub> SEA SALT MASS

### 3.6.1 IMPROVE

Estimates of sea salt (SS) discussed here are likely an underestimate, as chloride concentrations in the particle phase can be depleted by a gas–particle exchange of chloride to the atmosphere. The 2016–2019 regional monthly mean SS concentrations for the IMPROVE regions ranged from  $0.007 \mu\text{g m}^{-3}$  in the Central Rocky Mountains region in November to  $2.05 \mu\text{g m}^{-3}$  in the Virgin Islands region in January and  $1.81 \mu\text{g m}^{-3}$  in the California Coast region in June. SS concentrations were visible on the monthly bar charts relative to other species for only a few regions. In the eastern United States, coastal regions such as the Northeast, East Coast, and Southeast regions had noticeable SS concentrations relative to other species (Figure 3.1.1). In the East Coast and Southeast regions, concentrations reached  $0.7 \mu\text{g m}^{-3}$  in the late winter and spring months. Monthly mean SS concentrations near  $0.2 \mu\text{g m}^{-3}$  occurred in the Boundary Water region in February, and concentrations of  $\sim 0.1 \mu\text{g m}^{-3}$  were observed in the Central Great Plains region. In the northwestern United States, monthly mean SS concentrations neared  $0.2 \mu\text{g m}^{-3}$  in the Columbia River Gorge and Northwest regions in April (Figure 3.1.2), but in other regions, concentrations were typically  $<0.02 \mu\text{g m}^{-3}$ . In the Alaska region, monthly mean SS concentrations reached  $0.7 \mu\text{g m}^{-3}$  in February.

IMPROVE SS mass fractions ranged from 0.0013 in the Northern Rockies region in August to 0.48 in the Alaska region in December and 0.45 in the Virgin Islands region in March. The maximum CONUS region mass fraction was 0.33 in the California Coast region in June.

Regions closest to the coast in the eastern United States had noticeable contributions of SS to RCFM, such as the Northeast, East Coast, and Southeast regions (Figure 3.1.4). Mass fractions in the East Coast and Northeast regions reached 0.15 in spring and fall months, while in the Southeast region, mass fractions near 0.15 were observed in spring months. In the Virgin Islands region, monthly mean mass fractions were higher year round, ranging from 0.16 to 0.45. In the northwestern United States, noticeable mass fractions were observed in the Northwest, Columbia River Gorge, and Oregon/Northern California regions. In the Northwest region, mass fractions were highest early in the year, just greater than 0.1. Similar mass fractions occurred in the Oregon/Northern California region. Much greater contributions of SS to RCFM occurred in the Alaska region, with fractions that ranged from 0.05 during summer months to near 0.5 during winter months (Figure 3.1.5). The California Coast region had the highest contributions of SS to RCFM of any region in the southwestern United States; mass fractions ranged from 0.08 in August to higher contributions through spring and early summer that peaked in June (Figure 3.1.6). The Southern California and Southern Arizona regions both experienced noticeable but low contributions during the first half of the year (~0.05).

### 3.6.2 CSN

Estimates of SS concentrations were derived from chlorine mass concentrations because CSN did not start reporting chloride until 2017. SS monthly mean concentrations ranged from ~zero in the North Dakota region and  $0.0006 \mu\text{g m}^{-3}$  in the Northwest region, both in April, to  $1.03 \mu\text{g m}^{-3}$  in the Hawaii region in December and  $0.69 \mu\text{g m}^{-3}$  in the San Jose region in June. SS concentrations were relatively low and difficult to discern on the bar charts corresponding to regions in the eastern United States (Figure 3.1.7), with the exception of the Florida and East Texas/Gulf regions. In the Florida region, SS monthly mean concentrations reached  $0.65 \mu\text{g m}^{-3}$  in February and  $0.33 \mu\text{g m}^{-3}$  in the East Texas/Gulf region in June. Monthly mean SS concentrations in the regions in the northwestern United States were quite low, generally around  $0.1 \mu\text{g m}^{-3}$  or less. In the Puget Sound region, SS concentrations reached  $0.14 \mu\text{g m}^{-3}$  and  $0.11 \mu\text{g m}^{-3}$  in the Portland region in December (Figure 3.1.8). In the inland Alaska region, monthly mean SS concentrations did not rise above  $0.1 \mu\text{g m}^{-3}$  year round. Regions in the southwestern United States were also associated with low SS concentrations. The San Jose region had some of the highest monthly mean concentrations that reached  $0.69 \mu\text{g m}^{-3}$  in June. SS in other regions rarely exceeded  $0.15 \mu\text{g m}^{-3}$  (Figure 3.1.9). The Hawaii region had higher monthly mean concentrations year round, ranging from  $0.60 \mu\text{g m}^{-3}$  in September to  $1.03 \mu\text{g m}^{-3}$  in December.

SS contributions to RCFM ranged from ~0 in the North Dakota and 0.0002 in the Northwest region in April to 0.38 in the Hawaii region in July and 0.12 in the Florida region in February. The Florida and East Texas/Gulf regions were the only regions in the eastern United States with discernable SS contributions (Figure 3.1.10). Similar low contributions were observed for regions in the northwestern United States (Figure 3.11). The Puget Sound and Oregon regions had the highest monthly mean contributions, near 0.01–0.02. In the southwestern United States, contributions in the San Jose region reached 0.1 in late spring and early summer months, but most other regions had contributions that were low (<0.05) (Figure 3.1.12). The Hawaii region had SS contributions that ranged from 0.22 in February to 0.38 in July.

## **3.7 PM<sub>2.5</sub> GRAVIMETRIC FINE MASS**

### **3.7.1 IMPROVE**

IMPROVE regional monthly mean FM concentrations ranged from 0.59  $\mu\text{g m}^{-3}$  in the Great Basin region in January to 13.26  $\mu\text{g m}^{-3}$  in the Oregon/Northern California region in August. Regional monthly mean FM concentrations mirrored the combined species concentrations on the bar charts shown in previous figures in this chapter. Regional monthly mean concentrations in regions in the eastern United States peaked during summer, around 6–8  $\mu\text{g m}^{-3}$ , as was seen in Figure 3.1.1. The highest monthly mean concentrations occurred during summer in the Midsouth and Ohio River Valley regions. The Southeast region was influenced by biomass smoke during April, when POM concentrations increased over other months. In the northwestern United States, strong seasonal variability due to the impacts of biomass smoke and increased POM concentrations led to peaks in FM in the Northwest, Northern Rockies, Hells Canyon, and Oregon/Northern California regions, over 12  $\mu\text{g m}^{-3}$  (Figure 3.1.2). Biomass smoke impacts also influenced FM concentrations in regions in the southwestern United States, such as the Sierra Nevada region in July and August, when FM was over 10  $\mu\text{g m}^{-3}$  (Figure 3.1.3). Summer peaks in FM also occurred in many other regions but at lower concentrations (~6–8  $\mu\text{g m}^{-3}$ ). Seasonal variability in mean FM concentrations was lowest in the Southern Arizona region.

### **3.7.2 CSN**

Monthly mean FM concentrations ranged from 3.02  $\mu\text{g m}^{-3}$  in the Alaska region in May and 3.25  $\mu\text{g m}^{-3}$  in the Northwest region in April to 23.27  $\mu\text{g m}^{-3}$  in the Sacramento/Central Valley region in December. Monthly mean FM concentration peaked in both winter and summer in several northern regions in the eastern United States (Figure 3.1.7), such as the Northeast, New York City, Washington D.C./Philadelphia, and Ohio River Valley regions. Farther south, FM concentrations peaked in summer and were flatter during winter months. Monthly mean FM peaked in both summer and winter at regions in the northwestern United States and reached values near 10  $\mu\text{g m}^{-3}$ , such as in the Northwest, Puget Sound, and Portland regions (Figure 3.1.8). Similar seasonal patterns in monthly mean FM occurred in regions in the southwestern United States (Figure 3.1.9). Winter and summer peaks were observed in the Sacramento/Central Valley, Northwest Nevada, Utah, and Front Range CO regions, for example. FM monthly mean concentrations in the West Texas region were relatively flat, while concentrations in the Phoenix/Tucson region peaked during winter. In the Los Angeles region, monthly mean concentrations for the first half of the year were relatively low and increased in June for the rest of the year.

## **3.8 COARSE MASS**

CM is often assumed to be associated with mineral dust, although other studies have shown it also is associated with SS or biological particles and could include ionic species, such as sodium or nitrate, or organic carbon. Therefore, it may have seasonality similar to FD or could vary depending on sources and transport. IMPROVE 2016–2019 regional monthly mean CM concentrations ranged from 0.42  $\mu\text{g m}^{-3}$  in the Northwest region in December to 28.38  $\mu\text{g m}^{-3}$  in the Columbia River Gorge region in June. Regional monthly mean CM concentrations increased during late spring and early summer months in regions in the eastern United States, such as the

Boundary Waters, Ohio River Valley, East Coast, and Appalachia regions (Figure 3.8.1). Higher concentrations were observed in the East Coast and the Central Great Plains regions ( $\sim 10 \text{ } \mu\text{g m}^{-3}$ ). Seasonal patterns in the Midsouth and Southeast regions were similar, with peaks near  $8 \text{ } \mu\text{g m}^{-3}$  in July. Monthly mean concentrations in the Virgin Islands region peaked in summer months (near  $20 \text{ } \mu\text{g m}^{-3}$ ), likely associated with transport of North African dust and/or SS.

Regional monthly mean CM concentrations in regions in the northwestern United States were seasonally variable, with higher concentrations in summer and early fall months that dropped rapidly during winter months (Figure 3.8.2). Concentrations were highest in the Columbia River Gorge region, followed by the Northern Great Plains region. For most of the regions, the peak in monthly mean CM occurred in July or August and ranged around  $5\text{--}8 \text{ } \mu\text{g m}^{-3}$ . Concentrations were lowest in the Northwest region (peak  $\sim 3 \text{ } \mu\text{g m}^{-3}$ ), compared to monthly mean concentrations nearly ten times higher in the Columbia River Gorge region.

In the southwestern United States, the summer maxima observed in regions farther north (e.g., Sierra Nevada, Great Basin, Colorado Plateau, and Central Rockies regions) shifted toward the spring months for regions farther south (e.g., Southern Arizona, Mogollon Plateau, and West Texas regions; see Figure 3.8.3). The peaks in monthly mean CM during spring may be associated with dust source regions in the southwestern United States and Mexico and predominant meteorological conditions corresponding to dust episodes in those seasons. Some of the regions with the highest monthly mean CM concentrations ( $>10 \text{ } \mu\text{g m}^{-3}$ ) in the southwestern United States were located in California, including the California Coast, Southern California, and Sierra Nevada regions. The monthly mean CM concentrations in the Hawaii region were low ( $<2 \text{ } \mu\text{g m}^{-3}$ ) year round.

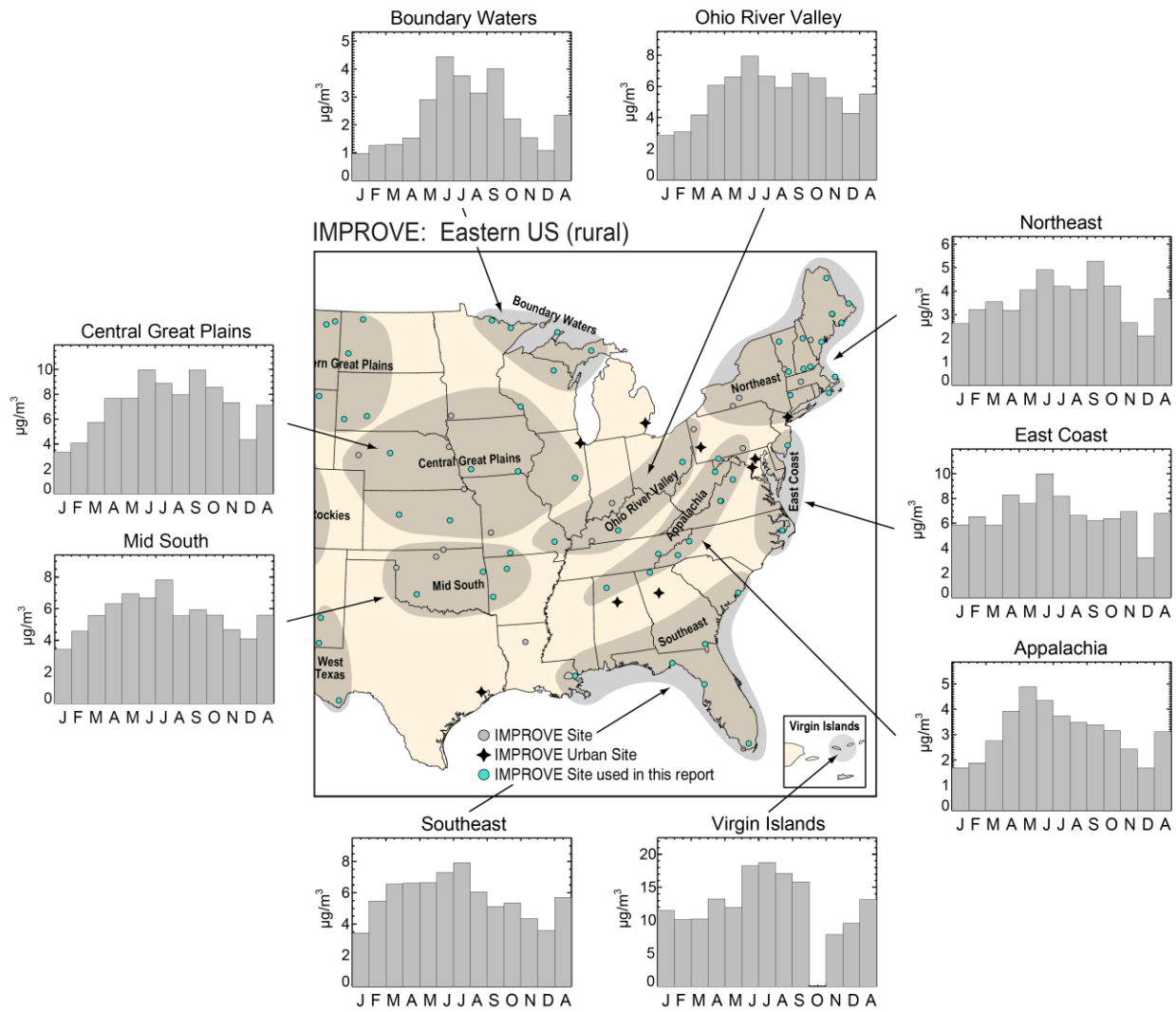


**Figure 3.8.1. IMPROVE 2016–2019 regional monthly mean coarse mass (CM) concentrations ( $\mu\text{g m}^{-3}$ ) for the eastern United States. Letters on the x-axis correspond to the month and “A” corresponds to annual mean. Shaded areas in the map correspond to regions that include the sites used in the analysis, shown as blue dots.**

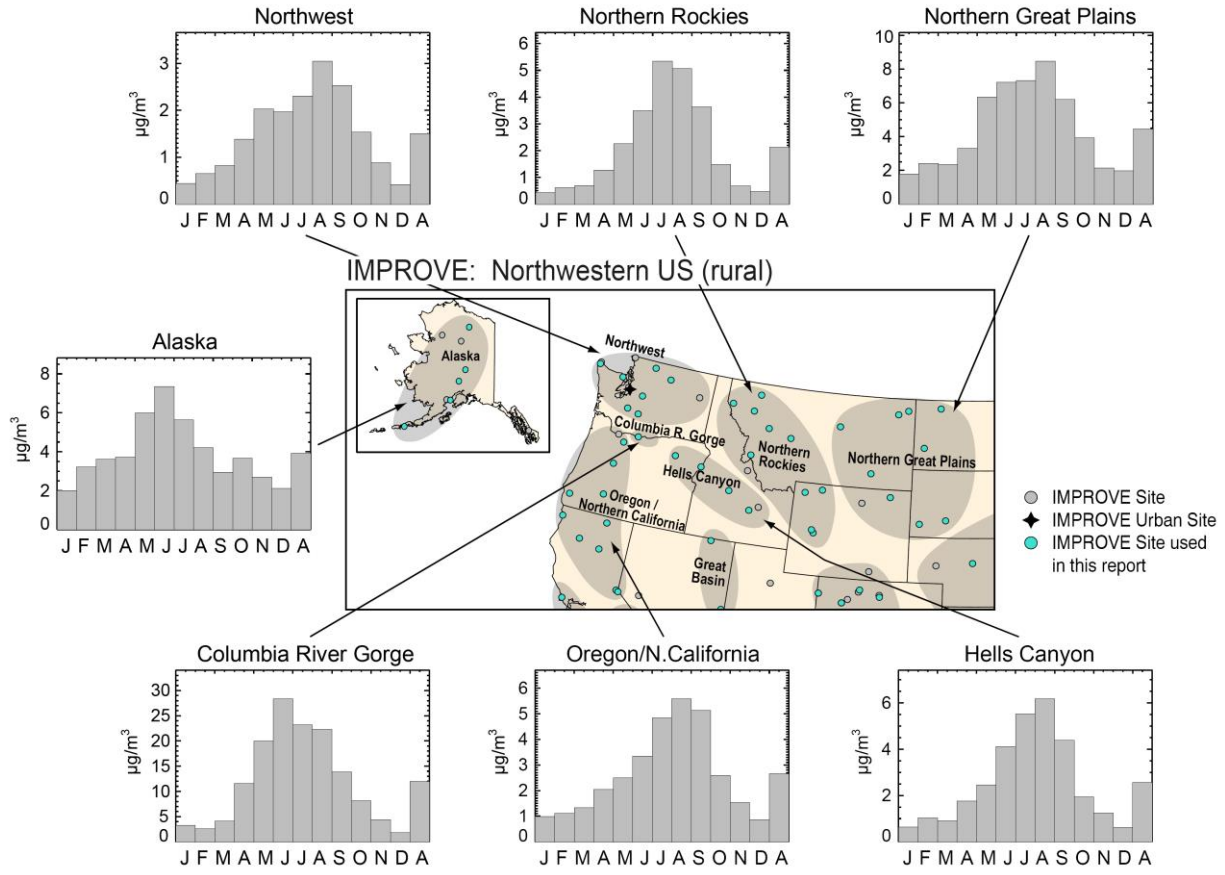


**Figure 3.8.2. IMPROVE 2016–2019 regional monthly mean coarse mass (CM) concentrations ( $\mu\text{g}/\text{m}^3$ ) for the northwestern United States. Letters on the x-axis correspond to the month and “A” corresponds to annual mean. Shaded areas in the map correspond to regions that include the sites used in the analysis, shown as orange dots.**

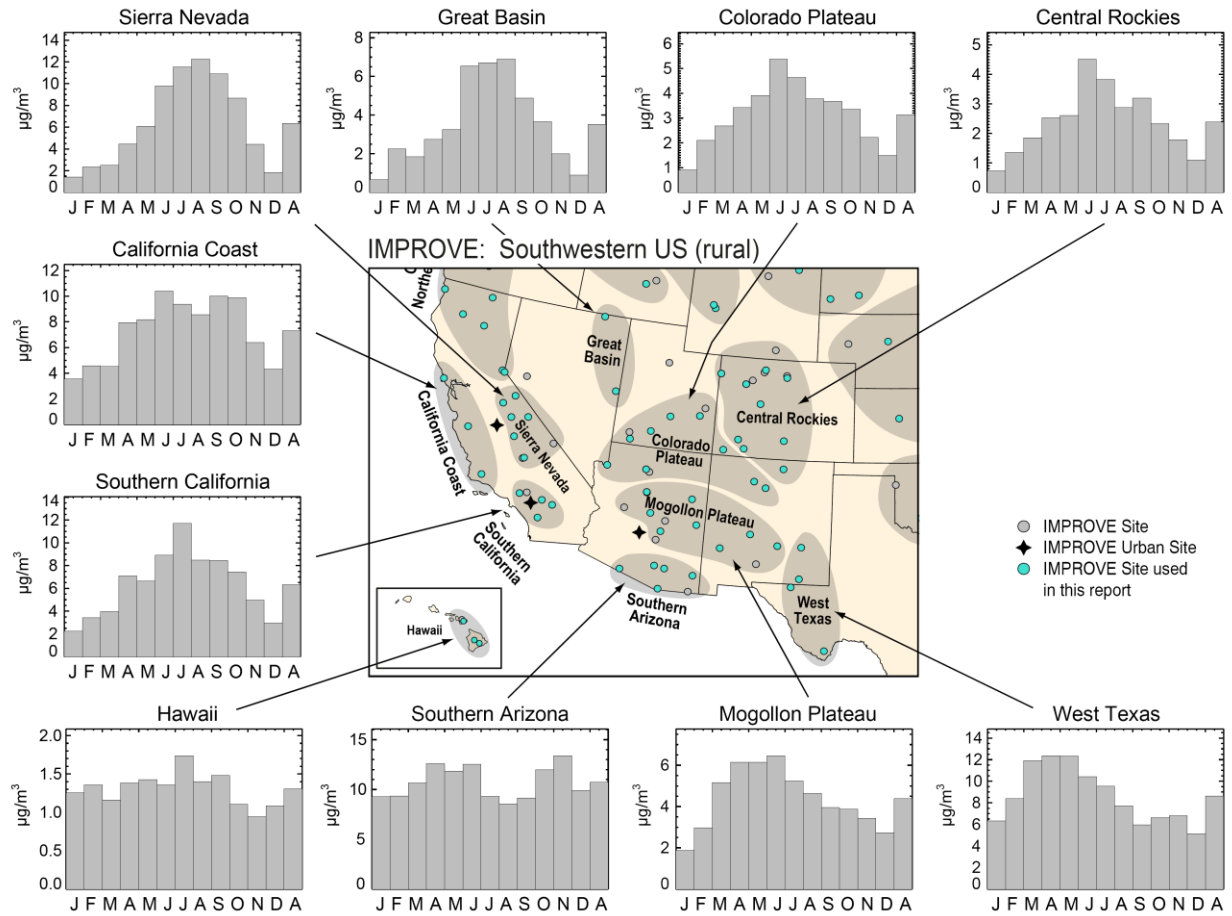


**Figure 3.8.3. IMPROVE 2016–2019 regional monthly mean coarse mass (CM) concentrations ( $\mu\text{g m}^{-3}$ ) for the southwestern United States. Letters on the x-axis correspond to the month and “A” corresponds to annual mean. Shaded areas in the map correspond to regions that include the sites used in the analysis, shown as orange dots.**

### 3.9 DISCUSSION

The differences observed in the seasonal and spatial patterns in species concentrations for the rural regions of the IMPROVE network and the urban/suburban regions in the CSN network were indicative of the spatial extent of aerosol sources, atmospheric processes, regional transport, and sinks. For example, AS seasonal patterns and concentrations were similar for both the IMPROVE rural and CSN urban regions. In the eastern United States, monthly mean AS concentrations were similar in magnitude and had low monthly variability in both urban and rural regions. For nearly all urban and rural regions, monthly mean concentrations were near  $2 \mu\text{g m}^{-3}$  or less and fractional contributions were  $<0.3$ . Concentrations in urban and rural regions in the northwestern United States were lower ( $<2 \mu\text{g m}^{-3}$ ) than in regions in the eastern United States, likely due to lower emissions of  $\text{SO}_2$ . The variability of monthly mean AS concentrations was more pronounced in rural regions compared to urban regions in the northwestern United States, in part because of the large contributions from POM during summer. Some urban regions also exhibited this pattern. Contributions of AS to RCFM in northwestern U.S. regions were typically  $<0.2$ , lower than for eastern U.S. regions. In urban CSN regions in the southwestern United States, AS concentrations peaked in summer at many regions. Less monthly variability

was seen in rural IMPROVE regions; however, similar magnitudes in concentration were observed.

Seasonal and spatial patterns in monthly mean AN concentrations were similar between urban and rural regions. For example, in the eastern United States, monthly mean concentrations were higher in regions farther north. Regions farther north were closer to areas with extensive agricultural activity, such as the Midwest United States. However, in urban regions AN concentrations were higher, although they peaked during winter months in both urban and rural regions, and often exceeded AS concentrations. Monthly variability and concentration magnitude decreased for regions farther south for both urban and rural regions. Contributions were a significant fraction of RCFM in urban and rural regions, especially during winter months in regions farther north. AN monthly mean concentrations were lower in regions in the northwestern United States, although concentrations in urban regions were still higher than in rural regions. Higher monthly mean concentrations were observed during winter months near areas of agricultural activity for both urban and rural regions. AN concentrations were higher than AS concentrations during winter months in many urban and rural regions in the northwestern United States. In the southwestern United States, higher urban mean AN concentrations were observed relative to rural regions, especially in California, Utah, and Colorado.

The strong summer maxima in POM concentrations in western rural regions suggested that wildfire activity was a major contributor to POM concentrations in rural areas, especially in the western and northwestern United States in summer. Biogenic secondary organic aerosol also could have contributed significantly to high summer POM concentrations. Urban regions experienced maxima in monthly mean POM concentrations during summer but also during winter months, which could be due to additional local sources and meteorological conditions. Summer maxima in regions in the northwestern United States were higher for rural regions, due largely to smoke impacts. In regions in the southwestern United States, both summer and winter maxima were common in urban regions, whereas most rural regions experienced maxima during summer. Seasonal and spatial variability in rural and urban regions was similar in the eastern United States, with higher concentrations during summer months. Less monthly variability was observed in urban regions farther south, which was not reflected at rural regions. POM monthly mean concentrations in eastern U.S. regions were typically higher than at rural regions. POM was the dominant contributor to RCFM at all areas of the United States. In the eastern United States, half of RCFM was composed of POM in both urban and rural regions, especially during summer months. These contributions were greater in both urban and rural regions in the northwestern United States; contributions over 0.7 were common. The contributions decreased for southwestern U.S. regions, but during summer, POM could dominate RCFM at both urban and rural regions, and in some urban regions, POM could be equally important during winter months.

Monthly mean EC concentrations were higher in urban regions across the United States. The urban regional monthly mean maxima were nearly three times higher than those in rural regions. In rural regions, EC seasonal and spatial patterns tended to follow those of POM, especially in northwestern U.S. regions where biomass smoke impacts were significant sources. Summer maxima in monthly mean EC reflected smoke contributions, but higher winter

contributions were also observed, especially in urban regions, likely due to residential heating. Contributions to RCFM were also higher in urban regions across the United States.

FD concentrations were influenced by both local and long-range transport. While it is difficult to make direct comparisons between IMPROVE and CSN monthly mean FD concentrations due to existing biases, some similar spatial patterns were evident. The long-range transport of North African dust influenced both urban and rural regions in the eastern United States during summer in regions farther south. This influence was especially evident in the relative contribution of FD to RCFM. Monthly mean FD concentrations were higher near agricultural areas for both urban and rural regions, such as the Central Great Plains/Central U.S. and Northern Great Plains. The spring dust phenomenon in the southwestern United States also influenced both rural and urban regions. Contributions of FD to RCFM were significant during spring months (~0.5), suggesting both local and regional sources influenced RCFM across the southwestern United States.

While the seasons corresponding to maxima and minima for CM and FD concentrations agreed in some regions (e.g., in the northwestern United States and many regions in the southwestern United States), for many regions these seasons did not coincide. If FD was the main contributor to CM, their seasonality would be similar. It is possible and probably quite likely that the seasonality of CM was influenced by the variability of species other than mineral dust.

SS concentrations and fractional contributions were negligible in most urban and rural regions. Coastal regions (including regions on both the east and west coasts, including the Hawaii and Alaska regions) were the only regions to correspond to non-negligible impacts from SS on RCFM. SS corresponded to a high degree of seasonality.

FM concentrations were noticeably higher in urban regions than rural regions. The regional mean urban maximum was nearly twice that of rural maximum. The rural monthly mean maximum was likely due to the impact of biomass smoke, given its occurrence in the Oregon/Northern California region in August and the dominant role of POM. The maximum urban monthly mean FM concentration occurred in the Sacramento/Central Valley region in December due to POM and AN concentrations. For most urban and rural regions across the United States, depending on season, the highest FM concentrations occurred due to high contributions of POM and AN, highlighting their importance to the FM budget.

Tables with regional monthly mean concentrations listed as a function of species, month, and region are provided in Appendix 3.1 for IMPROVE and the CSN. Regional monthly mean mass fractions are listed in Appendix 3.2 for IMPROVE and the CSN.

## REFERENCES

- Debell, L. J., Gebhart, K., Hand, J. L., Malm, W. C., Pitchford, M. L., Schichtel, B. S., and White, W. H. (2006), IMPROVE (Interagency Monitoring of Protected Visual Environments): Spatial and seasonal patterns and temporal variability of haze and its constituents in the United States: Report IV, Colorado State University, Fort Collins CO, ISSN 0737-5352-74.
- Hand, J. L., Copeland, S., Day, D., Dillner, A., Indresand, H., Malm, W., McDade, C., Moore, C., Pitchford, M., and Schichtel, B. (2011), IMPROVE (Interagency Monitoring of Protected Visual Environments): Spatial and seasonal patterns and temporal variability of haze and its constituents in the United States, Report V, Colorado State University, Fort Collins, CO.
- Hand, J. L., Schichtel, B. A., Pitchford, M., Malm, W. C., and Frank, N. H. (2012), Seasonal composition of remote and urban fine particulate matter in the United States, *Journal of Geophysical Research: Atmospheres*, 117(D5), D05209, doi:10.1029/2011jd017122.
- Hand, J. L., Gill, T., and Schichtel, B. (2017), Spatial and seasonal variability in fine mineral dust and coarse aerosol mass at remote sites across the United States, *Journal of Geophysical Research: Atmospheres*, 122(5), 3080-3097, doi:10.1002/2016JD026290.
- Malm, W., Sisler, J. F., Pitchford, M., Scruggs, M., Ames, R. B., Copeland, S., Gebhart, K., and Day, D. (2000), IMPROVE (Interagency Monitoring of Protected Visual Environments): Spatial and seasonal patterns and temporal variability of haze and its constituents in the United States: Report III, Colorado State University, Fort Collins, CO, ISSN 0737-5352-47.

## Chapter 4. Reconstructed Aerosol Light Extinction Coefficients

Light extinction occurs in the atmosphere when incident light is attenuated by the scattering and absorption of light from particles and gases in the layer through which it travels. The light extinction coefficient ( $b_{ext}$ ) is the fractional loss of intensity per unit path length. The Beer-Lambert law describes the intensity (F) of an incident flux ( $F_o$ ) through a layer of thickness (z) as

$$\frac{F}{F_o} = \exp(-b_{ext} z). \quad (4.1)$$

The extinction coefficient can be written as the sum of scattering and absorption by particles ( $b_{sp}$  and  $b_{ap}$ , respectively) and gases ( $b_{sg}$  and  $b_{ag}$ , respectively) and has units of inverse length:

$$b_{ext} = b_{sp} + b_{ap} + b_{sg} + b_{ag}. \quad (4.2)$$

Absorption of light by gases is a well-understood phenomenon and straightforward to estimate. Visible light absorption by gases in the atmosphere is dominated by nitrogen dioxide ( $\text{NO}_2$ ) and can be estimated by multiplying  $\text{NO}_2$  concentrations by an absorption efficiency (Pitchford et al., 2007). Rayleigh scattering theory describes scattering of light by molecules ( $b_{sg}$ ) and depends on the density of the atmosphere. The highest Rayleigh scattering values occur at sea level ( $\sim 12 \text{ Mm}^{-1}$  at 550 nm), compared to the lowest levels at high elevations ( $8 \text{ Mm}^{-1}$  at 550 nm at  $\sim 3.0 \text{ km}$ ). Rayleigh scattering can vary due to temperature and pressure variations; it can be accurately determined if elevation and meteorological conditions are known.

Light extinction by particles is more complicated and depends strongly on particle size, composition, and hygroscopic properties. All particles scatter light and, if their size and refractive index are known, light scattering coefficients can be computed using Mie theory, assuming spherical particles. Light absorption by particles in the visible wavelengths is due to light absorbing carbon as well as some crustal mineral species. Because all of the required information necessary for performing Mie calculations is typically unknown (size distribution and concurrent aerosol composition measurements are time intensive and costly), the IMPROVE algorithm was developed to estimate aerosol light extinction coefficients based on assumed size distributions and composition measurements (Malm et al., 1994).

### 4.1 IMPROVE AEROSOL LIGHT EXTINCTION COEFFICIENT ALGORITHM

Light extinction coefficients can be computed for an external mixture of aerosols by assuming a linear combination of species mass concentrations:

$$b_{ext} = \sum_j \alpha_j M_j. \quad (4.3)$$

The species (j) mass concentration is given by  $M_j (\mu\text{g m}^{-3})$ , and the dry speices mass extinction efficiency is given by  $\alpha_j (\text{m}^2 \text{ g}^{-1})$  (Hand and Malm, 2007). Equation (4.3) holds for an internally mixed aerosol where the chemical species are mixed in fixed proportions to each other,

the index of refraction is not a function of composition or size, and the aerosol density is independent of volume (Malm and Kreidenweis, 1997).

For species that absorb water, the linear relationship between light extinction coefficients and mass shown in equation (4.3) will not hold because of the nonlinear behavior of particle growth and  $b_{ext}$  with increased relative humidity (RH). To account for this effect, the extinction efficiencies are multiplied by a humidification factor ( $f(RH) = b_{sp,RH}/b_{sp,dry}$ ) that is the ratio of humidified ( $b_{sp,RH}$ ) to dry ( $b_{sp,dry}$ ) light scattering coefficients. Humidification factors are computed by assuming a size distribution and using composition-dependent growth factors.

The original IMPROVE equation has been used extensively to reconstruct  $b_{ext}$ , using measured aerosol composition (e.g., Malm et al., 1994; Lowenthal and Kumar, 2003; Malm et al., 2005; Malm and Hand, 2007; Prenni et al., 2019), and was adopted by the Environmental Protection Agency (EPA) as a metric for tracking progress in reducing haze levels under the 1999 Regional Haze Rule (RHR) (Pitchford et al., 2007). In 2005 a review was initiated by the IMPROVE steering committee to investigate possible biases in reconstructed light extinction coefficients as computed by the original algorithm (Hand and Malm, 2006; Malm and Hand, 2007). The review resulted in the development of the second IMPROVE algorithm that is now being used by most states in their state implementation plans (Pitchford et al., 2007).

Modifications made for the second IMPROVE algorithm included the addition of a sea salt (SS) term with associated hygroscopic growth; a change in the organic mass (OM) to organic carbon (OC) ratio (OM/OC) from 1.4 to 1.8 to calculate particulate organic mass from organic carbon (POM = (OM/OC)×OC); the use of site-specific Rayleigh scattering values rather than a constant 10  $Mm^{-1}$ ; and a split-component mass extinction efficiency algorithm for ammonium sulfate (AS), ammonium nitrate (AN), and POM to approximate a bimodal size distribution. The second IMPROVE equation also included light absorption for NO<sub>2</sub> (Pitchford et al., 2007) for locations with these measurements; this term is not included in the analysis here.

Recent examinations of biases between gravimetric and reconstructed fine mass and measured and reconstructed scattering have identified issues with the reconstructed mass and extinction algorithms, resulting in underestimations of reconstructed mass and extinction over time (Hand et al., 2019; Prenni et al., 2019). As discussed in Chapter 2, biases associated with the OM/OC ratio and underestimates of fine dust (FD) were identified as major contributors to the mass bias and were accounted for by applying monthly values of OM/OC and increasing FD by 15%. Biases in measured and reconstructed scattering were associated with the split-component mass extinction efficiency algorithm used to approximate bimodal size distributions for AS, AN, and POM. A potential correction to the reconstructed extinction algorithm was proposed by Prenni et al. (2019) but has not been finalized.

Given the changes to the reconstructed mass algorithm and issues related to the split-component extinction algorithm, the approach for calculating reconstructed extinction in this report is a modified version of the original IMPROVE algorithm (single size mode model), with the addition of SS and site-specific Rayleigh scattering. In addition, POM was calculated with monthly varying OM/OC ratios as described in Chapter 2, and FD was increased by 15%. The algorithm for calculating ambient total  $b_{ext}$  ( $b_{ext,tot}$ ) is presented in equation (4.4):

$$b_{ext\_tot} = 3 \times f(RH) \times [AS] + 3 \times f(RH) \times [AN] + 4 \times [POM] + 10 \times [EC] + 1 \times [FD] + 1.7 \times f(RH)_{ss} \times [SS] + 0.6 \times [CM] + \text{site-specific Rayleigh scattering} \quad (4.4)$$

EC is elemental carbon and CM is coarse mass. The units of  $b_{ext\_tot}$  and Rayleigh scattering are in inverse megameters ( $Mm^{-1}$ ). Mass concentrations of aerosol species are in units of  $\mu\text{g m}^{-3}$ , and mass extinction efficiencies have units of  $\text{m}^2 \text{ g}^{-1}$ . Dry mass extinction efficiencies (numerals multiplying each term in equation 4.4) were rounded to one significant digit to represent the degree of uncertainty associated with these values. Values of  $3 \text{ m}^2 \text{ g}^{-1}$  were used for both AS and AN,  $4 \text{ m}^2 \text{ g}^{-1}$  for POM,  $10 \text{ m}^2 \text{ g}^{-1}$  for EC,  $1 \text{ m}^2 \text{ g}^{-1}$  for FD,  $1.7 \text{ m}^2 \text{ g}^{-1}$  for SS, and  $0.6 \text{ m}^2 \text{ g}^{-1}$  for CM. These values correspond to a wavelength of 550 nm (Hand and Malm, 2007). Extinction coefficients for individual species correspond to their individual terms in equation (4.4).

The  $f(RH)$  values applied in equation (4.4) were computed using the algorithm outlined in the Regional Haze Rule Guidelines for Tracking Progress (EPA, 2003) and were the same values applied in previous IMPROVE reports. The  $f(RH)$  curve was calculated with Mie theory, assuming a lognormal AS mass size distribution with a geometric mass mean diameter of  $0.3 \mu\text{m}$  and a geometric standard deviation of 2.0 and interpolated between the deliquescence and efflorescence points. This  $f(RH)$  was applied to both AS and AN (see Figure 4.1a). The  $f(RH)_{ss}$  curve applied to SS was computed assuming a SS geometric mass mean diameter of  $2.5 \mu\text{m}$  and a geometric standard deviation of 2 and is shown in Figure 4.1b (Pitchford et al., 2007). Below the deliquescence point ( $RH = 47\%$ ) the  $f(RH)_{ss}$  is set to 1. POM was assumed to be nonhygroscopic. Humidification factors are unitless.

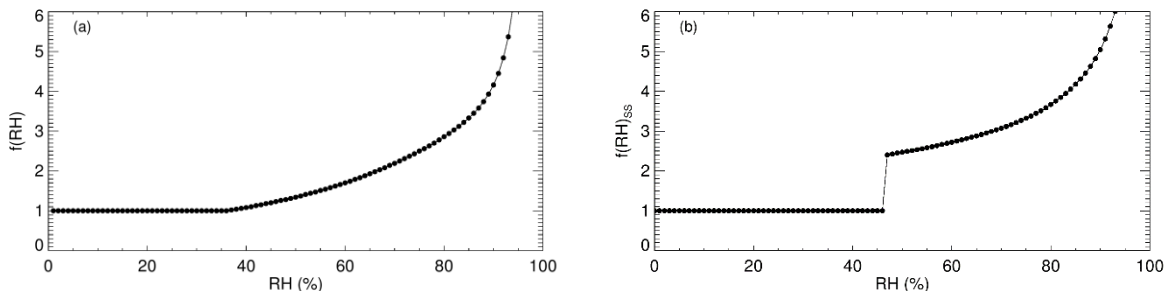


**Figure 4.1. (a) Humidification factors ( $f(RH)$ ) as a function of relative humidity (RH, %) for AS. A lognormal mass size distribution with a geometric mass mean diameter of  $0.3 \mu\text{m}$  and a geometric standard deviation of 2.0 was assumed. (b)  $f(RH)_{ss}$  for SS with an assumed lognormal mass size distribution with a geometric mass mean diameter of  $2.5 \mu\text{m}$  and a geometric standard deviation of 2.0. A wavelength of 550 nm was used.**

Monthly and site-specific  $f(RH)$  curves were generated based on monthly climatological mean RH values. These monthly RH values eliminate the effects of interannual variations in RH while maintaining typical regional and seasonal humidity patterns around the United States. The EPA produced recommended monthly  $f(RH)$  values for each Class I area, based on analysis of a 10-year record (1988–1997) of hourly RH data from 292 National Weather Service stations across the 50 states and the District of Columbia, as well as from 29 IMPROVE and IMPROVE-protocol monitoring sites, 48 Clean Air Status and Trends Network (CASTNet) sites, and 13 additional sites administered by the National Park Service. Values of  $f(RH)$  for other IMPROVE sites (non-Class I area sites) were generated using an interpolation scheme with an inverse distance weighting technique (EPA, 2001). The daily ambient AS, AN, and SS extinction

coefficients for each site were calculated using this lookup table. Values of  $f(RH)$  vary significantly depending on time of year and site location. For example, the  $f(RH)$  value at Great Basin National Park (NP), Nevada (GRBA1), in August is assumed to be 1.23, compared to 4.16 in at Redwood NP, California (REDW1). Estimates of  $f(RH)$  for Chemical Speciation Network (CSN) sites were determined similarly to non-Class I area IMPROVE sites by using an interpolation scheme. Values of  $f(RH)$  and site-specific Rayleigh scattering values used in this report are provided in Appendix 4.1 and 4.2 (IMPROVE and the CSN, respectively).

Visual range and extinction measurements are nonlinear with respect to human perception of visual scene changes caused by haze. The deciview ( $dv$ ) haze index was derived with a number of assumptions such that uniform changes in haze correspond to approximately uniform incremental changes in visual perception (Pitchford and Malm, 1994). Deciview is calculated from reconstructed  $b_{ext\_tot}$ , using equation (4.5):

$$dv = 10 \times \ln(b_{ext\_tot}/10) \quad (4.5)$$

In the original IMPROVE equation,  $dv = 0$  for pristine (Rayleigh scattering) conditions (elevation  $\sim 1.8$  km) for elevations where Rayleigh scattering =  $10 \text{ Mm}^{-1}$ . For different values of site-specific Rayleigh scattering, as specified in equation (4.4), it is possible to have a negative  $dv$  for pristine conditions ( $b_{ext\_tot} < 10 \text{ Mm}^{-1}$ ).

Daily  $b_{ext}$  values were computed using equation (4.4) for AS, AN, POM, EC, FD, SS, CM, reconstructed aerosol  $b_{ext}$  ( $b_{ext\_aer}$  = sum of speciated  $b_{ext}$ ),  $b_{ext\_tot}$  ( $b_{ext\_tot} = b_{ext\_aer} + \text{site-specific Rayleigh scattering}$ ), and  $dv$  for IMPROVE and CSN sites. Monthly, seasonal, and annual means were computed following the methods and completeness criteria outlined in Chapter 2. Spatial patterns of 2016–2019 annual mean speciated  $b_{ext}$  are presented. Differences between patterns in mass and  $b_{ext}$  are likely due to hygroscopic effects for species that uptake water. For nonhygroscopic species,  $b_{ext}$  values are scaled mass concentrations. Fractional contributions of speciated  $b_{ext}$  to  $b_{ext\_aer}$  are also presented. The top number in the scale of each contour map corresponds to the maximum  $b_{ext}$  for all sites, although the contours themselves were created with the highest level set to the 95<sup>th</sup> percentile in  $b_{ext}$ . Interpolated data are provided only to reflect general spatial patterns, not for strict interpretation.

Recall from Chapter 2 that CM is not available at CSN sites. For CSN, an estimate of urban CM  $b_{ext\_CM}$  was made by interpolating 2016–2019 monthly averaged EPA CM concentrations to CSN site locations. These interpolated monthly mean values were used to calculate daily estimates of  $b_{ext\_aer}$ ,  $b_{ext\_tot}$ , and  $dv$  at CSN sites. Comparisons of 2016–2019 monthly mean CM concentrations at collocated IMPROVE (measured) and CSN (interpolated) sites are shown in Figure 4.2 for Birmingham, Alabama (BIRM1), Fresno, California (FRES1), Phoenix, Arizona (PHOE1), and Puget Sound, Washington (PUSO1). Concentrations were highly correlated ( $r = 0.99$ ); however, monthly mean IMPROVE CM was higher than collocated interpolated CSN CM, with a 12% bias. For context, recall that biases between IMPROVE and CSN FD and SS were greater (20% and 81%, respectively), with higher IMPROVE values (see Chapter 1). CM was not interpolated at sites in Alaska or Hawaii, so  $b_{ext\_aer}$ ,  $b_{ext\_tot}$ ,  $dv$ , and fractional contributions of  $b_{ext\_CM}$  to  $b_{ext\_aer}$  were not calculated at those sites.

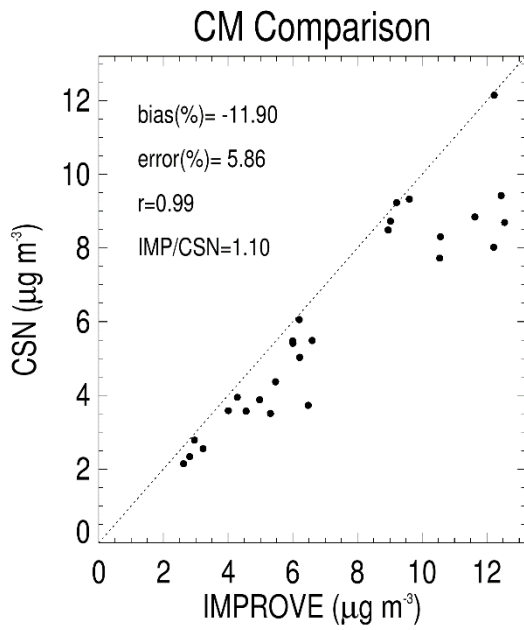


**Figure 4.2.** Comparisons of 2016–2019 monthly mean coarse mass concentrations (CM,  $\mu\text{g m}^{-3}$ ) for four collocated IMPROVE (measured) and CSN (interpolated) sites. CSN CM concentrations were spatially interpolated from EPA Federal Reference Method (FRM) sites.

## 4.2 SPATIAL PATTERNS IN ANNUAL MEAN AEROSOL LIGHT EXTINCTION COEFFICIENTS

### 4.2.1 PM<sub>2.5</sub> Ammonium Sulfate Light Extinction Coefficients

The 2016–2019 IMPROVE rural annual mean light extinction coefficients corresponding to AS ( $b_{\text{ext\_AS}}$ ) ranged from  $1.67 \text{ Mm}^{-1}$  in Sawtooth National Forest (NF), Idaho (SAWT1), to  $19.52 \text{ Mm}^{-1}$  in Breton Island, Louisiana (BRIS1) (Figure 4.2.1a). Annual mean  $b_{\text{ext\_AS}}$  was higher at sites in the eastern United States relative to the western United States. A similar pattern was observed for annual mean AS mass concentrations in Chapter 2. The highest values of annual mean  $b_{\text{ext\_AS}}$  occurred at sites along the Ohio River valley and the Gulf Coast regions in Louisiana and Florida ( $>15 \text{ Mm}^{-1}$ ). At sites in the Intermountain West,  $b_{\text{ext\_AS}}$  was typically less than  $5 \text{ Mm}^{-1}$ . Although AS annual mean mass concentrations increased along the southern coast of California, this increase was not as obvious for  $b_{\text{ext\_AS}}$ , perhaps due in part to lower relative humidity and hygroscopic effects in that region relative to regions in the East.

Similar spatial patterns of  $b_{\text{ext\_AS}}$  were observed with the addition of CSN sites (Figure 4.2.1b), with higher values at sites along the Ohio River valley and Gulf region, with a strong East-West gradient and low values in the western United States. The maximum annual mean  $b_{\text{ext\_AS}}$  for the CSN network occurred in Liberty, Pennsylvania ( $29.36 \text{ Mm}^{-1}$ , 420030064), compared to the lowest  $b_{\text{ext\_AS}}$  in Reno, Nevada ( $2.37 \text{ Mm}^{-1}$ , 320310016). The similarity in the spatial patterns and magnitudes of  $b_{\text{ext\_AS}}$  for the IMPROVE and CSN sites suggest sources and meteorological conditions that contribute to high  $b_{\text{ext\_AS}}$  on regional scales.

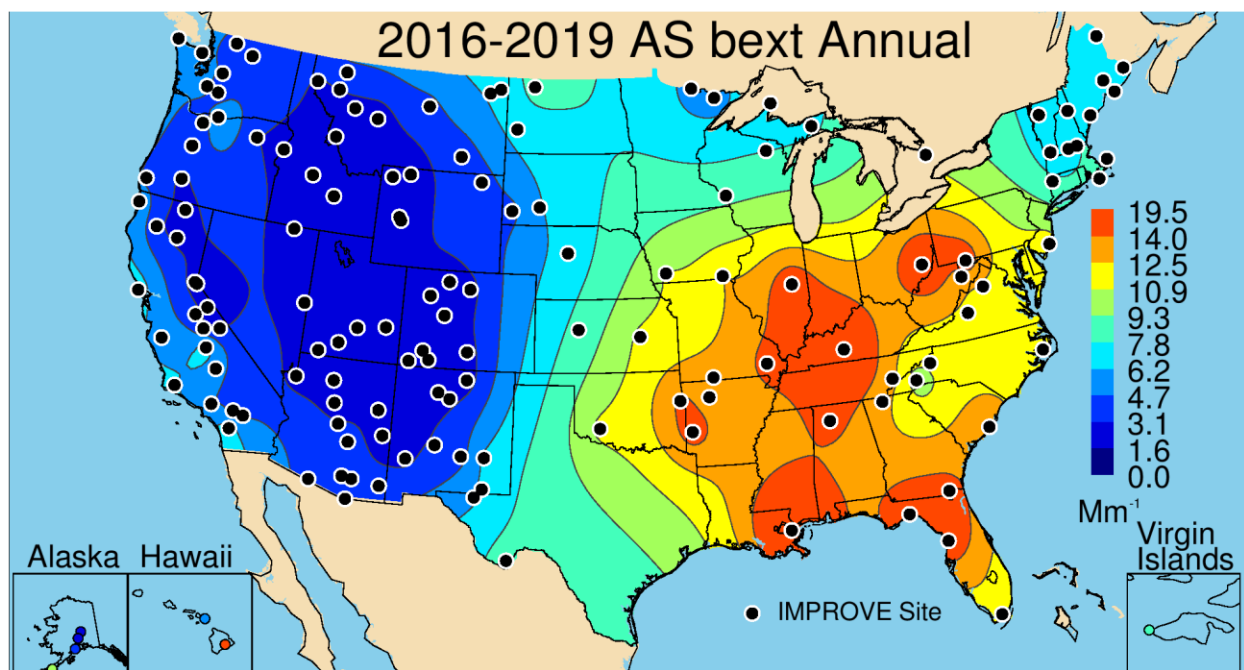


Figure 4.2.1a. IMPROVE 2016–2019 PM<sub>2.5</sub> reconstructed ambient annual mean light extinction coefficients for ammonium sulfate ( $b_{ext\_AS}$ ,  $Mm^{-1}$ ). Wavelength corresponds to 550 nm.

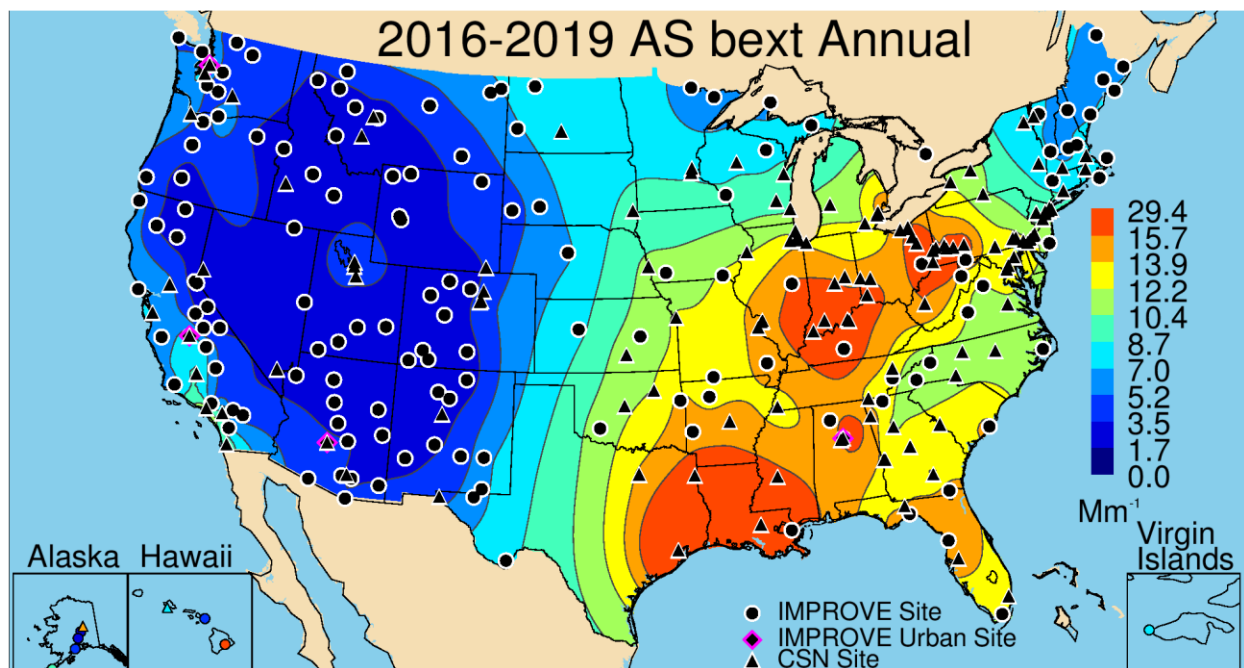
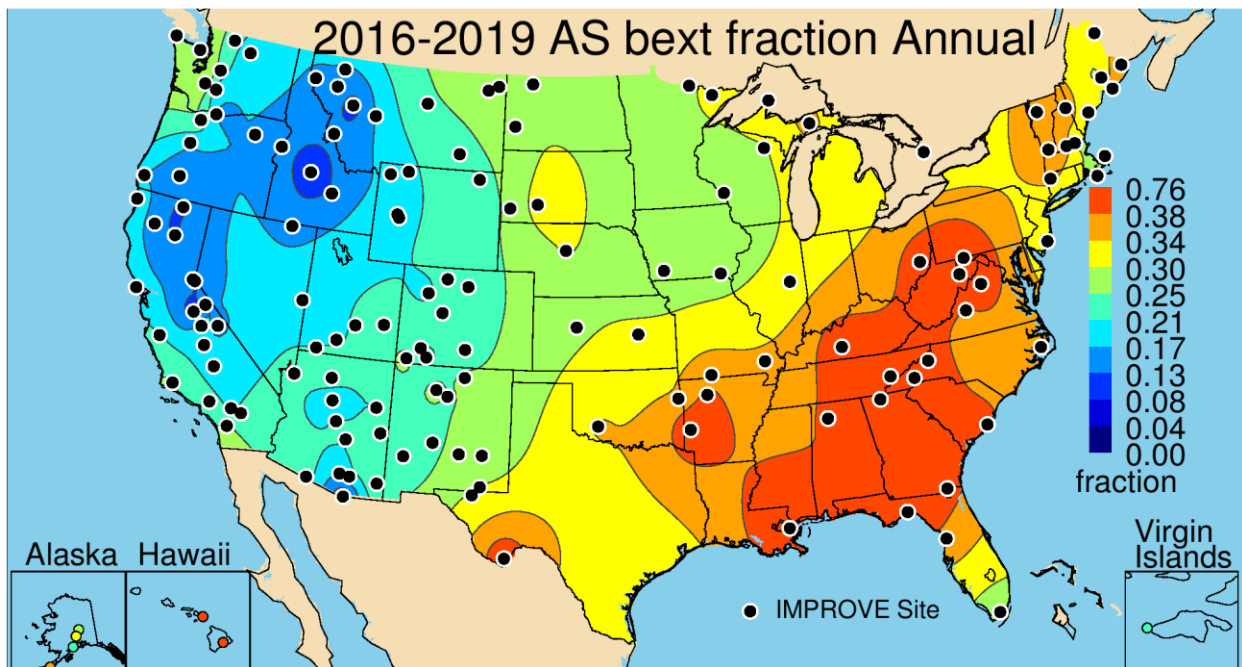


Figure 4.2.1b. IMPROVE and CSN 2016–2019 PM<sub>2.5</sub> reconstructed ambient annual mean light extinction coefficients for ammonium sulfate ( $b_{ext\_AS}$ ,  $Mm^{-1}$ ). Wavelength corresponds to 550 nm.

At sites in the eastern United States, the IMPROVE annual mean fractional contribution of  $b_{ext\_AS}$  to reconstructed  $b_{ext\_aer}$  ranged between 0.3 and 0.5 (Figure 4.2.1c), with the highest contributions at sites in the East along the Ohio River valley and the Southeast. Contributions decreased toward the West, with contributions around 0.25–0.30 across the central United States. The spatial pattern generally followed that of  $b_{ext\_AS}$ . The lowest contributions occurred at sites

in northern California, Idaho, and Oregon (<0.15). The sites with the highest contributions of  $b_{ext\_AS}$  were Hawaii Volcanoes NP, Hawaii (0.76, HAVO1), Breton Island, Louisiana (0.48, BRIS1), and Dolly Sods Wilderness Area (WA), West Virginia (0.47, DOSO1). The minimum contributions occurred at Nogales, Arizona (0.08, NOGA1) and Sawtooth NF, Idaho (0.09, SAWT1).

The fractional contribution of  $b_{ext\_AS}$  at the CSN sites ranged from 0.06 (Butte, Montana, 300930005) to 0.42 (Capitol, Louisiana, 220330009), with very similar spatial patterns as the IMPROVE network (Figure 4.2.1d). However, the addition of CSN sites often corresponded to lower contributions. For example, sites in the eastern United States showed lower contributions, especially at urban sites across the Southeast (~0.3). Lower contributions also occurred for urban sites around the Great Lakes, central United States, and urban sites across the West (e.g., Colorado, New Mexico, Arizona, Idaho, Montana, and California), likely due to the importance of the contribution of other species to  $b_{ext\_aer}$ , such as  $b_{ext\_POM}$  and  $b_{ext\_AN}$ .



**Figure 4.2.1c. IMPROVE 2016–2019 annual mean fraction contributions of ambient ammonium sulfate light extinction coefficient ( $b_{ext\_AS}$ ) to reconstructed aerosol  $b_{ext}$ . Wavelength corresponds to 550 nm.**

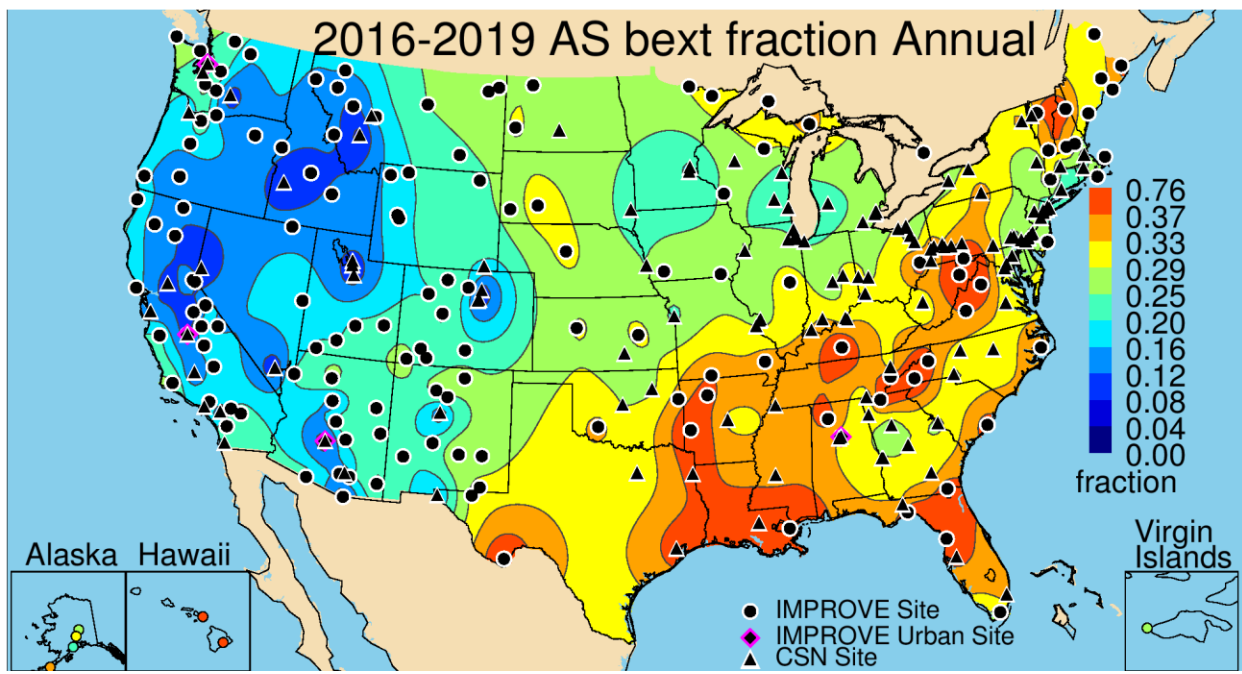


**Figure 4.2.1d. IMPROVE and CSN 2016–2019 annual mean fraction contributions of ambient ammonium sulfate light extinction coefficient ( $b_{ext\_AS}$ ) to reconstructed aerosol  $b_{ext}$ . Wavelength corresponds to 550 nm.**

#### 4.2.2 PM<sub>2.5</sub> Ammonium Nitrate Light Extinction Coefficients

The spatial pattern of the 2016–2019 rural IMPROVE annual mean AN light extinction coefficients ( $b_{ext\_AN}$ ; Figure 4.2.2a) was similar to the annual mean AN mass concentration pattern (Chapter 2). Rural IMPROVE estimates ranged from  $0.34 \text{ Mm}^{-1}$  at Denali NP, Alaska (DENA1), and  $0.49 \text{ Mm}^{-1}$  at Sawtooth NF, Idaho (SAWT1), to  $19.37 \text{ Mm}^{-1}$  in Bondville, Illinois (BOND1), located in the agricultural Midwest. The BOND1 site is in the center of the area of highest  $b_{ext\_AN}$  located in the central United States, where annual mean  $b_{ext\_AN}$  was typically greater than  $10 \text{ Mm}^{-1}$ . In general, however, most of the rural sites corresponded to low annual mean  $b_{ext\_AN}$  ( $<5 \text{ Mm}^{-1}$ ), except at the Columbia River Gorge (CORI1) site in Washington ( $14.74 \text{ Mm}^{-1}$ ) and sites in northern North Dakota and Montana ( $\sim 7 \text{ Mm}^{-1}$ ) near oil and gas development activity. Somewhat elevated levels of  $b_{ext\_AN}$  also occurred at sites along the West Coast ( $\sim 5 \text{ Mm}^{-1}$ ).

Annual mean  $b_{ext\_AN}$  at CSN sites ranged from  $1.25 \text{ Mm}^{-1}$  in Kapolei, Hawaii (150030010) and  $2.06 \text{ Mm}^{-1}$  at Tucson, Arizona (040191028) to  $34.08 \text{ Mm}^{-1}$  in Bakersfield, California (060290014). The spatial pattern of  $b_{ext\_AN}$  with CSN sites was similar to that of annual mean AN mass concentrations, with a region of high extinction in the central United States and hot spots of high  $b_{ext\_AN}$  at western sites in Utah, Washington, and the Central Valley of California (Figure 4.2.2b). CSN sites in the southeastern United States were relatively low ( $<10 \text{ Mm}^{-1}$ ).

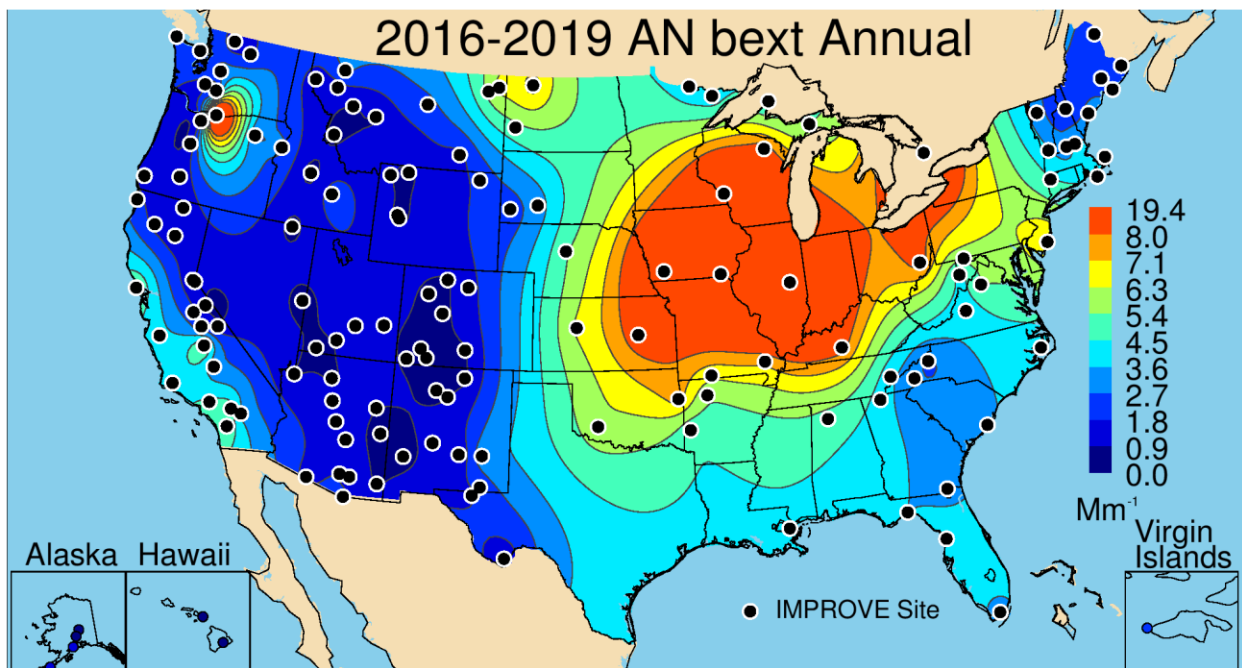


Figure 4.2.2a. IMPROVE 2016–2019 PM<sub>2.5</sub> reconstructed ambient annual mean light extinction coefficients for ammonium nitrate ( $b_{ext\_AN}$ ,  $Mm^{-1}$ ). Wavelength corresponds to 550 nm.

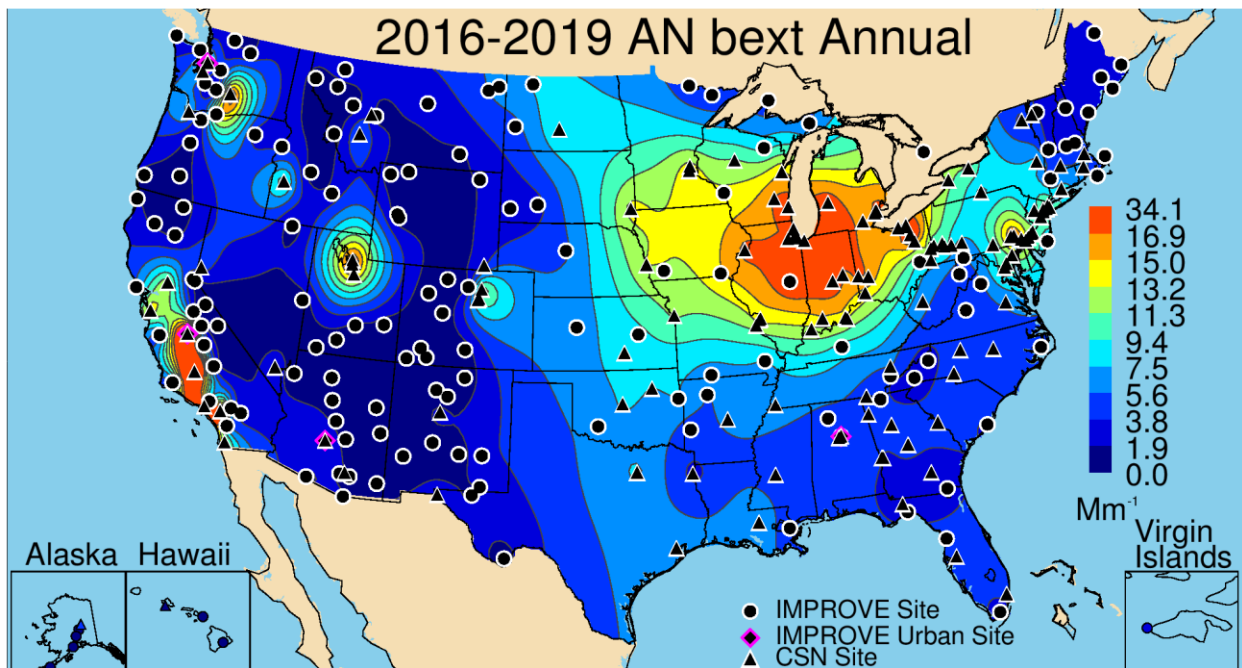
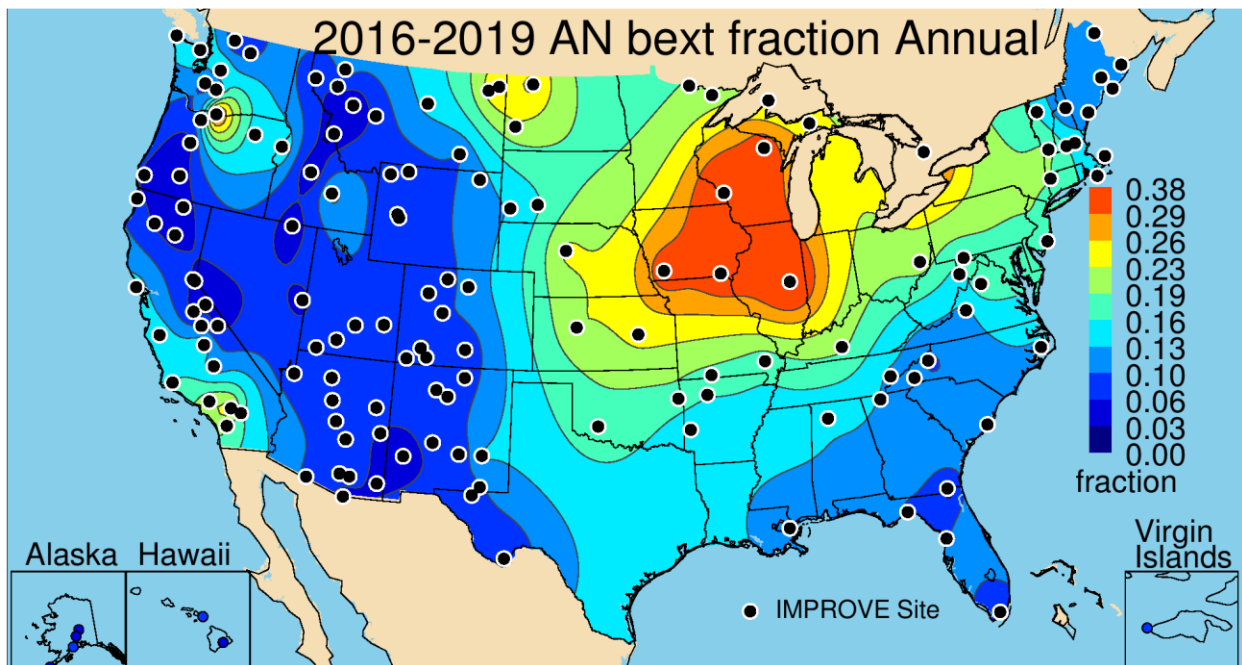


Figure 4.2.2b. IMPROVE and CSN 2016–2019 PM<sub>2.5</sub> reconstructed ambient annual mean light extinction coefficients for ammonium nitrate ( $b_{ext\_AN}$ ,  $Mm^{-1}$ ). Wavelength corresponds to 550 nm.

The spatial pattern of the annual mean fractional contributions of IMPROVE  $b_{ext\_AN}$  to  $b_{ext\_aer}$  reflects the  $b_{ext\_AN}$  pattern (see Figure 4.2.2c), with elevated fractional contributions (>0.3) of  $b_{ext\_AN}$  to  $b_{ext\_aer}$  in areas of high agricultural activity in the central United States. Sites in Southern California and the Central Valley had contributions near 0.2. Contributions of  $b_{ext\_AN}$  to  $b_{ext\_aer}$  were somewhat higher at sites in northern North Dakota and Montana (~0.25). However,

most sites in the Intermountain West corresponded to low annual mean contributions (<0.1), as did sites in the southeastern United States. The highest annual mean fractional contribution occurred at Bondville, Illinois (0.38, BOND1), and the lowest occurred at Sawtooth NF, Idaho (0.03, SAWT1).

The addition of CSN sites did not significantly alter the spatial patterns in annual mean  $b_{ext\_AN}$  contributions to  $b_{ext\_aer}$  (Figure 4.2.2d), with a region of high fractional contribution in the central United States. However, additional impacts at urban sites created hot spots (>0.3), such as at sites in the Colorado Front Range and around Salt Lake City, Utah, as well as the Central Valley of California. The highest annual mean fractional contribution of  $b_{ext\_AN}$  to  $b_{ext\_aer}$  occurred in Bountiful, Utah (0.44, 490110004), compared to the lowest in General Coffee, Georgia (0.06, 130690002).



**Figure 4.2.2c. IMPROVE 2016–2019 annual mean fraction contributions of ambient ammonium nitrate light extinction coefficient ( $b_{ext\_AN}$ ) to reconstructed aerosol  $b_{ext}$ . Wavelength corresponds to 550 nm.**

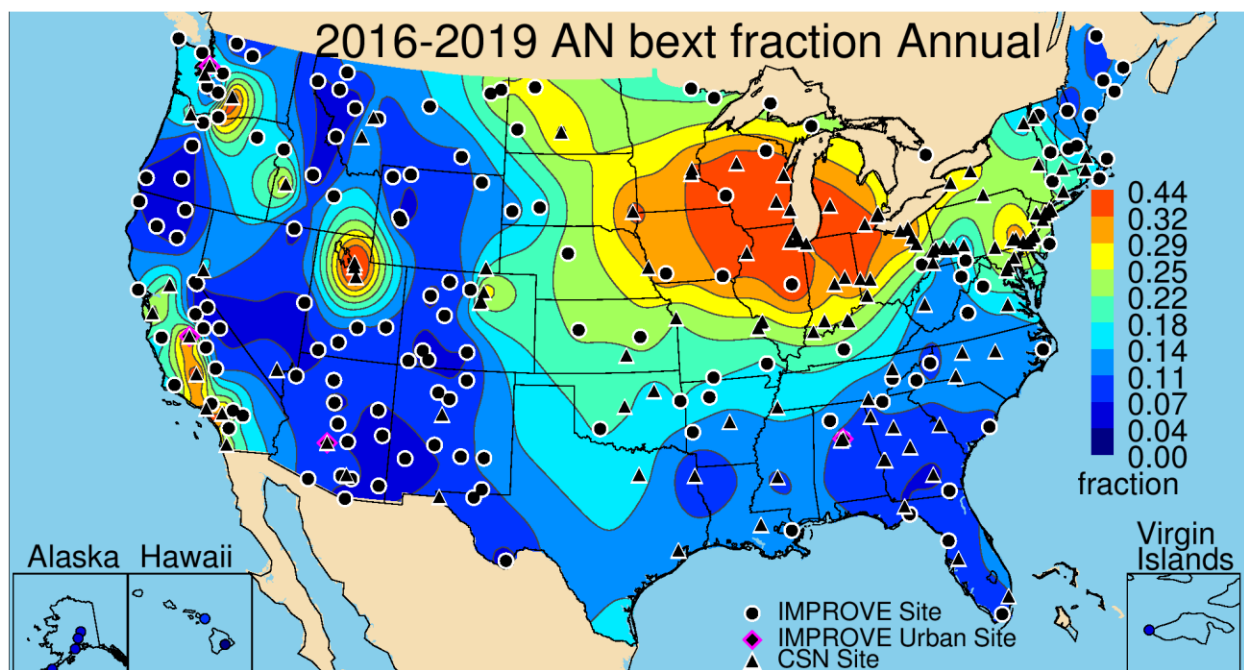


Figure 4.2.2d. IMPROVE and CSN 2016–2019 annual mean fraction contributions of ambient ammonium nitrate light extinction coefficient ( $b_{ext\_AN}$ ) to reconstructed aerosol  $b_{ext}$ . Wavelength corresponds to 550 nm.

#### 4.2.3 PM<sub>2.5</sub> Particulate Organic Matter Light Extinction Coefficients

The 2016–2019 IMPROVE annual mean light extinction coefficient due to POM ( $b_{ext\_POM}$ ) ranged from 0.60 Mm<sup>-1</sup> in Haleakala Crater NP, Hawaii (HACR1), and 2.95 Mm<sup>-1</sup> in White River NF, Colorado (WHRI1), to 27.01 Mm<sup>-1</sup> in Yosemite NP, California (YOSE1). POM was considered nonhygroscopic in equation (4.4), so the spatial pattern of  $b_{ext\_POM}$  (Figure 4.2.3a) reflects that of the POM annual mean mass concentration pattern. High levels of  $b_{ext\_POM}$  were observed at sites in the southern and southeastern United States. Regions of the northwestern United States also included sites with relatively high  $b_{ext\_POM}$ , such as the Central Valley of California (10–15 Mm<sup>-1</sup> and higher). Sites in northern Idaho and Montana also had high  $b_{ext\_POM}$ , likely associated with biomass burning impacts. Low  $b_{ext\_POM}$  occurred at sites across the southwestern United States and part of the Intermountain West, with values less than 5 Mm<sup>-1</sup>.

Urban annual mean  $b_{ext\_POM}$  was higher than at rural sites. Values ranged from 1.66 Mm<sup>-1</sup> in Kapolei, Hawaii (150030010), and 6.06 Mm<sup>-1</sup> at the base of Whiteface Mountain, New York (360310003), to 24.04 Mm<sup>-1</sup> in Fresno, California (020190011). Other urban sites in the Central Valley of California had annual mean  $b_{ext\_POM}$  over 15 Mm<sup>-1</sup>. Elevated  $b_{ext\_POM}$  was also observed at sites in the southeastern United States. Stronger gradients near cities were observed with the inclusion of CSN data, suggesting local urban sources of organic aerosols. Regional sources (perhaps biogenic or wildfire emissions) seemed more spatially extensive in the southeastern United States, compared to more localized sources for many urban centers in the West, such as the Front Range of Colorado; Phoenix, Arizona; and Las Vegas, Nevada.

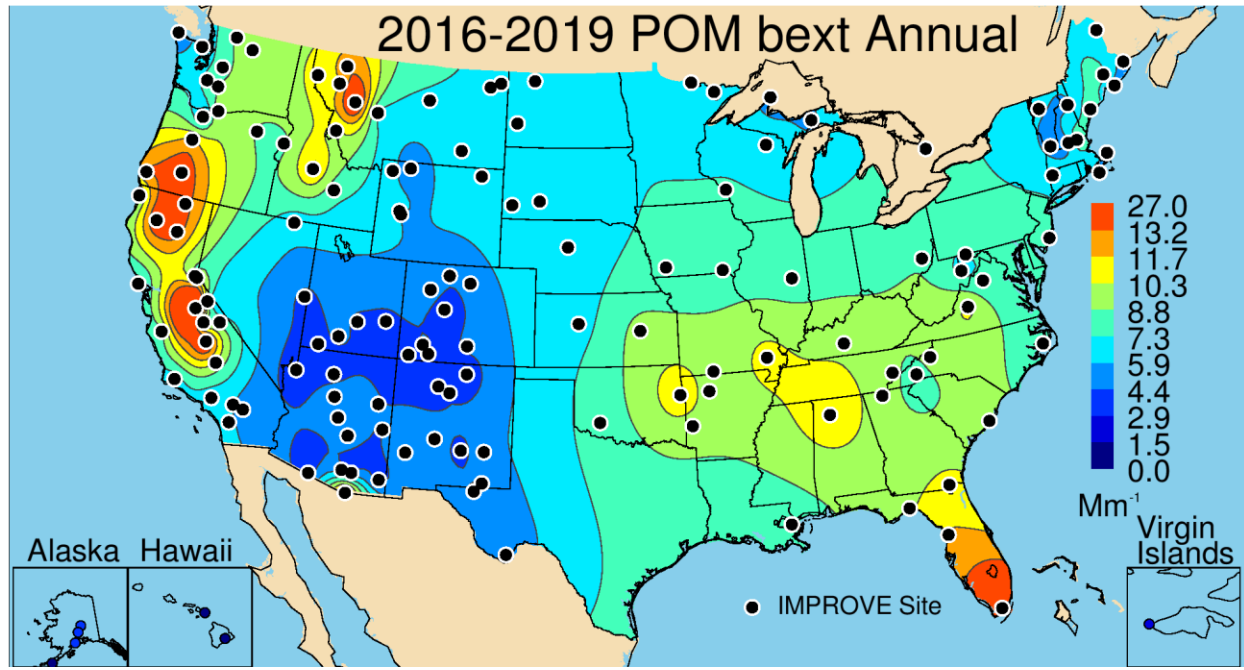


Figure 4.2.3a. IMPROVE 2016–2019 PM<sub>2.5</sub> reconstructed ambient annual mean light extinction coefficients for particulate organic matter ( $b_{ext\_POM}$ ,  $Mm^{-1}$ ). Wavelength corresponds to 550 nm.

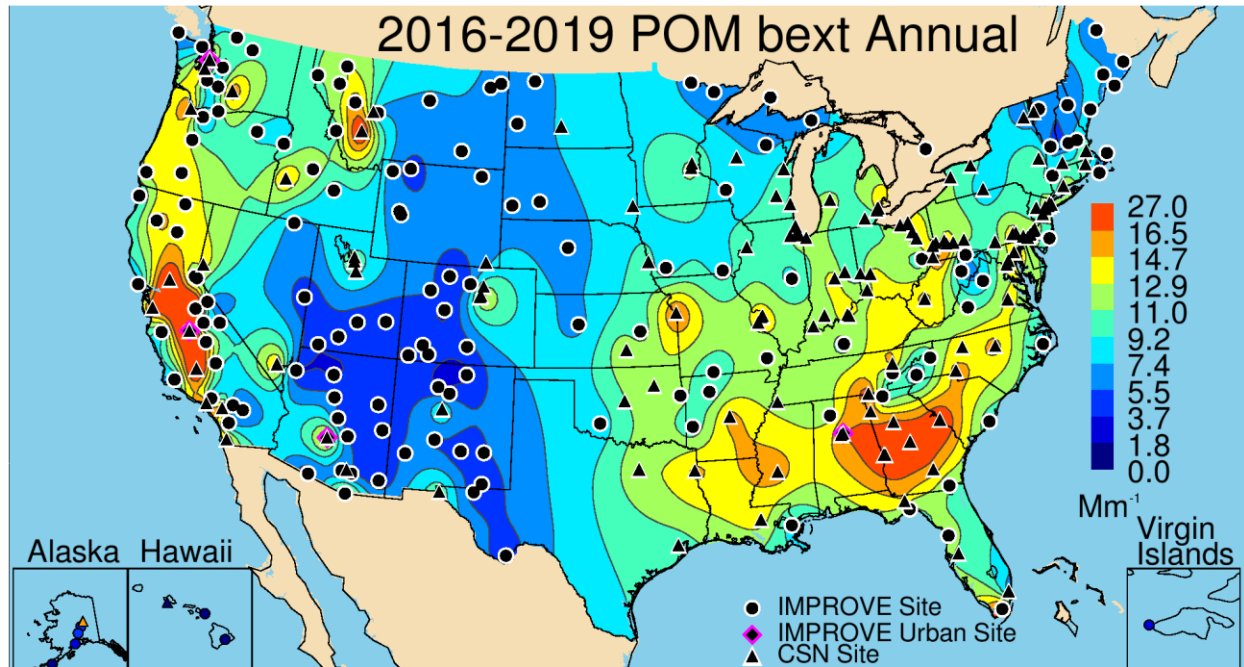


Figure 4.2.3b. IMPROVE and CSN 2016–2019 PM<sub>2.5</sub> reconstructed ambient annual mean light extinction coefficients for particulate organic matter ( $b_{ext\_POM}$ ,  $Mm^{-1}$ ). Wavelength corresponds to 550 nm.

The IMPROVE fractional contribution of  $b_{ext\_POM}$  to  $b_{ext\_aer}$  is presented in Figure 4.2.3c. Contributions of 0.5 or higher were observed at sites in the western United States, especially in northern California, southern Oregon, Idaho, and Montana, suggesting the strong impact of biomass burning emissions to  $b_{ext\_aer}$ . The east–west gradient observed for fractional  $b_{ext\_POM}$  shows lower fractions in the eastern United States (<0.3), a gradient mirroring that observed for

$b_{ext\_AS}$ . The maximum annual mean fractional contribution occurred at Sawtooth NF, Idaho (0.70, SAWT1), compared to the lowest at Hawaii Volcano NP, Hawaii (0.05, HAVO1), and Martha's Vineyard, Massachusetts (0.16, MAVI1).

A similar pattern was observed with the addition of the CSN sites, with higher fractional contributions at sites in the West (Figure 4.2.3d). Interestingly, urban sites in Utah had lower fractional contributions compared to surrounding areas, likely because of the contribution from  $b_{ext\_AN}$  to  $b_{ext\_aer}$  (see Figure 4.2.2d) at these sites. The lowest annual mean fractional contributions corresponded to sites in the central United States, also likely due to the role of  $b_{ext\_AN}$ . CSN sites in the southeastern United States had higher fractional contributions (0.35–0.4) relative to surrounding areas. The fractional contribution ranged from 0.17 (Davie, Florida, 120110034) to 0.49 in Butte, Montana (300930005).

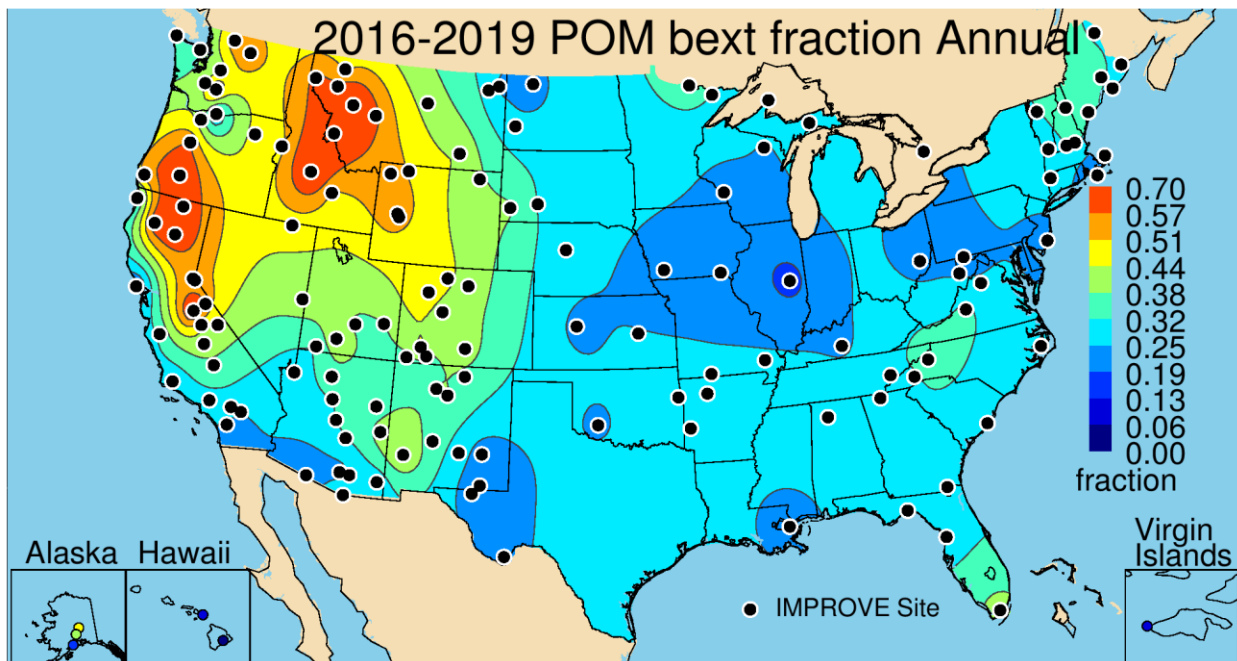
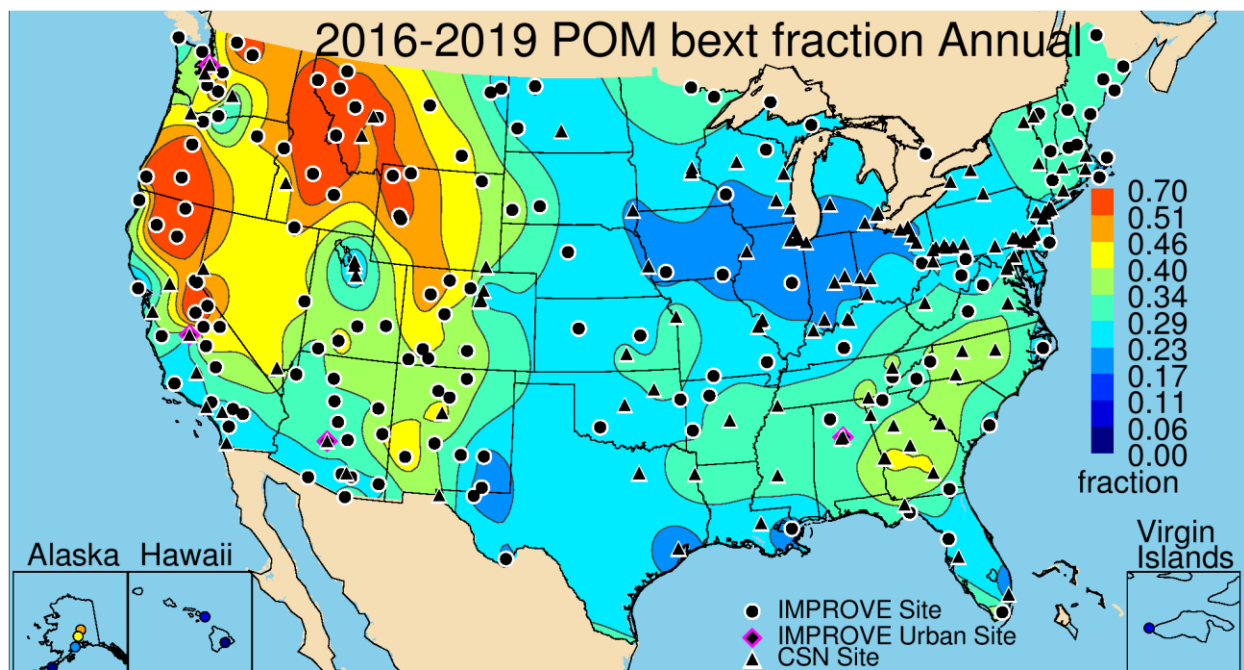


Figure 4.2.3c. IMPROVE 2016–2019 annual mean fraction contributions of particulate organic matter light extinction coefficient ( $b_{ext\_POM}$ ) to reconstructed aerosol  $b_{ext}$ . Wavelength corresponds to 550 nm.



**Figure 4.2.3d. IMPROVE and CSN 2016–2019 annual mean fraction contributions of particulate organic matter light extinction coefficient ( $b_{ext\_POM}$ ) to reconstructed aerosol  $b_{ext}$ .** Wavelength corresponds to 550 nm.

#### 4.2.4 PM<sub>2.5</sub> Elemental Carbon Light Extinction Coefficients

The IMPROVE spatial pattern of 2016–2019 annual mean EC extinction coefficients ( $b_{ext\_EC}$ ) was similar to the EC mass concentration patterns, with elevated levels at eastern sites (Figure 4.2.4a). The maximum annual mean  $b_{ext\_EC}$  ( $8.86 \text{ Mm}^{-1}$ ) occurred at Nogales, Arizona (NOGA1), and at Chassahowitzka NWR ( $3.37 \text{ Mm}^{-1}$ , CHAS1) in Florida, similar to the high EC mass concentrations. The lowest  $b_{ext\_EC}$  occurred at Haleakala Crater NP, Hawaii ( $0.15 \text{ Mm}^{-1}$  HACR1), and White River Face NF, Colorado ( $0.59 \text{ Mm}^{-1}$ , WHRI1). These sites also had the lowest annual mean  $b_{ext\_POM}$ . The highest  $b_{ext\_EC}$  occurred at sites across the eastern United States and some sites in the Northwest, while sites in the southwestern United States and Intermountain West had values less than  $2 \text{ Mm}^{-1}$ . Most (93%) IMPROVE sites corresponded to very low ( $< 3 \text{ Mm}^{-1}$ )  $b_{ext\_EC}$ .

Impacts of urban sources on  $b_{ext\_EC}$  was evident from the strong gradients surrounding urban sites, such as the Front Range of Colorado; Phoenix, Arizona; Las Vegas, Nevada; and sites in the Central Valley of California (Figure 4.2.4b). Elevated  $b_{ext\_EC}$  also occurred at sites along the Ohio River valley and at sites in Alabama and Georgia. The minimum annual mean urban  $b_{ext\_EC}$  ( $0.96 \text{ Mm}^{-1}$ ) occurred at Kapolei, Hawaii (150030010), and Whiteface Mountain Base, New York ( $1.17 \text{ Mm}^{-1}$ , 360310003). The maximum CSN annual mean  $b_{ext\_EC}$  occurred at Liberty, Pennsylvania ( $14.26 \text{ Mm}^{-1}$ , 420030064).

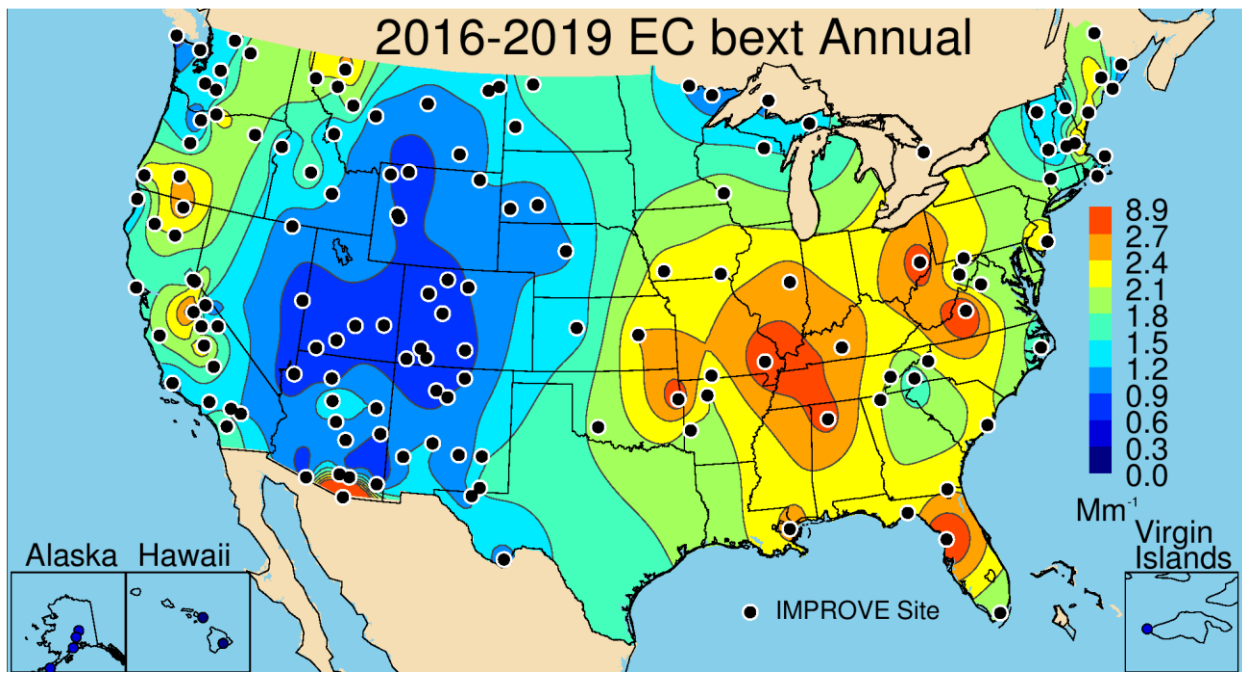


Figure 4.2.4a. IMPROVE 2016–2019 PM<sub>2.5</sub> reconstructed ambient annual mean light extinction coefficients for elemental carbon ( $b_{\text{ext\_EC}}$ ,  $\text{Mm}^{-1}$ ). Wavelength corresponds to 550 nm.

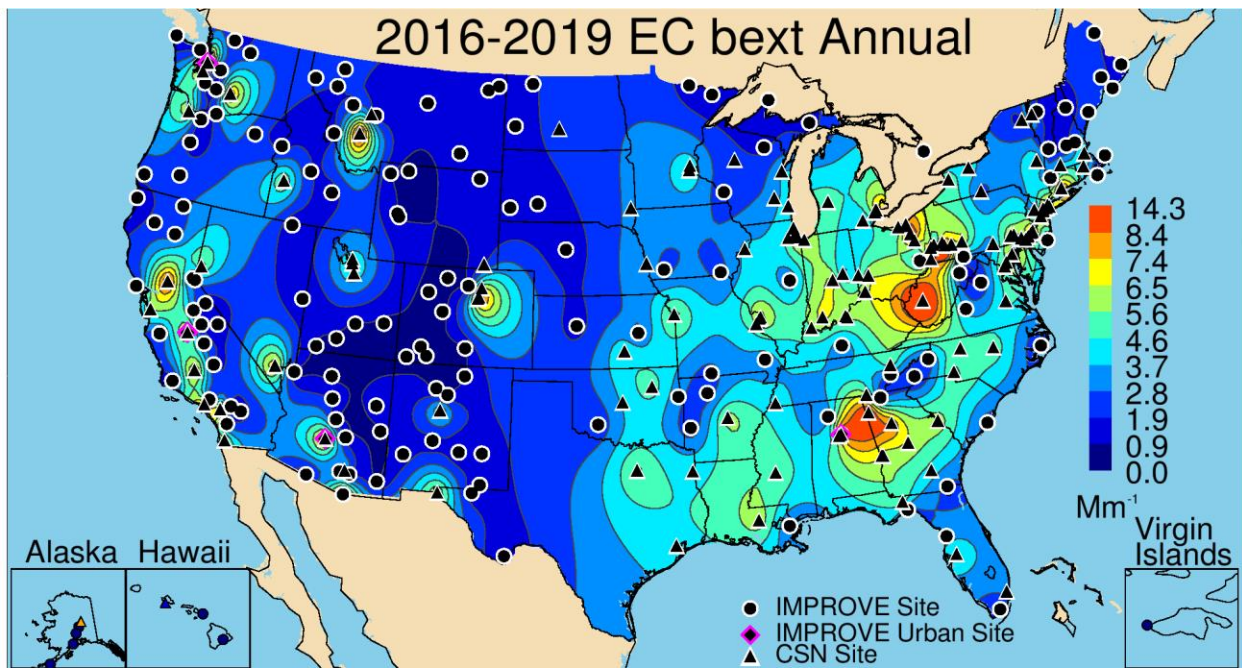


Figure 4.2.4b. IMPROVE and CSN 2016–2019 PM<sub>2.5</sub> reconstructed ambient annual mean light extinction coefficients for elemental carbon ( $b_{\text{ext\_EC}}$ ,  $\text{Mm}^{-1}$ ). Wavelength corresponds to 550 nm.

The IMPROVE annual mean fractional contribution of  $b_{\text{ext\_EC}}$  to  $b_{\text{ext\_aer}}$  ranged from 0.01 at Hawaii Volcanoes NP, Hawaii (HAVO1), and 0.04 at Redwood NP, California (REDW1), to 0.13 at Lake Tahoe Community College, California (LTCC1), and 0.19 at Nogales, Arizona (NOGA). Most of the IMPROVE sites corresponded to contributions of 0.05 or greater (Figure 4.2.4c). The sites with highest contributions were in the northwestern United States, the

Intermountain West, and the southwestern United States. Sites in the northeastern United States, Ohio River valley, and Appalachian Mountain region were also associated with elevated contributions.

Localized urban impacts on the fractional contribution of  $b_{ext\_EC}$  on  $b_{ext\_aer}$  were clear from the tight gradients surrounding several urban sites in Figure 4.2.4d. Many of the same sites with elevated  $b_{ext\_EC}$  also corresponded to high fractional contributions, such as around the Front Range of Colorado; Butte, Montana; El Paso, Texas; Las Vegas, Nevada, and others. Sites in Alabama, Georgia, and West Virginia also had elevated contributions. The minimum annual mean contribution was 0.06 at Whiteface Mountain Base, New York (360310003), compared to the maximum of 0.25 at Butte, Montana (300930005).

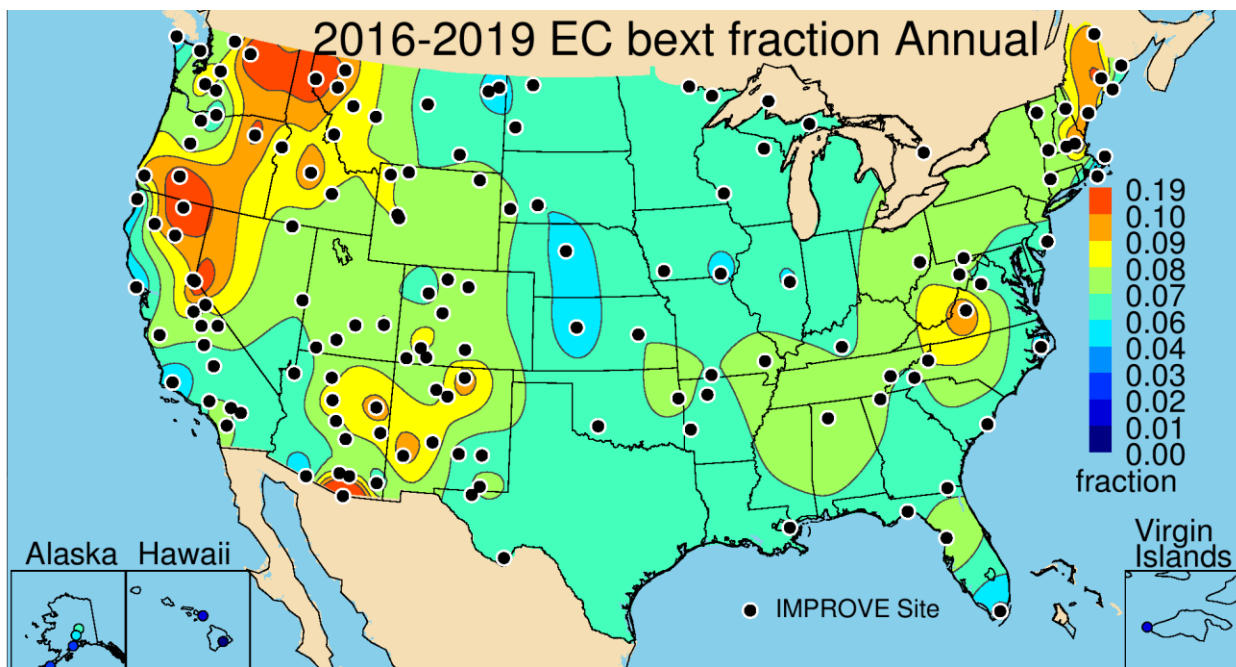
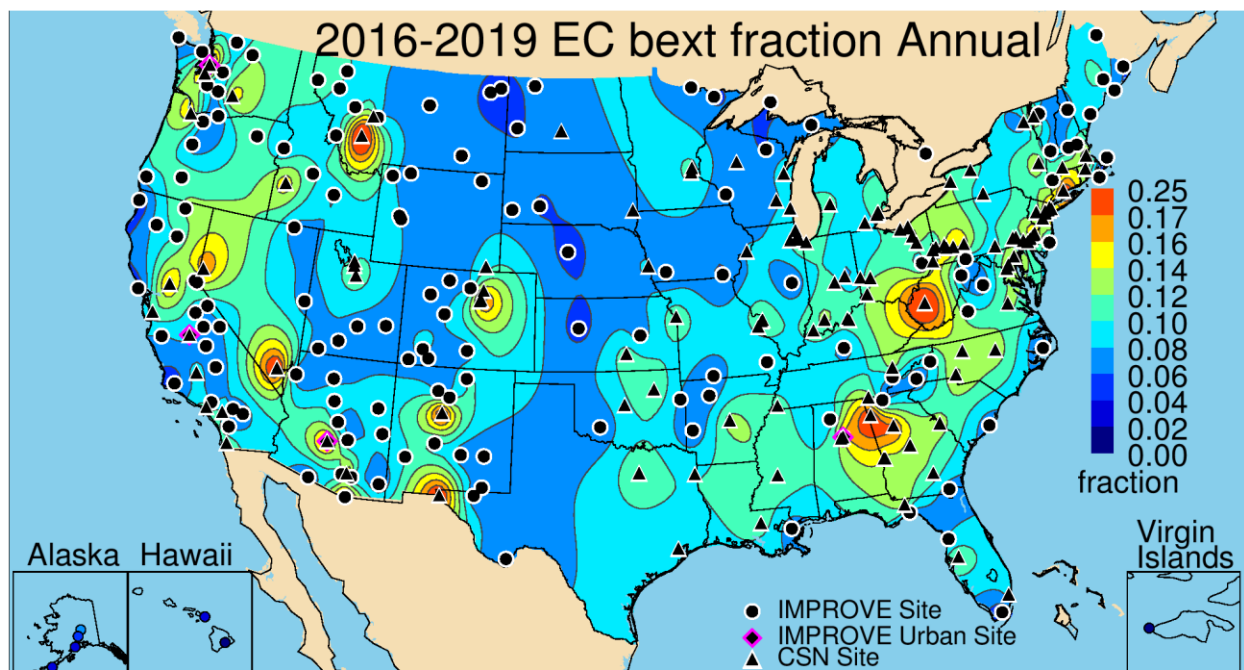


Figure 4.2.4c. IMPROVE 2016–2019 annual mean fraction contributions of elemental carbon light extinction coefficient ( $b_{ext\_EC}$ ) to reconstructed aerosol  $b_{ext}$ . Wavelength corresponds to 550 nm.



**Figure 4.2.4d. IMPROVE and CSN 2016–2019 annual mean fraction contributions of elemental carbon light extinction coefficient ( $b_{\text{ext\_EC}}$ ) to reconstructed aerosol  $b_{\text{ext}}$ . Wavelength corresponds to 550 nm.**

#### 4.2.5 PM<sub>2.5</sub> Fine Dust Light Extinction Coefficients

The annual mean FD  $b_{\text{ext}}$  ( $b_{\text{ext\_FD}}$ ) spatial pattern (Figure 4.2.5a) was the same as the FD mass concentration pattern. The rural IMPROVE annual mean  $b_{\text{ext\_FD}}$  ranged from  $0.07 \text{ Mm}^{-1}$  in the Makah Tribe site in Washington (MAKA2) to  $3.10 \text{ Mm}^{-1}$  in Sycamore Canyon, Arizona (SYCA2). The highest  $b_{\text{ext\_FD}}$  ( $\sim 1\text{--}3 \text{ Mm}^{-1}$ ) occurred at sites in the southwestern United States, with a lobed spatial pattern that followed the Mogollon Plateau. Somewhat higher values extended to sites northward and into the southeastern United States. The Virgin Islands NP (VIIS1) site also had high  $b_{\text{ext\_FD}}$  ( $1.95 \text{ Mm}^{-1}$ ), likely due to impacts of North African dust transport. Sites in the northwestern and northeastern United States had relatively low  $b_{\text{ext\_FD}}$  ( $<0.5 \text{ Mm}^{-1}$ ).

The addition of data from CSN sites provided further detail to the spatial pattern of  $b_{\text{ext\_FD}}$  (Figure 4.2.5b) but did not alter it substantially. Recall the bias in FD between IMPROVE and CSN sites discussed in Chapter 1, with higher IMPROVE FD concentrations. However, even with this bias, hot spots ( $1\text{--}2 \text{ Mm}^{-1}$ ) of annual mean  $b_{\text{ext\_FD}}$  for CSN sites occurred at sites around the Front Range of Colorado; Salt Lake City, Utah; the Central Valley of California; Birmingham, Alabama; Dallas, Texas; and St. Louis, Missouri, among others. Annual mean values ranged between the minimum of  $0.17 \text{ Mm}^{-1}$  at the Pinnacle SP site in New York (361010003) to  $2.07 \text{ Mm}^{-1}$  in El Paso, Texas (481410044).

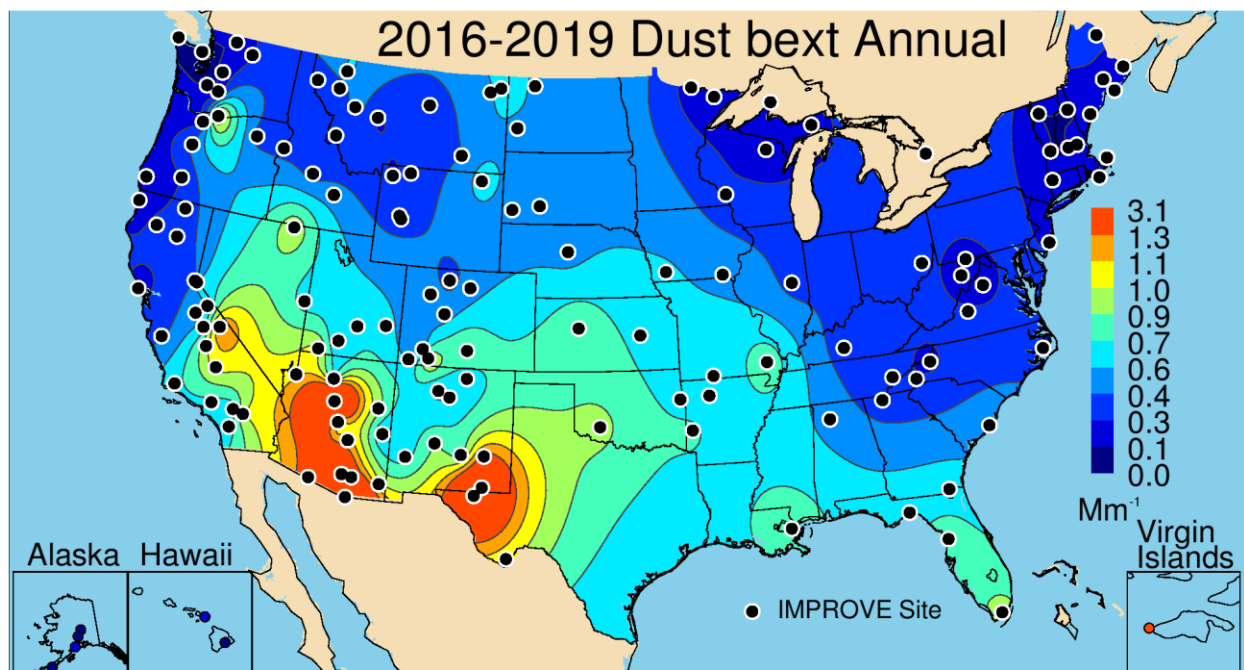


Figure 4.2.5a. IMPROVE 2016–2019 PM<sub>2.5</sub> reconstructed ambient annual mean light extinction coefficients for fine dust ( $b_{ext\_FD}$ ,  $Mm^{-1}$ ). Wavelength corresponds to 550 nm.

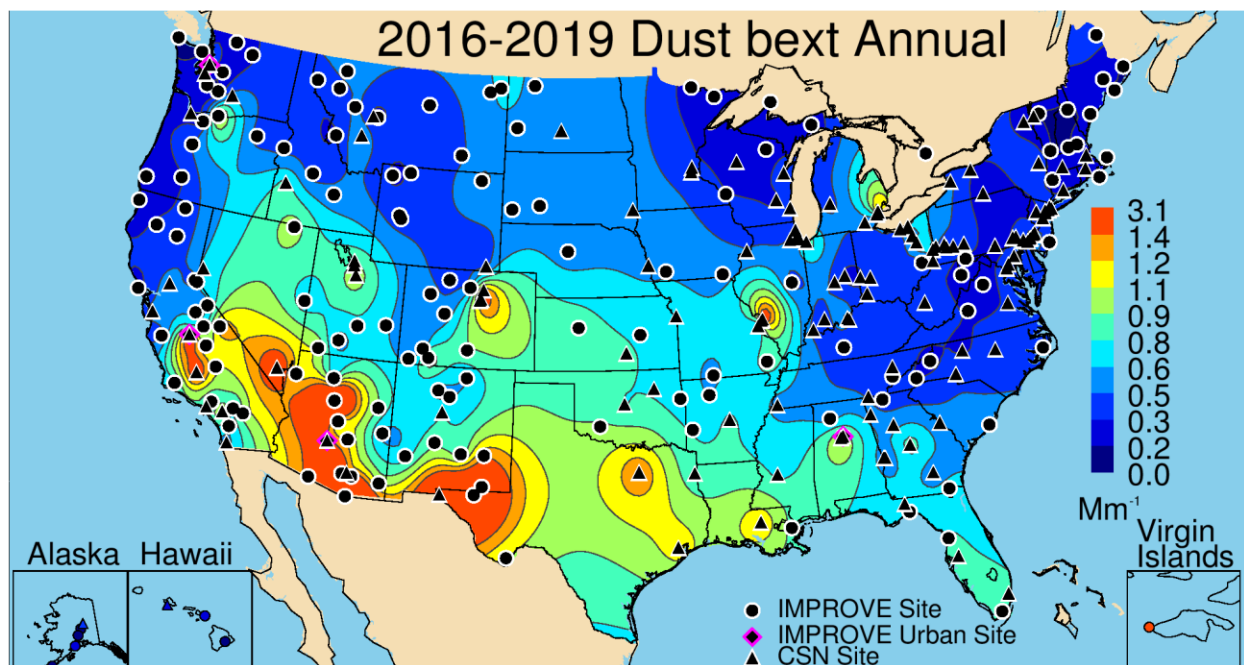


Figure 4.2.5b. IMPROVE and CSN 2016–2019 PM<sub>2.5</sub> reconstructed ambient annual mean light extinction coefficients for fine dust ( $b_{ext\_FD}$ ,  $Mm^{-1}$ ). Wavelength corresponds to 550 nm.

The largest  $b_{ext\_FD}$  annual mean fractional contributions to  $b_{ext\_aer}$  occurred at sites in the southwestern United States (Figure 4.2.5c), with values around 0.10–0.15. Fractional contributions ranged from 0.004 in Simeonof, Alaska (SIME1), and 0.005 at both the Makah Tribe site (MAKA2) in Washington and the Redwood NP site in California (REDW1) to 0.16 at Sycamore Canyon, Arizona (SYCA2). Most sites of the eastern United States corresponded to annual mean contributions less than 0.03.

The spatial pattern in fractional contribution of  $b_{ext\_FD}$  to  $b_{ext\_aer}$  did not change substantially with the addition of CSN sites (Figure 4.2.5d). The highest contributions occurred at sites in the southwestern United States, while fractional contributions at sites across the eastern United States and along the West Coast were low (~0.02 or below). The minimum annual mean contribution was 0.005 at Five Points, Ohio (391530023), and the maximum contribution was 0.07 in El Paso, Texas (481410044). No CSN sites had contributions greater than 0.1.

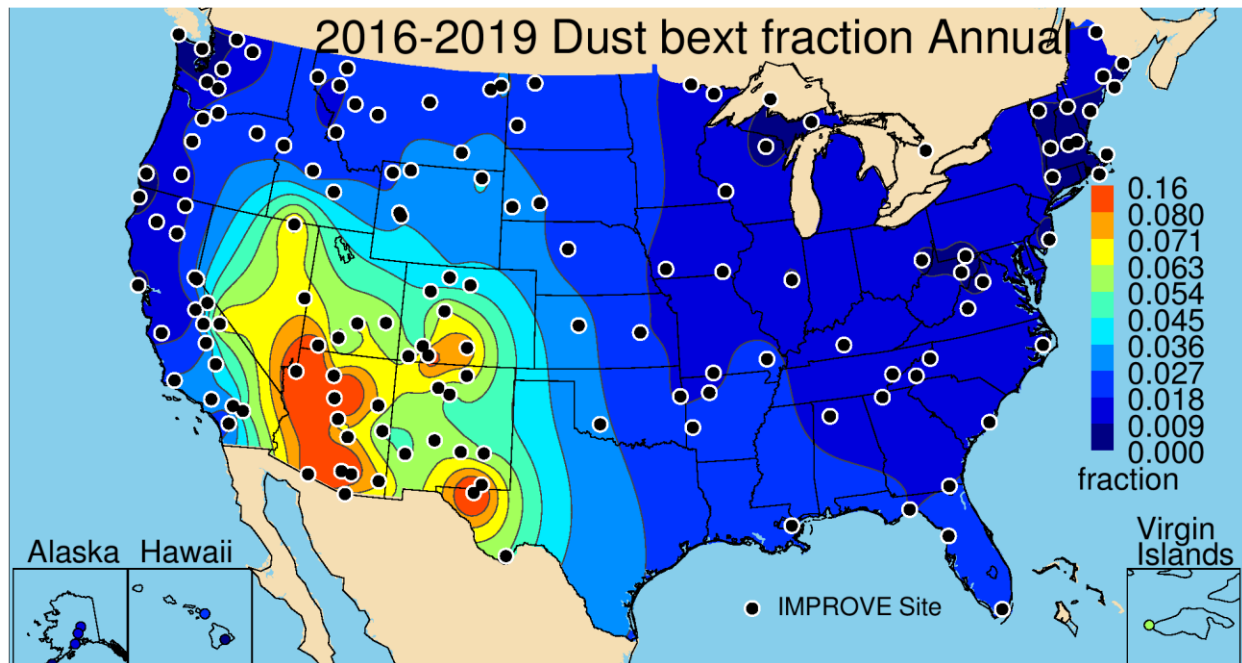


Figure 4.2.5c. IMPROVE 2016–2019 annual mean fraction contributions of fine dust light extinction coefficient ( $b_{ext\_FD}$ ) to reconstructed aerosol  $b_{ext}$ . Wavelength corresponds to 550 nm.

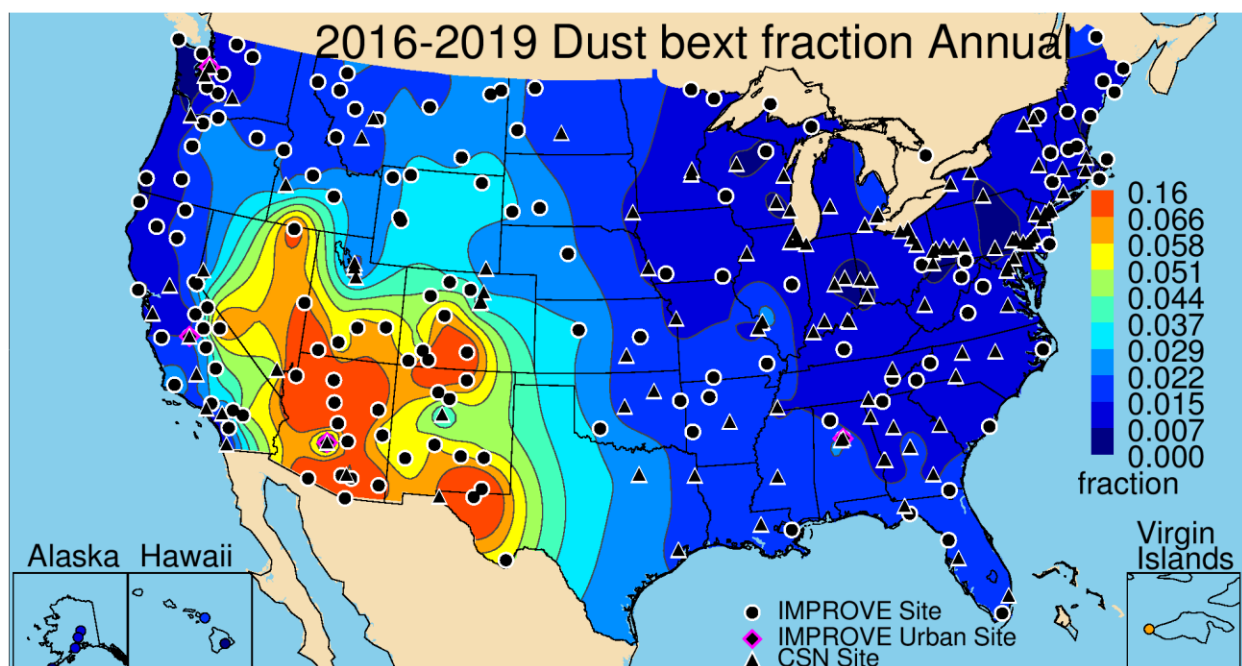


Figure 4.2.5d. IMPROVE and CSN 2016–2019 annual mean fraction contributions of fine dust light extinction coefficient ( $b_{ext\_FD}$ ) to reconstructed aerosol  $b_{ext}$ . Wavelength corresponds to 550 nm.

#### 4.2.6 PM<sub>2.5</sub> Sea Salt Extinction Coefficients

Spatial patterns of IMPROVE 2016–2019 monthly mean SS light extinction coefficients ( $b_{ext\_ss}$ ) were highest along the coasts (Figure 4.2.6a) and at sites in Alaska, Hawaii, and the Virgin Islands. Annual mean values were extremely low across the western United States (<0.3 Mm<sup>-1</sup>) and at sites along the Appalachian Mountains. Values ranged from 0.04 Mm<sup>-1</sup> in North Absaroka, Wyoming (NOAB1), to 12.73 Mm<sup>-1</sup> in Point Reyes National Seashore (NS), California (PORE1).

The coastal pattern of elevated  $b_{ext\_ss}$  was also observed with the inclusion of CSN sites (Figure 4.2.6b); however, recall the bias between IMPROVE and CSN SS estimates at collocated sites, with IMPROVE yielding higher concentrations. The maximum  $b_{ext\_ss}$  occurred at Kapolei, Hawaii (4.47 Mm<sup>-1</sup>, 150030010), and Davie, Florida (3.46 Mm<sup>-1</sup>, 120110034), and the minimum  $b_{ext\_ss}$  occurred at Pinnacle SP, New York (0.00 Mm<sup>-1</sup>, 361010003).

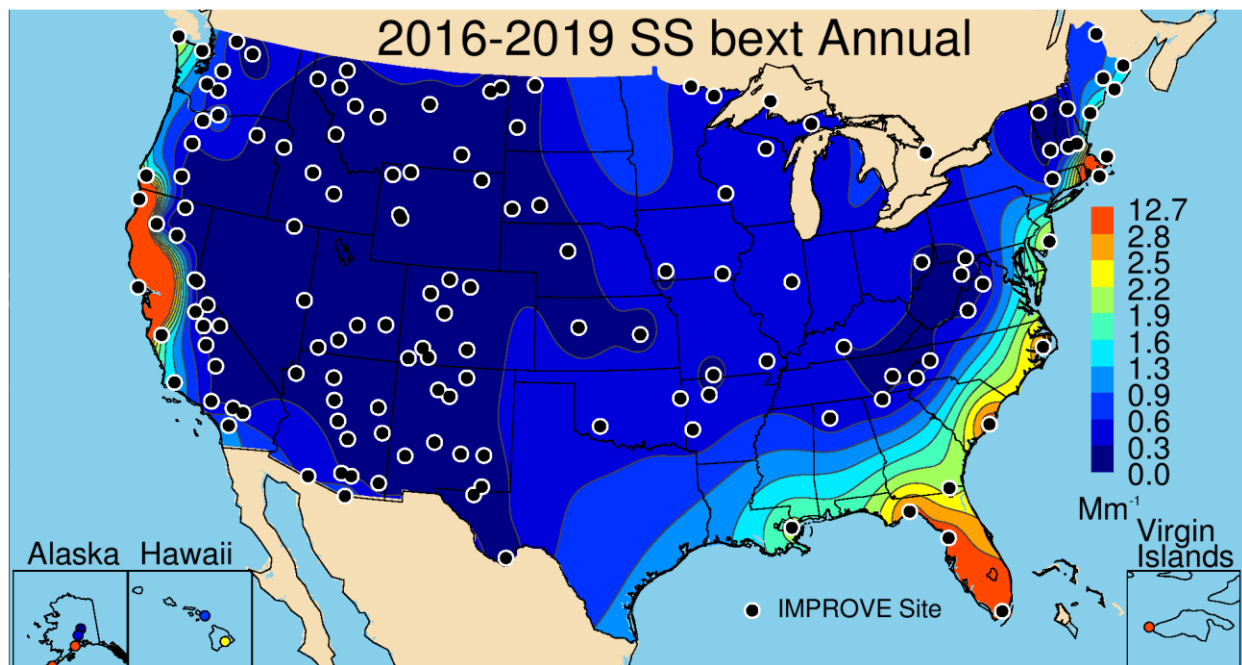
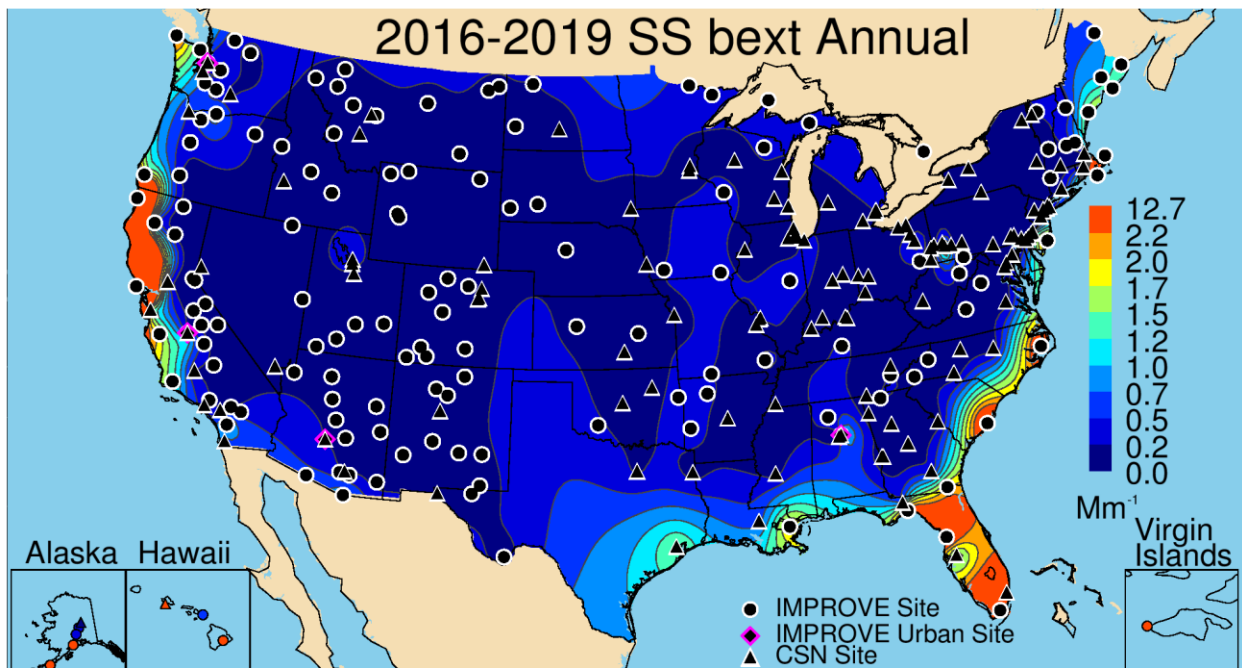


Figure 4.2.6a. IMPROVE 2016–2019 PM<sub>2.5</sub> reconstructed ambient annual mean light extinction coefficients for sea salt ( $b_{ext\_ss}$ , Mm<sup>-1</sup>). Wavelength corresponds to 550 nm.



**Figure 4.2.6b. IMPROVE and CSN 2016–2019 PM<sub>2.5</sub> reconstructed ambient annual mean light extinction coefficients for sea salt ( $b_{ext\_SS}$ ,  $Mm^{-1}$ ). Wavelength corresponds to 550 nm.**

The IMPROVE fractional contribution of  $b_{ext\_SS}$  to  $b_{ext\_aer}$  was low on an annual mean basis, except at coastal sites where the maximum IMPROVE contribution (0.41) occurred at Simeonof, Alaska (SIME1), and Point Reyes NS, California (PORE1, 0.33) (Figure 4.2.6c). Relatively high annual mean contributions also occurred at Redwood NP, California (0.31, REDW1), and Virgin Islands NP (0.28, VIIS1). However, most sites corresponded to contributions less than 0.05. The lowest contribution of SS to  $b_{ext\_aer}$  (0.003) occurred at both Monture, Montana (MONT1), and Thunder Basin, Wyoming (THBA1).

The largest annual mean fractional contribution for the CSN occurred at Davie, Florida (0.09, 120110034). No other sites had contributions greater than 0.05 (Figure 4.2.6d). Sites in Hawaii or Alaska were missing from fractional contribution analysis because other species were missing. The lowest fractional contribution occurred at Cheyenne, Wyoming (0.00, 560210100).

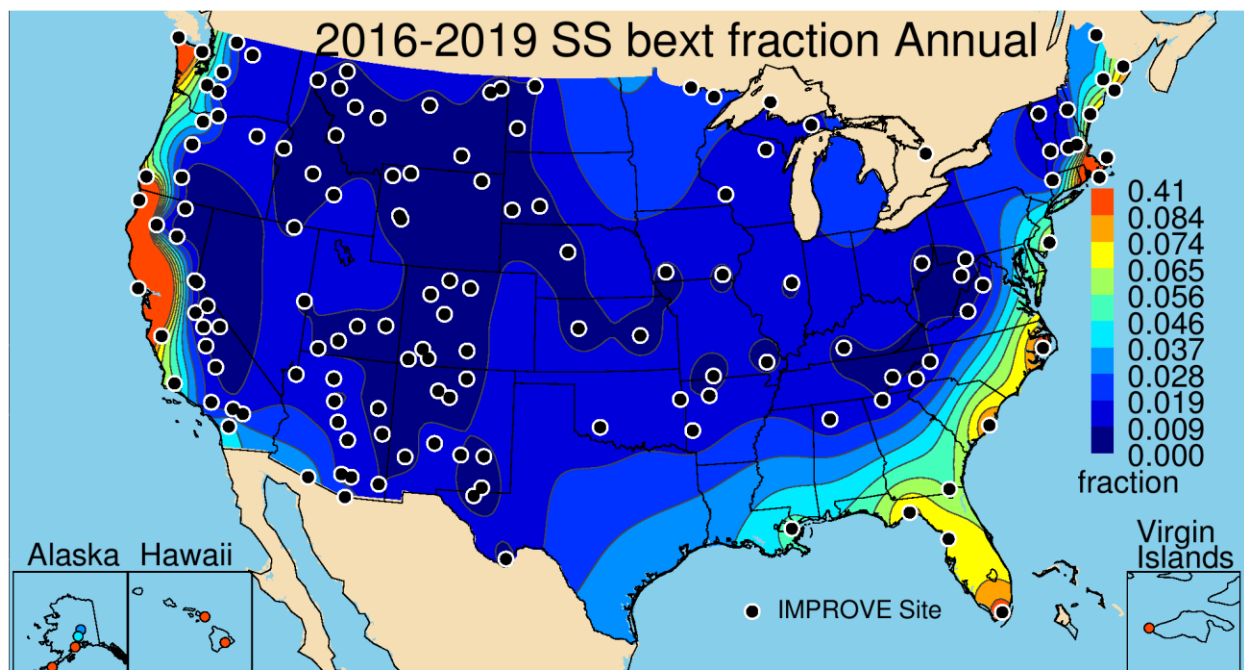


Figure 4.2.6c. IMPROVE 2016–2019 annual mean fraction contributions of sea salt light extinction coefficient ( $b_{ext\_SS}$ ) to reconstructed aerosol  $b_{ext}$ . Wavelength corresponds to 550 nm.

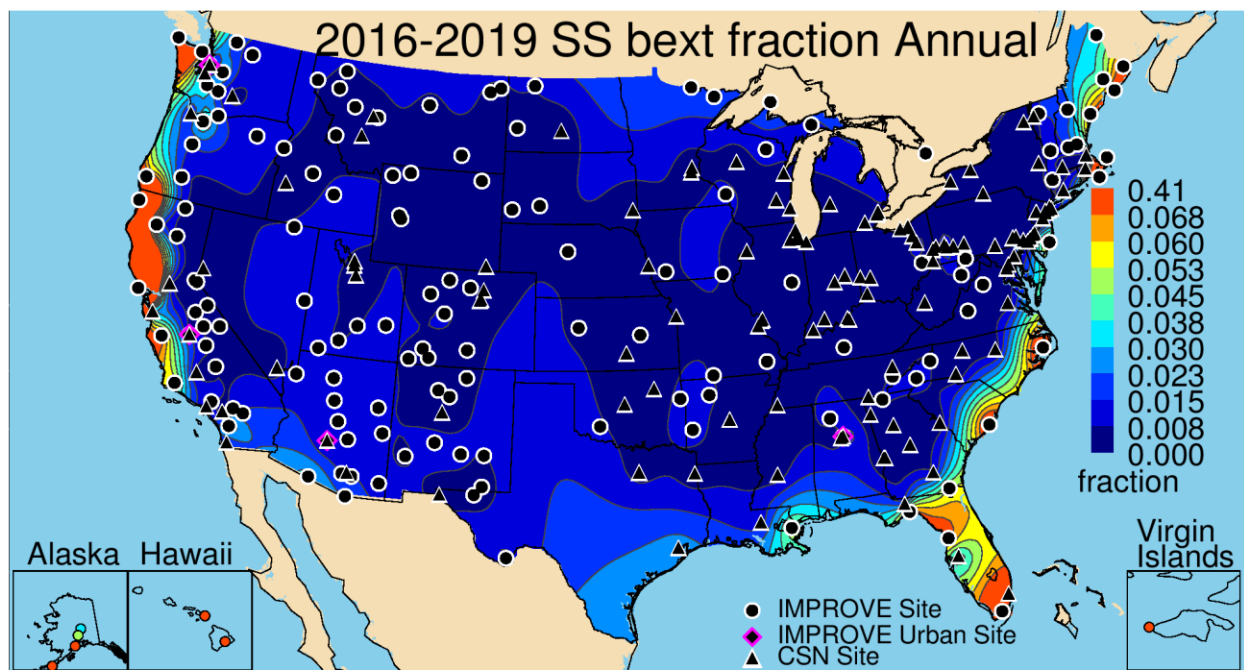


Figure 4.2.6d. IMPROVE and CSN 2016–2019 annual mean fraction contributions of sea salt light extinction coefficient ( $b_{ext\_SS}$ ) to reconstructed aerosol  $b_{ext}$ . Wavelength corresponds to 550 nm.

#### 4.2.7 Coarse Mass Light Extinction Coefficients

The spatial patterns of IMPROVE annual mean CM concentrations and  $b_{ext\_CM}$  were similar (Figure 4.2.7a) since CM is treated as nonhygroscopic in the extinction algorithm. The highest  $b_{ext\_CM}$  occurred at sites in southern New Mexico and stretched across the southern Great Plains into the central United States. Sites in regions of southern Arizona, Southern California,

and California's Central Valley also had higher  $b_{ext\_CM}$ . The maximum  $b_{ext\_CM}$  occurred at Virgin Islands NP ( $7.87 \text{ Mm}^{-1}$ , VIIS1), Salt Creek, New Mexico ( $7.20 \text{ Mm}^{-1}$ , SACR1), and Columbia River Gorge, Washington ( $7.19 \text{ Mm}^{-1}$ , CORI1). Lower annual mean  $b_{ext\_CM}$  occurred at sites across the Intermountain West, along the Appalachian Mountains, and in regions of the Northeast and Northwest ( $< 2 \text{ Mm}^{-1}$ ). The lowest  $b_{ext\_CM}$  occurred at Haleakala Crater NP, Hawaii ( $0.59 \text{ Mm}^{-1}$ , HACR1), and Crater Lake NP, Oregon ( $0.63 \text{ Mm}^{-1}$ , CRLA1).

The annual mean spatial pattern in urban  $b_{ext\_CM}$  followed that of the IMPROVE spatial pattern (Figure 4.2.7b). Higher  $b_{ext\_CM}$  occurred at sites across the central United States, southern New Mexico and Arizona, Southern California, and the Central Valley of California. Additional hot spots of  $b_{ext\_CM}$  occurred at sites in the Colorado Front Range, Salt Lake City, Utah, and Indianapolis, Indiana. The highest  $b_{ext\_CM}$  occurred in Rubidoux, California ( $13.15 \text{ Mm}^{-1}$ , 060658001). The lowest annual mean  $b_{ext\_CM}$  occurred in the Intermountain West, northwestern and northeastern United States, and many sites in the eastern United States ( $< 2 \text{ Mm}^{-1}$ ). Somewhat elevated levels of  $b_{ext\_CM}$  ( $\sim 4 \text{ Mm}^{-1}$ ) occurred at sites in the southeastern United States. The minimum annual mean  $b_{ext\_CM}$  occurred Sieben Flats, Montana, near Helena ( $1.04 \text{ Mm}^{-1}$ , 300490004).

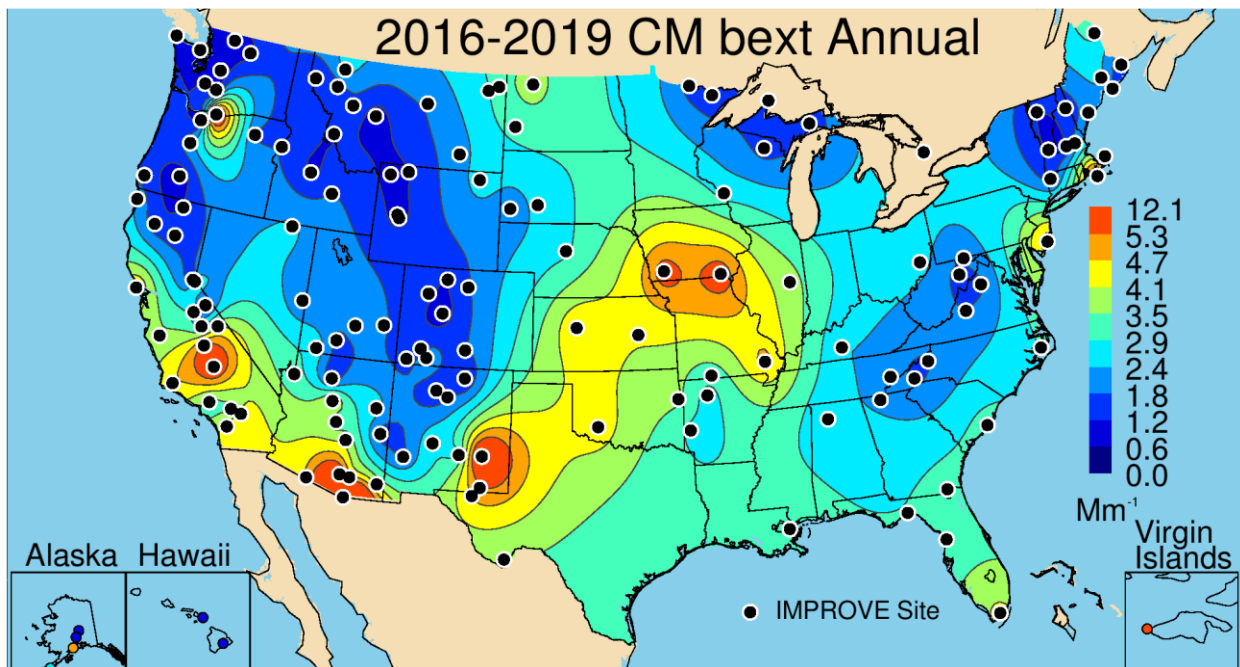


**Figure 4.2.7a. IMPROVE 2016–2019 PM<sub>2.5</sub> reconstructed ambient annual mean light extinction coefficients for coarse mass ( $b_{ext\_CM}$ ,  $\text{Mm}^{-1}$ ).** Wavelength corresponds to 550 nm.

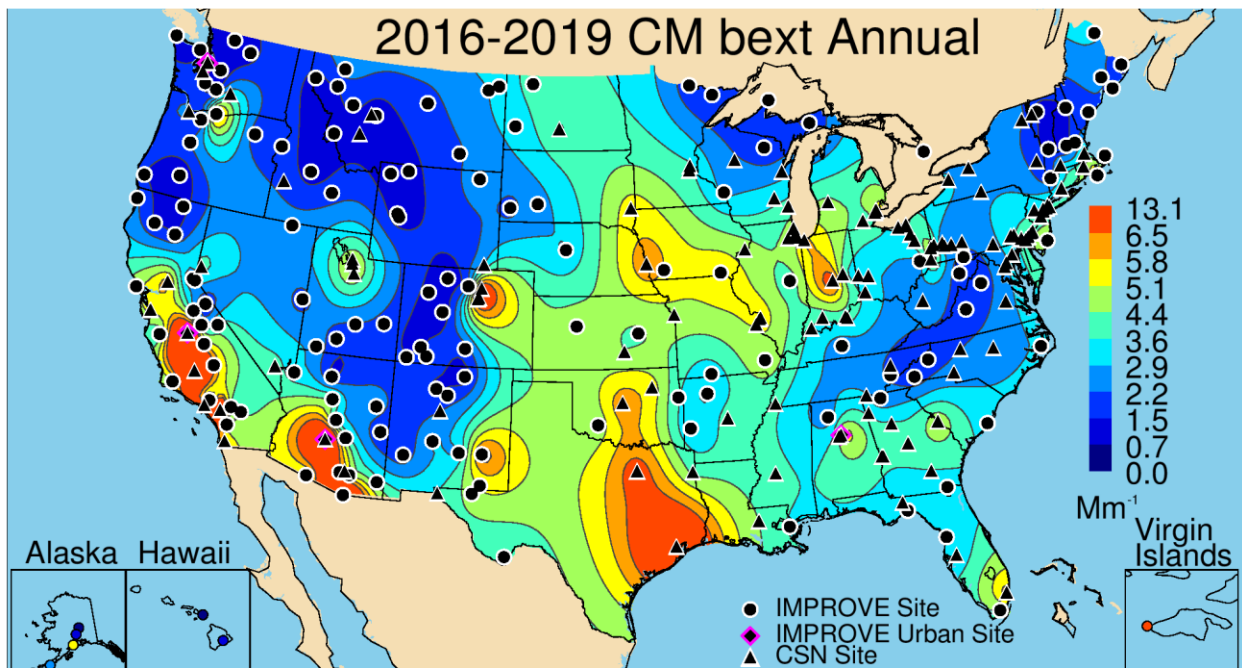


**Figure 4.2.7b. IMPROVE and CSN 2016–2019 PM<sub>2.5</sub> reconstructed ambient annual mean light extinction coefficients for coarse mass ( $b_{ext\_CM}$ ,  $Mm^{-1}$ ). Wavelength corresponds to 550 nm.**

The annual mean IMPROVE fractional contributions of  $b_{ext\_CM}$  to  $b_{ext\_aer}$  ranged from 0.03 at Crater Lake NP, Oregon (CRLA1), to 0.32 in Saguaro West NP, Arizona (SAWE1) (see Figure 4.2.7c). The contributions of  $b_{ext\_CM}$  to  $b_{ext\_aer}$  were most important at sites in the southwestern United States, where  $b_{ext\_CM}$  fractional contributions were ~0.25 or greater. Elevated fractions (0.10–0.15) occurred at sites across the western United States, reaching into the northern Great Plains. Fractional contributions at sites in the central United States were lower (<0.10) due to the importance of  $b_{ext\_AN}$  contributions to  $b_{ext\_aer}$ . Sites in the eastern United States and the northwestern United States had annual mean contributions of 0.10 or less.

The addition of annual mean  $b_{ext\_CM}$  fractional contributions to  $b_{ext\_aer}$  at sites with interpolated CM did not alter the spatial patterns seen for IMPROVE sites (Figure 4.2.7d). Contributions were highest at sites in the southwestern United States. Some urban hot spots occurred, such as increased contributions in the Front Range of Colorado (~0.19) and southern Florida (~0.15). Most of the eastern United States, especially sites in the Ohio River valley and Mid-Atlantic region had sites with low contributions (0.05 or less). Annual mean contributions ranged from 0.03 in Liberty, Pennsylvania (420030064), to 0.25 in Phoenix, Arizona (040139997).

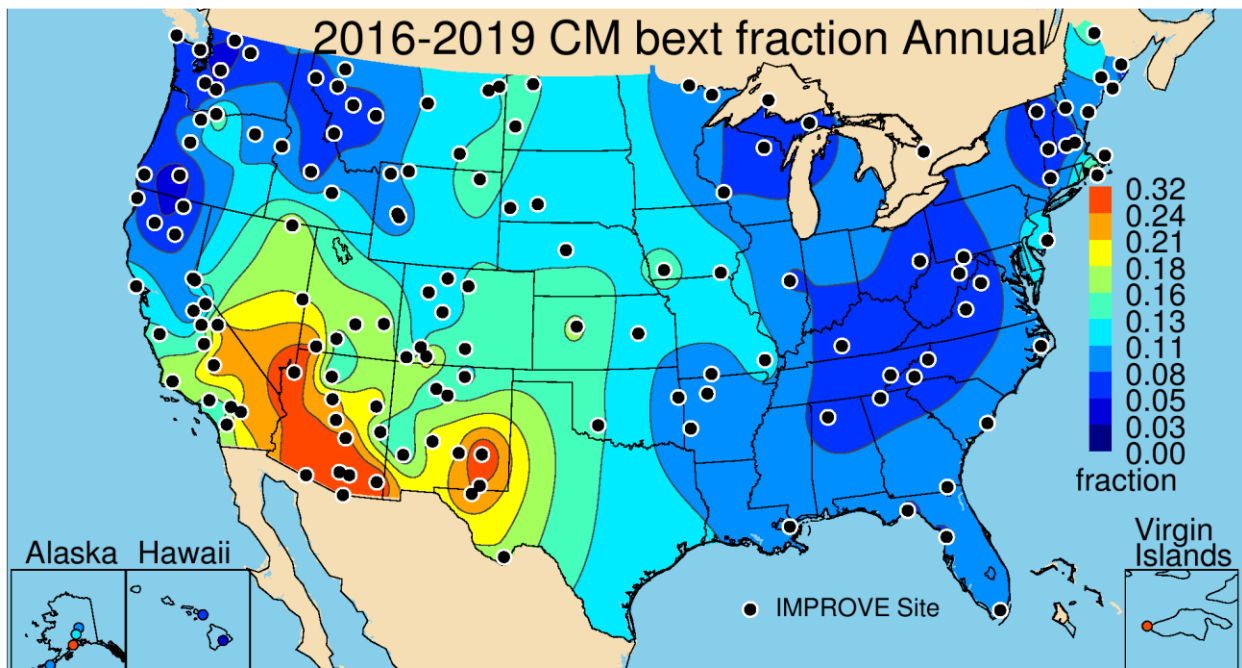


Figure 4.2.7c. IMPROVE 2016–2019 annual mean fraction contributions of coarse mass light extinction coefficient ( $b_{ext\_CM}$ ) to reconstructed aerosol  $b_{ext}$ . Wavelength corresponds to 550 nm.

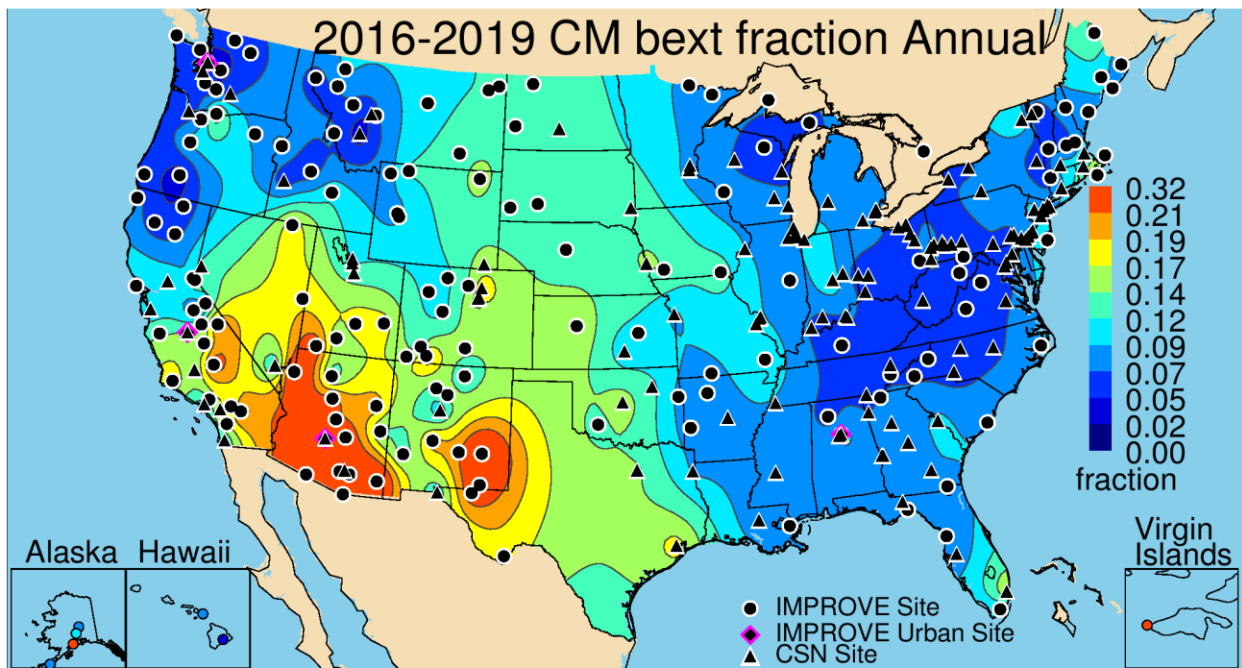


Figure 4.2.7d. IMPROVE and CSN 2016–2019 annual mean fraction contributions of coarse mass light extinction coefficient ( $b_{ext\_CM}$ ) to reconstructed aerosol  $b_{ext}$ . Wavelength corresponds to 550 nm.

#### 4.2.8 Reconstructed Aerosol Light Extinction Coefficients

The 2016–2019 IMPROVE annual mean  $b_{ext\_aer}$  is presented in Figure 4.2.8a. The east–west gradient observed for several species (especially  $b_{ext\_AS}$ ) was preserved in the aggregation of  $b_{ext\_aer}$ , but sites with the highest  $b_{ext\_aer}$  were in the central United States due to agricultural activity and in Florida due to biomass smoke impacts. Sites with the lowest  $b_{ext\_aer}$  occurred in

the southwestern United States and the Intermountain West. Higher  $b_{ext\_aer}$  occurred at sites in California and the northwestern United States. Annual mean  $b_{ext\_aer}$  ranged from  $7.48 \text{ Mm}^{-1}$  in Haleakala Crater NP, Hawaii (HACR1), and  $7.66 \text{ Mm}^{-1}$  in White River NF, Colorado (WHRI1), to  $50.65 \text{ Mm}^{-1}$  in Bondville, Illinois (BOND1). Recall that the highest  $b_{ext\_AN}$  fractional contribution to  $b_{ext\_aer}$  (0.38) occurred at Bondville, Illinois (BOND1).

The addition of CSN sites preserved the large-scale gradients observed with IMPROVE sites, with higher  $b_{ext\_aer}$  in the central and eastern United States compared to lower estimates at sites in the Intermountain West and southwestern United States (Figure 4.2.8b). The addition of sites in the eastern United States provided further spatial resolution that focused the area of high  $b_{ext\_aer}$  ( $>50 \text{ Mm}^{-1}$ ) in the central United States, especially Indiana and Pennsylvania. High  $b_{ext\_aer}$  also occurred at sites in Texas and at Gulf sites ( $>50 \text{ Mm}^{-1}$ ) and along the Central Valley of California. In fact, the highest annual mean  $b_{ext\_aer}$  occurred at Bakersfield, California ( $88.71 \text{ Mm}^{-1}$ , 0602090014). The maximum annual mean  $b_{ext\_AN}$  also occurred at Bakersfield. The lowest annual mean  $b_{ext\_aer}$  occurred in Cheyenne, Wyoming ( $18.49 \text{ Mm}^{-1}$ , 560210100).

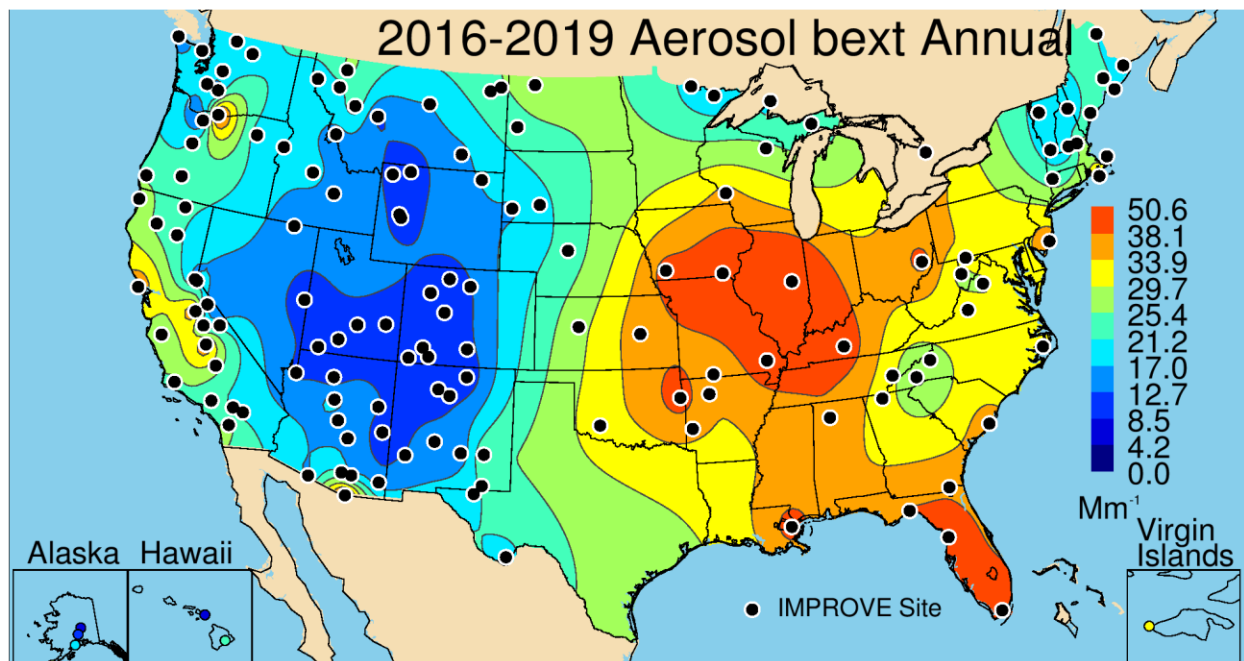


**Figure 4.2.8a.** IMPROVE 2016–2019 reconstructed ambient annual mean aerosol light extinction coefficients ( $b_{ext\_aer}$ ,  $\text{Mm}^{-1}$ ) (no Rayleigh scattering). Wavelength corresponds to 550 nm.

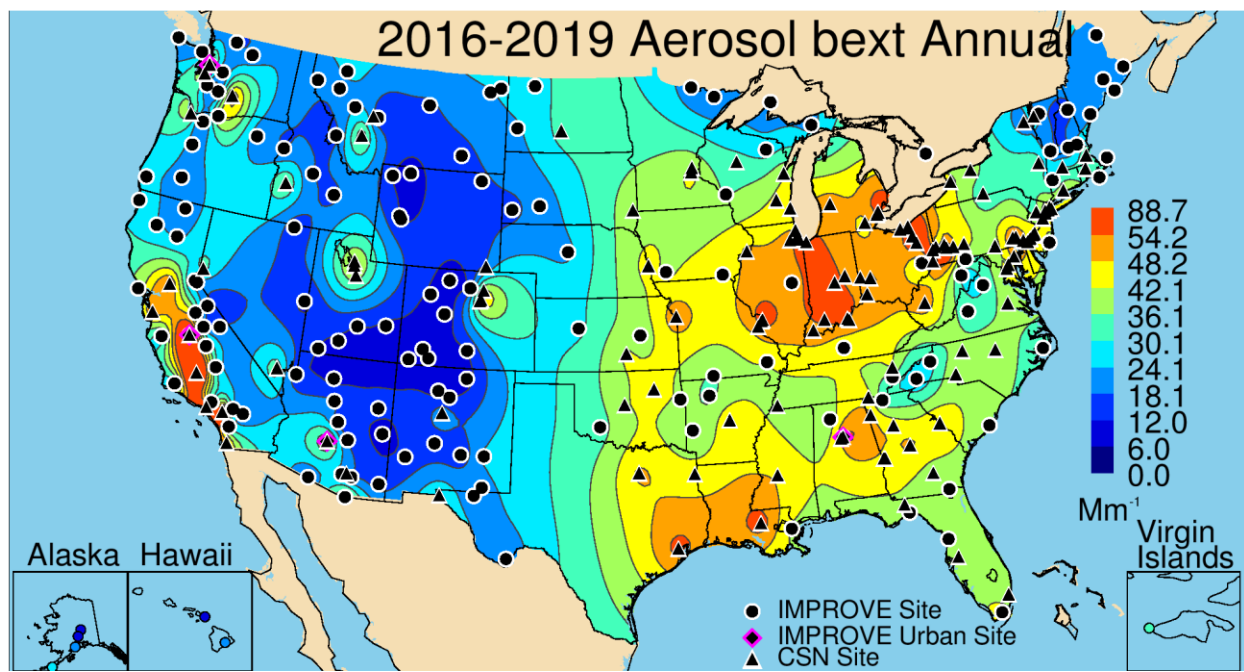
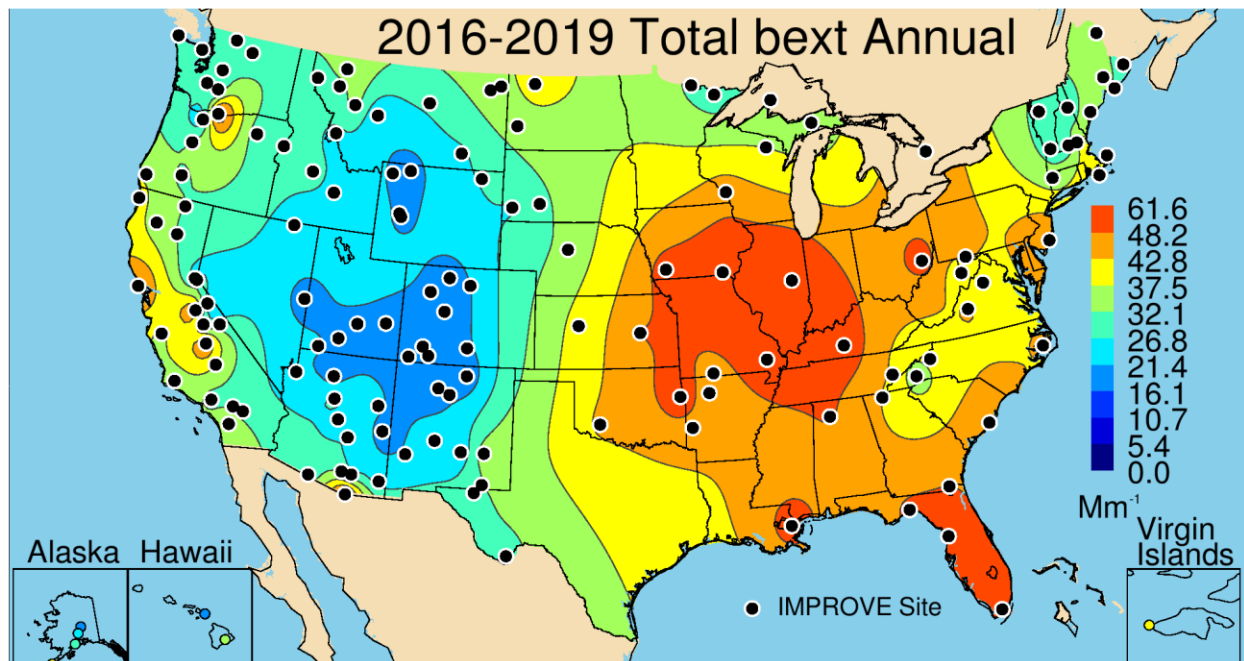


Figure 4.2.8b. IMPROVE and CSN 2016–2019 PM<sub>2.5</sub> reconstructed ambient annual mean aerosol light extinction coefficients ( $b_{ext\_aer}$ ,  $Mm^{-1}$ ) (no Rayleigh scattering). Wavelength corresponds to 550 nm.

#### 4.2.9 Reconstructed Total Light Extinction Coefficients

The spatial patterns in  $b_{ext\_tot}$  are similar to  $b_{ext\_aer}$  but increased by ~8–12  $Mm^{-1}$  to account for site-specific Rayleigh scattering. IMPROVE annual mean  $b_{ext\_tot}$  ranged from 15.67  $Mm^{-1}$  at White River NF, Colorado (WHRI1), to 61.65  $Mm^{-1}$  at Bondville, Illinois (BOND1) (see Figure 4.2.9a). Annual mean  $b_{ext\_tot}$  at CSN sites (Figure 4.2.9b) ranged from 27.49  $Mm^{-1}$  at Cheyenne, Wyoming (560210100), to 99.71  $Mm^{-1}$  at Bakersfield, California (060290014).



**Figure 4.2.9a.** IMPROVE 2016–2019 annual mean reconstructed ambient total light extinction coefficients ( $b_{ext\_tot}$ ,  $Mm^{-1}$ ) (aerosol + Rayleigh). Wavelength corresponds to 550 nm.

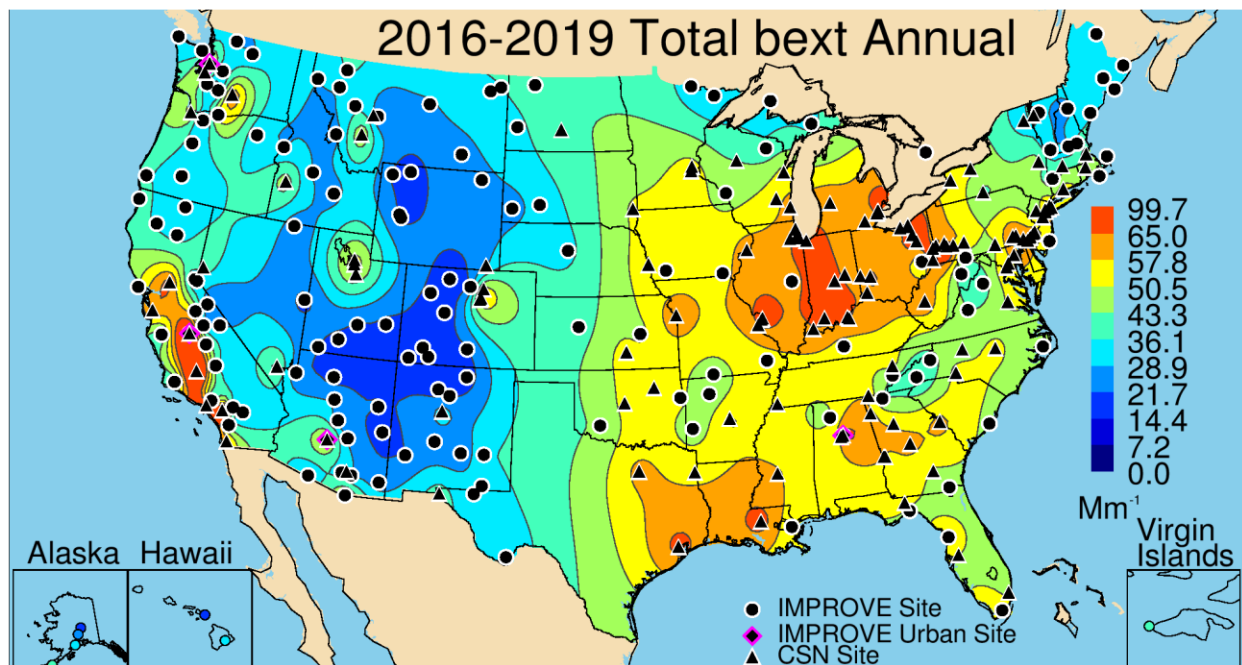


**Figure 4.2.9b.** IMPROVE 2016–2019 annual mean reconstructed ambient total light extinction coefficients ( $b_{ext\_tot}$ ,  $Mm^{-1}$ ) (aerosol + Rayleigh). Wavelength corresponds to 550 nm.

#### 4.2.10 Deciview

The 2016–2019 IMPROVE annual mean dv spatial pattern was very similar to the  $b_{ext\_tot}$  pattern, as expected (see Figure 4.2.10a). Higher dv values (>15 dv) were observed at sites in the eastern United States, with the exception of northeastern sites (10–11 dv). Lower values were observed at sites in the Intermountain West, especially at sites in the central Rocky Mountains of Colorado and northern New Mexico. Higher estimates were observed at sites in California (~15). Values at rural sites ranged from 4.49 dv at White River NF, Colorado (WHRI1), to 18.19 dv at Bondville, Illinois (BOND1).

Similar to the map of  $b_{ext\_tot}$ , the addition of urban sites to the dv map in Figure 4.2.10b provided additional spatial resolution but did not change the overall patterns. The highest annual mean dv occurred at sites in the central United States and the Gulf area, as well as at sites in the Central Valley of California. Additional hot spots included sites in the Front Range of Colorado; Salt Lake City, Utah; Phoenix, Arizona; and Las Vegas, Nevada. Estimates ranged from 10.11 dv at Cheyenne, Wyoming (560210100), to 23.0 dv at Bakersfield, California (060290014).

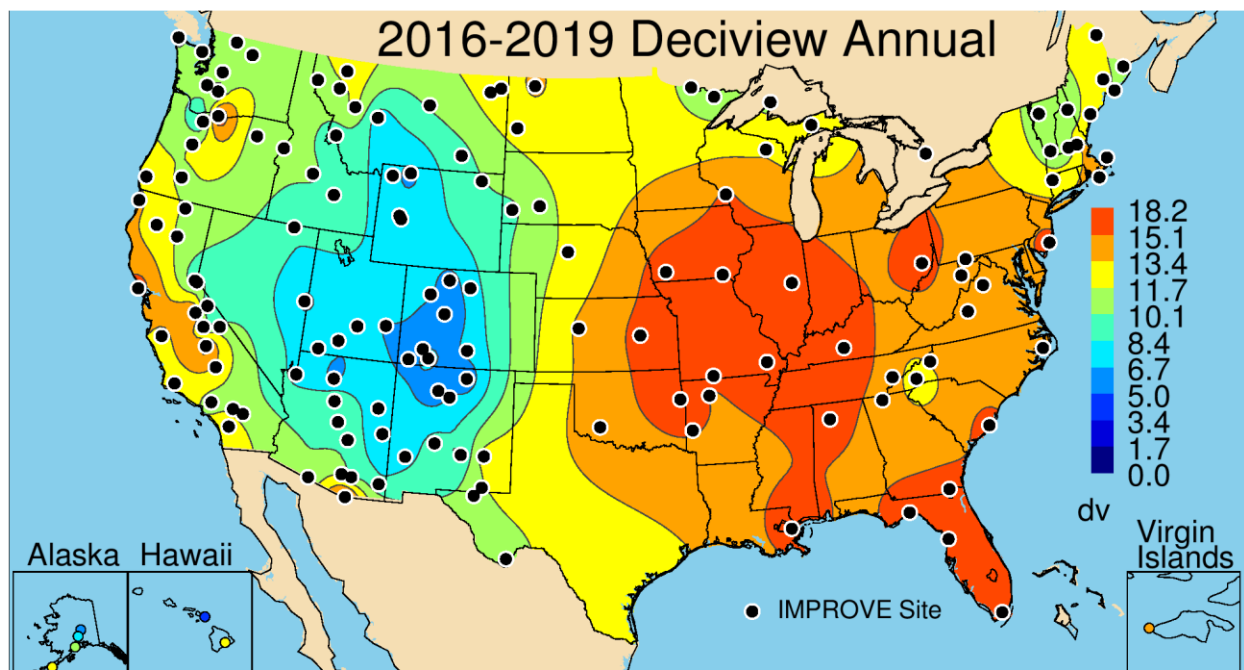


Figure 4.2.10a. IMPROVE 2016–2019 annual mean deciview (dv). Wavelength corresponds to 550 nm.

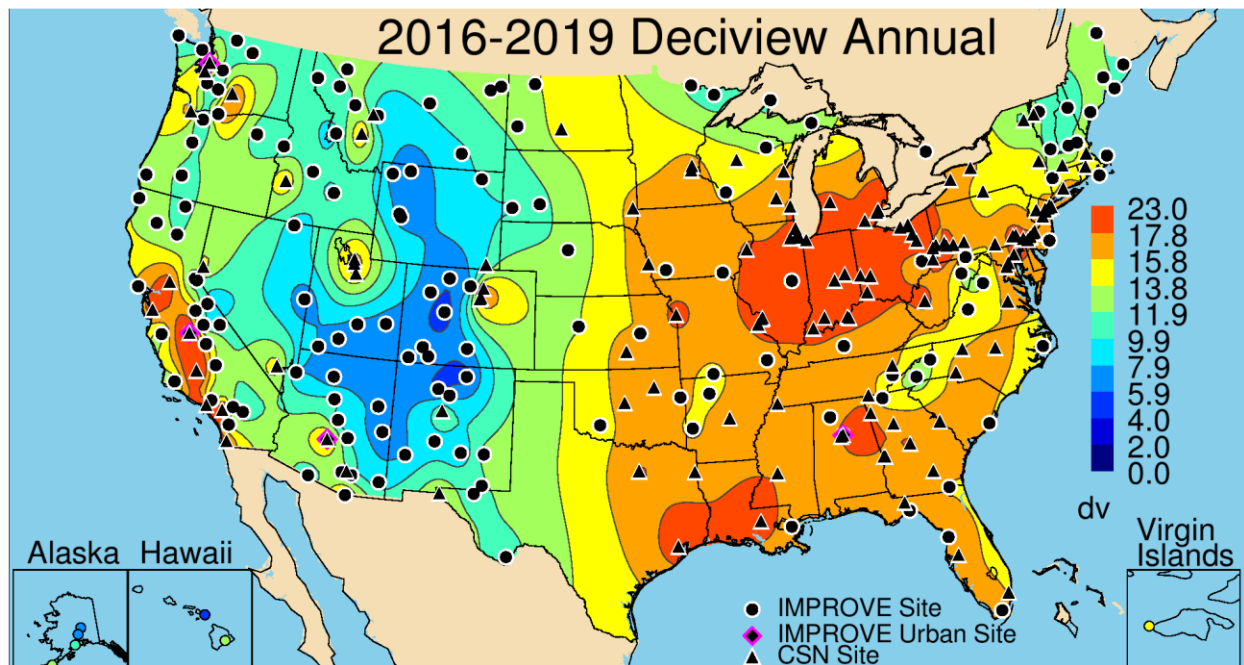


Figure 4.2.10b. IMPROVE and CSN 2016–2019 annual mean deciview (dv). Wavelength corresponds to 550 nm.

#### 4.2.11 Summary

The spatial variability of speciated and total  $b_{ext\_tot}$  depends on sources, transport, and environmental conditions, such as the impacts of RH on hygroscopic growth. While spatial patterns of speciated  $b_{ext}$  reflected the spatial patterns in mass presented in Chapter 2, they differed in some cases due to the uptake of water from species considered hygroscopic in the

reconstruction algorithm (i.e., AS, AN, and SS). For similar reasons, the spatial variability in fractional contributions of  $b_{ext}$  differed from species' fractional contributions to mass, depending on the roles of other species, some of which may be hygroscopic. In addition, the degree of light scattering efficiency of a particular species (e.g., mass scattering efficiency) will also influence the level of contribution of that species to  $b_{ext\_tot}$ .

The highest annual mean  $b_{ext\_AS}$  occurred at urban and rural sites in the eastern United States, where sources of SO<sub>2</sub> emissions are greatest, and high RH in summer can facilitate hygroscopic growth. Somewhat lower values occurred at sites in Virginia, West Virginia, and in the Northeast. A strong spatial gradient occurred along the central United States, resulting in relatively low  $b_{ext\_AS}$  at sites across the West, due to lower emissions. Contributions of  $b_{ext\_AS}$  to  $b_{ext\_aer}$  were also highest in the East, typically greater than 0.3, and highest at rural sites. With the exception of sites in Hawaii, the annual mean fractional contribution of  $b_{ext\_AS}$  to  $b_{ext\_aer}$  did not exceed 0.5 at any rural or urban site. Fractional contributions also decreased at sites toward the West. Sites in the central United States had contributions around 0.25–0.3, and the lowest contributions occurred at sites in Idaho, Montana, and northern California (<0.15), likely due to the role of  $b_{ext\_POM}$ .

Biomass smoke impacts at sites in the northwestern United States and Florida strongly influenced the  $b_{ext\_POM}$  spatial pattern at rural sites, where the highest estimates of annual mean rural  $b_{ext\_POM}$  occurred. Estimates were somewhat higher at sites in the southeastern United States, but still lower than at smoke-influenced sites. The lowest  $b_{ext\_POM}$  at rural sites occurred in the southwestern United States. The annual mean  $b_{ext\_POM}$  was higher in many urban areas, such as sites in the southeastern United States and the Central Valley of California, suggesting additional urban sources of POM. The contribution of  $b_{ext\_POM}$  to  $b_{ext\_aer}$  was highest at sites in the northwestern United States (>0.50), especially where contributions of  $b_{ext\_AS}$  were low. Contributions of  $b_{ext\_POM}$  at sites in the eastern United States were similar in magnitude or greater than contributions of  $b_{ext\_AS}$ . At some urban sites in the western United States, contributions of  $b_{ext\_POM}$  were lower than surrounding rural areas (e.g., the Central Valley of California and Salt Lake City, Utah) because of the role of  $b_{ext\_AN}$ .

The highest annual mean  $b_{ext\_AN}$  occurred at both urban and rural sites around the central United States due to agricultural activity in the region. Other hot spots occurred at urban sites in the West, such as Salt Lake City, Utah, and the Central Valley of California, suggesting additional urban and agricultural sources. Except for these areas, annual mean  $b_{ext\_AN}$  was low across the United States. The fraction of  $b_{ext\_aer}$  due to  $b_{ext\_AN}$  was also highest at sites in the central United States, exceeding 0.3 across the region. Higher contributions were also observed at sites with hot spots of  $b_{ext\_AN}$ .

Differences in urban and rural  $b_{ext}$  were most obvious for  $b_{ext\_EC}$  compared to other species. Annual mean  $b_{ext\_EC}$  at rural sites was high at some smoke-influenced sites in the northwestern United States and in Florida. However, at many rural sites in the eastern United States, annual mean  $b_{ext\_EC}$  exceeded levels observed in the western United States. The lowest rural  $b_{ext\_EC}$  occurred at sites across the Intermountain West. Urban annual mean  $b_{ext\_EC}$  was much higher and more localized, with several hot spots in the West, such as Phoenix, Arizona, Las Vegas, Nevada, and urban sites in the Central Valley of California. Both regional and local

impacts of  $b_{ext\_EC}$  occurred at sites in the East, such as hot spots in Georgia and Alabama, suggesting additional urban sources relative to surrounding rural areas.

Compared to other species, FD and CM have lower mass scattering efficiencies, which will reduce their influence on  $b_{ext\_tot}$  on a per mass basis. Similar spatial patterns in  $b_{ext\_FD}$  and  $b_{ext\_CM}$  were observed at sites in the Central Valley of California and at sites in the southwestern United States, where estimates were the highest, suggesting similar sources. However, unlike  $b_{ext\_FD}$ , annual mean  $b_{ext\_CM}$  was elevated at sites in the central United States, corresponding to areas of agricultural activity. Both  $b_{ext\_FD}$  and  $b_{ext\_CM}$  were elevated at sites in the southeastern United States and the Virgin Islands site (VIIS1), consistent with the influence of transport of dust from North Africa. The contributions of  $b_{ext\_FD}$  and  $b_{ext\_CM}$  to  $b_{ext\_aer}$  were highest at sites in the southwestern United States, around ~0.05–0.15 and 0.2–0.3, respectively.

Annual mean  $b_{ext\_SS}$  was elevated at sites along the eastern and western coasts of the United States, near sources and in some regions where hygroscopic impacts were likely higher. Impacts from  $b_{ext\_SS}$  farther inland were low, likely due to chloride loss from the filters. Sites in the Virgin Islands, Hawaii, and Alaska also had higher annual mean  $b_{ext\_ss}$ . At many of these sites the contributions of  $b_{ext\_ss}$  to  $b_{ext\_aer}$  were larger than 0.1.

The spatial patterns in  $b_{ext\_tot}$  and dv were similar and reflected the combined impacts from the species discussed above. Notably, the highest  $b_{ext\_tot}$  and dv occurred at sites in the central United States and the Central Valley of California. Both regions corresponded to sites with the highest  $b_{ext\_AN}$ , suggesting the importance of agricultural activity on visibility in these regions. Lower  $b_{ext\_tot}$  and dv occurred at sites along the Appalachian Mountains, the Northeast, and especially the Intermountain West. While the role of biomass smoke is important to  $b_{ext\_tot}$ , with elevated levels at sites in the Northwest and Florida, the role of agriculture appeared to dominate. The role of  $b_{ext\_AS}$  on  $b_{ext\_tot}$  was relatively low across the United States.

Tables of the 2016–2019 annual mean  $b_{ext}$  and  $b_{ext}$  fractions are reported for each site in Appendix 4.3 (IMPROVE and CSN  $b_{ext}$ ) and 4.4 (IMPROVE and CSN  $b_{ext}$  fraction).

## REFERENCES

- EPA, U. S. (2001), U.S. Environmental Protection Agency, Interpolating relative humidity weighting factors to calculate visibility impairment and the effects of IMPROVE monitor outliers, *68-D-98-113, WA No. 3-39*, <http://vista.cira.colostate.edu/Improve/wp-content/uploads/2016/03/DraftReportSept20.pdf>.
- EPA, U. S. (2003), U.S. Environmental Protection Agency, Guidance for tracking progress under the Regional Haze Rule, *EPA-454/B-03-004*, <https://www.epa.gov/sites/default/files/2021-03/documents/tracking.pdf>.
- Hand, J. L., and Malm, W. C. (2006), Review of the IMPROVE equation for estimating ambient light extinction coefficients, Colorado State University, Fort Collins, CO, ISSN 0737-5352-71.
- Hand, J. L., and Malm, W. (2007), Review of aerosol mass scattering efficiencies from ground-based measurements since 1990, *Journal of Geophysical Research: Atmospheres*, *112*(D16), 203, doi:10.1029/2007JD008484.
- Hand, J. L., Prenni, A. J., Schichtel, B. A., Malm, W. C., and Chow, J. C. (2019), Trends in remote PM<sub>2.5</sub> residual mass across the United States: Implications for aerosol mass reconstruction in the IMPROVE network, *Atmospheric Environment*, *203*, 141-152, doi:10.1016/j.atmosenv.2019.01.049.
- Lowenthal, D. H., and Kumar, N. (2003), PM<sub>2.5</sub> mass and light extinction reconstruction in IMPROVE, *Journal of the Air & Waste Management Association*, *53*(9), 1109-1120, <https://doi.org/10.1080/10473289.2003.10466264>.
- Malm, W. C., Sisler, J. F., Huffman, D., Eldred, R. A., and Cahill, T. A. (1994), Spatial and seasonal trends in particle concentration and optical extinction in the United States, *Journal of Geophysical Research: Atmospheres*, *99*(D1), 1347-1370, <https://doi.org/10.1029/93JD02916>.
- Malm, W. C., and Kreidenweis, S. M. (1997), The effects of models of aerosol hygroscopicity on the apportionment of extinction, *Atmospheric Environment*, *31*(13), 1965-1976, [https://doi.org/10.1016/S1352-2310\(96\)00355-X](https://doi.org/10.1016/S1352-2310(96)00355-X).
- Malm, W. C., Day, D. E., Carrico, C., Kreidenweis, S. M., Collett Jr, J. L., McMeeking, G., Lee, T., Carrillo, J., and Schichtel, B. (2005), Intercomparison and closure calculations using measurements of aerosol species and optical properties during the Yosemite Aerosol Characterization Study, *Journal of Geophysical Research: Atmospheres*, *110*(D14), D14302, doi:10.1029/2004JD005494.
- Malm, W. C., and Hand, J. L. (2007), An examination of the physical and optical properties of aerosols collected in the IMPROVE program, *Atmospheric Environment*, *41*(16), 3407-3427, doi:10.1016/j.atmosenv.2006.12.012.
- Pitchford, M. L., and Malm, W. C. (1994), Development and applications of a standard visual index, *Atmospheric Environment*, *28*(5), 1049-1054, [https://doi.org/10.1016/1352-2310\(94\)90264-X](https://doi.org/10.1016/1352-2310(94)90264-X).
- Pitchford, M., Malm, W. C., Schichtel, B. A., Kumar, N., Lowenthal, D., and Hand, J. L. (2007), Revised algorithm for estimating light extinction from IMPROVE particle speciation data, *Journal of the Air & Waste Management Association*, *57*(11), 1326-1336, doi:10.3155/1047-3289.57.11.1326.

Prenni, A., Hand, J., Malm, W., Copeland, S., Luo, G., Yu, F., Taylor, N., Russell, L., and Schichtel, B. (2019), An examination of the algorithm for estimating light extinction from IMPROVE particle speciation data, *Atmospheric Environment*, 214, 116880, <https://doi.org/10.1016/j.atmosenv.2019.116880>.

## **Chapter 5. Seasonal Distribution of Reconstructed Aerosol Light Extinction Coefficients**

Regional, monthly, and annual mean ambient speciated  $b_{ext}$  for 2016–2019 were calculated for major aerosol species including ammonium sulfate (AS), ammonium nitrate (AN), particulate organic matter (POM), elemental carbon (EC), fine dust (FD), sea salt (SS), and coarse mass (CM). Regional mean  $b_{ext}$  values were calculated for the IMPROVE and Chemical Speciation Network (CSN) regions discussed in Chapter 3. CM was not interpolated at CSN sites in Alaska and Hawaii, so  $b_{ext\_CM}$  is not available in those regions nor are speciated fractional contributions to  $b_{ext\_aer}$ . Monthly and annual mean  $b_{ext}$  values are presented as stacked bar charts, similar to the regional mean mass concentrations presented in the Chapter 3. For nonhygroscopic species, the seasonality of  $b_{ext}$  was the same as the seasonality in mass concentrations. Monthly mean  $b_{ext}$  values are depicted with the first letter of the month, followed by an “A” for annual mean. The seasonal distributions in fractional contribution of major aerosol species to aerosol  $b_{ext}$  ( $b_{ext\_aer}$ , the sum of speciated  $b_{ext}$ ) are also presented. Seasonal stacked bar charts for monthly mean  $b_{ext}$  are grouped into figures corresponding to three areas of the country: eastern, northwestern, and southwestern United States.

### **5.1 PM<sub>2.5</sub> AMMONIUM SULFATE LIGHT EXTINCTION COEFFICIENTS**

#### **5.1.1 IMPROVE**

Ambient reconstructed extinction coefficients from AS,  $b_{ext\_AS}$ , were computed using a dry extinction efficiency of  $3 \text{ m}^2 \text{ g}^{-1}$  and a humidification factor ( $f(\text{RH})$ ) to account for hygroscopic effects (see Chapter 4). The patterns in  $b_{ext\_AS}$  may closely resemble AS mass concentration patterns, but differences will arise due to hygroscopic effects. The IMPROVE 2016–2019 regional monthly mean rural  $b_{ext\_AS}$  ranged from  $1.08 \text{ Mm}^{-1}$  in the Great Basin region in January to  $23.41 \text{ Mm}^{-1}$  in the Hawaii region in March and  $24.51 \text{ Mm}^{-1}$  in the Ohio River Valley region in July. Recall that the maximum AS regional monthly mean mass concentration also occurred in the Ohio River Valley region in July (Chapter 3 and Figure 3.1.1). Many of the eastern IMPROVE regions corresponded to high  $b_{ext\_AS}$  in summer, but values were highest ( $>18 \text{ Mm}^{-1}$ ) in the Appalachia, Midsouth, Southeast, and Ohio River Valley regions (Figure 5.1.1). In the Northeast and Southeast regions,  $b_{ext\_AS}$  values were lower ( $10\text{--}20 \text{ Mm}^{-1}$ ), as were values toward the central United States, such as the Central Great Plains region. Regardless of the magnitude of  $b_{ext\_AS}$ , it peaked in the summer in most eastern regions.

In the northwestern United States, the maximum  $b_{ext\_AS}$  occurred in the Columbia River Gorge region in January ( $12.70 \text{ Mm}^{-1}$ ; Figure 5.1.2). With the exception of the winter maximum in the Columbia River Gorge, other regions experienced maximum monthly mean values in spring months (Northern Great Plains, Northern Rockies, and Hells Canyon) or during summer months (Northwest, Oregon/Northern California, Alaska). The lowest maximum monthly mean values occurred in the Hells Canyon, Northern Rockies, and Oregon/Northern California ( $\leq 5 \text{ Mm}^{-1}$ ). The minimum monthly mean  $b_{ext\_AS}$  occurred in the Northern Rockies region ( $1.59 \text{ Mm}^{-1}$ ) and the Oregon/Northern California region ( $1.54 \text{ Mm}^{-1}$ ), both in January. The largest minimum monthly mean  $b_{ext\_AS}$  occurred in the Columbia River Gorge region ( $4.66 \text{ Mm}^{-1}$ ) in June.

Most of the regions in the southwestern United States experienced maximum monthly mean  $b_{ext\_AS}$  in summer or early fall (Figure 5.1.3). The Hawaii region experienced the highest monthly mean maximum  $b_{ext\_AS}$  ( $23.41 \text{ Mm}^{-1}$ ) in March, followed by the West Texas region ( $11.26 \text{ Mm}^{-1}$ ) in September, and the California Coast and Southern California regions ( $\sim 9 \text{ Mm}^{-1}$ ), both in July. The lowest maximum monthly mean  $b_{ext\_AS}$  occurred in the Great Basin region ( $2.66 \text{ Mm}^{-1}$ ) in May. The minimum monthly mean  $b_{ext\_AS}$  occurred during winter months for all of the regions in the southwestern United States. The lowest occurred in the Great Basin region in January ( $1.08 \text{ Mm}^{-1}$ ), and the largest minimum occurred in the Hawaii region ( $5.22 \text{ Mm}^{-1}$ ) in December.

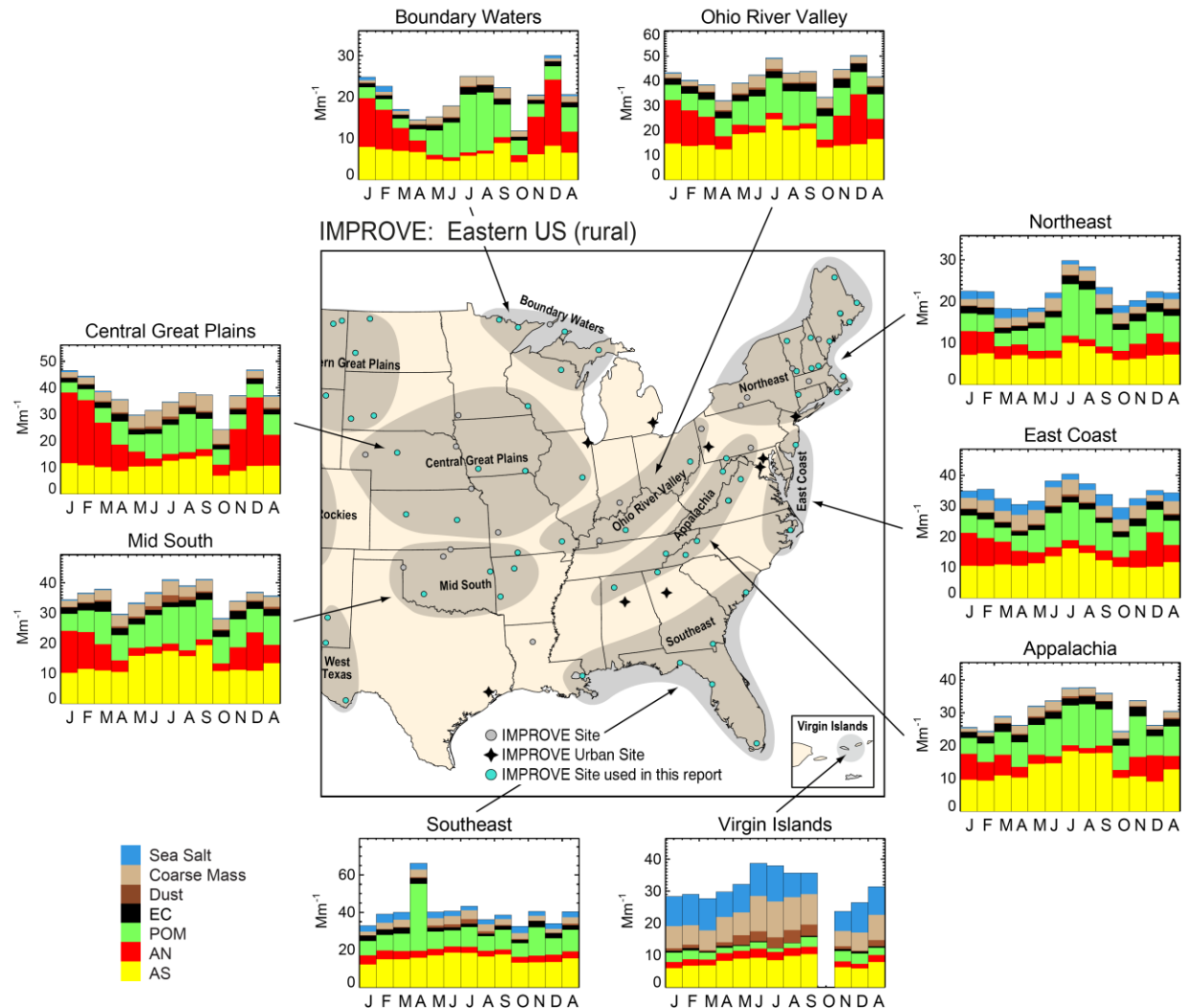


**Figure 5.1.1. IMPROVE 2016–2019 regional monthly mean ambient reconstructed spatiotemporal aerosol light extinction coefficients ( $\text{Mm}^{-1}$ ) for the eastern United States. Letters on the x-axis correspond to the month and “A” corresponds to annual mean. Shaded areas in the map correspond to regions that include sites used in the analysis, shown as blue dots. Wavelength corresponds to 550 nm.**

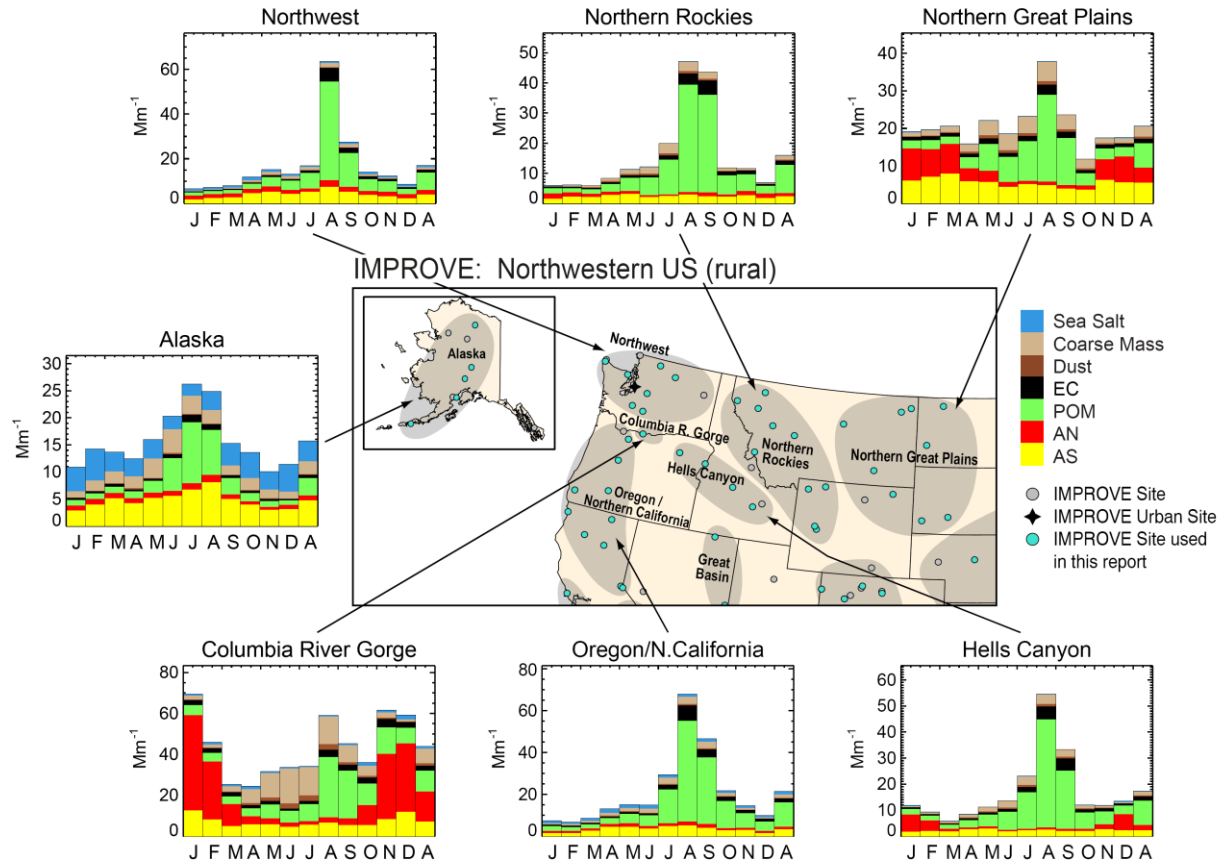


**Figure 5.1.2. IMPROVE 2016–2019 regional monthly mean ambient reconstructed speciated aerosol light extinction coefficients ( $\text{Mm}^{-1}$ ) for the northwestern United States. Letters on the x-axis correspond to the month and “A” corresponds to annual mean. Shaded areas in the map correspond to regions that include sites used in the analysis, shown as blue dots. Wavelength corresponds to 550 nm.**

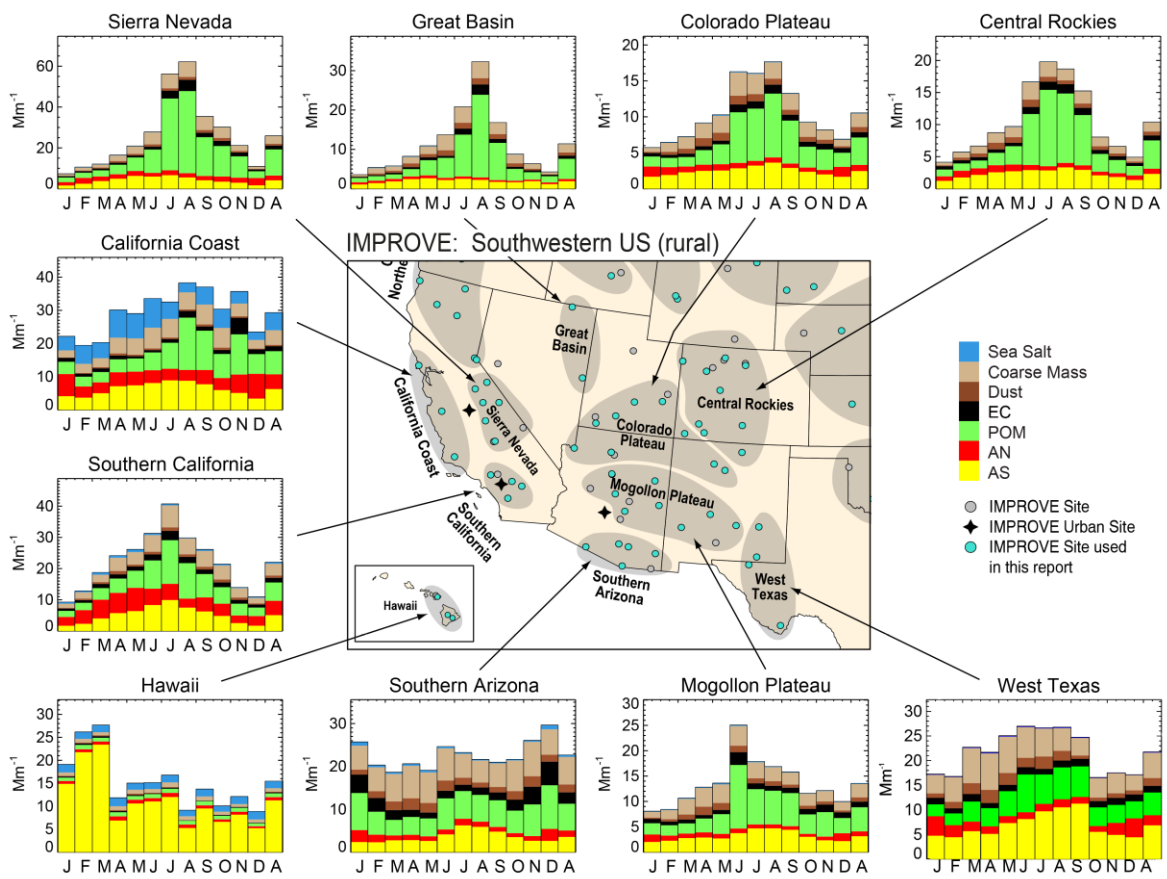


**Figure 5.1.3. IMPROVE 2016–2019 regional monthly mean ambient reconstructed spiculated aerosol light extinction coefficients ( $Mm^{-1}$ ) for the southwestern United States. Letters on the x-axis correspond to the month and “A” corresponds to annual mean. Shaded areas in the map correspond to regions that include sites used in the analysis, shown as blue dots. Wavelength corresponds to 550 nm.**

The IMPROVE fractional contribution of  $b_{ext\_AS}$  to  $b_{ext\_aer}$  ranged from 0.047 in the Hells Canyon region in August to 0.846 in Hawaii in March. The maximum fractions in continental U.S. (CONUS) regions were 0.498 in the Ohio River Valley region in July and 0.496 in the Appalachia region in September. Other regions in the eastern United States corresponded to maximum monthly mean fractions around 0.4–0.45 that occurred mostly during summer and early fall months (Figure 5.1.4). Fractions in the Midsouth, Northeast, and Boundary Waters regions peaked during spring months. The seasonal pattern in the Boundary Waters region differed from other regions with lower fractions in summer months, likely due to the contributions from  $b_{ext\_POM}$ . The lowest monthly mean maximum contribution in the eastern United States occurred in the Virgin Islands region in September (0.292). The lowest minimum monthly mean mass fraction also occurred in the Virgin Islands region in January (0.212). The minimum fractional contribution of  $b_{ext\_AS}$  in other regions was round 0.3 and typically occurred in winter months, except in the Northeast region in June, the Boundary Waters region in July, and the Midsouth and Southeast regions in spring months.

The seasonality of the fractional contribution of  $b_{ext\_AS}$  to  $b_{ext\_aer}$  in regions in the northwestern United States differed from that observed for eastern regions, with minima in  $b_{ext\_AS}$  contributions in summer months, largely due to the strong contributions from  $b_{ext\_POM}$  during summer (Figure 5.1.5). The fractional contribution ranged from 0.056 (Northern Rockies region in September) and 0.076 (Oregon/Northern California in August) to 0.392 in the Northwest (April) and 0.389 in the Northern Great Plains in March. The lowest maximum monthly mean contribution occurred in the Hells Canyon region (0.329) in March.

The seasonality of the fractional contribution of  $b_{ext\_AS}$  to  $b_{ext\_aer}$  in regions farther north in the southwestern United States followed those of the northwestern region, with lower contributions that occurred in the summer months due to the role of  $b_{ext\_POM}$  contributions (Figure 5.1.6). Contributions of  $b_{ext\_AS}$  in regions farther south tended to have flat seasonality, or summer/early fall maxima. The minimum monthly mean fractional contributions were 0.070 in the Great Basin region (August) and 0.089 in both the Sierra Nevada region (August) and the Southern Arizona region (December). The maximum contribution occurred in the Hawaii region in March (0.846) and in the West Texas region in September (0.455). Maximum contributions in other regions were around 0.3 and occurred either during spring months or late summer/early fall months.

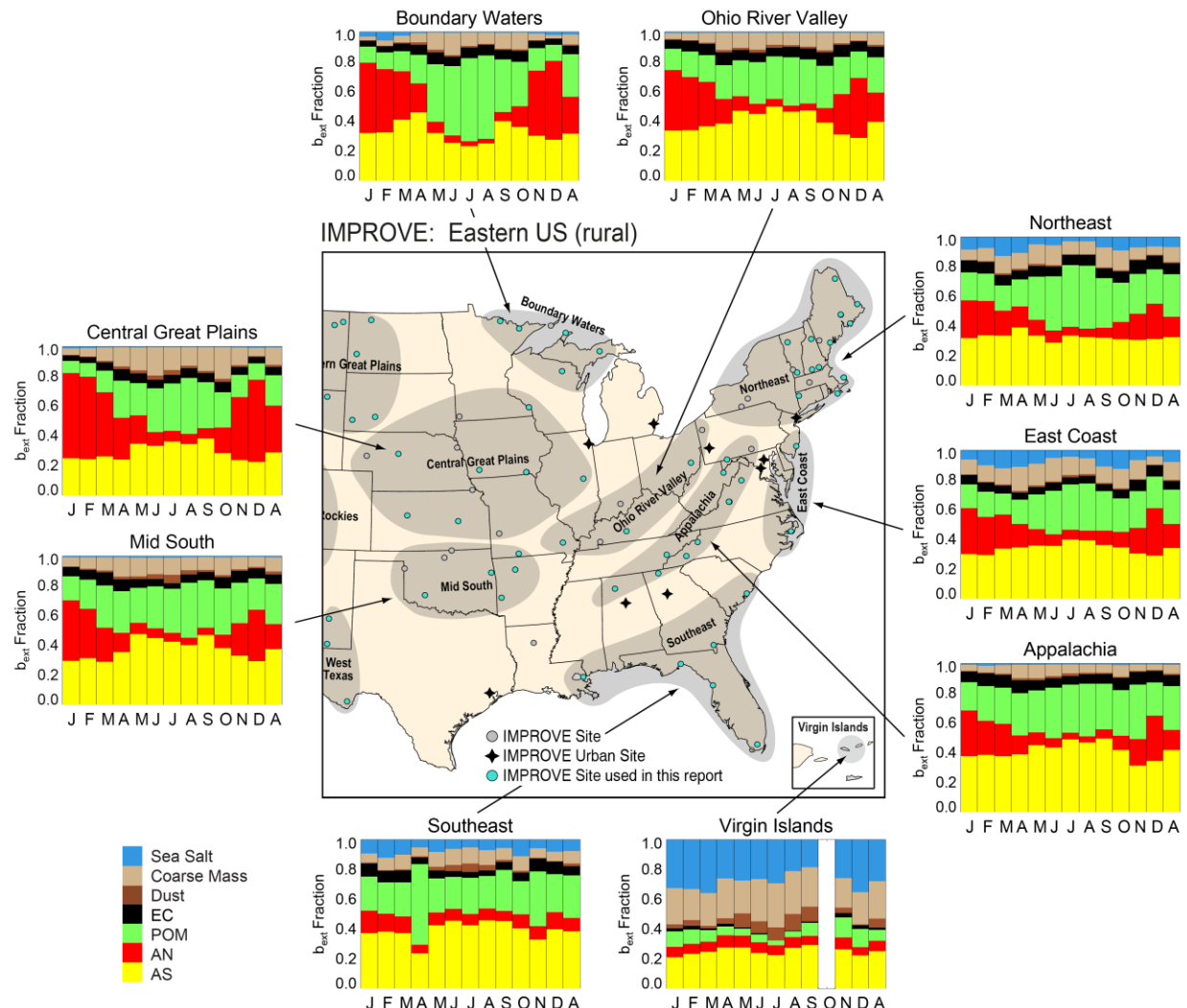


**Figure 5.1.4. IMPROVE 2016–2019 regional monthly mean speciated fractional contributions to ambient aerosol light extinction coefficients for the eastern United States. Letters on the x-axis correspond to the month and “A” corresponds to annual mean. Shaded areas in the map correspond to regions that include sites used in the analysis, shown as blue dots. Wavelength corresponds to 550 nm.**

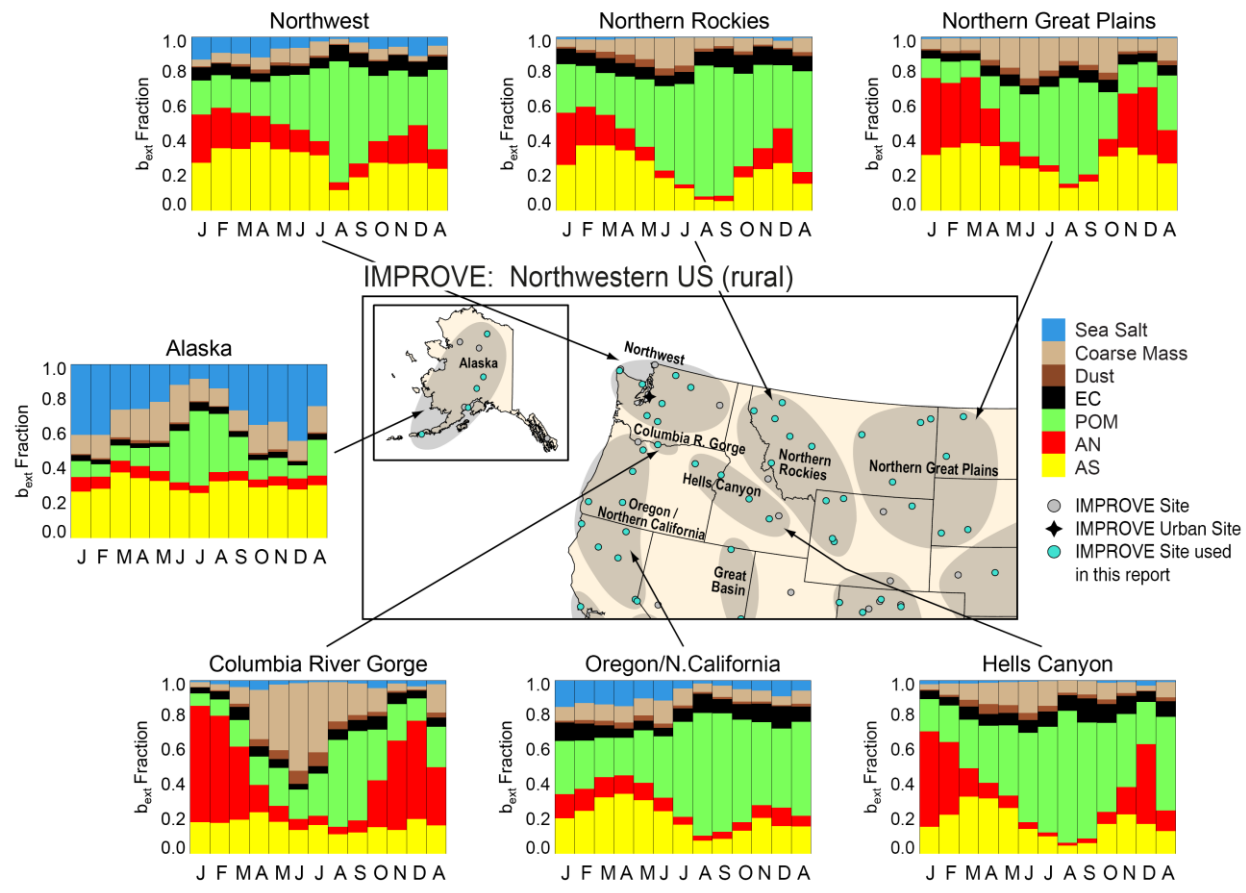


**Figure 5.1.5. IMPROVE 2016–2019 regional monthly mean speciated fractional contributions to ambient aerosol light extinction coefficients for the northwestern United States. Letters on the x-axis correspond to the month and “A” corresponds to annual mean. Shaded areas in the map correspond to regions that include sites used in the analysis, shown as blue dots. Wavelength corresponds to 550 nm.**

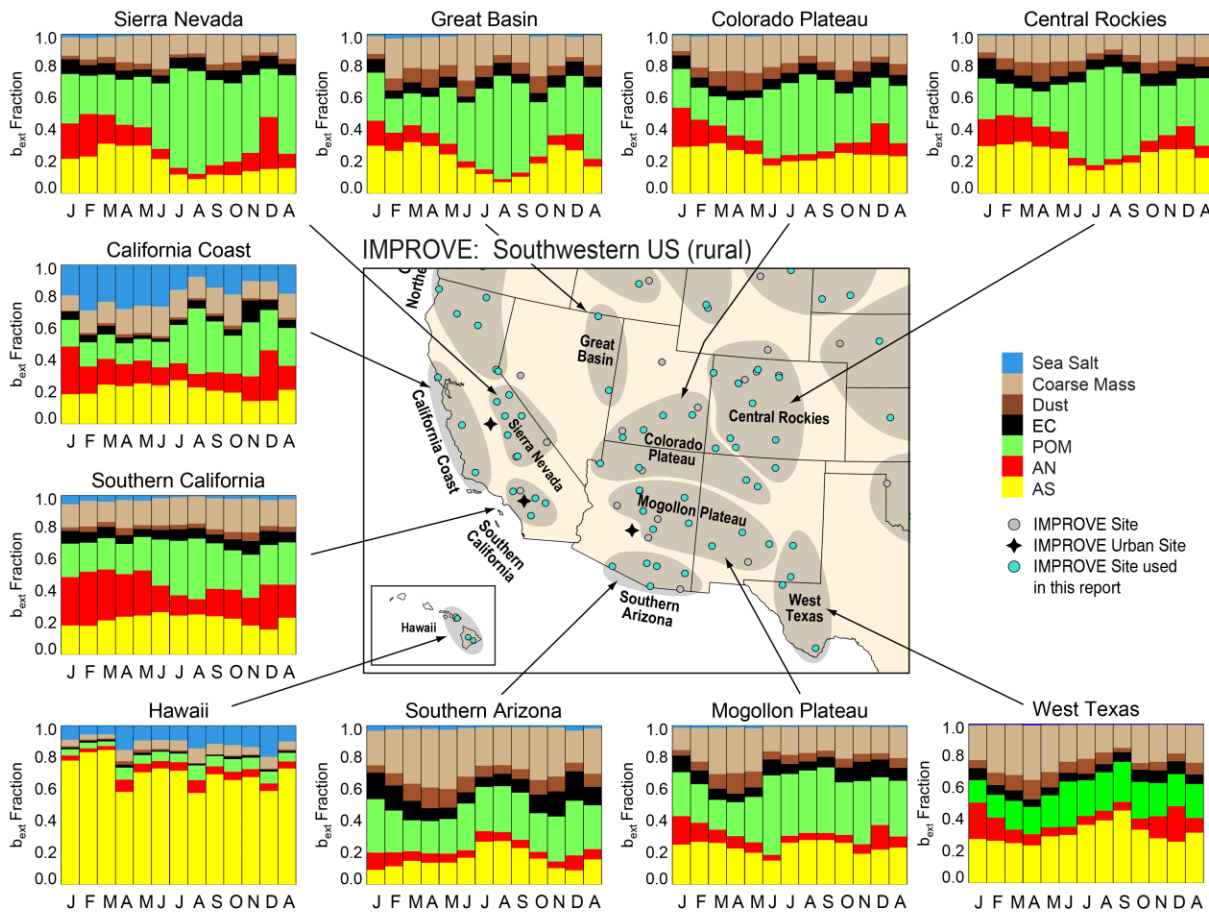


**Figure 5.1.6. IMPROVE 2016–2019 regional monthly mean speciated fractional contributions to ambient aerosol light extinction coefficients for the southwestern United States. Letters on the x-axis correspond to the month and “A” corresponds to annual mean. Shaded areas in the map correspond to regions that include sites used in the analysis, shown as blue dots. Wavelength corresponds to 550 nm.**

### 5.1.2 CSN

The lowest urban  $b_{ext\_AS}$  occurred in the Northwest Nevada region in February ( $1.61 \text{ Mm}^{-1}$ ). The highest CSN  $b_{ext\_AS}$  occurred in the Alaska region in January ( $42.0 \text{ Mm}^{-1}$ ) and the East Texas/Gulf region in March ( $29.33 \text{ Mm}^{-1}$ ). Most of the monthly mean maxima in other regions in the eastern United States were much lower, around  $15\text{--}18 \text{ Mm}^{-1}$ , although the maximum value in the Ohio River Valley region was  $23.28 \text{ Mm}^{-1}$  in July. Other maxima occurred in summer or early fall for eastern regions. Although maxima occurred mostly in summer, the seasonal variability was low, as can be seen in Figure 5.1.7. The minimum monthly mean  $b_{ext\_AS}$  for eastern regions occurred mostly in fall or spring months, with the lowest in the Central US region ( $7.15 \text{ Mm}^{-1}$ ) in October. Other minima were around  $8\text{--}10 \text{ Mm}^{-1}$ , except in the East Texas/Gulf region, where the minimum  $b_{ext\_AS}$  of  $18.62 \text{ Mm}^{-1}$  occurred in October.

With the exception of the Alaska region, maximum  $b_{ext\_AS}$  for regions in the northwestern United States (Figure 5.1.8) ranged from  $\sim 5$  to  $12 \text{ Mm}^{-1}$  and peaked in summer and winter months. The highest  $b_{ext\_AS}$  occurred in the North Dakota region ( $12.56 \text{ Mm}^{-1}$ ) in March, and the lowest maximum occurred in the Northwest region in January ( $5.34 \text{ Mm}^{-1}$ ). The minimum

monthly mean  $b_{ext\_AS}$  ranged from 2 to 5  $Mm^{-1}$ , with the lowest in the Northwest region (2.07  $Mm^{-1}$ ) and the Alaska region (2.18  $Mm^{-1}$ ), both in June. With the exception of the Alaska region, the seasonality in  $b_{ext\_AS}$  was relatively flat.

The range in the  $b_{ext\_AS}$  in regions in the southwestern United States was 1.61  $Mm^{-1}$  in the Northwest Nevada region in February to 23.74  $Mm^{-1}$  in the Los Angeles region in July, followed by the San Diego region (21.28  $Mm^{-1}$ ), also in July (Figure 5.1.9). Both regions had a strong seasonal pattern. Most other regions experienced monthly mean maximum  $b_{ext\_AS}$  from ~3 to 10  $Mm^{-1}$ , mostly during summer or early fall months. The exceptions were the Sacramento/Central Valley, Utah, Front Range CO, and Hawaii regions, which experienced maxima in January or February. Minimum monthly mean  $b_{ext\_AS}$  ranged from ~2 to 6  $Mm^{-1}$ , with the minima occurring during a variety of months depending on region, but none during summer months.

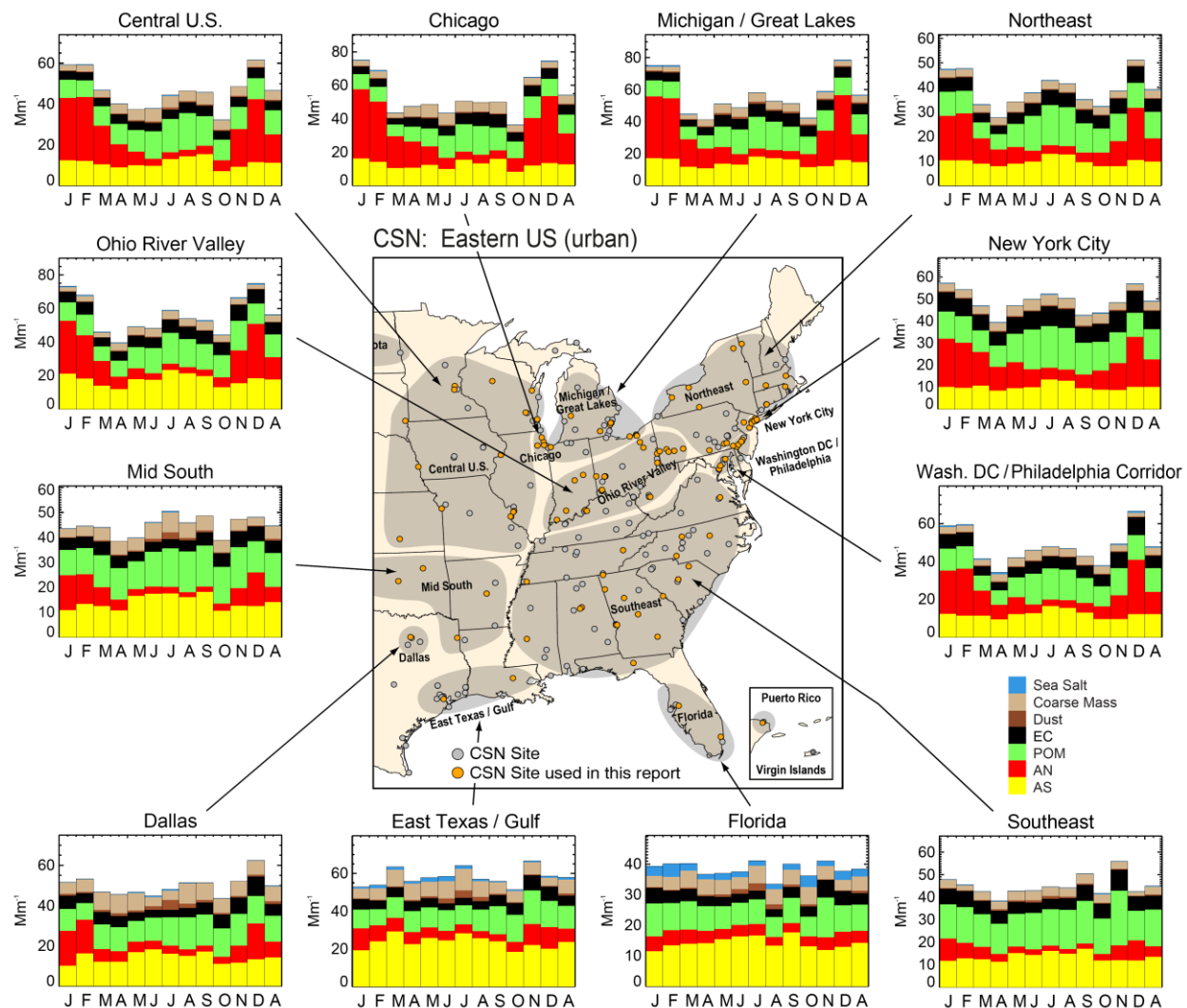


**Figure 5.1.7. CSN 2016–2019 regional monthly mean ambient reconstructed spatiotemporal aerosol light extinction coefficients ( $Mm^{-1}$ ) for the eastern United States. Letters on the x-axis correspond to the month and “A” corresponds to annual mean. Shaded areas in the map correspond to regions that include sites used in the analysis, shown as orange dots. Wavelength corresponds to 550 nm.**

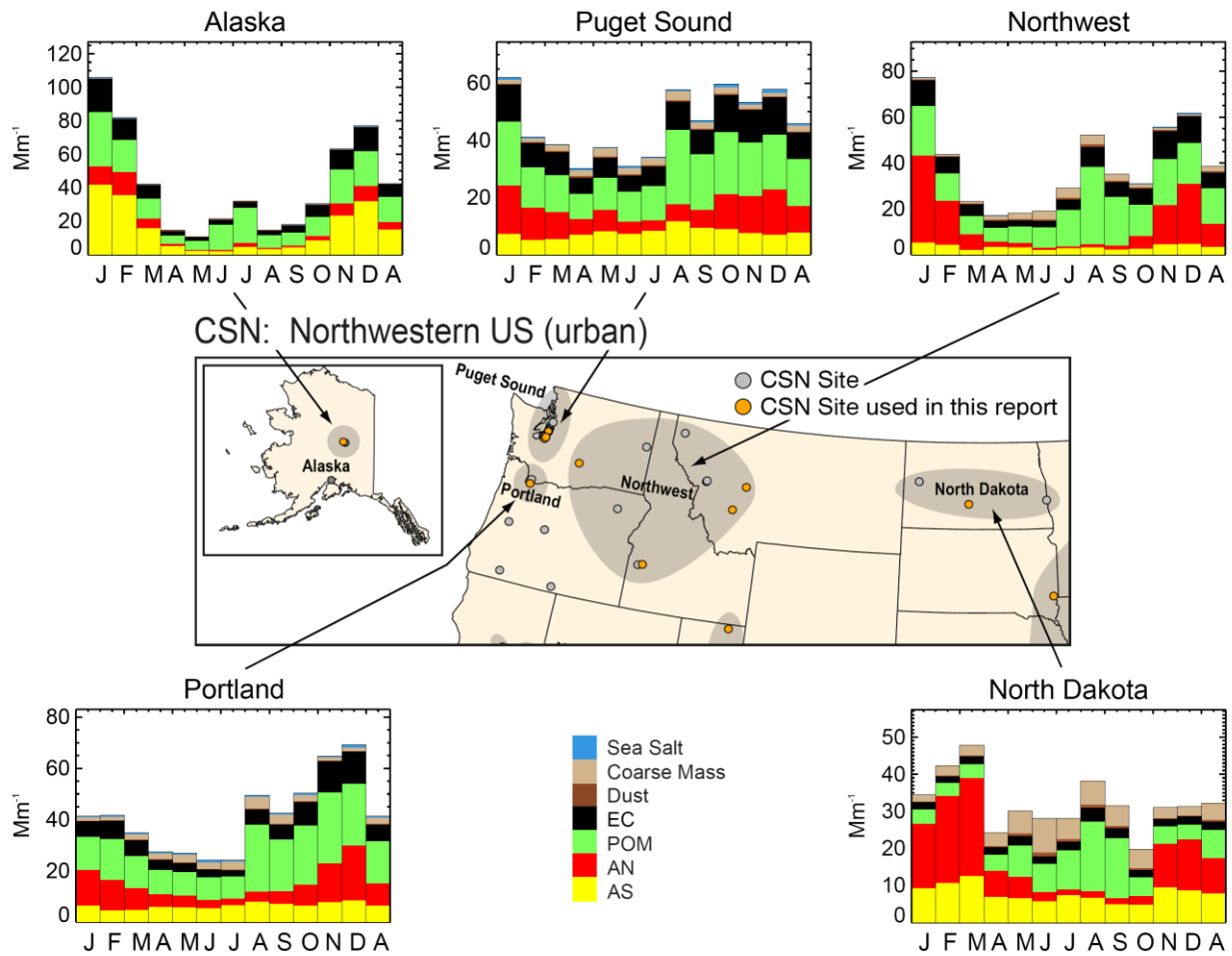


**Figure 5.1.8. CSN 2016–2019 regional monthly mean ambient reconstructed speciated aerosol light extinction coefficients ( $Mm^{-1}$ ) for the northwestern United States. Letters on the x-axis correspond to the month and “A” corresponds to annual mean. Shaded areas in the map correspond to regions that include sites used in the analysis, shown as orange dots. Wavelength corresponds to 550 nm.**

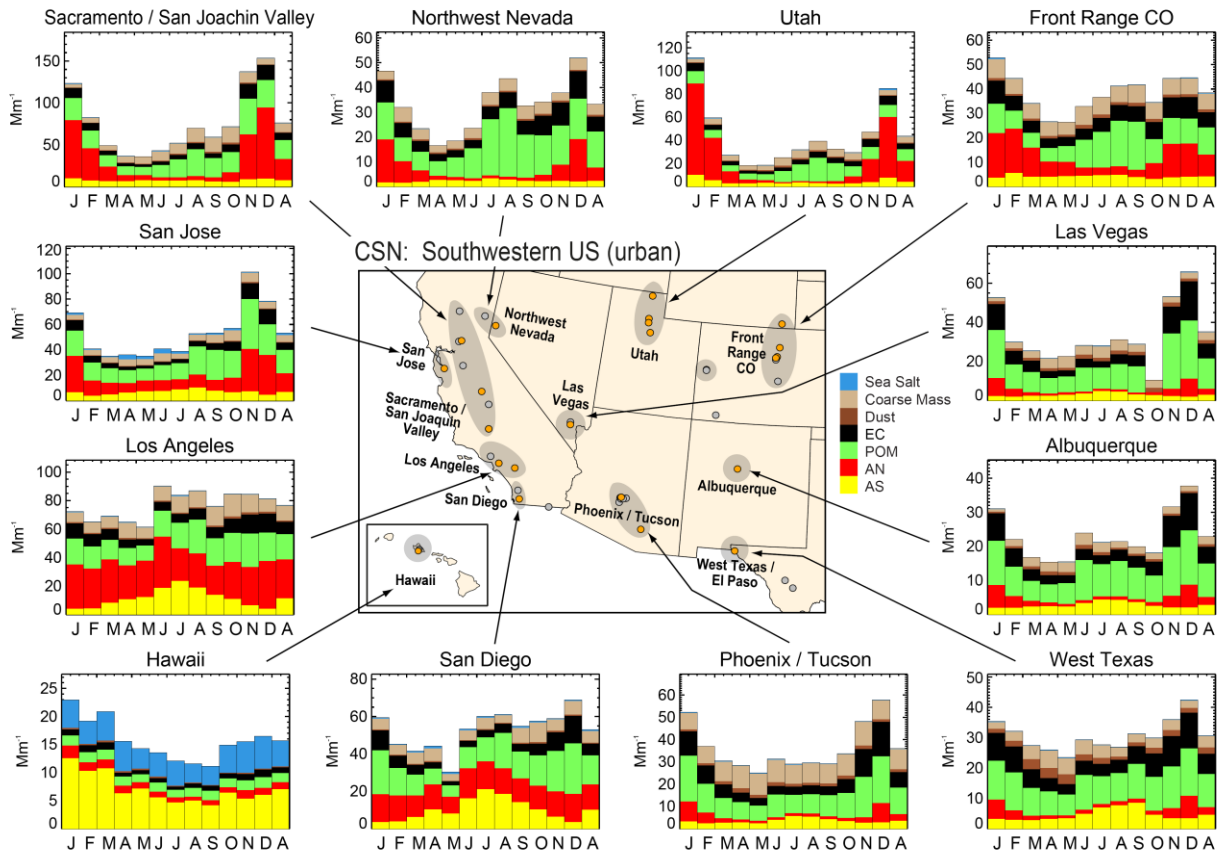


**Figure 5.1.9. CSN 2016–2019 regional monthly mean ambient reconstructed speciated aerosol light extinction coefficients ( $Mm^{-1}$ ) for the southwestern United States. Letters on the x-axis correspond to the month and “A” corresponds to annual mean. Shaded areas in the map correspond to regions that include sites used in the analysis, shown as orange dots. Wavelength corresponds to 550 nm.**

CSN regional mean  $b_{ext\_AS}$  fraction ranged from 0.032 in the Las Vegas region in December and 0.038 in the Northwest Nevada region in January to 0.464 in the East Texas/Gulf region in March. The maximum contributions of  $b_{ext\_AS}$  to  $b_{ext\_aer}$  in the eastern United States were typically around 0.3–0.4 (Figure 5.1.10) in summer and early fall months. The lowest contributions were around 0.2–0.3 in winter months, lending to low seasonal variability in  $b_{ext\_AS}$  contributions in regions in the eastern United States. While the seasonal patterns were quite similar across regions, the maximum contributions occurred in regions farther south.

The relative contribution of  $b_{ext\_AS}$  to  $b_{ext\_aer}$  decreased considerably in regions in the western United States. Minimum  $b_{ext\_AS}$  contributions in regions in the northwestern United States were around 0.1, with the highest minimum in the North Dakota region (0.158 in September; Figure 5.1.11). The maximum contributions for these regions reached 0.2–0.3, with the highest contribution (0.306) in the North Dakota region in November. Contributions were also relatively flat. The Alaska region was not included because CM estimates were not available there.

Monthly mean contributions of  $b_{ext\_AS}$  to  $b_{ext\_aer}$  were lowest in regions in the southwestern United States relative to other areas of the country (Figure 5.1.12). Minimum contributions were below 0.1, and maximum contributions were around 0.2–0.3, with the highest contribution of 0.354 in the San Diego region in July. A stronger seasonal variability occurred at regions in the southwestern United States relative to other regions, with summer maximum contributions common, especially in regions farther south, like the West Texas, Phoenix/Tucson, San Diego, and Los Angeles regions. However, the Sacramento/Central Valley, Northwest Nevada, and Utah regions had maximum contributions in spring months.

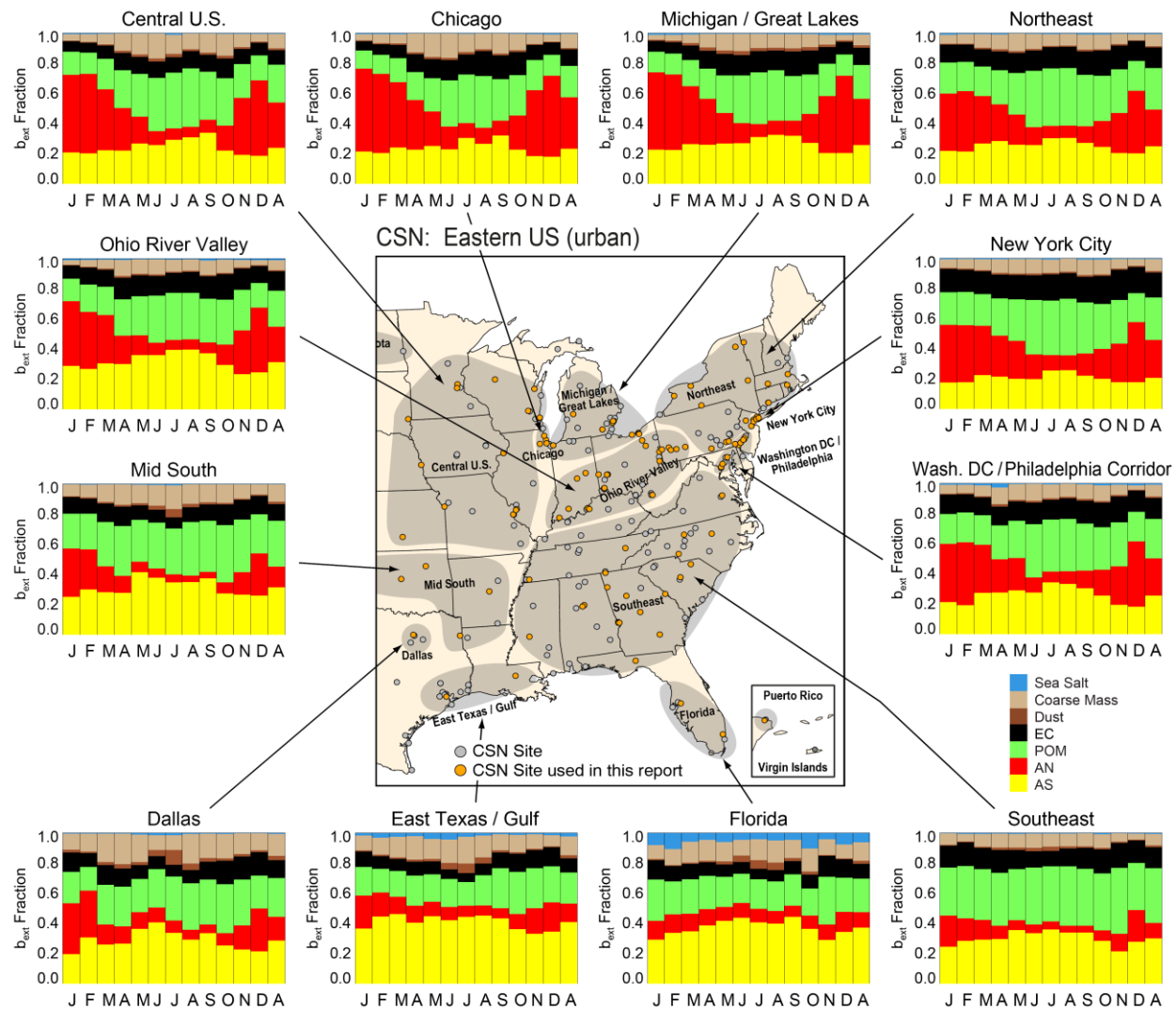


**Figure 5.1.10. CSN 2016–2019 regional monthly mean speciated fractional contributions to ambient aerosol light extinction coefficients for the eastern United States. Letters on the x-axis correspond to the month and “A” corresponds to annual mean. Shaded areas in the map correspond to regions that include sites used in the analysis, shown as orange dots. Wavelength corresponds to 550 nm.**

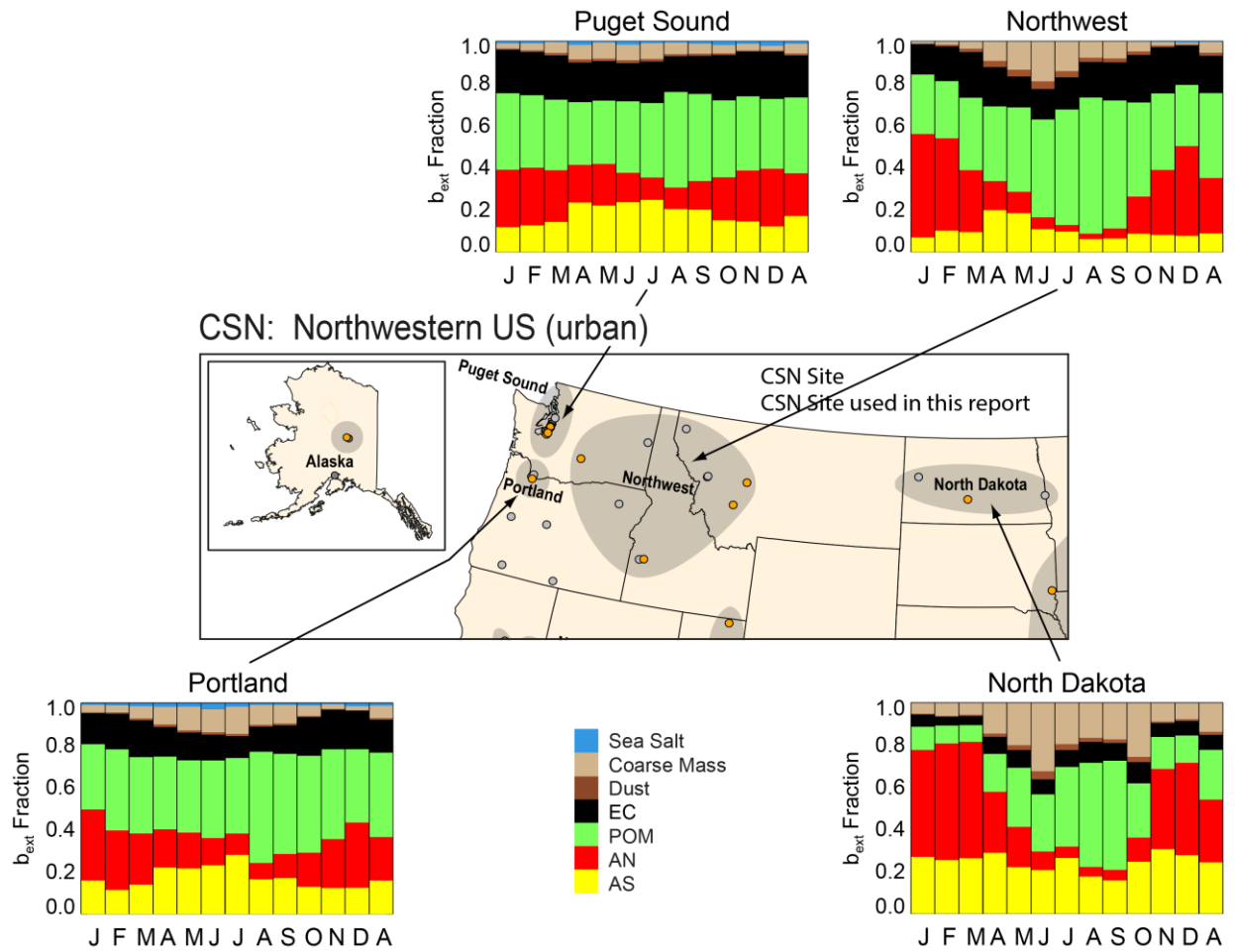


**Figure 5.1.11.** 2016–2019 regional monthly mean speciated fractional contributions to ambient aerosol light extinction coefficients for the northwestern United States. Letters on the x-axis correspond to the month and “A” corresponds to annual mean. Shaded areas in the map correspond to regions that include sites used in the analysis, shown as orange dots. Wavelength corresponds to 550 nm.

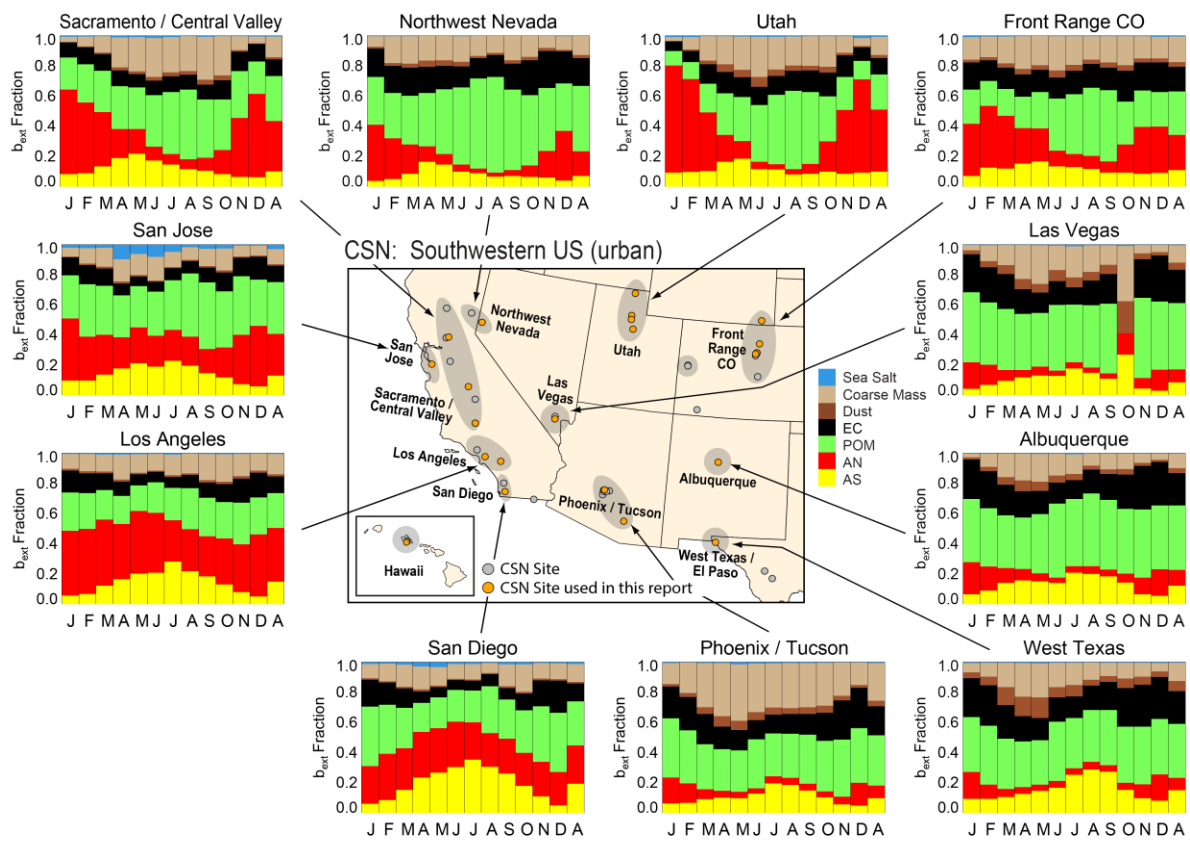


**Figure 5.1.12. CSN 2016–2019 regional monthly mean speciated fractional contributions to ambient aerosol light extinction coefficients for the southwestern United States. Letters on the x-axis correspond to the month and “A” corresponds to annual mean. Shaded areas in the map correspond to regions that include sites used in the analysis, shown as orange dots. Wavelength corresponds to 550 nm.**

## 5.2 PM<sub>2.5</sub> AMMONIUM NITRATE LIGHT EXTINCTION COEFFICIENTS

The extinction efficiency and  $f(RH)$  values used to compute reconstructed light extinction coefficients from AN,  $b_{ext\_AN}$ , were the same as those used to compute  $b_{ext\_AS}$ . In a similar manner, while general patterns of  $b_{ext\_AN}$  mostly follow AN mass concentrations, differences may occur due to hygroscopic effects.

### 5.2.1 IMPROVE

Winter maxima in 2016–2019 regional monthly mean  $b_{ext\_AN}$  were common in many IMPROVE regions, consistent with favorable AN formation in winter conditions. In fact, the maximum  $b_{ext\_AN}$  in rural IMPROVE regions occurred in winter ( $46.59 \text{ Mm}^{-1}$ ) in the Columbia River Gorge region in January. The minimum IMPROVE regional, monthly mean  $b_{ext\_AN}$  ( $0.378 \text{ Mm}^{-1}$ ) occurred in the Great Basin region in October.

Similar to AN mass concentrations,  $b_{ext\_AN}$  was highest in regions farther north in the eastern United States and those closer in proximity to agricultural activities (Figure 5.1.1). The highest monthly mean  $b_{ext\_AN}$  in the eastern United States occurred in the Central Great Plains

region ( $26.66 \text{ Mm}^{-1}$ ) in January and in the Ohio River Valley region ( $20.25 \text{ Mm}^{-1}$ ) in December. These regions also experienced relatively high seasonal variability, with low  $b_{\text{ext\_AN}}$  during summer months. The minimum  $b_{\text{ext\_AN}}$  for eastern regions was around  $1\text{--}2 \text{ Mm}^{-1}$ , with the lowest ( $0.755 \text{ Mm}^{-1}$ ) in the Boundary Waters region in August. In regions farther south, the seasonal variability was quite low; in the Southeast region, monthly mean maximum  $b_{\text{ext\_AN}}$  was less than  $5 \text{ Mm}^{-1}$  year round. In the Northeast region monthly mean maximum  $b_{\text{ext\_AN}}$  was around  $5 \text{ Mm}^{-1}$ , and the region experienced a larger seasonal variability.

Regional monthly mean  $b_{\text{ext\_AN}}$  varied considerably between regions in the northwestern United States (Figure 5.1.2). The Northern Great Plains, Hells Canyon, and Columbia River Gorge regions experienced higher  $b_{\text{ext\_AN}}$  relative to other regions, especially during winter months. The maximum monthly mean  $b_{\text{ext\_AN}}$  in the Northern Great Plains and Hells Canyon regions was  $8.51 \text{ Mm}^{-1}$  and  $6.49 \text{ Mm}^{-1}$ , respectively, both in January. In contrast, values in the Oregon/Northern California, Northwest, Alaska, and Northern Rockies regions were low, with maximum monthly mean  $b_{\text{ext\_AN}}$  below  $3 \text{ Mm}^{-1}$  and low seasonal variability. Maximum monthly mean  $b_{\text{ext\_AN}}$  occurred in August for the Northwest, Alaska, and Oregon/Northern California regions, coincident with peaks in  $b_{\text{ext\_POM}}$ .

With the exception of the California Coast ( $7.45 \text{ Mm}^{-1}$  in December) and Southern California ( $7.43 \text{ Mm}^{-1}$  in May) regions, maximum monthly mean  $b_{\text{ext\_AN}}$  was  $<4 \text{ Mm}^{-1}$  in regions in the southwestern United States (Figure 5.1.3). Most other regions had low seasonal variability, except the West Texas region where monthly mean  $b_{\text{ext\_AN}}$  ranged from a minimum of  $1.17 \text{ Mm}^{-1}$  in October to  $3.94 \text{ Mm}^{-1}$  in January. Monthly mean  $b_{\text{ext\_AN}}$  in the Hawaii region was  $<1 \text{ Mm}^{-1}$  year round.

The contribution of  $b_{\text{ext\_AN}}$  to  $b_{\text{ext\_aer}}$  ranged from 0.0169 in the Hells Canyon region in August to 0.671 in the Columbia River Gorge region in January. Regions farther north in the eastern United States experienced a high degree of seasonality in the fractional contribution of  $b_{\text{ext\_AN}}$  (Figure 5.1.4). Monthly mean contributions during summer months in the Boundary Waters, Central Great Plains, and Ohio River Valley regions were around 0.03–0.06, compared to over 0.5 during winter months. Regions farther from agricultural sources, such as the East Coast, Northeast, and Appalachia regions, had lower maximum monthly mean contributions (~0.3 or less) in winter months. The Southeast region had the lowest year-round monthly mean contributions, ranging from 0.06 to 0.15.

In the northwestern United States, the monthly mean contributions of  $b_{\text{ext\_AN}}$  to  $b_{\text{ext\_aer}}$  ranged from a minimum of 0.030 in the Oregon/Northern California region in August to 0.549 in the Hells Canyon region and 0.671 in the Columbia River Gorge region, both in January (Figure 5.1.5). Monthly mean contributions in the Northern Great Plains reached 0.443 in January. The regions with higher contributions were closer to agricultural activity and oil and gas development. Contributions in other regions, such as the Northern Rockies and Northwest regions, reached nearly 0.3 in winter. Contributions in the Alaska region were also low year round (0.042 in July to 0.084 in January).

The relative contribution of  $b_{\text{ext\_AN}}$  to  $b_{\text{ext\_aer}}$  was lower in the southwestern United States relative to other areas (Figure 5.1.6). Monthly mean contributions ranged from 0.019 in the Great

Basin region in August to 0.328 in the Sierra Nevada region in December and 0.338 in the Southern California region in February. Other regions experienced elevated monthly mean contributions during winter months, but values only reached 0.15–0.3. The Hawaii region experienced a maximum monthly mean contribution of 0.081 in August and low contributions the rest of the year.

## 5.2.2 CSN

The CSN regional monthly mean  $b_{ext\_AN}$  ranged from 0.53 Mm<sup>-1</sup> in the Alaska region in May, 0.64 Mm<sup>-1</sup> in the Hawaii region in August, and 0.82 Mm<sup>-1</sup> in the Albuquerque region in May to 84.82 Mm<sup>-1</sup> in the Sacramento/Central Valley region in December. Similar to the seasonal patterns observed in IMPROVE regions in the eastern United States,  $b_{ext\_AN}$  was highest (30–40 Mm<sup>-1</sup>) during winter months in regions farther north, such as the Central U.S., Michigan/Great Lakes, and Chicago regions (Figure 5.1.7). The range in seasonality decreased in regions farther south, such as the East Texas/Gulf, Florida, and Southeast regions, where values were near 10 Mm<sup>-1</sup> or less during winter months. These values were double what was observed in southern IMPROVE regions in the eastern United States.

In the northwestern United States, regional, monthly mean CONUS  $b_{ext\_AN}$  ranged from 0.91 Mm<sup>-1</sup> in the Northwest region in July to 37.97 Mm<sup>-1</sup> in the Northwest region in January, roughly four times higher than the IMPROVE maximum monthly mean value (Figure 5.1.8). The maximum  $b_{ext\_AN}$  occurred during winter months in all regions in the northwestern United States except in the North Dakota region, where the monthly mean maximum value of 26.40 Mm<sup>-1</sup> occurred in March. This is a region near oil and gas development activity. The maximum monthly mean values in the northwestern United States were lower than those observed in eastern CSN regions.

Maximum values of regional monthly mean  $b_{ext\_AN}$  in urban regions were considerably higher in the southwestern United States (5.1.9) compared to the northwestern United States. The Sacramento/Central Valley and Utah regions experienced high monthly mean  $b_{ext\_AN}$  (~80 Mm<sup>-1</sup> and higher) during winter months. These areas are subject to inversions and increased particulate matter concentrations during winter. Winter monthly mean maxima and strong seasonal variability in  $b_{ext\_AN}$  were also observed in regions farther south, such as the Phoenix/Tucson, Albuquerque, and West Texas regions, but monthly mean maxima  $b_{ext\_AN}$  were much lower (<10 Mm<sup>-1</sup>). In contrast, monthly mean  $b_{ext\_AN}$  values in regions in southern California, such as the Los Angeles, and San Diego regions, were elevated year round. In the Los Angeles region, monthly mean values ranged from 20.36 Mm<sup>-1</sup> in September to 35.84 Mm<sup>-1</sup> in June, also a different seasonal pattern from what was observed in most other regions in the southwestern United States.

CSN regional monthly mean  $b_{ext\_AN}$  fractional contributions ranged from 0.026 and 0.027 in August in the Northwest and Northwest Nevada regions, respectively, to 0.71 in the Utah region in January. Contributions of  $b_{ext\_AN}$  to  $b_{ext\_aer}$  in the eastern United States were highest in regions farther north (Figure 5.1.10). During winter months in the Central U.S., Chicago, and Michigan Great Lakes regions,  $b_{ext\_AN}$  contributed over half of  $b_{ext\_aer}$  and decreased to less than 0.1 during summer months. The range in seasonal contributions was much lower in regions

farther south, such as the East Texas/Gulf and Florida regions, where monthly mean contributions ranged from ~0.05 in summer months to ~0.2 or less during winter months.

The highest monthly mean contributions of  $b_{ext\_AN}$  to  $b_{ext\_aer}$  (0.55) in the northwestern United States occurred in the North Dakota region in February (Figure 5.1.11). Contributions in this region dropped by a factor of ten (0.05) during summer months. The Northwest region experienced a higher range in contributions from summer to winter months compared to the Puget Sound and Portland regions, where contributions during winter months were lower (~0.3) and summer contributions were higher (~0.10).

While the Utah region corresponded to the highest monthly mean contributions in winter months (0.71), other regions in the southwestern United States also experienced high contributions during winter months, such as the Sacramento/Central Valley region (0.56 in January), the Northwest Nevada region (0.49 in January), and the Front Range CO region (0.41 in February). These regions also experienced much lower contributions (~0.05) during summer months (Figure 5.1.12). Regions in California experienced less seasonality in  $b_{ext\_AN}$  contributions, such as the San Jose, Los Angeles, and San Diego regions, suggesting additional urban sources during summer months. The lowest contributions occurred in regions in the southwest areas, such as the Phoenix/Tucson, West Texas, and Albuquerque regions. These regions experienced higher monthly mean contributions in winter relative to summer but ranged from ~0.03 to ~0.2 or less.

## 5.3 PM<sub>2.5</sub> PARTICULATE ORGANIC MATTER LIGHT EXTINCTION COEFFICIENTS

### 5.3.1 IMPROVE

POM was considered to be nonhygroscopic in reconstructed  $b_{ext}$  calculations. On a similar dry mass basis,  $b_{ext\_POM}$  would be higher than  $b_{ext\_AS}$  or  $b_{ext\_AN}$  because its extinction efficiency is higher ( $4 \text{ m}^2 \text{ g}^{-1}$  compared to  $3 \text{ m}^2 \text{ g}^{-1}$ ; see section 4.1).

The minimum IMPROVE 2016–2019 regional monthly mean  $b_{ext\_POM}$  occurred in the Hawaii region in December ( $0.66 \text{ Mm}^{-1}$ ) and the Central Rockies region in January ( $1.06 \text{ Mm}^{-1}$ ). The maximum regional monthly mean  $b_{ext\_POM}$  occurred in the Oregon/Northern California region in August ( $47.99 \text{ Mm}^{-1}$ ). Monthly mean  $b_{ext\_POM}$  in the eastern United States ranged from ~3 to  $7 \text{ Mm}^{-1}$  to  $35 \text{ Mm}^{-1}$  (Figure 5.1.1), which occurred in April in the Southeast region due to the impacts of biomass smoke (see Chapter 2). Most regions in the eastern United States experienced monthly mean maxima during July and August, and values were consistently near  $14 \text{ Mm}^{-1}$ . The Virgin Islands region experienced a maximum monthly mean  $b_{ext\_POM}$  ( $3.25 \text{ Mm}^{-1}$ ) during December. Most of the regional minima monthly mean  $b_{ext\_POM}$  occurred during January or March, with the exception of the Southeast region, which occurred in October, and the Virgin Islands region in July.

Biomass smoke influence on  $b_{ext\_POM}$  was obvious in many northwestern United States regions, with strong impacts during summer months (Figure 5.1.2). All of the regions experienced maximum monthly mean values during August, with the exception of Alaska (July).

The highest monthly mean  $b_{ext\_POM}$  occurred in the Oregon/Northern California, Northwest, and Hells Canyon regions ( $>40 \text{ Mm}^{-1}$ ). Maximum monthly mean values were lower in the Columbia River Gorge region ( $29.50 \text{ Mm}^{-1}$ ) and the Northern Rockies region ( $35.11 \text{ Mm}^{-1}$ ). Minimum monthly mean values occurred from January through March for most regions and were less than  $4 \text{ Mm}^{-1}$ , with the exception of the Alaska region, which corresponded to a minimum in December.

The northerly regions in the southwestern United States were also influenced by biomass smoke with higher  $b_{ext\_POM}$  during summer months (July and August), such as the Sierra Nevada, Great Basin, and Central Rockies regions (Figure 5.1.3). The highest monthly mean  $b_{ext\_POM}$  occurred in the Sierra Nevada region ( $40.24 \text{ Mm}^{-1}$ ) in August. These regions also had their lowest ( $<2 \text{ Mm}^{-1}$ ) monthly mean  $b_{ext\_POM}$  during January. Less seasonality was observed in regions farther south. The Southern Arizona, Mogollon Plateau, and West Texas regions had  $b_{ext\_POM}$  that ranged from 2 to  $3 \text{ Mm}^{-1}$  in February and March to around  $10 \text{ Mm}^{-1}$  during summer months, except for the Southern Arizona region, which had a maximum in December.

The contributions of  $b_{ext\_POM}$  to  $b_{ext\_aer}$  ranged from 0.029 in the Hawaii region in March, 0.030 in the Virgin Islands region in July, and 0.071 in the Columbia River Gorge region in January to 0.76 in the Hells Canyon region in August. In the eastern United States, the regional maximum monthly mean  $b_{ext\_POM}$  contribution was  $\sim 0.3\text{--}0.5$ , with the highest contribution in the Boundary Waters region (0.56) in August (Figure 5.1.4). The April maximum in the Southeast region corresponded to biomass smoke influence. Other monthly mean maxima generally occurred in August, except the Appalachia region (November). Minimum contributions of  $b_{ext\_POM}$  to  $b_{ext\_aer}$  occurred mostly during winter months or early spring (e.g., the Northeast and East Coast regions). Minimum monthly mean contributions were around 0.1–0.2. The lowest occurred in the Virgin Islands region in July (0.03) and the Central Great Plains region in January (0.08).

Contributions of  $b_{ext\_POM}$  to  $b_{ext\_aer}$  were much higher for many northwestern U.S. regions relative to the eastern United States, and the maximum monthly mean contributions occurred in August for nearly all regions (Figure 5.1.5). The  $b_{ext\_POM}$  contributions ranged from 0.071 in the Columbia River Gorge (January) and Alaska (February) regions to 0.76 in the Hells Canyon region (August). With the exception of the Alaska region (0.43 in July) and the Columbia River Gorge (0.52 in September), the maximum monthly mean contributions were over 0.7, highlighting the importance of biomass burning influence on  $b_{ext\_aer}$  in these regions.

In the southwestern United States, contributions of  $b_{ext\_POM}$  ranged from 0.142 in the West Texas region (January) to 0.65 in the Great Basin and Sierra Nevada regions, both in August (Figure 5.1.6). Regions farther north were likely influenced by biomass smoke, similar to regions in the northwestern United States area. Minimum monthly mean contributions were typically around 0.15–0.2 for other regions and occurred in early spring or late winter months. Maximum monthly mean contributions were lower farther south and ranged from 0.3 to 0.4, such as in the Southern Arizona, Mogollon Plateau, and West Texas regions. The maximum contribution in the Southern Arizona region occurred in December; other regions experienced maxima during summer months.

### 5.3.2 CSN

The regional, monthly mean  $b_{ext\_POM}$  in CSN regions ranged from  $1.33 \text{ Mm}^{-1}$  in the Hawaii region (July) and  $3.58 \text{ Mm}^{-1}$  in the North Dakota region in February to  $42.69 \text{ Mm}^{-1}$  in the Sacramento/Central Valley region in November. In the eastern United States the monthly mean  $b_{ext\_POM}$  values were highest during July and August in most regions ( $\sim 15\text{--}20 \text{ Mm}^{-1}$ ) and reached  $24 \text{ Mm}^{-1}$  in the Southeast region in November (Figure 5.1.7). Minimum values in regions across the eastern United States ( $\sim 8\text{--}10 \text{ Mm}^{-1}$ ) were roughly half the maximum monthly mean values ( $\sim 15\text{--}18 \text{ Mm}^{-1}$ ).

The seasonal variability in  $b_{ext\_POM}$  in CSN regions in the northwestern United States was much lower than for IMPROVE regions (Figure 5.1.8). The strong influence of biomass smoke was not as evident. Monthly mean maximum  $b_{ext\_POM}$  occurred during August in the Puget Sound ( $26.11 \text{ Mm}^{-1}$ ), Northwest ( $33.72 \text{ Mm}^{-1}$ ), and North Dakota regions ( $18.84 \text{ Mm}^{-1}$ ). However, in the Portland region, the maximum monthly mean  $b_{ext\_POM}$  occurred in November ( $27.59 \text{ Mm}^{-1}$ ). Most regions experienced minimum monthly mean  $b_{ext\_POM}$  during spring or winter months ( $\sim 4\text{--}9 \text{ Mm}^{-1}$ ), except the Portland region with a minimum monthly mean  $b_{ext\_POM}$  in July ( $8.83 \text{ Mm}^{-1}$ ).

The maximum regional monthly mean  $b_{ext\_POM}$  in the southwestern United States occurred in the Sacramento/Central Valley region ( $42.69 \text{ Mm}^{-1}$ ), followed by the San Jose region ( $39.45 \text{ Mm}^{-1}$ ), both in November (Figure 5.1.9). Other regions had maximum monthly mean  $b_{ext\_POM}$  in December, such as the San Diego region and others in the southwest part of the country (e.g., Phoenix/Tucson, West Texas). However, in the Northwest Nevada, Los Angeles, Front Range CO, and Utah regions, monthly mean  $b_{ext\_POM}$  was highest in August or September, perhaps due to biomass smoke influence that affected some regions in the northwestern United States.

Monthly mean contributions of  $b_{ext\_POM}$  to  $b_{ext\_aer}$  ranged from 0.079 in the North Dakota region in March to 0.645 in the Northwest region in August (Figure 5.1.10). In the eastern United States, contributions ranged from 0.121 in January in the Chicago region to 0.437 in the Southeast region in November. Monthly mean contributions in the Southeast region were greater than 0.3 during all months. In regions farther north, contributions were greater in the summer months, in part due to contributions of  $b_{ext\_AN}$  to  $b_{ext\_aer}$  during winter months. All regions experienced their lowest monthly mean  $b_{ext\_POM}$  contributions ( $\sim 0.12\text{--}0.3$ ) during winter months, with the exception of Florida (October). Months corresponding to maximum contributions varied depending on region but mostly occurred during summer months, except for the Southeast and Florida regions in November and in October for the Dallas, East Texas/Gulf, and Midsouth regions.

In the northwestern United States regional monthly mean  $b_{ext\_POM}$  contributions to  $b_{ext\_aer}$  ranged from 0.079 in March in the North Dakota region to 0.645 in the Northwest region in August (Figure 5.1.11). Most of the maximum contributions occurred during summer months ( $\sim 0.45\text{--}0.65$ ), and with the exception of the North Dakota region, minimum contributions in other regions were around 0.3. Both the Puget Sound and Portland regions experienced relatively flat contributions of  $b_{ext\_POM}$  to  $b_{ext\_aer}$  compared to the Northwest and North Dakota regions, highlighting the importance of  $b_{ext\_POM}$  contributions during winter farther west.

Contributions of  $b_{ext\_POM}$  were significant in many southwestern urban regions (Figure 5.1.12), ranging from 0.278 in Los Angeles (November) to 0.635 in the Northwest Nevada region in August. Regions farther north experienced maximum contributions during summer, in part due to the contributions of  $b_{ext\_AN}$  during winter months, when  $b_{ext\_POM}$  contributions were lowest. Farther south, maximum contributions around 0.4–0.5 occurred during summer months (Albuquerque and West Texas) and in January in the Phoenix/Tucson region.

## 5.4 PM<sub>2.5</sub> ELEMENTAL CARBON LIGHT EXTINCTION COEFFICIENT

Monthly mean EC mass concentrations were low compared to other species, and urban concentrations were higher than rural concentrations. Recall that EC light extinction coefficients ( $b_{ext\_EC}$ ) were computed by scaling the EC mass by its extinction efficiency ( $10 \text{ m}^2 \text{ g}^{-1}$ ), which is higher than the other species, due to its ability to both scatter and absorb visible light. This higher extinction efficiency increased EC's relative contribution to  $b_{ext}$  compared to reconstructed fine mass (RCFM).

### 5.4.1 IMPROVE

The rural IMPROVE 2016–2019 regional monthly mean  $b_{ext\_EC}$  ranged from  $0.09 \text{ Mm}^{-1}$  in the Hawaii region in August and  $0.28 \text{ Mm}^{-1}$  in the Great Basin region in February to  $7.44 \text{ Mm}^{-1}$  in the Oregon/Northern California region in August. The lowest monthly mean  $b_{ext\_EC}$  in the eastern United States occurred in the Boundary Waters region in March; other eastern regions had minimum  $b_{ext\_EC}$  around  $1\text{--}2 \text{ Mm}^{-1}$  (Figure 5.1.1). Minimum values occurred during January for the Appalachia, Ohio River Valley, and Central Great Plains regions, while other regions had minimum values during spring and summer months. The highest monthly mean  $b_{ext\_EC}$  ( $3.69 \text{ Mm}^{-1}$ ) occurred in the Ohio River Valley region in November, similar to the Appalachia region ( $2.94 \text{ Mm}^{-1}$ ). The Midsouth and Southeast regions also had higher monthly mean maximum values ( $\sim 3 \text{ Mm}^{-1}$ ).

Maximum monthly mean  $b_{ext\_EC}$  values were highest in regions in the northwestern United States. Values ranged from  $0.47 \text{ Mm}^{-1}$  in February in the Northern Rockies region to  $7.44 \text{ Mm}^{-1}$  in the Oregon/Northern California region in August (Figure 5.1.2). Maximum monthly mean  $b_{ext\_EC}$  occurred during summer months for all of the regions with the exception of the Columbia River Gorge region (November). Summer maxima were likely associated with biomass burning influence.

In the southwestern United States, regional monthly mean  $b_{ext\_EC}$  ranged from  $0.28 \text{ Mm}^{-1}$  in February in the Great Basin region to  $5.47 \text{ Mm}^{-1}$  in the Sierra Nevada region in August and  $5.49 \text{ Mm}^{-1}$  in December in the Southern Arizona region. Regions farther north experienced maximum  $b_{ext\_EC}$  in summer months (usually August), such as the Sierra Nevada, Great Basin, Colorado Plateau, and Central Rockies regions, likely due to biomass smoke influence (Figure 5.1.3). Higher monthly mean  $b_{ext\_EC}$  in the Southern Arizona region during winter months suggests additional sources; this region corresponded to the largest minimum monthly mean  $b_{ext\_EC}$  in the southwestern United States ( $1.39 \text{ Mm}^{-1}$  in May).

Monthly mean  $b_{ext\_EC}$  contributions to  $b_{ext\_aer}$  ranged from 0.003 in the Virgin Islands region in July and 0.021 in the California Coast region in June to 0.185 in the Southern Arizona region in December. Contributions were less than 0.1 in all eastern IMPROVE regions (Figure 5.1.4) and generally higher during fall and winter months. The lowest monthly mean minimum contribution in eastern regions was 0.036 in the Central Great Plains region in January. Most of the minimum monthly contributions ranged between 0.03 and 0.06, while the maximum contributions were 0.090 in the Ohio River Valley in October and 0.092 in the Northeast region in November.

Contributions of  $b_{ext\_EC}$  to  $b_{ext\_aer}$  were higher in regions in the northwestern United States (Figure 5.1.5). In the Oregon/Northern California and Hells Canyon region, monthly mean maximum contributions were ~0.13 in December and September, respectively. The Northern Rockies and Northwest regions had maximum contributions around 0.1 in September and August, respectively. Minimum monthly mean contributions were around 0.05, meaning that contributions year round were greater than 0.05 in most regions. The lowest contributions occurred in the Alaska region (0.022) in May and the Columbia River Gorge region (0.033) in June.

In the southwestern United States, the maximum monthly contribution occurred in the Southern Arizona region (0.185) in December. Other regions had contributions higher than 0.1, such as the California Coast (0.139, November), Central Rockies (0.127, January), and the Mogollon Plateau (0.123, November). Maximum contributions in remaining regions were around 0.1, mostly during winter months (Figure 5.1.6). Minimum contributions were around 0.05, with the lowest in the California Coast region in June (0.021).

## 5.4.2 CSN

CSN regional monthly mean  $b_{ext\_EC}$  values ranged from 0.58  $Mm^{-1}$  in the Hawaii region in July and 1.77  $Mm^{-1}$  in the North Dakota region in February to 20.10  $Mm^{-1}$  in the Las Vegas region in December. In the eastern United States, the minimum monthly mean  $b_{ext\_EC}$  was 2.60  $Mm^{-1}$  in the Florida region in August (Figure 5.1.7). The largest minimum  $b_{ext\_EC}$  occurred in the New York City region (6.21  $Mm^{-1}$  in April). The New York City region also had the largest maximum  $b_{ext\_EC}$  of 9.88  $Mm^{-1}$  in December. Several other regions had the maximum monthly mean  $b_{ext\_EC}$  around 9  $Mm^{-1}$  (the Dallas, Ohio River Valley, Washington D.C./Philadelphia Corridor, and Southeast regions). Maximum  $b_{ext\_EC}$  occurred during November and December for most regions, except the Central U.S. and Chicago regions (both August) and the Michigan Great Lakes region (September). The lowest maximum  $b_{ext\_EC}$  occurred in the Central U.S. region (5.32  $Mm^{-1}$ ).

The North Dakota region of the northwestern United States had the lowest maximum monthly mean  $b_{ext\_EC}$  of the region (3.79  $Mm^{-1}$  in August). Other regions had maximum  $b_{ext\_EC}$  in winter months, with the highest in the Alaska region (19.59  $Mm^{-1}$ ) in January. This seasonal pattern is different from what was observed in rural regions, where  $b_{ext\_EC}$  peaked in summer months, suggesting additional urban sources. Minimum monthly mean  $b_{ext\_EC}$  was around 1–2  $Mm^{-1}$ , except in the Puget Sound region (5.62  $Mm^{-1}$ ) in June (Figure 5.1.8).

Monthly mean values of  $b_{ext\_EC}$  in the southwestern United States were comparable to other regions and ranged from  $0.58 \text{ Mm}^{-1}$  in Hawaii in July and  $2.08 \text{ Mm}^{-1}$  in the San Diego region in May to  $20.10 \text{ Mm}^{-1}$  in the Las Vegas region in December (Figure 5.1.9). All of the regions in the southwestern United States had maximum monthly mean  $b_{ext\_EC}$  during winter months, nearly all in December. Minimum monthly mean  $b_{ext\_EC}$  values were around  $2\text{--}5 \text{ Mm}^{-1}$  and nearly all occurred in May.

Monthly mean contributions of  $b_{ext\_EC}$  to  $b_{ext\_aer}$  were higher in CSN regions compared to IMPROVE regions. The contributions ranged from 0.042 in the North Dakota region in February to 0.305 in the Las Vegas region in December. In the eastern United States, maximum contributions were around 0.13 and higher, with a maximum contribution of 0.200 in the New York City region in November (Figure 5.1.10). Maximum contributions occurred mostly in fall months (November). Minimum monthly mean contributions were greater than 0.06 for all regions, and the largest minimum contribution occurred in the New York City region (0.147) in February; the seasonal range in  $b_{ext\_EC}$  contribution in the New York City region was low.

In the northwestern United States,  $b_{ext\_EC}$  contributions ranged from 0.042 in the North Dakota region in February to nearly 0.23 in the Puget Sound and Northwest regions in January and October, respectively (Figure 5.1.11). The North Dakota region was an outlier in the northwestern United States, where contributions were generally greater than 0.1.

Maximum monthly mean  $b_{ext\_EC}$  contributions in the southwestern United States were less than 0.3, with the maximum in Las Vegas. Regions in California (e.g., Sacramento/Central Valley, San Jose, and Los Angeles) had lower maximum contributions compared to those regions farther east, such as the Northwest Nevada, Front Range CO, Albuquerque, Las Vegas, West Texas, and Phoenix/Tucson regions. The minimum contribution of 0.143 occurred in July in the West Texas region (Figure 5.1.12).

## 5.5 PM<sub>2.5</sub> FINE DUST LIGHT EXTINCTION COEFFICIENTS

The FD extinction efficiency used to compute  $b_{ext\_FD}$  in the IMPROVE algorithm is  $1 \text{ m}^2 \text{ g}^{-1}$ . The dust extinction efficiency is lower than for most other species, and dust is nonhygroscopic; therefore the seasonal and spatial patterns in  $b_{ext\_FD}$  were similar to FD mass concentrations. However, the magnitude of  $b_{ext\_FD}$  may change relative to other species, as well as its relative contribution to  $b_{ext\_aer}$ .

### 5.5.1 IMPROVE

The IMPROVE 2016–2019 regional monthly mean  $b_{ext\_FD}$  ranged from  $0.034 \text{ Mm}^{-1}$  in the Northwest region in December to  $4.01 \text{ Mm}^{-1}$  in the Virgin Islands region in August and  $2.70 \text{ Mm}^{-1}$  in the Southern Arizona region in April and  $2.72 \text{ Mm}^{-1}$  in the Columbia River Gorge region in July. In the eastern United States, long-distance transport of dust from North Africa in summer is well documented and is the likely reason for high dust concentrations and consequent light extinction in summer in the Virgin Islands region (Figure 5.1.1). Monthly mean  $b_{ext\_FD}$  in the eastern United States ranged from  $0.087 \text{ Mm}^{-1}$  in the Boundary Waters region in January to  $2.38 \text{ Mm}^{-1}$  and  $2.46 \text{ Mm}^{-1}$  in the CONUS regions of the Midsouth and Southeast, respectively,

both in July. Nearly all eastern regions had maximum monthly mean  $b_{ext\_FD}$  during July, with the exception of the Boundary Waters and Northeast regions (May).

Monthly mean values of  $b_{ext\_FD}$  in northwestern U.S. regions were low; with the exception of the high value in the Columbia River Gorge region, maximum monthly  $b_{ext\_FD}$  was less than  $1\text{--}2 \text{ Mm}^{-1}$  in all other regions (Figure 5.1.2). The Northwest and Alaska regions had the lowest values year round ( $<0.3 \text{ Mm}^{-1}$ ). Maximum monthly mean values occurred in July and August, except for the Alaska region (April). Minimum values occurred in January and December, except for Alaska (September).

The highest maximum monthly mean  $b_{ext\_FD}$  in the southwestern United States occurred in regions farther south that are known to be influenced by dust, such as the Southern Arizona region ( $2.70 \text{ Mm}^{-1}$ ) and the West Texas region ( $2.66 \text{ Mm}^{-1}$ ), both in April. Other regions had maximum  $b_{ext\_FD}$  ranging from 1 to  $2 \text{ Mm}^{-1}$ , although during different months. The Central Rockies and Colorado Plateau regions experienced their highest monthly mean  $b_{ext\_FD}$  during June, while the maximum in the California Coast and Sierra Nevada regions occurred in October. The maximum  $b_{ext\_FD}$  in the Southern California region occurred in July (Figure 5.1.3).

Contributions of  $b_{ext\_FD}$  to  $b_{ext\_aer}$  ranged from 0.003 in the Hawaii region in September and the Columbia River Gorge region in January to 0.131 in the Southern Arizona region in April. Maximum monthly mean contributions  $b_{ext\_FD}$  to  $b_{ext\_aer}$  in the eastern United States were negligible, less than 0.03 in most regions, except the Midsouth (0.060) and the Southeast (0.060) regions, both in July (Figure 5.1.4), likely due to long-range transport of North African dust.

In the northwestern United States, contributions of monthly mean  $b_{ext\_FD}$  to  $b_{ext\_aer}$  ranged from a minimum of 0.003 (January) to 0.080 (July), both in the Columbia River Gorge region (Figure 5.1.5). The lowest maximum contribution occurred in the Alaska region (0.019) in April. Maxima in other regions in the northwestern United States were around 0.02–0.05, nearly all in April.

Monthly mean contributions of  $b_{ext\_FD}$  to  $b_{ext\_aer}$  in the southwestern United States ranged from 0.003 in the Hawaii region in September and 0.006 in the California Coast region in January to 0.130 in the Southern Arizona and West Texas regions in April (Figure 5.1.6). Other regions had maximum contributions in April of ~0.1. Southern California and the California Coast regions both experienced maximum contributions during fall months (0.02–0.05).

## 5.5.2 CSN

The CSN maximum monthly mean  $b_{ext\_FD}$  value of  $4.75 \text{ Mm}^{-1}$  occurred in the Dallas region in July, compared to the lowest value of  $0.09 \text{ Mm}^{-1}$  in the Hawaii region in September and  $0.15 \text{ Mm}^{-1}$  in the North Dakota region in January. In regions in the eastern United States,  $b_{ext\_FD}$  was negligible (Figure 5.1.7), except in regions farther south that have influence from transport of North African dust. For example, in addition to the Dallas region, the East Texas/Gulf ( $4.04 \text{ Mm}^{-1}$ ), Florida ( $2.39 \text{ Mm}^{-1}$ ), Midsouth ( $2.83 \text{ Mm}^{-1}$ ), and Southeast ( $1.23 \text{ Mm}^{-1}$ ) regions all had maximum  $b_{ext\_FD}$  during July. The Michigan/Great Lakes and Central U.S. regions also had maximum  $b_{ext\_FD}$  of ~ $1 \text{ Mm}^{-1}$  in summer months.

Regions in the northwestern United States experienced very low monthly mean  $b_{ext\_FD}$ , and the highest maximum occurred in the North Dakota region ( $1.06 \text{ Mm}^{-1}$ ) in June and  $1.01 \text{ Mm}^{-1}$  in the Northwest region in August. In other regions, the maximum monthly mean  $b_{ext\_FD}$  was less than  $1 \text{ Mm}^{-1}$  and not visible on the bar charts in Figure 5.1.8. Minimum monthly mean  $b_{ext\_FD}$  was  $\sim 0.1\text{--}0.3 \text{ Mm}^{-1}$  for all regions in the northwestern United States.

The relative values of  $b_{ext}$  for all species in the southwestern United States demonstrated that while a species may contribute significantly to RCFM, it may not contribute as significantly to  $b_{ext}$  because it is not as efficient at scattering light as other species. The effects of the larger extinction efficiency for EC compared to that for FD were obvious in magnitudes of speciated  $b_{ext}$  in Figure 5.1.9. For most regions, the  $b_{ext\_FD}$  values were much lower than  $b_{ext\_EC}$ . The range in monthly mean  $b_{ext\_FD}$  in the southwestern United States was  $0.09 \text{ Mm}^{-1}$  in Hawaii in September and  $0.31 \text{ Mm}^{-1}$  in the San Jose region in May to  $3.34 \text{ Mm}^{-1}$  in the West Texas region in April. The Sacramento/Central Valley and Las Vegas regions also had higher  $b_{ext\_FD}$  ( $2.23 \text{ Mm}^{-1}$ ) in October. Over half of the southwestern regions experienced their maximum  $b_{ext\_FD}$  during October and November, while the Front Range CO ( $1.51 \text{ Mm}^{-1}$ ), Albuquerque ( $1.13 \text{ Mm}^{-1}$ ), and Utah ( $1.62 \text{ Mm}^{-1}$ ) regions had maximums in June.

The highest CSN monthly mean contribution of  $b_{ext\_FD}$  to  $b_{ext\_aer}$  occurred in the Las Vegas region (0.213) in October. Several CONUS regions had minimum contributions of  $\sim 0.003$  (Portland, Northwest, and Sacramento/Central Valley). In the eastern United States, the maximum  $b_{ext\_FD}$  contribution occurred in the Dallas region (0.100) in July. Similar to  $b_{ext\_FD}$ , regions with the highest maximum  $b_{ext\_FD}$  contributions ( $\sim 0.05$ ) occurred in regions influenced by North African dust transport (e.g., East Texas/Gulf, Midsouth, and Florida regions) in July (Figure 5.1.10).

Contributions of  $b_{ext\_FD}$  to  $b_{ext\_aer}$  were insignificant in regions in the northwestern United States (Figure 5.1.11). Monthly mean maximum contributions were less than 0.04 in all regions. These occurred in April in the Puget Sound and Portland regions and in June in the Northwest and North Dakota regions.

The lowest minimum monthly mean  $b_{ext\_FD}$  contribution in the southwestern United States occurred in the Sacramento/Central Valley region (0.003) in January, compared to the maximum of 0.213 in the Las Vegas region in October and the West Texas (0.137) region in May. Other regions in California had low maximum contributions ( $< 0.03$ ), while regions farther south were closer to 0.05–0.07 (e.g., Albuquerque and Phoenix/Tucson) during spring months (Figure 5.12). Of all the urban regions, those in the southwestern United States corresponded to the highest contributions of  $b_{ext\_FD}$  to  $b_{ext\_aer}$ .

## 5.6 PM<sub>2.5</sub> SEA SALT LIGHT EXTINCTION COEFFICIENTS

SS was treated as a hygroscopic species in the algorithm for computing the reconstructed light extinction coefficient for sea salt ( $b_{ext\_SS}$ ). While SS mass concentrations were relatively low, except in coastal regions, values of  $b_{ext\_SS}$  were significant in some regions due to hygroscopic effects.

## 5.6.1 IMPROVE

IMPROVE 2016–2019 regional monthly mean  $b_{ext\_SS}$  ranged from  $0.032 \text{ Mm}^{-1}$  in the Central Rockies region in November to  $8.81 \text{ Mm}^{-1}$  in the California Coast region in June and  $11.09 \text{ Mm}^{-1}$  in July in the Virgin Islands region. Monthly mean  $b_{ext\_SS}$  was significant year round in the Virgin Islands region, with estimates over  $6 \text{ Mm}^{-1}$  (Figure 5.1.1), and the maximum monthly mean  $b_{ext\_SS}$  was higher than  $b_{ext\_FD}$  by nearly a factor of 3 due to hygroscopic effects of SS, as well as a higher SS dry extinction efficiency. In the eastern United States,  $b_{ext\_SS}$  was significantly lower than  $b_{ext}$  from other species in most regions ( $<5 \text{ Mm}^{-1}$ ) and was barely visible on the bar charts associated with the East Coast, Southeast, and Northeast regions. Maximum monthly mean  $b_{ext\_SS}$  values in these regions were  $3.93 \text{ Mm}^{-1}$  (March),  $4.67 \text{ Mm}^{-1}$  (February), and  $2.35 \text{ Mm}^{-1}$  (March), respectively.

The Alaska region in the northwestern United States had the highest maximum monthly mean  $b_{ext\_SS}$  in that area ( $5.76 \text{ Mm}^{-1}$ ) in February and had monthly mean  $b_{ext\_SS}$  over  $2 \text{ Mm}^{-1}$  year round. The Northwest, Oregon/Northern California, and Columbia River Gorge regions had maximum monthly mean  $b_{ext\_SS}$  around  $2 \text{ Mm}^{-1}$  or less (Figure 5.1.2). The maximum  $b_{ext\_SS}$  occurred in December for the Northern Rockies, Hells Canyon, and Columbia River Gorge regions.

In the southwestern United States, the California Coast region had the highest maximum monthly mean  $b_{ext\_SS}$  ( $8.81 \text{ Mm}^{-1}$ ) that peaked in June, and monthly mean  $b_{ext\_SS}$  was higher than  $2 \text{ Mm}^{-1}$  year round (Figure 5.1.3). The Hawaii region also had non-negligible  $b_{ext\_SS}$ , with monthly mean values that ranged from  $1.23 \text{ Mm}^{-1}$  (October) to  $1.83 \text{ Mm}^{-1}$  (April), with low seasonal variability. Other regions in the southwestern United States had maximum monthly mean  $b_{ext\_SS}$  less than  $1 \text{ Mm}^{-1}$ .

The fractional contribution of  $b_{ext\_SS}$  to  $b_{ext\_aer}$  ranged from 0.0013 in the Hells Canyon region in August to 0.440 in the Alaska region in December. The highest monthly mean contributions occurred outside of CONUS regions: Virgin Islands (0.358, March) and Hawaii (0.197, December). Coastal regions in the eastern United States also corresponded to higher maximum monthly mean contributions, such as the East Coast (0.126) in October, Northeast (0.129) in March, and the Southeast (0.119) in February. Contributions in noncoastal regions in the eastern United States were less than 0.05 (Figure 5.1.4).

Contributions of  $b_{ext\_SS}$  to  $b_{ext\_aer}$  in the northwestern United States were also highest at coastal regions, such as the Northwest (0.129) in January, Oregon/Northern California (0.153) in January, and Columbia River Gorge (0.054) in April. In the other regions, the contributions were 0.03 or less year round (Figure 5.1.5).

Similar to other areas, the southwestern United States had the only significant contributions of  $b_{ext\_SS}$  in coastal regions, such as the California Coast and Hawaii regions. The maximum monthly mean  $b_{ext\_SS}$  at other regions occurred in the Southern California region (0.055) in January; other regions had contributions of 0.03 or less (Figure 5.1.6).

## 5.6.2 CSN

The range in  $b_{ext\_SS}$  in CSN regions was similar to the range for IMPROVE regions, with the lowest in Albuquerque in September ( $0.012 \text{ Mm}^{-1}$ ) and the highest regional mean in the Florida region ( $4.30 \text{ Mm}^{-1}$ ) in February. In the eastern United States, maximum monthly mean  $b_{ext\_SS}$  was less than  $1 \text{ Mm}^{-1}$  in all regions except the Florida region ( $4.30 \text{ Mm}^{-1}$ , February) and the East Texas/Gulf region ( $2.50 \text{ Mm}^{-1}$ ) in June (Figure 5.1.7).

Only two regions in the northwestern United States had maximum monthly mean  $b_{ext\_SS}$  over  $1 \text{ Mm}^{-1}$ . The Puget Sound ( $1.32 \text{ Mm}^{-1}$ ) and Portland ( $1.08 \text{ Mm}^{-1}$ ) regions had the highest  $b_{ext\_SS}$  during December. The monthly mean  $b_{ext\_SS}$  values are not visible in the bar charts for the other regions (Figure 5.1.8).

Similar magnitudes of  $b_{ext\_SS}$  occurred in the southwestern United States (Figure 5.1.9), with maximum monthly mean values less than  $1 \text{ Mm}^{-1}$ , except in the San Jose ( $3.50 \text{ Mm}^{-1}$ ) and San Diego regions ( $1.24 \text{ Mm}^{-1}$ ), both in April, and the Utah region in December ( $1.29 \text{ Mm}^{-1}$ ).

Monthly mean contributions of  $b_{ext\_SS}$  to  $b_{ext\_aer}$  ranged from zero in the North Dakota region in April to 0.086 in the San Jose region in April. In the eastern United States the only regions with non-negligible contributions were the Florida region in February (0.104) and the East Texas/Gulf region in June (0.04). All other regions had maximum contributions of 0.01 or less (Figure 5.1.10).

The maximum  $b_{ext\_SS}$  contribution in the northwestern United States was around 0.02 in the Puget Sound region in December and the Portland region in June. The North Dakota and Northwest regions had maximum mean contributions of 0.002 and 0.005, respectively (Figure 5.1.11).

In the southwestern United States, maximum monthly mean  $b_{ext\_SS}$  values were ~0.1 or less. The highest occurred in the San Jose region in April (0.086). Other regions had maxima of 0.01 or less (Figure 5.1.12) and were not visible on the regional bar charts.

## 5.7 COARSE MASS LIGHT EXTINCTION COEFFICIENTS

CM concentrations are estimated routinely by the IMPROVE network and were interpolated to CSN sites from EPA FRM data in order to calculate  $b_{ext\_CM}$ ,  $b_{ext\_aer}$ ,  $b_{ext\_tot}$ , and  $dv$  at CSN sites (see Chapter 2). Therefore, estimates of light extinction coefficients from CM ( $b_{ext\_CM}$ ) for the CSN have additional uncertainty. The extinction efficiency for CM is  $0.6 \text{ m}^2 \text{ g}^{-1}$ , and since CM is considered to be nonhygroscopic,  $b_{ext\_CM}$  is scaled to CM concentrations (see section 4.1). The seasonality of  $b_{ext\_CM}$  often follows  $b_{ext\_FD}$ , especially if they have similar sources; differences in seasonality may indicate different sources or perhaps a non-mineral-dust-related composition of CM.

### 5.7.1 IMPROVE

Values of regional monthly mean  $b_{ext\_CM}$  ranged from  $0.28 \text{ Mm}^{-1}$  in the Northwest and Northern Rockies regions in December and January, respectively, to  $17.03 \text{ Mm}^{-1}$  in the Columbia

River Gorge in June. In the eastern United States, the regional monthly mean  $b_{ext\_CM}$  ranged from  $0.61 \text{ Mm}^{-1}$  in the Boundary Waters region in January to  $11.25 \text{ Mm}^{-1}$  in the Virgin Islands region in July and  $5.94 \text{ Mm}^{-1}$  and  $6.00 \text{ Mm}^{-1}$  in the Central Great Plains and East Coast regions, respectively, in June (Figure 5.1.1). The high  $b_{ext\_CM}$  in the Virgin Islands region was similar in magnitude to  $b_{ext\_SS}$  during that same month, suggesting that the  $b_{ext\_CM}$  was most likely related to SS and perhaps dust, as it increased during similar months. Maximum monthly mean values around  $4\text{--}5 \text{ Mm}^{-1}$  occurred during July in regions farther south that were influenced by North African dust transport in summer (Midsouth and Southeast regions). The lowest maximum monthly mean  $b_{ext\_CM}$  of  $\sim 3 \text{ Mm}^{-1}$  occurred in the Boundary Waters (June), Appalachia (May), and Northeast (September) regions. Minimum monthly mean  $b_{ext\_CM}$  values were around  $1\text{--}2 \text{ Mm}^{-1}$  in most regions, with the highest minimum  $b_{ext\_CM}$  in the Virgin Islands region ( $4.72 \text{ Mm}^{-1}$ ) in November. Only the Midsouth and Southeast regions had similar months with monthly mean maximum  $b_{ext\_CM}$  and  $b_{ext\_FD}$  (July).

Minimum monthly mean  $b_{ext\_CM}$  values in the northwestern United States were lower than minimum values in the eastern United States, with several regions having minimum monthly mean values around  $0.2\text{--}0.5 \text{ Mm}^{-1}$ , all in winter months (Figure 5.1.2). In addition to the high value in the Columbia River Gorge region, other maximum values were around  $4\text{--}5 \text{ Mm}^{-1}$  during summer months, roughly a third of that of the Columbia River Gorge region. About half of the regions had  $b_{ext\_CM}$  maxima during the same months as  $b_{ext\_FD}$  maxima, except for Alaska (April maximum for  $b_{ext\_FD}$ , June maximum for  $b_{ext\_CM}$ ) and Columbia River Gorge (July for  $b_{ext\_FD}$ , June for  $b_{ext\_CM}$ ) and Northern Rockies (August for  $b_{ext\_FD}$ , July for  $b_{ext\_CM}$ ). Other regions had maxima  $b_{ext\_CM}$  during August.

Minimum monthly mean  $b_{ext\_CM}$  occurred during winter months for all regions in the southwestern United States, except the Southern Arizona region ( $5.13 \text{ Mm}^{-1}$  in August; Figure 5.1.3). Other minimum monthly mean values ranged from  $0.5$  to  $3.0 \text{ Mm}^{-1}$ . Maximum monthly mean  $b_{ext\_CM}$  values ranged from  $7$  to  $8 \text{ Mm}^{-1}$  in the Sierra Nevada (August), Southern Arizona (November), Southern California (July), and West Texas (April) regions. Maxima in other regions were around  $2\text{--}4 \text{ Mm}^{-1}$  and occurred during summer months. Half of the regions had similar months for maximum  $b_{ext\_CM}$  and  $b_{ext\_FD}$  (Central Rockies, Colorado Plateau, Great Basin, Southern California, and West Texas).

Both the minimum (0.018) and maximum (0.506) monthly mean contributions of  $b_{ext\_CM}$  to  $b_{ext\_aer}$  occurred in the Columbia River Gorge region in December and June, respectively. In the eastern United States, minimum mean contributions of  $b_{ext\_CM}$  were around  $0.02\text{--}0.05$ , with the highest minimum of 0.20 in the Virgin Islands region (Figure 5.1.4). Contributions were lowest during winter months for all regions, except the Southeast region (April) and the Virgin Islands region (November). The largest maximum monthly mean  $b_{ext\_CM}$  contribution also occurred in the Virgin Islands region (0.30), but in other regions contributions were around  $0.1\text{--}0.2$ , with the Central Great Plains region having contributions of 0.212 in October, perhaps associated with agricultural harvesting. Other contributions were highest during spring and fall months.

In the northwestern United States, contributions from  $b_{ext\_CM}$  were the highest in the Columbia River Gorge region (0.506 in June), the Northern Great Plains (0.233 also in June),

and the Alaska region (0.225) in May (Figure 5.1.5). Other regions had maximum contributions around 0.13–0.18, all in June. Minimum monthly mean contributions ranged from 0.029 (Northwest region in August) to 0.101 (Alaska region in August). Minimum contributions occurred during summer months in the Northwest, Oregon/Northern California, and Alaska regions, perhaps due to the strong contributions from  $b_{ext\_POM}$  during summer months. Other regions experienced minimum contributions from  $b_{ext\_CM}$  during winter months.

The lowest monthly mean  $b_{ext\_CM}$  contributions in the southwestern United States were around 0.09 in the California Coast (January), Central Rockies (August), and Colorado Plateau (January) regions. The lowest contribution in the Hawaii region occurred in March (0.026). Maximum monthly mean contributions ranged from 0.175 in the Central Rockies region in October to 0.372 in the Southern Arizona region in May. Most of the regions had contributions around 0.2 or higher, such as the West Texas region (0.342 in April). For many regions in the southwestern United States,  $b_{ext\_CM}$  was one of the top third contributors, along with  $b_{ext\_AS}$  and  $b_{ext\_POM}$  (Figure 5.1.6).

## 5.7.2 CSN

The monthly mean  $b_{ext\_CM}$  interpolated to CSN sites ranged from  $0.46 \text{ Mm}^{-1}$  in the Northwest region in December to  $18.70 \text{ Mm}^{-1}$  in the Sacramento/Central Valley region in October. In the eastern United States, minimum monthly mean  $b_{ext\_CM}$  values were around  $2\text{--}3 \text{ Mm}^{-1}$ , with the highest minimums in the Dallas ( $4.33 \text{ Mm}^{-1}$  in June) and East Texas/Gulf ( $4.31 \text{ Mm}^{-1}$  in December) regions (Figure 5.1.7). Most of the eastern regions had minimum monthly mean  $b_{ext\_CM}$  during December or January. The maximum monthly mean  $b_{ext\_CM}$  occurred in the East Texas/Gulf ( $11.45 \text{ Mm}^{-1}$ , July) and Dallas regions ( $10.11 \text{ Mm}^{-1}$  in August), suggesting a large seasonality in those regions. Other maxima ranged from 4 to  $5 \text{ Mm}^{-1}$ . Values from 6 to  $7 \text{ Mm}^{-1}$  occurred in the Midsouth (July), Central United States (June), and Chicago (May) regions. Only the Midsouth, East Texas/Gulf, and Florida regions experienced maxima for both in  $b_{ext\_FD}$  and  $b_{ext\_CM}$  in July, as well as the Washington D.C./Philadelphia Corridor region in June.

In the northwestern United States, monthly mean  $b_{ext\_CM}$  minima were around  $1\text{--}2 \text{ Mm}^{-1}$ , with the lowest in the Northwest region and the highest minimum in the North Dakota region ( $1.78 \text{ Mm}^{-1}$ , January, Figure 5.1.8). Monthly mean maximum  $b_{ext\_CM}$  were around  $3\text{--}4 \text{ Mm}^{-1}$  in most regions, except in the North Dakota region ( $9.09 \text{ Mm}^{-1}$ ) in June, perhaps related to agricultural activity. Other regions had maximum  $b_{ext\_CM}$  during August. This is the same month that  $b_{ext\_FD}$  was highest in those regions.

The Sacramento/Central Valley region in the southwestern United States had the highest maximum monthly mean  $b_{ext\_CM}$  in that region ( $18.70 \text{ Mm}^{-1}$ ) in October (Figure 5.1.9), also likely related to agricultural activity. Most of the regions in California had maxima in October, and maximum values ranged from 8 to  $15 \text{ Mm}^{-1}$ . The Phoenix/Tucson region had a maximum monthly mean  $b_{ext\_CM}$  ( $10.62 \text{ Mm}^{-1}$ ) in November, while the maximum monthly mean  $b_{ext\_CM}$  in Albuquerque region was only  $3.47 \text{ Mm}^{-1}$ . The Sacramento/Central Valley, Los Angeles, Albuquerque, and West Texas regions all had similar months with monthly mean maximum  $b_{ext\_FD}$  and  $b_{ext\_CM}$ .

In CSN regions, the monthly mean  $b_{ext\_CM}$  contributions to  $b_{ext\_aer}$  ranged between 0.007 (Northwest region, December) to 0.376 (Phoenix/Tucson region, May). In regions in the eastern United States,  $b_{ext\_CM}$  contributed from 0.029 (Washington D.C./Philadelphia Corridor region in December) to 0.203 (Dallas region) in April (Figure 5.1.10). Most of the monthly mean maxima were around 0.1–0.2 across eastern regions, and most occurred in late spring to summer months.

The maximum monthly mean  $b_{ext\_CM}$  contributions in the northwestern United States were similar in magnitude (0.1–0.2), with the largest in the North Dakota region. Other maxima also occurred in June and July (Figure 5.1.11). Lower contributions occurred during winter months, around 0.01–0.05. With the exception of the North Dakota region, contributions of  $b_{ext\_CM}$  were generally similar to or less than contributions from  $b_{ext\_EC}$ .

Higher contributions of  $b_{ext\_CM}$  to  $b_{ext\_aer}$  were observed in the southwestern United States (Figure 5.1.12). Maximum contributions ranged from 0.158 in the San Jose region in June to 0.376 in the Phoenix/Tucson region in May and 0.356 in the Las Vegas in October. Otherwise, contributions were 0.2–0.3 in most regions. The lowest contributions (~0.02) occurred in the Albuquerque and Utah regions in January, with larger contributions from other species such as  $b_{ext\_AN}$  and  $b_{ext\_POM}$ .

## 5.8 RECONSTRUCTED AEROSOL LIGHT EXTINCTION COEFFICIENTS

The reconstructed aerosol light extinction coefficient ( $b_{ext\_aer}$ ), as defined earlier, is the sum of light extinction coefficients from the previous components discussed above, namely, AS, AN, POM, EC, FD, SS, and CM. Rayleigh scattering is not included but would add roughly 10–12  $Mm^{-1}$  to  $b_{ext\_aer}$ , depending on the site.

### 5.8.1 IMPROVE

The 2016–2019 regional monthly mean IMPROVE  $b_{ext\_aer}$  ranged from 3.61  $Mm^{-1}$  in the Great Basin region in January to 69.48  $Mm^{-1}$  in Columbia River Gorge region in January, where  $b_{ext\_AN}$  was the major contributor (0.671).

Maximum  $b_{ext\_aer}$  occurred in both summer and winter months, depending on region (Figure 5.1.1). In the Boundary Waters, Central Great Plains, and Ohio River Valley regions, the maximum monthly mean  $b_{ext\_aer}$  occurred in December (30–50  $Mm^{-1}$ ) and was associated mainly with the contributions from  $b_{ext\_AN}$ , followed by  $b_{ext\_AS}$ . These regions also had a peak in  $b_{ext\_aer}$  in summer months, due to  $b_{ext\_POM}$  and  $b_{ext\_AS}$ . In other eastern regions, such as the East Coast, Northeast, and Appalachia regions, the maximum  $b_{ext\_aer}$  occurred during summer months (~30–40  $Mm^{-1}$ ) and was associated with  $b_{ext\_AS}$  and  $b_{ext\_POM}$ . The maximum  $b_{ext\_aer}$  in the Southeast region (66.21  $Mm^{-1}$ ) occurred in April and was associated with elevated  $b_{ext\_POM}$  due to biomass smoke. The maximum  $b_{ext\_aer}$  in the Virgin Islands region (38.71  $Mm^{-1}$ ) occurred in June, with  $b_{ext\_AS}$ ,  $b_{ext\_CM}$ , and  $b_{ext\_SS}$  as the major contributors. The lowest minimum monthly mean  $b_{ext\_aer}$  in the eastern United States occurred in the Boundary Waters region in October (11.88  $Mm^{-1}$ ). Many regions experienced the lowest  $b_{ext\_aer}$  in October (~20–30  $Mm^{-1}$ ).

The maximum monthly mean  $b_{ext\_aer}$  occurred during summer months for all regions in the northwestern United States except the Columbia River Gorge region (January), where the highest monthly mean  $b_{ext\_aer}$  in the region occurred due to the contributions of  $b_{ext\_AN}$ . The Oregon/Northern California and Northwest regions also had elevated  $b_{ext\_aer}$  ( $67.85 \text{ Mm}^{-1}$  and  $63.55 \text{ Mm}^{-1}$ , respectively) in August due to  $b_{ext\_POM}$  from biomass smoke (Figure 5.1.2). The lowest monthly mean maximum  $b_{ext\_aer}$  occurred in the Alaska ( $26.24 \text{ Mm}^{-1}$ ) and Northern Great Plains regions ( $37.83 \text{ Mm}^{-1}$ ). Minimum monthly mean  $b_{ext\_aer}$  ranged from  $\sim 6 \text{ Mm}^{-1}$  (Northern Rockies and Hells Canyon regions in March) to  $24.49 \text{ Mm}^{-1}$  (Columbia River Gorge region in April).

In the southwestern United States, monthly mean  $b_{ext\_aer}$  ranged from  $3.62 \text{ Mm}^{-1}$  in the Great Basin region in January to  $62.23 \text{ Mm}^{-1}$  in the Sierra Nevada region in August. Maximum  $b_{ext\_aer}$  occurred in summer months for most of the regions, except for the Southern Arizona region ( $29.65 \text{ Mm}^{-1}$ ) in December, due to  $b_{ext\_POM}$ ,  $b_{ext\_EC}$  and  $b_{ext\_CM}$  (Figure 5.1.3). For regions farther north, the role of  $b_{ext\_POM}$  in the summer maxima, along with elevated  $b_{ext\_POM}$ , indicated the impacts of biomass smoke on  $b_{ext\_aer}$  in these regions. Farther south, such as in the West Texas region, additional contributions from  $b_{ext\_AS}$  and  $b_{ext\_CM}$  led to higher summer maxima ( $26.97 \text{ Mm}^{-1}$ ). Regions in California, such as the California Coast ( $38.30 \text{ Mm}^{-1}$ ) and Southern California ( $40.71 \text{ Mm}^{-1}$ ) regions also had significant contributions of  $b_{ext\_AS}$ .

## 5.8.2 CSN

The urban CSN regional monthly mean  $b_{ext\_aer}$  ranged from  $15.40 \text{ Mm}^{-1}$  in the Albuquerque region in April to  $153.69 \text{ Mm}^{-1}$  in the Sacramento/Central Valley region in December, when  $b_{ext\_AN}$  was the highest contributor. Most urban regional maxima occurred in winter months, along with peaks in  $b_{ext\_AN}$  and  $b_{ext\_POM}$ . In the eastern United States, maximum monthly mean  $b_{ext\_aer}$  occurred during winter months, and most of that was dominated by  $b_{ext\_AN}$  (Figure 5.1.7). Maxima occurred during summer monthly only in the Midsouth and Florida regions (July). In most eastern regions, smaller peaks in  $b_{ext\_aer}$  also occurred during summer months, such as in the Northeast region. The highest monthly mean maximum  $b_{ext\_aer}$  occurred in the Michigan/Great Lakes region in December ( $78.57 \text{ Mm}^{-1}$ ), but values greater than  $70 \text{ Mm}^{-1}$  also occurred in the Chicago and Ohio River Valley regions. Maxima in other regions were around  $50\text{--}65 \text{ Mm}^{-1}$ , with the lowest maximum in the Florida region ( $41.10 \text{ Mm}^{-1}$ ).

Regional monthly mean  $b_{ext\_aer}$  in the northwestern United States ranged from  $17.02 \text{ Mm}^{-1}$  to  $77.30 \text{ Mm}^{-1}$  in the Northwest region in April and January, respectively (Figure 5.1.8). Other minima were around  $20\text{--}30 \text{ Mm}^{-1}$ . Maximum monthly mean  $b_{ext\_aer}$  occurred during winter months in all regions except for the North Dakota region in March. Contributions from  $b_{ext\_AN}$  and  $b_{ext\_POM}$  led to high  $b_{ext\_aer}$  during winter.

For nearly all regions in the southwestern United States, monthly mean  $b_{ext\_aer}$  was highest during winter months, with the highest value in the Sacramento/Central Valley region (Figure 5.1.9). Other regions with maxima over  $100 \text{ Mm}^{-1}$  included the San Jose region ( $101.43 \text{ Mm}^{-1}$ ) and the Utah region ( $111.29 \text{ Mm}^{-1}$ ). For most winter maxima in  $b_{ext\_aer}$ ,  $b_{ext\_AN}$  was the major contributor, followed by  $b_{ext\_POM}$  in most regions. Farther south, contributions from  $b_{ext\_POM}$  were higher than  $b_{ext\_AN}$ . The only exception to winter maxima occurred in the Los

Angeles region in June ( $90.27 \text{ Mm}^{-1}$ ), where  $b_{\text{ext\_AN}}$ ,  $b_{\text{ext\_POM}}$ , and  $b_{\text{ext\_AS}}$  were all major contributors. The lowest maximum ( $37.77 \text{ Mm}^{-1}$ ) occurred in the Albuquerque region. Regional monthly mean maximum  $b_{\text{ext\_aer}}$  was higher in the southwestern United States area relative to the eastern and northwestern United States, largely due to the role of  $b_{\text{ext\_AN}}$  and  $b_{\text{ext\_POM}}$  during winter.

## 5.9 DECIVIEW

Estimates of deciview (dv) include the site-specific Rayleigh scattering coefficient, and therefore the regions corresponding to maximum and minimum dv may differ from  $b_{\text{ext\_aer}}$  described in the previous section.

### 5.9.1 IMPROVE

Regional monthly mean dv across the network ranged from 2.39 dv in the Central Rockies to 20.98 dv in the Columbia River Gorge region, both in January. In the eastern United States, the monthly mean dv ranged from 8.51 dv in the Boundary Waters region in October to 18.31 dv in the Southeast region in April and 18.16 dv in the Ohio River Valley in December. The high value in the Southeast was likely due to biomass smoke influence. Maxima in summer months occurred in the East Coast (16.55 dv), Appalachia (15.75 dv), and Northeast (14.14 dv) regions.

In the northwestern United States, monthly mean dv ranged from 3.94 dv in the Northern Rockies in January to 20.98 in the Columbia River Gorge, also in January. All other regions in the area had summer maxima in dv, with values ranging from 15 dv to 20 dv. Recall from the previous section that  $b_{\text{ext\_AN}}$  was the major contributor to  $b_{\text{ext\_aer}}$  during winter in the Columbia River Gorge region.

The highest maximum regional monthly mean dv in the southwestern United States occurred in the Sierra Nevada region (19.18 dv) and the lowest maximum in the Colorado Plateau region (9.71 dv), both in August. The minimum monthly mean dv ranged between 2.39 dv in the Central Rockies region in January to 10.76 dv in the California Coast region in February.

### 5.9.2 CSN

CSN regional monthly mean dv ranged from 9.32 dv in the Albuquerque region in April to 27.80 dv in the Sacramento/Central Valley region in December. The highest maximum monthly mean dv in the eastern United States occurred in the Michigan/Great Lakes region in December. Most of the maxima in the eastern United States occurred during winter months, around 18–20 dv. Summer maxima occurred in the Midsouth and Florida regions (16–18 dv). The lowest maxima occurred in the Florida region (16.50 dv). The lowest minimum monthly mean dv occurred in the Northeast region in April (13.51 dv).

Maximum regional monthly mean dv occurred during winter months in the northwestern United States, with values around 20 (20.92 dv in the Portland region in December and 20.75 dv in the Northwest region in January), except in the North Dakota region (17.73 dv) in March.

Minimum values in the northwestern United States were near 10–14 dv, with the lowest minimum monthly mean dv in the Northwest region (10.04 dv) compared to the highest minimum in the Puget Sound region (14.27 dv), both in April.

In the southwestern United States, monthly mean dv ranged from 9.79 dv (Northwest Nevada in April) to the highest in the Sacramento/Central Valley region. Most of the maximum monthly mean dv occurred during December and January (~15–30 dv) except in the Los Angeles region (23.15 dv, June). The lowest monthly mean maximum values occurred in farther south, such as the Albuquerque (15.64 dv) and West Texas (16.57 dv) regions.

## 5.10 SUMMARY

The seasonal patterns in  $b_{ext}$  corresponding to major aerosol species were similar to the seasonal distributions in mass concentrations presented in the Chapter 3. This similarity was expected for most species because mass concentrations were converted to  $b_{ext}$ , with mass extinction efficiencies that essentially just scaled the values to  $b_{ext}$ . However, for AS, AN, and SS, the conversion to  $b_{ext}$  accounted for relative humidity effects and hygroscopic growth that can be considerable in environments with high relative humidity. No significant differences were observed between the seasonal distributions in mass compared to  $b_{ext}$ . Occasionally, the season that corresponded to the majority of the maximum and minimum regional absolute  $b_{ext}$  or relative  $b_{ext}$  changed for many of the species examined here. In addition, some species that were important for their contributions to RCFM were less important in reconstructed  $b_{ext\_aer}$  (e.g., FD), while others became more important (e.g., EC, POM, and hygroscopic species). Differences in urban and rural  $b_{ext\_aer}$  were evident, especially in seasonal patterns. Many of the urban regions had maximum  $b_{ext\_aer}$  during winter, due to the role of  $b_{ext\_AN}$  and  $b_{ext\_POM}$ , whereas many rural areas across the United States experienced maximum  $b_{ext\_aer}$  during summer months, due to the role of  $b_{ext\_POM}$  and  $b_{ext\_AS}$ . The contributions of  $b_{ext\_CM}$  were important in both urban and rural regions in the southwestern United States.

In both urban and rural regions, monthly mean  $b_{ext\_AS}$  was higher in the eastern United States, with average maximum values that ranged from 16 to 18  $Mm^{-1}$ . The seasonal range was mostly flat, although with a small increase during summer months for both networks. The similarity in magnitude of  $b_{ext\_AS}$  suggested regional impacts of  $b_{ext\_AS}$  on visibility in both urban and rural regions. Average maximum monthly mean values of  $b_{ext\_AS}$  were similar for both the northwestern and southwestern United States regions, with somewhat higher values for CSN regions (9  $Mm^{-1}$  compared to 6  $Mm^{-1}$ ). Maximum values occurred mostly during summer months except in the CSN Alaska region, where maximum  $b_{ext\_AS}$  occurred during winter months. Contributions of  $b_{ext\_AS}$  to  $b_{ext\_aer}$  were higher in rural regions across the United States. In the eastern United States, contributions reached an average maximum of 0.45 for IMPROVE regions and 0.37 for CSN regions, compared to the northwestern United States (0.35 and 0.26 for IMPROVE and CSN, respectively), and the southwestern United States (0.31 and 0.23 for IMPROVE and CSN, respectively).

Regional average monthly mean maximum  $b_{ext\_AN}$  was higher in urban regions. For all CSN regions, average maximum  $b_{ext\_AN}$  ranged from 23 to 29  $Mm^{-1}$ , with the highest values in regions in the southwestern United States. Rural estimates varied considerably depending on

region, with average maximum values around  $13 \text{ Mm}^{-1}$  in the eastern United States, compared to  $11 \text{ Mm}^{-1}$  and  $3 \text{ Mm}^{-1}$  in the northwestern and southwestern United States, respectively. For nearly all regions, monthly mean maximum  $b_{\text{ext\_AN}}$  was highest during winter months, reflecting favorable formation conditions. Maximum contributions of  $b_{\text{ext\_AN}}$  were similar for urban and rural regions in the eastern and northwestern Untied States ( $\sim 0.4$ ), but in the southwestern regions, higher contributions occurred in urban (0.36) relative to rural regions (0.23). These contributions were usually higher during winter months, except in some urban and rural regions in the southern part of California that had higher contributions year round.

Discrepancies between urban and rural average monthly mean maximum  $b_{\text{ext\_POM}}$  suggested the importance of different sources in urban and rural areas. The influence of biomass smoke led to high average monthly mean maximum  $b_{\text{ext\_POM}}$  in the rural northwestern United States, with values near  $37 \text{ Mm}^{-1}$  (IMPROVE) and  $27 \text{ Mm}^{-1}$  (CSN) and differences in seasonality. Rural areas experienced strong summer peaks in  $b_{\text{ext\_POM}}$  while urban regions often had higher  $b_{\text{ext\_POM}}$  year round and during winter months, suggesting additional urban sources and lower impacts from biomass smoke. The opposite was true for the southwestern United States, where CSN regional mean  $b_{\text{ext\_POM}}$  was higher than in IMPROVE regions ( $26 \text{ Mm}^{-1}$  versus  $<16 \text{ Mm}^{-1}$ ). Regional mean  $b_{\text{ext\_POM}}$  was very similar for urban and rural regions in the eastern United States ( $\sim 16\text{--}17 \text{ Mm}^{-1}$ ), with summer peaks suggesting more regional sources, perhaps related to biogenic emissions. Maximum contributions of  $b_{\text{ext\_POM}}$  to  $b_{\text{ext\_aer}}$  were around 0.35–0.4 in both urban and rural regions in the East. Average maximum contributions were higher in the northwestern United States and higher in IMPROVE regions (0.7 versus 0.5 in CSN regions). Although  $b_{\text{ext\_POM}}$  contributions in urban and rural regions in the southwestern United States were higher than in the East, like in eastern regions they were similar in magnitude ( $\sim 0.46\text{--}0.48$ ).

The largest urban and rural discrepancies were observed for monthly mean maximum  $b_{\text{ext\_EC}}$ . Urban  $b_{\text{ext\_EC}}$  was higher, with values four times higher in the eastern and southwestern United States and over two times higher in the northwestern United States. In most urban regions,  $b_{\text{ext\_EC}}$  was higher during winter months, suggesting urban sources that led to higher  $b_{\text{ext\_EC}}$  relative to summer biomass smoke influence. Contributions from  $b_{\text{ext\_EC}}$  to  $b_{\text{ext\_aer}}$  were also higher in urban regions for all areas. In the eastern United States, regional average urban maximum contributions of  $b_{\text{ext\_EC}}$  were 0.16, compared to 0.09 in rural regions. This range was also observed in the northwestern United States (0.19 versus 0.10) and the southwestern United States (0.22 versus 0.11).

Even with the bias in FD between CSN and IMPROVE networks, the average maximum  $b_{\text{ext\_FD}}$  was similar ( $\sim 1\text{--}2 \text{ Mm}^{-1}$ ) at urban and rural regions across the United States. The highest monthly mean urban  $b_{\text{ext\_FD}}$  occurred in regions in the eastern and southwestern United States ( $1.6\text{--}1.7 \text{ Mm}^{-1}$ ), while rural regions experienced maximum  $b_{\text{ext\_FD}}$  in the southwestern United States, a region known to experience frequent dust impacts. The role of FD in visibility is reduced relative to its contributions to RCFM because FD is less efficient at scattering light due to its larger size. Visibility impacts of  $b_{\text{ext\_CM}}$  were higher than  $b_{\text{ext\_FD}}$  due to its greater mass, even though it has an even lower mass scattering efficiency ( $0.6 \text{ m}^2\text{g}^{-1}$  versus  $1 \text{ m}^2\text{g}^{-1}$ ). Average monthly mean maximum  $b_{\text{ext\_CM}}$  values were similar for urban and rural regions and were around  $5\text{--}6 \text{ Mm}^{-1}$ , except in the southwestern U.S. urban regions where the average maximum urban

$b_{ext\_CM}$  was  $9 \text{ Mm}^{-1}$ , due to higher values near the Central Valley. Contributions from  $b_{ext\_CM}$  were similar in urban and rural regions (0.15–0.25) and were higher for both in regions in the southwestern United States.

Visibility impacts of  $b_{ext\_SS}$  were low, except in coastal regions. For both urban and rural regions, the average monthly mean maximum  $b_{ext\_SS}$  was  $1\text{--}2 \text{ Mm}^{-1}$ , even with the large bias between the CSN and IMPROVE. Average contributions of  $b_{ext\_SS}$  to  $b_{ext\_aer}$  in CSN regions were 0.01–0.02 and were somewhat higher in rural regions (0.05–0.07).

Finally, reconstructed  $b_{ext\_aer}$  estimates suggested higher visibility impacts in urban regions. In the eastern United States, average maximum  $b_{ext\_aer}$  was  $\sim 62 \text{ Mm}^{-1}$ , around  $20 \text{ Mm}^{-1}$  greater than in IMPROVE regions, and dv values ranged from 16 (IMPROVE) to 20 (CSN). For rural regions, average maximum monthly mean  $b_{ext\_aer}$  was highest for regions in the northwestern United States ( $\sim 57 \text{ Mm}^{-1}$ ) but somewhat lower than in urban regions ( $64 \text{ Mm}^{-1}$ ) in the same area (dv values were 19 and 20 for IMPROVE and CSN, respectively). While average maximum  $b_{ext\_aer}$  was highest for urban regions in the southwestern United States ( $76 \text{ Mm}^{-1}$ , 21 dv), it was lowest in rural regions in the same area ( $33 \text{ Mm}^{-1}$ , 14 dv).

In both urban and rural regions, the role of  $b_{ext\_AN}$  and  $b_{ext\_POM}$  were very important, often driving the seasonality of the maximum  $b_{ext\_aer}$  due to the seasonality of specific sources (e.g., biomass smoke) or during periods with favorable formation conditions (e.g.,  $b_{ext\_AN}$ ). However,  $b_{ext\_AS}$  was within the top third contributing species in most regions, in part due to its hygroscopic nature, and was still an important contributor to  $b_{ext\_aer}$ .

Appendices associated with this chapter include tables of regional monthly mean  $b_{ext}$  for IMPROVE and the CSN (5.1) and tables of  $b_{ext}$  fraction for IMPROVE and the CSN (5.2).

## Chapter 6. Trends in IMPROVE Speciated Aerosol Concentrations

Site-specific trends were computed for eight parameters: 10<sup>th</sup>, 50<sup>th</sup>, and 90<sup>th</sup> percentiles and winter (DJF), spring (MAM), summer (JJA), fall (SON), and annual mean. December data from the previous year were included in winter mean calculations. Fifty percent of daily data was required for a valid seasonal mean, and annual means were calculated from four valid seasonal means. Annual percentiles were calculated for 60% of valid daily data. Long- and short-term trends required 70% of the years to be valid. These completeness criteria differed from those applied for 4-year aggregated data (see Chapter 2). A Theil regression was performed with the concentration data as the dependent variable and the year as the independent variable. Theil regressions avoid heavy influence by outliers on the regression results (Theil, 1950). Kendall tau statistics were used to determine the statistical significance, assuming the slope was statistically significant at 5% ( $p \leq 0.05$ ), meaning that there was a 95% chance that the slope was not due to random chance. Trends (% yr<sup>-1</sup>) were calculated by dividing the slope by the median concentration value over the time period of the trend, multiplied by 100%. Reporting trends instead of slopes normalizes the range in concentrations that occur across the United States. However, trends can be large when median concentrations are very low (e.g., 10<sup>th</sup> percentile).

Short-term, regional mean trends were calculated for ten regions of the United States. Sites were grouped by their state into the following regions: Northeast, Southeast, Midsouth, Central, Southwest, Northwest, California, Alaska, Hawaii, Virgin Islands (see Table 6.0 and Figure 6.0) and the continental United States (CONUS). The Virgin Islands region included one site. Although some names are the same, these regions are broader and do not necessarily correspond to the regions shown in Chapters 3 and 5. The regions were qualitatively determined only as a means for summarizing trends. Regional mean trends were computed by aggregating site-specific seasonal mean concentrations (or percentiles) for a given region and year and then performing a Theil regression on regional mean concentrations. Sites that met the 70% valid data trend requirement were included in the regional trend calculation. Regional mean trends were calculated for seasonal and annual means and for the 10<sup>th</sup>, 50<sup>th</sup>, and 90<sup>th</sup> percentiles. Annual mean trends can be driven by specific seasons, and different parts of the mass distribution may have different trends, so comparisons of regional mean trends provide further insight into temporal behavior of major aerosol components.

**Table 6.0. Regions and states (abbreviations) used for regional mean trends. Sites within listed states were included in the corresponding region.**

Region	State
Northeast	ME, NH, VT, MA, RI, CT, NY, PA, NJ, DE, MD, OH, WV, VA, IN, KY
Southeast	TN, NC, SC, MS, LA, AL, GA, FL
Midsouth	OK, LA, AR
Central	ND, SD, MN, MI, WI, IL, MO, KS, NE, IA
Southwest	NV, UT, CO, NM, AZ, TX
Northwest	WA, OR, ID, MT, WY
California	CA
Alaska	AK
Hawaii	HI
Virgin Islands	Virgin Islands

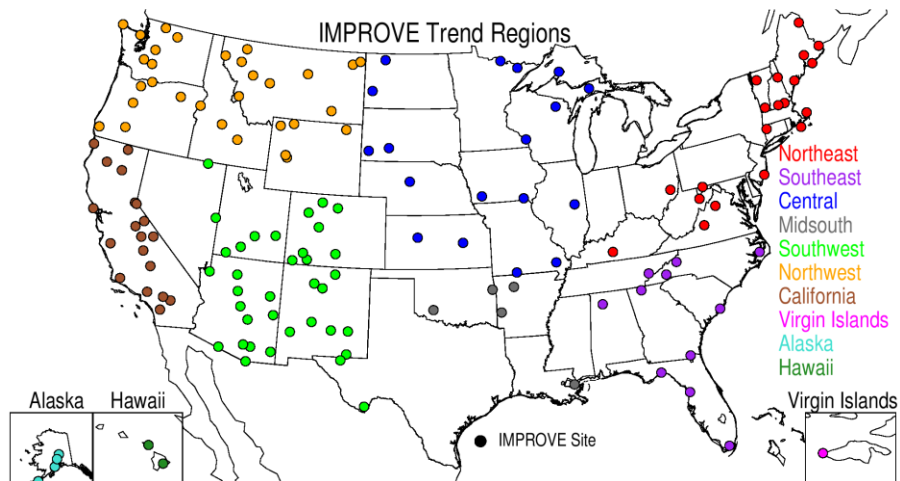


**Figure 6.0. IMPROVE regions defined to summarize regional mean trends.**

Trend results were interpolated to provide isopleths to guide the eye (Isaaks and Mohan Srivastava, 1989). Positive trends are denoted with an upward-pointing triangle and contoured with warm colors. Negative trends are shown with downward-pointing triangles and contoured with cold colors. Statistically significant trends ( $p \leq 0.05$ ) are denoted with filled triangles. Scales were kept similar for all parameters so that trends can be compared. Long-term trend maps suffer from lower site densities, and therefore interpolations in regions without long-term sites (such as the central United States) should be viewed only as a spatial transition.

## 6.1 SULFATE ION TRENDS

Missing sulfate ion concentrations after 1 May 1995 were replaced with  $3 \times$  sulfur concentrations to reduce the impacts of missing data on trend results. Before 1995, filters were masked and could result in an underestimation of sulfur concentrations (Schichtel, 2003); therefore sulfur was not used as a replacement before this date. Long-and short-term annual mean sulfate ion trends are shown in Figures 6.1.1a and 6.1.1b, respectively. Fifty-five sites met long-term annual mean trend completeness criteria, and most long-term sites are in the western United States. Annual mean sulfate ion concentrations have decreased significantly for all CONUS long-term sites. Long-term annual mean sulfate ion trends ranged from  $-7.78\% \text{ yr}^{-1}$  ( $p < 0.001$ ) at Shining Rock Wilderness Area (WA), North Carolina (SHRO1), to  $-1.01\% \text{ yr}^{-1}$  ( $p = 0.01$ ) at Lassen Volcanic National Park (NP), California (LAVO1). The greatest long-term decrease in annual mean sulfate ion concentrations occurred for sites along the Appalachian region where sulfur dioxide emissions have also dramatically decreased (Krotkov et al., 2016; Kharol et al., 2017; Feng et al., 2020; Hand et al., 2020). Less progress occurred for sites in California, Nevada, and Idaho, as well as southwestern Texas. Trends at these sites were between  $-1\% \text{ yr}^{-1}$  and  $-2\% \text{ yr}^{-1}$ . Emissions in the West have historically been lower than in the East (Hand et al., 2012; Hand et al., 2020), and therefore the reduction of those regulated emissions has had less of an impact on already-low concentrations.

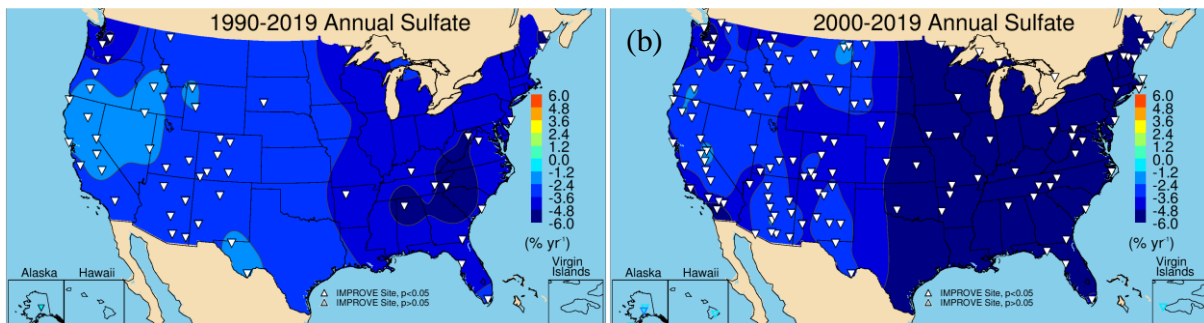


**Figure 6.1.1.** Annual mean sulfate ion mass trends ( $\% \text{ yr}^{-1}$ ) for (a) long-term (1990–2019) and (b) short-term (2000–2019) periods. Filled triangles correspond to statistically significant trends ( $p \leq 0.05$ ).

Annual mean sulfate ion concentrations also decreased for all of the short-term sites shown in Figure 6.1.1b. Out of the 135 valid sites, all but five had statistically significant annual mean sulfate ion trends that ranged from  $-11.23\% \text{ yr}^{-1}$  ( $p < 0.001$ ) at Cohutta, Georgia (COHU1), to  $-1.76\% \text{ yr}^{-1}$  ( $p = 0.012$ ) at Fort Peck, Montana (FOPE1). Insignificant trends occurred at sites in Hawaii, Alaska, and the Virgin Islands. As seen in Figure 6.1.1b, a strong spatial gradient in annual mean trends existed between the eastern and western United States, with stronger rates of change for sites in the East. Sites east of  $-100^\circ$  nearly all had concentrations decrease at rates greater than  $-4\% \text{ yr}^{-1}$ , and at sites in the Appalachia and Ohio River valley regions, trends were around  $-7\% \text{ yr}^{-1}$  to  $-10\% \text{ yr}^{-1}$ , corresponding to a 140–200% decrease over the past two decades. Trends at sites in the western United States were about  $-2\% \text{ yr}^{-1}$  to  $-4\% \text{ yr}^{-1}$ .

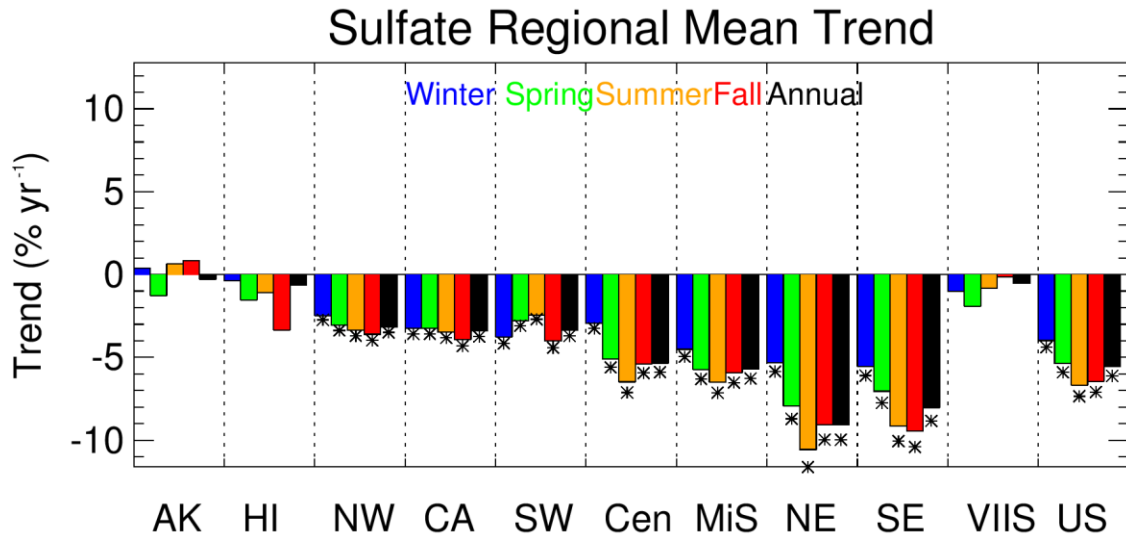


**Figure 6.1.2.** Short-term (2000–2019) regional seasonal mean sulfate ion trends ( $\% \text{ yr}^{-1}$ ) for major U.S. regions for winter, spring, summer, fall, and annual means. Regions are arranged from western to eastern United States (AK = Alaska, HI = Hawaii, NW = Northwest, CA = California, SW = Southwest, Cen = Central, MiS = Midsouth, NE = Northeast, SE = Southeast, VIIS = Virgin Islands, and US = all sites). Statistically significant trends ( $p \leq 0.05$ ) are denoted with “\*”.

The spatial gradients and seasonal distribution in sulfate ion trends are also shown in the regional mean trends presented in Figure 6.1.2, with regional mean trends ordered from west to

east. The largest reductions in seasonal mean sulfate ion concentrations occurred for sites in the Northeast region ( $-10.56\% \text{ yr}^{-1}$  in summer), followed by the Southeast region ( $-9.46\% \text{ yr}^{-1}$  in fall). For the Northeast, Midsouth, and Central regions, the largest decrease in sulfate ion concentrations occurred during summer (in the Southeast decreases in fall were slightly larger), and the lowest decreases occurred during winter. This difference in the seasonal mean trends has led to a decrease in the seasonality of sulfate ion concentrations at eastern regions, as was discussed in Chapter 3. In regions in the western United States, the rate of decrease was lower, roughly half of the rate of decrease relative to eastern regions. The differences in seasonal mean trends were also smaller, suggesting that sulfate ion concentrations decreased by similar rates across seasons. The exception to this is at the Southwest region, where the largest decreases occurred during both winter and fall. Overall, across the United States, sulfate ion concentrations have decreased at a higher rate during summer and fall. Seasonal mean trends at sites in Alaska, Hawaii, and the Virgin Islands were all relatively flat and insignificant.

Long-term 10<sup>th</sup> and 90<sup>th</sup> percentile sulfate ion trends are shown in Figure 6.1.3a and 6.1.3b, respectively. The 50<sup>th</sup> percentile trends are not shown, as they are similar to the annual mean trends previously discussed. The spatial variability for the 10<sup>th</sup> and 90<sup>th</sup> percentile trends were similar, with larger reductions in the eastern United States. The 10<sup>th</sup> percentile trends ranged from  $-6.01\% \text{ yr}^{-1}$  ( $p < 0.001$ ) at Snoqualmie Pass, Washington (SNPA1), to  $-1.13\% \text{ yr}^{-1}$  ( $p = 0.04$ ) at Yosemite NP, California (YOSE1), and 54 out of 57 sites had statistically significant trends. Insignificant trends occurred at Hawaii Volcanoes NP, Hawaii (HAVO1), Lassen Volcanic NP, California (LAVO1), and Three Sisters WA, Oregon (THSI1). Trends in the 10<sup>th</sup> percentile sulfate ion concentrations at sites in California were weaker ( $\sim -2\% \text{ yr}^{-1}$ ) than for other areas in the United States.

Trend values did not differ greatly for the long-term 90<sup>th</sup> percentile in sulfate concentrations (Figure 6.1.3b) compared to the 10<sup>th</sup> percentile trends, and 55 out of 57 sites had statistically significant trends. The largest negative trend occurred at Shining Rock WA, North Carolina (SHRO1,  $-7.31\% \text{ yr}^{-1}$ ,  $p < 0.001$ ) compared to the least negative trend at Big Bend NP, Texas, (BIBE1,  $-0.81\% \text{ yr}^{-1}$ ,  $p = 0.03$ ). Trends for sites in Arizona and New Mexico were somewhat larger for the 90<sup>th</sup> percentile compared to the 10<sup>th</sup> percentile, while trends at sites in California were similar. Greater reductions in the 90<sup>th</sup> percentile concentration trends ( $-5\% \text{ yr}^{-1}$ ) occurred at sites in the East.

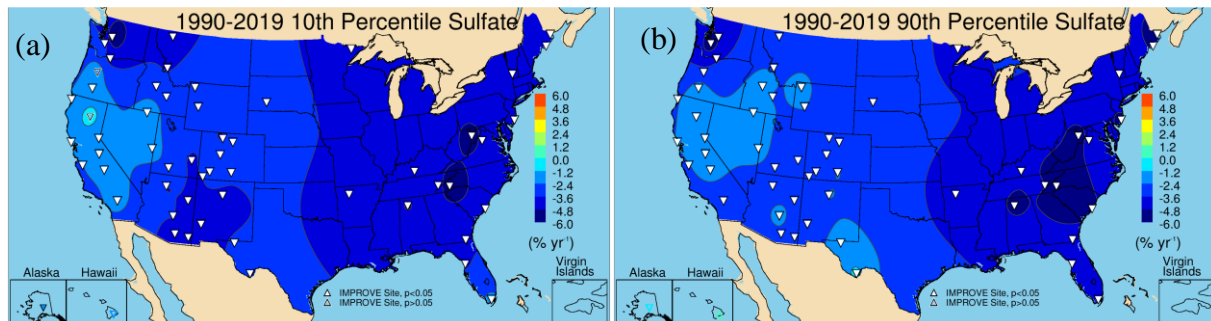


**Figure 6.1.3. IMPROVE long-term (1990-2019) trends ( $\% \text{ yr}^{-1}$ ) in (a) 10<sup>th</sup> percentile sulfate ion concentrations and (b) 90<sup>th</sup> percentile concentrations. Filled triangles correspond to statistically significant trends ( $p \leq 0.05$ ).**

Short-term trends in the 10<sup>th</sup> and 90<sup>th</sup> percentile sulfate ion concentrations are shown in Figure 6.1.4a and 6.1.4b, respectively. Large-scale spatial variability in trends was similar for both percentiles, with greater reductions in sulfate ion concentrations at sites in the eastern United States. Differences in the spatial patterns occurred in the central United States and for some sites in California that experienced insignificant 10<sup>th</sup> percentile trends. For 138 sites with valid 10<sup>th</sup> percentile trends, 126 were statistically significant, compared to 132 for 90<sup>th</sup> percentile trends. The largest reduction in 10<sup>th</sup> percentile concentrations occurred at Cohutta, Georgia (COHU1, -8.30% yr<sup>-1</sup>, p < 0.001), compared to the least reduction at Bliss State Park (SP), California (BLIS1, -1.73% yr<sup>-1</sup>, p = 0.03). The largest reduction in the 90<sup>th</sup> percentile concentrations also occurred at Cohutta, Georgia (COHU1, -14.22% yr<sup>-1</sup>, p < 0.001), compared to Kaiser, California (KAIS1, -1.40% yr<sup>-1</sup>, p = 0.03). For both the 10<sup>th</sup> and 90<sup>th</sup> percentiles, trends were negative but insignificant at Alaska, Hawaii, and Virgin Island sites.

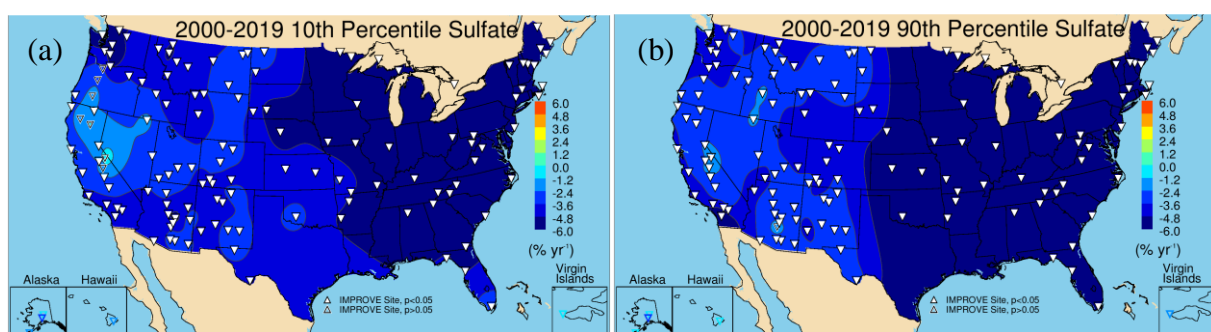


**Figure 6.1.4. IMPROVE short-term (2000–2019) trends (% yr<sup>-1</sup>) in (a) 10<sup>th</sup> percentile sulfate ion concentrations and (b) 90<sup>th</sup> percentile concentrations. Filled triangles correspond to statistically significant trends ( $p \leq 0.05$ ).**

Comparisons of short-term regional mean percentile trends are shown in Figure 6.1.5. For most regions in the western United States, the 10<sup>th</sup>, 50<sup>th</sup>, and 90<sup>th</sup> percentiles were similar, with the Northwest and Southwest regions having slightly greater reductions in the 10<sup>th</sup> percentile concentrations and the California region having somewhat greater reductions in the regional mean 90<sup>th</sup> percentile concentrations. However, for eastern regions, the regional 90<sup>th</sup> percentile trends decreased at a much greater rate than the 10<sup>th</sup> and 50<sup>th</sup> percentile concentrations. The Northeast region 90<sup>th</sup> percentile trend was -10.51% yr<sup>-1</sup> (p < 0.001) compared to the 10<sup>th</sup> percentile trend of -6.46% yr<sup>-1</sup> (p < 0.001). The Southeast region had a similar difference in 90<sup>th</sup> and 10<sup>th</sup> percentile trends (-9.63% yr<sup>-1</sup>, p < 0.001, compared to -5.28% yr<sup>-1</sup>, p < 0.001, respectively). These trends are consistent with the seasonal mean trends, as the highest sulfate ion concentrations typically occurred during summer.

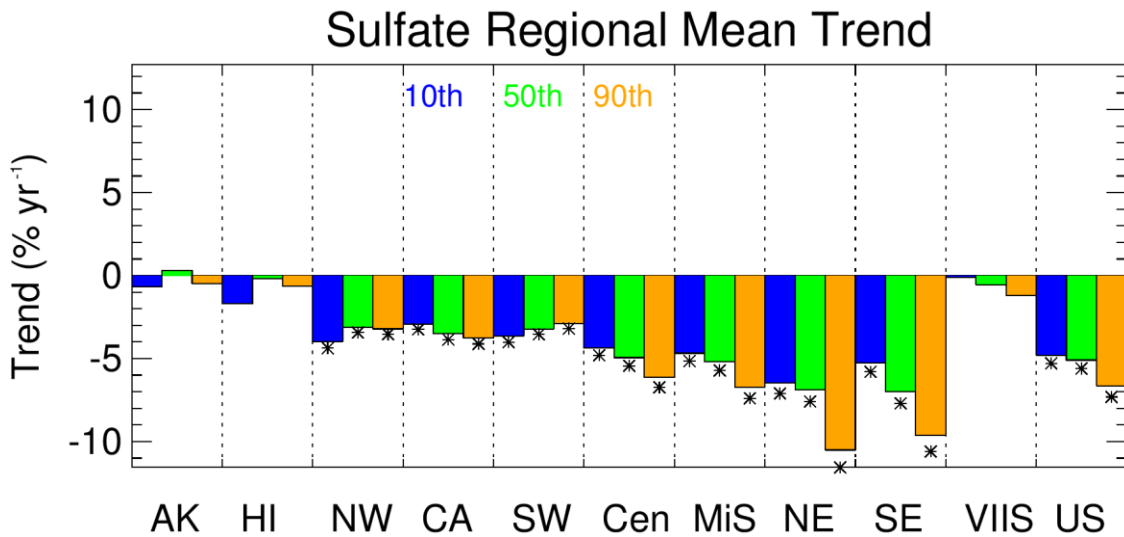


**Figure 6.1.5.** Short-term (2000–2019) regional mean trends ( $\% \text{ yr}^{-1}$ ) in 10<sup>th</sup>, 50<sup>th</sup>, and 90<sup>th</sup> percentile sulfate ion concentrations. Regions are arranged from western to eastern United States (AK = Alaska, HI = Hawaii, NW = Northwest, CA = California, SW = Southwest, Cen = Central, MiS = Midsouth, NE = Northeast, SE = Southeast, VIIS = Virgin Islands, and US = all sites). Statistically significant trends ( $p \leq 0.05$ ) are denoted with “\*”.

## 6.2 NITRATE ION TRENDS

During the late 1990s, IMPROVE nitrate ion concentrations at many sites fell below historical values during winter months. Investigations into the period from 1996 through 2000 revealed lower than usual concentrations during winter months, and the cause remains unknown (McDade, 2004; McDade, 2007). Concentrations returned to normal levels after 2000, after which the data were deemed valid. Given the number of sites influenced by this anomaly (Debell, 2006), nitrate ion data were considered invalid for winters from 1996 through 2000, which invalidated annual mean and percentile concentrations for those years.

Long-term annual mean nitrate ion trends are shown in Figure 6.2.1a. Of the 42 valid trend sites, 36 had statistically significant trends. The largest reductions in the annual mean nitrate ion concentrations occurred at sites in southern California and were about  $-3\% \text{ yr}^{-1}$ , except at the site with the largest negative trend, San Gorgonio WA, California (SAGO1,  $-7.95\% \text{ yr}^{-1}$ ,  $p < 0.001$ ). Strong reductions in nitrate ion concentrations in California are associated with reduced nitrogen dioxide emissions from vehicles (Krotkov et al., 2016; Hand et al., 2020). Insignificant trends occurred at sites in the southwestern United States and were associated with nearly flat reductions. The lowest statistically significant trend occurred at Bridger WA, Wyoming (BRID1,  $-0.92\% \text{ yr}^{-1}$ ,  $p = 0.04$ ). Sites in the eastern United States corresponded to reductions about  $-1\% \text{ yr}^{-1}$  to  $-2\% \text{ yr}^{-1}$ .

Short-term annual mean nitrate trends also showed strong reductions at sites in southern California (Figure 6.2.1b). The strongest reductions for short-term trends occurred at San Gorgonio, California (SAGO1,  $-8.89\% \text{ yr}^{-1}$ ,  $p < 0.001$ ). Around 80% of short-term annual mean nitrate trends were statistically significant (109 out of 134 valid sites). Sites in the northern Great

Plains were associated with insignificant trends ( $-1\% \text{ yr}^{-1}$  to  $-2\% \text{ yr}^{-1}$ ), likely due to the influence of oil and gas development in the region (Prenni et al., 2016; Evanoski-Cole et al., 2017; Gebhart et al., 2018). The lowest statistically significant annual mean nitrate ion trend occurred at Swanquarter, North Carolina (SWAN1,  $-0.88\% \text{ yr}^{-1}$ ,  $p = 0.04$ ).

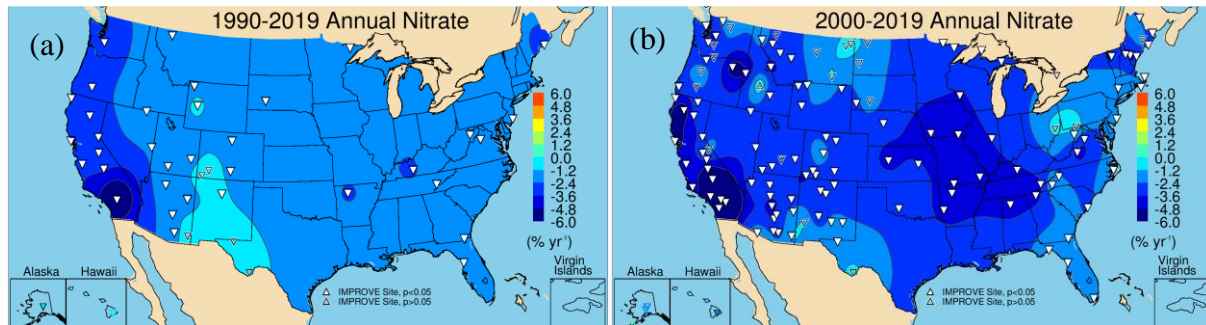


**Figure 6.2.1. Annual mean nitrate ion mass trends ( $\% \text{ yr}^{-1}$ ) for (a) long-term (1990–2019) and (b) short-term (2000–2019) periods. Filled triangles correspond to statistically significant trends ( $p \leq 0.05$ ).**

Comparisons of short-term regional seasonal mean nitrate ion concentration trends are shown in Figure 6.2.2. As seen in Figure 6.2.1b, the strongest reductions occurred in the California region, especially in fall ( $-7.46\% \text{ yr}^{-1}$ ,  $p < 0.001$ ) and spring ( $-7.00\% \text{ yr}^{-1}$ ,  $p < 0.001$ ). In other regions, there were differences in seasonal mean trends. For example, the regions of the Northwest, Southwest, and Southeast followed a similar pattern, with winter trends having the largest reductions, compared to the lowest reductions in summer, and spring and fall were in-between and comparable. This pattern is different from what occurred in the Midsouth region, with the strongest trends in spring, and the Central region, where the fall trends were the strongest and summer trends were lowest and insignificant. In contrast, very little range in seasonal trends occurred in the Northeast region (and winter had the lowest reductions). This range in seasonal mean trends indicates potentially different sources and atmospheric processes controlling nitrate concentrations in these regions.

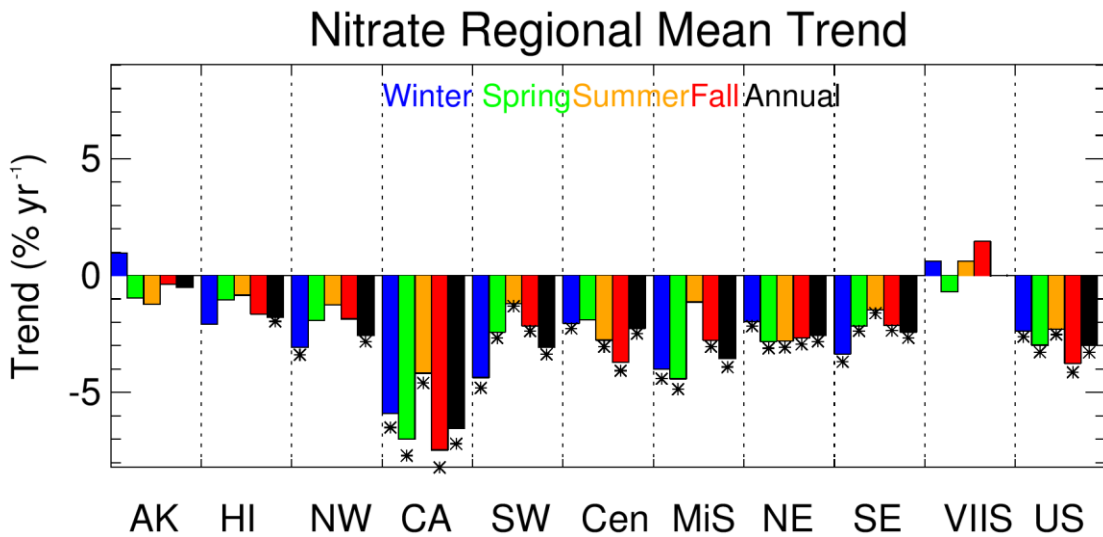


**Figure 6.2.2.** Short-term (2000–2019) regional seasonal mean nitrate ion trends ( $\% \text{ yr}^{-1}$ ) for major U.S. regions for winter, spring, summer, fall, and annual means. Regions are arranged from western to eastern United States (AK = Alaska, HI = Hawaii, NW = Northwest, CA = California, SW = Southwest, Cen = Central, MiS = Midsouth, NE = Northeast, SE = Southeast, VIIS = Virgin Islands, and US = all sites). Statistically significant trends ( $p \leq 0.05$ ) are denoted with “\*”.

Long-term trends in the 10<sup>th</sup> and 90<sup>th</sup> percentile nitrate concentrations are shown in Figure 6.2.3a and 6.2.3b, respectively. Of the 45 valid sites, only 25 of them were associated with statistically significant trends, and these occurred mainly at sites in California and the eastern United States. Similar to the annual mean trend, the strongest reduction in the 10<sup>th</sup> percentile nitrate concentration occurred at San Gorgonio WA, California (SAGO1,  $-6.03\% \text{ yr}^{-1}$ ,  $p < 0.001$ ), compared to  $-1.00\% \text{ yr}^{-1}$  ( $p = 0.02$ ) at Great Sand Dunes NP, Colorado (GRSA1). Many of the sites associated with insignificant and flat trends were located in the southwestern United States and the Intermountain West.

The spatial patterns in the 10<sup>th</sup> and 90<sup>th</sup> percentile long-term trends were similar, with the strongest reductions at sites in California, and weak and insignificant trends at sites in the Southwest. However, more sites met statistical significance criteria (30 out of 45) for 90<sup>th</sup> percentile trends. Some long-term trends at sites in the eastern United States were not as strong for the 90<sup>th</sup> percentile relative to the 10<sup>th</sup> percentile concentrations, and some 90<sup>th</sup> percentile trends were insignificant while the 10<sup>th</sup> percentile trends were not (Great Smoky Mountains NP, Tennessee, GRSM1 and Mammoth Cave NP, Kentucky, MACA1).

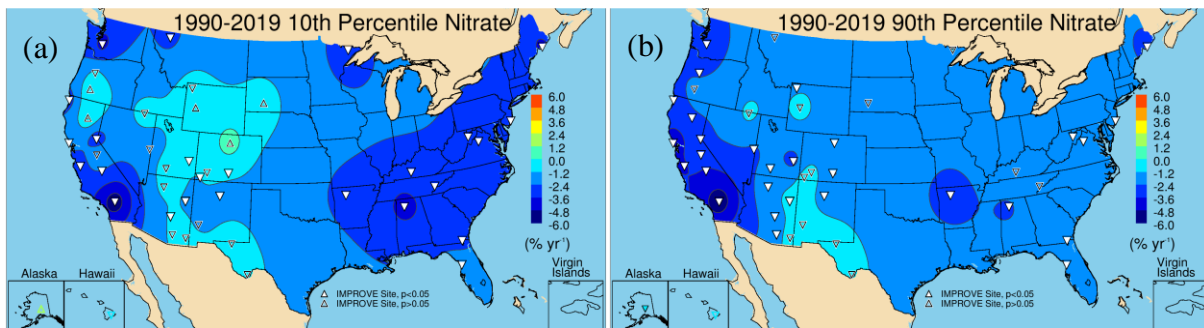


**Figure 6.2.3. IMPROVE long-term (1990–2019) trends ( $\% \text{ yr}^{-1}$ ) in (a) 10<sup>th</sup> percentile nitrate ion concentrations and (b) 90<sup>th</sup> percentile concentrations. Filled triangles correspond to statistically significant trends ( $p \leq 0.05$ ).**

The strongest reductions in short-term 10<sup>th</sup> percentile nitrate concentration trends also occurred at San Gorgonio WA, California (SAGO1,  $-10.34\% \text{ yr}^{-1}$ ,  $p < 0.001$ ) (Figure 6.2.4a). Several sites in the eastern United States also experienced strong reductions in the 10<sup>th</sup> percentile concentrations ( $-5\% \text{ yr}^{-1}$  to  $-6\% \text{ yr}^{-1}$ ), such as Cohutta, Georgia (COHU1); Seney, Michigan (SENE1); James River Face WA, Virginia (JARI1); and Quabbin Summit, Massachusetts (QURE1). Insignificant trends occurred at 81 of 138 valid sites. Positive but insignificant trends occurred at sites in the northern Great Plains, where oil and gas development has influenced nitrate concentrations. Other insignificant trends occurred at sites in Wyoming, Colorado, and Texas. The weakest significant trend occurred at Wichita Mountains, Oklahoma (WIMO1,  $-1.34\% \text{ yr}^{-1}$ ,  $p = 0.04$ ).

The spatial pattern in the short-term 90<sup>th</sup> percentile trend (Figure 6.2.4b) was similar to the 10<sup>th</sup> percentile trend pattern, with the strongest negative trends at sites in southern California, and at sites in Appalachian Mountains. Out of 138 valid sites, 98 met statistical significance requirements. Most of the insignificant trends also occurred at sites in the northern Great Plains area and near Maryland and Ohio (Frostburg Reservoir, Maryland, FRRE1, and Quaker City, Ohio, QUCI1, respectively).

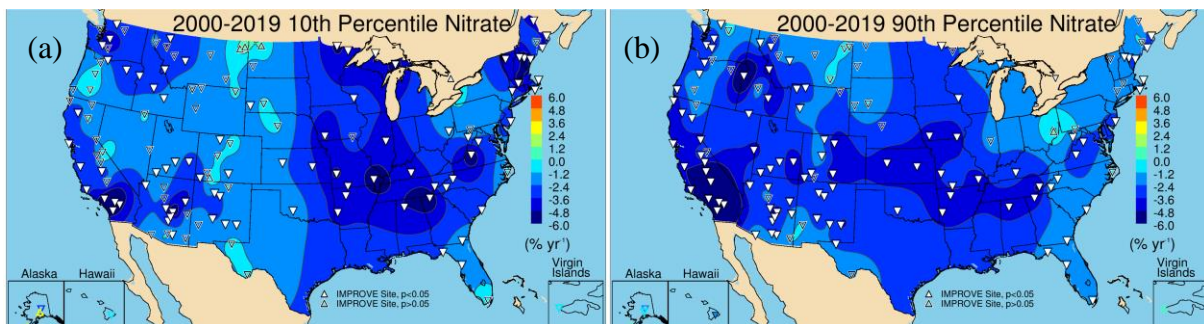


**Figure 6.2.4. IMPROVE short-term (2000–2019) trends ( $\% \text{ yr}^{-1}$ ) in (a) 10<sup>th</sup> percentile nitrate ion concentrations and (b) 90<sup>th</sup> percentile concentrations. Filled triangles correspond to statistically significant trends ( $p \leq 0.05$ ).**

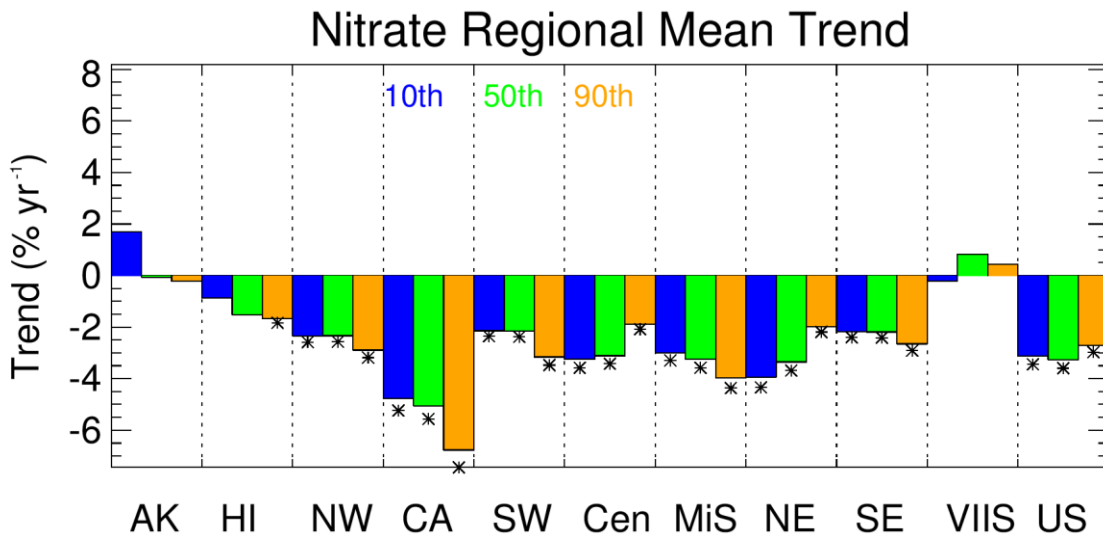


**Figure 6.2.5.** Short-term (2000–2019) regional mean trends ( $\% \text{ yr}^{-1}$ ) in 10<sup>th</sup>, 50<sup>th</sup>, and 90<sup>th</sup> percentile nitrate ion concentrations. Regions are arranged from western to eastern United States (AK = Alaska, HI = Hawaii, NW = Northwest, CA = California, SW = Southwest, Cen = Central, MiS = Midsouth, NE = Northeast, SE = Southeast, VIIS = Virgin Islands, and US = all sites). Statistically significant trends ( $p \leq 0.05$ ) are denoted with “\*”.

A summary of the regional 10<sup>th</sup>, 50<sup>th</sup>, and 90<sup>th</sup> percentile nitrate ion concentration trends is shown in Figure 6.2.5. As was seen in the maps, the strongest trends occurred in the California region, with the 90<sup>th</sup> percentile trends being the greatest ( $-6.77\% \text{ yr}^{-1}$ ,  $p < 0.001$ ). For all of the regions, except the Central and Northeast regions, reductions in the 90<sup>th</sup> percentile concentrations were strongest. In the Central and Northeast regions, the 90<sup>th</sup> percentile trends were the weakest, and the 10<sup>th</sup> percentile trends were the strongest. Reasons for this pattern for these regions is unknown.

### 6.3 ORGANIC CARBON TRENDS

Trends in OC and EC may be affected by changes in analytical methods. A recent review of carbonaceous measurements in the IMPROVE program identified shifts in analytical methods and their impacts on the fraction of EC to total carbon (OC + EC), i.e., EC/TC (Schichtel et al., 2021). One such shift occurred with hardware upgrades in 2005 that resulted in changes in the split between OC and EC that introduced uncertainty to trend analyses (Chow et al., 2007; White, 2007). Other shifts in EC/TC have also occurred over the history of the program due to new analyzers, new calibrations, and undetermined reasons. These effects have motivated discussions regarding future carbonaceous aerosol measurements within the program (Schichtel et al., 2021).

Annual mean OC trends for long-term sites are shown in Figure 6.3.1a. Of the 51 valid sites, 32 had statistically significant trends, including all of the sites in the eastern United States. Insignificant trends occurred at sites in the Intermountain West and at sites along eastern California. Positive but insignificant trends occurred at Bridger WA, Wyoming (BRID1); Crater Lake NP, Oregon (CRLA1); and Lassen Volcanic NP, California (LAVO1), sites likely

associated with impacts from biomass burning. The strongest statistically significant reductions in OC occurred at Mount Rainier NP, Washington (MORA1,  $-3.36\% \text{ yr}^{-1}$ ,  $p < 0.001$ ), and the least reduction occurred at Guadalupe Mountains, NP, Texas (GUMO1,  $-1.06\% \text{ yr}^{-1}$ ,  $p = 0.009$ ). Other strong reductions in the West occurred at Point Reyes National Seashore, California (PORE1,  $-3.24\% \text{ yr}^{-1}$ ,  $p < 0.001$ ), and San Gorgonio WA, California (SAGO1,  $-2.97\% \text{ yr}^{-1}$ ,  $p < 0.001$ ). Strong reductions in the East occurred at Dolly Sods WA, West Virginia (DOSO1,  $-2.93\% \text{ yr}^{-1}$ ,  $p < 0.001$ ); Shenandoah NP, Virginia (SHEN1,  $-2.44\% \text{ yr}^{-1}$ ,  $p < 0.001$ ); and Moosehorn National Wildlife Refuge (NWR), Maine, (MOOS1,  $-2.98\% \text{ yr}^{-1}$ ,  $p < 0.001$ ). Reductions in anthropogenic emissions have led to a decrease in OC in the East (e.g., Blanchard et al., 2016; Malm et al., 2017).

With the addition of short-term sites, the area with insignificant short-term trends increased farther north (Figure 6.3.1b), at sites in Montana, Idaho, and Washington, where biomass smoke has influenced trends in particulate matter and OC (McClure and Jaffe, 2018). All of the sites with insignificant trends occurred in the western United States and in Alaska, Hawaii, and the Virgin Islands. Positive, but insignificant, trends occurred at Craters of the Moon National Monument (NM), Idaho (CRMO1); White Pass, Washington (WHPA1); and Hoover, California (HOOV1), among others. Of the 136 valid sites, 67 had statistically significant trends. The strongest reduction occurred at Agua Tibia, California (AGTI1,  $-4.25\% \text{ yr}^{-1}$ ,  $p < 0.001$ ), and the least reduction occurred at Isle Royale NP, Michigan (ISLE1,  $-1.39\% \text{ yr}^{-1}$ ,  $p = 0.003$ ). Relatively strong reductions in annual mean OC occurred at sites in the eastern and northeastern United States. In the western United States, strong reductions also occurred at sites in southern California and parts of Arizona and New Mexico.

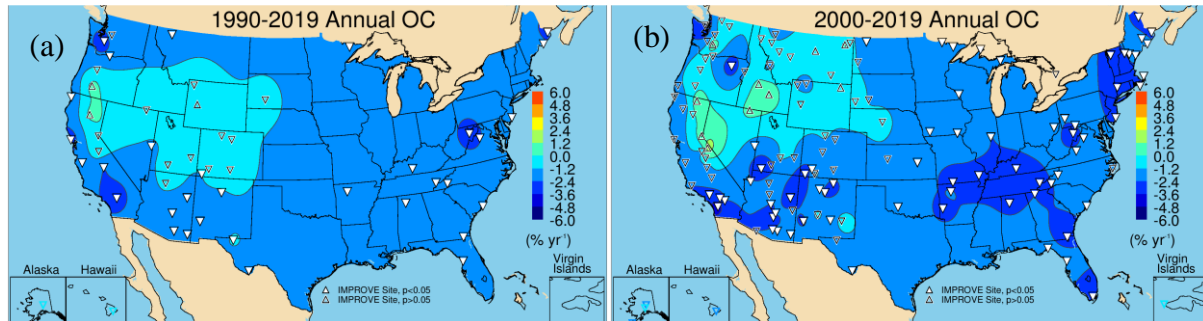


**Figure 6.3.1.** Annual mean organic carbon (OC) mass trends ( $\% \text{ yr}^{-1}$ ) for (a) long-term (1990–2019) and (b) short-term (2000–2019) periods. Filled triangles correspond to statistically significant trends ( $p \leq 0.05$ ).

Regional seasonal mean OC trends are shown in Figure 6.3.2. Statistically significant trends occurred during all seasons in the Southeast, Northeast, and the Midsouth regions, about  $-3\% \text{ yr}^{-1}$ . The strongest reductions in most these regions occurred for winter and spring. Trends in the Central region were lower ( $\sim -2\% \text{ yr}^{-1}$ ) than regions in the East and statistically significant in all seasons except summer. Seasonal mean trends at western regions were more variable than in the East. All of the winter and spring trends were statistically significant, and OC declined more strongly in these months ( $-3\% \text{ yr}^{-1}$  to  $-4\% \text{ yr}^{-1}$ ). Summer and fall trends were insignificant and summer trends were flat in the Northwest and California regions. Trends during these seasons have been influenced by biomass burning emissions.

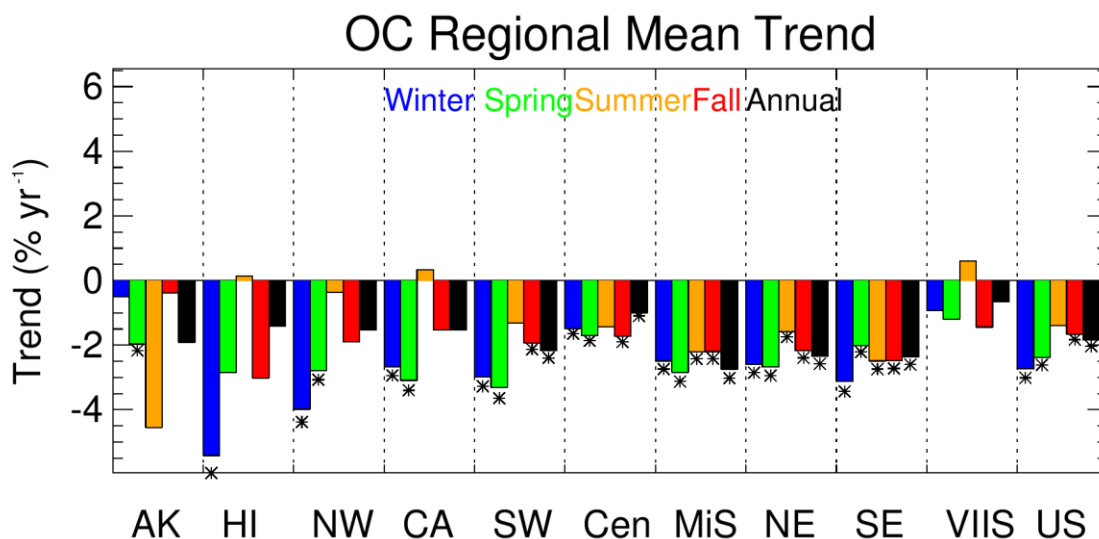


**Figure 6.3.2.** Short-term (2000–2019) regional seasonal mean organic carbon (OC) trends ( $\% \text{ yr}^{-1}$ ) for major U.S. regions for winter, spring, summer, fall, and annual means. Regions are arranged from western to eastern United States (AK = Alaska, HI = Hawaii, NW = Northwest, CA = California, SW = Southwest, Cen = Central, MiS = Midsouth, NE = Northeast, SE = Southeast, VIIS = Virgin Islands, and US = all sites). Statistically significant trends ( $p \leq 0.05$ ) are denoted with “\*\*”.

Differences in spatial patterns for long-term trends in the 10<sup>th</sup> and 90<sup>th</sup> percentile OC concentrations were evident from comparing Figure 6.3.3a and 6.3.3b, respectively. Reductions in the 10<sup>th</sup> percentile OC concentrations were much greater than for the 90<sup>th</sup> percentile concentrations, especially for sites in the West. Of the 51 long-term valid sites, 49 had statistically significant trends in 10<sup>th</sup> percentile OC concentrations. Strong reductions occurred at sites in northern California, Oregon, and Washington ( $-5\% \text{ yr}^{-1}$  to  $-6\% \text{ yr}^{-1}$ ), with the strongest at Mount Rainier NP, Washington (MORA1,  $-7.07\% \text{ yr}^{-1}$ ,  $p < 0.001$ ). However, sites across the United States experienced reductions around  $-2\% \text{ yr}^{-1}$  or greater. The lowest reduction occurred at Great Sand Dunes NP, Colorado (GRSA1,  $-1.01\% \text{ yr}^{-1}$ ,  $p = 0.02$ ). In contrast, 90<sup>th</sup> percentile trends at sites across the western United States were mostly insignificant, with over half (26) of the sites not meeting the statistical significance criterion. Ten of these sites were associated with positive but insignificant trends. These results suggest different influences on trends for different parts of the OC mass distribution. The trends in the highest OC concentrations were likely influenced by biomass burning impacts.

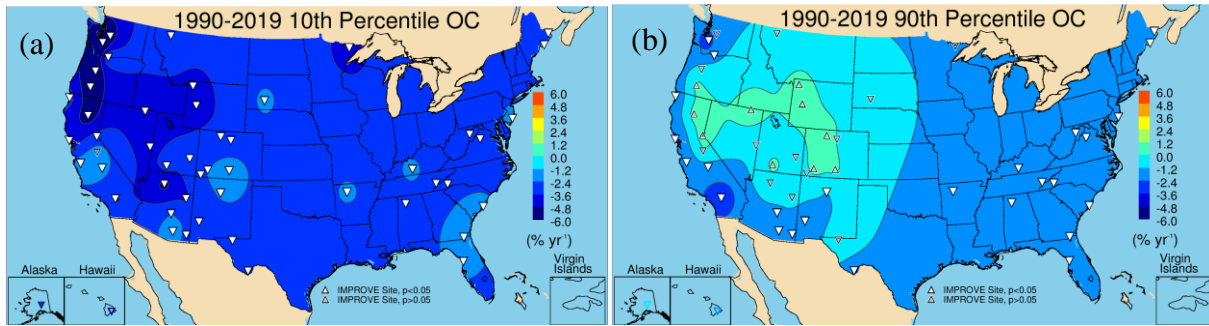


**Figure 6.3.3. IMPROVE long-term (1990–2020) trends ( $\% \text{ yr}^{-1}$ ) in (a) 10<sup>th</sup> percentile organic carbon (OC) concentrations and (b) 90<sup>th</sup> percentile concentrations. Filled triangles correspond to statistically significant trends ( $p \leq 0.05$ ).**

A similar spatial pattern occurred for short-term 10<sup>th</sup> and 90<sup>th</sup> percentile OC trends (Figure 6.3.4a and 6.3.4b, respectively). Most of the 10<sup>th</sup> percentile trends were statistically significant (90 out of 138 valid sites), and nearly all of these sites were in the eastern United States. Many of the trends at sites in the West were negative and insignificant, except for five sites. The greatest reductions occurred at North Absaroka, Wyoming (NOAB1,  $-11.68\% \text{ yr}^{-1}$ ,  $p = 0.009$ ), compared to the positive trend at Virgin Islands NP (VIIS1,  $12.76\% \text{ yr}^{-1}$ ,  $p = 0.011$ ). The strongly positive trend at VIIS1 is likely due to very low 10<sup>th</sup> percentile OC concentrations. Recall that trends were calculated by dividing the slope from the regression by the median of the concentration over the period, so sites with very low 10<sup>th</sup> percentile concentrations may have elevated trends.

While most of the sites in the eastern United States had statistically significant short-term 90<sup>th</sup> percentile trends, many of the sites in the West did not (51 out of 138 valid sites). Many of these same insignificant trend sites also had insignificant trends in annual mean OC; however, these sites did not have insignificant 10<sup>th</sup> percentile trends. It appears that the influences on the high OC concentrations were not similarly affecting the lowest OC concentrations over time. The strongest reductions in the 90<sup>th</sup> percentile trends occurred at Starkey, Oregon (STAR1,  $-4.22\% \text{ yr}^{-1}$ ,  $p = 0.03$ ), compared to  $-1.54\% \text{ yr}^{-1}$  ( $p = 0.003$ ) at Quaker City, Ohio (QUCI1).

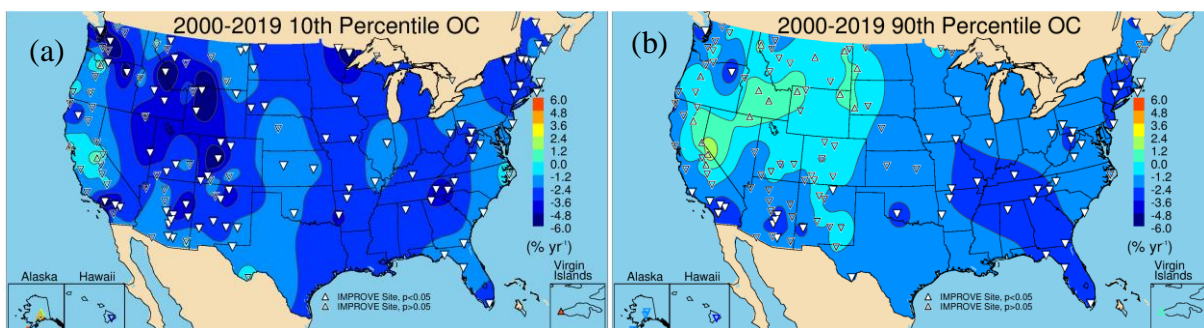


**Figure 6.3.4. IMPROVE short-term (2000–2019) trends ( $\% \text{ yr}^{-1}$ ) in (a) 10<sup>th</sup> percentile organic carbon (OC) concentrations and (b) 90<sup>th</sup> percentile concentrations. Filled triangles correspond to statistically significant trends ( $p \leq 0.05$ ).**

Differences in the trends in the 10<sup>th</sup> and 90<sup>th</sup> percentiles are shown in the regional mean percentile trends in Figure 6.3.5. The 90<sup>th</sup> percentile trends were the weakest and statistically

insignificant for regions in the West, such as the Northwest, California, and the Southwest regions. For regions in the East, the trends were similar for the lowest and highest OC concentrations, and all were statistically significant, indicating different influences on OC trends in the eastern and western United States, especially for the highest OC concentration in the West. Very large 10<sup>th</sup> percentile trends in the Virgin Islands and Hawaii regions were likely due to very low normalizing concentrations.

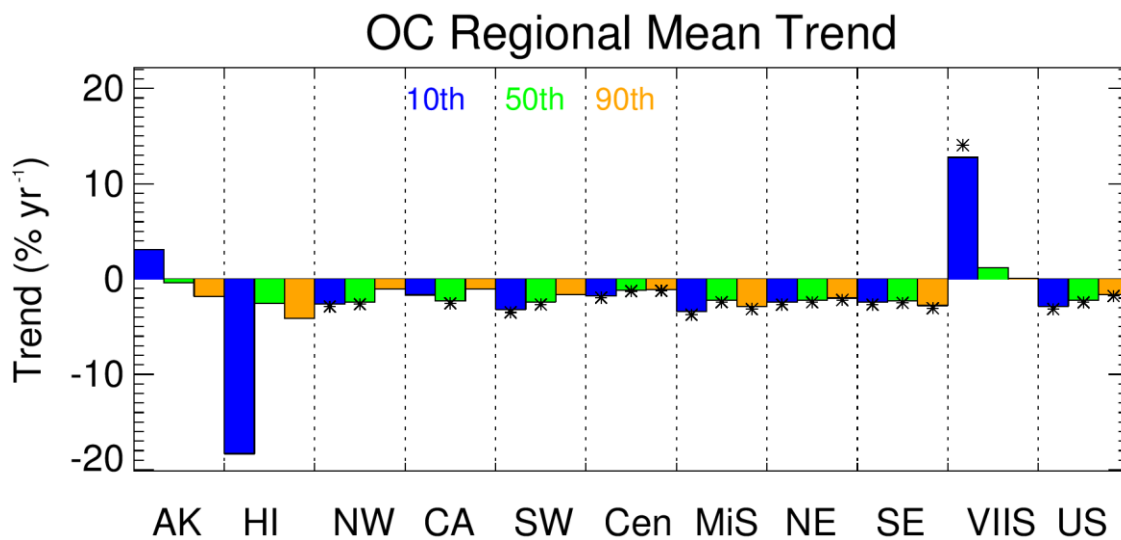


**Figure 6.3.5.** Short-term (2000-2019) regional mean trends (% yr<sup>-1</sup>) in 10<sup>th</sup>, 50<sup>th</sup>, and 90<sup>th</sup> percentile organic carbon (OC) concentrations. Regions are arranged from western to eastern United States (AK = Alaska, HI = Hawaii, NW = Northwest, CA = California, SW = Southwest, Cen = Central, MiS = Midsouth, NE = Northeast, SE = Southeast, VIIS = Virgin Islands, and US = all sites). Statistically significant trends ( $p \leq 0.05$ ) are denoted with “\*”.

#### 6.4 ELEMENTAL CARBON TRENDS

EC trends are affected by hardware and analytic changes, similar to issues that affect OC trends, as discussed in Section 6.3. In addition, Malm et al. (2020) suggested EC may be inadvertently and incorrectly assigned to the OC fraction during the thermal optical reflectance analysis, resulting in an underestimate of true EC concentrations. As discussed by Schichtel et al. (2021), EC concentrations have decreased at rural sites to the point that many sites have concentrations that are below the lower quantifiable limits (LQL, defined as  $3 \times$  minimum detection limit, MDL). From 2017 to 2019, about 30% of all EC concentrations were below the LQL. More sites in the West were below LQL than in the East. These low concentrations make tracking trends difficult, especially for the 10<sup>th</sup> percentile concentrations.

Long-term trends in annual mean EC are shown in Figure 6.4.1a. Of the 51 valid sites, 48 had statistically significant negative trends. The strongest reduction occurred at Hawaii Volcanoes NP, Hawaii (HAVO1,  $-6.23\% \text{ yr}^{-1}$ ,  $p < 0.001$ ), followed by Moosehorn NWR, Maine (MOOS1,  $-5.10\% \text{ yr}^{-1}$ ,  $p < 0.001$ ), compared to  $-1.4\% \text{ yr}^{-1}$  ( $p = 0.002$ ) at Guadalupe Mountains NP, Texas (GUMO1). EC concentrations decreased at a rate greater than  $-2\% \text{ yr}^{-1}$  at 41 long-term sites. The weakest trends occurred at sites in the West, and sites with insignificant trends

occurred in areas influenced by biomass smoke (Bridger WA, Wyoming, BRID1; Jarbidge WA, Nevada, JARB1; and Lassen Volcanic NP, LAVO1).

Of the 136 valid short-term sites, 102 had statistically significant negative trends (Figure 6.4.1b). Sites with the strongest reductions (-5 to -6%  $\text{yr}^{-1}$ ) were located in southern California, the northwestern United States, and regions of the northeastern United States. The Moosehorn NWR, Maine (MOOS1), site had the strongest reduction in EC (-7.77%  $\text{yr}^{-1}$ ,  $p < 0.001$ ) compared to -2.09%  $\text{yr}^{-1}$  ( $p = 0.03$ ) at Big Bend NP, Texas (BIBE1). Most of the statistically insignificant trends occurred in the West at sites influenced by biomass smoke and in northern Montana and North Dakota, where oil and gas development has been demonstrated to impact EC concentrations (Gebhart et al., 2018).

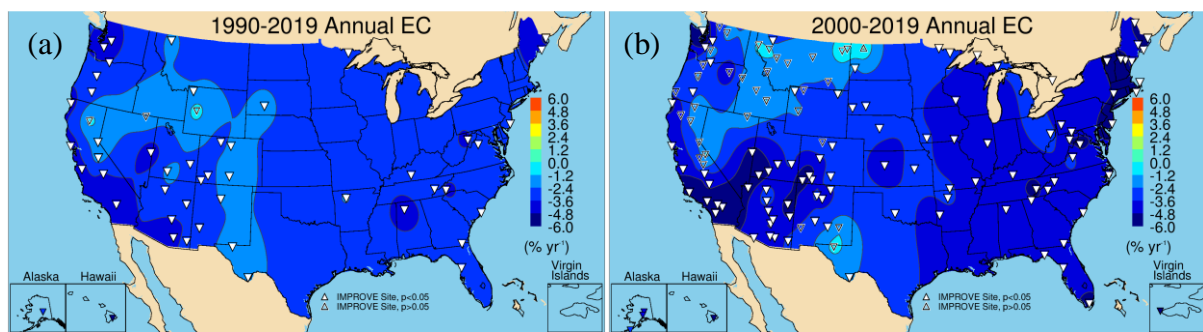


**Figure 6.4.1.** Annual mean elemental carbon (EC) mass trends ( $\text{yr}^{-1}$ ) for (a) long-term (1990–2019) and (b) short-term (2000–2019) periods. Filled triangles correspond to statistically significant trends ( $p \leq 0.05$ ).

A summary of short-term regional seasonal mean trends is shown in Figure 6.4.2. Negative trends occurred for all regions and seasons. Some of the strongest reductions occurred during all seasons in the Virgin Islands region. In regions in the eastern United States, the largest negative trends occurred during summer. Trends in the Southeast region were somewhat larger than other eastern regions, especially in winter and summer. The lowest negative trends occurred in the Central region, similar to OC trends. In the West, the strongest reductions in EC occurred mainly in winter and spring (e.g., California). Negative trends in the summer were weakest, and in the Northwest region were insignificant, likely reflecting the role of biomass smoke on EC concentrations. The difference in seasonal and regional trends implies different sources influencing EC depending on region.

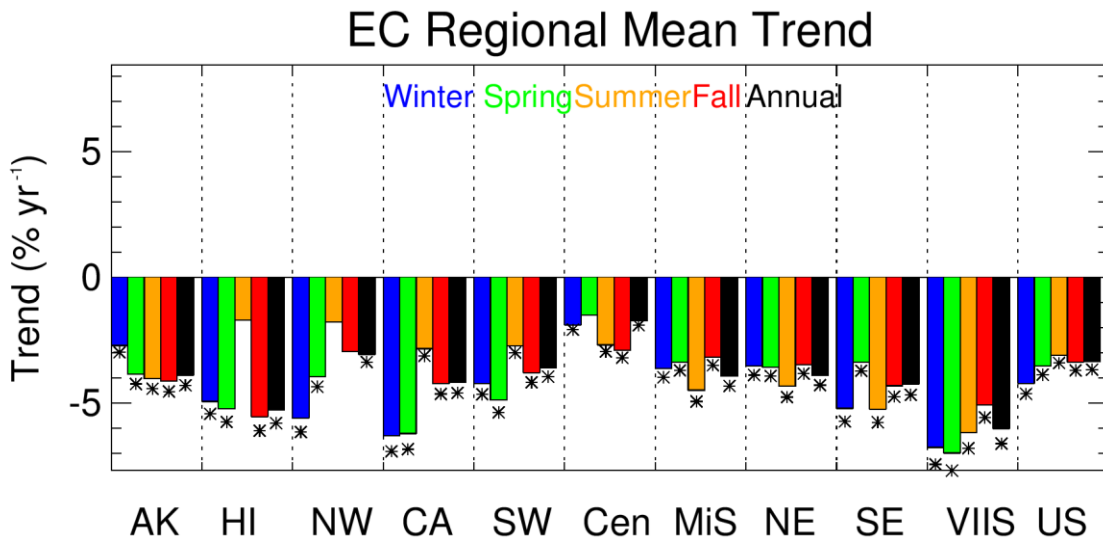


**Figure 6.4.2.** Short-term (2000–2019) regional seasonal mean elemental carbon (EC) trends ( $\% \text{ yr}^{-1}$ ) for major U.S. regions for winter, spring, summer, fall, and annual means. Regions are arranged from western to eastern United States (AK = Alaska, HI = Hawaii, NW = Northwest, CA= California, SW = Southwest, Cen = Central, MiS = Midsouth, NE = Northeast, SE = Southeast, VIIS = Virgin Islands, and US = all sites). Statistically significant trends ( $p \leq 0.05$ ) are denoted with “\*\*”.

Long-term trends in 10<sup>th</sup> and 90<sup>th</sup> percentile EC concentrations are shown in Figure 6.4.3a and 6.4.3b, respectively. The strongest reductions in the 10<sup>th</sup> percentile EC concentrations occurred at sites in the western United States. Of the 51 valid sites, 47 had statistically significant trends. Insignificant trends occurred at Bridger WA, Wyoming (BRID1); Point Reyes NP, California (PORE1); Guadalupe Mountains NP, Texas (GUMO1); and Jarbidge WA, Nevada (JARB1). The largest negative trend occurred at Hawaii Volcanoes NP, Hawaii (HAVO1,  $-15.46\% \text{ yr}^{-1}$ ,  $p = 0.006$ ), likely due to normalization by very low EC concentrations, followed by Three Sisters WA, Oregon (THSI1,  $-9.09\% \text{ yr}^{-1}$ ,  $p = 0.009$ ). The weakest negative trend occurred at Glacier NP, Montana (GLAC1,  $-2.16\% \text{ yr}^{-1}$ ,  $p = 0.003$ ).

The 90<sup>th</sup> percentile EC concentrations declined at all of the valid long-term sites, with 46 of the 51 sites having statistically significant trends. The strongest reductions were around  $-4\% \text{ yr}^{-1}$ , at sites in the northwestern United States, northeastern United States, and southern California. The strongest trend occurred at Saguaro NM, Arizona (SAGU1,  $-4.83\% \text{ yr}^{-1}$ ,  $p < 0.001$ ), and the weakest at Great Sand Dunes NP, Colorado (GRSA1,  $-0.95\% \text{ yr}^{-1}$ ,  $p = 0.02$ ). Sites in Intermountain West and parts of California corresponded to weak and insignificant trends.

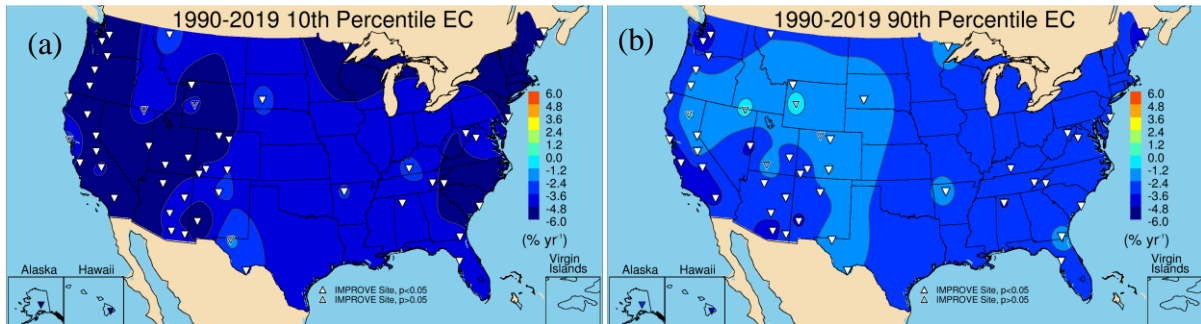


**Figure 6.4.3. IMPROVE long-term (1990–2019) trends ( $\% \text{ yr}^{-1}$ ) in (a) 10<sup>th</sup> percentile elemental carbon (EC) concentrations and (b) 90<sup>th</sup> percentile concentrations. Filled triangles correspond to statistically significant trends ( $p \leq 0.05$ ).**

Reductions in the 10<sup>th</sup> percentile EC occurred across the United States for short-term sites (Figure 6.4.4a). Recall that EC concentrations at many sites, especially in the West, may be below LQL, and therefore trends may be more uncertain. In addition, the normalized trend may be large because the normalizing concentration over the period is very low. Short-term trends in the 90<sup>th</sup> percentile EC concentrations are shown in Figure 6.4.4b. The strongest reduction occurred at San Gorgonio WA, California (SAGO1,  $-7.57\% \text{ yr}^{-1}$ ,  $p < 0.001$ ), compared to  $-1.92\% \text{ yr}^{-1}$  ( $p = 0.04$ ) at Theodore Roosevelt NP, North Dakota (THRO1). Insignificant trends occurred at sites across the Intermountain West and northwestern United States. Some of these sites may be influenced by biomass smoke, and some, like THRO1, may be influenced by oil and gas development (Gebhart et al., 2018). Six sites in these regions had positive, although insignificant, trends. Out of the 138 valid sites, 96 had statistically significant trends. Strong reductions in 90<sup>th</sup> percentile EC occurred at sites in southern California and at sites in the northeastern and northwestern United States.

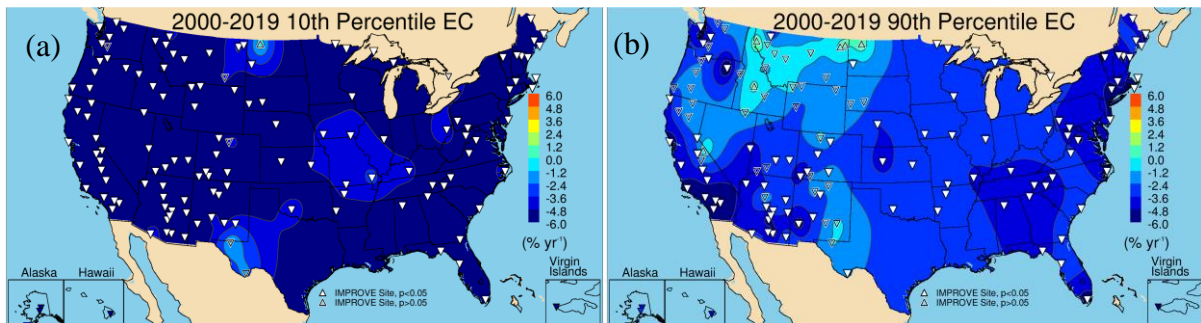


**Figure 6.4.4. IMPROVE short-term (2000–2019) trends ( $\% \text{ yr}^{-1}$ ) in (a) 10<sup>th</sup> percentile elemental carbon (EC) concentrations and (b) 90<sup>th</sup> percentile concentrations. Filled triangles correspond to statistically significant trends ( $p \leq 0.05$ ).**

Regional mean trends in percentile concentrations are shown in Figure 6.4.5. For nearly all regions, the 10<sup>th</sup> percentile trends were the greatest, although these are likely affected by low concentrations (e.g., sites in Alaska, Hawaii, and Virgin Islands). For most regions, the 90<sup>th</sup> percentile concentrations decreased at a lower rate than the median concentrations. Both the Northwest and Alaska regions had insignificant trends in 90<sup>th</sup> percentile EC concentrations, perhaps related to increased smoke impacts.

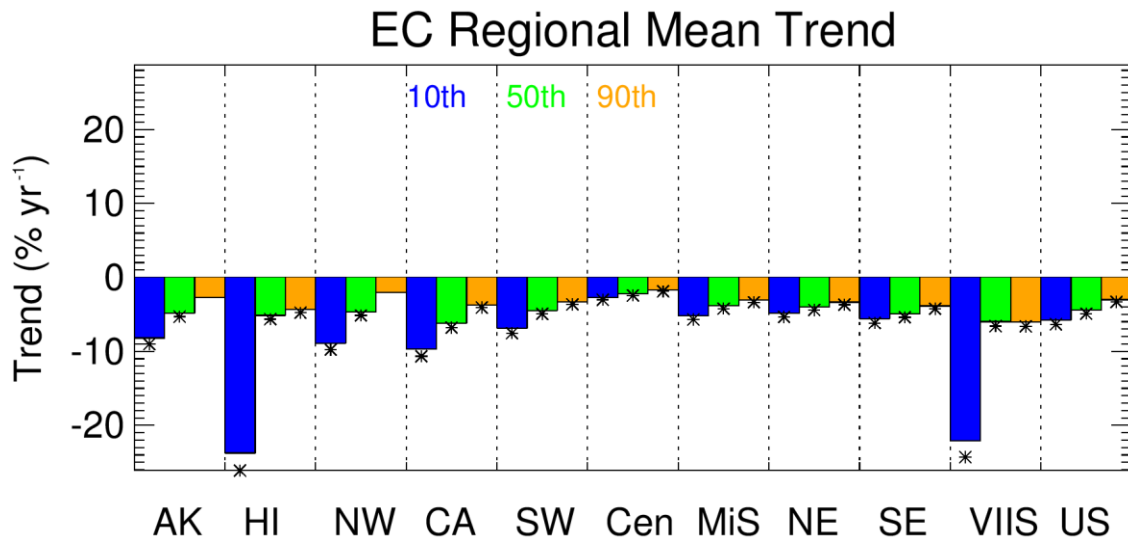


**Figure 6.4.5.** Short-term (2000–2019) regional mean trends ( $\% \text{ yr}^{-1}$ ) in  $10^{\text{th}}$ ,  $50^{\text{th}}$ , and  $90^{\text{th}}$  percentile elemental carbon (EC) percentile concentrations. Regions are arranged from western to eastern United States (AK = Alaska, HI = Hawaii, NW = Northwest, CA = California, SW = Southwest, Cen = Central, MiS = Midsouth, NE = Northeast, SE = Southeast, VIIS = Virgin Islands, and US = all sites). Statistically significant trends ( $p \leq 0.05$ ) are denoted with “\*\*”.

## 6.5 FINE DUST MASS TRENDS

Recall from Chapter 2.1 that FD concentrations were determined by combining the oxides of elemental mass concentrations of Al, Si, Ca, Fe, and Ti (see Table 2.1). The analytical methods used to determine these species have evolved over time and included PIXE (proton induced X-ray emission) and XRF (X-ray fluorescence) techniques. The transitions from PIXE to XRF methods, the change in XRF anodes from Mo to Cu, as well as different calibration procedures affect the data by changing MDLs (Hyslop et al., 2015). In 2011, the analysis method switched to the PANalytical XRF system that resolved issues related to undetected Al with concentrations above the MDL (White, 2006). Before 2011, XRF data below the MDL were replaced by  $0.5 \times \text{MDL}$ . Changes in analytical methods may not equally affect data for each FD species; therefore, the integrated dust concentration may be less susceptible to possible variability introduced by the analytical methods, although this has not been specifically demonstrated.

Long-term and short-term annual mean FD trends are shown in Figures 6.5.1a and 6.5.1b, respectively. Roughly 40% of long-term trends were insignificant (23 out of 56 valid sites); nearly all of these were located at sites in the western United States, and many (12) of them were positive. In the West, statistically significant reductions in FD occurred in California, Oregon, Washington State, Wyoming, and Colorado. Across the eastern United States, FD decreased at all sites. The strongest reductions occurred at Yellowstone NP, Wyoming (YELL1,  $-3.94\% \text{ yr}^{-1}$ ,  $p < 0.001$ ), compared to an increase in FD at Guadalupe Mountains NP, Texas (GUMO1,  $1.22\% \text{ yr}^{-1}$ ,  $p = 0.05$ ).

Annual mean trends in FD for 2000–2019 were significantly negative at sites across the eastern United States, especially at sites in the northeastern United States, and across the Intermountain West and northwestern United States. Out of 134 sites, 68 had statistically significant trends. These ranged from  $-6.04\% \text{ yr}^{-1}$  ( $p < 0.001$ ) in Great Gulf WA, New Hampshire (GRGU1), to  $-1.57\% \text{ yr}^{-1}$  ( $p = 0.03$ ) at Northern Cheyenne, Montana (NOCH1). Many of the insignificant trends were positive (11) at sites near the Central Valley of California, Oklahoma, Texas, Oregon, and North Dakota. Many of the sites in the southwestern United States had statistically insignificant trends.

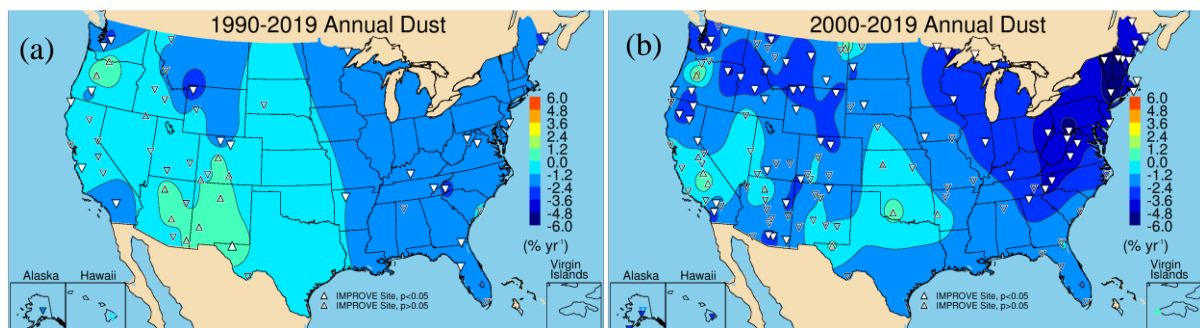


**Figure 6.5.1 Annual mean fine dust mass trends ( $\% \text{ yr}^{-1}$ ) for (a) long-term (1990–2019) and (b) short-term (2000–2019) periods. Filled triangles correspond to statistically significant trends ( $p \leq 0.05$ ).**

Compared to other species, trends in FD showed greater seasonal and spatial variability. Trends were mostly insignificant and generally not strongly negative as is the case for other species. The Northeast region was the only region with statistically significant trends during all seasons. The Southeast region had statistically significant reductions in FD during all seasons except summer. Similarly, the Midsouth region had insignificant but positive trends during summer; this is the season with impacts from North African dust transport. In the Central region, only winter and spring corresponded to statistically significant negative trends. Across the West, regions were associated with insignificant though negative trends. The California region had insignificant but positive trends during summer, and the summer trends in the Northwest region were flat. FD has not experienced the levels of reduction that have occurred for other species.

## Dust Regional Mean Trend

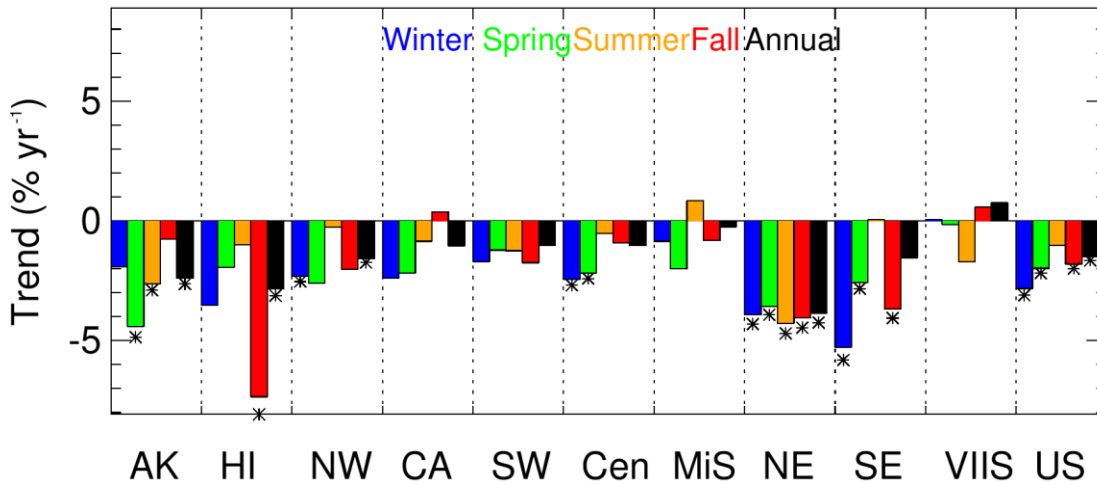


Figure 6.5.2. Short-term (2000–2019) regional seasonal mean fine dust mass trends ( $\% \text{ yr}^{-1}$ ) for major U.S. regions for winter, spring, summer, fall, and annual means. Regions are arranged from western to eastern United States (AK = Alaska, HI = Hawaii, NW = Northwest, CA = California, SW = Southwest, Cen = Central, MiS = Midsouth, NE = Northeast, SE = Southeast, VIIS = Virgin Islands, and US = all sites). Statistically significant trends ( $p \leq 0.05$ ) are denoted with “\*\*”.

Long-term trends in the 10<sup>th</sup> percentile FD concentrations are shown in Figure 6.5.3a. For most of the United States, sites experienced reductions in the lowest FD concentrations. Of the 59 valid sites, 46 had statistically significant trends, ranging from  $-6.25\% \text{ yr}^{-1}$  ( $p < 0.001$ ) in Three Sisters WA, Oregon (THSI1), to  $1.80\% \text{ yr}^{-1}$  ( $p = 0.010$ ) in Guadalupe Mountains NP, Texas (GUMO1). All of the insignificant trends occurred at sites in the southwestern United States. In contrast, for the 90<sup>th</sup> percentile, of the 59 valid sites only 17 had statistically significant trends, and many of these sites were in the eastern United States (Figure 6.5.3b). Sites across the southwestern United States were associated with positive although insignificant trends. Trends in the 90<sup>th</sup> percentile FD ranged from  $-3.78\% \text{ yr}^{-1}$  ( $p < 0.001$ ) at Yellowstone NP, Wyoming (YELL1), to  $2.38\% \text{ yr}^{-1}$  ( $p = 0.011$ ) at Columbia River Gorge, Washington (CORI1).

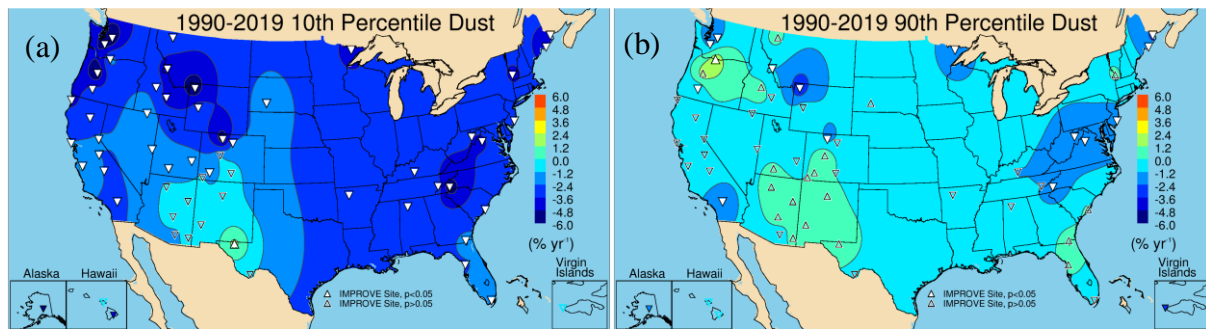
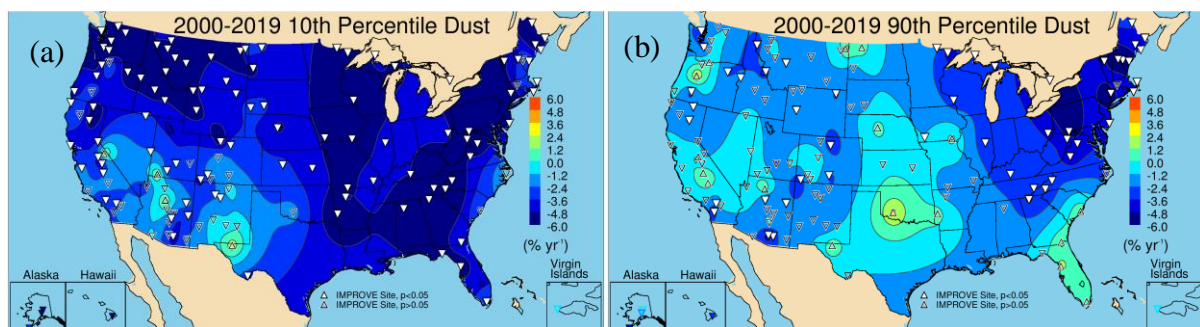


Figure 6.5.3. IMPROVE long-term (1990–2019) trends ( $\% \text{ yr}^{-1}$ ) in (a) 10<sup>th</sup> percentile fine dust concentrations and (b) 90<sup>th</sup> percentile concentrations. Filled triangles correspond to statistically significant trends ( $p \leq 0.05$ ).

Short-term trends in 10<sup>th</sup> percentile FD concentrations were negative at sites across the United States, with stronger reductions across the eastern and Intermountain West and

northwestern United States (Figure 6.5.4a). Insignificant trends occurred at 34 sites out of 137 valid sites, and most of these were in the southwestern United States. Trends ranged from  $-9.34\% \text{ yr}^{-1}$  ( $p = 0.006$ ) at White Pass, Washington (WHPA1), to  $-1.72\% \text{ yr}^{-1}$  ( $p = 0.019$ ) at Pinnacles NM, California (PINN1).

Most of the short-term 90<sup>th</sup> percentile trends in FD at sites in the West were insignificant (Figure 6.5.4b), with 84 insignificant trends out of 137 valid sites. Positive though insignificant trends occurred at sites in the central United States, the Central Valley of California, Oregon, the northern Great Plains, and Florida. The 90<sup>th</sup> percentile trends ranged from  $-6.67\% \text{ yr}^{-1}$  ( $p < 0.001$ ) at Great Gulf WA, New Hampshire (GRGU1), to  $-1.18\% \text{ yr}^{-1}$  ( $p = 0.013$ ) at Viking Lake, Iowa (VILA1). Comparisons of trends from these two maps suggests that the influences that govern the FD trend 10<sup>th</sup> and 90<sup>th</sup> percentiles are different, although low 10<sup>th</sup> percentile concentrations could also play a role.



**Figure 6.5.4.** IMPROVE short-term (2000–2019) trends ( $\% \text{ yr}^{-1}$ ) in (a) 10<sup>th</sup> percentile fine dust concentrations and (b) 90<sup>th</sup> percentile concentrations. Filled triangles correspond to statistically significant trends ( $p \leq 0.05$ ).

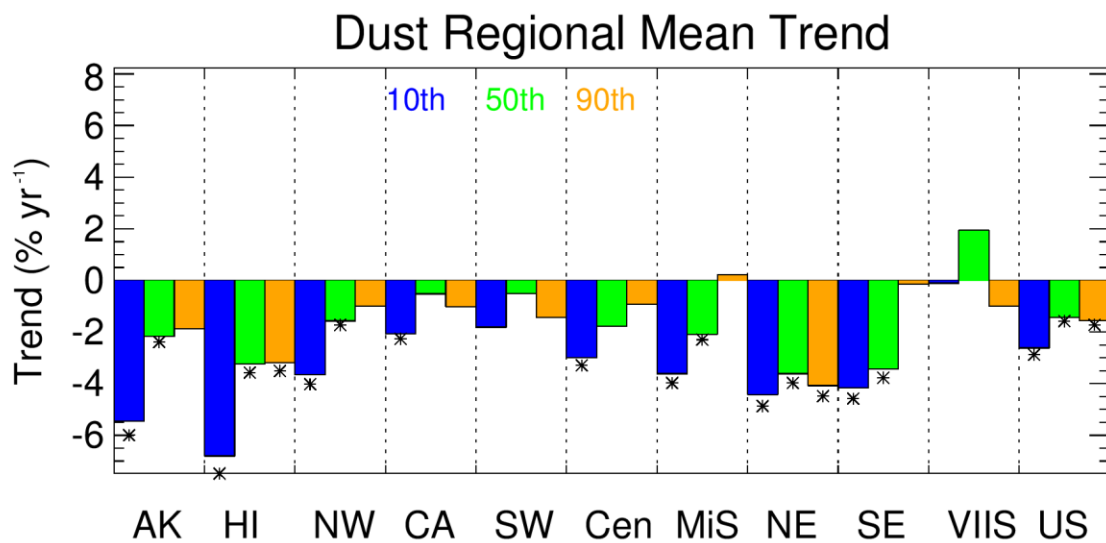


**Figure 6.5.5.** Short-term (2000–2019) regional mean trends ( $\% \text{ yr}^{-1}$ ) trends in 10<sup>th</sup>, 50<sup>th</sup>, and 90<sup>th</sup> percentile fine dust concentrations. Regions are arranged from western to eastern United States (AK = Alaska, HI = Hawaii, NW = Northwest, CA = California, SW = Southwest, Cen = Central, MiS = Midsouth, NE = Northeast, SE = Southeast, VIIS = Virgin Islands, and US = all sites). Statistically significant trends ( $p \leq 0.05$ ) are denoted with “\*”.

For most regions, the 10<sup>th</sup> percentile FD trends were strongest, which may be in part due to low 10<sup>th</sup> percentile FD concentrations (Figure 6.5.5). For nearly all regions, the 90<sup>th</sup> percentile trends were insignificant (except the Northeast and Hawaii regions). These insignificant trends may imply that the influences on the highest FD concentrations have not decreased steadily to result in statistically significant negative trends. For other regions in the West, such as the California, Southwest, and Central regions, the median trends were also insignificant.

## 6.6 GRAVIMETRIC PM<sub>2.5</sub> FINE MASS TRENDS

Trends in PM<sub>2.5</sub> fine mass (FM) may be driven by trends in a particular species, depending on the degree of its contribution; however, inferring FM trends based on the trends of other species is complicated because of the spatial and seasonal variability of a specific species relative to another. The statistical significance level of trends at a given site differs for each species and for FM trends, complicating comparisons of trends from different species at a specific location. In addition, sampling or analytical artifacts, such as particle bound water, may influence FM trends (see Chapter 1, Section 1.3.1.2). For example, beginning in 2011, higher laboratory relative humidity during weighing resulted in an increase in particle bound water associated with FM data (White, 2016). This issue was resolved in 2019, but it may influence trends in FM (Hand et al., 2019).

Long-term trends in annual mean FM are shown in Figure 6.6.1a. Of the 56 valid sites, 44 had statistically significant trends, ranging from -4.39% yr<sup>-1</sup> ( $p < 0.001$ ) at Shining Rock WA, North Carolina (SHRO1), to -0.85% yr<sup>-1</sup> ( $p < 0.001$ ) at Tonto NM, Arizona (TONT1). The strongest trends occurred at sites in the eastern United States, likely associated with reductions in sulfate concentrations (see Figure 6.1.1a). Most of the insignificant trends occurred in the western United States, similar to trends in OC (Figure 6.3.1a).

Short-term trends in annual mean FM are shown in Figure 6.6.1b. The spatial pattern in short-term trends follows that of long-term trends, with the strongest reduction in FM at sites in the eastern United States, again, likely associated with sulfate reductions. Of the 134 valid short-term sites, only 78 were associated with statistically significant trends, and nearly all of the insignificant trends occurred at sites in the western United States, especially at sites in the Intermountain West, northwestern United States, and northern California, where OC trends were also insignificant. Sites in southern California had strong negative trends, likely associated with nitrate ion reductions. The short-term trends ranged from -5.79% yr<sup>-1</sup> ( $p < 0.001$ ) at Frostburg Reservoir, Maryland (FRRE1), to -1.02 % yr<sup>-1</sup> ( $p = 0.016$ ) at Theodore Roosevelt NP, North Dakota (THRO1).

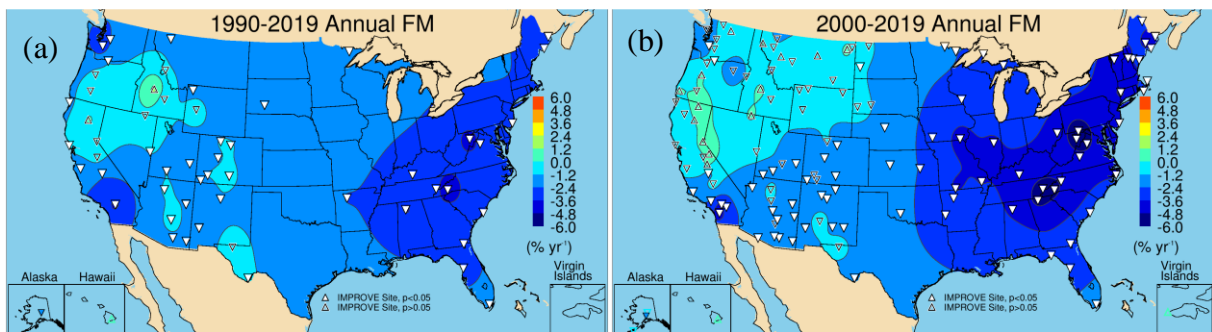


**Figure 6.6.1.** Annual mean gravimetric PM<sub>2.5</sub> fine mass (FM) trends (% yr<sup>-1</sup>) for (a) long-term (1990–2019) and (b) short-term (2000–2019) periods. Filled triangles correspond to statistically significant trends ( $p \leq 0.05$ ).

The short-term regional seasonal mean trends in the eastern United States were similar to regional seasonal mean sulfate trends (compare Figure 6.6.2 to Figure 6.1.2). The strongest reductions in FM occurred in the Northeast and Southeast regions (-4% yr<sup>-1</sup> to -5% yr<sup>-1</sup>). Trends were weaker moving west, and in regions such as the Northwest and California, FM trends were similar to OC trends. Summer and fall trends in these regions were insignificant and positive, indicating the role of biomass smoke in FM trends. In the Southwest region, all of the seasons except summer had statistically significant reductions in FM. Only summer had an insignificant (negative) trend, similar to both OC and FD trends.

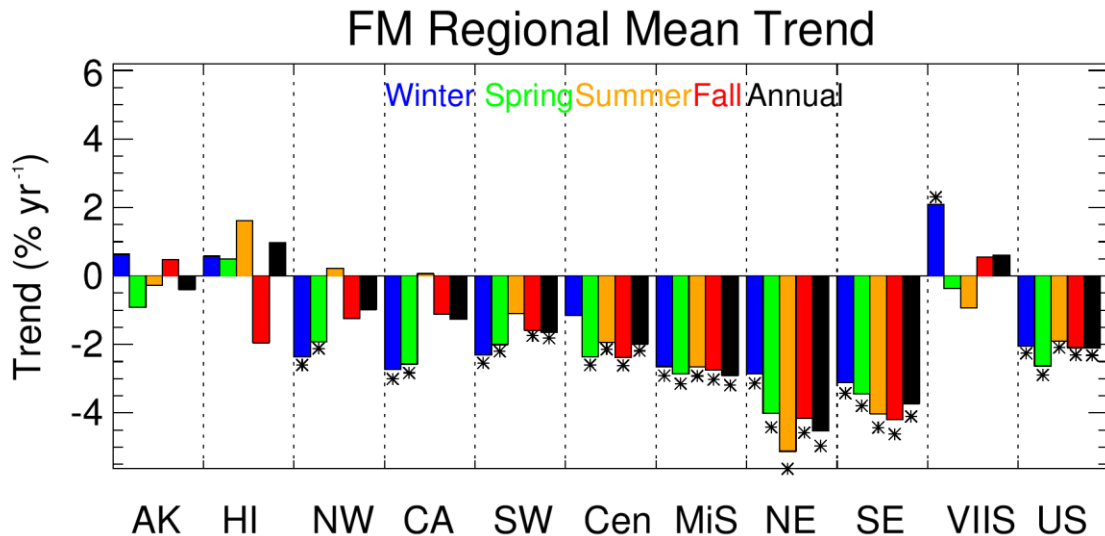


**Figure 6.6.2.** Short-term (2000–2019) regional seasonal mean gravimetric PM<sub>2.5</sub> fine mass (FM) trends (% yr<sup>-1</sup>) for major U.S. regions for winter, spring, summer, fall, and annual means. Regions are arranged from western to eastern United States (AK = Alaska, HI = Hawaii, NW = Northwest, CA = California, SW = Southwest, Cen = Central, MiS = Midsouth, NE = Northeast, SE = Southeast, VIIS = Virgin Islands, and US = all sites). Statistically significant trends ( $p \leq 0.05$ ) are denoted with “\*”.

Long-term trends in 10<sup>th</sup> percentile FM concentrations are shown in Figure 6.6.3a. All but four of the 58 valid sites had statistically significant trends. The lowest reductions occurred at sites in California and in the southwestern United States. The strongest reductions occurred at

Snoqualmie Pass, Washington (SNPA1,  $-5.93\% \text{ yr}^{-1}$ ,  $p < 0.001$ ), and the weakest reductions occurred at Guadalupe Mountains NP, Texas (GUMO1,  $-0.75\% \text{ yr}^{-1}$ ,  $p = 0.05$ ).

The long-term 90<sup>th</sup> percentile trends are shown in Figure 6.6.3b. More sites had insignificant trends (19 sites) and most of them were in the western United States, especially in the northwestern United States, likely influenced by OC trends given similarities in their spatial patterns. Strong reductions at sites in the eastern United States were likely influenced by sulfate reductions. The trends in 90<sup>th</sup> percentile FM ranged from  $-4.83\% \text{ yr}^{-1}$  ( $p < 0.001$ ) at Shining Rock WA, North Carolina (SHRO1), to  $-0.71\% \text{ yr}^{-1}$  ( $p = 0.02$ ) at Tonto NM, Arizona (TONT1); these maximum and minimum trends occurred at the same sites as for annual mean trends.

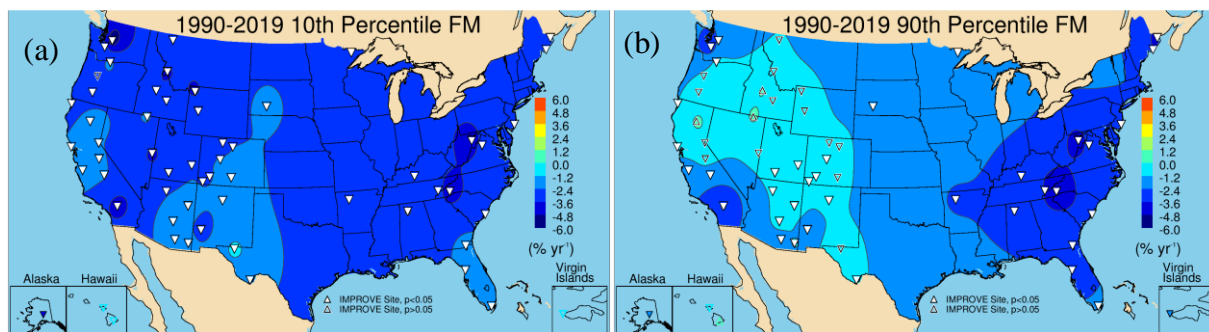


**Figure 6.6.3. IMPROVE long-term (1990–2019) trends ( $\% \text{ yr}^{-1}$ ) in (a) 10<sup>th</sup> percentile gravimetric PM<sub>2.5</sub> fine mass (FM) concentrations and (b) 90<sup>th</sup> percentile concentrations. Filled triangles correspond to statistically significant trends ( $p \leq 0.05$ ).**

Of the 137 valid short-term sites for the 10<sup>th</sup> percentile trends in FM, 101 were statistically significant (Figure 6.6.4a). All of the trends for sites in the eastern United States were negative and statistically significant, with the strongest reductions at sites along the Ohio River valley and Appalachia areas. Reductions also occurred at sites in the northwestern United States. Insignificant trends occurred at sites in California and Oregon. Trends in the 10<sup>th</sup> percentile FM ranged from  $-5.31\% \text{ yr}^{-1}$  ( $p < 0.001$ ) at Dolly Sods WA, West Virginia (DOSO1), to  $-1.14\% \text{ yr}^{-1}$  ( $p = 0.03$ ) at Organ Pipe, Arizona (ORPI1).

Spatial patterns in the short-term 90<sup>th</sup> percentile FM trends were similar to those for OC trends in the western United States and sulfate trends in the eastern United States (Figure 6.6.4b). The strongest reductions occurred at sites in the East ( $-8.36\% \text{ yr}^{-1}$ ,  $p < 0.001$  at Frostburg Reservoir, Maryland, FRRE1). Of the 137 valid sites, 67 had trends that were statistically insignificant, and nearly all of these occurred in the western United States, especially in the northwestern United States, California, and Oregon, where biomass smoke has influenced OC as well as FM trends. The weakest reduction occurred at Voyageurs NP, Minnesota, (VOYA2,  $-0.78\% \text{ yr}^{-1}$ ,  $p = 0.04$ ).

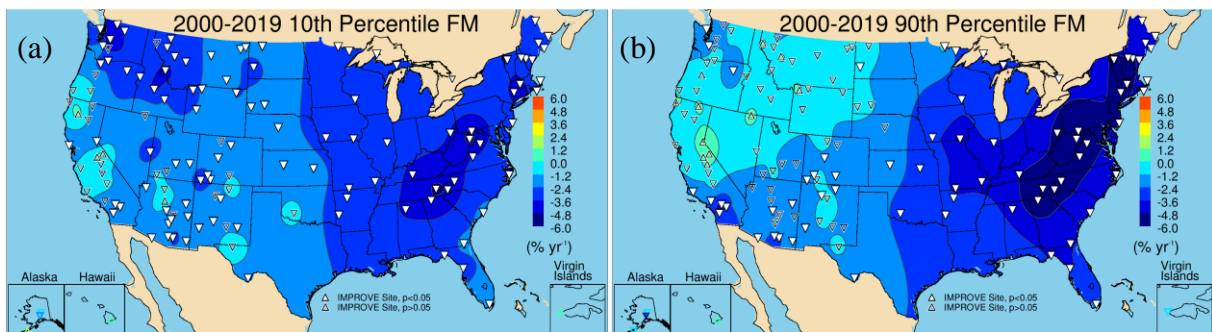


**Figure 6.6.4. IMPROVE short-term (2000–2019) trends ( $\% \text{ yr}^{-1}$ ) in (a) 10<sup>th</sup> percentile gravimetric PM<sub>2.5</sub> fine mass (FM) concentrations and (b) 90<sup>th</sup> percentile concentrations. Filled triangles correspond to statistically significant trends ( $p \leq 0.05$ ).**

The strongest short-term regional FM percentile trends occurred in the Northeast and Southeast regions (Figure 6.6.5). In both regions, the 90<sup>th</sup> percentile FM concentrations decreased most strongly (-4%  $\text{yr}^{-1}$  to -5%  $\text{yr}^{-1}$ ), especially in the Northeast region, likely related to sulfate reductions. Recall that the summer seasonal mean trends were also greatest in the Northeast region (Figure 6.6.2). In the western United States, 90<sup>th</sup> percentile reductions were either insignificant and/or the lowest of the 10<sup>th</sup> and 50<sup>th</sup> percentiles, due to the impacts of OC trends from biomass smoke influence. In both the Northwest and Southwest regions, the lowest FM concentrations decreased at a faster rate. Trends at OCONUS regions (outside CONUS) were insignificant.

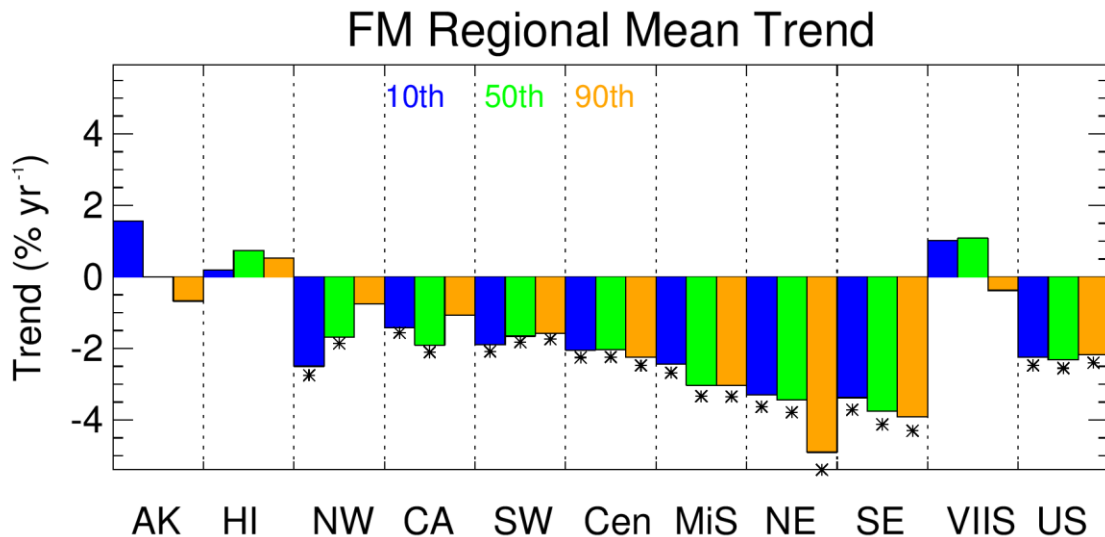


**Figure 6.6.5. Short-term (2000–2019) regional mean trends ( $\% \text{ yr}^{-1}$ ) in 10<sup>th</sup>, 50<sup>th</sup>, and 90<sup>th</sup> percentile gravimetric PM<sub>2.5</sub> fine mass (FM) concentrations. Regions are arranged from western to eastern United States (AK = Alaska, HI = Hawaii, NW = Northwest, CA = California, SW = Southwest, Cen = Central, MiS = Midsouth, NE = Northeast, SE = Southeast, VIIS = Virgin Islands, and US = all sites). Statistically significant trends ( $p \leq 0.05$ ) are denoted with “\*”.**

## 6.7 PM<sub>10</sub> TRENDS

PM<sub>10</sub> concentrations are determined gravimetrically and correspond to particles with an aerodynamic diameter less than 10  $\mu\text{m}$ . PM<sub>10</sub> mass concentrations include all the species presented in the previous sections, in addition to coarse mass, and are similar to PM<sub>2.5</sub> trends except for when contributions from CM are significant.

The spatial pattern in long-term annual mean PM<sub>10</sub> trends was similar to the annual mean FM trends pattern (Figure 6.7.1a). The strongest reductions occurred at sites in the eastern United States and in southern California. Of the 49 valid sites, 37 had statistically significant trends. Sites with lower and insignificant trends occurred in California, Oregon, and Nevada, similar to FM trends. However, unlike for FM trends, sites in the southwestern United States also had insignificant trends, likely associated with CM. Trends in PM<sub>10</sub> ranged from -3.70%  $\text{yr}^{-1}$  ( $p < 0.001$ ) at Dolly Sods WA, West Virginia (DOSO1), to -0.93%  $\text{yr}^{-1}$  ( $p = 0.02$ ) at Big Bend NP, Texas (BIBE1).

The differences in trends between the eastern and western United States also existed for short-term trends in annual mean PM<sub>10</sub>, with the strongest trends at sites in the eastern United States, due to sulfate reductions (Figure 6.7.1b). Positive but insignificant trends occurred at sites in California, Oregon, Washington, northern Montana, and North Dakota. This spatial pattern was similar to FM trends, except for the addition of insignificant PM<sub>10</sub> trends at sites in the southwestern and central United States, likely associated with CM. The strongest reduction occurred at Frostburg Reservoir, Maryland (FRRE1, -4.02%  $\text{yr}^{-1}$ ,  $p < 0.001$ ), and annual mean PM<sub>10</sub> increased at Three Sisters WA, Oregon (1.73%  $\text{yr}^{-1}$ ,  $p = 0.03$ ).

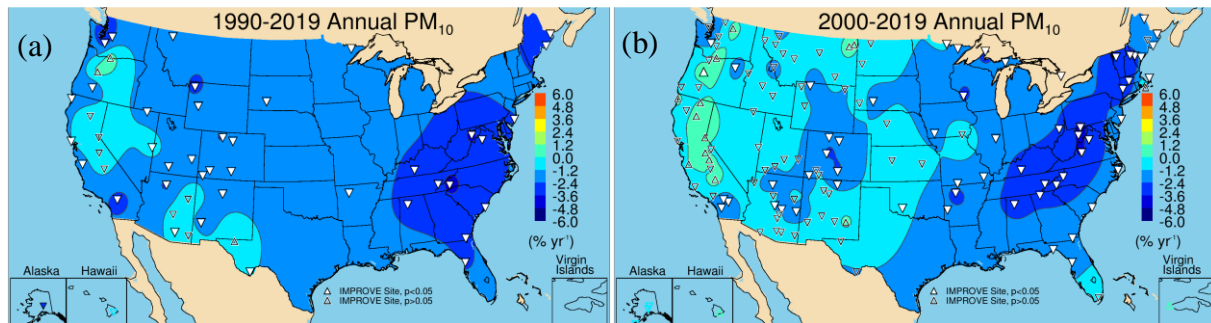
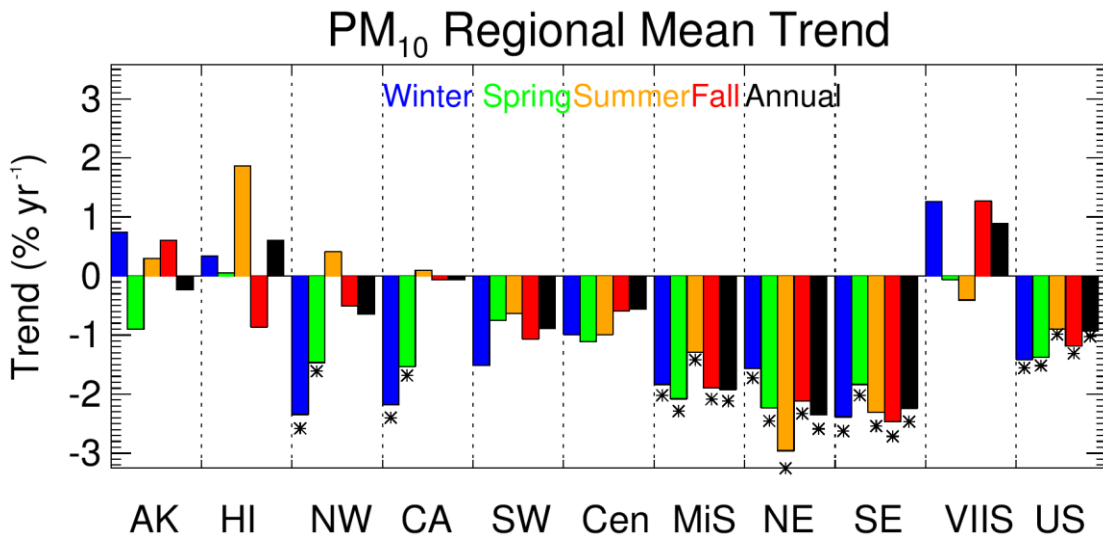


Figure 6.7.1. Annual mean gravimetric PM<sub>10</sub> mass trends (%  $\text{yr}^{-1}$ ) for (a) long-term (1990–2019) and (b) short-term (2000–2019) periods. Filled triangles correspond to statistically significant trends ( $p \leq 0.05$ ).

Comparisons of short-term regional and seasonal mean trends in PM<sub>10</sub> are shown in Figure 6.7.2. The strong reductions in PM<sub>10</sub> in eastern regions (-2%  $\text{yr}^{-1}$  to -3%  $\text{yr}^{-1}$ ) were similar to those for FM, suggesting that in the Northeast and Southeast regions, PM<sub>10</sub> trends were largely driven by FM species. None of the seasonal mean trends in the Central region was statistically significant, unlike for FM trends, suggesting the additional role of CM in that region. This was also apparent for the Southwest region. In the California region, both winter and spring PM<sub>10</sub> and FM trends were similar, suggesting trends in those seasons were driven by FM trends. However, summer and fall PM<sub>10</sub> trends in the California region were flat and insignificant, while FM trends were either flat or negative but insignificant. All of the seasonal mean trends in the Southwest region were insignificant, unlike FM trends.



**Figure 6.7.2.** Short-term (2000–2019) regional seasonal mean gravimetric PM<sub>10</sub> mass trends (% yr<sup>-1</sup>) for major U.S. regions for winter, spring, summer, fall, and annual means. Regions are arranged from western to eastern United States (AK = Alaska, HI = Hawaii, NW = Northwest, CA = California, SW = Southwest, Cen = Central, MiS = Midsouth, NE = Northeast, SE = Southeast, VIIS = Virgin Islands, and US = all sites). Statistically significant trends ( $p \leq 0.05$ ) are denoted with “\*\*”.

The long-term 10<sup>th</sup> percentile trends in PM<sub>10</sub> are shown in Figure 6.7.3a. Nearly all of the trends at 50 valid sites were statistically significant, with the only insignificant trend at Guadalupe Mountains NP, Texas (GUMO1). The strongest reductions occurred at sites in the Intermountain West and Northwest, and trends ranged from -7.40% yr<sup>-1</sup> ( $p < 0.001$ ) at Mount Zirkel WA, Colorado (MOZI1), to -1.52% yr<sup>-1</sup> ( $p < 0.001$ ) at Saguaro NM, Arizona (SAGU1).

The long-term 90<sup>th</sup> percentile trends in PM<sub>10</sub> (Figure 6.7.3b) were similar to the 90<sup>th</sup> percentile FM trends, with the strong reductions at sites in the eastern United States, and were likely driven by reductions in FM and specifically sulfate. Most of the sites in the West had insignificant trends (32 out of 50 valid sites had statistically significant trends). Most of these trends occurred at sites in California, Oregon, and the southwestern United States. Trends ranged from -4.03% yr<sup>-1</sup> ( $p < 0.001$ ) at Shining Rock WA, North Carolina (SHRO1), to 1.70% yr<sup>-1</sup> ( $p = 0.014$ ) at Columbia River Gorge, Washington (CORI1). This site had the only statistically significant positive trend and was negative for FM, suggesting that CM played an important role.

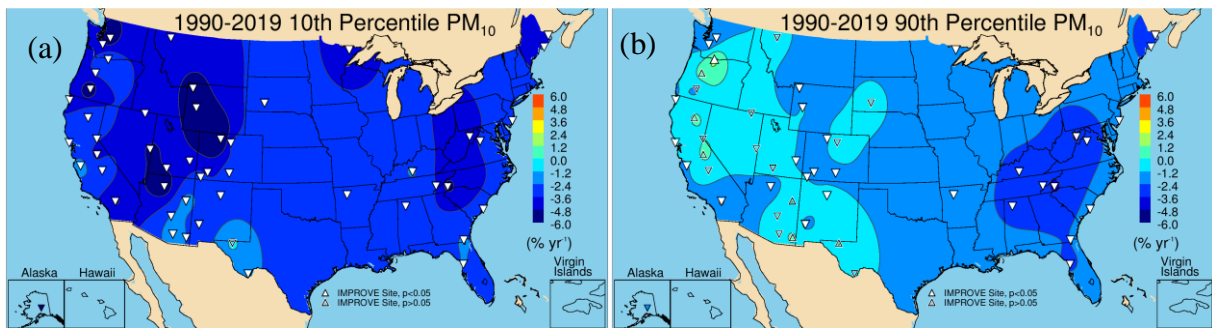


**Figure 6.7.3. IMPROVE long-term (1990–2019) trends ( $\% \text{ yr}^{-1}$ ) in (a) 10<sup>th</sup> percentile gravimetric PM<sub>10</sub> mass concentrations and (b) 90<sup>th</sup> percentile concentrations. Filled triangles correspond to statistically significant trends ( $p \leq 0.05$ ).**

The short-term 10<sup>th</sup> percentile PM<sub>10</sub> concentrations declined significantly at most valid sites (Figure 6.7.4a), especially at sites in the eastern United States. However, unlike FM trends, many sites in the southwestern United States had insignificant trends in PM<sub>10</sub>. Out of 137 valid sites, 78 were statistically significant, but many insignificant trends occurred at sites in California or the southwestern United States. Trends ranged from -4.35% yr<sup>-1</sup> ( $p = 0.002$ ) at Olympic, Washington (OLYM1), to -0.77% yr<sup>-1</sup> ( $p = 0.046$ ) at San Pedro Parks, New Mexico (SAPE1).

The spatial pattern in the short-term 90<sup>th</sup> percentile PM<sub>10</sub> trends was similar to the FM trends (Figure 6.7.4b), with the exception of sites in the southwestern and central United States. At sites in these areas, trends were flat and insignificant. Three sites had statistically significant positive trends, including Lassen Volcanic NP, California (LAVO1, 1.64% yr<sup>-1</sup>,  $p = 0.03$ ), Three Sisters WA, Oregon (THSI1, 2.26% yr<sup>-1</sup>,  $p = 0.004$ ), and Columbia River Gorge, Washington (CORI1, 2.42% yr<sup>-1</sup>,  $p = 0.03$ ). The largest negative trend occurred at Frostburg Reservoir, Maryland (FRRE1, -4.76% yr<sup>-1</sup>,  $p < 0.001$ ), similar to FM trends.

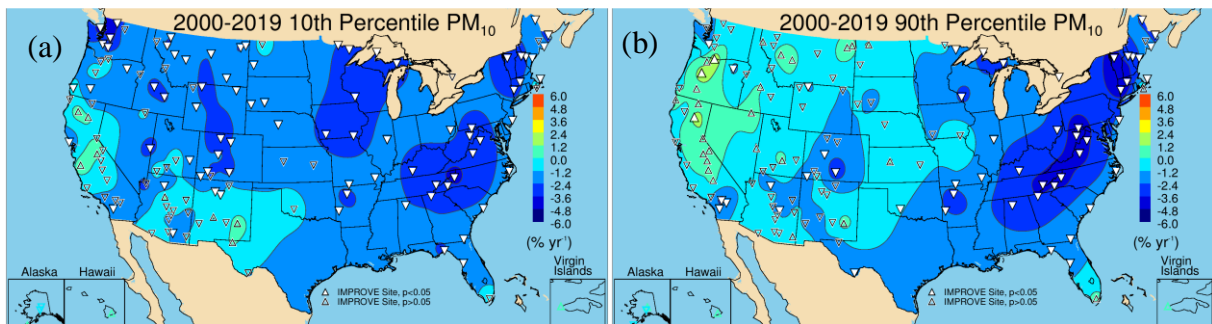


**Figure 6.7.4. IMPROVE short-term (2000–2019) trends ( $\% \text{ yr}^{-1}$ ) in (a) 10<sup>th</sup> percentile gravimetric PM<sub>10</sub> mass concentrations and (b) 90<sup>th</sup> percentile concentrations. Filled triangles correspond to statistically significant trends ( $p \leq 0.05$ ).**

Both of the PM<sub>10</sub> regional mean trends in the Northeast and Southeast regions were similar to FM trends, with the 90<sup>th</sup> percentile PM<sub>10</sub> concentration trends being the largest, which were likely driven by reductions in FM, specifically sulfate (Figure 6.7.5). In the Central region, only the 10<sup>th</sup> percentile trends were significant, unlike for FM when all percentile trends were significant, suggesting additional influence on the 50<sup>th</sup> and 90<sup>th</sup> percentile trends. Similar results occurred in the Southwest and California regions, where none of the PM<sub>10</sub> trends was significant

but nearly all of the FM trends were. Trends in the Northwest region were similar for PM<sub>10</sub> and FM, suggesting that PM<sub>10</sub> trends were driven by FM trends.

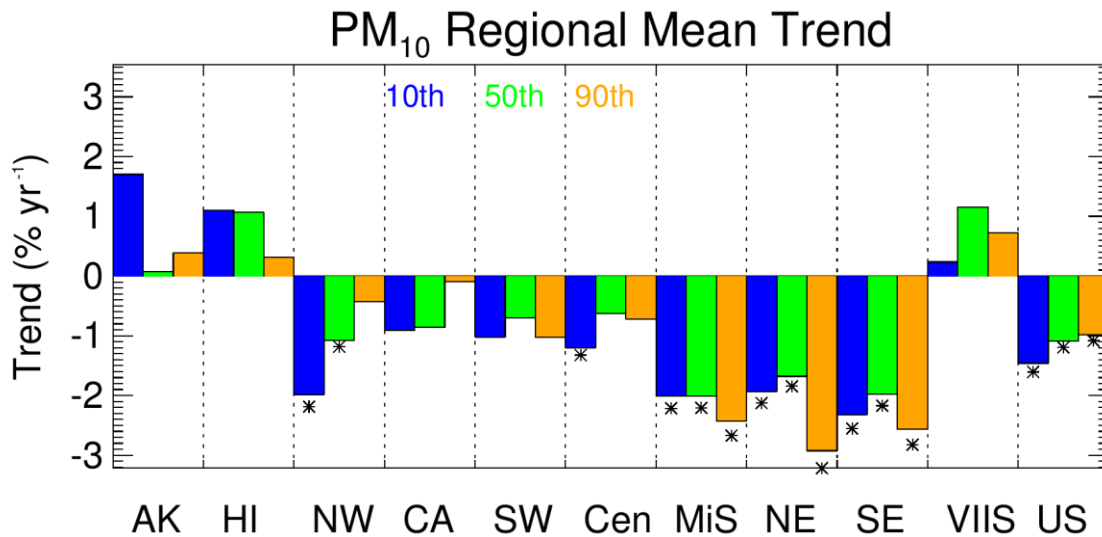


**Figure 6.7.5.** Short-term (2000–2019) regional mean trends ( $\% \text{ yr}^{-1}$ ) in 10<sup>th</sup>, 50<sup>th</sup>, and 90<sup>th</sup> percentile gravimetric PM<sub>10</sub> mass concentrations. Regions are arranged from western to eastern United States (AK = Alaska, HI = Hawaii, NW = Northwest, CA = California, SW = Southwest, Cen = Central, MiS = Midsouth, NE = Northeast, SE = Southeast, VIIS = Virgin Islands, and US = all sites). Statistically significant trends ( $p \leq 0.05$ ) are denoted with “\*”.

## 6.8 COARSE MASS TRENDS

CM is calculated as the difference between PM<sub>10</sub> and PM<sub>2.5</sub> (FM) gravimetric mass. CM is often associated with mechanically generated sources and assumed to be composed of mineral dust, but as discussed in Section 2.2.12, it can also include carbonaceous and inorganic ion material. Spatial patterns in CM trends may be similar to FD trends, assuming FD is the tail of the coarse dust mode, but could vary if CM is composed of material other than mineral dust, or if the coarse mode size distribution is shifted to a larger size.

Annual mean long-term trends in CM are shown in Figure 6.8.1a. The strongest reductions in CM occurred at sites in Wyoming and Colorado. Of the 49 valid sites, 30 of them had statistically significant trends. Insignificant trends mostly occurred at sites in the western United States, in California, Arizona, and Texas. One positive trend occurred at Columbia River Gorge, Washington (CORI1,  $1.83\% \text{ yr}^{-1}$ ,  $p = 0.04$ ). The strongest reduction in CM occurred at Crater Lake NP, Oregon (CRLA1,  $-5.39\% \text{ yr}^{-1}$ ,  $p < 0.001$ ).

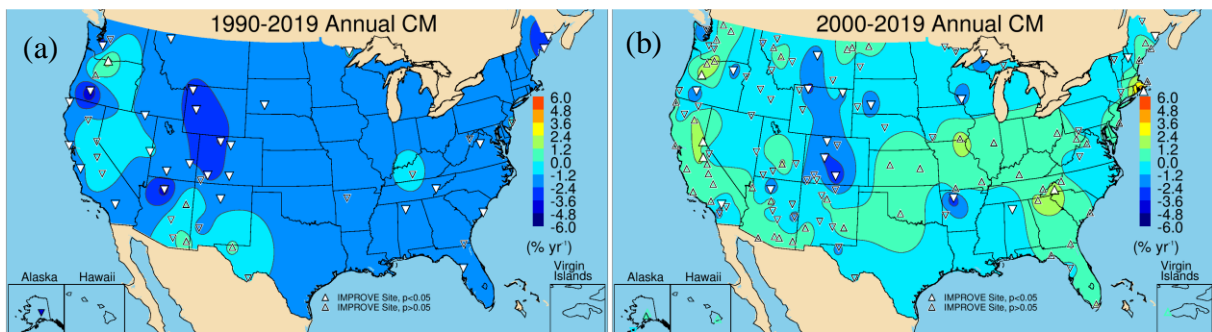


**Figure 6.8.1. Annual mean coarse mass (CM) trends ( $\% \text{ yr}^{-1}$ ) for (a) long-term (1990–2019) and (b) short-term (2000–2019) periods. Filled triangles correspond to statistically significant trends ( $p \leq 0.05$ ).**

Short-term annual mean CM trends are shown in Figure 6.8.1b. Only 23 of 131 valid sites had statistically significant trends, suggesting that at most sites, trends were variable. CM declined significantly at some sites, for example, in Colorado, Wyoming, and Montana, and in Arkansas, where the strongest reductions occurred at Upper Buffalo WA, Arkansas (UPBU1 -3.85%  $\text{yr}^{-1}$ ,  $p = 0.045$ ). Positive trends (mostly insignificant) occurred at 61 sites, with six being statistically significant (Martha's Vineyard, Massachusetts, MAVI1; Shining Rock WA, North Carolina, SHRO1; Three Sisters WA, Oregon, THSI1; Yosemite NP, California, YOSE1; Bliss SP, California, BLIS1; and Trapper Creek, Alaska, TRCR1). The spatial pattern in short-term CM trends was different from FD trends (Figure 6.5.1b), suggesting that different composition or size distribution of coarse-mode aerosols influenced CM trends.

Regional seasonal mean trends are shown in Figure 6.8.2. As suggested in Figure 6.8.1b, nearly all of the regions were associated with insignificant and weak trends, especially relative to other species already discussed. The Northeast region had significant positive trends in summer, as did the Alaska and Hawaii regions. All of the seasonal mean trends in the Central region were positive but insignificant. The Midsouth and Southwest regions had weak but negative insignificant trends, while the California region had weak, positive insignificant trends in summer and fall but negative, insignificant trends in winter and spring. The Northwest region had statistically significant trends in winter but weak and insignificant trends during other seasons.

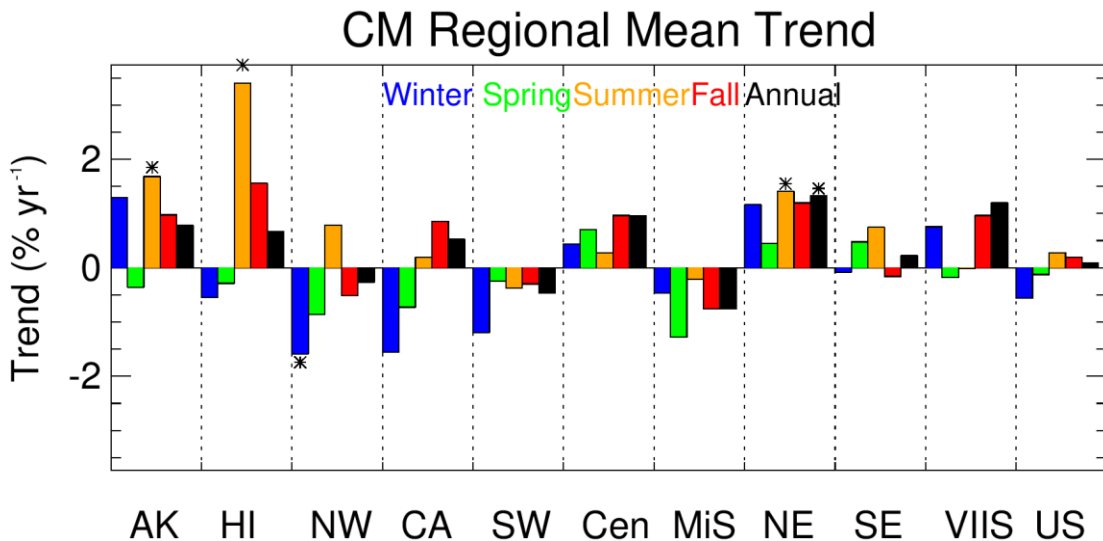


**Figure 6.8.2.** Short-term (2000–2019) regional seasonal mean coarse mass (CM) trends ( $\% \text{ yr}^{-1}$ ) for major U.S. regions for winter, spring, summer, fall, and annual means. Regions are arranged from western to eastern United States (AK = Alaska, HI = Hawaii, NW = Northwest, CA = California, SW = Southwest, Cen = Central, MiS = Midsouth, NE = Northeast, SE = Southeast, VIIS = Virgin Islands, and US = all sites). Statistically significant trends ( $p \leq 0.05$ ) are denoted with “\*”.

The 10<sup>th</sup> percentile long-term trends were negative at most sites (44 out of 50 valid sites), with the strongest reductions at sites in the Intermountain West and southwestern United States (Figure 6.8.3a). Of the 50 valid sites, 31 had statistically significant trends, ranging from  $-8.94\% \text{ yr}^{-1}$  ( $p < 0.001$ ) at Mount Zirkel WA, Colorado (MOZI1), to  $-1.64\% \text{ yr}^{-1}$  ( $p = 0.016$ ) at Tonto NM, Arizona (TONT1). The trends in 90<sup>th</sup> percentile CM did not decrease to the same degree as the 10<sup>th</sup> percentile trends (Figure 6.8.3b). Of the 50 valid sites, 30 had statistically significant trends, ranging from  $-5.32\% \text{ yr}^{-1}$  ( $p < 0.001$ ) at Crater Lake NP, Oregon (CRLA1), to  $2.82\% \text{ yr}^{-1}$  ( $p = 0.002$ ) at Columbia River Gorge, Washington (CORI1). Recall that the 90<sup>th</sup> percentile trend in FD at CRLA1 was also positive, suggesting CM is likely associated with mineral dust at this site. The 90<sup>th</sup> percentile CM trends decreased at a higher rate than the 90<sup>th</sup> percentile FD trends, especially for sites in the southwestern United States. Similarities in FD and CM trends occurred for sites in Arizona and Texas. Insignificant positive 90<sup>th</sup> percentile CM trends at sites in California were insignificant but negative for the 90<sup>th</sup> percentile FD trends.

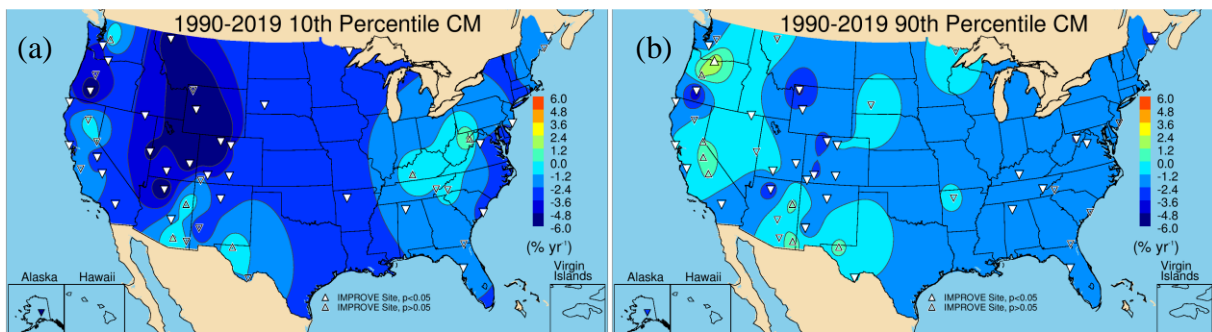


**Figure 6.8.3. IMPROVE long-term (1990–2019) trends ( $\% \text{ yr}^{-1}$ ) in (a) 10<sup>th</sup> percentile coarse mass (CM) concentrations and (b) 90<sup>th</sup> percentile concentrations. Filled triangles correspond to statistically significant trends ( $p \leq 0.05$ ).**

Short-term trends in the 10<sup>th</sup> and 90<sup>th</sup> percentile CM concentrations (Figure 6.8.4a and 6.8.4b, respectively) showed more spatial variability than the long-term trends, with many more insignificant and positive trends. The 10<sup>th</sup> percentile trends had only 22 statistically significant trends out of 137 valid sites. Of the valid sites, 72 had positive although mostly insignificant trends. The strongest statistically insignificant negative trends occurred at sites in Colorado and Montana and parts of southern California and Oregon. Statistically significant positive trends occurred at several sites, with the strongest at Shining Rock WA, North Carolina (SHRO1); Dolly Sods WA, West Virginia (DOSO1); Cohutta, Georgia (COHU1); Sawtooth National Forest (NF), Idaho (SAWT1); Lassen Volcanic NP, California (LAVO1); and Bliss SP, California (BLIS1). Trends ranged from  $-10.37\% \text{ yr}^{-1}$  ( $p = 0.025$ ) at Gates of the Mountains, Montana (GAMO1), to  $9.08\% \text{ yr}^{-1}$  ( $p = 0.005$ ) at Shining Rock WA, North Carolina (SHRO1).

Similar spatial patterns were seen for the short-term 90<sup>th</sup> percentile trends, with sites in the central United States, California, and the Northwest and sites in the Southeast having positive but insignificant trends. Sites with strongly decreased CM included those in Colorado. Of the 137 sites, 21 were statistically significant and ranged from  $-4.77\% \text{ yr}^{-1}$  ( $p = 0.005$ ) at Upper Buffalo WA, Arkansas (UPBU1), to  $5.41\% \text{ yr}^{-1}$  ( $p = 0.004$ ) at Martha's Vineyard, Massachusetts (MAVI1). Several sites had both significant positive 10<sup>th</sup> and 90<sup>th</sup> percentile trends, such as Shining Rock WA, North Carolina (SHRO1); Cohutta, Georgia (COHU1); and Bliss SP, California (BLIS1). The short-term 10<sup>th</sup> and 90<sup>th</sup> percentiles trend maps did not reflect the corresponding FD trend maps, with the CM trends having much larger spatial variability, more insignificant trends, and fewer sites with negative trends.

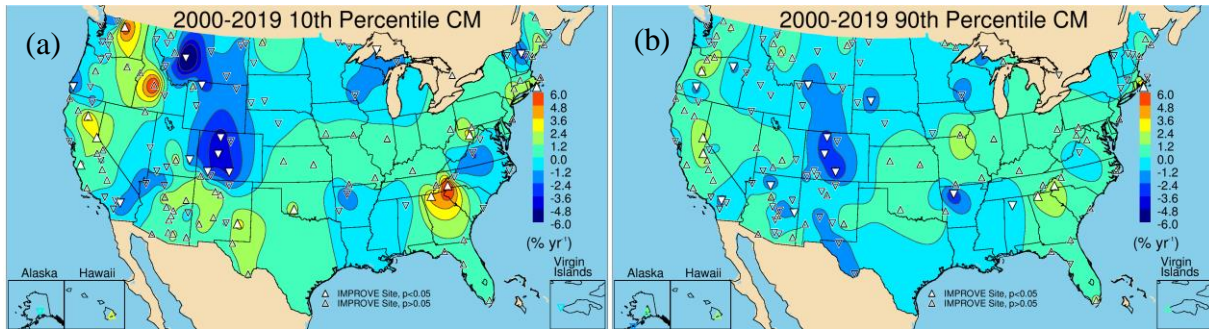


**Figure 6.8.4. IMPROVE short-term (2000–2019) trends ( $\% \text{ yr}^{-1}$ ) in (a) 10<sup>th</sup> percentile coarse mass (CM) concentrations and (b) 90<sup>th</sup> percentile concentrations. Filled triangles correspond to statistically significant trends ( $p \leq 0.05$ ).**

Comparisons of short-term regional mean percentile CM trends are shown in Figure 6.8.5. Unlike the results for FD trends (Figure 6.5.5), most of the regional mean trends were statistically insignificant, except for the positive 50<sup>th</sup> percentile trend in the Northeast region. The Central region had positive trends for all percentiles, although insignificant, while the Midsouth had negative trends, also insignificant. The California region had insignificant but weakly positive trends. CM trends were notable because they indicate that CM has not decreased across large regions of the United States, unlike FM.

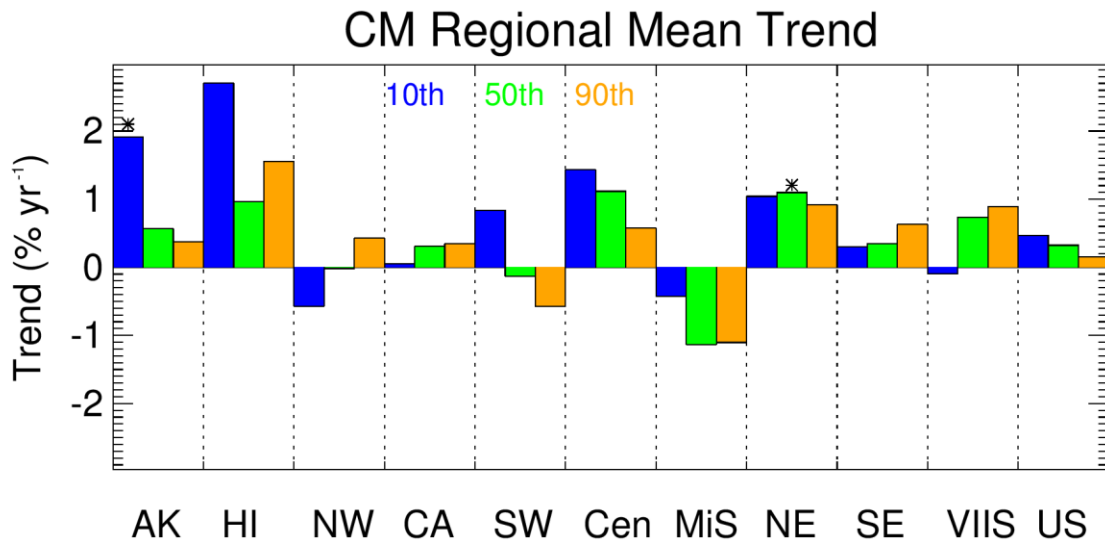


**Figure 6.8.5. Short-term (2000–2019) regional mean trends ( $\% \text{ yr}^{-1}$ ) in 10<sup>th</sup>, 50<sup>th</sup>, and 90<sup>th</sup> percentile coarse mass (CM) concentrations. Regions are arranged from western to eastern United States (AK = Alaska, HI = Hawaii, NW = Northwest, CA = California, SW = Southwest, Cen = Central, MiS = Midsouth, NE = Northeast, SE = Southeast, VIIS = Virgin Islands, and US = all sites). Statistically significant trends ( $p \leq 0.05$ ) are denoted with “\*”.**

## 6.9 $f_{\text{abs}}$ TRENDS

Recalibration of  $f_{\text{abs}}$  began in 2003 (White et al., 2016); therefore, only short-term trends were computed. Trends in  $f_{\text{abs}}$  could be influenced by changes in absorbing aerosol due to both

EC and/or FD. The short-term annual mean  $f_{abs}$  trend is shown in Figure 6.9.1. Of the 127 valid sites, 59 were statistically significant and ranged from  $-4.72\% \text{ yr}^{-1}$  ( $p < 0.001$ ) at San Gorgonio WA, California (SAGO1), to  $3.99\% \text{ yr}^{-1}$  ( $p = 0.024$ ) at Lostwood, North Dakota (LOST1). Several sites in North Dakota and Montana were associated with positive  $f_{abs}$  trends, likely associated with oil and gas development (Gebhart et al., 2018). EC trends were insignificant in this same region. Trends at sites across the northwestern United States were also largely insignificant and many were positive, likely due to biomass smoke impacts. Trends were also insignificant and positive at sites across parts of the southwestern United States, such as New Mexico and Colorado. These regions also experienced positive and insignificant FD trends.

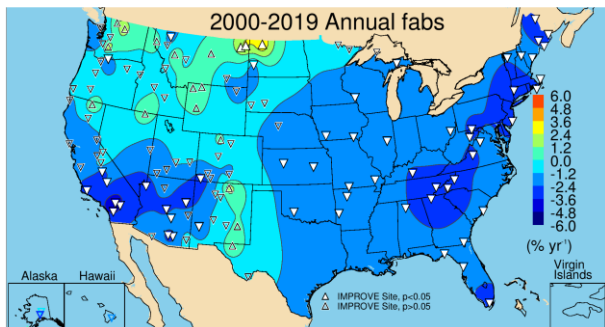


**Figure 6.9.1. Annual mean filter absorption ( $f_{abs}$ ) short-term (2000–2019) trends ( $\% \text{ yr}^{-1}$ ). Filled triangles correspond to statistically significant trends ( $p \leq 0.05$ ).**

Comparisons of regional seasonal mean short-term trends are shown in Figure 6.9.2. Statistically significant reductions in seasonal mean  $f_{abs}$  occurred at most regions but especially in the eastern United States. The Northeast, Southeast, and Midsouth regions all experienced similar reductions across all seasons ( $-2\% \text{ yr}^{-1}$  to  $-3\% \text{ yr}^{-1}$ ). In comparison, EC trends in the same regions were stronger during summer relative to other seasons. Weaker reductions in  $f_{abs}$  occurred in the Central and Southwest regions, with some seasonal trends that were insignificant, especially during summer. In the California region, strong reductions in  $f_{abs}$  occurred in spring and fall, while negative but insignificant trends occurred during winter and summer. The Northwest region had no statistically significant trends; most seasons were negative except for summer, which was weakly positive and likely influenced by biomass smoke. Seasonal mean trends in the Hawaii, Alaska, and Virgin Islands regions were mostly insignificant.

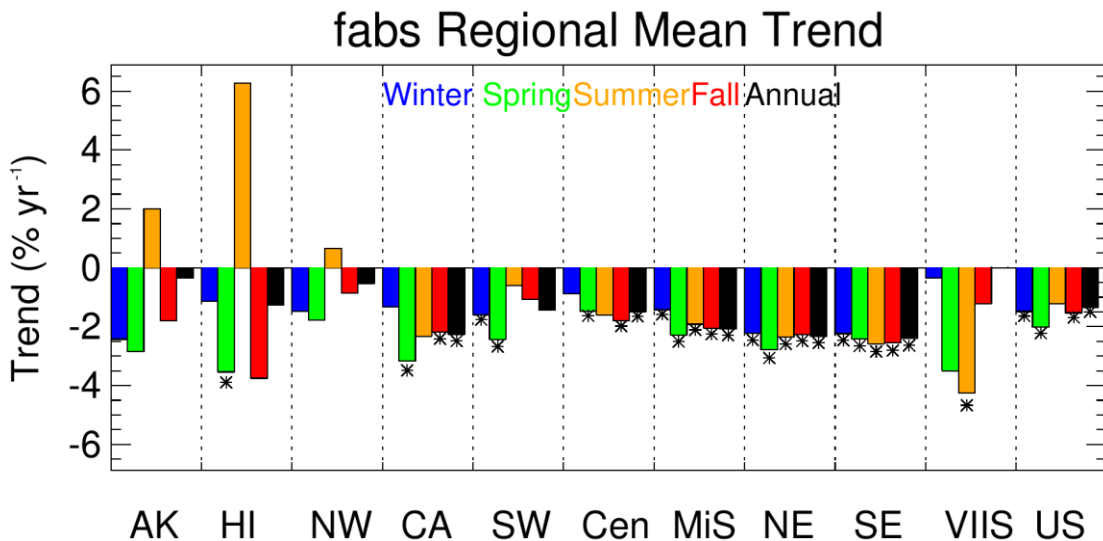


**Figure 6.9.2.** Short-term (2000–2019) regional seasonal mean filter absorption ( $f_{abs}$ ) trends ( $\% \text{ yr}^{-1}$ ) for major U.S. regions for winter, spring, summer, fall, and annual means. Regions are arranged from western to eastern United States (AK = Alaska, HI = Hawaii, NW = Northwest, CA = California, SW = Southwest, Cen = Central, MiS = Midsouth, NE = Northeast, SE = Southeast, VIIS = Virgin Islands, and US = all sites). Statistically significant trends ( $p \leq 0.05$ ) are denoted with “\*”.

Short-term trends in the 10<sup>th</sup> percentile  $f_{abs}$  showed strong reductions at sites in the eastern United States, where most sites had statistically significant trends, except in the northeastern United States (Figure 6.9.3a). Of the 132 valid sites, 45 sites had statistically significant trends, most in the eastern United States. Trends ranged from  $-16.92\% \text{ yr}^{-1}$  ( $p = 0.028$ ) in Mount Hood, Oregon (MOHO1), to  $3.77\% \text{ yr}^{-1}$  ( $p = 0.022$ ) at Lostwood, North Dakota (LOST1). Many of the 10<sup>th</sup> percentile trends could be affected by normalization by very low  $f_{abs}$  median values. The spatial patterns are different from those observed in the 10<sup>th</sup> percentile EC trends.

The 90<sup>th</sup> percentile  $f_{abs}$  trends (Figure 6.9.3b) showed similar spatial patterns as the 10<sup>th</sup> percentile trends. Strong reductions in  $f_{abs}$  at sites across the eastern United States were statistically significant, while reductions at sites in the West were much weaker, positive, and insignificant. However, sites in southern California, Arizona, and parts of Oregon also experienced strong reductions. Many of the insignificant and positive trends at sites in the northwestern and southwestern United States were similar to EC and FD trends, respectively, and these likely influenced the  $f_{abs}$  trends. The 90<sup>th</sup> percentile trends ranged from  $-4.48\% \text{ yr}^{-1}$  ( $p < 0.001$ ) at San Gorgonio WA, California (SAGO1), to  $3.03\% \text{ yr}^{-1}$  ( $p = 0.017$ ) at Medicine Lake, Montana (MELA1).

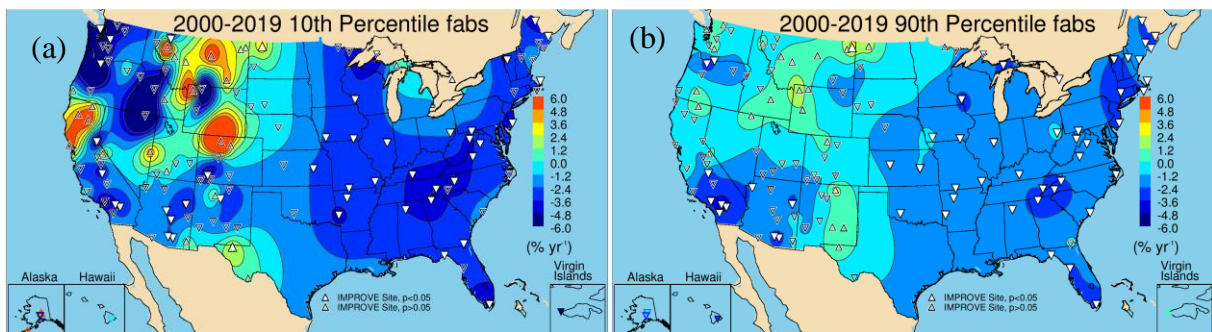


**Figure 6.9.3. IMPROVE short-term (2000–2019) trends ( $\% \text{ yr}^{-1}$ ) in (a) 10<sup>th</sup> percentile filter absorption ( $f_{\text{abs}}$ ) and (b) 90<sup>th</sup> percentile  $f_{\text{abs}}$ . Filled triangles correspond to statistically significant trends ( $p \leq 0.05$ ).**

Regional mean percentile trends are shown in Figure 6.9.4. The Northeast, Southeast, and Central regions had statistically significant trends, with somewhat higher reductions for the 10<sup>th</sup> percentile  $f_{\text{abs}}$ , which may be an artifact of normalization by very low  $f_{\text{abs}}$  values. In the Southwest region, the 50<sup>th</sup> percentile had significant reductions in  $f_{\text{abs}}$ , but the 90<sup>th</sup> percentile trend was weak and insignificant. This was the general pattern for the Northwest and California regions, where the 90<sup>th</sup> percentile  $f_{\text{abs}}$  trends were negative but insignificant.

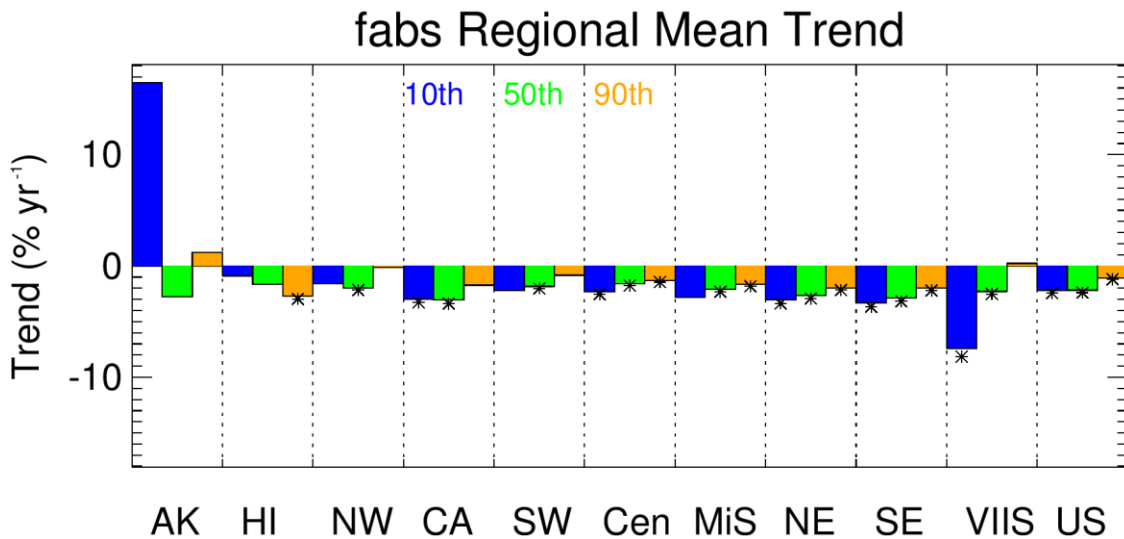


**Figure 6.9.4. Short-term (2000–2019) regional mean trends ( $\% \text{ yr}^{-1}$ ) in 10<sup>th</sup>, 50<sup>th</sup>, and 90<sup>th</sup> percentile filter absorption ( $f_{\text{abs}}$ ). Regions are arranged from western to eastern United States (AK = Alaska, HI = Hawaii, NW = Northwest, CA = California, SW = Southwest, Cen = Central, MiS = Midsouth, NE = Northeast, SE = Southeast, VIIS = Virgin Islands, and US = all sites). Statistically significant trends ( $p \leq 0.05$ ) are denoted with “\*”.**

## 6.10 DISCUSSION

Timelines of regional, annual mean mass concentrations for PM<sub>2.5</sub> sulfate ion, nitrate ion, OC, EC, and FD that correspond to previous trend results are shown in Figure 6.10.1(a-j) for 2001 through 2019. Regional mean concentrations for 2000 were not included due to the expansion of the network in that year (Hand et al., 2020). Similar timelines for CM

concentrations are shown in Figure 6.10.2(a-j). These mass concentrations do not include mass correction factors for sulfate, nitrate, or OC (e.g., concentrations are for sulfate ion, not ammonium sulfate); therefore, the sum of individual bars should not be interpreted as RCFM, such as is shown in Chapter 3. However, the basic patterns are similar and reflect both RCFM and FM. It is clear from these timelines and the previous trend discussions that strong reductions in FM have occurred at nearly all remote regions across the United States. These reductions were greatest in the East and driven by strong negative trends in sulfate ion concentrations. Sulfate concentrations have decreased in response to dramatic reductions in sulfur dioxide emissions due to regulatory activity (Hand et al., 2020). In addition, reductions in nitrate ion and OC concentrations (especially in the East) have contributed to reduced FM. Negative trends in nitrate concentrations at sites in southern California occurred at sites where nitrogen dioxide emissions, especially mobile emissions, have declined due to regulatory activity.

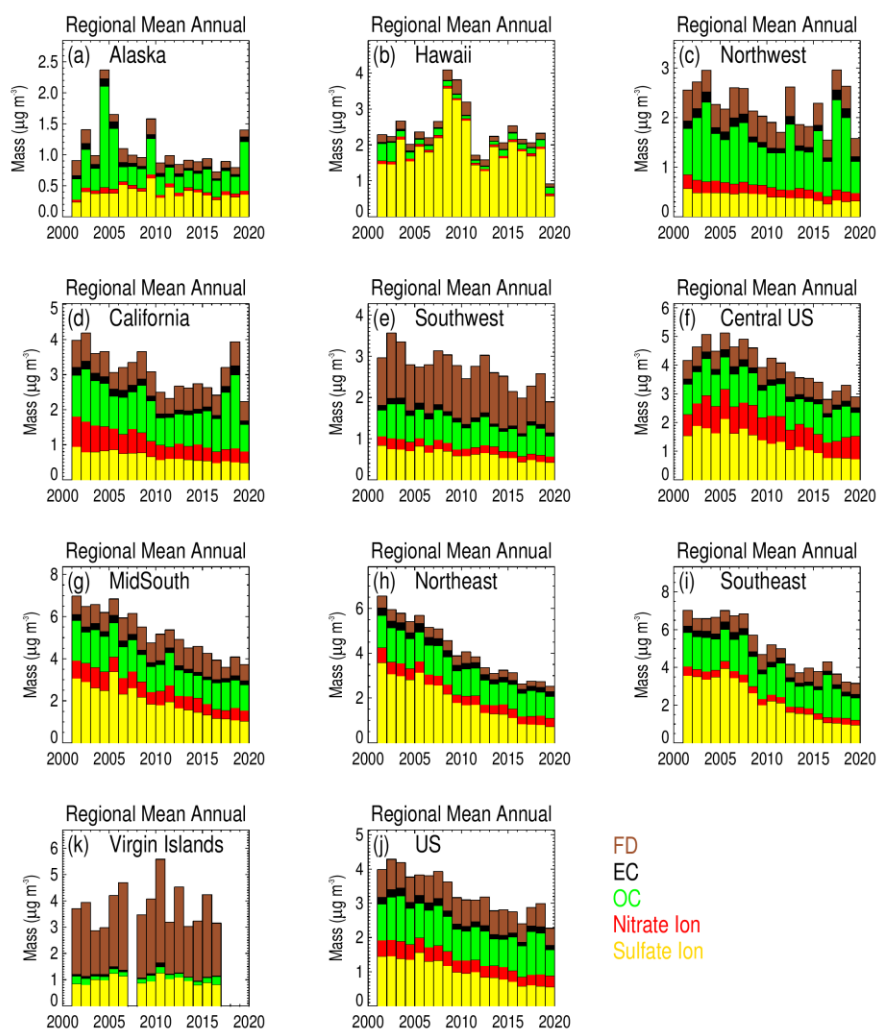


**Figure 6.10.1. Short-term (2001–2019) timelines in IMPROVE regional, annual mean mass concentrations ( $\mu\text{g m}^{-3}$ ) for sulfate ion, nitrate ion, organic carbon (OC), elemental carbon (EC), and fine dust (FD).**

At sites in the western United States, especially the Northwest, FM has declined at a weaker rate relative to sites in the East. Comparisons of OC and EC trends suggest that FM is influenced by an increase in biomass burning impacts that have led to an increase in OC, or at the very least flat and insignificant trends. Hire fire years are especially evident for 2017 and 2018 in Figure 6.10.1.c. OC is a major contributor to FM, especially at western sites, and has influenced FM trends in the region (McClure and Jaffe, 2018).

FM concentrations at sites in the Southwest have decreased (many insignificantly), although to a lower extent relative to sites in the East. The FM budget at these sites includes a significant fraction of FD, and trends in FD were insignificant (Figure 6.10.1e). OC trends were also insignificant at many southwestern sites, suggesting that the role of FD and OC may have influenced FM trends in the region.

PM<sub>10</sub> trends were spatially similar to FM trends at sites in the East, where CM concentrations were relatively low, and therefore declines in sulfate and OC concentrations also led to reductions in PM<sub>10</sub>. However, FM and PM<sub>10</sub> trends at sites in the West were different, mainly at sites in the central and southwestern United States. Sites in these regions have a large contribution from CM (Figure 6.10.2). CM trends were notably different from PM<sub>2.5</sub> speciated trends in that only a few sites across the United States had statistically significant negative CM trends. Several sites had statistically significant positive trends. These CM trends appeared to affect the PM<sub>10</sub> trends at those sites.

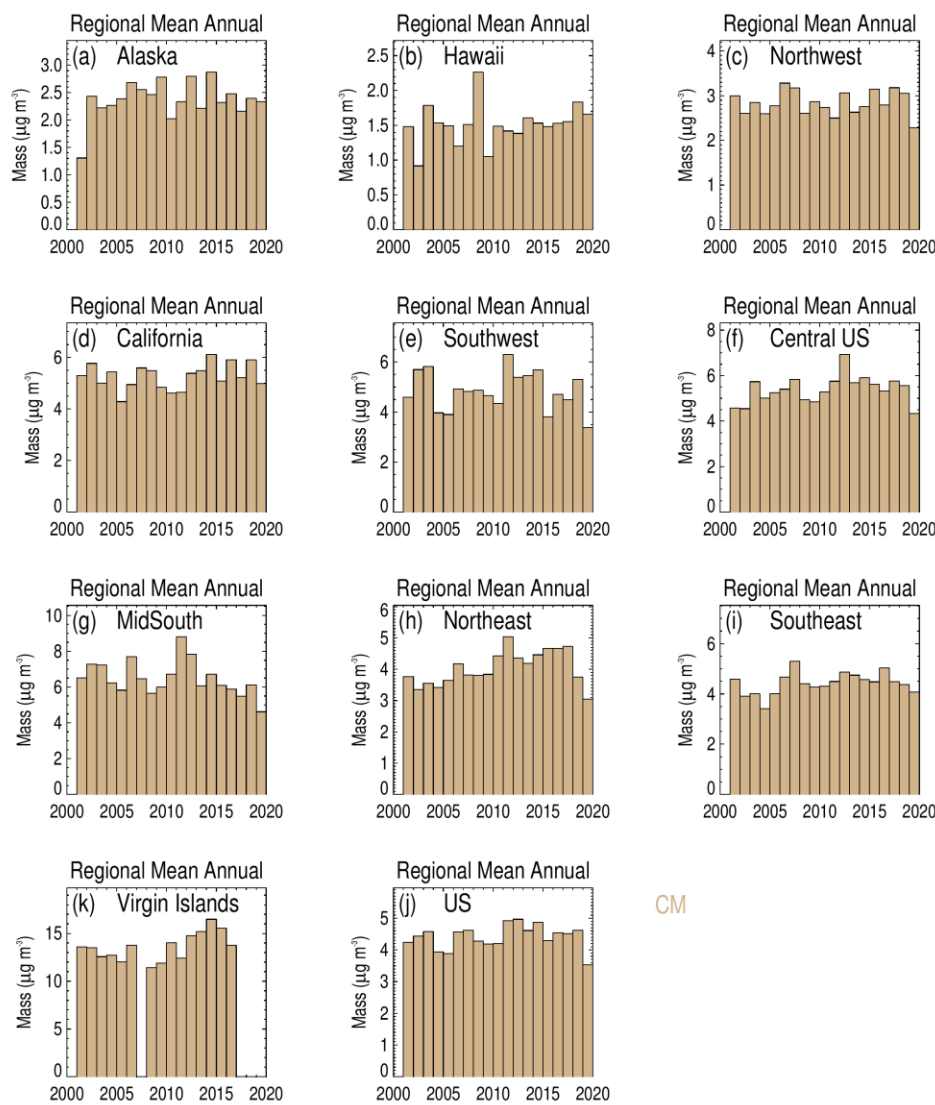


**Figure 6.10.2. Short-term (2001–2019) timelines in IMPROVE regional, annual mean coarse mass (CM) concentrations ( $\mu\text{g m}^{-3}$ ).**

Regulatory activity has been very successful at reducing pollutant emissions that lead to secondary aerosols, such as sulfate, nitrate, and OC, as well as reductions in primary aerosols such as EC, and some OC, depending on its sources. Reductions in these species have driven negative trends in FM and  $\text{PM}_{10}$  at sites across the United States. However, the role of natural aerosols, such as those derived from biomass smoke and dust storms have not declined and for some sites and seasons have increased. The impact of these positive trends have and likely will continue to impede progress in reducing FM and  $\text{PM}_{10}$  concentrations.

Site-specific long-term and short-term annual mean trend results are provided in Appendix 6.1, short-term percentile trends in Appendix 6.2, and long-term percentile trends in Appendix 6.3.

## REFERENCES

- Blanchard, C., Hidy, G., Shaw, S., Baumann, K., and Edgerton, E. (2016), Effects of emission reductions on organic aerosol in the southeastern United States, *Atmospheric Chemistry and Physics*, 16(1), 215-238, doi:10.5194/acp-16-215-2016.
- Chow, J. C., Watson, J. G., Chen, L.-W. A., Chang, M. O., Robinson, N. F., Trimble, D., and Kohl, S. (2007), The IMPROVE\_A temperature protocol for thermal/optical carbon analysis: maintaining consistency with a long-term database, *Journal of the Air & Waste Management Association*, 57(9), 1014-1023, <https://doi.org/10.3155/1047-3289.57.9.1014>.
- Debell, L. J. (2006), Data Validation Historical Report No 3, [http://vista.cira.colostate.edu/improve/wp-content/uploads/2022/09/044\\_Historical\\_QA\\_Report\\_Nitrate.pdf](http://vista.cira.colostate.edu/improve/wp-content/uploads/2022/09/044_Historical_QA_Report_Nitrate.pdf).
- Evanoski-Cole, A., Gebhart, K., Sive, B., Zhou, Y., Capps, S., Day, D., Prenni, A., Schurman, M., Sullivan, A., and Li, Y. (2017), Composition and sources of winter haze in the Bakken oil and gas extraction region, *Atmospheric Environment*, 156, 77-87, <http://dx.doi.org/10.1016/j.atmosenv.2017.02.019>.
- Feng, J., Chan, E., and Vet, R. (2020), Air quality in the eastern United States and eastern Canada for 1990–2015: 25 years of change in response to emission reductions of SO<sub>2</sub> and NO<sub>x</sub> in the region, *Atmospheric Chemistry and Physics*, 20(5), 3107-3134, doi:10.5194/acp-20-3107-2020.
- Gebhart, K. A., Day, D. E., Prenni, A. J., Schichtel, B. A., Hand, J. L., and Evanoski-Cole, A. R. (2018), Visibility impacts at Class I areas near the Bakken oil and gas development, *Journal of the Air & Waste Management Association*, 68(5), 477-493, doi:10.1080/10962247.2018.1429334.
- Hand, J. L., Schichtel, B. A., Malm, W. C., and Pitchford, M. L. (2012), Particulate sulfate ion concentration and SO<sub>2</sub> emission trends in the United States from the early 1990s through 2010, *Atmospheric Chemistry and Physics*, 12(21), 10353-10365, doi:10.5194/acp-12-10353-2012.
- Hand, J. L., Prenni, A. J., Schichtel, B. A., Malm, W. C., and Chow, J. C. (2019), Trends in remote PM<sub>2.5</sub> residual mass across the United States: Implications for aerosol mass reconstruction in the IMPROVE network, *Atmospheric Environment*, 203, 141-152, doi:10.1016/j.atmosenv.2019.01.049.
- Hand, J. L., Prenni, A. J., Copeland, S., Schichtel, B. A., and Malm, W. C. (2020), Thirty years of the Clean Air Act Amendments: Impacts on haze in remote regions of the United States (1990–2018), *Atmospheric Environment*, 243, 117865, <https://doi.org/10.1016/j.atmosenv.2020.117865>.
- Hyslop, N. P., Trzepla, K., and White, W. H. (2015), Assessing the suitability of historical PM<sub>2.5</sub> element measurements for trend analysis, *Environmental Science & Technology*, 49(15), 9247-9255, doi:10.1021/acs.est.5b01572.
- Isaaks, E. H., and Mohan Srivastava, R. (1989), *An Introduction to Applied Geostatistics*, Oxford University Press, New York, ISBN 978-0195050134.

Kharol, S. K., McLinden, C. A., Sioris, C. E., Shephard, M. W., Fioletov, V., van Donkelaar, A., Philip, S., and Martin, R. V. (2017), OMI satellite observations of decadal changes in ground-level sulfur dioxide over North America, *Atmospheric Chemistry and Physics*, 17(9), 5921-5929, doi:10.5194/acp-17-5921-2017.

Krotkov, N. A., McLinden, C. A., Li, C., Lamsal, L. N., Celarier, E. A., Marchenko, S. V., Swartz, W. H., Bucsela, E. J., Joiner, J., Duncan, B. N., Boersma, K. F., Veefkind, J. P., Levelt, P. F., Fioletov, V. E., Dickerson, R. R., He, H., Lu, Z., and Streets, D. G. (2016), Aura OMI observations of regional SO<sub>2</sub> and NO<sub>2</sub> pollution changes from 2005 to 2015, *Atmos. Chem. Phys.*, 16(7), 4605-4629, doi:10.5194/acp-16-4605-2016.

Malm, W. C., Schichtel, B. A., Hand, J. L., and Collett Jr, J. L. (2017), Concurrent temporal and spatial trends in sulfate and organic mass concentrations measured in the IMPROVE monitoring program, *Journal of Geophysical Research: Atmospheres*, 122, 10462-10476, doi:10.1002/2017JD026865.

Malm, W., Schichtel, B., Hand, J., and Prenni, A. (2020), Implications of organic mass to carbon ratios increasing over time in the rural United States, *Journal of Geophysical Research: Atmospheres*, 125(5), e2019JD031480, doi:10.1029/2019JD031480.

McClure, C. D., and Jaffe, D. A. (2018), US particulate matter air quality improves except in wildfire-prone areas, *Proceedings of the National Academy of Sciences*, 115(31), 7901-7906, doi:doi:10.1073/pnas.1804353115.

McDade, C. (2004), Summary of IMPROVE nitrate measurements, [http://vista.cira.colostate.edu/improve/Publications/GrayLit/025\\_IMPROVEnitrate/Nitrate%20Summary\\_1004.pdf](http://vista.cira.colostate.edu/improve/Publications/GrayLit/025_IMPROVEnitrate/Nitrate%20Summary_1004.pdf).

McDade, C. (2007), Diminished wintertime nitrate concentrations in late 1990s, *IMPROVE Data Advisory*, [http://vista.cira.colostate.edu/improve/Data/QA\\_QC/Advisory/da0002/da0002\\_WinterNO3.pdf](http://vista.cira.colostate.edu/improve/Data/QA_QC/Advisory/da0002/da0002_WinterNO3.pdf).

Prenni, A., Day, D., Evanoski-Cole, A., Sive, B., Hecobian, A., Zhou, Y., Gebhart, K., Hand, J., Sullivan, A., and Li, Y. (2016), Oil and gas impacts on air quality in federal lands in the Bakken region: An overview of the Bakken Air Quality Study and first results, *Atmospheric Chemistry and Physics*, 16(3), 1401-1416, doi:10.5194/acp-16-1401-2016.

Schichtel, B. A. (2003), Underestimation of sulfur concentrations during high loadings and humidity conditions in the eastern US, *IMPROVE Data Advisory*, [http://vista.cira.colostate.edu/improve/Data/QA\\_QC/Advisory/da0001/da0001\\_S\\_underestimation.htm](http://vista.cira.colostate.edu/improve/Data/QA_QC/Advisory/da0001/da0001_S_underestimation.htm).

Schichtel, B. A., Malm, W. C., Beaver, M., Copeland, S., Hand, J. L., Prenni, A. J., Rice, J., and Vimont, J. (2021), The future of carbonaceous aerosol measurement in the IMPROVE monitoring program, [http://vista.cira.colostate.edu/improve/wp-content/uploads/2021/10/041\\_CarbonReport\\_Final.pdf](http://vista.cira.colostate.edu/improve/wp-content/uploads/2021/10/041_CarbonReport_Final.pdf).

Theil, H. (1950), A rank-invariant method of linear and polynomial regression analysis., *Proc. Kon. Ned. Akad. v Wetensch.*, A(53), 386-392, [https://doi.org/10.1007/978094-011-2546-8\\_20](https://doi.org/10.1007/978094-011-2546-8_20).

White, W. H. (2006), Elemental concentrations above the MDL can go undetected, *IMPROVE Data Advisory* (da0010),

[http://vista.cira.colostate.edu/improve/Data/QA\\_QC/Advisory/da0010/da0010\\_Almdl.pdf](http://vista.cira.colostate.edu/improve/Data/QA_QC/Advisory/da0010/da0010_Almdl.pdf).

White, W. H. (2007), Shift in EC/OC split with 1 January 2005 TOR hardware upgrade, *IMPROVE Data Advisory* (da0016),

[http://vista.cira.colostate.edu/improve/Data/QA\\_QC/Advisory/da0016/da0016\\_TOR2005.pdf](http://vista.cira.colostate.edu/improve/Data/QA_QC/Advisory/da0016/da0016_TOR2005.pdf).

White, W. H. (2015), Changed reporting of light absorption, *IMPROVE Data Advisory* (da0033),  
[http://vista.cira.colostate.edu/improve/Data/QA\\_QC/Advisory/da0033/da0033\\_Fabs.pdf](http://vista.cira.colostate.edu/improve/Data/QA_QC/Advisory/da0033/da0033_Fabs.pdf).

White, W. H. (2016), Increased variation of humidity in the weighing laboratory, *IMPROVE Data Advisory* (da0035),

[http://vista.cira.colostate.edu/improve/Data/QA\\_QC/Advisory/da0035/da0035\\_IncreasedRH.pdf](http://vista.cira.colostate.edu/improve/Data/QA_QC/Advisory/da0035/da0035_IncreasedRH.pdf).

White, W. H., Trzepla, K., Hyslop, N. P., and Schichtel, B. A. (2016), A critical review of filter transmittance measurements for aerosol light absorption, and de novo calibration for a decade of monitoring on PTFE membranes, *Aerosol Science and Technology*, 50(9), 984-1002,  
<http://dx.doi.org/10.1080/02786826.2016.1211615>.

Zhang, X. (2019), Correction of chloride concentrations for filter blank levels, *IMPROVE Data Advisory* (da0039),

[http://vista.cira.colostate.edu/improve/Data/QA\\_QC/Advisory/da0039/da0039\\_ChlorideOverCorrection.pdf](http://vista.cira.colostate.edu/improve/Data/QA_QC/Advisory/da0039/da0039_ChlorideOverCorrection.pdf).

## Chapter 7. Trends in IMPROVE Reconstructed Light Extinction Coefficients

Temporal trends were calculated for speciated aerosol extinction coefficients, including extinction due to ammonium sulfate ( $b_{ext\_AS}$ ), ammonium nitrate ( $b_{ext\_AN}$ ), particulate organic matter ( $b_{ext\_POM}$ ), elemental carbon ( $b_{ext\_EC}$ ), fine dust ( $b_{ext\_FD}$ ), coarse mass ( $b_{ext\_CM}$ ), aerosol extinction ( $b_{ext\_aer}$ ), total extinction (aerosol and Rayleigh,  $b_{ext\_tot}$ ), and deciview (dv). Trends in sea salt extinction ( $b_{ext\_SS}$ ) were not calculated because of negative biases in chloride concentrations from 2007 to 2011 (Zhang, 2019). For all of the parameters, long-term (30 years, 1990–2019) and short-term (20 years, 2000–2019) trends were computed. Short-term trends take advantage of the network expansion in 2000 that resulted in greater site coverage across the country. Trend analyses were not performed for Chemical Speciation Network data because of the many changes starting in 2016 that resulted in some shifts to the data that require further evaluation before trends can be accurately interpreted (see Appendix 1.2).

Site-specific trends were computed for the same eight parameters as mass trends: 10<sup>th</sup>, 50<sup>th</sup>, and 90<sup>th</sup> percentiles and winter (DJF), spring (MAM), summer (JJA), fall (SON), and annual means. Winter means include the December data from the previous year. Fifty percent of daily data was required for a valid seasonal mean, and annual means were calculated from four valid seasonal means. Annual percentiles were calculated for 60% of valid daily data. Sites for long- and short-term trends required 70% of the years to be valid. A Theil regression was performed with the  $b_{ext}$  data as the dependent variable and the year as the independent variable. An advantage to the Theil regression is that heavy influence by outliers on the regression results is avoided (Theil, 1950). Kendall tau statistics were used to determine the statistical significance, assuming the slope was statistically significant at 5% ( $p \leq 0.05$ ), meaning that there was a 95% chance that the slope was not due to random chance. Trends (% yr<sup>-1</sup>) were calculated by dividing the slope by the median  $b_{ext}$  value over the time period of the trend, multiplied by 100%. Reporting trends instead of slopes normalizes the range in  $b_{ext}$  values that occurred across the United States. However, trends can be large (>100%) when median  $b_{ext}$  values are very low (e.g., 10<sup>th</sup> percentile).

Short-term regional mean trends were calculated for ten regions of the United States. Sites were grouped by their state into the following regions: Northeast, Southeast, Midsouth, Central, Southwest, Northwest, California, Alaska, Hawaii, Virgin Islands (See Table 6.0 and Figure 6.0), and the continental United States (CONUS). The Virgin Islands region included one site. Only sites that met the 70% valid data trend requirement were included in the regional trend calculation. Although some names are the same, these regions are broader and do not correspond to the regions shown in Chapters 3 and 5. The regions were qualitatively determined only as a means for summarizing trends. Regional mean trends were computed by aggregating site-specific seasonal mean  $b_{ext}$  (or percentiles) for a given region and year and then performing a Theil regression on regional mean  $b_{ext}$ . Regional mean trends were calculated for seasonal and annual means and for the 10<sup>th</sup>, 50<sup>th</sup>, and 90<sup>th</sup> percentiles. Annual mean trends can be driven by trends during specific seasons, and different percentiles may correspond to different trends, so regional mean trends were categorized by these aggregations to provide further insight into the temporal behavior of major aerosol extinction components.

Trend results were interpolated to provide isopleths to guide the eye (Isaaks and Mohan Srivastava, 1989). Site-specific positive trends were denoted with an upward-pointing triangle and contoured with warm colors. Negative trends were shown with downward-pointing triangles and contoured with cold colors. Statistically significant trends ( $p \leq 0.05$ ) were denoted with filled triangles. Scales were kept similar for all parameters so that trends can be compared. Long-term trend maps suffer from lower site densities, and therefore interpolations in regions without long-term sites (such as the central United States) should be viewed only as a spatial transition.

Speciated  $b_{ext}$  trends were similar to mass trends, especially for nonhygroscopic species. Differences in trends may arise depending on treatment of negative extinction values, which can occur for (very small) negative mass concentrations. While negative mass values reflect uncertainties in the measurements, negative  $b_{ext}$  values are unphysical and were set to zero.

## 7.1 AMMONIUM SULFATE LIGHT EXTINCTION COEFFICIENT TRENDS

Long-and short-term annual mean  $b_{ext\_AS}$  trends are shown in Figures 7.1.1a and 7.1.1b, respectively. All of the 55 valid sites met long-term completeness criteria, and all were statistically significant. Reductions of  $b_{ext\_AS}$  were strongest at sites in the eastern United States, in the Appalachian Mountains and Ohio River valley areas, where sulfur dioxide emissions have decreased dramatically and have led to improvements in visibility (Hand et al., 2014; Hand et al., 2020). Long-term annual mean  $b_{ext\_AS}$  trends ranged from  $-7.91\% \text{ yr}^{-1}$  ( $p < 0.001$ ) at Shining Rock Wilderness Area (WA), North Carolina (SHRO1), to  $-0.97\% \text{ yr}^{-1}$  ( $p = 0.02$ ) at Lassen Volcanic National Park (NP), California (LAVO1). Less progress occurred for sites in California, Nevada, and Idaho, as well as southwest Texas. Trends at these sites were between  $-1$  and  $-2\% \text{ yr}^{-1}$ . The West has historically had lower sulfur dioxide emissions than the eastern United States (Hand et al., 2012; Hand et al., 2020), and therefore the reduction of those regulated emissions has had less of an impact on already-low extinction values.

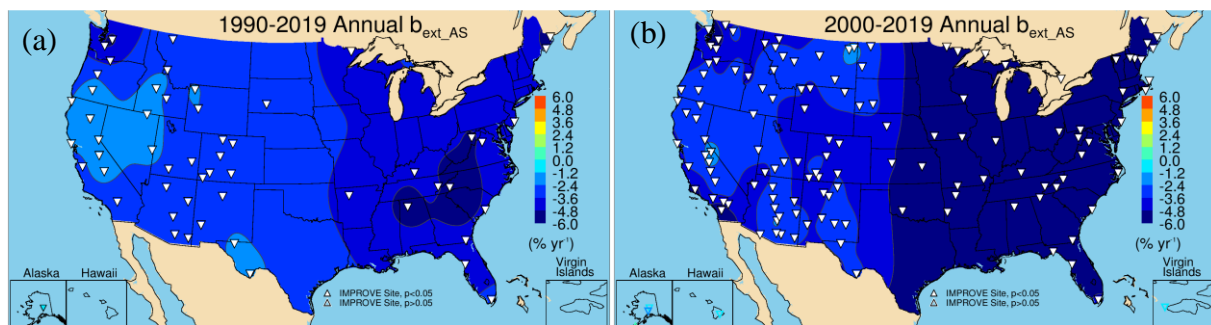


**Figure 7.1.1.** Annual mean ammonium sulfate  $b_{ext}$  ( $b_{ext\_AS}$ ) trends ( $\% \text{ yr}^{-1}$ ) for (a) long-term (1990–2019) and (b) short-term (2000–2019) periods. Filled triangles correspond to statistically significant trends ( $p \leq 0.05$ ).

Trends in short-term annual mean  $b_{ext\_AS}$  were negative for all valid sites shown in Figure 7.1.1b. Out of the 135 valid sites, 130 were statistically significant and ranged from  $-11.55\% \text{ yr}^{-1}$  ( $p < 0.001$ ) at (FRRE1) to  $1.93\% \text{ yr}^{-1}$  ( $p = 0.003$ ) at (HOOV1). Insignificant trends occurred at sites in Hawaii, Alaska, and the Virgin Islands. A strong spatial gradient in annual mean trends existed between the eastern and western United States, with stronger rates of change for sites in the East. Sites east of  $-100^\circ$  nearly all had  $b_{ext\_AS}$  decrease at rates greater than  $-4\% \text{ yr}^{-1}$ , and in the Appalachia and Ohio River valley areas, trends were around  $-7\% \text{ yr}^{-1}$  to  $-10\% \text{ yr}^{-1}$ ,

corresponding to a 140–200% decrease over the past two decades. Trends in the western United States were about  $-2\text{ \% yr}^{-1}$  to  $-4\text{ \% yr}^{-1}$ .

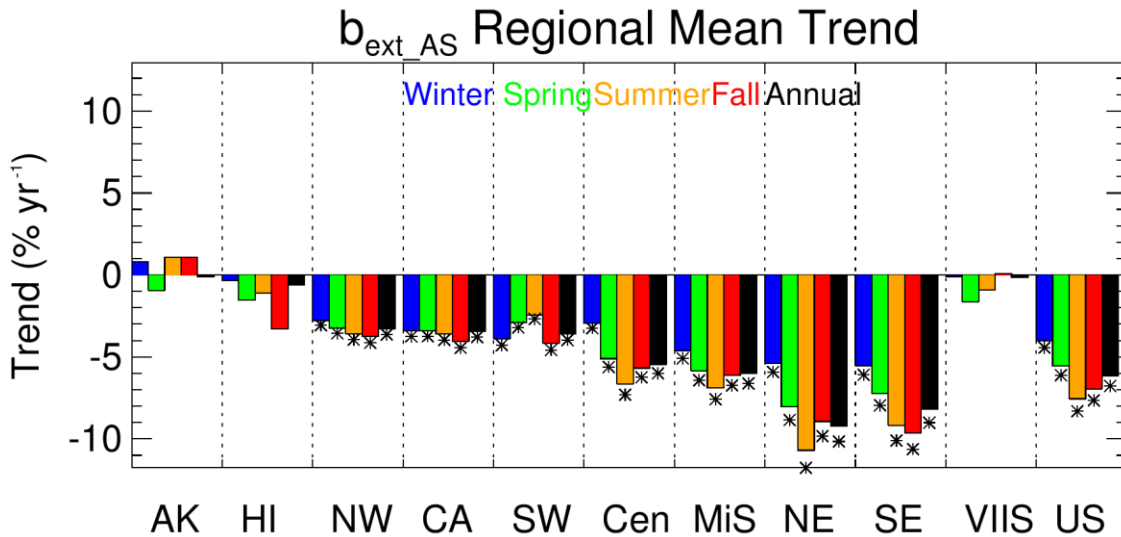


**Figure 7.1.2.** Short-term (2000–2019) regional seasonal mean ammonium sulfate  $b_{\text{ext}}$  ( $b_{\text{ext\_AS}}$ ) trends ( $\text{ \% yr}^{-1}$ ) for major U.S. regions for winter, spring, summer, fall, and annual means. Regions are arranged from western to eastern United States (AK = Alaska, HI = Hawaii, NW = Northwest, CA = California, SW = Southwest, Cen = Central, MiS = Midsouth, NE = Northeast, SE = Southeast, VIIS = Virgin Islands, and US = all sites). Statistically significant trends ( $p \leq 0.05$ ) are denoted with “\*\*”.

Regional seasonal mean  $b_{\text{ext\_AS}}$  trends are presented in Figure 7.1.2 and were similar to regional mean mass trends. The largest reductions in seasonal mean  $b_{\text{ext\_AS}}$  occurred for sites in the Northeast region ( $-10.70\text{ \% yr}^{-1}$  in summer), followed by the Southeast region ( $-9.66\text{ \% yr}^{-1}$  in fall). The least negative regional mean trends in the East occurred during winter. Trends were lower at regions in the western United States ( $-3\text{ \% yr}^{-1}$  to  $-4\text{ \% yr}^{-1}$ ), and the range in seasonal mean trends were lower. The exception to this is in the Southwest region, where summer trends were lower relative to other seasons. Overall, across the United States, negative  $b_{\text{ext\_AS}}$  trends were strongest during summer and fall. Seasonal regional mean trends at sites in Alaska, Hawaii, and the Virgin Islands were all relatively flat and insignificant.

Long-term 10<sup>th</sup> and 90<sup>th</sup> percentile  $b_{\text{ext\_AS}}$  trends are shown in Figure 7.1.3a and 7.1.3b, respectively. The spatial variability for the 10<sup>th</sup> and 90<sup>th</sup> percentile trends were similar, with larger reductions at sites in the eastern United States. The 10<sup>th</sup> percentile trends ranged from  $-5.74\text{ \% yr}^{-1}$  ( $p < 0.001$ ) at Shining Rock WA, North Carolina (SHRO1), to  $-1.34\text{ \% yr}^{-1}$  ( $p = 0.008$ ) at Jarbidge WA, Nevada (JARB1), and 54 out of 57 sites had statistically significant trends. Insignificant trends occurred at Hawaii Volcanoes NP, Hawaii (HAVO1), Lassen Volcanic NP, California (LAVO1), and Three Sisters WA, Oregon (THSI1). Trends in the 10<sup>th</sup> percentile  $b_{\text{ext\_AS}}$  at sites in California were weaker ( $\sim 2\text{ \% yr}^{-1}$ ) than at other sites in the United States.

Trend values did not differ greatly for the long-term 90<sup>th</sup> percentile  $b_{\text{ext\_AS}}$  (Figure 7.1.3b) compared to the 10<sup>th</sup> percentile  $b_{\text{ext\_AS}}$  trends, and 56 out of 57 sites had statistically significant

trends. The largest negative trend occurred at Shining Rock WA, North Carolina (SHRO1,  $-7.20\% \text{ yr}^{-1}$ ,  $p < 0.001$ ), compared to the lowest negative trend at Big Bend NP, Texas (BIBE1,  $-1.02\% \text{ yr}^{-1}$ ,  $p = 0.012$ ).

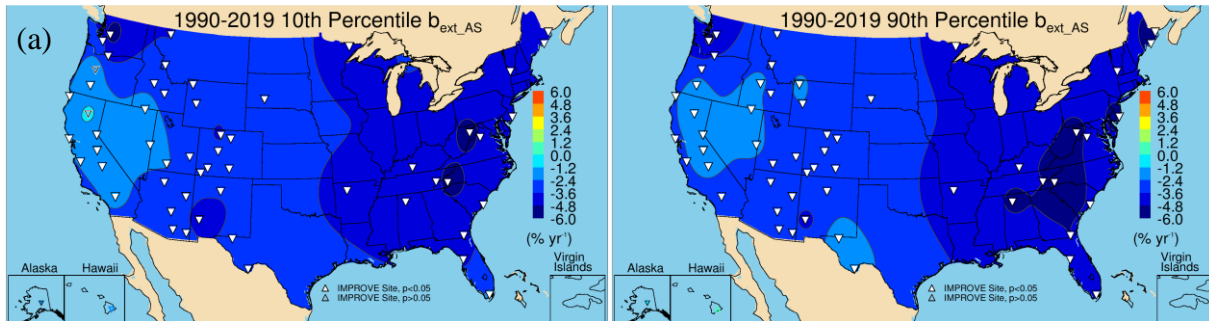


**Figure 7.1.3. IMPROVE long-term (1990–2019) trends ( $\% \text{ yr}^{-1}$ ) in (a) 10<sup>th</sup> percentile ammonium sulfate  $b_{\text{ext}}$  ( $b_{\text{ext\_AS}}$ ) and (b) 90<sup>th</sup> percentile  $b_{\text{ext\_AS}}$ . Filled triangles correspond to statistically significant trends ( $p \leq 0.05$ ).**

Short-term trends in the 10<sup>th</sup> and 90<sup>th</sup>  $b_{\text{ext\_AS}}$  are shown in Figure 7.1.4a and 7.1.4b, respectively. Large-scale spatial variability in trends was similar for both percentiles, with greater reductions in  $b_{\text{ext\_AS}}$  at sites in the eastern United States. Differences in the spatial patterns occurred at sites in the central United States where the 90<sup>th</sup> percentile trends were stronger (e.g., Kansas and Oklahoma and in southern California). At sites in the northwestern United States, 10<sup>th</sup> percentile trends were stronger. For 138 valid sites with 10<sup>th</sup> percentile trends, 126 were statistically significant, compared to 132 for 90<sup>th</sup> percentile trends. The largest reductions in 10<sup>th</sup> percentile  $b_{\text{ext\_AS}}$  occurred at Cohutta, Georgia (COHU1,  $-8.32\% \text{ yr}^{-1}$ ,  $p < 0.001$ ), compared to lowest reduction at Crater Lake NP, California (CRLA1,  $-1.78\% \text{ yr}^{-1}$ ,  $p = 0.04$ ). The largest reduction in the 90<sup>th</sup> percentile  $b_{\text{ext\_AS}}$  also occurred at Cohutta, Georgia (COHU1,  $-14.38\% \text{ yr}^{-1}$ ,  $p < 0.001$ ), compared to the lowest reduction at Kaiser, California (KAIS1,  $-1.45\% \text{ yr}^{-1}$ ,  $p = 0.009$ ). For both the 10<sup>th</sup> and 90<sup>th</sup> percentiles, trends were insignificant at sites in Alaska, Hawaii, and the Virgin Islands.

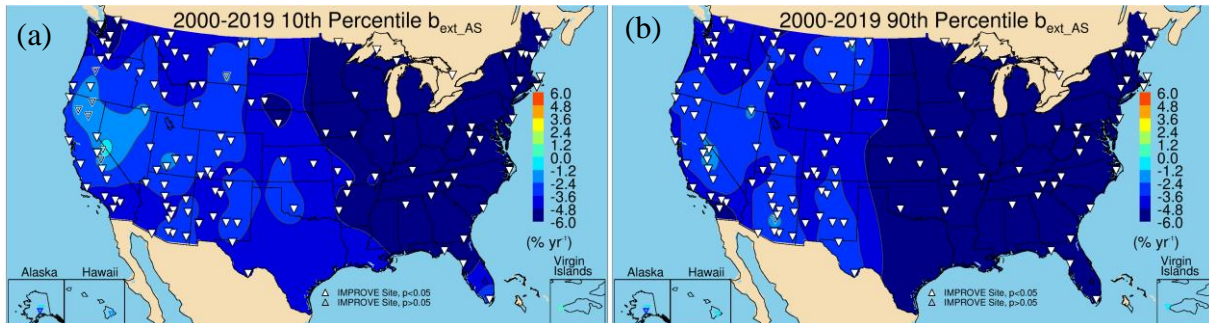


**Figure 7.1.4. IMPROVE short-term (2000–2019) trends ( $\% \text{ yr}^{-1}$ ) in (a) 10<sup>th</sup> percentile ammonium sulfate  $b_{\text{ext}}$  ( $b_{\text{ext\_AS}}$ ) and (b) 90<sup>th</sup> percentile  $b_{\text{ext\_AS}}$ . Filled triangles correspond to statistically significant trends ( $p \leq 0.05$ ).**

Comparisons of regional mean percentile trends are shown in Figure 7.1.5. For most regions in the western United States, the 10<sup>th</sup>, 50<sup>th</sup>, and 90<sup>th</sup> percentile trends were similar, with the Northwest region having slightly greater reductions in the 10<sup>th</sup> percentile  $b_{\text{ext\_AS}}$  as suggested in Figures 7.1.4a and 7.1.4b. However, for eastern regions, the regional mean 90<sup>th</sup> percentile trends decreased at a much greater rate than the other percentile trends. The 90<sup>th</sup> percentile trend

in the Northeast region was  $-11.25\% \text{ yr}^{-1}$  compared to the 10<sup>th</sup> percentile trend of  $-6.37\% \text{ yr}^{-1}$ . The Southeast region had similar differences in the 90<sup>th</sup> and 10<sup>th</sup> percentile trends ( $-9.83\% \text{ yr}^{-1}$  compared to  $-5.44\% \text{ yr}^{-1}$ ,  $p < 0.001$ , respectively). These trends are consistent with the strongest seasonal mean trends occurring in summer, when the highest  $b_{\text{ext\_AS}}$  typically occurred.

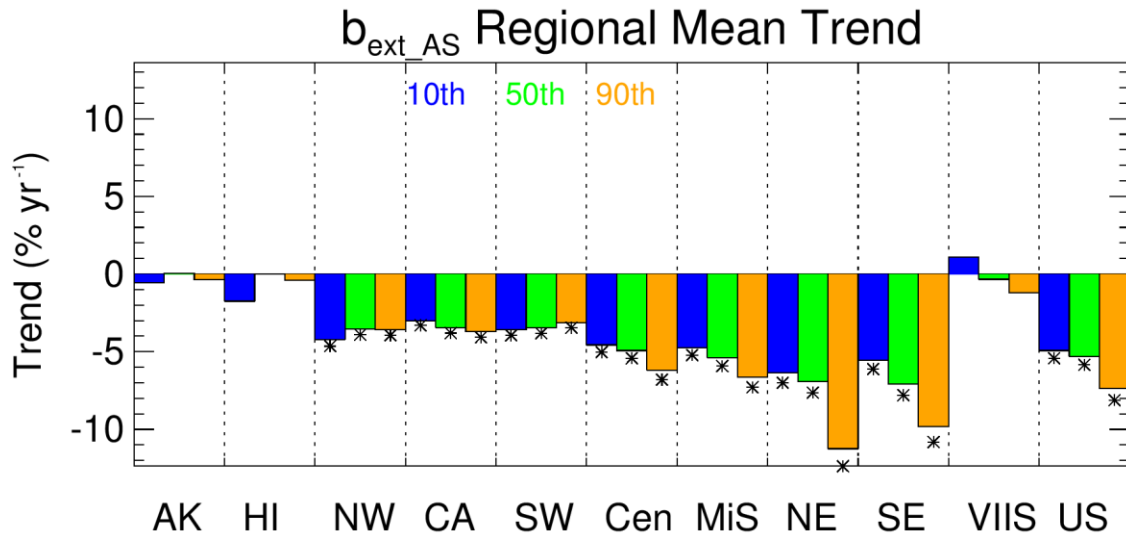


**Figure 7.1.5.** Short-term (2000–2019) regional mean trends ( $\% \text{ yr}^{-1}$ ) in 10<sup>th</sup>, 50<sup>th</sup>, and 90<sup>th</sup> percentile ammonium sulfate  $b_{\text{ext}}$  ( $b_{\text{ext\_AS}}$ ). Regions are arranged from western to eastern United States (AK = Alaska, HI = Hawaii, NW = Northwest, CA = California, SW = Southwest, Cen = Central, MiS = Midsouth, NE = Northeast, SE = Southeast, VIIS = Virgin Islands, and US = all sites). Statistically significant trends ( $p \leq 0.05$ ) are denoted with “\*”.

## 7.2 AMMONIUM NITRATE LIGHT EXTINCTION COEFFICIENT TRENDS

Long-term annual mean  $b_{\text{ext\_AN}}$  trends are shown in Figure 7.2.1a. Of the 42 valid trend sites, 36 had statistically significant trends. The largest reductions ( $\sim -3\% \text{ yr}^{-1}$ ) in the annual mean  $b_{\text{ext\_AN}}$  occurred at sites in southern California, with the largest negative trend at San Gorgonio WA, California (SAGO1,  $-7.75\% \text{ yr}^{-1}$ ,  $p < 0.001$ ). Strong reductions in  $b_{\text{ext\_AN}}$  at sites in California are associated with reduced nitrogen dioxide emissions from vehicles (Russell et al., 2012; Tong et al., 2015). Insignificant trends occurred at sites in Colorado, Texas, and New Mexico and were associated with nearly flat reductions. The lowest statistically significant trend occurred at Bridger WA, Wyoming (BRID1,  $-0.94\% \text{ yr}^{-1}$ ,  $p = 0.03$ ). Trends at sites in the eastern United States were about  $-1\% \text{ yr}^{-1}$  to  $-2\% \text{ yr}^{-1}$ .

Short-term annual mean  $b_{\text{ext\_AN}}$  trends also showed strong reductions at sites in southern California (Figure 7.2.1b). The strongest reduction for short-term trends occurred at Joshua Tree NP, California (JOSH1,  $-8.92\% \text{ yr}^{-1}$ ,  $p < 0.001$ ). Of the 134 valid trends, 110 were statistically significant. Insignificant trends at sites in the northern Great Plains ( $-1\% \text{ yr}^{-1}$  to  $-2\% \text{ yr}^{-1}$ ) were likely associated with oil and gas development in the region (Gebhart et al., 2018). The lowest statistically significant annual mean  $b_{\text{ext\_AN}}$  trend occurred at Medicine Lake, Montana (MELA1,  $-0.89\% \text{ yr}^{-1}$ ,  $p = 0.04$ ).

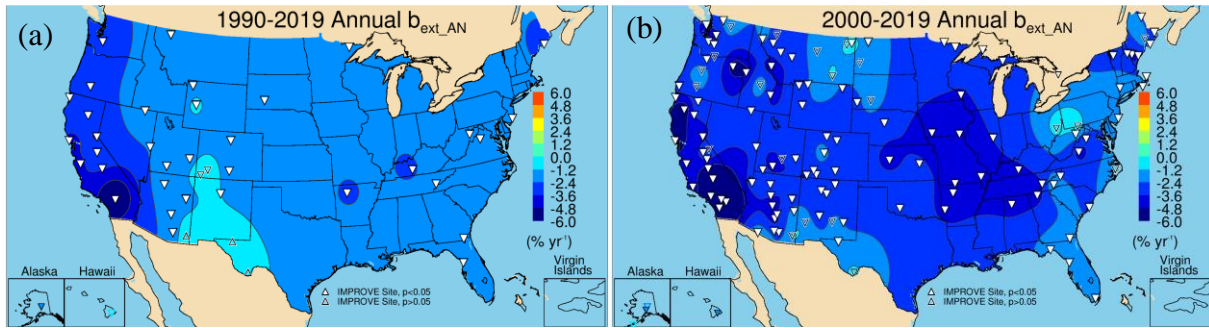


**Figure 7.2.1.** Annual mean ammonium nitrate  $b_{ext}$  ( $b_{ext\_AN}$ ) trends ( $\% \text{ yr}^{-1}$ ) for (a) long-term (1990–2019) and (b) short-term (2000–2019) periods. Filled triangles correspond to statistically significant trends ( $p \leq 0.05$ ).

Comparisons of short-term regional seasonal mean  $b_{ext\_AN}$  trends are shown in Figure 7.2.2. The strongest reductions occurred in the California region, especially in the spring (-6.97%  $\text{yr}^{-1}$ ) and fall (-7.10%  $\text{yr}^{-1}$ ). Most regions had the strongest reductions during winter and least reductions in summer, with a large seasonal range. The exception was in the Northeast region where trends for all seasons were similar (~-2%  $\text{yr}^{-1}$  to -3%  $\text{yr}^{-1}$ ). This range in seasonal mean trends indicates potentially different sources and atmospheric processes controlling  $b_{ext\_AN}$  in these regions.

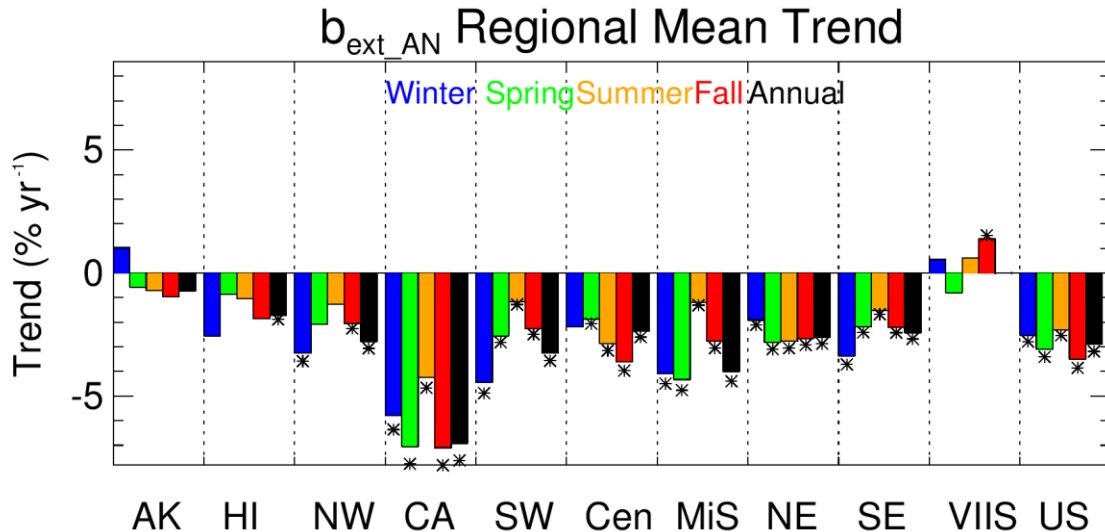


**Figure 7.2.2.** Short-term (2000–2019) regional seasonal mean ammonium nitrate  $b_{ext}$  ( $b_{ext\_AN}$ ) trends ( $\% \text{ yr}^{-1}$ ) for major U.S. regions for winter, spring, summer, fall, and annual means. Regions are arranged from western to eastern United States (AK = Alaska, HI = Hawaii, NW = Northwest, CA = California, SW = Southwest, Cen = Central, MiS = Midsouth, NE = Northeast, SE = Southeast, VIIS = Virgin Islands, and US = all sites). Statistically significant trends ( $p \leq 0.05$ ) are denoted with “\*”.

Long-term trends in the 10<sup>th</sup> and 90<sup>th</sup> percentile  $b_{ext\_AN}$  are shown in Figure 7.2.3a and 7.2.3b, respectively. Of the 45 valid 10<sup>th</sup> percentile trends, only 26 of them were statistically significant, and these occurred mainly at sites in California and the eastern United States. The strongest reduction in the 10<sup>th</sup> percentile  $b_{ext\_AN}$  occurred at San Gorgonio WA, California (SAGO1, -6.25%  $\text{yr}^{-1}$ ,  $p < 0.001$ ), compared to -0.88%  $\text{yr}^{-1}$  ( $p = 0.03$ ) at Weminuche WA,

Colorado (WEMI1). Flat and insignificant trends occurred at sites located in the southwestern United States and the Intermountain West.

The spatial patterns in the long-term 90<sup>th</sup> percentile trends were similar to the 10<sup>th</sup> percentile trends, with the strongest reductions at sites in California and weak and insignificant trends at sites in the Southwest (Figure 7.2.3b). Trends ranged from -5.96% yr<sup>-1</sup> ( $p < 0.001$ ) at San Gorgonio WA (SAGO1), to -0.88% yr<sup>-1</sup> ( $p = 0.05$ ) at Jarbidge WA, Nevada (JARB1). However, more sites met statistical significance limits (32 out of 45) for 90<sup>th</sup> percentile trends. Some long-term 90<sup>th</sup> percentile trends in the eastern United States were weaker relative to the 10<sup>th</sup> percentile trends, but sites in the Intermountain West had stronger and statistically significant 90<sup>th</sup> percentile trends.

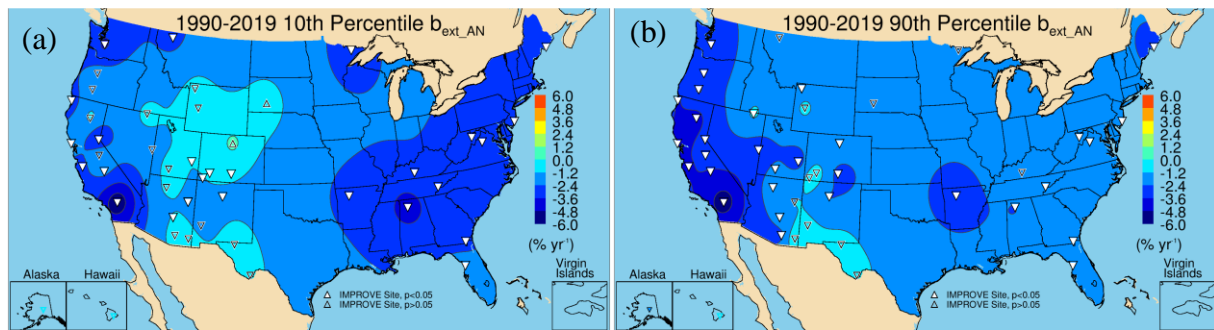


**Figure 7.2.3. IMPROVE long-term (1990–2019) trends (% yr<sup>-1</sup>) in (a) 10<sup>th</sup> percentile ammonium nitrate  $b_{ext}$  ( $b_{ext\_AN}$ ) and (b) 90<sup>th</sup> percentile  $b_{ext\_AN}$ . Filled triangles correspond to statistically significant trends ( $p \leq 0.05$ ).**

The strongest reductions in short-term 10<sup>th</sup> percentile  $b_{ext\_AN}$  trends also occurred at San Gorgonio WA, California (SAGO1, -8.58 % yr<sup>-1</sup>,  $p < 0.001$ ) (Figure 7.2.4a). Several sites in the eastern United States also experienced strong reductions in the 10<sup>th</sup> percentile  $b_{ext\_AN}$  (-5% yr<sup>-1</sup> to -6% yr<sup>-1</sup>). Insignificant trends occurred at 81 of 138 valid sites. Positive but insignificant trends occurred at sites in the northern Great Plains, where oil and gas development has influenced  $b_{ext\_AN}$ . Other insignificant and flat trends occurred at sites in Colorado, Nebraska, South Dakota, Oregon, and Texas. The weakest significant trend occurred at Thunder Basin, Wyoming (THBA1, -1.09% yr<sup>-1</sup>,  $p = 0.04$ ).

The spatial patterns in the short-term 10<sup>th</sup> and 90<sup>th</sup> percentile trends (Figure 7.2.4b) were similar, with the strongest trends at sites in southern California and at sites in the Appalachian Mountains. Out of 138 valid 90<sup>th</sup> percentile trends, 101 met statistical significance requirements. Most of the insignificant trends also occurred at sites in the northern Great Plains area and near Maryland and Ohio (Frostburg Reservoir, Maryland, FRRE1, and Quaker City, Ohio, QUCI1, respectively). The short-term 90<sup>th</sup> percentile trends ranged from -9.68% yr<sup>-1</sup> ( $p = 0.011$ ) at Hells Canyon, Oregon (HECA1), to -1.43% yr<sup>-1</sup> ( $p = 0.04$ ) at Hawaii Volcanoes NP, Hawaii (HAVO1).

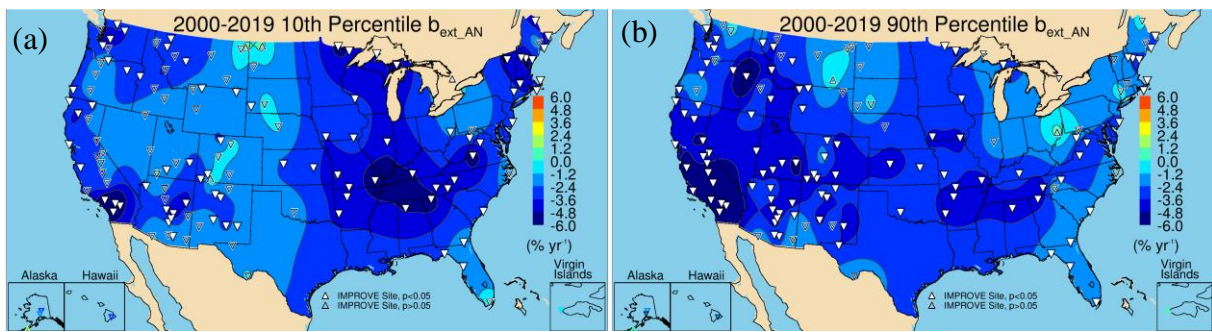


**Figure 7.2.4. IMPROVE short-term (2000–2019) trends ( $\% \text{ yr}^{-1}$ ) in (a) 10<sup>th</sup> percentile ammonium nitrate  $b_{\text{ext\_AN}}$  ( $b_{\text{ext\_AN}}$ ) and (b) 90<sup>th</sup> percentile  $b_{\text{ext\_AN}}$ . Filled triangles correspond to statistically significant trends ( $p \leq 0.05$ ).**

A summary of the regional mean 10<sup>th</sup>, 50<sup>th</sup>, and 90<sup>th</sup> percentile  $b_{\text{ext\_AN}}$  trends is shown in Figure 7.2.5. The strongest trends occurred in the California region, with the 90<sup>th</sup> percentile trends being the greatest (-6.77%  $\text{yr}^{-1}$ ,  $p < 0.001$ ). For all of the regions except the Central and Northeast regions, the 90<sup>th</sup> percentile trends were strongest. In the Central and Northeast regions, the 90<sup>th</sup> percentile trends were the weakest, and the 10<sup>th</sup> percentile trends were the strongest.

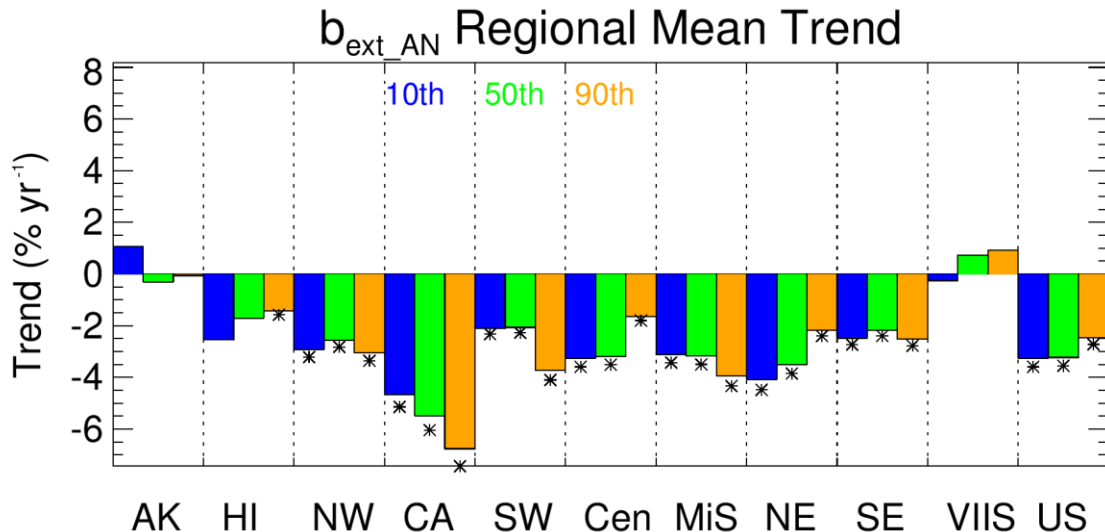


**Figure 7.2.5. Short-term (2000–2019) regional mean trends ( $\% \text{ yr}^{-1}$ ) in 10<sup>th</sup>, 50<sup>th</sup>, and 90<sup>th</sup> percentile ammonium nitrate  $b_{\text{ext}}$  ( $b_{\text{ext\_AN}}$ ). Regions are arranged from western to eastern United States (AK = Alaska, HI = Hawaii, NW = Northwest, CA = California, SW = Southwest, Cen = Central, MiS = Midsouth, NE = Northeast, SE = Southeast, VIIS = Virgin Islands, and US = all sites). Statistically significant trends ( $p \leq 0.05$ ) are denoted with “\*”.**

### 7.3 PARTICULATE ORGANIC MATTER LIGHT EXTINCTION COEFFICIENT TRENDS

Annual mean  $b_{\text{ext\_POM}}$  trends for long-term sites are shown in Figure 7.3.1a. Of the 50 valid sites, 32 had statistically significant trends, including all of the sites in the eastern United States. Sites in the Intermountain West and parts of California were associated with insignificant

and flat trends. Small positive but insignificant trends occurred at Bridger WA, Wyoming (BRID1), Jarbidge, Nevada (JARB1), Crater Lake NP, Oregon (CRLA1), Lassen Volcanic NP, California (LAVO1), and Bliss SP, California (BLIS1), all sites likely associated with impacts from biomass burning. The strongest statistically significant reductions in  $b_{ext\_POM}$  occurred at Mount Rainier NP, Washington (MORA1,  $-3.14\% \text{ yr}^{-1}$ ,  $p < 0.001$ ), and the least reduction occurred at Guadalupe Mountains, NP, Texas (GUMO1,  $-0.94\% \text{ yr}^{-1}$ ,  $p = 0.015$ ). Strong reductions at sites in the East occurred at Dolly Sods WA, West Virginia (DOSO1,  $-2.89\% \text{ yr}^{-1}$ ,  $p < 0.001$ ), Shenandoah NP, Virginia (SHEN1,  $-2.46\% \text{ yr}^{-1}$ ,  $p < 0.001$ ), and Moosehorn National Wildlife Refuge (NWR), Maine, (MOOS1,  $-2.88\% \text{ yr}^{-1}$ ,  $p < 0.001$ ).

With the addition of short-term sites, the area with sites having insignificant short-term trends expanded farther north (Figure 7.3.1b) into Montana, Idaho, and Washington, where biomass smoke has influenced trends in fine mass and organic carbon (McClure and Jaffe, 2018). All of the sites with insignificant trends occurred in the western United States and in Alaska, Hawaii, and the Virgin Islands. Of the 136 valid sites, 63 of them had statistically significant trends. The strongest reduction occurred at Agua Tibia, California (AGTI1,  $-4.27\% \text{ yr}^{-1}$ ,  $p < 0.001$ ), and the least reduction occurred at Big Bend NP, Texas (BIBE,  $-1.33\% \text{ yr}^{-1}$ ,  $p = 0.019$ ). Relatively strong reductions in annual mean  $b_{ext\_POM}$  occurred in the southeastern and northeastern United States, Arizona, New Mexico, and southern California.

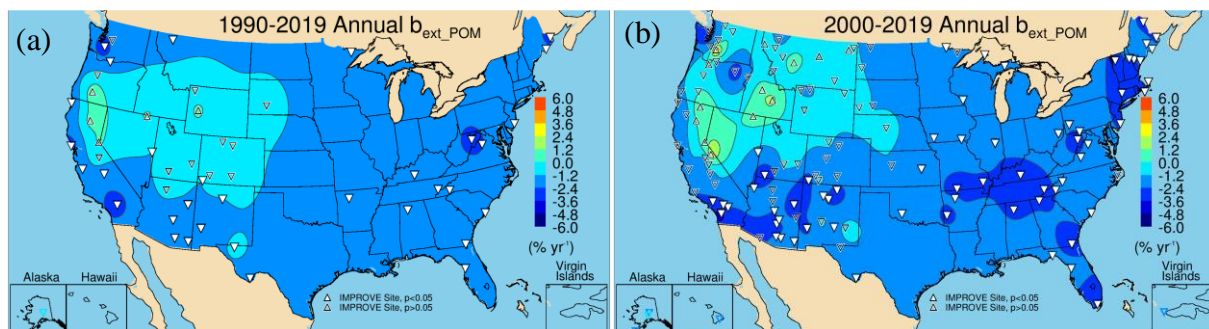


**Figure 7.3.1. Annual mean particulate organic matter  $b_{ext}$  ( $b_{ext\_POM}$ ) trends ( $\% \text{ yr}^{-1}$ ) for (a) long-term (1990–2019) and (b) short-term (2000–2019) periods. Filled triangles correspond to statistically significant trends ( $p \leq 0.05$ ).**

Regional seasonal mean  $b_{ext\_POM}$  trends are shown in Figure 7.3.2. Statistically significant trends occurred during all seasons in the Southeast, Northeast, and the Midsouth regions ( $\sim -3\% \text{ yr}^{-1}$ ). The strongest reductions in most of these regions occurred for winter and spring. Trends in the Central region were lower ( $\sim -1\% \text{ yr}^{-1}$  to  $-2\% \text{ yr}^{-1}$ ) than regions in the East and statistically significant in all seasons except summer. Seasonal mean trends in western regions were more variable than in regions in the East. All of the winter and spring trends were statistically significant, and  $b_{ext\_POM}$  declined more strongly in these seasons ( $-3\% \text{ yr}^{-1}$  to  $-4\% \text{ yr}^{-1}$ ). Summer and fall trends were insignificant and summer trends were flat in the Northwest and California regions. These seasons have been influenced by biomass burning emissions.

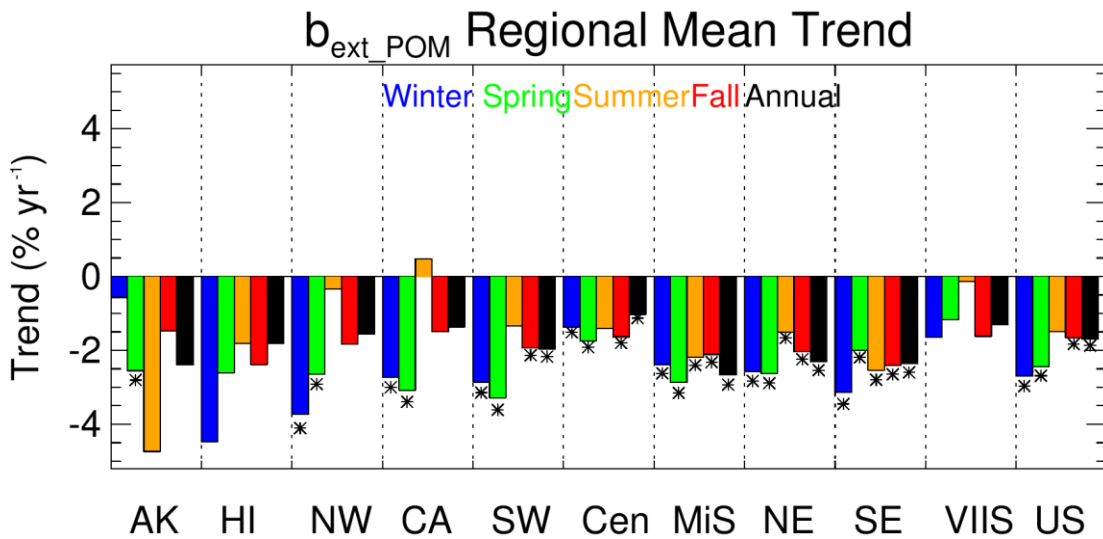


**Figure 7.3.2.** Short-term (2000–2019) regional, seasonal mean particulate organic matter  $b_{\text{ext}}\text{-POM}$  trends ( $\% \text{ yr}^{-1}$ ) for major U.S. regions for winter, spring, summer, fall, and annual means. Regions are arranged from western to eastern United States (AK = Alaska, HI = Hawaii, NW = Northwest, CA = California, SW = Southwest, Cen = Central, MiS = Midsouth, NE = Northeast, SE = Southeast, VIIS = Virgin Islands, and US = all sites). Statistically significant trends ( $p \leq 0.05$ ) are denoted with “\*\*”.

Long-term trends in the 10<sup>th</sup> percentile and 90<sup>th</sup> percentile  $b_{\text{ext}}\text{-POM}$  (Figure 7.3.3a and 7.3.3b, respectively) had different spatial patterns. At sites in the West, 10<sup>th</sup> percentile  $b_{\text{ext}}\text{-POM}$  trends were much stronger than for the 90<sup>th</sup> percentile  $b_{\text{ext}}\text{-POM}$  trends. Of the 50 long-term valid sites, 49 had statistically significant trends in 10<sup>th</sup> percentile  $b_{\text{ext}}\text{-POM}$ . Strong reductions occurred at sites in northern California, Oregon, and Washington ( $-5\% \text{ yr}^{-1}$  to  $-6\% \text{ yr}^{-1}$ ), with the strongest at Mount Rainier NP, Washington (MORA1,  $-6.48\% \text{ yr}^{-1}$ ,  $p < 0.001$ ). However, some sites across the United States experienced reductions around  $-2\% \text{ yr}^{-1}$  or greater. The lowest reduction occurred at Great Sand Dunes NP, Colorado (GRSA1,  $-1.31\% \text{ yr}^{-1}$ ,  $p < 0.001$ ).

In contrast, long-term 90<sup>th</sup> percentile trends at sites across the western United States were mostly insignificant, with over half (27) of the sites meeting statistical significance. The strongest trend occurred at San Gorgonio WA, California (SAGO1,  $-3.50\% \text{ yr}^{-1}$ ,  $p < 0.001$ ), compared to the weakest at Bandelier NM, New Mexico (BAND1,  $-1.03\% \text{ yr}^{-1}$ ,  $p = 0.015$ ). These results suggest different influences on trends for low and high  $b_{\text{ext}}\text{-POM}$ . The trends in the highest  $b_{\text{ext}}\text{-POM}$  in the western United States were likely influenced by biomass burning impacts.

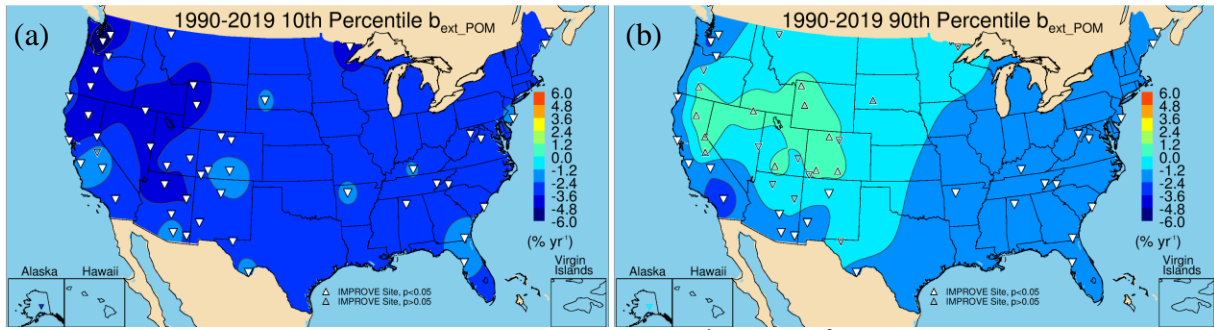


**Figure 7.3.3. IMPROVE long-term (1990–2019) trends ( $\% \text{ yr}^{-1}$ ) in (a) 10<sup>th</sup> percentile particulate organic matter  $b_{\text{ext\_POM}}$  and (b) 90<sup>th</sup> percentile  $b_{\text{ext\_POM}}$ . Filled triangles correspond to statistically significant trends ( $p \leq 0.05$ ).**

Spatial patterns in short-term trends in the 10<sup>th</sup> and 90<sup>th</sup> percentile  $b_{\text{ext\_POM}}$  were similar to long-term trends (Figure 7.3.4a and 7.3.4b, respectively). Many of the 10<sup>th</sup> percentile trends were statistically significant (93 out of 138 valid sites) and nearly all of these sites were in the eastern United States. However, some of the strongest reductions in the 10<sup>th</sup> percentile  $b_{\text{ext\_POM}}$  occurred at sites in the West, such as Colorado, Wyoming, Nevada, Washington, and southern California. The greatest reductions occurred at North Absaroka, Wyoming (NOAB1,  $-8.37\% \text{ yr}^{-1}$ ,  $p = 0.003$ ), compared to Ike's Backbone, Arizona (IKBA1,  $-1.70\% \text{ yr}^{-1}$ ,  $p = 0.002$ ).

Many of the short-term trends in the 90<sup>th</sup> percentile  $b_{\text{ext\_POM}}$  at sites in the West were insignificant, except for sites in southern California and Arizona (Figure 7.3.4b). Influences on the highest  $b_{\text{ext\_POM}}$  trends do not appear to be affecting the lowest  $b_{\text{ext\_POM}}$  over time. The strongest reductions in the 90<sup>th</sup> percentile trends occurred at Sierra Ancha, Arizona (SIAN1,  $-4.16\% \text{ yr}^{-1}$ ,  $p = 0.009$ ), compared to  $-1.31\% \text{ yr}^{-1}$  ( $p = 0.016$ ) at Moosehorn NWR, Maine (MOOS1). Although all insignificant, 22 trends were positive.

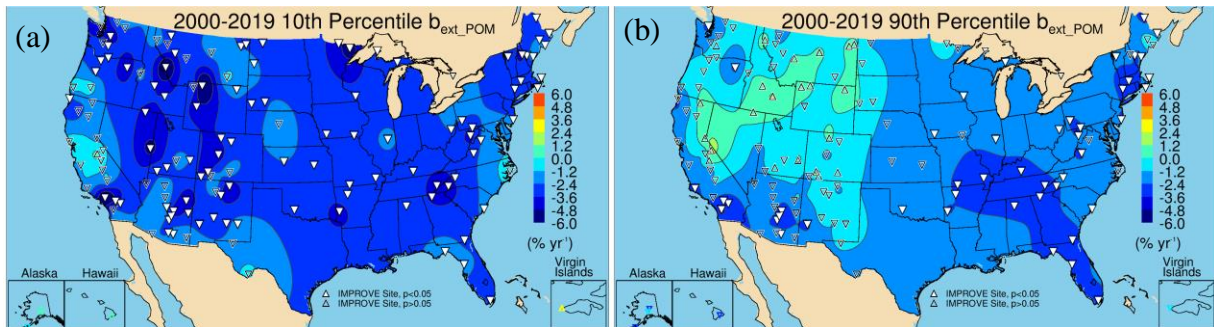


**Figure 7.3.4. IMPROVE short-term (2000–2019) trends ( $\% \text{ yr}^{-1}$ ) in (a) 10<sup>th</sup> percentile particulate organic matter  $b_{\text{ext\_POM}}$  and (b) 90<sup>th</sup> percentile  $b_{\text{ext\_POM}}$ . Filled triangles correspond to statistically significant trends ( $p \leq 0.05$ ).**

Comparisons of regional mean percentile trends are shown in Figure 7.3.5. The 90<sup>th</sup> percentile trends were the weakest and statistically insignificant for regions in the West, such as the Northwest, California, and the Southwest regions. The 10<sup>th</sup> percentile trends in the California region were also insignificant. For the Southeast region, the range in trends for different percentiles was low. Almost all regions had stronger reductions in the 10<sup>th</sup> percentile  $b_{\text{ext\_POM}}$  relative to other percentile trends.

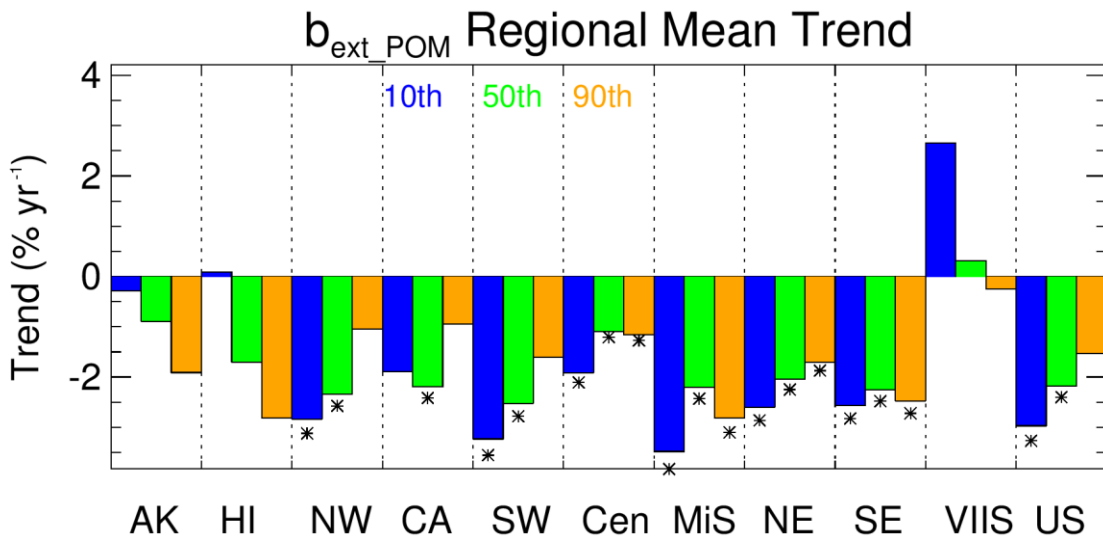


**Figure 7.3.5.** Short-term (2000–2019) regional mean trends ( $\% \text{ yr}^{-1}$ ) in 10<sup>th</sup>, 50<sup>th</sup>, and 90<sup>th</sup> percentile particulate organic matter  $b_{ext}$  ( $b_{ext\_POM}$ ). Regions are arranged from western to eastern United States (AK = Alaska, HI = Hawaii, NW = Northwest, CA = California, SW = Southwest, Cen = Central, MiS = Midsouth, NE = Northeast, SE = Southeast, VIIS = Virgin Islands, and US = all sites). Statistically significant trends ( $p \leq 0.05$ ) are denoted with “\*\*”.

#### 7.4 ELEMENTAL CARBON LIGHT EXTINCTION COEFFICIENT TRENDS

Long-term trends in annual mean  $b_{ext\_EC}$  are shown in Figure 7.4.1a. Of the 50 valid trends, 47 were statistically significant, and all were negative. The strongest reduction occurred at Point Reyes NP, California (PORE1,  $-5.73\% \text{ yr}^{-1}$ ,  $p < 0.001$ ), compared to the weakest at Guadalupe Mountains NP, Texas (GUMO1,  $-1.45\% \text{ yr}^{-1}$ ,  $p < 0.001$ ). The weakest trends occurred at sites in the West, and sites with insignificant trends occurred in areas influenced by biomass smoke (Bridger WA, Wyoming, BRID1; Jarbidge WA, Nevada, JARB1; and Lassen Volcanic NP, LAVO1).

Of the 136 valid short-term sites, 103 had statistically significant negative trends (Figure 7.4.1b). Sites with the strongest reductions ( $-5\% \text{ yr}^{-1}$  to  $-6\% \text{ yr}^{-1}$ ) were in southern California, the northwestern United States, and regions of the northeastern United States. The Moosehorn NWR, Maine (MOOS1), site had the strongest reduction in  $b_{ext\_EC}$  ( $-7.77\% \text{ yr}^{-1}$ ,  $p < 0.001$ ) compared to the weakest at White Mountain, New Mexico (WHIT1,  $-2.14\% \text{ yr}^{-1}$ ,  $p = 0.03$ ). Most of the statistically insignificant trends occurred in the West at sites influenced by biomass smoke and in northern Montana and North Dakota, where oil and gas development has been demonstrated to impact EC concentrations (Gebhart et al., 2018).

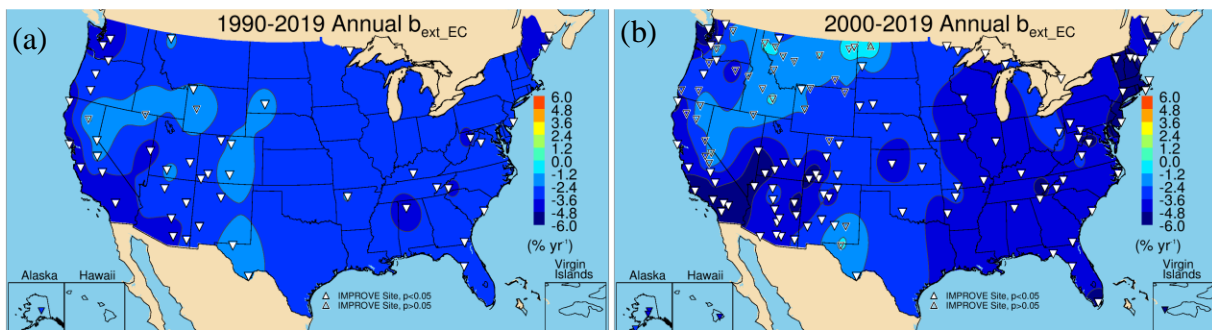


**Figure 7.4.1.** Annual mean elemental carbon  $b_{ext}$  ( $b_{ext\_EC}$ ) trends for (a) long-term (1990–2019) and (b) short-term (2000–2019) periods. Filled triangles correspond to statistically significant trends ( $p \leq 0.05$ ).

A summary of short-term regional seasonal mean trends is shown in Figure 7.4.2. Negative trends occurred for all regions and seasons, with large ranges in trends for some regions. Some of the strongest reductions occurred during all seasons in the Virgin Islands region. In eastern regions, the largest negative trends occurred during summer ( $\sim -5\% \text{ yr}^{-1}$ ). Trends in the Southeast region were somewhat larger than in other eastern regions and were large in both winter and summer. The lowest negative trends occurred in the Central region, especially in winter ( $-1.89\% \text{ yr}^{-1}$ ). In the West, the strongest reductions in  $b_{ext\_EC}$  ( $\sim -6\% \text{ yr}^{-1}$ ) occurred mainly in winter and spring (e.g., California) and were larger than regional trends in the East. Trends for all western regions were lowest in the summer and in the Northwest were insignificant, likely reflecting the role of biomass smoke on  $b_{ext\_EC}$ . The difference in seasonal and regional trends implies different sources and temporal behavior on  $b_{ext\_EC}$  depending on location.

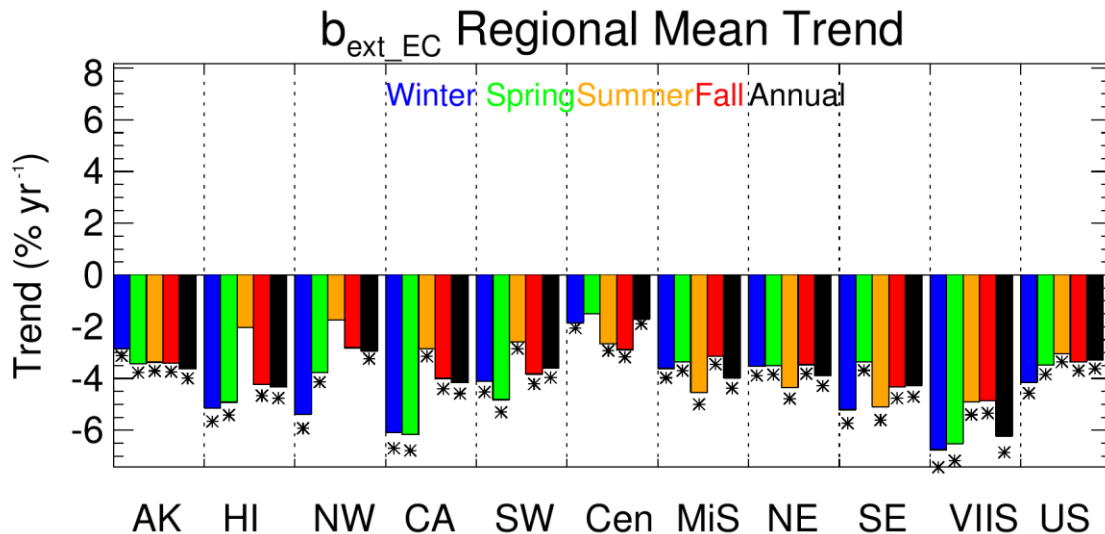


**Figure 7.4.2.** Short-term (2000–2019) regional seasonal mean elemental carbon  $b_{ext}$  ( $b_{ext\_EC}$ ) trends ( $\% \text{ yr}^{-1}$ ) for major U.S. regions for winter, spring, summer, fall, and annual means. Regions are arranged from western to eastern United States (AK = Alaska, HI = Hawaii, NW = Northwest, CA = California, SW = Southwest, Cen = Central, MiS = Midsouth, NE = Northeast, SE = Southeast, VIIS = Virgin Islands, and US = all sites). Statistically significant trends ( $p \leq 0.05$ ) are denoted with “\*”.

Long-term trends in 10<sup>th</sup> and 90<sup>th</sup> percentile  $b_{ext\_EC}$  are shown in Figure 7.4.3a and 7.4.3b, respectively. The strongest reductions in the 10<sup>th</sup> percentile  $b_{ext\_EC}$  occurred at sites in the western United States. Of the 51 valid sites, all had statistically significant trends. The largest negative trend occurred at Three Sisters WA, Oregon (THSI1, -9.29% yr<sup>-1</sup>, p < 0.001), compared to the weakest trend at Glacier NP, Montana (GLAC1, -2.16% yr<sup>-1</sup>, p = 0.002).

The 90<sup>th</sup> percentile  $b_{ext\_EC}$  declined at all of the valid long-term sites, with 46 of the 51 sites having statistically significant trends (Figure 7.4.3b). The strongest reductions were around -4% yr<sup>-1</sup> to -5% yr<sup>-1</sup> at sites in the northwestern United States, northeastern United States, and southern California. The strongest trend occurred at Point Reyes NP, California (PORE1, -5.46% yr<sup>-1</sup>, p < 0.001), and the weakest at Great Sand Dunes NP, Colorado (GRSA1, -1.00% yr<sup>-1</sup>, p = 0.02). Sites in Intermountain West and parts of California and Texas had weak and insignificant trends.

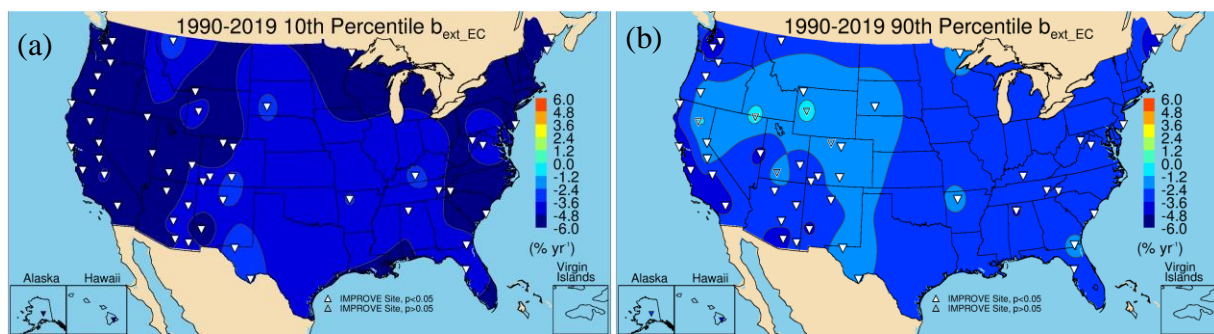


**Figure 7.4.3. IMPROVE long-term (1990–2019) trends (% yr<sup>-1</sup>) in (a) 10<sup>th</sup> percentile elemental carbon  $b_{ext}$  ( $b_{ext\_EC}$ ) and (b) 90<sup>th</sup> percentile  $b_{ext\_EC}$ . Filled triangles correspond to statistically significant trends (p ≤ 0.05).**

Negative short-term trends in 10<sup>th</sup> percentile  $b_{ext\_EC}$  occurred at all sites except Lostwood, North Dakota (LOST1), which was insignificant (Figure 7.4.4a). Recall that EC concentrations at many sites, especially in the West, may be below the lower quantifiable limit (LQL), and therefore 10<sup>th</sup> percentile trends in  $b_{ext\_EC}$  may be more uncertain. The strongest reduction occurred at Starkey, Oregon (STAR1, -13.79% yr<sup>-1</sup>, p < 0.001), compared to -2.25% yr<sup>-1</sup> (p = 0.04) at Big Bend NP, Texas (BIBE1). Short-term trends in the 90<sup>th</sup> percentile  $b_{ext\_EC}$  are shown in Figure 7.4.4b. Insignificant trends occurred at sites across the Intermountain West and northwestern United States. Some of these sites may be influenced by biomass smoke, and some, such as Theodore Roosevelt NP, North Dakota (THRO1), may be influenced by oil and gas development (Gebhart et al., 2018). Out of the 138 valid sites, 129 had statistically significant trends. Strong reductions in the 90<sup>th</sup> percentile  $b_{ext\_EC}$  occurred at sites in southern California and the northeastern and northwestern United States. Short-term 90<sup>th</sup> percentile trends ranged from -7.56% yr<sup>-1</sup> (p < 0.001) at San Gorgonio WA, California (SAGO1), to -1.92% yr<sup>-1</sup> (p = 0.04) at Theodore Roosevelt NP, North Dakota (THRO1).

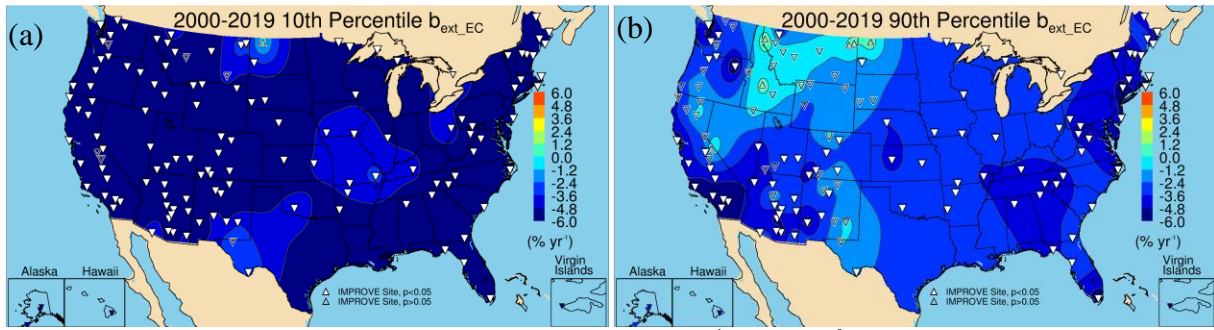


**Figure 7.4.4. IMPROVE short-term (2000–2019) trends ( $\% \text{ yr}^{-1}$ ) in (a) 10<sup>th</sup> percentile elemental carbon  $b_{ext}$  ( $b_{ext\_EC}$ ) and (b) 90<sup>th</sup> percentile  $b_{ext\_EC}$ . Filled triangles correspond to statistically significant trends ( $p \leq 0.05$ ).**

Regional mean trends in percentile  $b_{ext\_EC}$  are shown in Figure 7.4.5. For nearly all regions, the 10<sup>th</sup> percentile trends were the greatest, although these were likely affected by low  $b_{ext\_EC}$  (e.g., Alaska, Hawaii, and Virgin Islands). For most regions, the 90<sup>th</sup> percentile  $b_{ext\_EC}$  decreased at a lower rate than the median  $b_{ext\_EC}$ . Both the Northwest and Alaska regions had insignificant trends in 90<sup>th</sup> percentile  $b_{ext\_EC}$ , perhaps related to increased smoke impacts.

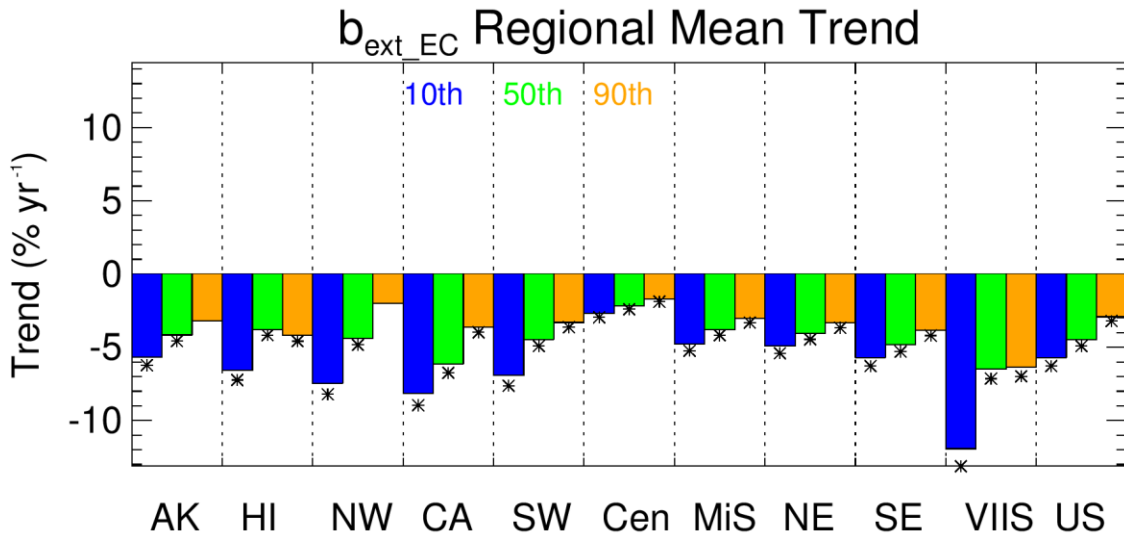


**Figure 7.4.5. Short-term (2000–2019) regional mean trends ( $\% \text{ yr}^{-1}$ ) in 10<sup>th</sup>, 50<sup>th</sup>, and 90<sup>th</sup> percentile elemental carbon  $b_{ext}$  ( $b_{ext\_EC}$ ). Regions are arranged from western to eastern United States (AK = Alaska, HI = Hawaii, NW = Northwest, CA = California, SW = Southwest, Cen = Central, MiS = Midsouth, NE = Northeast, SE = Southeast, VIIS = Virgin Islands, and US = all sites). Statistically significant trends ( $p \leq 0.05$ ) are denoted with “\*”.**

## 7.5 FINE DUST LIGHT EXTINCTION COEFFICIENT TRENDS

Long-term and short-term annual mean  $b_{ext\_FD}$  trends are shown in Figures 7.5.1a and 7.5.1b, respectively. Many of the long-term trends were statistically insignificant, nearly all of these were located at sites in the western United States, and many of them were positive. In the West, statistically significant reductions in  $b_{ext\_FD}$  occurred at sites in California, Oregon, Washington State, Wyoming, and Colorado. Across the eastern United States, sites were

associated with reduced  $b_{ext\_FD}$ , although with some insignificant trends. The strongest reductions occurred at Yellowstone NP, Wyoming (YELL2,  $-3.94\% \text{ yr}^{-1}$ ,  $p < 0.001$ ), compared to an increase in annual mean  $b_{ext\_FD}$  at Guadalupe Mountains NP, Texas (GUMO1,  $1.22\% \text{ yr}^{-1}$ ,  $p = 0.05$ ).

Annual mean trends in  $b_{ext\_FD}$  for 2000 to 2019 were significantly negative across the eastern United States, especially at sites in the northeastern United States and across the Intermountain West and northwestern United States (Figure 7.5.1b). Out of 137 sites, 62 had statistically significant trends. These ranged from  $-7.12\% \text{ yr}^{-1}$  ( $p < 0.001$ ) at Mohawk Mountain, Connecticut (MOMO1), to  $-2.40\% \text{ yr}^{-1}$  ( $p = 0.03$ ) at Northern Cheyenne, Montana (NOCH1). Many sites near the Central Valley of California, Oklahoma, Texas, Oregon, and North Dakota had positive but insignificant trends. Many of the sites in the southwestern United States corresponded to statistically insignificant negative trends.

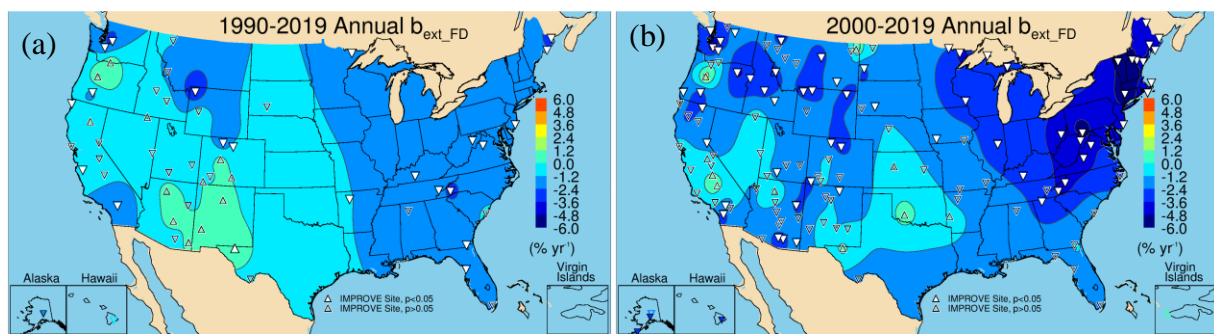


**Figure 7.5.1** Annual mean fine dust  $b_{ext}$  ( $b_{ext\_FD}$ ) trends ( $\% \text{ yr}^{-1}$ ) for (a) long-term (1990–2019) and (b) short-term (2000–2019) periods. Filled triangles correspond to statistically significant trends ( $p \leq 0.05$ ).

Compared to other species, regional seasonal mean trends in  $b_{ext\_FD}$  showed greater variability. Trends were mostly insignificant and generally not strongly negative as was the case for other species. The Northeast region was the only region with statistically significant trends during all seasons ( $-3\% \text{ yr}^{-1}$  to  $-5\% \text{ yr}^{-1}$ ). The Southeast region had statistically significant reductions in  $b_{ext\_FD}$  during all seasons except summer. Similarly, the Midsouth region had insignificant but positive trends during summer; this is the season with impacts from North African dust transport. In the Central region, only winter and spring corresponded to statistically significant negative trends ( $\sim -2\% \text{ yr}^{-1}$ ). Across the West, regions were associated with insignificant though negative trends. The California region had insignificant but positive trends during fall. The levels of progress that have been observed in reducing extinction from other species have not been experienced by  $b_{ext\_FD}$ .

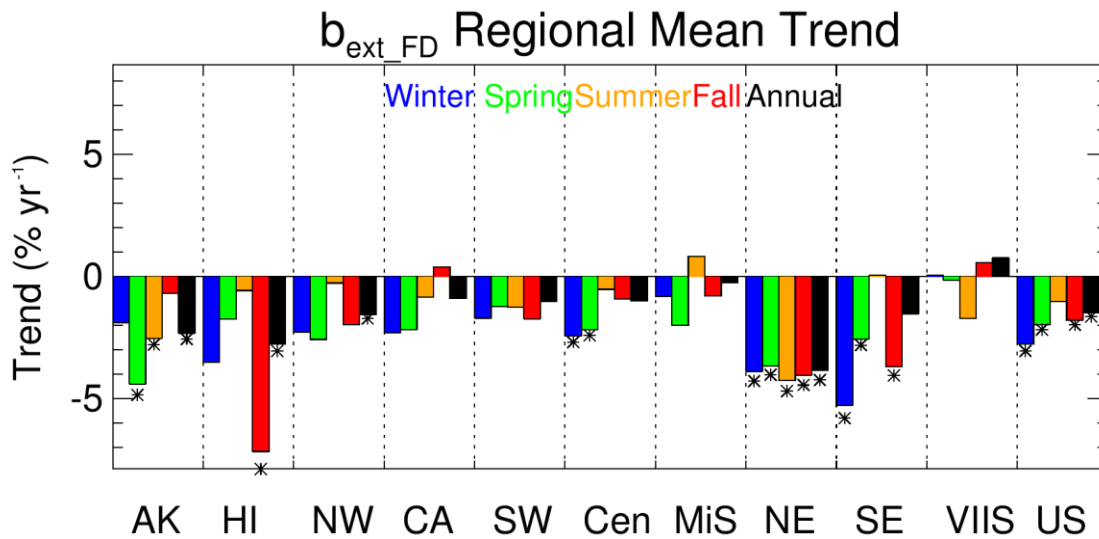


**Figure 7.5.2.** Short-term (2000–2019) regional seasonal mean fine dust  $b_{ext}$  ( $b_{ext\_FD}$ ) trends ( $\% \text{ yr}^{-1}$ ) for major U.S. regions for winter, spring, summer, fall, and annual means. Regions are arranged from western to eastern United States (AK = Alaska, HI = Hawaii, NW = Northwest, CA= California, SW = Southwest, Cen = Central, MiS = Midsouth, NE = Northeast, SE = Southeast, VIIS = Virgin Islands, and US = all sites). Statistically significant trends ( $p \leq 0.05$ ) are denoted with “\*\*”.

Long-term trends in the 10<sup>th</sup> percentile  $b_{ext\_FD}$  are shown in Figure 7.5.3a. For most of the United States, sites experienced reductions in the lowest  $b_{ext\_FD}$ . Of the 59 valid sites, 46 had statistically significant trends, ranging from  $-5.97\% \text{ yr}^{-1}$  ( $p < 0.001$ ) in Three Sisters WA, Oregon (THSI1), to  $1.80\% \text{ yr}^{-1}$  ( $p = 0.010$ ) in Guadalupe Mountains NP, Texas (GUMO1). All of the insignificant trends occurred in the southwestern United States. In contrast, for the 90<sup>th</sup> percentile  $b_{ext\_FD}$ , of the 59 valid sites only 17 had statistically significant trends, and many of these were in the eastern United States (Figure 7.5.3b). Sites across the southwestern United States were associated with positive although insignificant trends. Trends ranged from  $-3.78\% \text{ yr}^{-1}$  ( $p < 0.001$ ) at Yellowstone NP, Wyoming (YELL2), to  $2.38\% \text{ yr}^{-1}$  ( $p = 0.012$ ) at Columbia River Gorge, Washington (CORI1).

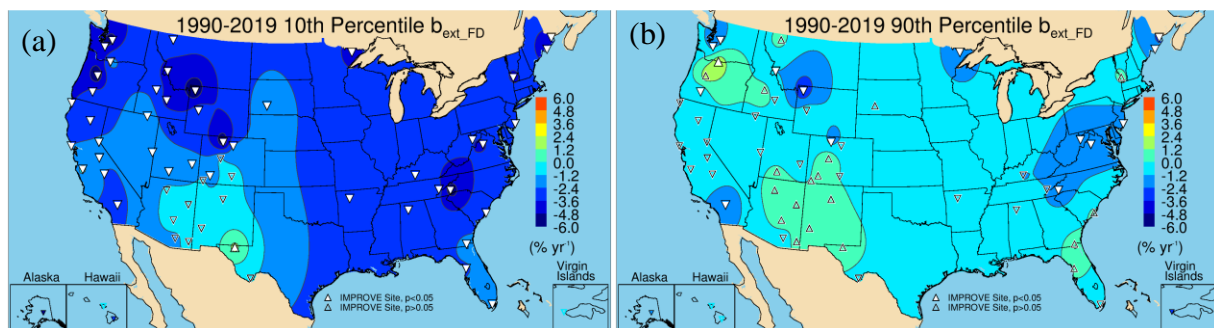


**Figure 7.5.3.** IMPROVE long-term (1990–2019) trends ( $\% \text{ yr}^{-1}$ ) in (a) 10<sup>th</sup> percentile fine dust  $b_{ext}$  ( $b_{ext\_FD}$ ) and (b) 90<sup>th</sup> percentile  $b_{ext\_FD}$ . Filled triangles correspond to statistically significant trends ( $p \leq 0.05$ ).

Short-term trends in 10<sup>th</sup> percentile  $b_{ext\_FD}$  were negative at sites across the United States, with stronger reductions at sites across the eastern United States, Intermountain West, and

northwestern United States, but with several sites having insignificant trends in the Southwest. Insignificant trends occurred at 34 sites (out of 137), and most of these were in the southwestern United States (Figure 7.5.4a). Trends ranged from  $-8.59\% \text{ yr}^{-1}$  ( $p < 0.001$ ) at Shining Rock WA, North Carolina (SHRO1), to  $-1.72\% \text{ yr}^{-1}$  ( $p = 0.019$ ) at Pinnacles NM, California (PINN1). Most of the 90<sup>th</sup> percentile  $b_{\text{ext\_FD}}$  trends in the West were insignificant (Figure 7.5.4b), with 83 insignificant trends. Positive though insignificant trends occurred at sites in the central United States, the Central Valley of California, Oregon, the northern Great Plains, and Florida. The 90<sup>th</sup> percentile trends ranged from  $-6.67\% \text{ yr}^{-1}$  ( $p < 0.001$ ) at Great Gulf WA, New Hampshire (GRGU1), to  $2.87\% \text{ yr}^{-1}$  ( $p = 0.03$ ) at Three Sisters WA, Oregon (THSI1). Comparison of trends from these two maps suggests that the influences that govern the changes in the 10<sup>th</sup> and 90<sup>th</sup> percentiles are different, although low 10<sup>th</sup> percentile  $b_{\text{ext\_FD}}$  could also play a role.

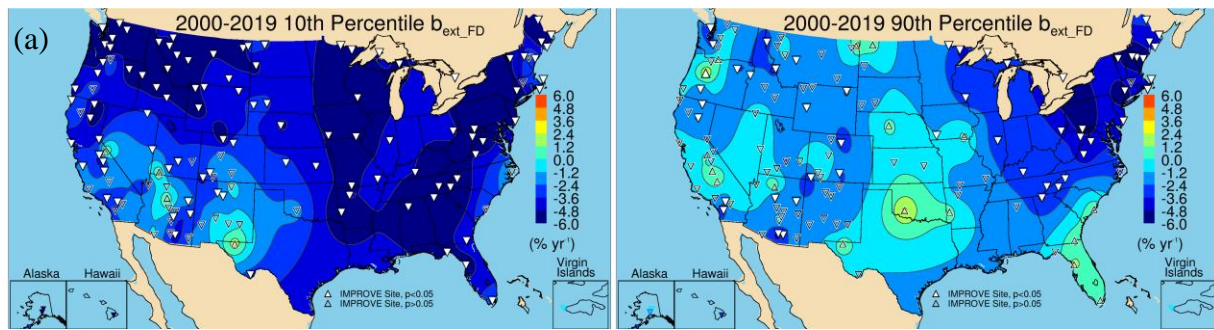


**Figure 7.5.4. IMPROVE short-term (2000–2019) trends ( $\% \text{ yr}^{-1}$ ) in (a) 10<sup>th</sup> percentile fine dust  $b_{\text{ext}}$  ( $b_{\text{ext\_FD}}$ ) and (b) 90<sup>th</sup> percentile  $b_{\text{ext\_FD}}$ . Filled triangles correspond to statistically significant trends ( $p \leq 0.05$ ).**

Regional mean percentile trends are shown in Figure 7.5.5. For most regions, the 10<sup>th</sup> percentile trends were strongest, which may be in part due to low 10<sup>th</sup> percentile  $b_{\text{ext\_FD}}$ . For nearly all regions, the 90<sup>th</sup> percentile trends were insignificant (except the Northeast and Hawaii regions). These insignificant trends may imply that the influences on the highest  $b_{\text{ext\_FD}}$  have not decreased enough to result in statistically significant negative trends. For other regions in the West, such as California, Southwest, and Central, the median trends were also insignificant.

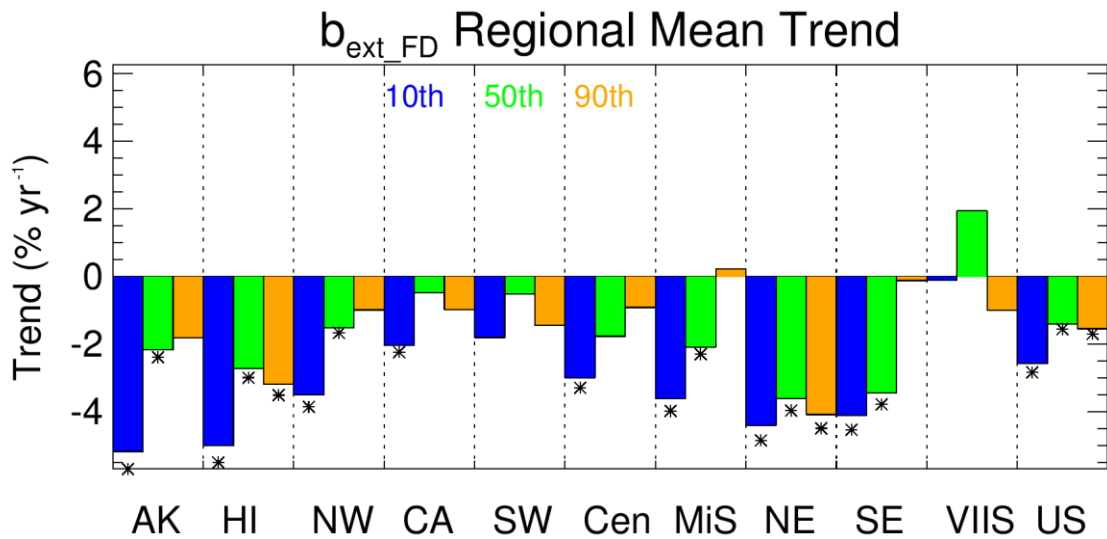


**Figure 7.5.5.** Short-term (2000–2019) regional mean trends ( $\% \text{yr}^{-1}$ ) in 10<sup>th</sup>, 50<sup>th</sup>, and 90<sup>th</sup> percentile fine dust  $b_{ext}$  ( $b_{ext\_FD}$ ). Regions are arranged from western to eastern United States (AK = Alaska, HI = Hawaii, NW = Northwest, CA = California, SW = Southwest, Cen = Central, MiS = Midsouth, NE = Northeast, SE = Southeast, VIIS = Virgin Islands, and US = all sites). Statistically significant trends ( $p \leq 0.05$ ) are denoted with “\*”.

## 7.6 COARSE MASS LIGHT EXTINCTION COEFFICIENT TRENDS

Annual mean long-term trends in  $b_{ext\_CM}$  are shown in Figure 7.6.1a. The strongest reductions in  $b_{ext\_CM}$  occurred at sites in Wyoming, Colorado, and Oregon. Of the 49 valid sites, 30 had statistically significant trends. Insignificant trends mostly occurred in the western United States, at sites in California, Arizona, and Texas. One positive trend occurred at Columbia River Gorge, Washington (CORI1,  $1.83\% \text{ yr}^{-1}$ ,  $p = 0.04$ ). The strongest reduction in  $b_{ext\_CM}$  occurred at Crater Lake NP, Oregon (CRLA1,  $-5.39\% \text{ yr}^{-1}$ ,  $p < 0.001$ ).

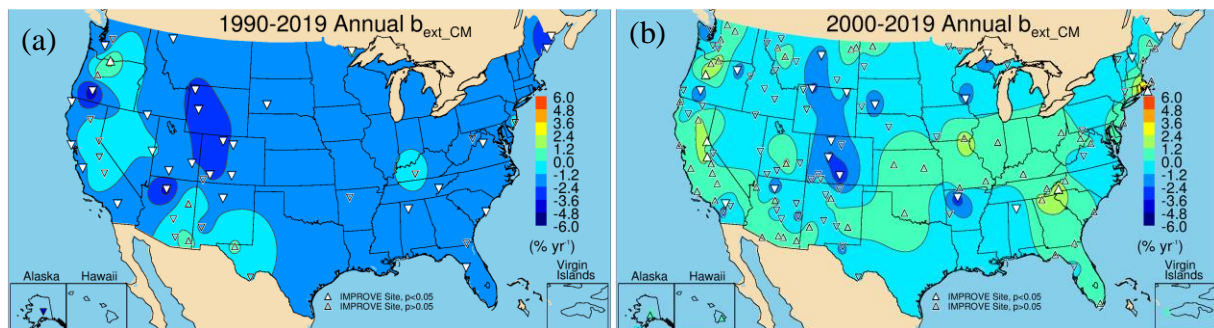


**Figure 7.6.1.** Annual mean coarse mass  $b_{ext}$  ( $b_{ext\_CM}$ ) trends ( $\% \text{yr}^{-1}$ ) for (a) long-term (1990–2019) and (b) short-term (2000–2019) periods. Filled triangles correspond to statistically significant trends ( $p \leq 0.05$ ).

Short-term annual mean  $b_{ext\_CM}$  trends are shown in Figure 7.6.1b. Only 24 of 131 valid sites had statistically significant trends, suggesting that at most sites, trends were variable. Significant reductions in  $b_{ext\_CM}$  occurred at sites in Colorado, Wyoming, Montana, and Arkansas, where the strongest reductions occurred at Upper Buffalo WA, Arkansas

(UPBU1, -3.92%  $\text{yr}^{-1}$ ,  $p = 0.037$ ). Positive trends (mostly insignificant) occurred at 61 sites, with seven being statistically significant (Martha's Vineyard, Massachusetts, MAVI1; Shining Rock WA, North Carolina, SHRO1; Three Sisters WA, Oregon, THSI1; Yosemite NP, California, YOSE1; Bliss SP, California, BLIS1; Trapper Creek, Alaska, TRCR1; and Hawaii Volcanoes NP, Hawaii, HAVO1). The spatial pattern in short-term  $b_{\text{ext\_CM}}$  trends was different from  $b_{\text{ext\_FD}}$  trends (Figure 7.5.1b), suggesting that different composition or size distribution of coarse-mode aerosols influenced  $b_{\text{ext\_CM}}$  trends.

Regional seasonal mean trends are shown in Figure 7.6.2. As suggested in Figure 7.6.1b, nearly all of the regions were associated with insignificant and weak trends, especially relative to other species already discussed. The Northeast region had significant positive trends in summer, as did the Alaska and Hawaii regions. All of the seasonal mean trends in the Central region were positive but insignificant. The Midsouth and Southwest regions had weak but negative insignificant trends, while the California region had weak, positive insignificant trends in summer and fall but negative insignificant trends in winter and spring. The Northwest region had statistically significant trends in winter but weak and insignificant trends during other seasons.

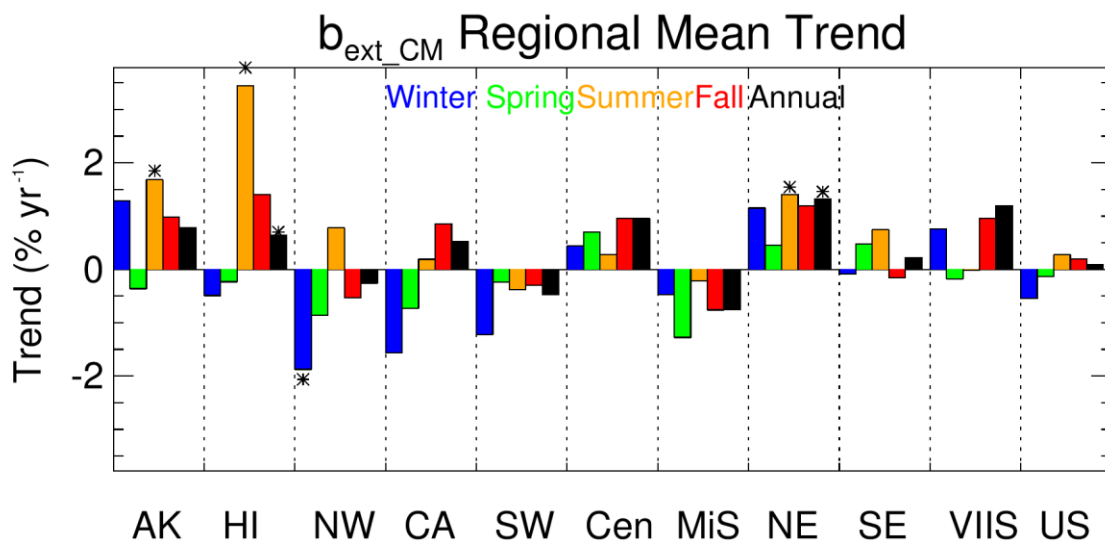


**Figure 7.6.2.** Short-term (2000–2019) regional seasonal mean coarse mass  $b_{\text{ext}}$  ( $b_{\text{ext\_CM}}$ ) trends (%  $\text{yr}^{-1}$ ) for major U.S. regions for winter, spring, summer, fall, and annual means. Regions are arranged from western to eastern United States (AK = Alaska, HI = Hawaii, NW = Northwest, CA = California, SW = Southwest, Cen = Central, MiS = Midsouth, NE = Northeast, SE = Southeast, VIIS = Virgin Islands, and US = all sites). Statistically significant trends ( $p \leq 0.05$ ) are denoted with “\*\*”.

The long-term 10<sup>th</sup> percentile trends in  $b_{\text{ext\_CM}}$  were negative at most sites, with the strongest reductions at sites in the Intermountain West and southwestern United States (Figure 7.6.3a). Of the 50 valid sites, 31 had statistically significant trends, ranging from -8.94%  $\text{yr}^{-1}$  ( $p < 0.001$ ) at Mount Zirkel WA, Colorado (MOZI1), to -1.64%  $\text{yr}^{-1}$  ( $p = 0.016$ ) at Tonto NM, Arizona (TONT1). The trends in 90<sup>th</sup> percentile  $b_{\text{ext\_CM}}$  did not decrease to the same degree as the 10<sup>th</sup> percentile trends (Figure 7.6.3b). Of the 50 valid sites, 30 had statistically significant trends, ranging from -5.32%  $\text{yr}^{-1}$  ( $p < 0.001$ ) at Crater Lake NP, Oregon (CRLA1), to 2.82%  $\text{yr}^{-1}$  ( $p = 0.002$ ) at Columbia River Gorge, Washington (CORI1). Recall that the 90<sup>th</sup> percentile trend

in  $b_{ext\_FD}$  at CRLA1 was also positive, suggesting CM is likely associated with mineral dust at this site. The 90<sup>th</sup> percentile CM trends decreased more than the 90<sup>th</sup> percentile  $b_{ext\_FD}$  trends, especially for sites in the southwestern United States. Similarities in trends of  $b_{ext\_FD}$  and  $b_{ext\_CM}$  occurred for sites in Arizona and Texas. Sites in California had positive (insignificant)  $b_{ext\_CM}$  trends but negative  $b_{ext\_FD}$  90<sup>th</sup> percentile trends.

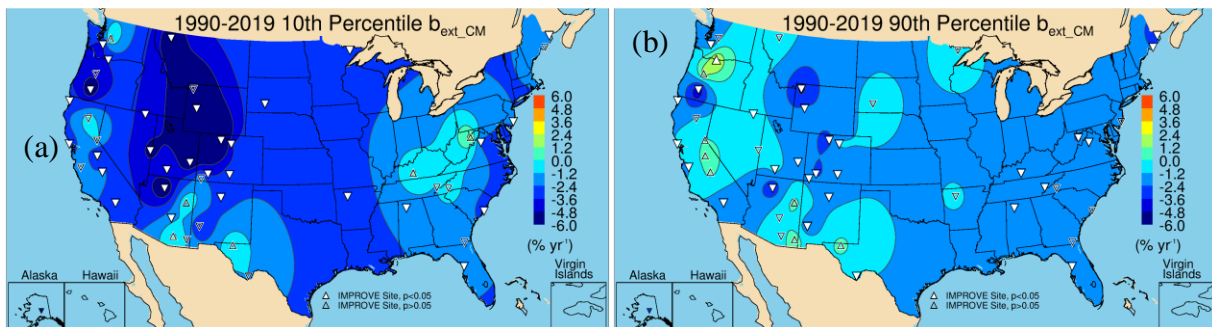


**Figure 7.6.3. IMPROVE long-term (1990–2019) trends ( $\% \text{ yr}^{-1}$ ) in (a) 10<sup>th</sup> percentile coarse mass  $b_{ext}$  ( $b_{ext\_CM}$ ) and (b) 90<sup>th</sup> percentile  $b_{ext\_CM}$ . Filled triangles correspond to statistically significant trends ( $p \leq 0.05$ ).**

Short-term trends in the 10<sup>th</sup> and 90<sup>th</sup> percentile  $b_{ext\_CM}$  (Figure 7.6.4a and 7.6.4b, respectively) showed more spatial variability than the long-term trends, with many more sites having insignificant and positive trends. The 10<sup>th</sup> percentile trends had only 22 statistically significant trends out of 137 valid sites. The strongest statistically insignificant negative trends occurred at sites in Colorado and Montana and parts of southern California and Oregon. Statistically significant positive trends occurred at several sites, with the strongest ( $>3\% \text{ yr}^{-1}$ ) at Shining Rock WA, North Carolina (SHRO1); Dolly Sods WA, West Virginia (DOSO1); Cohutta, Georgia (COHU1); Lassen Volcanic NP, California (LAVO1); and Pasayten, Washington (PASA1). Trends ranged from  $-9.50\% \text{ yr}^{-1}$  ( $p = 0.025$ ) at Gates of the Mountains, Montana (GAMO1), to  $7.66\% \text{ yr}^{-1}$  ( $p = 0.006$ ) at Shining Rock WA, North Carolina (SHRO1). Some of these trends may be affected by low  $b_{ext\_CM}$ .

Similar spatial patterns were seen for the short-term 90<sup>th</sup> percentile trends, with sites in the central United States, California, the Northwest, and the Southeast having positive but insignificant trends (Figure 7.6.4b). Sites with strongly decreased  $b_{ext\_CM}$  included those in Colorado. Of the 137 sites, 21 were statistically significant and ranged from  $-4.77\% \text{ yr}^{-1}$  ( $p = 0.005$ ) at Upper Buffalo WA, Arkansas (UPBU1), to  $5.31\% \text{ yr}^{-1}$  ( $p = 0.004$ ) at Martha's Vineyard, Massachusetts (MAVI1). Several of the sites with significant positive 10<sup>th</sup> percentile trends also had positive 90<sup>th</sup> percentile trends, such as Shining Rock WA, North Carolina (SHRO1); Cohutta, Georgia (COHU1); and Bliss SP, California (BLIS1). The short-term 10<sup>th</sup> and 90<sup>th</sup> percentiles trend maps did not reflect the corresponding  $b_{ext\_FD}$  trend maps, with the  $b_{ext\_CM}$  trends having much larger variability, more insignificant trends, and fewer sites with decreased trends.

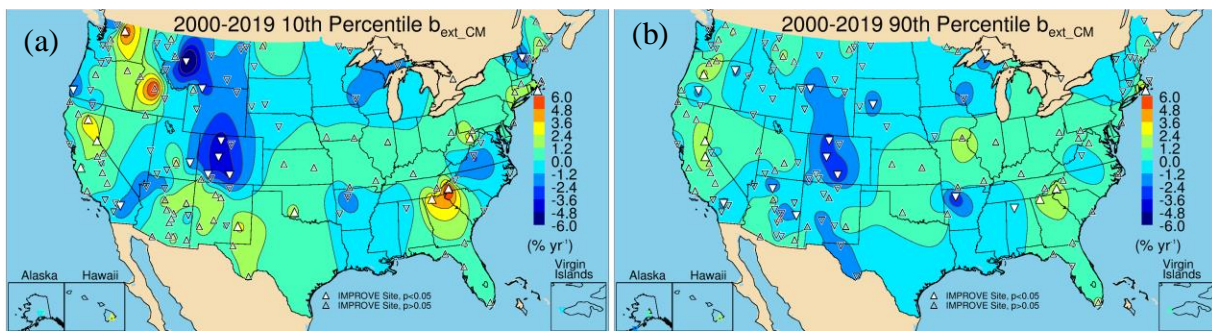


**Figure 7.6.4. IMPROVE short-term (2000–2019) trends ( $\% \text{yr}^{-1}$ ) in (a) 10<sup>th</sup> percentile coarse mass  $b_{ext\_CM}$  ( $b_{ext\_CM}$ ) and (b) 90<sup>th</sup> percentile  $b_{ext\_CM}$ . Filled triangles correspond to statistically significant trends ( $p \leq 0.05$ ).**

Comparisons of short-term regional mean percentile  $b_{ext\_CM}$  trends are shown in Figure 7.6.5. Unlike the results for  $b_{ext\_FD}$  trends (Figure 7.5.5), most of the regional mean trends are statistically insignificant, except for the positive 50<sup>th</sup> percentile trend in the Northeast region. The Central region had positive trends for all percentiles, although insignificant, while the Midsouth region had negative trends. The California region had weak to positive trends. Both the Hawaii and Alaska regions had positive but insignificant trends. Trends in  $b_{ext\_CM}$  were notable and indicated that  $b_{ext\_CM}$  has not decreased across large regions of the United States, unlike trends in extinction from other species.

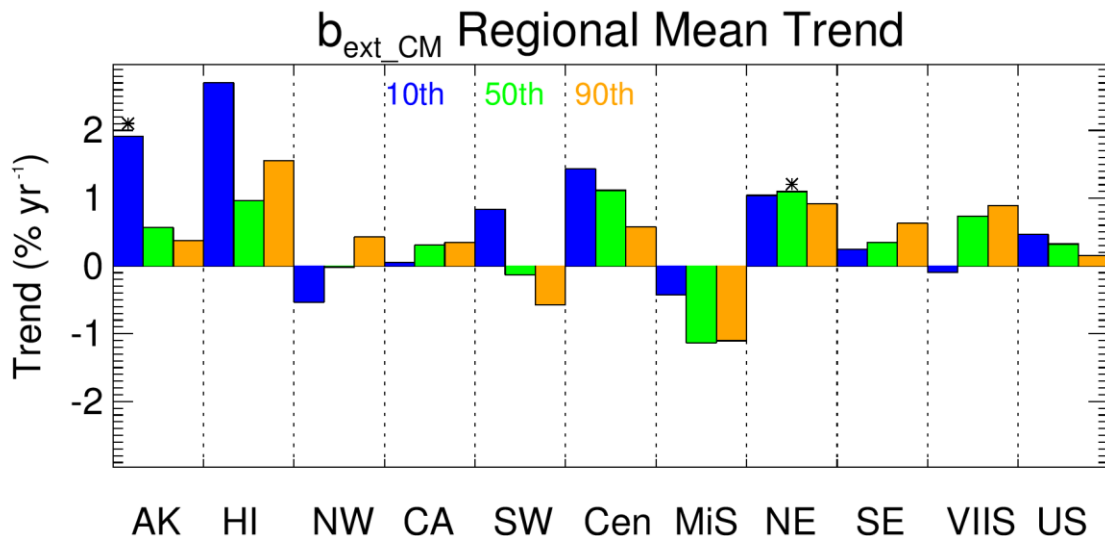


**Figure 7.6.5. Short-term (2000–2019) regional mean trends ( $\% \text{yr}^{-1}$ ) in 10<sup>th</sup>, 50<sup>th</sup>, and 90<sup>th</sup> percentile coarse mass  $b_{ext}$  ( $b_{ext\_CM}$ ). Regions are arranged from western to eastern United States (AK = Alaska, HI = Hawaii, NW = Northwest, CA = California, SW = Southwest, Cen = Central, MiS = Midsouth, NE = Northeast, SE = Southeast, VIIS = Virgin Islands, and US = all sites). Statistically significant trends ( $p \leq 0.05$ ) are denoted with \*\*.**

## 7.7 AEROSOL EXTINCTION COEFFICIENT TRENDS

Reconstructed  $b_{ext\_aer}$  includes extinction from the previous aerosol species discussed, as well as  $b_{ext\_ss}$ . Rayleigh scattering contributions are not included. Trends in  $b_{ext\_aer}$  are likely similar to trends in total aerosol mass but could differ due to hygroscopic effects of some species, and because species with lower mass scattering efficiencies will have less contributions to extinction relative to mass (e.g., CM and FD).

The spatial patterns in long-term annual mean  $b_{ext\_aer}$  trends are shown in Figure 7.7.1a. The strongest reductions occurred at sites in the eastern United States, southern California, and the Northwest. Of the 38 valid sites, 34 had statistically significant trends. Sites with weak and insignificant trends were in California, Nevada, and Wyoming. Trends in  $b_{ext\_aer}$  ranged from  $-6.38\% \text{ yr}^{-1}$  ( $p < 0.001$ ) at Dolly Sods WA, West Virginia (DOSO1), to  $-0.57\% \text{ yr}^{-1}$  ( $p = 0.02$ ) at Guadalupe NP, Texas (GUMO1). The strong reduction of  $b_{ext\_aer}$  at eastern sites was likely associated with sulfate reductions (Hand et al., 2020).

The differences in long-term trends at sites in the eastern and western United States were also observed for short-term trends in annual mean  $b_{ext\_aer}$ , with the strongest reductions in the eastern United States where  $b_{ext\_AS}$  also significantly declined (Figure 7.7.1b). Positive but insignificant trends occurred at sites in California, Oregon, Washington, northern Montana, and North Dakota. This spatial pattern was similar to  $b_{ext\_POM}$  trends, and  $b_{ext\_aer}$  trends were likely influenced by the impacts of biomass smoke, especially at sites in the western United States. Short-term significant  $b_{ext\_aer}$  trends ranged from  $-8.44\% \text{ yr}^{-1}$  ( $p < 0.001$ ) at Shining Rock WA, North Carolina (SHRO1), to  $-1.16\% \text{ yr}^{-1}$  ( $p = 0.011$ ) at Salt Creek, New Mexico (SACR1).

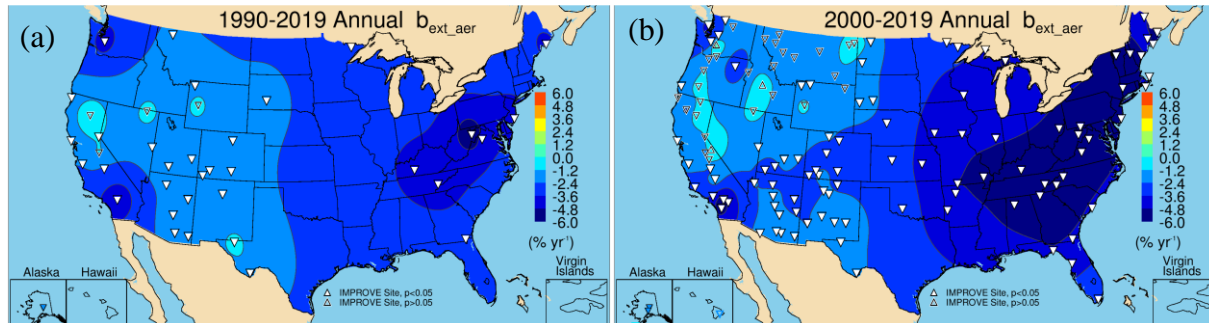


**Figure 7.7.1** Annual mean aerosol  $b_{ext}$  ( $b_{ext\_aer}$ ) trends ( $\% \text{ yr}^{-1}$ ) for (a) long-term (1990–2019) and (b) short-term (2000–2019) periods. Filled triangles correspond to statistically significant trends ( $p \leq 0.05$ ).

Comparisons of short-term regional and seasonal trends in  $b_{ext\_aer}$  are shown in Figure 7.7.2. The strong reductions in  $b_{ext\_aer}$  in eastern regions are similar to those for  $b_{ext\_AS}$  (Figure 7.1.2), suggesting that in the Northeast and Southeast regions,  $b_{ext\_aer}$  trends were largely driven by  $b_{ext\_AS}$ . The strongest regional reductions occurred during summer in the Northeast ( $-7.85\% \text{ yr}^{-1}$ ) and summer/fall in the Southeast region ( $-6.7\% \text{ yr}^{-1}$ ). While still negative, the magnitude of the trends decreased for western regions, around  $-2\% \text{ yr}^{-1}$  to  $-3\% \text{ yr}^{-1}$ . Regional trends in the western regions were influenced by biomass smoke, as indicated by the weak but insignificant trends during summer at sites in the Northwest and California regions, similar to  $b_{ext\_POM}$  (Figure 7.3.2). In addition,  $b_{ext\_AS}$  was lower in the western regions and did not decline at the same rate as in eastern regions (Hand et al., 2020).

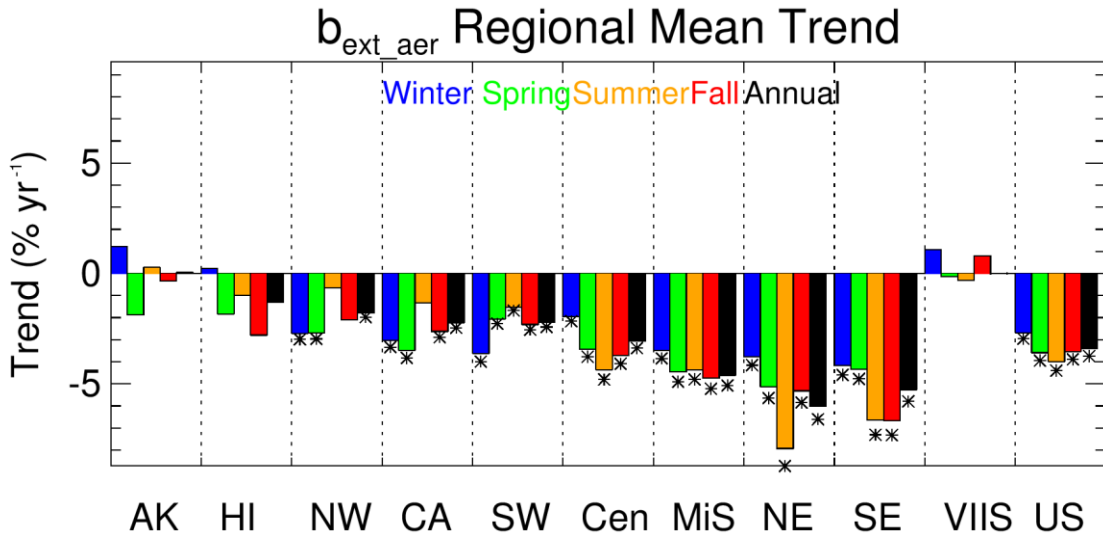


**Figure 7.7.2.** Short-term (2000–2019) regional seasonal mean aerosol  $b_{ext}$  ( $b_{ext\_aer}$ ) trends ( $\% \text{yr}^{-1}$ ) for major U.S. regions for winter, spring, summer, fall, and annual means. Regions are arranged from western to eastern United States (AK = Alaska, HI = Hawaii, NW = Northwest, CA= California, SW = Southwest, Cen = Central, MiS = Midsouth, NE = Northeast, SE = Southeast, VIIS = Virgin Islands, and US = all sites). Statistically significant trends ( $p \leq 0.05$ ) are denoted with “\*\*”.

The long-term 10<sup>th</sup> percentile trends in  $b_{ext\_aer}$  are shown in Figure 7.7.3a. All of the 40 valid trends were statistically significant. The strongest reductions occurred at sites in the Intermountain West, southern California, and the Appalachian Mountains. Trends ranged from  $-5.12\% \text{ yr}^{-1}$  ( $p < 0.001$ ) at Dolly Sods WA, West Virginia (DOSO1), to  $-1.80\% \text{ yr}^{-1}$  ( $p < 0.001$ ) at Pinnacles NM, California (PINN1). The 90<sup>th</sup> percentile trends in  $b_{ext\_aer}$  are shown in Figure 7.7.3b. Strong reductions in the eastern United States were likely associated with reductions in  $b_{ext\_AS}$ . Several sites in the West had insignificant trends, especially in California, Oregon, Nevada, Wyoming, and Texas. Trends ranged from  $-6.54\% \text{ yr}^{-1}$  ( $p < 0.001$ ) at DOSO1 to  $-0.89\% \text{ yr}^{-1}$  ( $p = 0.009$ ) at Bryce Canyon NP, Utah (BRCA1).

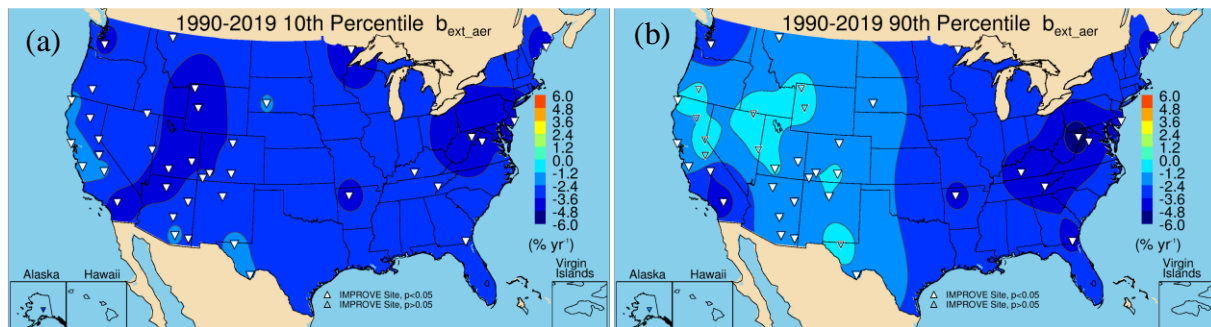


**Figure 7.7.3.** IMPROVE long-term (1990–2019) trends ( $\% \text{yr}^{-1}$ ) in (a) 10<sup>th</sup> percentile aerosol  $b_{ext}$  ( $b_{ext\_aer}$ ) and (b) 90<sup>th</sup> percentile  $b_{ext\_aer}$ . Filled triangles correspond to statistically significant trends ( $p \leq 0.05$ ).

The short-term trends in 10<sup>th</sup> percentile  $b_{ext\_aer}$  were significant at 118 of the 136 valid sites (Figure 7.7.4a), with the strongest negative trends at sites in the eastern United States. Weaker trends occurred at sites in California and Oregon and in the northern Great Plains.

Trends ranged from  $-6.18\% \text{ yr}^{-1}$  ( $p < 0.001$ ) at Dolly Sods WA, West Virginia (DOSO1), to  $1.57\% \text{ yr}^{-1}$  ( $p = 0.03$ ) at Virgin Islands NP (VIIS1).

The spatial patterns in the short-term 90<sup>th</sup> percentile  $b_{\text{ext\_aer}}$  trends were similar to the long-term 90<sup>th</sup> percentiles trends (Figure 7.7.4b), with the strongest reductions at sites in the eastern United States. Of the 136 valid trends, 90 were statistically significant. Most of the insignificant trends occurred at sites in the West, likely influenced by biomass smoke. Trends ranged from  $-9.33\% \text{ yr}^{-1}$  at Cohutta, Georgia (COHU1), to  $-1.29\% \text{ yr}^{-1}$  ( $p = 0.03$ ) at Bandelier NM, New Mexico (BAND1).

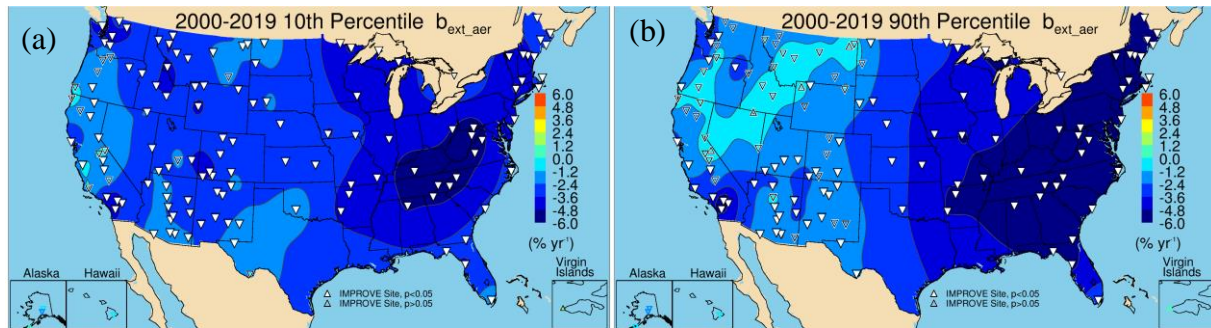


**Figure 7.7.4. IMPROVE short-term (2000–2019) trends ( $\% \text{ yr}^{-1}$ ) in (a) 10<sup>th</sup> percentile aerosol  $b_{\text{ext\_aer}}$  and (b) 90<sup>th</sup> percentile  $b_{\text{ext\_aer}}$ . Filled triangles correspond to statistically significant trends ( $p \leq 0.05$ ).**

The strongest regional mean short-term trends in  $b_{\text{ext\_aer}}$  occurred for the 90<sup>th</sup> percentile in the Northeast and Southeast regions ( $\sim -6.5\% \text{ yr}^{-1}$ ) and likely coincided with the strong summer mean  $b_{\text{ext\_aer}}$  trends (Figure 7.7.5). These trends are also consistent with strong reductions in summer mean  $b_{\text{ext\_AS}}$  in those regions. Trends in  $b_{\text{ext\_aer}}$  percentiles were weaker for regions in the West. The 10<sup>th</sup> and 50<sup>th</sup> percentile trends were the strongest in the Northwest and California regions, and the 90<sup>th</sup> percentile trends were likely associated with smoke influence. The Southwest region was the only western region with significant 90<sup>th</sup> percentile trends.

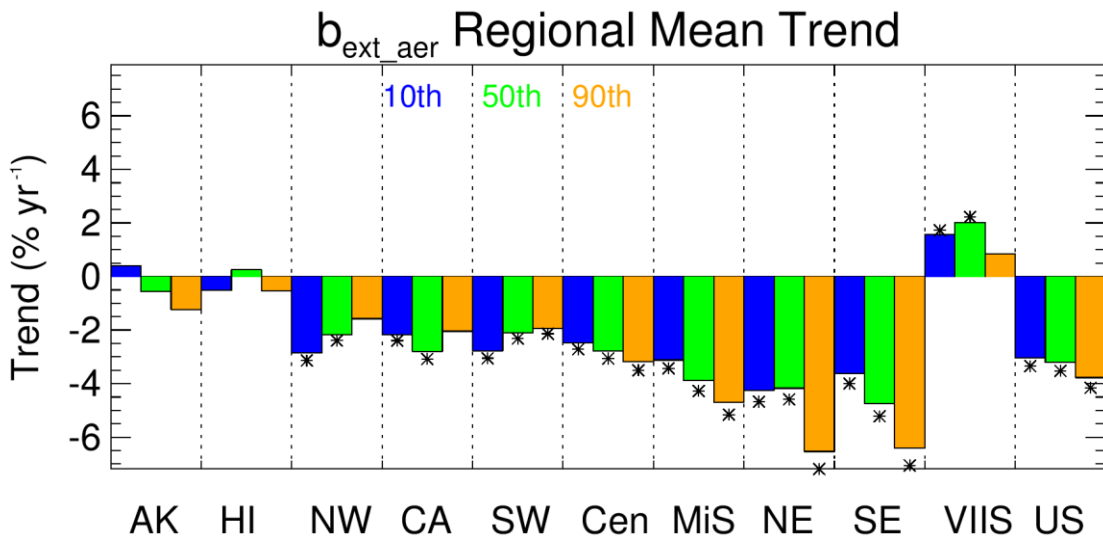


**Figure 7.7.5.** Short-term (2000–2019) regional mean trends ( $\% \text{ yr}^{-1}$ ) in 10<sup>th</sup>, 50<sup>th</sup>, and 90<sup>th</sup> percentile aerosol  $b_{ext}$  ( $b_{ext\_aer}$ ). Regions are arranged from western to eastern United States (AK = Alaska, HI = Hawaii, NW = Northwest, CA = California, SW = Southwest, Cen = Central, MiS = Midsouth, NE = Northeast, SE = Southeast, VIIS = Virgin Islands, and US = all sites). Statistically significant trends ( $p \leq 0.05$ ) are denoted with “\*\*”.

## 7.8 TOTAL EXTINCTION COEFFICIENT TRENDS

Reconstructed  $b_{ext\_tot}$  includes  $b_{ext\_aer}$  and site-specific Rayleigh scattering. Although the slopes from the linear regression will be the same for  $b_{ext\_aer}$  and  $b_{ext\_tot}$ , the trends in  $b_{ext\_tot}$  may be different because the normalization differs. However, general patterns in  $b_{ext\_tot}$  trends will follow trends in  $b_{ext\_aer}$ .

The spatial patterns in long-term annual mean  $b_{ext\_tot}$  trends are shown in (Figure 7.8.1a). The strongest reductions occurred at sites in the eastern United States, southern California, and the Northwest. Of the 38 valid sites, 34 had statistically significant trends. Sites with weaker and insignificant trends occurred in California, Nevada, and Wyoming. Trends in  $b_{ext\_tot}$  ranged from  $-6.38\% \text{ yr}^{-1}$  ( $p < 0.001$ ) at Dolly Sods WA, West Virginia (DOSO1), to  $-0.79\% \text{ yr}^{-1}$  ( $p = 0.02$ ) at Guadalupe NP, Texas (GUMO1). The strong reduction of  $b_{ext\_tot}$  at eastern sites was likely associated with sulfate reductions (Hand et al., 2020).

Similar spatial patterns occurred for short-term trends in annual mean  $b_{ext\_tot}$ , with the strongest reductions at sites in the eastern United States where  $b_{ext\_AS}$  significantly declined (Figure 7.8.1b). Positive but insignificant trends occurred at sites in California, Oregon, Washington, northern Montana, and North Dakota. This spatial pattern was similar to  $b_{ext\_POM}$  trends, and  $b_{ext\_tot}$  trends were likely influenced by the impacts of biomass smoke, especially at sites in the western United States. Short-term significant  $b_{ext\_tot}$  trends ranged from  $-6.53\% \text{ yr}^{-1}$  ( $p < 0.001$ ) at Shining Rock WA, North Carolina (SHRO1), to  $-0.71\% \text{ yr}^{-1}$  ( $p = 0.04$ ) at Trapper Creek, Alaska (TRCR1).

(b)

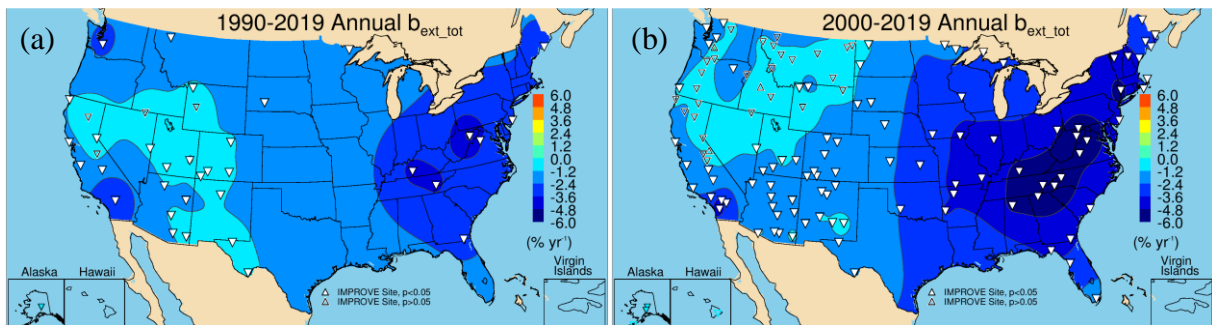


**Figure 7.8.1.** Annual mean total  $b_{ext}$  ( $b_{ext\_tot}$ ) trends ( $\% \text{ yr}^{-1}$ ) for (a) long-term (1990–2019) and (b) short-term (2000–2019) periods. Filled triangles correspond to statistically significant trends ( $p \leq 0.05$ ).

Comparisons of short-term regional and seasonal trends in  $b_{ext\_tot}$  are shown in Figure 7.8.2. The strong reductions in  $b_{ext\_tot}$  in eastern regions are similar to those for  $b_{ext\_AS}$  (Figure 7.1.2), suggesting that in the Northeast and Southeast regions,  $b_{ext\_tot}$  trends are largely driven by  $b_{ext\_AS}$ . The strongest regional reductions occurred during summer in the Northeast region ( $-6.51\% \text{ yr}^{-1}$ ) and summer/fall in the Southeast region ( $\sim -5.5\% \text{ yr}^{-1}$ ). While still negative, the magnitude of the trends decreased for western regions, around  $-2\% \text{ yr}^{-1}$  to  $-3\% \text{ yr}^{-1}$ . Regional trends in the western regions were influenced by biomass smoke, as evidenced by the weak but insignificant trends during summer in the Northwest and California regions, similar to  $b_{ext\_POM}$  (Figure 7.3.2). In addition,  $b_{ext\_AS}$  was lower in the western regions and did not decline at the same rate as in eastern regions.

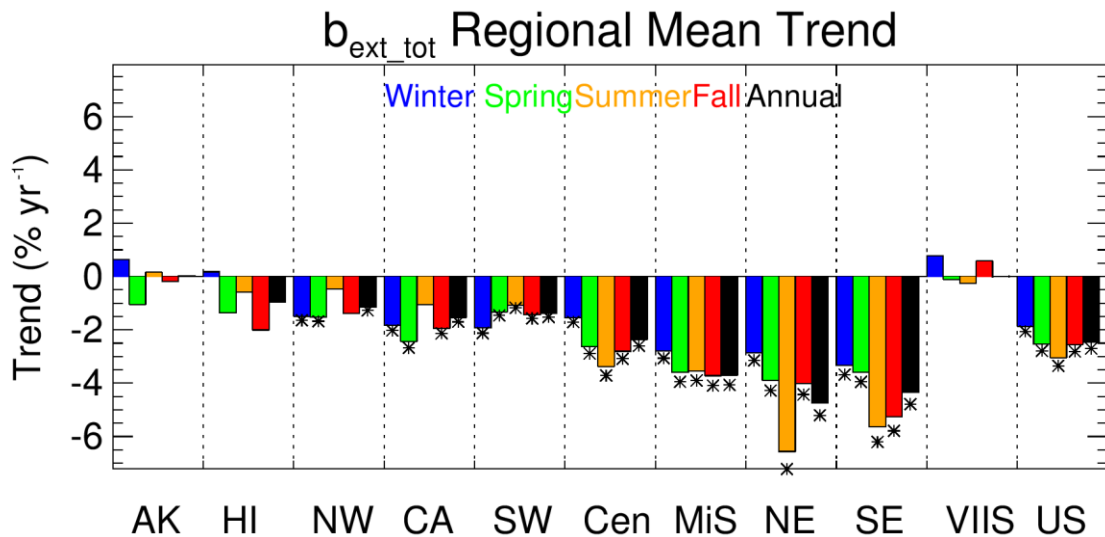


**Figure 7.8.2.** Short-term (2000–2019) regional seasonal mean total  $b_{ext}$  ( $b_{ext\_tot}$ ) trends ( $\% \text{ yr}^{-1}$ ) for major U.S. regions for winter, spring, summer, fall, and annual means. Regions are arranged from western to eastern United States (AK = Alaska, HI = Hawaii, NW = Northwest, CA = California, SW = Southwest, Cen = Central, MiS = Midsouth, NE = Northeast, SE = Southeast, VIIS = Virgin Islands, and US = all sites). Statistically significant trends ( $p \leq 0.05$ ) are denoted with “\*”.

The long-term 10<sup>th</sup> percentile trends in  $b_{ext\_tot}$  are shown in Figure 7.8.3a. All of the 40 valid trends were statistically significant. The strongest reductions occurred at sites in the

Intermountain West, southern California, and the Appalachian Mountains. Trends ranged from  $-3.39\% \text{ yr}^{-1}$  ( $p < 0.001$ ) at Dolly Sods WA, West Virginia (DOSO1), to  $-0.65\% \text{ yr}^{-1}$  ( $p < 0.001$ ) at Denali NP, Alaska (DENA1). The 90<sup>th</sup> percentile trends in  $b_{\text{ext\_tot}}$  are shown in Figure 7.8.3b. Strong reductions in the eastern United States were likely associated with reductions in  $b_{\text{ext\_AS}}$ . Several sites in the West had insignificant trends, especially at sites in California, Oregon, Nevada, Wyoming, and Texas. Trends ranged from  $-5.97\% \text{ yr}^{-1}$  ( $p < 0.001$ ) at DOSO1 to  $-0.63\% \text{ yr}^{-1}$  ( $p = 0.009$ ) at Bryce Canyon NP, Utah (BRCA1).

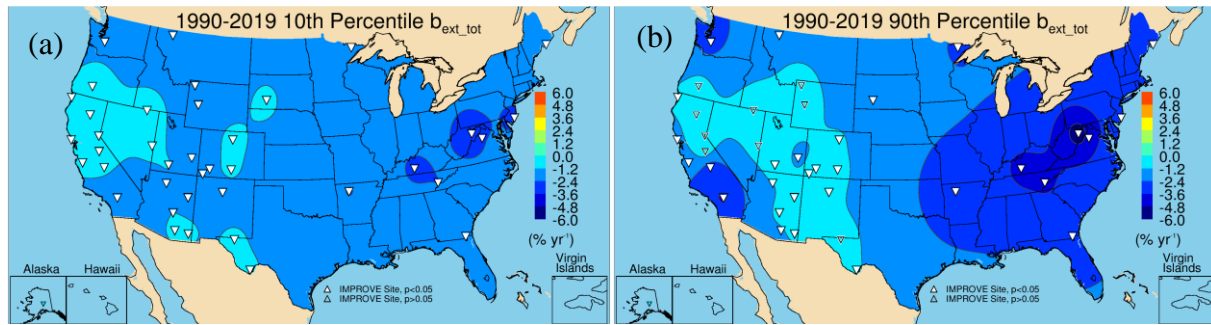


**Figure 7.8.3. IMPROVE long-term (1990–2019) trends ( $\% \text{ yr}^{-1}$ ) in (a) 10<sup>th</sup> percentile total  $b_{\text{ext}}$  ( $b_{\text{ext\_tot}}$ ) and (b) 90<sup>th</sup> percentile  $b_{\text{ext\_tot}}$ . Filled triangles correspond to statistically significant trends ( $p \leq 0.05$ ).**

The short-term trends in 10<sup>th</sup> percentile  $b_{\text{ext\_tot}}$  were significant at 118 of the 136 valid sites (Figure 7.8.4a), with the strongest negative trends at sites in the eastern United States. Weaker trends occurred at sites in California, Oregon, and the northern Great Plains. Trends ranged from  $-4.26\% \text{ yr}^{-1}$  ( $p < 0.001$ ) at Mammoth Cave NP, Kentucky (MACA1), to  $0.94\% \text{ yr}^{-1}$  ( $p = 0.03$ ) at Virgin Islands NP (VIIS1).

The spatial patterns in the short-term 90<sup>th</sup> percentile  $b_{\text{ext\_tot}}$  trends were similar to the long-term 90<sup>th</sup> percentiles trends (Figure 7.8.4b), with the strongest reductions at sites in the eastern United States. Of the 136 valid trends, 90 were statistically significant. Most of the insignificant trends occurred at sites in the West, likely influenced by biomass smoke. Trends ranged from  $-8.28\% \text{ yr}^{-1}$  at Cohutta, Georgia (COHU1), to  $-0.93\% \text{ yr}^{-1}$  ( $p = 0.03$ ) at Bandelier NM, New Mexico (BAND1).

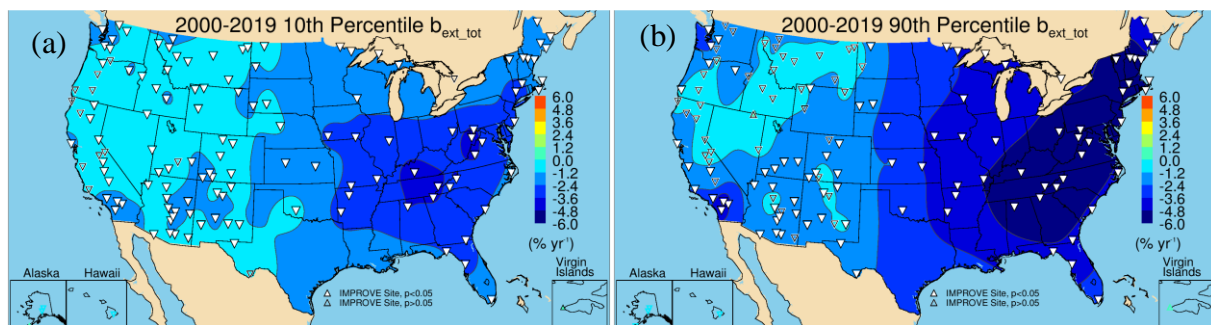


**Figure 7.8.4. IMPROVE short-term (2000–2019) trends ( $\% \text{ yr}^{-1}$ ) in (a) 10<sup>th</sup> percentile total  $b_{\text{ext}}$  ( $b_{\text{ext\_tot}}$ ) and (b) 90<sup>th</sup> percentile  $b_{\text{ext\_tot}}$ . Filled triangles correspond to statistically significant trends ( $p \leq 0.05$ ).**

The strongest regional mean short-term trends in  $b_{\text{ext\_tot}}$  occurred for the 90<sup>th</sup> percentile in the Northeast and Southeast regions ( $\sim -5.5\% \text{ yr}^{-1}$ ) and coincided with the strong summer mean

$b_{ext\_tot}$  trends (Figure 7.8.5). These trends were consistent with strong reductions in summer mean  $b_{ext\_AS}$  in those regions. Trends in  $b_{ext\_tot}$  percentiles were weaker for regions in the West. The 10<sup>th</sup> and 50<sup>th</sup> percentile trends were the strongest in the Northwest and California regions, and insignificant 90<sup>th</sup> percentile trends were likely associated with smoke influence. The Southwest region was the only western region with significant 90<sup>th</sup> percentile trends.

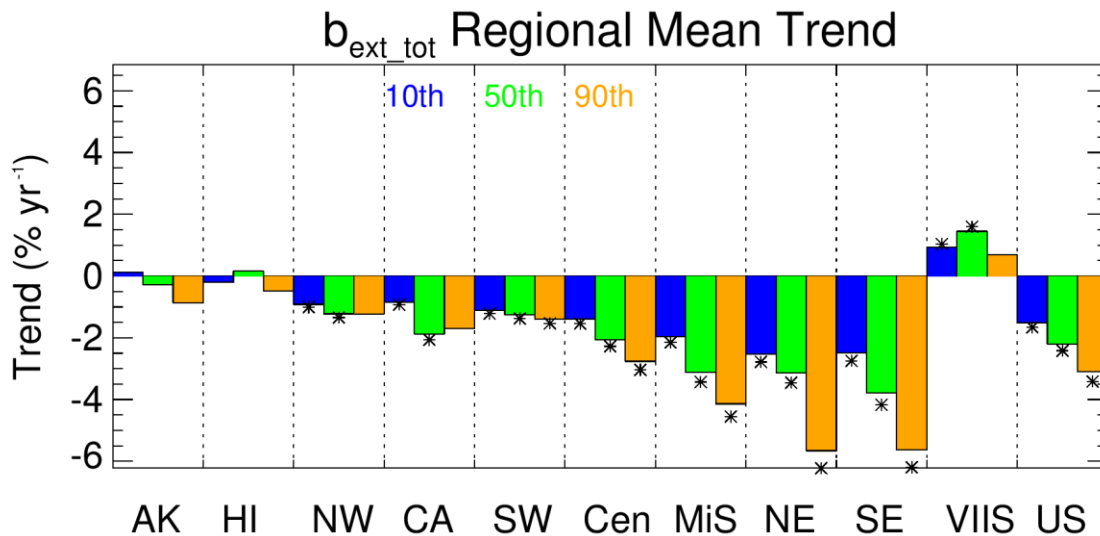


**Figure 7.8.5.** Short-term (2000–2019) regional mean trends ( $\% \text{ yr}^{-1}$ ) in 10<sup>th</sup>, 50<sup>th</sup>, and 90<sup>th</sup> percentile total  $b_{ext}$  ( $b_{ext\_tot}$ ). Regions are arranged from western to eastern United States (AK = Alaska, HI = Hawaii, NW = Northwest, CA = California, SW = Southwest, Cen = Central, MiS = Midsouth, NE = Northeast, SE = Southeast, VIIS = Virgin Islands, and US = all sites). Statistically significant trends ( $p \leq 0.05$ ) are denoted with “\*”.

## 7.9 DECIVIEW TRENDS

The deciview (dv) haze index is a logarithmic transformation of  $b_{ext\_tot}$  (see Chapter 4.1); therefore, the spatial and seasonal patterns in dv trends will generally follow trends in  $b_{ext\_tot}$ . The spatial patterns in long-term annual mean dv trends are shown in (Figure 7.9.1a). The strongest reductions occurred at sites in the eastern United States, southern California, and the Northwest. Of the 38 valid sites, 37 had statistically significant trends. Sites with lower and insignificant trends were in California, Nevada, and Wyoming. Trends in dv ranged from  $-2.85\% \text{ yr}^{-1}$  ( $p < 0.001$ ) at Dolly Sods WA, West Virginia (DOSO1), to  $-0.53\% \text{ yr}^{-1}$  ( $p = 0.009$ ) at Guadalupe NP, Texas (GUMO1).

The differences in annual mean dv trends that were observed between sites in the eastern and western United States were also observed for the short-term trends, with the strongest reductions in the eastern United States where  $b_{ext\_AS}$  significantly declined (Figure 7.9.1b). Insignificant trends occurred at sites in California, Oregon, Washington, northern Montana, and North Dakota. This spatial pattern was similar to  $b_{ext\_POM}$  trends, and dv trends were influenced by the impacts of biomass smoke, especially at sites in the western United States. Short-term significant dv trends ranged from  $-3.81\% \text{ yr}^{-1}$  ( $p < 0.001$ ) at Shining Rock WA, North Carolina (SHRO1), to  $-0.67\% \text{ yr}^{-1}$  ( $p = 0.013$ ) at Salt Creek, New Mexico (SACR1).

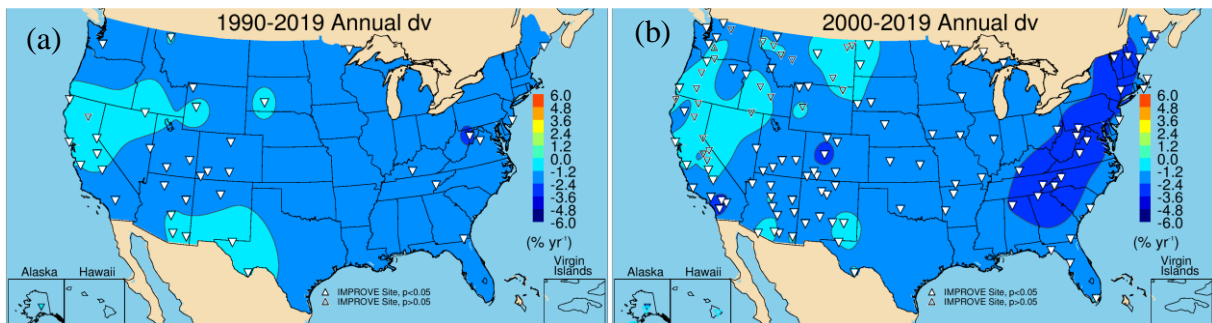


**Figure 7.9.1** Annual mean deciview (dv) trends ( $\% \text{ yr}^{-1}$ ) for (a) long-term (1990–2019) and (b) short-term (2000–2019) periods. Filled triangles correspond to statistically significant trends ( $p \leq 0.05$ ).

Comparisons of short-term regional and seasonal mean trends in dv are shown in Figure 7.9.2. The strong reductions in dv in eastern regions are similar to those for  $b_{\text{ext\_AS}}$  (Figure 7.1.2), suggesting that in the Northeast and Southeast regions, dv trends were largely driven by  $b_{\text{ext\_AS}}$ . The strongest regional reductions occurred during summer in the Northeast region ( $-3.24\% \text{ yr}^{-1}$ ) and summer/fall in the Southeast region ( $\sim -2.7\% \text{ yr}^{-1}$ ). While still negative, the magnitude of the trends decreased for western regions, around  $-1\% \text{ yr}^{-1}$  to  $-2\% \text{ yr}^{-1}$ . Regional trends in the western regions were influenced by biomass smoke, as evidenced by the weak but insignificant trends during summer in the Northwest and California regions, similar to  $b_{\text{ext\_POM}}$  (Figure 7.3.2). In addition,  $b_{\text{ext\_AS}}$  was lower in the western regions and did not decline at the same rate as in eastern regions.

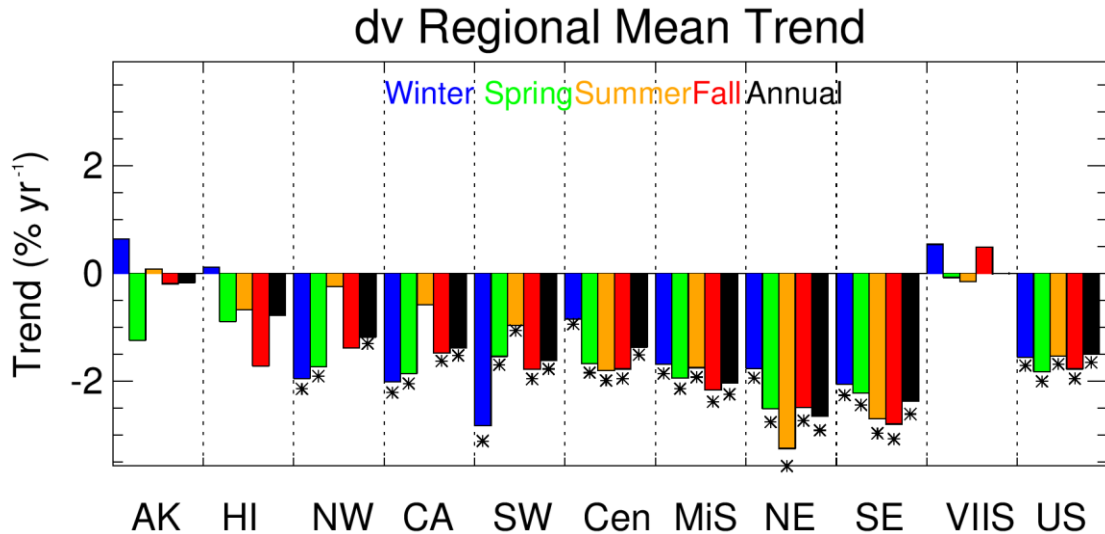


**Figure 7.9.2.** Short-term (2000–2019) regional seasonal mean deciview (dv) trends ( $\% \text{ yr}^{-1}$ ) for major U.S. regions for winter, spring, summer, fall, and annual means. Regions are arranged from western to eastern United States (AK = Alaska, HI = Hawaii, NW = Northwest, CA = California, SW = Southwest, Cen = Central, MiS = Midsouth, NE = Northeast, SE = Southeast, VIIS = Virgin Islands, and US = all sites). Statistically significant trends ( $p \leq 0.05$ ) are denoted with “\*”.

The long-term 10<sup>th</sup> percentile trends in dv are shown in Figure 7.9.3a. All of the 40 valid trends were statistically significant. The strongest reductions occurred at sites in the

Intermountain West, southern California, and the Appalachian Mountains. Trends ranged from  $-6.32\% \text{ yr}^{-1}$  ( $p < 0.001$ ) at Bridger, Wyoming (BRID1), to  $-1.08\% \text{ yr}^{-1}$  ( $p < 0.001$ ) at Pinnacles NM, California (PINN1). The 90<sup>th</sup> percentile long-term trends in dv are shown in Figure 7.9.3b. Strong reductions in the eastern United States were likely associated with reductions in  $b_{\text{ext\_AS}}$ . Several sites in the West had insignificant trends, especially at sites in California, Oregon, Nevada, Wyoming, and Texas. Trends ranged from  $-2.41\% \text{ yr}^{-1}$  ( $p < 0.001$ ) at Dolly Sods WA, West Virginia (DOSO1), to  $-0.41\% \text{ yr}^{-1}$  ( $p = 0.03$ ) at Redwood NP, California (REDW1).

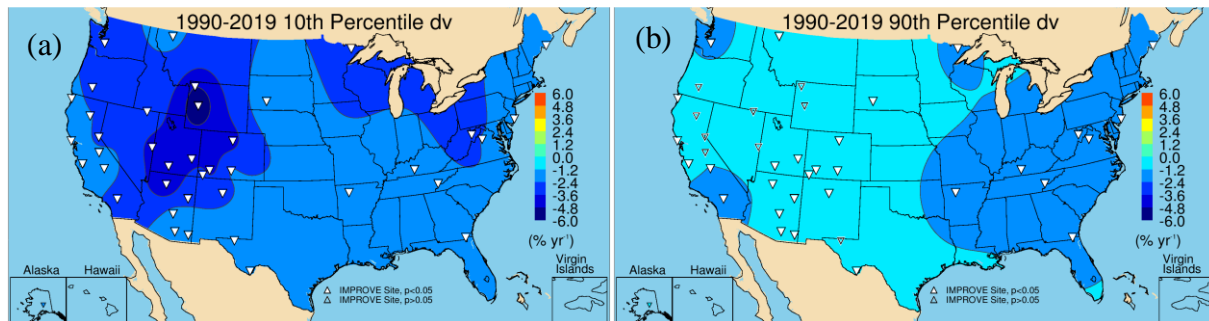


**Figure 7.9.3. IMPROVE long-term (1990–2019) trends ( $\% \text{ yr}^{-1}$ ) in (a) 10<sup>th</sup> percentile deciview (dv) and (b) 90<sup>th</sup> percentile dv. Filled triangles correspond to statistically significant trends ( $p \leq 0.05$ ).**

The short-term trends in 10<sup>th</sup> percentile dv were significant at 118 of the 136 valid sites (Figure 7.9.4a), with the strongest negative trends at sites in the eastern United States. Weaker trends occurred at sites in California, Oregon, and the northern Great Plains. Trends ranged from  $-9.42\% \text{ yr}^{-1}$  ( $p < 0.001$ ) at White River NF, Colorado (WHRI1), to  $0.92\% \text{ yr}^{-1}$  ( $p = 0.03$ ) at Virgin Islands NP (VIIS1).

The spatial pattern in the short-term 90<sup>th</sup> percentile dv trends (Figure 7.9.4b) showed the strongest reductions at sites in the eastern United States. Of the 136 valid trends, 90 were statistically significant. Most of the insignificant trends occurred at sites in the West, likely influenced by biomass smoke. Trends ranged from  $-3.47\% \text{ yr}^{-1}$  ( $p < 0.001$ ) at Shining Rock WA, North Carolina (SHRO1), to  $-0.74\% \text{ yr}^{-1}$  ( $p = 0.03$ ) at Kalmiopsis, Oregon (KALM1).

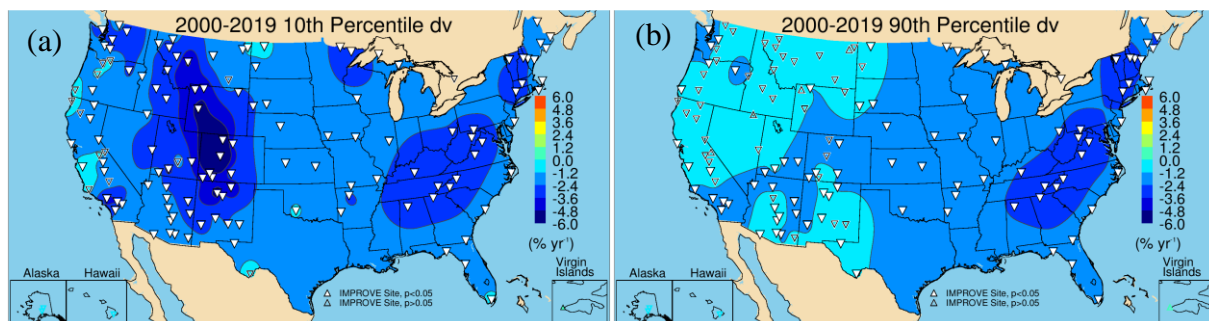


**Figure 7.9.4. IMPROVE short-term (2000–2019) trends ( $\% \text{ yr}^{-1}$ ) in (a) 10<sup>th</sup> percentile deciview (dv) and (b) 90<sup>th</sup> percentile dv. Filled triangles correspond to statistically significant trends ( $p \leq 0.05$ ).**

The strongest regional short-term trends in dv occurred for the 90<sup>th</sup> percentile in the Northeast and Southeast regions ( $\sim -2.5\% \text{ yr}^{-1}$ ) and likely coincided with the strong summer mean

$dv$  trends (Figure 7.9.5). These trends were consistent with strong reductions in summer mean  $b_{ext\_AS}$  in those regions. Trends in  $dv$  percentiles decreased for regions in the West. The 10<sup>th</sup> and 50<sup>th</sup> percentile trends were the strongest in the Northwest and California regions, and insignificant 90<sup>th</sup> percentile trends were likely associated with smoke influence. The Southwest region was the only western region with significant 90<sup>th</sup> percentile trends.

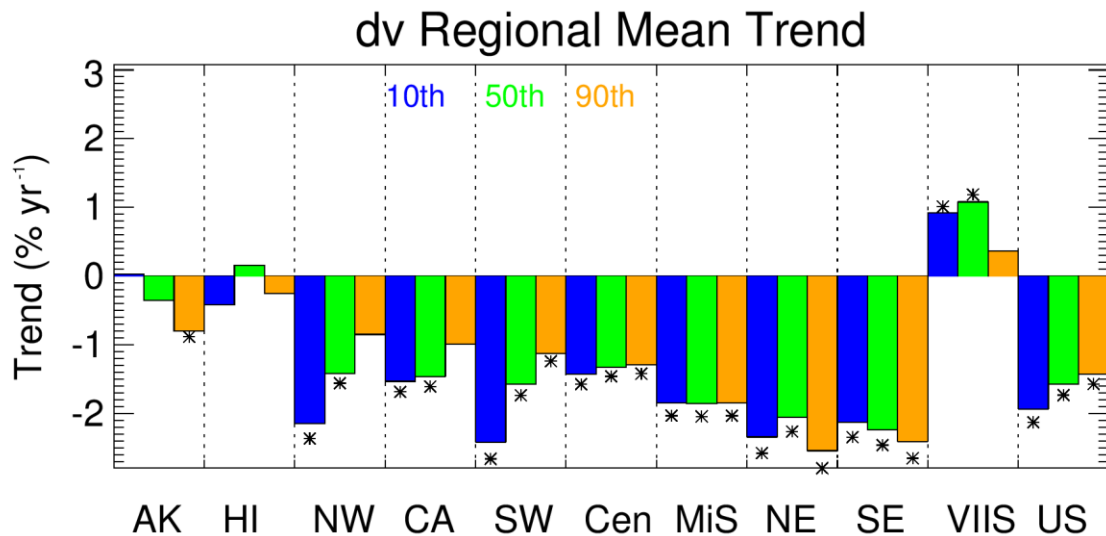


**Figure 7.9.5.** Short-term (2000–2019) trends ( $\% \text{ yr}^{-1}$ ) trends in 10<sup>th</sup>, 50<sup>th</sup>, and 90<sup>th</sup> percentile deciview ( $dv$ ). Regions are arranged from western to eastern United States (AK = Alaska, HI = Hawaii, NW = Northwest, CA = California, SW = Southwest, Cen = Central, MiS = Midsouth, NE = Northeast, SE = Southeast, VIIS = Virgin Islands, and US = all sites). Statistically significant trends ( $p \leq 0.05$ ) are denoted with “\*”.

## 7.10 DISCUSSION

Timelines of regional, annual mean speciated  $b_{ext}$  corresponding to the previous trend results are shown in Figure 7.10.1(a-j) for 2000 through 2019 due to the expansion of the network in 2000 (Hand et al., 2020). Strong reductions in  $b_{ext\_tot}$  have occurred at remote sites across the United States. These reductions were greatest in the eastern United States and driven by strong negative trends in  $b_{ext\_AS}$ . Sulfate concentrations and associated  $b_{ext\_AS}$  have decreased in response to major reductions in sulfur dioxide emissions (Hand et al., 2020). In addition, reductions in  $b_{ext\_AN}$  and  $b_{ext\_POM}$  (especially in the East) have contributed to reduced  $b_{ext\_tot}$ . Negative trends in  $b_{ext\_tot}$  occurred at sites in California where  $b_{ext\_AN}$  decreased due to reductions in nitrogen dioxide emissions, especially mobile emissions.

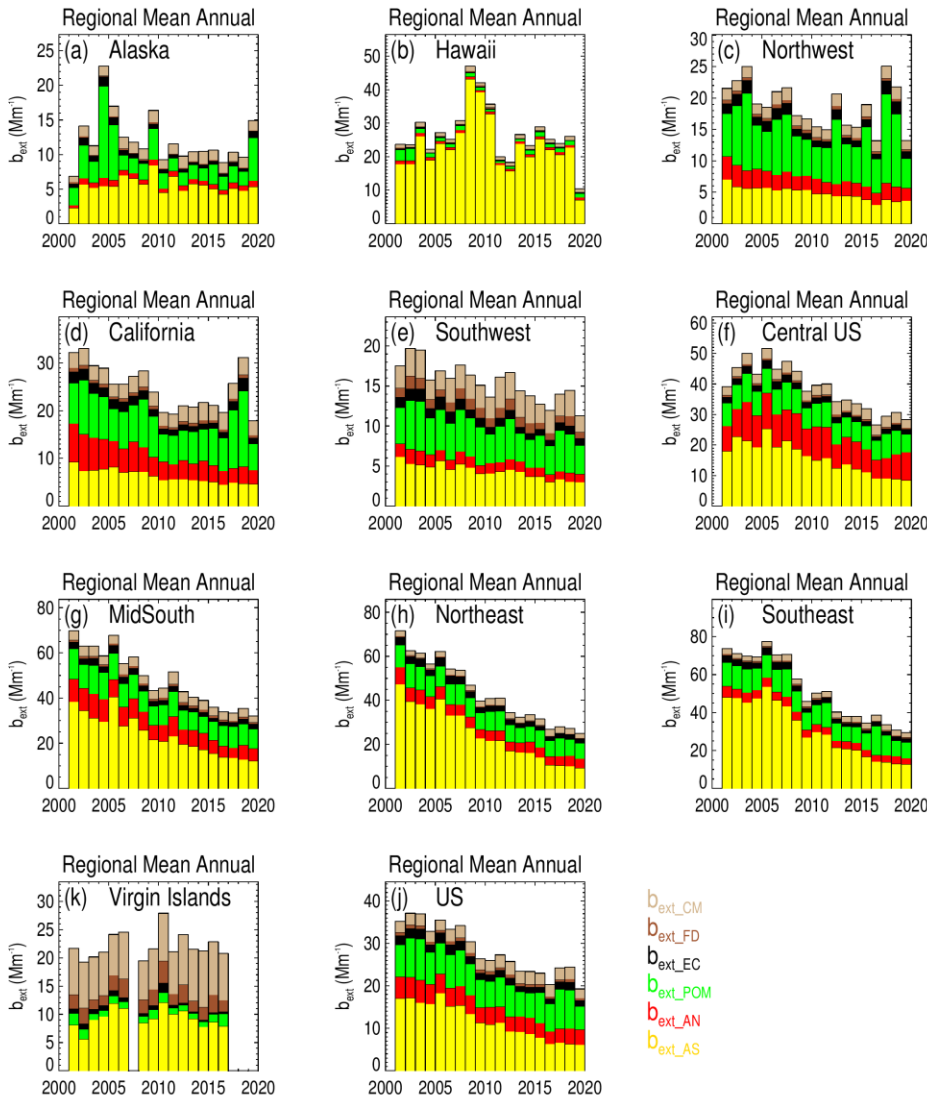


**Figure 7.10.1. Short-term (2001–2019) timelines in IMPROVE regional, annual mean ambient speciated  $b_{ext}$  ( $Mm^{-1}$ ) for ammonium sulfate ( $b_{ext\_AS}$ ), ammonium nitrate ( $b_{ext\_AN}$ ), particulate organic matter ( $b_{ext\_POM}$ ), elemental carbon ( $b_{ext\_EC}$ ), fine dust ( $b_{ext\_FD}$ ), and coarse mass ( $b_{ext\_CM}$ ). Wavelength corresponds to 550 nm.**

In the western United States, especially the Northwest,  $b_{ext\_tot}$  has declined at a weaker rate relative to sites in the East. Comparisons of  $b_{ext\_POM}$  and  $b_{ext\_EC}$  trends suggest that  $b_{ext\_tot}$  is influenced by an increase in biomass burning impacts that have led to an increase in  $b_{ext\_POM}$ , or at the very least flat and insignificant trends (Figure 7.10.1c). Extinction from carbonaceous aerosols is a major contributor to  $b_{ext\_tot}$  especially at western sites (Hand et al., 2020).

Although  $b_{ext\_FD}$  and  $b_{ext\_CM}$  have not decreased at the same rate as extinction from other species, and in some regions have increased, their impact on  $b_{ext\_tot}$  was not as pronounced as their impact on mass. This difference is due to their lower mass scattering efficiencies (compare Figure 7.10.1 to Figures 6.10.1 and 6.10.2). However, the fraction of  $b_{ext\_tot}$  due to  $b_{ext\_FD}$  and  $b_{ext\_CM}$  has increased, especially as  $b_{ext\_AS}$  and  $b_{ext\_AN}$  have decreased.

Regulatory activity has been very successful at reducing pollutant emissions that lead to secondary aerosols, such as sulfate, nitrate, and POM, and their contributions to haze. Reductions in these species have driven negative trends in  $b_{ext\_tot}$  at sites across the United States. However, the role of natural aerosols, such as those derived from biomass smoke and dust storms, have not declined and for some sites and seasons, have increased. The impacts of these positive trends have and likely will continue to impede progress in improving visibility, especially in the western United States.

To demonstrate the visibility conditions associated with the trends in  $b_{ext\_tot}$ , the computer software program, WinHaze 2.9.9.1 (<http://vista.cira.colostate/Improve/winhaze>) was used to simulate visibility conditions from user-specified scenes and speciated aerosol concentrations or visibility levels. The 90<sup>th</sup> percentile  $b_{ext\_tot}$  values were chosen for the initial and end years for Great Smoky Mountains NP, Tennessee (GRSM1), San Gorgonio WA, California (SAGO1), and Yosemite NP, California (YOSE1). These sites were chosen to represent trends in visibility in the East and West, respectively.

The 90<sup>th</sup> percentile visibility conditions in GRSM1 in 1990 (256 Mm<sup>-1</sup>) and 2019 (58 Mm<sup>-1</sup>) are shown in Figure 7.10.2. The dramatic improvement in the visibility conditions is evident. These changes are largely due to the reductions of sulfate aerosols in the region and were evidenced by the strong reduction in  $b_{ext\_tot}$  shown in Figure 7.8.4b. Similar results for the 1990 (127 Mm<sup>-1</sup>) and 2019 (43 Mm<sup>-1</sup>) 90<sup>th</sup> percentile  $b_{ext\_tot}$  at SAGO1 are shown in Figure 7.10.3. The striking improvement in visibility at this site was largely due to the reduction of nitrate aerosols. In contrast, visibility conditions at Yosemite NP, California, are shown in Figure 7.10.4 for the 90<sup>th</sup> percentile  $b_{ext\_tot}$  in 1990 (58 Mm<sup>-1</sup>) and 2019 (40 Mm<sup>-1</sup>). The changes in the conditions are imperceptible, in part because the initial conditions were initially very low. This site had insignificant trends and was influenced by biomass smoke impacts. While the trend analyses presented here provide a quantifiable measure of the changes in haze over time, the ability to visualize the changes is a powerful means by which to communicate the progress that has been achieved through regulatory activity, as well as to identify future challenges.



**Figure 7.10.2.** Split-image of visibility conditions in Great Smoky Mountains NP, Tennessee (GRSM1), for 90<sup>th</sup> percentile total extinction levels in 1990 (left side) and 2019 (right side).



**Figure 7.10.3.** Split-image of visibility conditions in San Gorgonio WA, California (SAGO1), for 90<sup>th</sup> percentile total extinction levels in 1990 (left side) and 2019 (right side).



**Figure 7.10.4. Split-image of visibility conditions in Yosemite NP, California (YOSE1), for 90<sup>th</sup> percentile total extinction levels in 1990 (left side) and 2019 (right side).**

Site-specific long-term and short-term trend results are provided in Appendix 7.1 for annual mean trends, short-term percentile trends in Appendix 7.2, and long-term percentile trends in Appendix 7.3.

## REFERENCES

- Gebhart, K. A., Day, D. E., Prenni, A. J., Schichtel, B. A., Hand, J. L., and Evanoski-Cole, A. R. (2018), Visibility impacts at Class I areas near the Bakken oil and gas development, *Journal of the Air & Waste Management Association*, 68(5), 477-493, doi:10.1080/10962247.2018.1429334.
- Hand, J. L., Schichtel, B. A., Malm, W. C., and Pitchford, M. L. (2012), Particulate sulfate ion concentration and SO<sub>2</sub> emission trends in the United States from the early 1990s through 2010, *Atmospheric Chemistry and Physics*, 12(21), 10353-10365, doi:10.5194/acp-12-10353-2012.
- Hand, J. L., Schichtel, B. A., Malm, W. C., Copeland, S., Molenar, J. V., Frank, N. H., and Pitchford, M. (2014), Widespread reductions in haze across the United States from the early 1990s through 2011, *Atmospheric Environment*, 94, 671-679, doi:10.1016/j.atmosenv.2014.05.062.
- Hand, J. L., Prenni, A. J., Copeland, S., Schichtel, B. A., and Malm, W. C. (2020), Thirty years of the Clean Air Act Amendments: Impacts on haze in remote regions of the United States (1990–2018), *Atmospheric Environment*, 243, 117865, <https://doi.org/10.1016/j.atmosenv.2020.117865>.
- Isaaks, E. H., and Mohan Srivastava, R. (1989), *An Introduction to Applied Geostatistics*, Oxford University Press, New York, ISBN 978-0195050134.
- McClure, C. D., and Jaffe, D. A. (2018), US particulate matter air quality improves except in wildfire-prone areas, *Proceedings of the National Academy of Sciences*, 115(31), 7901-7906, doi:10.1073/pnas.1804353115.
- Russell, A., Valin, L., and Cohen, R. (2012), Trends in OMI NO<sub>2</sub> observations over the United States: Effects of emission control technology and the economic recession, *Atmospheric Chemistry and Physics*, 12(24), 12197-12209, doi:doi:10.5194/acp-12-12197-2012.
- Theil, H. (1950), A rank-invariant method of linear and polynomial regression analysis., *Proc. Kon. Ned. Akad. v Wetensch.*, A(53), 386-392, [https://doi.org/10.1007/978094-011-2546-8\\_20](https://doi.org/10.1007/978094-011-2546-8_20).
- Tong, D. Q., Lamsal, L., Pan, L., Ding, C., Kim, H., Lee, P., Chai, T., Pickering, K. E., and Stajner, I. (2015), Long-term NO<sub>x</sub> trends over large cities in the United States during the great recession: Comparison of satellite retrievals, ground observations, and emission inventories, *Atmospheric Environment*, 107, 70-84, <http://dx.doi.org/10.1016/j.atmosenv.2015.01.035>.
- Zhang, X. (2019), Correction of chloride concentrations for filter blank levels, *IMPROVE Data Advisory* (da0039), [http://vista.cira.colostate.edu/improve/Data/QA\\_QC/Advisory/da0039/da0039\\_ChlorideOverCorrection.pdf](http://vista.cira.colostate.edu/improve/Data/QA_QC/Advisory/da0039/da0039_ChlorideOverCorrection.pdf).

## Chapter 8. IMPROVE Bibliography 2010 to Present

Compiled by John G. Watson, Desert Research Institute and Warren White, U.C. Davis

Abbasi, B., Wang, X. L., Chow, J. C., Watson, J. G., Peik, B., Nasiri, V., Riemschnitter, K. B., and Elahifard, M. (2021), Review of respirable coal mine dust characterization for mass concentration, size distribution and chemical composition, *Minerals*, 11(4), 426, doi:10.3390/min11040426.

Aldhaif, A. M., Lopez, D. H., Dadashazar, H., and Sorooshian, A. (2020), Sources, frequency, and chemical nature of dust events impacting the United States East Coast, *Atmospheric Environment*, 231, doi:10.1016/j.atmosenv.2020.117456.

Ali, K., Panicker, A. S., Beig, G., Srinivas, R., and Acharja, P. (2016), Carbonaceous aerosols over Pune and Hyderabad (India) and influence of meteorological factors, *Journal of Atmospheric Chemistry*, 73(1), 1-27, doi:10.1007/s10874-015-9314-4.

Ancelet, T., Davy, P. K., Trompetter, W. J., Markwitz, A., and Weatherburn, D. C. (2011), Carbonaceous aerosols in an urban tunnel, *Atmospheric Environment*, 45(26), 4463-4469.

Appel, K. W., Pouliot, G. A., Simon, H., Sarwar, G., Pye, H. O. T., Napelenok, S. L., Akhtar, F., and Roselle, S. J. (2013), Evaluation of dust and trace metal estimates from the Community Multiscale Air Quality (CMAQ) model version 5.0, *Geoscientific Model Development*, 6(4), 883-899.

Arora, P., and Jain, S. (2015), Estimation of organic and elemental carbon emitted from wood burning in traditional and improved cookstoves using controlled cooking test, *Environmental Science & Technology*, 49(6), 3958-3965.

Bahadur, R., Feng, Y., Russell, L. M., and Ramanathan, V. (2011), Impact of California's air pollution laws on black carbon and their implications for direct radiative forcing, *Atmospheric Environment*, 45(5), 1162-1167.

Bahadur, R., Feng, Y., Russell, L. M., and Ramanathan, V. (2011), Response to comments on "Impact of California's air pollution laws on black carbon and their implications for direct radiative forcing" by R. Bahadur et al, *Atmospheric Environment*, 45(24), 4119-4121.

Batmunkh, T., Lee, K. Y., Kim, Y. J., Bae, M. S., Maskey, S., and Park, K. (2016), Optical and thermal characteristics of carbonaceous aerosols measured at an urban site in Gwangju, Korea, in the winter of 2011, *Journal of the Air & Waste Management Association*, 66(2), 151-163, doi:10.1080/10962247.2015.1101031.

Bautista, A. T., Pabroa, P. C. B., Santos, F. L., Racho, J. M. D., and Quirit, L. L. (2014), Carbonaceous particulate matter characterization in an urban and a rural site in the Philippines, *Atmospheric Pollution Research*, 5(2), 245-252,  
<http://www.atmospolres.com/articles/volume5/issue2/apr-14-030.pdf>.

Begum, B. A., and Hopke, P. K. (2013), Identification of haze-creating sources from fine particulate matter in Dhaka aerosol using carbon fractions, *Journal of the Air & Waste Management Association*, 63(9), 1046-1057.

Bell, S. W., Hansell, R. A., Chow, J. C., Tsay, S. C., Wang, S. H., Ji, Q., Li, C., Watson, J. G., and Khlystov, A. Y. (2013), Constraining aerosol optical models using ground-based, collocated

particle size and mass measurements in variable air mass regimes during the 7-SEAS/Dongsha experiment, *Atmospheric Environment*, 78, 163-173,  
[https://www.researchgate.net/publication/235341396\\_Constraining\\_aerosol\\_optical\\_models\\_using\\_ground-based\\_collocated\\_particle\\_size\\_and\\_mass\\_measurements\\_in\\_variable\\_air\\_mass\\_regimes\\_during\\_the\\_7-SEASDongsha\\_experiment](https://www.researchgate.net/publication/235341396_Constraining_aerosol_optical_models_using_ground-based_collocated_particle_size_and_mass_measurements_in_variable_air_mass_regimes_during_the_7-SEASDongsha_experiment).

Bergen, S., Sheppard, L., Sampson, P. D., Kim, S. Y., Richards, M., Vedral, S., Kaufman, J. D., and Szpiro, A. A. (2013), A national prediction model for PM2.5 component exposures and measurement error-corrected health effect inference, *Environ. Health Perspect*, 121(9), 1017-1025, <http://ehp.niehs.nih.gov/wp-content/uploads/121/9/ehp.1206010.pdf>.

Berkowitz, C. M., Berg, L. K., Yu, X. Y., Alexander, M. L., Laskin, A., Zaveri, R. A., Jobson, B. T., Andrews, E., and Ogren, J. A. (2011), The influence of fog and airmass history on aerosol optical, physical and chemical properties at Pt. Reyes National Seashore, *Atmospheric Environment*, 45(15), 2559-2568.

Bian, Q. J., Ford, B., Pierce, J. R., and Kreidenweis, S. M. (2020), A cecadal climatology of chemical, physical, and optical properties of ambient smoke in the western and southeastern United States, *Journal of Geophysical Research-Atmospheres*, 125(1), doi:10.1029/2019jd031372.

Bladt, H., Ivleva, N. P., and Niessner, R. (2014), Internally mixed multicomponent soot: Impact of different salts on soot structure and thermo-chemical properties, *Journal of Aerosol Science*, 70, 26-35.

Blanchard, C. L., Tanenbaum, S., and Motallebi, N. (2011), Spatial and temporal characterization of PM2.5 mass concentrations in California, 1980-2007, *Journal of the Air & Waste Management Association*, 61(3), 339-351.

Blanchard, C. L., Hidy, G. M., Tanenbaum, S., Edgerton, E. S., and Hartsell, B. E. (2013), The Southeastern Aerosol Research and Characterization (SEARCH) study: Spatial variations and chemical climatology, 1999-2010, *Journal of the Air & Waste Management Association*, 63(3), 260-275, <http://www.tandfonline.com/doi/pdf/10.1080/10962247.2012.749816>.

Blanchard, C. L., Hidy, G. M., Tanenbaum, S., Edgerton, E. S., and Hartsell, B. E. (2013), The Southeastern Aerosol Research and Characterization (SEARCH) study: Temporal trends in gas and PM concentrations and composition, 1999-2010, *Journal of the Air & Waste Management Association*, 63(3), 247-259,  
<http://www.tandfonline.com/doi/pdf/10.1080/10962247.2012.748523>.

Blanchard, C. L., Tanenbaum, S., and Hidy, G. M. (2014), Spatial and temporal variability of air pollution in Birmingham, Alabama, *Atmospheric Environment*, 89, 382-391.

Blanchard, C. L., Chow, J. C., Edgerton, E. S., Watson, J. G., Hidy, G. M., and Shaw, S. (2014), Organic aerosols in the southeastern United States: Speciated particulate carbon measurements from the SEARCH network, 2006 to 2010, *Atmospheric Environment*, 95, 327-333.

Buchard, V., da Silva, A. M., Randles, C. A., Colarco, P., Ferrare, R., Hair, J., Hostetler, C., Tackett, J., and Winker, D. (2016), Evaluation of the surface PM2.5 in Version 1 of the NASA MERRA Aerosol Reanalysis over the United States, *Atmospheric Environment*, 125, 100-111, doi:10.1016/j.atmosenv.2015.11.004.

- Bürki, C., Reggente, M., M. Dillner, A., L. Hand, J., L. Shaw, S., and Takahama, S. (2020), Analysis of functional groups in atmospheric aerosols by infrared spectroscopy: Method development for probabilistic modeling of organic carbon and organic matter concentrations, *Atmospheric Measurement Techniques*, 13(3), 1517-1538, doi:10.5194/amt-13-1517-2020.
- Cao, J. J., Chow, J. C., Tao, J., Lee, S. C., Watson, J. G., Ho, K. F., Wang, G. H., Zhu, C. S., and Han, Y. M. (2011), Stable carbon isotopes in aerosols from Chinese cities: Influence of fossil fuels, *Atmospheric Environment*, 45(6), 1359-1363.
- Cao, J. J., Li, H., Chow, J. C., Watson, J. G., Lee, S. C., Rong, B., Dong, J. G., and Ho, K. F. (2011), Chemical composition of indoor and outdoor atmospheric particles at Emperor Qin's terra-cotta museum, Xi'an, China, *Aerosol and Air Quality Research*, 11(1), 70-79, [http://aaqr.org/VOL11\\_No1\\_February2011/8\\_AAQR-10-10-OA-0088\\_70-79.pdf](http://aaqr.org/VOL11_No1_February2011/8_AAQR-10-10-OA-0088_70-79.pdf).
- Cao, J. J., Huang, H., Lee, S. C., Chow, J. C., Zou, C. W., Ho, K. F., and Watson, J. G. (2012), Indoor/outdoor relationships for organic and elemental carbon in PM<sub>2.5</sub> at residential homes in Guangzhou, China, *Aerosol and Air Quality Research*, 12(5), 902-910, [http://aaqr.org/VOL12\\_No5\\_October2012/18\\_AAQR-12-02-OA-0026\\_902-910.pdf](http://aaqr.org/VOL12_No5_October2012/18_AAQR-12-02-OA-0026_902-910.pdf).
- Cao, J. J., Shen, Z. X., Chow, J. C., Lee, S. C., Watson, J. G., Tie, X. X., Ho, K. F., Wang, G. H., and Han, Y. M. (2012), Winter and summer PM<sub>2.5</sub> chemical compositions in 14 Chinese cities, *Journal of the Air & Waste Management Association*, 62(10), 1214-1226, doi:10.1080/10962247.2012.701193.
- Cao, J. J., Wang, Q. Y., Chow, J. C., Watson, J. G., Tie, X. X., Shen, Z. X., and An, Z. S. (2012), Impacts of aerosol compositions on visibility impairment in Xi'an, China, *Atmospheric Environment*, 59, 559-566, [https://www.researchgate.net/publication/263854060\\_Impacts\\_of\\_aerosol\\_compositions\\_on\\_visibility\\_impairment\\_in\\_Xian\\_China](https://www.researchgate.net/publication/263854060_Impacts_of_aerosol_compositions_on_visibility_impairment_in_Xian_China).
- Cao, J. J., Xu, H. M., Xu, Q., Chen, B. H., and Kan, H. D. (2012), Fine particulate matter constituents and cardiopulmonary mortality in a heavily polluted Chinese city, *Environ. Health Perspect*, 120(3), 373-378.
- Cao, J. J., Zhu, C. S., Tie, X. X., Geng, F. H., Xu, H. M., Ho, S. S. H., Wang, G. H., Han, Y. M., and Ho, K. F. (2013), Characteristics and sources of carbonaceous aerosols from Shanghai, China, *Atmospheric Chemistry and Physics*, 13(2), 803-817.
- Carter, T. S., Heald, C. L., Jimenez, J. L., Campuzano-Jost, P., Kondo, Y., Moteki, N., Schwarz, J. P., Wiedinmyer, C., Darmenov, A. S., da Silva, A. M., and Kaiser, J. W. (2020), How emissions uncertainty influences the distribution and radiative impacts of smoke from fires in North America, *Atmospheric Chemistry and Physics*, 20(4), 2073-2097, doi:10.5194/acp-20-2073-2020.
- Castaneda, C. M., Ashbaugh, L. L., and Wakabayashi, P. (2010), Use of proton backscattering to determine the carbon and oxygen content in fine particle samples deposited on PTFE((CF<sub>2</sub>)<sub>n</sub>) membrane disk filters, *Journal of Aerosol Science*, 41(1), 99-107.
- Celo, V., Dabek-Zlotorzynska, E., and McCurdy, M. (2015), Chemical characterization of exhaust emissions from selected Canadian marine vessels: The case of trace metals and lanthanoids, *Environmental Science & Technology*, 49(8), 5220-5226.

Chakrabarty, R. K., Pervez, S., Chow, J. C., Dewangan, S., Robles, J. A., Tian, G. X., and Watson, J. G. (2014), Funeral pyres in south Asia: Large-scale brown carbon emissions and associated warming, *Environmental Science & Technology Letters*, 1(1), 44-48, <http://pubs.acs.org/doi/pdf/10.1021/ez4000669>.

Chen, D., Zhao, Y., Zhang, J., Yu, H., and Yu, X. N. (2020), Characterization and source apportionment of aerosol light scattering in a typical polluted city in the Yangtze River Delta, China, *Atmospheric Chemistry and Physics*, 20(17), 10193-10210, doi:10.5194/acp-20-10193-2020.

Chen, L.-W. A., Watson, J. G., Chow, J. C., DuBois, D. W., and Herschberger, L. (2010), Chemical mass balance source apportionment for combined PM<sub>2.5</sub> measurements from U.S. non-urban and urban long-term networks, *Atmospheric Environment*, 44(38), 4908-4918.

Chen, L.-W. A., Watson, J. G., Chow, J. C., DuBois, D. W., and Herschberger, L. (2011), PM<sub>2.5</sub> source apportionment: Reconciling receptor models for U.S. non-urban and urban long-term networks, *Journal of the Air & Waste Management Association*, 61(11), 1204-1217, <http://www.tandfonline.com/doi/pdf/10.1080/10473289.2011.619082>.

Chen, L.-W. A., Watson, J. G., Chow, J. C., DuBois, D. W., and Herschberger, L. (2012), Chemical mass balance source apportionment for combined PM<sub>2.5</sub> measurements from U.S. non-urban and urban long-term networks (vol 44, pg 4908, 2010), *Atmospheric Environment*, 51, 335-335.

Chen, L.-W. A., Watson, J. G., Chow, J. C., Green, M. C., Inouye, D., and Dick, K. (2012), Wintertime particulate pollution episodes in an urban valley of the western U.S.: A case study, *Atmospheric Chemistry and Physics*, 12(21), 10051-10064, <http://www.atmos-chem-phys.net/12/10051/2012/acp-12-10051-2012.pdf>.

Chen, L.-W. A., Tropp, R. J., Li, W.-W., Zhu, D. Z., Chow, J. C., Watson, J. G., and Zielinska, B. (2012), Aerosol and air toxics exposure in El Paso, Texas: A pilot study, *Aerosol and Air Quality Research*, 12(2), 169-189, [http://aaqr.org/VOL12\\_No2\\_April2012/3\\_AAQR-11-10-OA-0169\\_169-179.pdf](http://aaqr.org/VOL12_No2_April2012/3_AAQR-11-10-OA-0169_169-179.pdf).

Chen, L.-W. A., Chow, J. C., Watson, J. G., and Schichtel, B. A. (2012), Consistency of long-term elemental carbon trends from thermal and optical measurements in the IMPROVE network, *Atmospheric Measurement Techniques*, 5, 2329-2338, <http://www.atmos-meas-tech.net/5/2329/2012/amt-5-2329-2012.pdf>.

Chen, L.-W. A., Malamakal, T., Wang, X. L., Green, M. C., Chow, J. C., and Watson, J. G. (2014), Evaluation of prescribed burning emissions and impacts on air quality in the Lake Tahoe basin, Desert Research Institute, Reno, NV, [http://www.fs.fed.us/psw/partnerships/tahoescience/documents/p076\\_Prescribed Burning Report 20141231.pdf](http://www.fs.fed.us/psw/partnerships/tahoescience/documents/p076_Prescribed Burning Report 20141231.pdf).

Chen, L.-W. A., Chow, J. C., Wang, X. L., Robles, J. A., Sumlin, B. J., Lowenthal, D. H., Zimmermann, R., and Watson, J. G. (2015), Multi-wavelength optical measurement to enhance thermal/optical analysis for carbonaceous aerosol, *Atmospheric Measurement Techniques*, 8, 451-461, <http://www.atmos-meas-tech.net/8/451/2015/amt-8-451-2015.html>.

Chen, L.-W. A., Chow, J. C., Wang, X. L., Cao, J. J., Mao, J. Q., and Watson, J. G. (2021), Brownness of organic aerosol over the United States: Evidence for seasonal biomass burning and

photobleaching effects, *Environmental Science & Technology*, 55(13), 8561-8572, doi:10.1021/acs.est.0c08706.

Chen, X., Day, D., Schichtel, B., Malm, W., Matzoll, A. K., Mojica, J., McDade, C. E., Hardison, E. D., Hardison, D. L., Walters, S., De Water, M. V., and Collett, J. L. (2014), Seasonal ambient ammonia and ammonium concentrations in a pilot IMPROVE NH<sub>x</sub> monitoring network in the western United States, *Atmospheric Environment*, 91, 118-126.

Chen, X. C., Zhang, Z. S., Engling, G., Zhang, R. J., Tao, J., Lin, M., Sang, X. F., Chan, C. Y., Li, S. Y., and Li, Y. P. (2014), Characterization of fine particulate black carbon in Guangzhou, a megacity of South China, *Atmospheric Pollution Research*, 5(3), 361-370.

Chen, Y. J., Tian, C. G., Feng, Y. L., Zhi, G. R., Li, J., and Zhang, G. (2015), Measurements of emission factors of PM2.5, OC, EC, and BC for household stoves of coal combustion in China, *Atmospheric Environment*, 109, 190-196.

Chen, Y., Dombek, T., Hand, J., Zhang, Z., Gold, A., Ault, A. P., Levine, K. E., and Surratt, J. D. (2021), Seasonal Contribution of Isoprene-Derived Organosulfates to Total Water-Soluble Fine Particulate Organic Sulfur in the United States, *ACS Earth and Space Chemistry*, 5(9), 2419-2432, doi:10.1021/acsearthspacechem.1c00102.

Cheng, Y., He, K. B., Duan, F. K., Zheng, M., Ma, Y. L., Tan, J. H., and Du, Z. Y. (2010), Improved measurement of carbonaceous aerosol: evaluation of the sampling artifacts and inter-comparison of the thermal-optical analysis methods, *Atmospheric Chemistry and Physics*, 10(17), 8533-8548.

Cheng, Y., Duan, F. K., He, K. B., Zheng, M., Du, Z. Y., Ma, Y. L., and Tan, J. H. (2011), Intercomparison of thermal-optical methods for the determination of organic and elemental carbon: Influences of aerosol composition and implications, *Environmental Science & Technology*, 45(23), 10117-10123.

Cheng, Y. A., He, K. B., Duan, F. K., Zheng, M., Du, Z. Y., Ma, Y. L., and Tan, J. H. (2011), Ambient organic carbon to elemental carbon ratios: Influences of the measurement methods and implications, *Atmospheric Environment*, 45(12), 2060-2066.

Cheng, Y. A., Zhen, M., He, K. B., Chen, Y. J., Yan, B., Russell, A. G., Shi, W. Y., Jiao, Z., Sheng, G. Y., Fu, J. M., and Edgerton, E. S. (2011), Comparison of two thermal-optical methods for the determination of organic carbon and elemental carbon: Results from the southeastern United States, *Atmospheric Environment*, 45(11), 1913-1918.

Cheng, Y., Duan, F. K., He, K. B., Du, Z. Y., Zheng, M., and Ma, Y. L. (2012), Intercomparison of thermal-optical method with different temperature protocols: Implications from source samples and solvent extraction, *Atmospheric Environment*, 61, 453-462.

Cheng, S. Y., Lang, J. L., Zhou, Y., Han, L. H., Wang, G., and Chen, D. S. (2013), A new monitoring-simulation-source apportionment approach for investigating the vehicular emission contribution to the PM2.5 pollution in Beijing, China, *Atmospheric Environment*, 79, 308-316.

Cheng, Y., He, K. B., Duan, F. K., Du, Z. Y., Zheng, M., and Ma, Y. L. (2014), Ambient organic carbon to elemental carbon ratios: Influence of the thermal-optical temperature protocol and implications, *Science of the Total Environment*, 468, 1103-1111.

Cheng, Y., Lee, S. C., Gu, Z. L., Ho, K. F., Zhang, Y. W., Huang, Y., Chow, J. C., Watson, J. G., Cao, J. J., and Zhang, R. J. (2015), PM<sub>2.5</sub> and PM<sub>10-2.5</sub> chemical composition and source apportionment near a Hong Kong roadway, *Particuology*, 18, 96-104, [https://www.researchgate.net/publication/259523926\\_PM2.5\\_and\\_PM10-2.5\\_chemical\\_composition\\_and\\_source\\_apportionment\\_near\\_a\\_Hong\\_Kong\\_roadway](https://www.researchgate.net/publication/259523926_PM2.5_and_PM10-2.5_chemical_composition_and_source_apportionment_near_a_Hong_Kong_roadway).

Cheng, Y., Chow, J. C., Watson, J. G., Zhou, J. M., Liu, S. X., and Cao, J. J. (2021), Decreasing concentrations of carbonaceous aerosols in China from 2003 to 2013 *Scientific Reports*, 11, 5352, doi:10.1038/s41598-021-84429-w.

Cheng, Z., Wang, S. X., Fu, X., Watson, J. G., Jiang, J. K., Fu, Q. Y., Chen, C. H., Xu, B. Y., Yu, J. S., Chow, J. C., and Hao, J. M. (2014), Impact of biomass burning on haze pollution in the Yangtze River Delta, China: A case study of summer in 2011, *Atmospheric Chemistry and Physics*, 14, 4573-4585, <http://www.atmos-chem-phys.net/14/4573/2014/acp-14-4573-2014.html>.

Chow, J. C., Wang, X. L., Kohl, S. D., Gronstal, S. B., and Watson, J. G. (2010), Heavy-duty diesel emissions in the Athabasca Oil Sands Region, in *Proceedings, 103rd Annual Meeting of the Air & Waste Management Association*, edited by R. J. Tropp and A. H. Legge, pp. 1-5, Air & Waste Management Association, Pittsburgh, PA.

Chow, J. C., Watson, J. G., Chen, L.-W. A., Rice, J., and Frank, N. H. (2010), Quantification of PM<sub>2.5</sub> organic carbon sampling artifacts in US networks, *Atmospheric Chemistry and Physics*, 10(12), 5223-5239, <http://www.atmos-chem-phys.net/10/5223/2010/acp-10-5223-2010.pdf>.

Chow, J. C., Watson, J. G., Green, M. C., and Frank, N. H. (2010), Filter light attenuation as a surrogate for elemental carbon, *Journal of the Air & Waste Management Association*, 60(11), 1365-1375, <http://www.tandfonline.com/doi/pdf/10.3155/1047-3289.60.11.1365>.

Chow, J. C., Watson, J. G., Lowenthal, D. H., Chen, L.-W. A., and Motallebi, N. (2010), Black and organic carbon emission inventories: Review and application to California, *Journal of the Air & Waste Management Association*, 60(4), 497-507, <http://www.tandfonline.com/doi/pdf/10.3155/1047-3289.60.4.497>.

Chow, J. C., Watson, J. G., Robles, J., Wang, X. L., Chen, L.-W. A., Trimble, D. L., Kohl, S. D., Tropp, R. J., and Fung, K. K. (2011), Quality assurance and quality control for thermal/optical analysis of aerosol samples for organic and elemental carbon, *Analytical and Bioanalytical Chemistry*, 401(10), 3141-3152, doi:10.1007/s00216-011-5103-3.

Chow, J. C., Watson, J. G., Chen, L.-W. A., Lowenthal, D. H., and Motallebi, N. (2011), PM<sub>2.5</sub> source profiles for black and organic carbon emission inventories, *Atmospheric Environment*, 45(31), 5407-5414, [https://www.researchgate.net/publication/232410705\\_PM25\\_source\\_profiles\\_for\\_black\\_and\\_organic\\_carbon\\_emission\\_inventories](https://www.researchgate.net/publication/232410705_PM25_source_profiles_for_black_and_organic_carbon_emission_inventories).

Chow, J. C., Lowenthal, D. H., Watson, J. G., and Chen, L.-W. A. (2013), Source apportionment of SEARCH PM<sub>2.5</sub> measurements with organic markers, Desert Research Institute, Reno, NV.

Chow, J. C., and Watson, J. G. (2013), Chemical analyses of particle filter deposits, in *Aerosols Handbook : Measurement, Dosimetry, and Health Effects*, edited by L. Ruzer and N. H. Harley, pp. 179-204, CRC Press/Taylor & Francis, New York, NY,

<https://www.researchgate.net/publication/235341535> Chemical Analyses of Particle Filter Deposits.

Chow, J. C., Lowenthal, D. H., Chen, L.-W. A., Wang, X. L., and Watson, J. G. (2015), Mass reconstruction methods for PM<sub>2.5</sub>: A review, *Air Quality, Atmosphere, and Health*, 8, 243-263, <http://link.springer.com/article/10.1007%2Fs11869-015-0338-3#page-1>.

Chow, J. C., Wang, X. L., Sumlin, B. J., Gronstal, S. B., Chen, L.-W. A., Trimble, D. L., Kohl, S. D., Mayorga, S. R., Riggio, G. M., Hurbain, P. R., Johnson, M., Zimmermann, R., and Watson, J. G. (2015), Optical calibration and equivalence of a multiwavelength thermal/optical carbon analyzer, *Aerosol and Air Quality Research*, 15(4), 1145-1159, doi:10.4209/aaqr.2015.02.0106.

Chow, J. C., Yang, X. F., Wang, X. L., Kohl, S. D., and Watson, J. G. (2015), Characterization of ambient PM<sub>10</sub> bioaerosols in a California agricultural town, *Aerosol and Air Quality Research*, 15(4), 1433-1447, <http://www.aaqr.org/article/detail/AAQR-14-12-OA-0313>.

Chow, J. C., Watson, J. G., Green, M. C., Wang, X. L., Chen, L.-W. A., Trimble, D. L., Cropper, P. M., Kohl, S. D., and Gronstal, S. B. (2018), Separation of brown carbon from black carbon for IMPROVE and CSN PM<sub>2.5</sub> samples, *Journal of the Air & Waste Management Association*, 68(5), 494-510.

Chow, J. C., Chen, L.-W. A., Wang, X. L., Green, M. C., and Watson, J. G. (2021), Improved estimation of PM<sub>2.5</sub> brown carbon contributions to filter light attenuation, *Particuology*, 56, 1-9, doi:10.1016/j.partic.2021.01.001.

Christiansen, A. E., Carlton, A. G., and Henderson, B. H. (2020), Differences in fine particle chemical composition on clear and cloudy days, *Atmospheric Chemistry and Physics*, 20(19), 11607-11624, doi:10.5194/acp-20-11607-2020.

Christiansen, A. E., Carlton, A. G., and Porter, W. C. (2020), Changing nature of organic carbon over the United States, *Environmental Science and Technology*, 54(17), 10524-10532, doi:10.1021/acs.est.0c02225.

Chuang, M. T., Chang, S. C., Lin, N. H., Wang, J. L., Sheu, G. R., Chang, Y. J., and Lee, C. T. (2013), Aerosol chemical properties and related pollutants measured in Dongsha Island in the northern South China Sea during 7-SEAS/Dongsha Experiment, *Atmospheric Environment*, 78, 82-92.

Chuang, M. T., Lee, C. T., Chou, C. C. K., Lin, N. H., Sheu, G. R., Wang, J. L., Chang, S. C., Wang, S. H., Chi, K. H., Young, C. Y., Huang, H., Chen, H. W., Weng, G. H., Lai, S. Y., Hsu, S. P., Chang, Y. J., Chang, J. H., and Wu, X. C. (2014), Carbonaceous aerosols in the air masses transported from Indochina to Taiwan: Long-term observation at Mt. Lulin, *Atmospheric Environment*, 89, 507-516.

Collaud-Coen, M. C., Andrews, E., Asmi, A., Baltensperger, U., Bukowiecki, N., Day, D., Fiebig, M., Fjaeraa, A. M., Flentje, H., Hyvarinen, A., Jefferson, A., Jennings, S. G., Kouvarakis, G., Lihavainen, H., Myhre, C. L., Malm, W. C., Mihapopoulos, N., Molenar, J. V., O'Dowd, C., Ogren, J. A., Schichtel, B. A., Sheridan, P., Virkkula, A., Weingartner, E., Weller, R., and Laj, P. (2013), Aerosol decadal trends - Part 1: In-situ optical measurements at GAW and IMPROVE stations, *Atmospheric Chemistry and Physics*, 13(2), 869-894.

Creamean, J. M., Spackman, J. R., Davis, S. M., and White, A. B. (2014), Climatology of long-range transported Asian dust along the West Coast of the United States, *Journal of Geophysical Research-Atmospheres*, 119(21), 12171-12185.

Dabek-Zlotorzynska, E., Dann, T. F., Martinelango, P. K., Celo, V., Brook, J. R., Mathieu, D., Ding, L. Y., and Austin, C. C. (2011), Canadian National Air Pollution Surveillance (NAPS) PM2.5 speciation program: Methodology and PM2.5 chemical composition for the years 2003-2008, *Atmospheric Environment*, 45(3), 673-686.

Das, K. K., Bancroft, L., Wang, X. L., Chow, J. C., Xing, B. S., and Yang, Y. (2018), Digestion coupled with programmed thermal analysis for quantification of multiwall carbon nanotubes in plant tissues, *Environmental Science & Technology Letters*, 5(7), 442-447, doi:10.1021/acs.estlett.8b00287.

Debus, B., S. Takahama, A. T. Weakley, K. Seibert, and A. M. Dillner (2019), Long-Term Strategy for Assessing Carbonaceous Particulate Matter Concentrations from Multiple Fourier Transform Infrared (FT-IR) Instruments: Influence of Spectral Dissimilarities on Multivariate Calibration Performance, *Applied Spectroscopy*, 73(3), 271-283, doi:<https://opg.optica.org/as/abstract.cfm?URI=as-73-3-271>.

Deng, X. J., Wu, D., Yu, J. Z., Lau, A. K. H., Li, F., Tan, H. B., Yuan, Z. B., Ng, W. M., Deng, T., Wu, C., and Zhou, X. J. (2013), Characterization of secondary aerosol and its extinction effects on visibility over the Pearl River Delta Region, China, *Journal of the Air & Waste Management Association*, 63(9), 1012-1021, <http://www.tandfonline.com/doi/pdf/10.1080/10962247.2013.782927>.

Diab, J., Streibel, T., Cavalli, F., Lee.S.C., Saathoff, H., Mamakos, T., Chow, J. C., Chen, L.-W. A., Watson, J. G., Sippula, O., and Zimmermann, R. (2015), Hyphenation of a EC/OC thermal-optical carbon analyzer to photo ionization time-of-flight mass spectrometry: A new off-line aerosol mass spectrometric approach for characterization of primary and secondary particulate matter, *Atmospheric Measurement Techniques*, 8, 3337-3353, <http://www.atmos-meas-tech.net/8/3337/2015/amt-8-3337-2015.pdf>.

Diaz-Robles, L. A., Moncada-Herrera, J., Etcharren, P., Araneda, N., Perez, I., and Schiappacasse P., N. (2010), Source apportionment of PM2.5 in Temuco, Chile, using factor analysis and IMPROVE sampling. A seasonal analysis, in *Proceedings, Leapfrogging Opportunities for Air Quality Improvement*, edited by J. C. Chow, J. G. Watson and J. J. Cao, pp. 845-852, Air & Waste Management Association, Pittsburgh, PA.

Dillner, A. M., and Takahama, S. (2015), Predicting ambient aerosol thermal-optical reflectance (TOR) measurements from infrared spectra: Organic carbon, *Atmospheric Measurement Techniques*, 8(3), 1097-1109, <http://www.atmos-meas-tech.net/8/1097/2015/amt-8-1097-2015.pdf>.

Draxler, R. R., Ginoux, P., and Stein, A. F. (2010), An empirically derived emission algorithm for wind-blown dust, *Journal of Geophysical Research-Atmospheres*, 115.

DRI (2012), SOP 2-216r3: DRI Model 2001 thermal/optical carbon analysis (TOR/TOT) of aerosol filter samples - Method IMPROVE\_A, Desert Research Institute, Reno, NV, [http://www.epa.gov/ttn/amtic/files/ambient/pm25/spec/DRI\\_SOPforIMPROVEAFINAL.pdf](http://www.epa.gov/ttn/amtic/files/ambient/pm25/spec/DRI_SOPforIMPROVEAFINAL.pdf).

Drury, E., Jacob, D. J., Spurr, R. J. D., Wang, J., Shinozuka, Y., Anderson, B. E., Clarke, A. D., Dibb, J., McNaughton, C., and Weber, R. (2010), Synthesis of satellite (MODIS), aircraft (ICARTT), and surface (IMPROVE, EPA-AQS, AERONET) aerosol observations over eastern North America to improve MODIS aerosol retrievals and constrain surface aerosol concentrations and sources, *Journal of Geophysical Research-Atmospheres*, 115.

Du, Y. Y., Chen, J., Zhang, J. L., Gan, G. C., Liu, Y. C., Su, M. X., Lou, S. R., Zhou, M., Tao, S. K., and Qiao, L. P. (2020), Observation of aerosol optical properties and new particle formation in the Yangtze River Delta, *Huanjing Kexue/Environmental Science*, 41(9), 3932-3940, doi:10.13227/j.hjkx.201911271.

Eklund, A. G., Chow, J. C., Greenbaum, D. S., Hidy, G. M., Kleinman, M. T., Watson, J. G., and Wyzga, R. E. (2014), Public health and components of particulate matter: The changing assessment of black carbon-Critical review discussion, *Journal of the Air & Waste Management Association*, 64(11), 1221-1231,  
<http://www.tandfonline.com/doi/pdf/10.1080/10962247.2014.913954>.

Farina, S. C., Adams, P. J., and Pandis, S. N. (2010), Modeling global secondary organic aerosol formation and processing with the volatility basis set: Implications for anthropogenic secondary organic aerosol, *Journal of Geophysical Research-Atmospheres*, 115.

Ford, B., and Heald, C. L. (2013), Aerosol loading in the Southeastern United States: reconciling surface and satellite observations, *Atmospheric Chemistry and Physics*, 13(18), 9269-9283.

Fujii, Y., Iriana, W., Oda, M., Puriwigati, A., Tohno, S., Lestari, P., Mizohata, A., and Huboyo, H. S. (2014), Characteristics of carbonaceous aerosols emitted from peatland fire in Riau, Sumatra, Indonesia, *Atmospheric Environment*, 87, 164-169, doi:10.1016/j.atmosenv.2014.01.037.

Fujii, Y., Mahmud, M., Oda, M., Tohno, S., Matsumoto, J., and Mizohata, A. (2016), A key indicator of transboundary particulate matter pollution derived from Indonesian peatland fires in Malaysia, *Aerosol and Air Quality Research*, 16(1), 69-78, doi:10.4209/aaqr.2015.04.0215.

Fujita, E. M., Campbell, D. E., Zielinska, B., Chow, J. C., Lindhjem, C. E., DenBleyker, A., Bishop, G. A., Schuchmann, B. G., Stedman, D. H., and Lawson, D. R. (2012), Comparison of the MOVES2010a, MOBILE6.2 and EMFAC2007 mobile source emissions models with on-road traffic tunnel and remote sensing measurements, *Journal of the Air & Waste Management Association*, 62(10), 1134-1149,

<http://www.tandfonline.com/doi/pdf/10.1080/10962247.2012.699016>.

Gan, C. M., Pleim, J., Mathur, R., Hogrefe, C., Long, C. N., Xing, J., Roselle, S., and Wei, C. (2014), Assessment of the effect of air pollution controls on trends in shortwave radiation over the United States from 1995 through 2010 from multiple observation networks, *Atmospheric Chemistry and Physics*, 14(3), 1701-1715.

Gan, T. H., Hanhela, P., Mazurek, W., and Gillett, R. (2010), Characteristics of submarine engine diesel particulates in the maritime environment, *Journal of Aerosol Science*, 41(1), 23-35.

Gantt, B., Beaver, M., Timin, B., and Lorang, P. (2018), Recommended metric for tracking visibility progress in the Regional Haze Rule, *Journal of the Air & Waste Management Association*, 68(5), 438-445, doi: 10.1080/10962247.2018.1424058.

- Gantt, B., McDonald, K., Henderson, B., and Mannhardt, E. (2020), Incorporation of remote PM<sub>2.5</sub> concentrations into the downscaler model for spatially fused air quality surfaces, *Atmosphere*, 11(1), doi:10.3390/ATMOS11010103.
- Gargava, P., Chow, J. C., Watson, J. G., and Lowenthal, D. H. (2014), Speciated PM<sub>10</sub> emission inventory for Delhi, India, *Aerosol and Air Quality Research*, 14(5), 1515-1526, [http://www.aaqr.org/files/article/720/18\\_AAQR-13-02-OA-0047\\_1515-1526.pdf](http://www.aaqr.org/files/article/720/18_AAQR-13-02-OA-0047_1515-1526.pdf).
- Gebhart, K. A., Schichtel, B. A., Malm, W. C., Barna, M. G., Rodriguez, M. A., and Collett, J. L., Jr. (2011), Back-trajectory-based source apportionment of airborne sulfur and nitrogen concentrations at Rocky Mountain National Park, Colorado, USA, *Atmospheric Environment*, 45(3), 621-633.
- Gebhart, K. A., Day, D. E., Prenni, A. J., Schichtel, B. A., Hand, J. L., and Evanowski-Cole, A. R. (2018), Visibility impacts at Class I areas near the Bakken oil and gas development, *Journal of the Air & Waste Management Association*, 68(5), 477-493, doi:10.1080/10962247.2018.1429334.
- Gebhart, K. A., Farber, R. J., Hand, J. L., Eatough, D. J., Schichtel, B. A., Vimont, J. C., Green, M. C., and Malm, W. C. (2021), Long-term trends in particulate sulfate at the Grand Canyon National Park, *Atmospheric Environment*, 253, 118339, <https://doi.org/10.1016/j.atmosenv.2021.118339>.
- Geiser, L. H., Jovan, S. E., Glavich, D. A., and Porter, M. K. (2010), Lichen-based critical loads for atmospheric nitrogen deposition in Western Oregon and Washington Forests, USA, *Environ. Poll.*, 158(7), 2412-2421.
- Gilardoni, S., Vignati, E., and Wilson, J. (2011), Using measurements for evaluation of black carbon modeling, *Atmospheric Chemistry and Physics*, 11(2), 439-455, <http://www.atmos-chem-phys.net/11/439/2011/acp-11-439-2011.pdf>.
- Ginzburg, H., Liu, X. B., Baker, M., Shreeve, R., Jayanty, R. K. M., Campbell, D., and Zielinska, B. (2015), Monitoring study of the near-road PM<sub>2.5</sub> concentrations in Maryland, *Journal of the Air & Waste Management Association*, 65(9), 1062-1071, doi:10.1080/10962247.2015.1056887.
- Gong, W. M., Stroud, C., and Zhang, L. M. (2011), Cloud processing of gases and aerosols in air quality modeling, *Atmosphere*, 2(4), 567-616, <http://www.mdpi.com/2073-4433/2/4/567>.
- Gonzalez, M. E., Garfield, J. G., Corral, A. F., Edwards, E. L., Zeider, K., and Sorooshian, A. (2021), Extreme aerosol events at Mesa Verde, Colorado: Implications for air quality management, *Atmosphere*, 12(9), doi:10.3390/atmos12091140.
- Gordon, T. D., Prenni, A. J., Renfro, J. R., McClure, E., Hicks, B., Onasch, T. B., Freedman, A., McMeeking, G. R., and Chen, P. (2018), Open-path, closed-path, and reconstructed aerosol extinction at a rural site, *Journal of the Air & Waste Management Association*, 68(8), 824-835, doi:10.1080/10962247.2018.1452801.
- Gorham, K. A., Raffuse, S. M., Hyslop, N. P., and White, W. H. (2021), Comparison of recent speciated PM<sub>2.5</sub> data from collocated CSN and IMPROVE measurements, *Atmospheric Environment*, 244, doi:10.1016/j.atmosenv.2020.117977.

Grabowsky, J., Streibel, T., Sklorz, M., Chow, J. C., Mamakos, A., and Zimmermann, R. (2011), Hyphenation of a carbon analyzer to photo-ionization mass spectrometry to unravel the organic composition of particulate matter on a molecular level, *Analytical and Bioanalytical Chemistry*, 401(10), 3153-3164.

Green, M. C., Chen, L.-W. A., DuBois, D. W., and Molenar, J. V. (2012), Fine particulate matter and visibility in the Lake Tahoe Basin: Chemical characterization, trends, and source apportionment, *Journal of the Air & Waste Management Association*, 62(8), 953-965.

Green, M. C., Chow, J. C., Chang, M.-C. O., Chen, L.-W. A., Kuhns, H. D., Etyemezian, V. R., and Watson, J. G. (2013), Source apportionment of atmospheric particulate carbon in Las Vegas, Nevada, USA, *Particuology*, 11, 110-118,

doi:<https://www.researchgate.net/publication/235341593> Source apportionment of atmospheric particulate carbon in Las Vegas Nevada USA.

Green, M. C., Chow, J. C., Watson, J. G., Dick, K., and Inouye, D. (2015), Effects of snow cover and atmospheric stability on winter PM<sub>2.5</sub> concentrations in western US valleys, *Journal of Applied Meteorology and Climatology*, 54, 1191-1201, doi:dx.doi.org/10.1175/JAMC-D-14-0191.1.

Gu, J. X., Bai, Z. P., Liu, A. X., Wu, L. P., Xie, Y. Y., Li, W. F., Dong, H. Y., and Zhang, X. (2010), Characterization of atmospheric organic carbon and element carbon of PM<sub>2.5</sub> and PM<sub>10</sub> at Tianjin, China, *Aerosol and Air Quality Research*, 10(2), 167-176.

Gu, J. X., Bai, Z. P., Li, W. F., Wu, L. P., Liu, A. X., Dong, H. Y., and Xie, Y. Y. (2011), Chemical composition of PM<sub>2.5</sub> during winter in Tianjin, China, *Particuology*, 9(3), 215-221.

Gu, J. X., Du, S. Y., Han, D. W., Hou, L. J., Yi, J., Xu, J., Liu, G. H., Han, B., Yang, G. W., and Bai, Z. P. (2014), Major chemical compositions, possible sources, and mass closure analysis of PM<sub>2.5</sub> in Jinan, China, *Air Quality, Atmosphere & Health*, 7(3), 251-262.

Guerrette, J. J., and Henze, D. K. (2017), Four-dimensional variational inversion of black carbon emissions during ARCTAS-CARB with WRFDA-Chem, *Atmospheric Chemistry and Physics*, 17(12), 7605-7633, doi:10.5194/acp-17-7605-2017.

Guo, L., Cui, Y., He, Q., Gao, W., Pei, K., Zhu, L., Li, H., and Wang, X. (2021), Contributions of aerosol chemical composition and sources to light extinction during haze and non-haze days in Taiyuan, China, *Atmospheric Pollution Research*, 12(8), doi:10.1016/j.apr.2021.101140.

Gutknecht, W., Flanagan, J., McWilliams, A., Jayanty, R. K. M., Kellogg, R., Rice, J., Duda, P., and Sarver, R. H. (2010), Harmonization of uncertainties of x-ray fluorescence data for PM<sub>2.5</sub> air filter analysis, *Journal of the Air & Waste Management Association*, 60(2), 184-194.

Hadley, O. L. (2017), Background PM<sub>2.5</sub> source apportionment in the remote Northwestern United States, *Atmospheric Environment*, 167, 298-308, doi:10.1016/j.atmosenv.2017.08.030.

Hallar, A. G., Lowenthal, D. H., Clegg, S. L., Samburova, V., Taylor, N., Mazzoleni, L. R., Zielinska, B. K., Kristensen, T. B., Chirokova, G., McCubbin, I. B., Dodson, C., and Collins, D. (2013), Chemical and hygroscopic properties of aerosol organics at Storm Peak Laboratory, *Journal of Geophysical Research-Atmospheres*, 118(10), 4767-4779.

Hallar, A. G., Molotch, N. P., Hand, J. L., Livneh, B., McCubbin, I. B., Petersen, R., Michalsky, J., Lowenthal, D., and Kunkel, K. E. (2017), Impacts of increasing aridity and wildfires on

aerosol loading in the intermountain Western US, *Environmental Research Letters*, 12, doi:10.1088/1748-9326/aa510a.

Han, Y. M., Cao, J. J., Lee, S. C., Ho, K. F., and An, Z. S. (2010), Different characteristics of char and soot in the atmosphere and their ratio as an indicator for source identification in Xi'an, China, *Atmospheric Chemistry and Physics*, 10(2), 595-607.

Han, Y. M., Cao, J. J., Yan, B. Z., Kenna, T. C., Jin, Z. D., Cheng, Y., Chow, J. C., and An, Z. S. (2011), Comparison of elemental carbon in lake sediments measured by three different methods and 150-year pollution history in eastern China, *Environmental Science & Technology*, 45(12), 5287-5293.

Han, Y. M., Marlon, J. R., Cao, J. J., Jin, Z. D., and An, Z. S. (2012), Holocene linkages between char, soot, biomass burning and climate from Lake Daihai, China, *Global Biogeochemical Cycles*, 26.

Han, Y., Chen, A., Cao, J., Fung, K., Ho, F., Yan, B., Zhan, C., Liu, S., Wei, C., and An, Z. (2013), Thermal/optical methods for elemental carbon quantification in soils and urban dusts: Equivalence of different analysis protocols, *PLoS ONE*, 8(12), doi:10.1371/journal.pone.0083462.

Han, Y. M., Chen, L.-W. A., Cao, J. J., Fung, K. K., Ho, K. F., Yan, B. Z., Zhan, C. L., Liu, S. X., Wei, and An, Z. H. (2013), Thermal/optical methods for elemental carbon quantification in soils and urban dusts: Equivalence of different analysis protocols, *Plos One*, 8(12), e83462.

Han, Y. M., Bandowe, B. A. M., Wei, C., Cao, J. J., Wilcke, W., Wang, G. H., Ni, H. Y., Jin, Z. D., An, Z. S., and Yan, B. Z. (2015), Stronger association of polycyclic aromatic hydrocarbons with soot than with char in soils and sediments, *Chemosphere*, 119, 1335-1345.

Han, Y. M., Chen, L.-W. A., Huang, R. J., Chow, J. C., Watson, J. G., Ni, H. Y., Liu, S. X., Fung, K. K., Shen, Z. X., Wei, C., Wang, Q. Y., Tian, J., Zhao, Z. Z., Prevot, A. S. H., and Cao, J. J. (2016), Carbonaceous aerosols in megacity Xi'an, China: Implications of thermal/optical protocols comparison, *Atmospheric Environment*, 132, 58-68.

Hand, J. L., Copeland, S. A., McDade, C. E., Day, D. E., Moore, J., C.T., Dillner, A. M., Pitchford, M. L., Indresand, H., Schichtel, B. A., Malm, W. C., and Watson, J. G. (2011), Spatial and seasonal patterns and temporal variability of haze and its constituents in the United States, IMPROVE Report V, Cooperative Institute for Research in the Atmosphere, Fort Collins, CO, <http://vista.cira.colostate.edu/Improve/spatial-and-seasonal-patterns-and-temporal-variability-of-haze-and-its-constituents-in-the-united-states-report-v-june-2011/>.

Hand, J. L., Gebhart, K. A., Schichtel, B. A., and Malm, W. C. (2012), Increasing trends in wintertime particulate sulfate and nitrate ion concentrations in the Great Plains of the United States (2000-2010), *Atmospheric Environment*, 55, 107-110.

Hand, J. L., Schichtel, B. A., Malm, W. C., and Pitchford, M. L. (2012), Particulate sulfate ion concentration and SO<sub>2</sub> emission trends in the United States from the early 1990s through 2010, *Atmospheric Chemistry and Physics*, 12(21), 10353-10365.

Hand, J. L., Schichtel, B. A., Pitchford, M. L., Malm, W. C., and Frank, N. H. (2012), Seasonal composition of remote and urban fine particulate matter in the United States, *Journal of Geophysical Research-Atmospheres*, 117.

- Hand, J. L., Schichtel, B. A., Malm, W. C., and Frank, N. H. (2013), Spatial and temporal trends in PM<sub>2.5</sub> organic and elemental carbon across the United States, *Advances in Meteorology*, 2013, 1-13, doi:10.1155/2013/367674.
- Hand, J. L., Schichtel, B. A., Malm, W. C., Pitchford, M. L., and Frank, N. H. (2014), Spatial and seasonal patterns in urban influence on regional concentrations of speciated aerosols across the United States, *Journal of Geophysical Research-Atmospheres*, 119(22), 12832-12849.
- Hand, J. L., Schichtel, B. A., Malm, W. C., Copeland, S., Molnar, J. V., Frank, N. H., and Pitchford, M. L. (2014), Widespread reductions in haze across the United States from the early 1990s through 2011, *Atmospheric Environment*, 94, 671-679.
- Hand, J. L., White, W. H., Gebhart, K. A., Hyslop, N. P., Gill, T. E., and Schichtel, B. A. (2016), Earlier onset of the spring fine dust season in the southwestern United States, *Geophysical Research Letters*, 43(8), 4001-4009, doi:10.1002/2016gl068519.
- Hand, J. L., Gill, T. E., and Schichtel, B. A. (2017), Spatial and seasonal variability in fine mineral dust and coarse aerosol mass at remote sites across the United States, *Journal of Geophysical Research-Atmospheres*, 122(5), 3080-3097, doi:10.1002/2016jd026290.
- Hand, J. L., Gill, T. E., and Schichtel, B. A. (2019), Urban and rural coarse aerosol mass across the United States: Spatial and seasonal variability and long-term trends, *Atmospheric Environment*, 218, doi:10.1016/j.atmosenv.2019.117025.
- Hand, J. L., Prenni, A. J., Schichtel, B. A., Malm, W. C., and Chow, J. C. (2019), Trends in remote PM<sub>2.5</sub> residual mass across the United States: Implications for aerosol mass reconstruction in the IMPROVE network, *Atmospheric Environment*, 203, 141-152, doi:10.1016/j.atmosenv.2019.01.049.
- Hand, J. L., Prenni, A. J., Copeland, S., Schichtel, B. A., and Malm, W. C. (2020), Thirty years of the Clean Air Act Amendments: Impacts on haze in remote regions of the United States (1990-2018), *Atmospheric Environment*, 243, doi:10.1016/j.atmosenv.2020.117865.
- Heald, C. L., Collett, J. L., Lee, T., Benedict, K. B., Schwandner, F. M., Li, Y., Clarisse, L., Hurtmans, D. R., Van Damme, M., Clerbaux, C., Coheur, P. F., Philip, S., Martin, R. V., and Pye, H. O. T. (2012), Atmospheric ammonia and particulate inorganic nitrogen over the United States, *Atmospheric Chemistry and Physics*, 12(21), 10295-10312.
- Ho, K. F., Zhang, R. J., Lee, S. C., Ho, S. S. H., Liu, S. X., Fung, K., Cao, J. J., Shen, Z. X., and Xu, H. M. (2011), Characteristics of carbonate carbon in PM<sub>2.5</sub> in a typical semi-arid area of Northeastern China, *Atmospheric Environment*, 45(6), 1268-1274.
- Ho, S. S. H., Ho, K. F., Liu, S. X., Liu, W. D., Lee, S. C., Fung, K. K., Cao, J. J., Zhang, R. J., Huang, Y., Feng, N. S. Y., and Cheng, Y. (2012), Quantification of carbonate carbon in aerosol filter samples using a modified thermal/optical carbon analyzer (M-TOCA), *Analytical Methods*, 4(8), 2578-2584.
- Holden, A. S., Sullivan, A. P., Munchak, L. A., Kreidenweis, S. M., Schichtel, B. A., Malm, W. C., and Collett, J. L., Jr. (2011), Determining contributions of biomass burning and other sources to fine particle contemporary carbon in the western United States, *Atmospheric Environment*, 45(11), 1986-1993.

- Hu, Y., Balachandran, S., Pachon, J. E., Baek, J., Ivey, C., Holmes, H., Odman, M. T., Mulholland, J. A., and Russell, A. G. (2014), Fine particulate matter source apportionment using a hybrid chemical transport and receptor model approach, *Atmospheric Chemistry and Physics*, 14(11), 5415-5431, doi:<http://www.atmos-chem-phys.net/14/5415/2014/>.
- Hua, Y., Cheng, Z., Wang, S. X., Jiang, J. K., Chen, D. R., Cai, S. Y., Fu, X., Fu, Q. Y., Chen, C. H., Xu, B. Y., and Yu, J. Q. (2015), Characteristics and source apportionment of PM<sub>2.5</sub> during a fall heavy haze episode in the Yangtze River Delta of China, *Atmospheric Environment*, 123, 380-391, doi:10.1016/j.atmosenv.2015.03.046.
- Huang, H., Zou, C. W., Cao, J. J., and Tsang, P. (2011), Carbonaceous aerosol characteristics in outdoor and indoor environments of Nanchang, China, during summer 2009, *Journal of the Air & Waste Management Association*, 61(11), 1262-1272.
- Huang, M., Tong, D., Lee, P., Pan, L., Tang, Y., Stajner, I., Pierce, R. B., McQueen, J., and Wang, J. (2015), Toward enhanced capability for detecting and predicting dust events in the western United States: the Arizona case study, *Atmospheric Chemistry and Physics*, 15(21), 12595-12610, doi:10.5194/acp-15-12595-2015.
- Hyslop, N. P., and White, W. H. (2011), Identifying sources of uncertainty from the inter-species covariance of measurement errors, *Environmental Science & Technology*, 45(9), 4030-4037.
- Hyslop, N. P., Trzepla, K., and White, W. H. (2012), Reanalysis of archived IMPROVE PM<sub>2.5</sub> samples previously analyzed over a 15-year period, *Environmental Science & Technology*, 46(18), 10106-10113.
- Hyslop, N. K., Trzepla, C., Wallis, A., Matzoll, and W. White (2013), A 23-year record of twice-weekly aerosol composition measurements at Mauna Loa Observatory, *Atmospheric Environment*, 80, 259-263, doi:<http://dx.doi.org/10.1016/j.atmosenv.2013.07.038>.
- Hyslop, N. P., Trzepla, K., and White, W. H. (2015), Assessing the suitability of historical PM<sub>2.5</sub> element measurements for trend analysis, *Environmental Science & Technology*, 49(15), 9247-9255, doi:10.1021/acs.est.5b01572.
- Hyslop, N. P., et al. (2019), An inter-laboratory evaluation of new multi-element reference materials for atmospheric particulate matter measurements, *Aerosol Science and Technology*, 53(7), 771-782, doi:10.1080/02786826.2019.1606413.
- Hyslop, N. P., Y. Liu, S. Yatkin, and K. Trzepla (2022), Application of the U.S. EPA procedure for determining method detection limits to EDXRF measurement of filter-based aerosol samples, *Journal of the Air & Waste Management Association*, 72(8), 905-913, doi:10.1080/10962247.2022.2064005.
- Indresand, H., and Dillner, A. M. (2012), Experimental characterization of sulfur interference in IMPROVE aluminum and silicon XRF data, *Atmospheric Environment*, 61, 140-147.
- Indresand, H., White, W. H., Trzepla, K., and Dillner, A. M. (2013), Preparation of sulfur reference materials that reproduce atmospheric particulate matter sample characteristics for XRF calibration, *X-Ray Spectrometry*, 42(5), 359-367.
- Jain, S., Sharma, S. K., Choudhary, N., Masiwal, R., Saxena, M., Sharma, A., Mandal, T. K., Gupta, A., Gupta, N. C., and Sharma, C. (2017), Chemical characteristics and source apportionment of PM<sub>2.5</sub> using PCA/APCS, UNMIX, and PMF at an urban site of Delhi, India,

*Environmental Science and Pollution Research*, 24(17), 14637-14656, doi:10.1007/s11356-017-8925-5.

Jathar, S. H., Farina, S. C., Robinson, A. L., and Adams, P. J. (2011), The influence of semi-volatile and reactive primary emissions on the abundance and properties of global organic aerosol, *Atmospheric Chemistry and Physics*, 11(15), 7727-7746, <http://www.atmos-chem-phys.net/11/7727/2011/acp-11-7727-2011.pdf>.

Jeong, C. H., Herod, D., Dabek-Zlotorzynska, E., Ding, L. Y., McGuire, M. L., and Evans, G. (2013), Identification of the sources and geographic origins of black carbon using factor analysis at paired rural and urban sites, *Environmental Science & Technology*, 47(15), 8462-8470.

Jeronimo, M., Q. Stewart, A. T. Weakley, J. Giacomo, X. Zhang, N. Hyslop, A. M. Dillner, M. Shupler, and M. Brauer (2020), Analysis of black carbon on filters by image-based reflectance, *Atmospheric Environment*, 223, 117300, doi:<https://doi.org/10.1016/j.atmosenv.2020.117300>.

Jiang, L., Zhang, Z. F., Zhu, B., Shen, Y., Wang, H. L., Shi, S. S., and Sha, D. D. (2018), Comparison of parameterizations for the atmospheric extinction coefficient in Lin'an, China, *Science of the Total Environment*, 621, 507-515, doi:10.1016/j.scitotenv.2017.11.182.

Jo, D. S., Park, R. J., Kim, M. J., and Spracklen, D. V. (2013), Effects of chemical aging on global secondary organic aerosol using the volatility basis set approach, *Atmospheric Environment*, 81, 230-244.

June, N. A., Wang, X., Chen, L.-W. A., Chow, J. C., Watson, J. G., Wang, X. L., Henderson, B. H., Zheng, Y. Q., and Mao, J. Q. (2020), Spatial and temporal variability of brown carbon in the United States: Implications for direct radiative effects, *Geophysical Research Letters*, 47(23), doi:10.1029/2020GL090332.

Kamboures, M. A., Hu, S. S., Yu, Y., Sandoval, J., Rieger, P., Huang, S. M., Zhang, S., Dzhema, I., Huo, D., Ayala, A., and Chang, M.-C. O. (2013), Black carbon emissions in gasoline vehicle exhaust: A measurement and instrument comparison, *Journal of the Air & Waste Management Association*, 63(8), 886-901.

Kamruzzaman, M., Takahama, S., and Dillner, A. M. (2018), Quantification of amine functional groups and their influence on OM/OC in the IMPROVE network, *Atmospheric Environment*, 172, 124-132, doi:10.1016/j.atmosenv.2017.10.053.

Kavouras, I. G., Nikolich, G., Etyemezian, V. R., DuBois, D. W., King, J., and Shafer, D. (2012), In situ observations of soil minerals and organic matter in the early phases of prescribed fires, *Journal of Geophysical Research-Atmospheres*, 117.

Khan, B., Hays, M. D., Geron, C., and Jetter, J. (2012), Differences in the OC/EC ratios that characterize ambient and source aerosols due to thermal-optical analysis, *Aerosol Science and Technology*, 46(2), 127-137, <http://www.tandfonline.com/doi/pdf/10.1080/02786826.2011.609194>.

Kim, K. H., Sekiguchi, K., Furuuchi, M., and Sakamoto, K. (2011), Seasonal variation of carbonaceous and ionic components in ultrafine and fine particles in an urban area of Japan, *Atmospheric Environment*, 45(8), 1581-1590.

Kim, K. H., Sekiguchi, K., Kudo, S., Kinoshita, M., and Sakamoto, K. (2013), Carbonaceous and ionic components in ultrafine and fine particles at four sampling sites in the vicinity of roadway intersection, *Atmospheric Environment*, 74, 83-92.

Kim, P. S., Jacob, D. J., Fisher, J. A., Travis, K., Yu, K., Zhu, L., Yantosca, R. M., Sulprizio, M. P., Jimenez, J. L., Campuzano-Jost, P., Froyd, K. D., Liao, J., Hair, J. W., Fenn, M. A., Butler, C. F., Wagner, N. L., Gordon, T. D., Welti, A., Wennberg, P. O., Crounse, J. D., St Clair, J. M., Teng, A. P., Millet, D. B., Schwarz, J. P., Markovic, M. Z., and Perring, A. E. (2015), N Sources, seasonality, and trends of southeast US aerosol: an integrated analysis of surface, aircraft, and satellite observations with the GEOS-Chem chemical transport model, *Atmospheric Chemistry and Physics*, 15(18), 10411-10433, doi:10.5194/acp-15-10411-2015.

Kim, S. Y., Sheppard, L., Larson, T. V., Kaufman, J. D., and Vedral, S. (2015), Combining PM2.5 component data from multiple sources: Data consistency and characteristics relevant to epidemiological analyses of predicted long-term exposures, *Environmental Health Perspectives*, 123(7), 651-658, doi:10.1289/ehp.1307744.

Kim, S. Y., Olives, C., Sheppard, L., Sampson, P. D., Larson, T. V., Keller, J. P., and Kaufman, J. D. (2017), Historical prediction modeling approach for estimating long-term concentrations of PM2.5 in cohort studies before the 1999 implementation of widespread monitoring, *Environmental Health Perspectives*, 125(1), 38-46, doi:10.1289/ehp131.

Knue, J. (2016), Comparison of Four Thermal/Optical Carbon Analysis Protocols by Chemical Standards, B.S. Senior Thesis in Biochemistry and Molecular Biology, University of Nevada, Reno.

Kong, S. F., Ji, Y. Q., Lu, B., Chen, L., Han, B., Li, Z. Y., and Bai, Z. P. (2011), Characterization of PM(10) source profiles for fugitive dust in Fushun-a city famous for coal, *Atmospheric Environment*, 45(30), 5351-5365.

Kong, S. F., Ji, Y. Q., Lu, B., Bai, Z. P., Chen, L., Han, B., and Li, Z. Y. (2012), Chemical compositions and sources of atmospheric PM10 in heating, non-heating and sand periods at a coal-based city in northeastern china, *Journal of Environmental Monitoring*, 14(3), 852-865.

Kotchenruther, R. A. (2013), A regional assessment of marine vessel PM2.5 impacts in the U.S. Pacific Northwest using a receptor-based source apportionment method, *Atmospheric Environment*, 68, 103-111.

Kotchenruther, R. A. (2015), The effects of marine vessel fuel sulfur regulations on ambient PM2.5 along the west coast of the US, *Atmospheric Environment*, 103, 121-128.

Kotchenruther, R. A. (2017), The effects of marine vessel fuel sulfur regulations on ambient PM2.5 at coastal and near coastal monitoring sites in the US, *Atmospheric Environment*, 151, 52-61, doi:10.1016/j.atmosenv.2016.12.012.

Kumar, A., Singh, S., Kumar, N., Singh, N., Kumar, K., and Chourasiya, S. (2021), Assessment of carbonaceous fractions in ambient aerosols at high altitude and lowland urban locations of Kumaon Province, Indian Himalaya, *Sn Applied Sciences*, 3(1), doi:10.1007/s42452-020-04010-4.

Kumar, A., Singh, S., Kumar, N., Singh, N., Kumar, K., Mishra, A. K., Chourasiya, S., and Kushwaha, H. S. (2021), Seasonal abundance and source attribution of carbonaceous aerosols at

different altitude of mountainous locations in Uttarakhand Himalaya, *Aerosol Science and Engineering*, 5(2), 233-246, doi:10.1007/s41810-021-00098-2.

Kuzmiakova, A., Dillner, A. M., and Takahama, S. (2016), An automated baseline correction protocol for infrared spectra of atmospheric aerosols collected on polytetrafluoroethylene (Teflon) filters, *Atmospheric Measurement Techniques*, 9(6), 2615-2631, doi:10.5194/amt-9-2615-2016.

Lai, S. C., Ho, K. F., Zhang, Y. Y., Lee, S. C., Huang, Y., and Zou, S. C. (2010), Characteristics of residential indoor carbonaceous aerosols: A case study in Guangzhou, Pearl River Delta region, *Aerosol and Air Quality Research*, 10(5), 472-478.

Laidlaw, M. A. S., Zahran, S., Mielke, H. W., Taylor, M. P., and Filippelli, G. M. (2012), Re-suspension of lead contaminated urban soil as a dominant source of atmospheric lead in Birmingham, Chicago, Detroit and Pittsburgh, USA, *Atmospheric Environment*, 49, 302-310.

Lambert, A., Hallar, A. G., Garcia, M., Strong, C., Andrews, E., and Hand, J. L. (2020), Dust impacts of rapid agricultural expansion on the Great Plains, *Geophysical Research Letters*, 47(20), doi:10.1029/2020GL090347.

Lee, C. T., Ram, S. S., Nguyen, D. L., Chou, C. C. K., Chang, S. Y., Lin, N. H., Chang, S. C., Hsiao, T. C., Sheu, G. R., Ou-Yang, C. F., Chi, K. H., Wang, S. H., and Wu, X. C. (2016), Aerosol chemical profile of near-source biomass burning smoke in Sonla, Vietnam during 7-SEAS campaigns in 2012 and 2013, *Aerosol and Air Quality Research*, 16(11), 2603-2617, doi:10.4209/aaqr.2015.07.0465.

Levin, E. J. T., McMeeking, G. R., Carrico, C. M., Mack, L. E., Kreidenweis, S. M., Wold, C. E., Moosmüller, H., Arnott, W. P., Hao, W. M., Collett, J. L., Jr., and Malm, W. C. (2010), Biomass burning smoke aerosol properties measured during Fire Laboratory at Missoula Experiments (FLAME), *Journal of Geophysical Research-Atmospheres*, 115.

Li, B., Zhang, J., Zhao, Y., Yuan, S. Y., Zhao, Q. Y., Shen, G. F., and Wu, H. S. (2015), Seasonal variation of urban carbonaceous aerosols in a typical city Nanjing in Yangtze River Delta, China, *Atmospheric Environment*, 106, 223-231.

Li, N., Wei, X., Han, W. H., Sun, S. Y., and Wu, J. H. (2020), Characteristics and temporal variations of organic and elemental carbon aerosols in PM1 in Changchun, Northeast China, *Environmental Science and Pollution Research*, 27(8), 8653-8661, doi:10.1007/s11356-019-07494-9.

Li, S., Zhu, M., Yang, W. Q., Tang, M. J., Huang, X. L., Yu, Y. G., Fang, H., Yu, X., Yu, Q. Q., Fu, X. X., Song, W., Zhang, Y. L., Bi, X. H., and Wang, X. M. (2018), Filter-based measurement of light absorption by brown carbon in PM2.5 in a megacity in South China, *Science of the Total Environment*, 633, 1360-1369, doi:10.1016/j.scitotenv.2018.03.235.

Li, X., Xie, P., Li, A., Xu, J., Ren, H., Ren, B., Li, Y., and Li, J. (2021), Study of aerosol characteristics and sources using MAX-DOAS measurement during haze at an urban site in the Fenwei Plain, *Journal of Environmental Sciences (China)*, 107, 1-13, doi:10.1016/j.jes.2020.12.015.

Liao, H. T., Chou, C. C.-K., Chow, J. C., Watson, J. G., Hopke, P. K., and Wu, C. F. (2015), Source and risk apportionment of selected VOCs and PM<sub>2.5</sub> species using partially constrained receptor models with multiple time resolution data, *Environmental Pollution*, 205, 121-130.

Liao, W. J., Zhou, J. B., Zhu, S. J., Xiao, A. S., Li, K., and Schauer, J. J. (2020), Characterization of aerosol chemical composition and the reconstruction of light extinction coefficients during winter in Wuhan, China, *Chemosphere*, 241, doi:10.1016/j.chemosphere.2019.125033.

Lim, S., Lee, M., Lee, G., Kim, S., Yoon, S., and Kang, K. (2012), Ionic and carbonaceous compositions of PM10, PM2.5 and PM1.0 at Gosan ABC Superstation and their ratios as source signature, *Atmospheric Chemistry and Physics*, 12(4), 2007-2024.

Lin, G., Penner, J. E., Sillman, S., Taraborrelli, D., and Lelieveld, J. (2012), Global modeling of SOA formation from dicarbonyls, epoxides, organic nitrates and peroxides, *Atmospheric Chemistry and Physics*, 12(10), 4743-4774, <http://www.atmos-chem-phys.net/12/4743/2012/acp-12-4743-2012.pdf>.

Lin, Z. J., Tao, J., Chai, F. H., Fan, S. J., Yue, J. H., Zhu, L. H., Ho, K. F., and Zhang, R. J. (2013), Impact of relative humidity and particles number size distribution on aerosol light extinction in the urban area of Guangzhou, *Atmospheric Chemistry and Physics*, 13(3), 1115-1128.

Liu, C. N., Chiao, S., and Ryoo, J. M. (2019), Asian long-range transport in relation to atmospheric rivers in Northern California, *Atmosphere*, 10(6), doi:10.3390/atmos10060313.

Liu, Y., and Liu, Z. (2016), Source apportionment of ambient PM2.5 by using Unmix and PMF reception models at Flint Hills rural site and Kansas City urban site, in *Proceedings, 2016 ASABE Annual International Meeting*, edited, American Society of Agricultural and Biological Engineers, doi:10.13031/aim.20162447784.

Lowenthal, D. H., Watson, J. G., Koracin, D., Chen, L.-W. A., DuBois, D. W., Vellore, R., Kumar, N. K., Knipping, E. M., Wheeler, N., Craig, K., and Reid, S. (2010), Evaluation of regional scale receptor modeling, *Journal of the Air & Waste Management Association*, 60(1), 26-42, <http://www.tandfonline.com/doi/pdf/10.3155/1047-3289.60.1.26>.

Lowenthal, D. H., Zielinska, B., Samburova, V., Collins, D., Taylor, N. K., and Kumar, N. (2015), Evaluation of assumptions for estimating chemical light extinction at US national parks, *Journal of the Air & Waste Management Association*, 65(3), 249-260, <http://www.tandfonline.com/doi/pdf/10.1080/10962247.2014.986307?needAccess=true>.

Lowenthal, D. H., and Kumar, N. K. (2016), Evaluation of the IMPROVE Equation for estimating aerosol light extinction, *Journal of the Air & Waste Management Association*, 66(7), 726-737, doi:10.1080/10962247.2016.1178187.

Ma, Q. X., Wu, Y. F., Fu, S. L., Zhang, D. Z., Han, Z. W., and Zhang, R. J. (2020), Pollution severity-dependent aerosol light scattering enhanced by inorganic species formation in Beijing haze, *Science of the Total Environment*, 719, doi:10.1016/j.scitotenv.2020.137545.

MageeScientific (2021), DRI Model 2015, Magee Scientific Instruments, Berkeley, CA, <https://mageesci.com/mproducts/dri-model-2015/>.

Malamakal, T., Chen, L.-W. A., Wang, X. L., Green, M. C., Gronstal, S., Chow, J. C., and Watson, J. G. (2013), Prescribed burn smoke impact in the Lake Tahoe Basin: Model simulation and field verification, *International Journal of Environment and Pollution*, 52(3/4), 225-243, [https://www.researchgate.net/publication/260391315\\_Prescribed\\_burn\\_smoke\\_impact\\_in\\_the\\_Lake\\_Tahoe\\_Basin\\_Model\\_simulation\\_and\\_field\\_verification](https://www.researchgate.net/publication/260391315_Prescribed_burn_smoke_impact_in_the_Lake_Tahoe_Basin_Model_simulation_and_field_verification).

Malm, W. C., Schichtel, B. A., and Pitchford, M. L. (2011), Uncertainties in PM2.5 gravimetric and speciation measurements and what we can learn from them, *Journal of the Air & Waste Management Association*, 61(11), 1131-1149.

Malm, W. C., Schichtel, B. A., Hand, J. L., and Collett, J. L., Jr. (2017), Concurrent temporal and spatial trends in sulfate and organic mass concentrations measured in the IMPROVE monitoring program, *Journal of Geophysical Research: Atmospheres*, 122(19), 10462-10476, doi:10.1002/2017JD026865.

Malm, W. C., Schichtel, B. A., Hand, J. L., and Prenni, A. J. (2020), Implications of organic mass to carbon ratios increasing over time in the rural United States, *Journal of Geophysical Research-Atmospheres*, 125(5), doi:10.1029/2019jd031480.

Mao, Y. H., Li, Q. B., Zhang, L., Chen, Y., Randerson, J. T., Chen, D., and Liou, K. N. (2011), Biomass burning contribution to black carbon in the Western United States mountain ranges, *Atmospheric Chemistry and Physics*, 11(21), 11253-11266.

Mao, Y. H., Li, Q. B., Chen, D., Zhang, L., Hao, W. M., and Liou, K. N. (2014), Top-down estimates of biomass burning emissions of black carbon in the Western United States, *Atmospheric Chemistry and Physics*, 14(14), 7195-7211.

Mao, Y. H., Li, Q. B., Henze, D. K., Jiang, Z., Jones, D. B. A., Kopacz, M., He, C., Qi, L., Gao, M., Hao, W. M., and Liou, K. N. (2015), Estimates of black carbon emissions in the western United States using the GEOS-Chem adjoint model, *Atmospheric Chemistry and Physics*, 15(13), 7685-7702, <http://www.atmos-chem-phys.net/15/7685/2015/acp-15-7685-2015.pdf>.

MARAMA (2011), Mid-Atlantic/Northeast Visibility Union second interim report, Mid-Atlantic Regional Air Management Association, Baltimore, MD, [http://www.marama.org/publications\\_folder/reports/VisibilityInterimReport\\_sep2011](http://www.marama.org/publications_folder/reports/VisibilityInterimReport_sep2011).

Mardi, A. H., Dadashazar, H., Painemal, D., Shingler, T., Seaman, S. T., Fenn, M. A., Hostetler, C. A., and Sorooshian, A. (2021), Biomass burning over the United States east coast and western North Atlantic Ocean: Implications for clouds and air quality, *Journal of Geophysical Research-Atmospheres*, 126(20), doi:10.1029/2021jd034916.

McClure, C. D., and Jaffe, D. A. (2018), US particulate matter air quality improves except in wildfire-prone areas, *Proceedings of the National Academy of Sciences of the United States of America*, 115(31), 7901-7906, doi:10.1073/pnas.1804353115.

McDonald, J. D., White, R. K., Holmes, T., Mauderly, J. L., Zielinska, B., and Chow, J. C. (2012), Simulated downwind coal combustion emissions for laboratory inhalation exposure atmospheres, *Inhalation Toxicology*, 24(5), 310-319.

McDonald, J. D., Chow, J. C., Peccia, J., Liu, Y. S., Chand, R., Hidy, G. M., and Mauderly, J. L. (2013), Influence of collection region and site type on the composition of paved road dust, *Air Quality, Atmosphere & Health*, 6(3), 615-628, [https://www.researchgate.net/publication/257762872\\_Influence\\_of\\_collection\\_region\\_and\\_site\\_type\\_on\\_the\\_composition\\_of\\_paved\\_road\\_dust](https://www.researchgate.net/publication/257762872_Influence_of_collection_region_and_site_type_on_the_composition_of_paved_road_dust).

McKendry, I. G., and Gutzler, D. S. (2015), A possible link between wildfire aerosol and North American Monsoon precipitation in Arizona-New Mexico, *International Journal of Climatology*, 35(10), 3178-3184.

Meng, X., Hand, J. L., Schichtel, B. A., and Liu, Y. (2018), Space-time trends in PM<sub>2.5</sub> constituents in the conterminous United States estimated by a machine learning approach, 2005-2015, *Environmental International*, 121, 1137-1147, <https://doi.org/10.1016/j.envint.2018.10.029>.

Miguel, A. H., and Hansen, A. D. A. (2012), High-time resolution measurements of black carbon particles in the exhaust emissions of a diesel engine during acceleration, deceleration and cruise conditions, *Journal of the Brazilian Chemical Society*, 23(6), 1140-1145, <http://www.scielo.br/pdf/jbchs/v23n6/20.pdf>.

Miller, D. J., Sun, K., Zondlo, M. A., Kanter, D., Dubovik, O., Welton, E. J., Winker, D. M., and Ginoux, P. (2011), Assessing boreal forest fire smoke aerosol impacts on U.S. air quality: A case study using multiple data sets, *Journal of Geophysical Research-Atmospheres*, 116.

Molders, N., Porter, S. E., Cahill, C. F., and Grell, G. A. (2010), Influence of ship emissions on air quality and input of contaminants in southern Alaska National Parks and Wilderness Areas during the 2006 tourist season, *Atmospheric Environment*, 44(11), 1400-1413.

Murillo, J. H., Marin, J. F. R., Roman, S. R., Guerrero, V. H. B., Arias, D. S., Ramos, A. C., Gonzalez, B. C., and Baumgardner, D. G. (2013), Temporal and spatial variations in organic and elemental carbon concentrations in PM10/PM2.5 in the metropolitan area of Costa Rica, Central America, *Atmospheric Pollution Research*, 4(1), 53-63.

Murphy, B. N., and Pandis, S. N. (2010), Exploring summertime organic aerosol formation in the eastern United States using a regional-scale budget approach and ambient measurements, *Journal of Geophysical Research-Atmospheres*, 115.

Murphy, D. M., Chow, J. C., Leibensperger, E. M., Malm, W. C., Pitchford, M. L., Schichtel, B. A., Watson, J. G., and White, W. H. (2011), Decreases in elemental carbon and fine particle mass in the United States, *Atmospheric Chemistry and Physics*, 11, 4679-4686, <http://www.atmos-chem-phys.net/11/4679/2011/acp-11-4679-2011.pdf>.

Nava, V., Das, K. C., Amin, V., Gronstal, S., Wang, X. L., Chow, J. C., Watson, J. G., and Yang, Y. (2021), Quantification of carboxyl-functionalized multiwall carbon nanotubes in plant tissues with programmed thermal analysis, *Journal of Environmental Quality*, 50, 278–285, doi:10.1002/jeq2.20180.

Ni, D. F., Lin, J. J., Gao, J., Xie, J. F., Wang, J., Guo, Y. Z., and Ren, J. N. (2020), Comparative analysis of new observation methods for carbonaceous aerosol (OC/EC), *Zhongguo Huanjing Kexue/China Environmental Science*, 40(12), 5191-5197.

Ni, H. Y., Han, Y. M., Cao, J. J., Chen, L.-W. A., Tian, J., Wang, X. L., Chow, J. C., Watson, J. G., Wang, Q. Y., Wang, P., Li, H., and Huang, R. J. (2015), Emission characteristics of carbonaceous particles and trace gases from open burning of crop residue in China, *Atmospheric Environment*, 123, 399-406.

Niu, X. Y., Chuang, H. C., Wang, X. L., Ho, S. S. H., Li, L. J., Qu, L. L., Chow, J. C., Watson, J. G., Sun, J., Lee, S. C., Cao, J. J., and Ho, K. F. (2020), Cytotoxicity of PM<sub>2.5</sub> vehicular emissions in the Shing Mun Tunnel, Hong Kong, *Environmental Pollution*, 263, 114386, doi:10.1016/j.envpol.2020.114386.

O'Dell, K., Ford, B., Fischer, E. V., and Pierce, J. R. (2019), Contribution of wildland-fire smoke to US PM<sub>2.5</sub> and its influence on recent trends, *Environmental Science & Technology*, 53(4), 1797-1804, doi:10.1021/acs.est.8b05430.

O'Neill, S. M., Lahm, P. W., Fitch, M. J., and Broughton, M. (2013), Summary and analysis of approaches linking visual range, PM<sub>2.5</sub> concentrations, and air quality health impact indices for wildfires, *Journal of the Air & Waste Management Association*, 63(9), 1083-1090.

Ofosu, F. G., Hopke, P. K., Aboh, I. J. K., and Bamford, S. A. (2012), Characterization of fine particulate sources at Ashaiman in Greater Accra, Ghana, *Atmospheric Pollution Research*, 3(3), 301-310, doi:10.5094/apr.2012.033.

Ofosu, F. G., Hopke, P. K., Aboh, I. J. K., and Bamford, S. A. (2013), Biomass burning contribution to ambient air particulate levels at Navrongo in the Savannah zone of Ghana, *Journal of the Air & Waste Management Association*, 63(9), 1036-1045.

Olson, M. R., Graham, E., Hamad, S., Uchupalanun, P., Ramanathan, N., and Schauer, J. J. (2016), Quantification of elemental and organic carbon in atmospheric particulate matter using color space sensing-hue, saturation, and value (HSV) coordinates, *Science of the Total Environment*, 548, 252-259, doi:10.1016/j.scitotenv.2016.01.032.

Orasche, J., Seidel, T., Hartmann, H., Schnelle-Kreis, J., Chow, J. C., Ruppert, H., and Zimmermann, R. (2012), Comparison of emissions from wood combustion. Part 1: Emission factors and characteristics from different small-scale residential heating appliances considering particulate matter and polycyclic aromatic hydrocarbon (PAH)-related toxicological potential of particle-bound organic species, *Energy & Fuels*, 26(11), 6695-6704.

Pan, L., Kim, H., Lee, P., Saylor, R., Tang, Y., Tong, D., Baker, B., Kondragunta, S., Xu, C., G. Ruminski, M., Chen, W., McQueen, J., and Stajner, I. (2020), Evaluating a fire smoke simulation algorithm in the National Air Quality Forecast Capability (NAQFC) by using multiple observation data sets during the Southeast Nexus (SENEX) field campaign, *Geoscientific Model Development*, 13(5), 2169-2184, doi:10.5194/gmd-13-2169-2020.

Pant, P., Shukla, A., Kohl, S. D., Chow, J. C., Watson, J. G., and Harrison, R. M. (2015), Characterization of ambient PM<sub>2.5</sub> at a pollution hotspot in New Delhi, India and inference of sources, *Atmospheric Environment*, 109, 178-189,  
<https://www.sciencedirect.com/science/article/pii/S1352231015002034>.

Papp, M. (2012), Documentation of measurement uncertainty estimates of collocated Chemical Speciation Network and IMPROVE data for use in secondary PM<sub>2.5</sub> standard for visibility, U.S. Environmental Protection Agency, Research Triangle Park, NC,  
<http://www.epa.gov/ttn/naaqs/standards/pm/data/20120613Papp.pdf>.

Peng, C., Tian, M., Wang, X. L., Yang, F. M., Shi, G. M., Huang, R. J., Yao, X. J., Wang, Q. Y., Zhai, C. Z., Zhang, S. M., Qian, R. Z., Cao, J. J., and Chen, Y. (2020), Light absorption of brown carbon in PM<sub>2.5</sub> in the Three Gorges Reservoir region, southwestern China: Implications of biomass burning and secondary formation, *Atmospheric Environment*, 229, doi:10.1016/j.atmosenv.2020.117409.

Peng, Y., Wang, H., Hou, M. L., Jiang, T., Zhang, M., Zhao, T. L., and Che, H. Z. (2020), Improved method of visibility parameterization focusing on high humidity and aerosol

concentrations during fog-haze events: Application in the GRAPES\_CAUCE model in Jing-Jin-Ji, China, *Atmospheric Environment*, 222, doi:10.1016/j.atmosenv.2019.117139.

Pervez, S., Chakrabarty, R. K., Dewangan, S., Watson, J. G., Chow, J. C., Matawle, J. L., and Pervez, Y. (2015), Cultural and ritual burning emission factors and activity levels in India, *Aerosol and Air Quality Research*, 15, 72-80,  
[http://aaqr.org/VOL15\\_No1\\_February2015/7\\_AAQR-14-01-OA-0022\\_72-80.pdf](http://aaqr.org/VOL15_No1_February2015/7_AAQR-14-01-OA-0022_72-80.pdf).

Pongpiachan, S., Ho, K. F., and Cao, J. J. (2013), Estimation of gas-particle partitioning coefficients (K-p) of carcinogenic polycyclic aromatic hydrocarbons in carbonaceous aerosols collected at Chiang-Mai, Bangkok and Hat-Yai, Thailand, *Asian Pacific Journal of Cancer Prevention*, 14(4), 2461-2476.

Prabhakar, G., Sorooshian, A., Toffol, E., Arellano, A. F., and Betterton, E. A. (2014), Spatiotemporal distribution of airborne particulate metals and metalloids in a populated arid region, *Atmospheric Environment*, 92, 339-347.

Prenni, A. J., Levin, E. J. T., Benedict, K. B., Sullivan, A. P., Schurman, M. I., Gebhart, K. A., Day, D. E., Carrico, C. M., Malm, W. C., Schichtel, B. A., Collett, J. L., and Kreidenweis, S. M. (2014), Gas-phase reactive nitrogen near Grand Teton National Park: Impacts of transport, anthropogenic emissions, and biomass burning, *Atmospheric Environment*, 89, 749-756.

Prenni, A. J., Hand, J. L., Malm, W. C., Copeland, S., Luo, G., Yu, F., Taylor, N., Russell, L. M., and Schichtel, B. A. (2019), An examination of the algorithm for estimating light extinction from IMPROVE particle speciation data, *Atmospheric Environment*, 214, 116880,  
<https://doi.org/10.1016/j.atmosenv.2019.116880>.

Priyadarshini, B., Verma, S., Chatterjee, A., Sharma, S. K., and Mandal, T. K. (2019), Chemical characterization of fine atmospheric particles of water-soluble ions and carbonaceous species in a tropical urban atmosphere over the eastern Indo-Gangetic Plain, *Aerosol and Air Quality Research*, 19(1), 129-147, doi:10.4209/aaqr.2017.12.0606.

Pu, B., and Ginoux, P. (2018), Climatic factors contributing to long-term variations in surface fine dust concentration in the United States, *Atmospheric Chemistry and Physics*, 18(6), 4201-4215, doi:10.5194/acp-18-4201-2018.

Qadir, R. M., Abbaszade, G., Schnelle-Kreis, J., Chow, J. C., and Zimmermann, R. (2013), Concentrations and source contributions of particulate organic matter before and after implementation of a low emission zone in Munich, Germany, *Environ. Poll.*, 175, 158-167.

Raman, A., Arellano, A. F., and Brost, J. J. (2014), Revisiting haboobs in the southwestern United States: An observational case study of the 5 July 2011 Phoenix dust storm, *Atmospheric Environment*, 89, 179-188.

Rasool, Q. Z., Zhang, R., Lash, B., Cohan, D. S., Cooter, E. J., Bash, J. O., and Lamsal, L. N. (2016), Enhanced representation of soil NO emissions in the Community Multiscale Air Quality (CMAQ) model version 5.0.2, *Geoscientific Model Development*, 9(9), 3177-3197, doi:10.5194/gmd-9-3177-2016.

Rattigan, O. V., Felton, H. D., Bae, M. S., Schwab, J. J., and Demerjian, K. L. (2011), Comparison of long-term PM(2.5) carbon measurements at an urban and rural location in New York, *Atmospheric Environment*, 45(19), 3228-3236.

Ravi, V., Vaughan, J. K., Wolcott, M. P., and Lamb, B. K. (2019), Impacts of prescribed fires and benefits from their reduction for air quality, health, and visibility in the Pacific Northwest of the United States, *Journal of the Air & Waste Management Association*, 69(3), 289-304, doi:10.1080/10962247.2018.1526721.

Rea, P., Ma, L., Gill, T. E., Gardea-Torresdey, J., Tamez, C., and Jin, L. (2020), Tracing gypsumiferous White Sand aerosols in the shallow critical zone in the northern Sacramento Mountains, New Mexico using Sr/Ca and  $^{87}\text{Sr}/^{86}\text{Sr}$  ratios, *Geoderma*, 372, 114387, <https://doi.org/10.1016/j.geoderma.2020.114387>.

Reggente, M., Dillner, A. M., and Takahama, S. (2016), Predicting ambient aerosol thermal-optical reflectance (TOR) measurements from infrared spectra: extending the predictions to different years and different sites, *Atmospheric Measurement Techniques*, 9(2), 441-454, doi:10.5194/amt-9-441-2016.

Reggente, M., A. M. Dillner, and S. Takahama (2019), Analysis of functional groups in atmospheric aerosols by infrared spectroscopy: systematic intercomparison of calibration methods for US measurement network samples, *Atmos. Meas. Tech.*, 12(4), 2287-2312, doi:10.5194/amt-12-2287-2019.

Reid, J. S., et al. (2017), Ground-based High Spectral Resolution Lidar observation of aerosol vertical distribution in the summertime Southeast United States, *J. Geophys. Res. Atmos.*, 122, 2970-3004, doi:10.1002/2016JD025798.

Requia, W. J., Coull, B. A., and Koutrakis, P. (2019), The impact of wildfires on particulate carbon in the western USA, *Atmospheric Environment*, 213, 1-10, doi:10.1016/j.atmosenv.2019.05.054.

Requia, W. J., Coull, B. A., and Koutrakis, P. (2019), The influence of spatial patterning on modeling PM<sub>2.5</sub> constituents in Eastern Massachusetts, *Science of the Total Environment*, 682, 247-258, doi:10.1016/j.scitotenv.2019.05.012.

Requia, W. J., Jhun, I., Coull, B. A., and Koutrakis, P. (2019), Climate impact on ambient PM<sub>2.5</sub> elemental concentration in the United States: A trend analysis over the last 30 years, *Environment International*, 131, doi:10.1016/j.envint.2019.05.082.

Riggio, G. M. (2015), Development and application of thermal/optical- quadrupole TOA-QMS mass spectrometry for quantitative analysis of major particulate matter constituents, M.S. Thesis, University of Nevada, Reno, NV.

Rodriguez, M. A., Barna, M. G., Gebhart, K. A., Hand, J. L., Adelman, Z. E., Schichtel, B. A., Collett, J. L., Jr., and Malm, W. C. (2011), Modeling the fate of atmospheric reduced nitrogen during the Rocky Mountain Atmospheric Nitrogen and Sulfur Study (RoMANS): Performance evaluation and diagnosis using integrated processes rate analysis, *Atmospheric Environment*, 45(1), 223-234.

Ruthenburg, T. C., Perlin, P. C., Liu, V., McDade, C. E., and Dillner, A. M. (2014), Determination of organic matter and organic matter to organic carbon ratios by infrared spectroscopy with application to selected sites in the IMPROVE network, *Atmospheric Environment*, 86(0), 47-57, <http://www.sciencedirect.com/science/article/pii/S1352231013009795>.

Ruzer, L., and Harley, N. H. (2013), *Aerosols Handbook : Measurement, Dosimetry, and Health Effects, Second Edition*, CRC Press/Taylor & Francis, New York, NY.

Sahu, M., Hu, S., Ryan, P. H., LeMasters, G., Grinshpun, S. A., Chow, J. C., and Biswas, P. (2011), Chemical compositions and source identification of PM<sub>2.5</sub> aerosols for estimation of a diesel source surrogate, *Science of the Total Environment*, 409(13), 2642-2651, <\\joint\eaflReferences\DRIPDFs\Articles\Sahuetal2011STOTENDieselSource.pdf>.

Salako, G. O., Hopke, P. K., Cohen, D. D., Begum, B. A., Biswas, S. K., Pandit, G. G., Chung, Y. S., Abd Rahman, S., Hamzah, M. S., Davy, P., Markwitz, A., Shagjamba, D., Lodoysamba, S., Wimolwattanapun, W., and Bunprapob, S. (2012), Exploring the variation between EC and BC in a variety of locations, *Aerosol and Air Quality Research*, 12(1), 1-7.

Sarkar, C., N. Spada, S. Xu, M. M. Shafer, and N. P. Hyslop (2023), An inter-laboratory comparison of elemental loadings of PM<sub>2.5</sub> samples using energy-dispersive XRF and magnetic-sector ICP-MS, *Atmospheric Environment*, 293, 119463, doi:<https://doi.org/10.1016/j.atmosenv.2022.119463>.

Schichtel, B. A., Pitchford, M. L., and White, W. H. (2011), Comments on "Impact of California's Air Pollution Laws on Black Carbon and their Implications for Direct Radiative Forcing" by R. Bahadur et al, *Atmospheric Environment*, 45(24), 4116-4118.

Schichtel, B. A., RodriguezB, M. A., Barna, M. G., Gebhart, K. A., Pitchford, M. L., and Malm, W. C. (2012), A semi-empirical, receptor-oriented Lagrangian model for simulating fine particulate carbon at rural sites, *Atmospheric Environment*, 61, 361-370.

Schichtel, B. A., Hand, J. L., Barna, M. G., Gebhart, K. A., Copeland, S., Vimont, J., and Malm, W. C. (2017), Origin of fine particulate carbon in the rural United States, *Environmental Science & Technology*, 51(17), 9846-9855, doi:10.1021/acs.est.7b00645.

Schlosser, J. S., Braun, R. A., Bradley, T., Dadashazar, H., MacDonald, A. B., Aldhaif, A. A., Aghdam, M. A., Mardi, A. H., Xian, P., and Sorooshian, A. (2017), Analysis of aerosol composition data for western United States wildfires between 2005 and 2015: Dust emissions, chloride depletion, and most enhanced aerosol constituents, *Journal of Geophysical Research: Atmospheres*, 122(16), 8951-8966, doi:10.1002/2017JD026547.

Schwander, S., Okello, C. D., Freers, J., Chow, J. C., Watson, J. G., M., C., and Q.Y., M. (2014), Particulate matter air pollution in Mpererwe District, Kampala, Uganda - A pilot study, *Journal of Environmental and Public Health*, 2014(763934), 1-7, doi:<dx.doi.org/10.1155/2014/763934>.

Shakya, K. M., and Peltier, R. E. (2015), Non-sulfate sulfur in fine aerosols across the United States: Insight for organosulfate prevalence, *Atmospheric Environment*, 100, 159-166.

Shen, G. F., Xue, M., Yuan, S. Y., Zhang, J., Zhao, Q. Y., Li, B., Wu, H. S., and Ding, A. J. (2014), Chemical compositions and reconstructed light extinction coefficients of particulate matter in a mega-city. in the western Yangtze River Delta, China, *Atmospheric Environment*, 83, 14-20.

Shen, J. Y., Zhao, Q. B., Cheng, Z., Huo, J. T., Zhu, W. F., Zhang, Y. H., Duan, Y. S., Wang, X. L., Chen, L.-W. A., and Fu, Q. Y. (2020), Evolution of source contributions during heavy fine particulate matter (PM<sub>2.5</sub>) pollution episodes in eastern China through online measurements, *Atmospheric Environment*, 232, doi:10.1016/j.atmosenv.2020.117569.

Shen, Z. X., Lei, Y. L., Zhang, L. M., Zhang, Q., Zeng, Y. L., Tao, J., Zhu, C. H., Cao, J. J., Xu, H. M., and Liu, S. X. (2017), Methanol extracted brown carbon in PM<sub>2.5</sub> over Xi'an, China: Seasonal variation of optical properties and sources identification, *Aerosol Science and Engineering*, 1(2), 57-65, doi:10.1007/s41810-017-0007-z.

Shi, X. Y., He, K. B., Song, W. W., Wang, X. T., and Tan, J. H. (2012), Effects of a diesel oxidation catalyst on gaseous pollutants and fine particles from an engine operating on diesel and biodiesel, *Frontiers of Environmental Science & Engineering*, 6(4), 463-469.

Shimada, K., Takami, A., Ishida, T., Taniguchi, Y., Hasegawa, S., Chan, C. K., Kim, Y. P., Lin, N. H., and Hatakeyama, S. (2021), Long-term measurements of carbonaceous aerosol at Cape Hedo, Okinawa, Japan: Effects of changes in emissions in East Asia, *Aerosol and Air Quality Research*, 21(9), doi:10.4209/aaqr.200505.

Shrivastava, M., Easter, R. C., Liu, X. H., Zelenyuk, A., Singh, B., Zhang, K., Ma, P. L., Chand, D., Ghan, S., Jimenez, J. L., Zhang, Q., Fast, J., Rasch, P. J., and Tiitta, P. (2015), Global transformation and fate of SOA: Implications of low-volatility SOA and gas-phase fragmentation reactions, *Journal of Geophysical Research-Atmospheres*, 120(9), 4169-4195.

Simon, H., Bhave, P. V., Swall, J. L., Frank, N. H., and Malm, W. C. (2011), Determining the spatial and seasonal variability in OM/OC ratios across the US using multiple regression, *Atmospheric Chemistry and Physics*, 11(6), 2933-2949.

Singh, R., Kulshrestha, M. J., Kumar, B., and Chandra, S. (2016), Impact of anthropogenic emissions and open biomass burning on carbonaceous aerosols in urban and rural environments of Indo-Gangetic Plain, *Air Quality Atmosphere and Health*, 9(7), 809-822, doi:10.1007/s11869-015-0377-9.

Smiley, J. (2010), Technical memorandum: Experimental intercomparison of speciation laboratories, U.S. Environmental Protection Agency, Montgomery, AL, <http://www.epa.gov/ttn/amtic/files/ambient/pm25/spec/multilabspeciationpt2009.pdf>.

Snider, G., Weagle, C. L., Murdymootoo, K. K., Ring, A., Ritchie, Y., Stone, E., Walsh, A., Akoshile, C., Anh, N. X., Balasubramanian, R., Brook, J., Qonitan, F. D., Dong, J. L., Griffith, D., He, K. B., Holben, B. N., Kahn, R., Lagrosas, N., Lestari, P., Ma, Z. W., Misra, A., Norford, L. K., Quel, E. J., Salam, A., Schichtel, B., Segev, L., Tripathi, S., Wang, C., Yu, C., Zhang, Q., Zhang, Y. X., Brauer, M., Cohen, A., Gibson, M. D., Liu, Y., Martins, J. V., Rudich, Y., and Martin, R. V. (2016), Variation in global chemical composition of PM<sub>2.5</sub>: Emerging results from SPARTAN, *Atmospheric Chemistry and Physics*, 16(15), 9629-9653, doi:10.5194/acp-16-9629-2016.

Solomon, P. A., Crumpler, D., Flanagan, J. B., Jayanty, R. K. M., Rickman, E. E., and McDade, C. E. (2014), US National PM<sub>2.5</sub> Chemical Speciation Monitoring Networks-CSN and IMPROVE: Description of networks, *Journal of the Air & Waste Management Association*, 64(12), 1410-1438, <http://www.tandfonline.com/doi/pdf/10.1080/10962247.2014.956904>.

Soto-Garcia, L. L., Andreae, M. O., Andreae, T. W., Artaxo, P., Maenhaut, W., Kirchstetter, T. W., Novakov, T., Chow, J. C., and Mayol-Bracero, O. L. (2011), Evaluation of the carbon content of aerosols from the burning of biomass in the Brazilian Amazon using thermal, optical and thermal-optical analysis methods, *Atmospheric Chemistry and Physics*, 11(9), 4425-4444.

Spada, N. J., Cheng, X., White, W. H., and Hyslop, N. P. (2018), Decreasing vanadium footprint of bunker fuel emissions, *Environmental Science and Technology*, 52(20), 11528-11534, doi:10.1021/acs.est.8b02942.

Spada, N. J., and N. P. Hyslop (2018), Comparison of elemental and organic carbon measurements between IMPROVE and CSN before and after method transitions, *Atmospheric Environment*, 178, 173-180, doi:<https://doi.org/10.1016/j.atmosenv.2018.01.043>.

Sturtz, T. M., Schichtel, B. A., and Larson, T. V. (2014), Coupling chemical transport model source attributions with positive matrix factorization: Application to two IMPROVE sites impacted by wildfires, *Environmental Science & Technology*, 48(19), 11389-11396.

Sumlin, B. J. (2015), Development, characterization, and application of the DRI Model 2015 multiwavelength thermal-optical carbon analyzer, M.S. Thesis, University of Nevada, Reno, NV.

Tai, A. P. K., Mickley, L. J., and Jacob, D. J. (2010), Correlations between fine particulate matter (PM2.5) and meteorological variables in the United States: Implications for the sensitivity of PM2.5 to climate change, *Atmospheric Environment*, 44(32), 3976-3984.

Takahama, S., A. M. Dillner, A. T. Weakley, M. Reggente, C. Bürki, M. Lbadaoui-Darvas, B. Debus, A. Kuzmiakova, and A. S. Wexler (2019), Atmospheric particulate matter characterization by Fourier transform infrared spectroscopy: a review of statistical calibration strategies for carbonaceous aerosol quantification in US measurement networks, *Atmospheric Measurement Techniques*, 12(1), 525-567, doi:<https://doi.org/10.5194/amt-12-525-2019>.

Tang, D. L., Li, T. Y., Chow, J. C., Kulkarni, S. U., Watson, J. G., Ho, S. S. H., Quan, Z. Y., Qu, L. R., and Perera, F. (2014), Air pollution effects on fetal and child development: A cohort comparison in China, *Environ. Poll.*, 185, 90-96,  
[https://www.researchgate.net/publication/258635235\\_Air\\_pollution\\_effects\\_on\\_fetal\\_and\\_child\\_development\\_A\\_cohort\\_comparison\\_in\\_China](https://www.researchgate.net/publication/258635235_Air_pollution_effects_on_fetal_and_child_development_A_cohort_comparison_in_China).

Tanner, R. L., Bairai, S. T., and Mueller, S. F. (2015), Trends in concentrations of atmospheric gaseous and particulate species in rural eastern Tennessee as related to primary emission reductions, *Atmospheric Chemistry and Physics*, 15(17), 9781-9797, doi:10.5194/acp-15-9781-2015.

Tao, J., Cao, J. J., Zhang, R. J., Zhu, L. H., Zhang, T., Shi, S., and Chan, C. Y. (2012), Reconstructed light extinction coefficients using chemical compositions of PM2.5 in winter in urban Guangzhou, China, *Advances in Atmospheric Sciences*, 29(2), 359-368,  
[http://www.scies.org/UploadPic/Files\\_2012111173320826.pdf](http://www.scies.org/UploadPic/Files_2012111173320826.pdf).

Tao, J., Shen, Z. X., Zhu, C. S., Yue, J. H., Cao, J. J., Liu, S. X., Zhu, L. H., and Zhang, R. J. (2012), Seasonal variations and chemical characteristics of sub-micrometer particles (PM1) in Guangzhou, China, *Atmospheric Research*, 118, 222-231, doi:10.1016/j.atmosres.2012.06.025.

Tao, J., Zhang, L. M., Engling, G., Zhang, R. J., Yang, Y. H., Cao, J. J., Zhu, C. S., Wang, Q. Y., and Luo, L. (2013), Chemical composition of PM2.5 in an urban environment in Chengdu, China: Importance of springtime dust storms and biomass burning, *Atmospheric Research*, 122, 270-283.

Tao, J., Zhang, L. M., Cao, J. J., Hsu, S. C., Xia, X. G., Zhang, Z. S., Lin, Z. J., Cheng, T. T., and Zhang, R. J. (2014), Characterization and source apportionment of aerosol light extinction in Chengdu, southwest China, *Atmospheric Environment*, 95, 552-562.

- Tao, J., Zhang, L. M., Ho, K. F., Zhang, R. J., Lin, Z. J., Zhang, Z. S., Lin, M., Cao, J. J., Liu, S. X., and Wang, G. H. (2014), Impact of PM<sub>2.5</sub> chemical compositions on aerosol light scattering in Guangzhou - the largest megacity in South China, *Atmospheric Research*, 135, 48-58.
- Tao, J., Zhang, L. M., Wu, Y. F., and Zhang, Z. S. (2020), Evaluation of the IMPROVE formulas based on Mie model in the calculation of particle scattering coefficient in an urban atmosphere, *Atmospheric Environment*, 222, doi:10.1016/j.atmosenv.2019.117116.
- Terhorst, J., and Berkman, M. (2010), Effect of coal-fired power generation on visibility in a nearby national park, *Atmospheric Environment*, 44(21-22), 2524-2531.
- Tian, J., Wang, Q. Y., Han, Y. M., Ye, J. H., Wang, P., Pongpiachan, S., Ni, H. Y., Zhou, Y. Q., Wang, M., Zhao, Y. Z., and Cao, J. J. (2020), Contributions of aerosol composition and sources to particulate optical properties in a southern coastal city of China, *Atmospheric Research*, 235, doi:10.1016/j.atmosres.2019.104744.
- Tian, P., Wang, G. F., Zhang, R. J., Wu, Y. F., and Yan, P. (2015), Impacts of aerosol chemical compositions on optical properties in urban Beijing, China, *Particuology*, 18, 155-164.
- Tolocka, M. P., and Turpin, B. J. (2012), Contribution of organosulfur compounds to organic aerosol mass, *Environmental Science & Technology*, 46(15), 7978-7983.
- Tong, D. Q., Dan, M., Wang, T., and Lee, P. (2012), Long-term dust climatology in the western United States reconstructed from routine aerosol ground monitoring, *Atmospheric Chemistry and Physics*, 12(11), 5189-5205.
- Tong, D. Q., Wang, J. X. L., Gill, T. E., Lei, H., and Wang, B. Y. (2017), Intensified dust storm activity and Valley fever infection in the southwestern United States, *Geophysical Research Letters*, 44(9), 4304-4312, doi:10.1002/2017gl073524.
- Trivitayanurak, W., and Adams, P. J. (2014), Does the POA-SOA split matter for global CCN formation?, *Atmospheric Chemistry and Physics*, 14(2), 995-1010.
- U.S.EPA (2012), PM 2.5 -Visibility (IMPROVE), U.S. Environmental Protection Agency, Research Triangle Park, NC, <http://www.epa.gov/ttnamti1/visdata.html>.
- U.S.EPA (2017), Chemical speciation, U.S. Environmental Protection Agency, Research Triangle Park, NC, <http://www.epa.gov/ttn/amtic/speciepg.html>.
- Vega, E., López-Veneroni, D., Ramírez, O., Chow, J. C., and Watson, J. G. (2021), Particle-bound PAHs and chemical composition, Sources and health risk of PM<sub>2.5</sub> in a highly industrialized area, *Aerosol and Air Quality Research*, 21, 210047, doi:10.4209/aaqr.210047.
- Verma, M., Pervez, S., Chow, J. C., Majumdar, D., Watson, J. G., Pervez, Y. F., Deb, M. K., Shrivastava, K., Jain, V. K., Khan, N. A., Mandal, P., and Chakrabarty, R. K. (2021), Assessing the magnitude of PM<sub>2.5</sub> polycyclic aromatic hydrocarbon emissions from residential solid fuel combustion and associated health hazards in South Asia, *Atmospheric Pollution Research*, 12, 101142, doi:10.1016/j.apr.2021.101142.
- Walker, J. M., Philip, S., Martin, R. V., and Seinfeld, J. H. (2012), Simulation of nitrate, sulfate, and ammonium aerosols over the United States, *Atmospheric Chemistry and Physics*, 12(22), 11213-11227.

Wang, H. B., Li, X. H., Shi, G. M., Cao, J. J., Li, C. C., Yang, F. M., Ma, Y. L., and He, K. B. (2015), PM2.5 chemical compositions and aerosol optical properties in Beijing during the late fall, *Atmosphere*, 6(2), 164-182.

Wang, M., Xu, B. Q., Zhao, H. B., Cao, J. J., Joswiak, D., Wu, G. J., and Lin, S. B. (2012), The influence of dust on quantitative measurements of black carbon in ice and snow when using a thermal optical method, *Aerosol Science and Technology*, 46(1), 60-69.

Wang, Q. Y., Cao, J. J., Shen, Z. X., Tao, J., Xiao, S., Luo, L., He, Q. Y., and Tang, X. Y. (2013), Chemical characteristics of PM2.5 during dust storms and air pollution events in Chengdu, China, *Particuology*, 11(1), 70-77.

Wang, Q. Y., Cao, J. J., Tao, J., Li, N., Su, X. O., Chen, L.-W. A., Wang, P., Shen, Z. X., Liu, S. X., and Dai, W. T. (2013), Long-term trends in visibility and at Chengdu, China, *Plos One*, 8(7), e68894.

Wang, Q. Y., Liu, S. X., Li, N., Dai, W. T., Wu, Y. F., Tian, J., Zhou, Y. Q., Wang, M., Sai, S., Ho, H., Chen, Y., Zhang, R. J., Zhao, S. Y., Zhu, C. S., Han, Y. M., Tie, X. X., and Cao, J. J. (2019), Impacts of short-term mitigation measures on PM2.5 and radiative effects: a case study at a regional background site near Beijing, China, *Atmospheric Chemistry and Physics*, 19(3), 1881-1899, doi:10.5194/acp-19-1881-2019.

Watson, J. G., Chow, J. C., Chen, L.-W. A., Green, M. C., and Kohl, S. D. (2011), Wintertime PM<sub>2.5</sub> source contributions in Reno, NV, Desert Research Institute, Reno, NV.

Watson, X. L., Watson, J. G., Chow, J. C., Kohl, S. D., Chen, L.-W. A., Sodeman, D. A., Legge, A. H., and Percy, K. E. (2012), Measurement of real-world stack emissions with a dilution sampling system, in *Alberta Oil Sands: Energy, Industry, and the Environment*, edited by K. E. Percy, pp. 171-192, Elsevier Press, Amsterdam, The Netherlands,  
[https://www.researchgate.net/publication/235341714\\_Measurement\\_of\\_Real-World\\_Stack\\_Emissions\\_with\\_a\\_Dilution\\_Sampling\\_System](https://www.researchgate.net/publication/235341714_Measurement_of_Real-World_Stack_Emissions_with_a_Dilution_Sampling_System).

Watson, J. G., Chow, J. C., Lowenthal, D. H., Chen, L.-W. A., and Wang, X. L. (2012), Reformulation of PM<sub>2.5</sub> mass reconstruction assumptions for the San Joaquin Valley: Literature review, Desert Research Institute, Reno, NV.

Watson, J. G., and Chow, J. C. (2013), Source apportionment, in *Encyclopedia of Environmetrics*, edited by A. H. El-Shaarwi and W. W. Piegorsch, pp. 1-8, John Wiley & Sons, Ltd., Chichester, UK,  
<http://onlinelibrary.wiley.com/doi/10.1002/9780470057339.vas034.pub2/abstract>.

Watson, J. G., Chow, J. C., Wang, X. L., Kohl, S. D., Gronstal, S., and Zielinska, B. (2013), Measurement of real-world stack emissions in the Athabasca Oil Sands Region with a dilution sampling system during March, 2011, Desert Research Institute, Reno, NV, USA.

Watson, J. G., Chow, J. C., Wang, X. L., Kohl, S. D., and Sodeman, D. A. (2013), Measurement of real-world stack emissions in the Athabasca Oil Sands Region with a dilution sampling system during August, 2008, Desert Research Institute, Reno, NV, USA.

Watson, J. G., Chow, J. C., Wang, X. L., Lowenthal, D. H., Kohl, S. D., and Gronstal, S. (2013), Characterization of real-world emissions from nonroad mining trucks in the Athabasca Oil Sands Region during October, 2010, Desert Research Institute, Reno, NV.

Watson, J. G., Chow, J. C., Wang, X. L., and Kohl, S. D. (2014), Chemical source profiles for geological dust samples from the Athabasca Oil Sands Region, Desert Research Institute, Reno, NV.

Wang, X. L., Chow, J. C., Kohl, S. D., Percy, K. E., Legge, A. H., and Watson, J. G. (2015), Characterization of PM<sub>2.5</sub> and PM<sub>10</sub> fugitive dust source profiles in the Athabasca Oil Sands Region, *Journal of the Air & Waste Management Association*, 65(12), 1421-1433, <http://www.tandfonline.com/doi/full/10.1080/10962247.2015.1100693>.

Watson, J. G., and Chow, J. C. (2015), Receptor models and measurements for identifying and quantifying air pollution sources, in *Introduction to Environmental Forensics, 3rd Edition*, edited by B. L. Murphy and R. D. Morrison, pp. 677-706, Elsevier, Amsterdam, The Netherlands, [https://www.researchgate.net/publication/269394107\\_Receptor\\_Models\\_and\\_Measurements\\_for\\_Identifying\\_and\\_Quantifying\\_Air\\_Pollution\\_Sources](https://www.researchgate.net/publication/269394107_Receptor_Models_and_Measurements_for_Identifying_and_Quantifying_Air_Pollution_Sources).

Watson, J. G., Chow, J. C., Lowenthal, D. H., Chen, L.-W. A., Shaw, S., Edgerton, E. S., and Blanchard, C. L. (2015), PM<sub>2.5</sub> source apportionment with organic markers in the Southeastern Aerosol Research and Characterization (SEARCH) Study, *Journal of the Air & Waste Management Association*, 65(9), 1104-1118, <http://www.tandfonline.com/doi/pdf/10.1080/10962247.2015.1063551>.

Watson, J. G., Chow, J. C., Engling, G., Chen, L.-W. A., and Wang, X. L. (2016), Source apportionment: Principles and methods, in *Airborne Particulate Matter: Sources, Atmospheric Processes and Health*, edited by R. M. Harrison, pp. 72-125, Royal Society of Chemistry, London, UK, [https://www.researchgate.net/publication/308372849\\_Source\\_Apportionment\\_Principles\\_and\\_Methods](https://www.researchgate.net/publication/308372849_Source_Apportionment_Principles_and_Methods).

Watson, J. G., Cao, J. J., Wang, X. L., and Chow, J. C. (2021), PM<sub>2.5</sub> pollution in China's Guanzhong Basin and the USA's San Joaquin Valley mega-regions, *Faraday Discussions*, 226, 255-289, doi:10.1039/D0FD00094A.

Wei, C., Bandowe, B. A. M., Han, Y. M., Cao, J. J., Watson, J. G., Chow, J. C., and Wilcke, W. (2021), Polycyclic aromatic compounds (PAHs, oxygenated PAHs, nitrated PAHs, and azaarenes) in air from four climate zones of China: Occurrence, gas/particle partitioning, and health risks, *Science of The Total Environment*, 786, 147234, doi:10.1016/j.scitotenv.2021.147234.

White, W. H., Farber, R. J., Malm, W. C., Nuttall, M., Pitchford, M. L., and Schichtel, B. A. (2012), Comment on "Effect of coal-fired power generation on visibility in a nearby National Park (Terhorst and Berkman, 2010)", *Atmospheric Environment*, 55, 173-178.

White, W. H., Hyslop, N. P., Trzepla, K., Yatkin, S., Rarig, R. S., Gill, T. E., and Jin, L. X. (2015), Regional transport of a chemically distinctive dust: Gypsum from White Sands, New Mexico (USA), *Aeolian Research*, 16, 1-10, doi:10.1016/j.aeolia.2014.10.001.

White, W. H., Trzepla, K., Hyslop, N. P., and Schichtel, B. A. (2016), A critical review of filter transmittance measurements for aerosol light absorption, and de novo calibration for a decade of monitoring on PTFE membranes, *Aerosol Science and Technology*, 50(9), 984-1002, doi:10.1080/02786826.2016.1211615.

Winquist, A., Schauer, J. J., Turner, J. R., Klein, M., and Sarnat, S. E. (2015), Impact of ambient fine particulate matter carbon measurement methods on observed associations with acute cardiorespiratory morbidity, *Journal of Exposure Science & Environmental Epidemiology*, 25(2), 215-221.

Wu, C., Ng, W. M., Huang, J. X., Wu, D., and Yu, J. Z. (2012), Determination of elemental and organic carbon in PM<sub>2.5</sub> in the Pearl River Delta Region: Inter-instrument (Sunset vs. DRI Model 2001 Thermal/Optical Carbon Analyzer) and inter-protocol comparisons (IMPROVE vs. ACE-Asia Protocol), *Aerosol Science and Technology*, 46(6), 610-621, <http://www.tandfonline.com/doi/pdf/10.1080/02786826.2011.649313>.

Wu, F., Chow, J. C., An, Z. S., Watson, J. G., and Cao, J. J. (2011), Size-differentiated chemical characteristics of Asian Paleo dust: Records from aeolian deposition on the Chinese loess plateau, *Journal of the Air & Waste Management Association*, 61(2), 180-189, <http://www.tandfonline.com/doi/pdf/10.3155/1047-3289.61.2.180>.

Xiao, S., Wang, Q. Y., Cao, J. J., Huang, R. J., Chen, W. D., Han, Y. M., Xu, H. M., Liu, S. X., Zhou, Y. Q., Wang, P., Zhang, J. Q., and Zhan, C. L. (2014), Long-term trends in visibility and impacts of aerosol composition on visibility impairment in Baoji, China, *Atmospheric Research*, 149, 88-95.

Xing, L., Fu, T. M., Cao, J. J., Lee, S. C., Wang, G. H., Ho, K. F., Cheng, M. C., You, C. F., and Wang, T. J. (2013), Seasonal and spatial variability of the OM/OC mass ratios and high regional correlation between oxalic acid and zinc in Chinese urban organic aerosols, *Atmospheric Chemistry and Physics*, 13(8), 4307-4318.

Xu, H. M., Tao, J., Ho, S. S. H., Ho, K. F., Cao, J. J., Li, N., Chow, J. C., Wang, G. H., Han, Y. M., Zhang, R. J., Watson, J. G., and Zhang, J. Q. (2013), Characteristics of fine particulate non-polar organic compounds in Guangzhou during the 16th Asian Games: Effectiveness of air pollution controls, *Atmospheric Environment*, 76, 94-101, doi:j.atmosenv.2012.12.037.

Yang, F. M., Brook, J., He, K. B., Duan, F. K., and Ma, Y. L. (2010), Temporal variability in fine carbonaceous aerosol over two years in two Megacities: Beijing and Toronto, *Advances in Atmospheric Sciences*, 27(3), 705-714.

Yang, X. F., Robles, J. A., Wang, X. L., Chen, L.-W. A., Watson, J. G., and Chow, J. C. (2013), CHNS analysis of aerosols on a modified thermal/optical carbon analyzer: System setup and calibration protocol, presented at Proceedings, 106th Annual Meeting of the Air & Waste Management Association, Pittsburgh, PA.

Yatkin, S., H. S. Amin, K. Trzepla, and A. M. Dillner (2016), Preparation of lead (Pb) X-ray fluorescence reference materials for the EPA Pb monitoring program and the IMPROVE network using an aerosol deposition method, *Aerosol Science and Technology*, 50(4), 309-320, doi:10.1080/02786826.2016.1150956.

Yatkin, S., K. Trzepla, W. H. White, and N. P. Hyslop (2018), Generation of multi-element reference materials on PTFE filters mimicking ambient aerosol characteristics, *Atmospheric Environment*, 189, 41-49, doi:<https://doi.org/10.1016/j.atmosenv.2018.06.034>.

Yatkin, S., K. Trzepla, W. H. White, N. J. Spada, and N. P. Hyslop (2020), Development of single-compound reference materials on polytetrafluoroethylene filters for analysis of aerosol

- samples, *Spectrochimica Acta Part B: Atomic Spectroscopy*, 171, 105948, doi:<https://doi.org/10.1016/j.sab.2020.105948>.
- Yazdani, A., A. M. Dillner, and S. Takahama (2021), Estimating mean molecular weight, carbon number, and OM/OC with mid-infrared spectroscopy in organic particulate matter samples from a monitoring network, *Atmos. Meas. Tech.*, 14(7), 4805-4827, doi:10.5194/amt-14-4805-2021.
- Yelverton, T. L. B., Hays, M. D., Gullett, B. K., and Linak, W. P. (2014), Black carbon measurements of flame-generated soot as determined by optical, thermal-optical, direct absorption, and laser incandescence methods, *Environmental Engineering Science*, 31(4), 209-215.
- Yu, S., Mathur, R., Pleim, J., Pouliot, G., Wong, D., Eder, B., Schere, K., Gilliam, R., and Rao, S. T. (2012), Comparative evaluation of the impact of WRF/NMM and WRF/ARW meteorology on CMAQ simulations for PM2.5 and its related precursors during the 2006 TexAQS/GoMACCS study, *Atmospheric Chemistry and Physics*, 12(9), 4091-4106.
- Yu, S., Mathur, R., Pleim, J., Wong, D., Gilliam, R., Alapaty, K., Zhao, C., and Liu, X. (2014), Aerosol indirect effect on the grid-scale clouds in the two-way coupled WRF-CMAQ: model description, development, evaluation and regional analysis, *Atmospheric Chemistry and Physics*, 14(20), 11247-11285.
- Zeng, T., and Wang, Y. H. (2011), Nationwide summer peaks of OC/EC ratios in the contiguous United States, *Atmospheric Environment*, 45(3), 578-586.
- Zhan, C. L., Zhang, J. Q., Zheng, J. R., Yao, R. Z., Wang, P., Liu, H. X., Xiao, W. S., Liu, X. L., and Cao, J. J. (2019), Characterization of carbonaceous fractions in PM2.5 and PM10 over a typical industrial city in central China, *Environmental Science and Pollution Research*, 26(17), 16855-16867, doi:10.1007/s11356-017-9970-9.
- Zhang, Q., Shen, Z. X., Lei, Y. L., Wang, Y. S., Zeng, Y. L., Wang, Q. Y., Ning, Z., Cao, J. J., Wang, L. Q., and Xu, H. M. (2018), Variations of particle size distribution, black carbon, and brown carbon during a severe winter pollution event over Xi'an, China, *Aerosol and Air Quality Research*, 18(6), 1419-1430, doi:10.4209/aaqr.2018.01.0007.
- Zhang, R. J., Tao, J., Ho, K. F., Shen, Z. X., Wang, G. H., Cao, J. J., Liu, S. X., Zhang, L. M., and Lee, S. C. (2012), Characterization of atmospheric organic and elemental carbon of PM2.5 in a typical semi-arid area of northeastern China, *Aerosol and Air Quality Research*, 12(5), 792-802.
- Zhang, R., Bian, Q. J., Fung, J. C. H., and Lau, A. K. H. (2013), Mathematical modeling of seasonal variations in visibility in Hong Kong and the Pearl River Delta region, *Atmospheric Environment*, 77, 803-816.
- Zhang, R., Jing, J., Tao, J., Hsu, S. C., Wang, G., Cao, J. J., Lee, C. S. L., Zhu, L., Chen, Z., Zhao, Y., and Shen, Z. (2013), Chemical characterization and source apportionment of PM2.5 in Beijing: seasonal perspective, *Atmospheric Chemistry and Physics*, 13(14), 7053-7074, <http://www.atmos-chem-phys.net/13/7053/2013/>.
- Zhang, T., Cao, J. J., Chow, J. C., Shen, Z. X., Ho, K. F., Ho, S. S. H., Liu, S. X., Han, Y. M., Watson, J. G., Wang, G. H., and Huang, R. J. (2014), Characterization and seasonal variations of levoglucosan in fine particulate matter in Xi'an, China, *Journal of the Air & Waste Management Association*, 64(11), 1317-1327, doi:doi: 10.1080/10962247.2014.944959.

Zhang, X. L., Trzepla, K., White, W. H., Raffuse, S., and Hyslop, N. P. (2021), Intercomparison of thermal-optical carbon measurements by Sunset and Desert Research Institute (DRI) analyzers using the IMPROVE\_A protocol, *Atmospheric Measurement Techniques*, 14(4), 3217-3231, doi:10.5194/amt-14-3217-2021.

Zhang, X. Y., Wang, Y. Q., Niu, T., Zhang, X. C., Gong, S. L., Zhang, Y. M., and Sun, J. Y. (2012), Atmospheric aerosol compositions in China: spatial/temporal variability, chemical signature, regional haze distribution and comparisons with global aerosols, *Atmospheric Chemistry and Physics*, 12(2), 779-799, <http://www.atmos-chem-phys.net/12/779/2012/acp-12-779-2012.pdf>.

Zhang, Y. Y., Obrist, D., Zielinska, B., and Gertler, A. W. (2013), Particulate emissions from different types of biomass burning, *Atmospheric Environment*, 72, 27-35.

Zhang, Y. Y., Jia, Y., Li, M., and Hou, L. A. (2018), Characterization of carbonaceous species in PM<sub>2.5</sub> in Xi'an during spring, *Environmental Forensics*, 19(2), 150-154, doi:10.1080/15275922.2018.1448910.

Zhang, Z. Z., Gao, Y., Yuan, Q., Tan, Y., Li, H. W., Cui, L., Huang, Y., Cheng, Y., Xiu, G. L., Lai, S. C., Chow, J. C., Watson, J. G., and Lee, S. C. (2020), Effects of indoor activities and outdoor penetration on PM<sub>2.5</sub> and associated organic/elemental carbon at residential homes in four Chinese cities during winter, *Science of The Total Environment*, 739, 139684, doi:10.1016/j.scitotenv.2020.139684.

Zhao, C., Leung, L. R., Easter, R., Hand, J. L., and Avise, J. (2013), Characterization of speciated aerosol direct radiative forcing over California, *Journal of Geophysical Research-Atmospheres*, 118(5), 2372-2388.

Zhao, H. M., Tong, D. Q., Lee, P., Kim, H., and Lei, H. (2016), Reconstructing fire records from ground-based routine aerosol monitoring, *Atmosphere*, 7(3), doi:10.3390/atmos7030043.

Zhao, Z. Z., Cao, J. J., Shen, Z. X., Xu, B. Q., Zhu, C. S., Chen, L.-W. A., Su, X. L., Liu, X. S., Han, Y. M., Wang, G. H., and Ho, K. F. (2013), Aerosol particles at a high-altitude site in Southeast Tibetan Plateau, China: Implication of pollution, *Journal of Geophysical Research-Atmospheres*, 118(19), 11360-11375.

Zhang, X., K. Trzepla, W. White, and N. P. Hyslop (2022), Quantifying residual elemental carbon by thermal-optical analysis using an extended IMPROVE\_A protocol with higher maximum temperature, *Journal of the Air & Waste Management Association*, 72(11), 1316-1325, doi:10.1080/10962247.2022.2119306.

Zheng, N., Song, S. J., Jin, X. L., Jia, H. Y., Wang, Y., Ji, Y. Q., Guo, L. Q., and Li, P. H. (2019), Assessment of carbonaceous aerosols at Mount Tai, North China: Secondary formation and regional source analysis, *Aerosol and Air Quality Research*, 19(8), 1708-1720, doi:10.4209/aaqr.2019.06.0316.

Zhi, G. R., Chen, Y. J., Sun, J. Y., Chen, L. G., Tian, W. J., Duan, J. C., Zhang, G., Chai, F. H., Sheng, G. Y., and Fu, J. M. (2011), Harmonizing aerosol carbon measurements between two conventional thermal/optical analysis methods, *Environmental Science & Technology*, 45(7), 2902-2908.

Zhou, J. M., Cao, J. J., Zhang, R. J., Chow, J. C., and Watson, J. G. (2012), Carbonaceous and ionic components of atmospheric fine particles in Beijing and their impact on atmospheric

visibility, *Aerosol and Air Quality Research*, 12(4), 492-502,  
[http://aaqr.org/VOL12\\_No4\\_August2012/4\\_AAQR-11-11-OA-0218\\_492-502.pdf](http://aaqr.org/VOL12_No4_August2012/4_AAQR-11-11-OA-0218_492-502.pdf).

Zhou, Y. Q., Wang, Q. Y., Huang, R. J., Liu, S. X., Tie, X. X., Su, X. L., Niu, X. Y., Zhao, Z. Z., Ni, H. Y., Wang, M., Zhang, Y. G., and Cao, J. J. (2017), Optical properties of aerosols and implications for radiative effects in Beijing during the Asia-Pacific Economic Cooperation Summit 2014, *Journal of Geophysical Research-Atmospheres*, 122(18), 10119-10132, doi:10.1002/2017jd026997.

Zhu, C. S., Cao, J. J., Tsai, C. J., Shen, Z. X., Ho, K. F., and Liu, S. X. (2010), The indoor and outdoor carbonaceous pollution during winter and summer in rural areas of Shaanxi, China, *Aerosol and Air Quality Research*, 10(6), 550-558.

Zhu, C. S., Chen, C. C., Cao, J. J., Tsai, C. J., Chou, C. C. K., Liu, S. C., and Roam, G. D. (2010), Characterization of carbon fractions for atmospheric fine particles and nanoparticles in a highway tunnel, *Atmospheric Environment*, 44(23), 2668-2673.

Zhu, C. S., Tsai, C. J., Chen, S. C., Cao, J. J., and Roam, G. D. (2012), Positive sampling artifacts of organic carbon fractions for fine particles and nanoparticles in a tunnel environment, *Atmospheric Environment*, 54, 225-230.

Zhu, C. S., Cao, J. J., Shen, Z. X., Liu, S. X., Zhang, T., Zhao, Z. Z., Xu, H. M., and Zhang, E. K. (2012), Indoor and outdoor chemical components of PM2.5 in the rural areas of northwestern China, *Aerosol and Air Quality Research*, 12(6), 1157-1165.

Zhu, C. S., Cao, J. J., Tsai, C. J., Shen, Z. X., Han, Y. M., Liu, S. X., and Zhao, Z. Z. (2014), Comparison and implications of PM2.5 carbon fractions in different environments, *Science of the Total Environment*, 466, 203-209.

Zong, P., Zhu, Y., Wang, H., and Liu, D. (2020), WRF-Chem simulation of winter visibility in Jiangsu, China, and the application of a neural network algorithm, *Atmosphere*, 11(5), doi:10.3390/atmos11050520.